

ISBN 978-80-969-672-4-7



Institute of Measurement Science
Slovak Academy of Sciences
Dúbravská cesta 9
841 04 Bratislava, Slovakia



MEASUREMENT 2011

Proceedings

MEASUREMENT 2011



8th International Conference on Measurement

Smolenice, Slovakia, April 27 - 30, 2011



The 8^h International Conference **MEASUREMENT 2011** is organized by the Institute of Measurement Science of the Slovak Academy of Sciences, Bratislava, Slovakia.

MEASUREMENT 2011

Proceedings of the
8th International Conference on Measurement

Congress center of the Slovak Academy of Sciences
April 27-30, 2011, Smolenice Castle, Slovakia

MEASUREMENT 2011

Copyright © 2011 by Institute of Measurement Science, SAS

Editors: Ján Maňka, Viktor Witkovský, Milan Tyšler, Ivan Frollo
Publisher: Institute of Measurement Science
Slovak Academy of Sciences
Dúbravská cesta 9, 841 04 Bratislava

ISBN 978 - 80 - 969 - 672 - 4 - 7

Printed in Slovakia
by VEDA, Publishing House of the Slovak Academy of Sciences

Cover page aerial photo: courtesy of Andrej Kuruc, Bratislava

ORGANIZERS OF THE CONFERENCE

Organizer

Institut für Fertigungstechnik und Hochleistungslasertechnik, Technische Universität Wien, Austria
Faculty of Biomedical Engineering, Czech Technical University in Prague, Kladno, Czech Republic
Faculty of Electrical Engineering and Information Technology, STU Bratislava, Slovakia
Faculty of Mechanical Engineering, Technical University Košice, Slovakia
Slovak Institute of Metrology, Bratislava, Slovakia

Technical sponsorship:

IMEKO, its TC7 and TC13 committees, Slovak National Committee
U.R.S.I., Slovak National Committee
Slovak Metrological Society
Slovak Society of Biomedical Engineering and Medical Informatics

Conference Chairman

Milan Tyšler, Slovakia

Steering Committee

I. Frollo, Slovakia, chairman
S. Adamczak, Poland
R. Durný, Slovakia
V. Havlíček, Czech Republic
J. Rosina, Czech Republic
P. H. Osanna, Austria
J. Vajda, Slovakia
J. Živčák, Slovakia

Local Organizing Committee

M. Tyšler
J. Maňka
V. Witkovský
P. Andris
M. Hain
E. Bukovenová
K. Bartošová
A. Dvurečenskij
V. Juráš
J. Lenková
R. Ševčík
M. Škrátek
M. Teplan
L. Valkovič

International Program Committee

J. Maňka, Slovakia, Chairman
J. Bartl, Slovakia
V. Boháč, Slovakia
M.N. Durakbasa, Austria
D. Eidukas, Lithuania
M. Halaj, Slovakia
R. Hudák, Slovakia
Y. V. Chugui, Russia
E. Kawate, Japan
P. Kneppo, Czech Republic
K. Kováč, Slovakia
G. Kozmann, Hungary
L. Laurinavičius, Lithuania
F. Lehocki, Slovakia
L. Lhotská, Czech Republic
R. Maniewski, Poland
K. Meigas, Estonia
L. Michaeli, Slovakia
P.P.L. Regtien, The Netherlands
K. Roubík, Czech Republic
V. Smieško, Slovakia
D. Šimšík, Slovakia
M. Štork, Czech Republic
S. Takayama, Japan
M. Tarata, Romania
L.I. Titomir, Russia
E. Tkacz, Poland
G. Wimmer, Slovakia
V. Witkovský, Slovakia
E.G. Woschni, Germany
J. Zakrzewski, Poland

Preface

*We find no sense in talking about something unless we specify how we measure it;
a definition by the method of measuring a quantity is the one sure way
of avoiding talking nonsense ...*

Sir Hermann Bondi (1919 – 2005)

The words of Austrian astronomer who lived in the United Kingdom and managed also the European Space Research Organization (predecessor of the European Space Agency) wittily underline the important role of measurement in science and everyday life that has been stressed by many outstanding thinkers since ancient times.

Being aware of this fact, the international conferences MEASUREMENT have been always focused on new developments in measurement science, on advances in measuring methods and their practical implementations in measuring devices.

Following this tradition also the 8th International Conference MEASUREMENT 2011 is devoted to the disciplines of measurement science, metrology, and selected application areas and covers topics from theoretical problems of measurement, measurements of physical quantities and measurements in biomedicine. It will include also such actual themes as measurements in micro- and nano- dimensions or measurements using imaging techniques. The main aim of the Conference is to continue in passing and exchanging of know-how in measurement among scientists and experienced specialists but also to contribute to education of young students and investigators. That is why also this time the competition for Young Investigator Award was announced and is sponsored by the conference organizers.

As usual, the conference is organized by the Institute of Measurement Science, Slovak Academy of Sciences with valuable support of several co-organizers and technical sponsors. Representatives of them contributed to preparation of the conference program and proceedings.

Since 1997 every two years the conference participants from many countries inside and outside of Europe are guests of the beautiful conference center in the Smolenice Castle that offers its comfortable environment for scientific talks, fruitful working discussions and friendly relaxation moments.

I hope that also the 8th international conference on measurement will come into history as a high quality scientific and pleasurable social event. The editors of these proceedings also believe that the book reflects the high professional level of the conference, will be of help for all its readers and will become a valuable quoted reference in measurement science.

Milan Tyšler
Conference Chairman

CONTENTS

Theoretical Problems of Measurement

<i>P. Otomański, P. Fotowicz</i> Coverage Interval as a Measure of Uncertainty of Measurement	3
<i>F. Rublík</i> On a Non-Parametric Two-Sample Test of Equality of Location Parameters of Multivariate Populations	7
<i>A. Horníková, E. Güclü, G. Bas, N.M. Durakbasa</i> Data Mining – Novel Statistical Method for the Measurement Confirmation System	12
<i>M. Chvosteková</i> A Comparison of Simultaneous Tolerance Intervals in a Simple Linear Regression Model	16
<i>J. Zakrzewski</i> Accuracy in Analytical Measurements	20
<i>R. Palenčár, S. Ďuriš</i> Influence of Covariances on Uncertainties of Temperature Measurement by calibrated SPRT	24
<i>Godla, L. Michaeli, J. Šaliga, R. Palenčár</i> Estimation of ADC Nonlinearities from the Measurement in Input Voltage Intervals	28
<i>A. Kowalczyk, R. Hanus, A. Szlachta</i> Time Delay Estimation of Stochastic Signals Using Conditional Averaging	32
<i>J. Hribik, B. Lojko, P. Fuchs</i> Accuracy Verification of Simplified Error Correction Method in Digital Electricity Meters	38
<i>M. Kamenský, K. Kováč, G. Valky</i> Analyses of Quantization Noise Spectrum for Multiresolution Quantization of Harmonic Signal	42
<i>J. Holcik</i> Decomposition of Time Series – from Statistical to Linear System Approach	46
<i>A. Krakovská, K. Mezeiová</i> Choice of Measurement for Phase-Space Analysis: Review of the Actual Findings	51
<i>K. Mezeiová, A. Krakovská</i> Choice of Measurement for Phase-Space Reconstruction: Decision Based on False Nearest Neighbors Method	55
<i>S. Štolc, I. Bajla, K. Valentín, R. Škoviera</i> Temporal Pooling Method for Rapid HTM Learning Applied to Geometric Object Recognition	59

<i>V. Svendova, J. Holcik</i> Comparison of Time Series Decomposition Methods	65
<i>B. Arendacká</i> Bootstrap in Common Mean Estimation – a Case Study	69
<i>K. Hornišová</i> Performance of Likelihood Calibration Method by Gruet from the Posterior Point of View. Simulation Study	73
<i>K. Bartošová</i> The Influence of Increasing Number of Breath Gas Compounds on Binary Classification of Noisy Data	76
<i>G. Wimmer, K. Karovič, V. Witkovský, R. Köning</i> Confidence Interval for the Distance of Two Micro/Nano Structures and Its Applications in Dimensional Metrology	80
<i>M. Kollár, K. Kováč</i> Application of Cluster Analysis on Antenna Factor Measurements Data	84
<i>E. Kureková, M. Halaj, R. Palenčár, T. Loeb</i> The Positional Deviation in Two Numerically Controlled Axes	88
 Measurement of Physical Quantities	
<i>R. Köning, J. Flügge, D. Hüser, W. Haessler-Grohne, H.U. Danzebrink, G. Dai, U. Brand, V. Nesterov, S. Bütefisch, G. Ehret, M. Wurm, B. Bodermann, E. Buhr, H. Bosse</i> Dimensional Micro- and Nanometrology at PTB	95
<i>A. J. Moses, P. I. Anderson, N. Chukwuchekwa, J. P. Hall, P. I. Williams and X. T. Xu</i> Analysis of Magnetic Fields on the Surface of Grain Oriented Electrical Steel.....	107
<i>J. Kemppinen, H. Mainaud Durand, F. Lackner</i> Validation of CLIC Re-Adjustment System Based on Eccentric Cam Movers – One Degree of Freedom Mock-Up	111
<i>O. Strbak, D. Gogola, I. Frollo</i> Cube Model Approach in Simulating of Magnetite Nanoparticles Behaviour in External Magnetic Fields	115
<i>V. Štrbik, Š. Beňačka, V. Šmatko, Š. Gaži, Š. Chromik, A. Dujavová, I. Vávra, P. Vrabček</i> SFS heterostructures prepared by focused-ion-beam technique	119
<i>M. Hain, M. Nosko, F. Simančík, T. Dvůrák, R. Florek</i> X-Ray Microtomography and Its Use for Non-destructive Characterisation of Materials	123
<i>K. Kovářová, R. Ševčík, M. Chmelíková, M. Bednarik, R. Holzer</i> Comparison and Use of Hg Porosimetry and X-ray Computed Microtomography in Durability Tests of Sandstone on the Charles bridge in Prague	127

<i>R. Kořínek, K. Bartušek, J. Vondrák, M. Musil</i> Measurement and Calculation of Relaxation Time T_2 and Diffusion of Gel Electrolytes Based on the NaClO_4 Inorganic Salt During Polymerization by NMR Method with Focusing on ^{23}Na and ^1H Nuclei	131
<i>M. N. Durakbasa, P. H. Osanna, B. Sagbas, A. Hornikova</i> High Precision Production Metrology for Quality Improvement in Biomedical Applications	135
<i>Yu. Baksheeva, K. Sapozhnikova, R. Taymanov</i> Metrological Self-Check of Platinum Resistance Thermometer	141
<i>I. Bačić, K. Malaric</i> Measurements of ASTRA Satellite Signal Parameters	145
<i>R. Špánek, P. Tyl, M. Hernych, M. Hokr, P. Svoboda, M. Řimnáč, J. Štuller</i> Bedřichov Tunnel – Continual Automated Measurement of Physical Quantities	150
<i>J. Pacheco de Carvalho, H. Veiga, C. Pacheco, N. Marques, A. Reis</i> Performance Measurements of Laboratory IEEE 802.11 b, g WEP Point-to-Point Links	154
<i>L. Laurinavičius</i> High Magnetic Field Sensing by the Help of Semiconductor Resonator	158
<i>O. Stupakov</i> Advantages of Direct Field Approach in Application to Magnetic Hysteresis Measurements	162
<i>P. Andris, I. Frollo</i> Static Magnetic Field Instability and Its Inhomogeneity Distribution Mapping in NMR	166
<i>M. Truhlář, M. Košek, A. Richter</i> Experimental and Theoretical Study of Effects in Power Distribution Net	170
<i>P.P.L. Regtien, I.M.P. van Wieringen</i> Online Measurement of the Penetration Depth in Arc Welding	174
<i>I. Mori, O. Fujiwara, H. Garbe</i> A New Circuit Approach to Predict Discharge Currents for Air Discharges of ESD Generators	178
<i>V. Boháč, P. Dieška, L. Kubičár, V. Vretenár</i> Uncertainty Analysis of Model for Cuboid Shape Samples Applied on Thermophysical Measurement of Stone Porous Material	182
<i>M. Pavúk, M. Miglierini</i> Synchrotron X-ray Diffraction Study of the Crystallization Process in the As-Prepared Amorphous Fe–Mo–Cu–B System	188
<i>E. Kawate, M. Hain</i> Development of a Scatterometer for Spatial Distribution Measurements of Reflected and Transmitted Light from Diffuse Surfaces	192

<i>Yu.V. Chugui, E.S. Senchenko</i> High Precision Algorithms for Shadow Inspection of 3D Objects in Partially Coherent Light	197
<i>V.E. Kalikin, A.G. Verkhogliad, S.V. Kalichkin, S.N. Makarov, V.S. Bazin, S.G. Savkov</i> Automatic Optoelectronic System for Inspection of Wire Wear Using High-Speed Image Analysis	201
<i>M. Rückwardt, A. Göpfert, M. Schellhorn, S. Holder, G. Linß, S. Kienast</i> Using a Structured LED Linear Light Instead of a Laser Line Generator for High Measurement Tasks	205
<i>D. Hofmann, P.-G. Dittrich, E. Diintsch</i> Smartphones, Cloud Computing and Apps- Green Game Changers for Measurement Science and Education	209
<i>P. Marcon, K. Bartusek, M. Cap</i> Modeling and Measuring of the Changes of the Magnetic Field Next to Non- Ferromagnetic Substances for Magnetic Susceptibility Calculation	213
<i>K. Bartusek, D. Nespor, P. Drexler, P. Fiala</i> Properties of Magnetoinductive Resonator Array for MRI Application	217
<i>N.K. Andreev, A.S. Malatsion</i> Dependence of NMR Spin Echo Form on Liquid Flow Structures	221
<i>A. Krammer, R. Hart'anský</i> Generation of Homogeneous EM Field for EMC Test Purposes	225
<i>J. Hallon, M. Bittera, R. Hart'anský, K. Kováč, V. Smieško</i> Reproducibility of Long Cable Test-Setup of EMC Measurements	229
<i>R. Ravas, L. Syrová, J. Grman</i> The Iterative Method of Parameters and Centre of Radial Distortion Estimation	233
<i>M. Kwacz, M. Mrowka, J. Wysocki</i> Round Window Membrane Vibration Measured by Laser Doppler Vibrometer	237
<i>L. Marsalka, R. Hartansky</i> Analysis of Possible Short Length Measurement Using Energy Sucking of Electromagnetic Field	241
<i>M. Novák, L. Slavík, M. Košek, M. Truhlář</i> Measuring Low Magnetic Field in Electromagnetic Flow Meter	245
<i>M. Okrouhlý, J. Novák</i> Model of Electromechanical Valve in the Anti-lock Braking System	249
<i>M. Vogel, K. Weissensee, G. Linss</i> New Approaches to the Improvement in Efficiency of Dimensional Measurements on Multi-Sensor Coordinate Measuring Machines	253
<i>E.S. Senchenko, V.V. Atuchin, T. Khasanov, V.A. Kochubey, L.D. Pokrovsky</i> Measurements of Optical Parameters of γ -Mo ₂ N/Si(100) Thin Films	257

<i>A. Göpfert, R. Fütterer, M. Rückwardt, M. Rosenberger, M. Schellhorn, G. Linß</i> Prospects of a Fully Scalable Stabilized LED-Source for Illumination of Measuring Systems	261
<i>V. Stofanik, M. Minarik, I. Balaz, E. Cocherova, V. Bohac</i> Enhanced Method of the Quartz Resonator Self-Temperature-Sensing	265
<i>A. Prnová, D. Galusek, M. Škrátek, R. Karell, R. Klement, J. Kraxner</i> Preparation and Characterization of Yb ₂ O ₃ – Al ₂ O ₃ Glass Microspheres with High Alumina Content	269
<i>M. Godla, L. Michaeli, J. Šaliga, M. Sekerák</i> The Measuring Workplace for Studying Basic Characteristic of Operational Amplifiers Distributing Through Internet	274
<i>M. Stork</i> Frequency Synthesizer Based on Flying Adder Architecture and Phase Locked Loop	278
 Measurement in Biomedicine	
<i>R. Stojanovic, M. Mirkovic and D. Karadaglic</i> An FPGA System for QRS Complex Detection Based on Integer Wavelet Transform.....	285
<i>M. Stork, J. Novak, V. Zeman</i> Cardiac Output Estimation Based on Oxygen Consumption during Exercise Test on Bicycle Ergometer	289
<i>G. Tuboly</i> Body Surface Potential Mapping Data Conversion Method	293
<i>J. Švehlíková, J. Lenková, A. Drkošová, M. Foltín, M. Tyšler</i> Assessment of Heart Position in a Torso Model Using an Inverse Solution	297
<i>E. A. I. Aidu, V. G. Trunov, L. I. Titomir, T. A. Sakhnova, E. V. Blinova</i> Computer Atlas of the Dipole Electrocardiotopography	301
<i>J. Lenkova, J. Svehlikova, M. Tysler</i> Individual vs. Adjusted Standard Torso Model in the Solution of the Inverse Problem in Electrocardiology	305
<i>M. Tkáčová, R. Hudák, J. Živčák, J. Švehlík</i> Infrared Thermography as a Screening Method for Carpal Tunnel Syndrome Diagnosis	309
<i>P. Kaňuch, R. Hudák, J. Živčák</i> Industrial Computed Tomography in Biomedical Engineering	314
<i>I. Frollo, P. Andris, J. Přibíl, L. Vojtišek, T. Dermek, L. Valkovič, D. Gogola, O.Štrbák</i> Magnetic Resonance Imaging Methods Used for Weak Magnetic Materials Detection	319
<i>P. Szomolányi, E. Pittschieler, V. Juráš, I. Frollo, S. Trattnig</i> Development of Dedicated dGEMRIC Protocol for Biochemical Imaging of the Temporomandibular Joint Disc at 3 Tesla: A Feasibility Study	323

<i>L. Vojtišek, I. Frollo, L. Valkovič, D. Gogola, T. Dermek, V. Juráš, P. Szomolányi</i> Radiofrequency Coil Array Design and Optimisation for Magnetic Resonance Low Field Imaging	327
<i>S. Takayama, Y. Matsuda, N. Takahashi, T. Tanaka, K. Kariya</i> Dynamic Measurement of Body Inclination in Walking by Body Area Network Sensing System	331
<i>F. Hlavačka, D. Bzdúšková, Z. Halická, J. Lobotková, V. Szathmáry</i> Assessment of Human Balance during Stance Using Accelerometer Sensors	335
<i>M. Kopáni, M. Melník, M. Čaplovičová, J. Ivan, J. Maňka, J. Jakubovský</i> Iron Oxides Particles in Globus Pallidus of Human Brain	339
<i>M. Teplan, L. Molčan, M. Zeman</i> Spectral Analysis of Cardiovascular Parameters of Rats under Irregular Light-Dark Regime	343
<i>R. Jiřík, I. Peterlík, J. Jan, J. Fousek, M. Zapf, N. Ruiter</i> 3D Ultrasound Transmission Tomography Using Synthetic Aperture Focusing and Regularized Algebraic Reconstruction	347
<i>V. Juras, S. Zbyn, Ch. Pressl, P. Szomolanyi, I. Frollo, S. Trattinig</i> In Vivo Measurement of Fast Transversal Relaxation Times of Achilles Tendon Using Ultra-High Field MRI	352
<i>L. Valkovic, V. Juras, I. Frollo</i> Low-Field BOLD Effect Induced by Alcohol and Caffeine Measured in the Upper Limb: A Feasibility Study	356
<i>D. Gogola, L. Valkovič, T. Dermek, L. Vojtišek, I. Frollo</i> Design and Construction of a Head Probe Coil for Vocal Tract Imaging	360
<i>J. Přibíl, J. Horáček, P. Horák, I. Frollo</i> Noise Reduction of Recorded Speech in an NMR Imager during Phonation for 3D Vocal Tract Modeling	364
<i>M. Kwacz, M. Mrowka, J. Wysocki</i> The Measurement System for Experimental Investigation of Middle Ear Mechanics	368
<i>D. Janusek, M. Kania, R. Zaczek, H. Zavala-Fernandez, A. Zbieć, G. Opolski, R. Maniewski</i> Application of the Wavelet Based Denoising Methods for T-Wave Alternans Analysis in High Resolution ECG Maps	373
<i>J. Schlenker, T. Funda, T. Nedělka</i> Evaluation of Heart Rate Variability Using Recurrence Analysis	375
<i>P. Kal'avský, V. Rosík, S. Karas, M. Tyšler</i> Measuring System with Compound Software Architecture for Measurement and Evaluation of Biosignals from Isolated Animal Hearts	379
<i>V. Uspenskiy</i> Information Function of the Heart. A Measurement Model	383

<i>A. Takeda, K. Takata, J. Wang, O. Fujiwara</i> Dielectric Characterization of Limited Volume of Human Blood by Open-Ended Coaxial Measurement Probe	387
<i>S. Takayama, T. Tanaka, N. Takahashi, Y. Matsuda, K. Kariya</i> Dynamic Measurement to Keep Suitable Physical Strength in Exercise by Body Area Network Sensing System	391
<i>A. Wolf, V. Caithaml, L. Nestával</i> Telemonitoring of Blood Glucose and Energy Expenditure of Patients with Diabetes Mellitus to Support Optimization of Insulin Dosing	395
<i>M. Škrátek, I. Šimáček, A. Dvurečenskij and J. Maňka</i> Some Aspects of Liver Iron Stores Measurement with the SQUID System	398
<i>R. Kliment, P. Smrčka, J. Jeřábek, M. Vítězník</i> Selected Methods for Automatical Classification of Psychophysiological States in Experimentally Controlled Psychological Load	402
<i>M. Tkáčová, J. Živčák, P. Foffová</i> A Reference for Human Eye Surface Temperature Measurements in Diagnostic Process of Ophthalmologic Diseases	406
Authors Index	411

Theoretical Problems of Measurement

Coverage Interval as a Measure of Uncertainty of Measurement

¹P. Otomański, ²P. Fotowicz

¹Poznan University of Technology, Institute of Electrical Engineering and Electronics, Piotrowo street 3a, 60-965 Poznań, Poland

²Central Office of Measures, Elektoralna street 2, 00-139 Warszawa, Poland
Email: otoman@et.put.poznan.pl

Abstract. *The paper presents two methods for the evaluation of the expanded uncertainty of measurement result. The first one, in accordance with the classical method, consists in determining the uncertainty of type A and type B together with the coverage factor. The other method consists in calculating the coverage interval, which is a measure of uncertainty, and can be defined in two ways. The whole paper is completed with examples of the determination of measurement uncertainty by applying the latter method, for symmetric as well as asymmetric distribution.*

Keywords: Measurement Uncertainty, Coverage Interval, Monte Carlo Method

1. Introduction

As everybody knows, no measurement or test is perfect and the imperfections give rise to errors in the measurement result. Consequently, every measurement result is only an approximation of the value of measurand and is only complete when accompanied by a statement of the uncertainty of that approximation. It seems appropriate for the experimenter, who takes decisions about the choice of method for evaluating the expanded uncertainty, to be aware of the effects of choosing a given method with respect to its accuracy.

According to document [1], the uncertainty of measurement is the non-negative parameter characterizing the dispersion of the quantity values, being attributed to a measurand based on the information used. The parameter may be, for example, a standard deviation called standard measurement uncertainty (or a specified multiple of it), or the half-width of an interval, having a stated coverage probability.

It is obvious that expanded uncertainty U is a parameter allowing the determination of the limits of confidence interval comprising an unknown true value with a defined probability $1 - \alpha$. To determine the confidence interval for an arbitrary parameter of population, it is necessary to know the probability distribution of the estimator of that parameter. A detailed description of determining the value of uncertainty of type A and type B as well as the value of combined uncertainty u_c can be found, among others, in documents [2] and [3].

2. Evaluation of Uncertainty

Document [4] sets a new standard for calculating the measurement uncertainty. According to its interpretation, a measure of measurement uncertainty is the coverage interval, which can be defined in two ways. The first definition reads: “coverage interval for a quantity such that the probability that the quantity is less than the smallest value in the interval is equal to the probability that the quantity is greater than the largest value in the interval”. The other definition states: “coverage interval for a quantity with the shortest length among all coverage intervals for that quantity having the same coverage probability”. Determination of coverage interval, based on the first definition assumes that the probability of values on both sides of the interval is equal. If we assume that the coverage probability equals 0,95, then the interval

limits are determined by the quantiles of distribution $G^{-1}(0,025)$ and $G^{-1}(0,975)$. Symbolically this interval can be denoted as:

$$I_{\text{sym}} = [G^{-1}(0,025), G^{-1}(0,975)] \quad (1)$$

Determination of coverage interval based on the other definition demands the shortest interval from the set of all intervals for the same probability to be assumed. For the coverage probability 0.95 it will be an interval with the limit values for which the difference of upper value $G^{-1}(\alpha + 0.95)$ and lower value $G^{-1}(\alpha)$ will be the smallest. Symbolically this interval can be written as:

$$I_{\text{min}} = [G^{-1}(\alpha), G^{-1}(\alpha + 0,95)], G^{-1}(\alpha + 0.95) - G^{-1}(\alpha) = \min \quad (2)$$

The numeric procedure recommended by document [4] for calculating the coverage interval for probability 0.95, based on the Monte Carlo method, expects the number of draws $M = 10000$. Each of 10000 determined values is an element of the set of possible values of the distribution of output value. After the elements of this set are ordered in the form of an increasing sequence of values and after a successive probability is assigned to each of them, starting from $p = 0.0001$ and ending with $p = 1$, the boundaries of coverage interval, according to the first definition, are determined by the values represented by elements with number 250 and number 9750. If the other definition is applied, we will get 500 coverage intervals for probability 0.95. These will be successive intervals between pairs of elements of the set, numbered from 1 and 9501 up to 500 and 10000, respectively. The smallest element should be chosen among them.

3. Experiment Results

As far as the above considerations are concerned, a significant problem appears whether the lengths of both intervals: probabilistically symmetric and the shortest, are close to one another. This problem will be presented with an example of symmetric and asymmetric distribution. The representative of symmetric distribution will be the normal distribution, widely applied in metrological practice. As asymmetric distribution, on the other hand, the chi square - χ^2 distribution was applied. The normal distribution was analysed firstly. Using a generator of random numbers with standardised normal distribution $N(0,1)$, a set of 10000 values was set up. Sorting the set of these values in increasing order, and assigning a successive probability to each of the values, starting from $p = 0.0001$ and ending with $p = 1$, we get the numerical distribution function for normal distribution, presented in Figure 1.

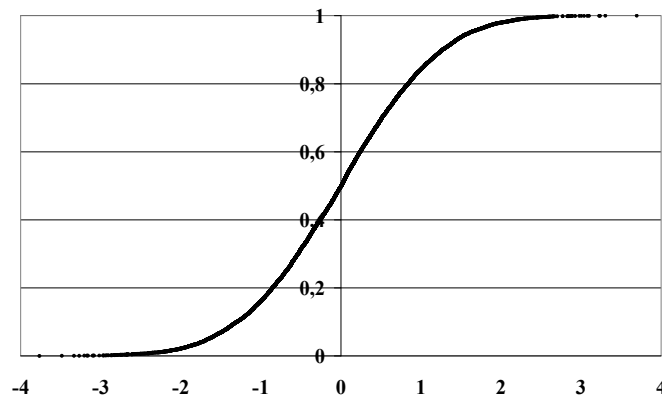


Fig. 1. Numerical distribution function for normal distribution

Based on the calculations carried out, exemplary values of the lengths of coverage intervals were obtained: 3.91 for the shortest interval and 3.93 for the symmetric interval, respectively, which are very close to each other. The obtained values are in accordance with the length of the confidence interval for normal distribution, which for confidence interval 95% is determined by the difference between two quantiles of distribution 1.96 and -1.96. A set of exemplary values of all 500 coverage intervals for this distribution is shown in Figure 2.

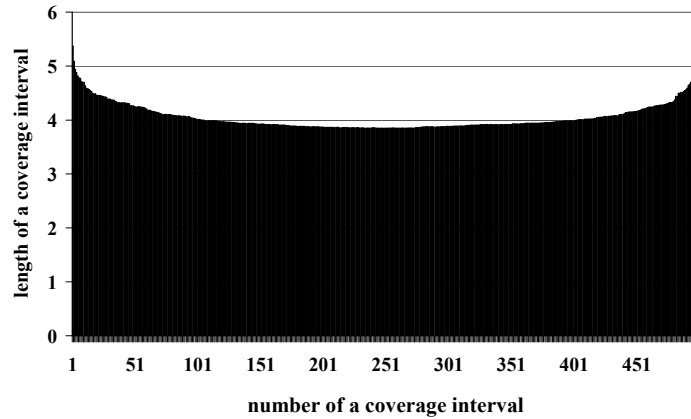


Fig. 2. Numerical coverage intervals for normal distribution

Asymmetric distribution χ^2 , with one degree of freedom, can be obtained from normal distribution with the operation of squaring, which is presented in the equation below:

$$\chi_1^2 = [N(0,1)]^2 \quad (3)$$

Carrying out the calculations for the above equation 10000 times, we get a set of values with chi square distribution and one degree of freedom. Similarly as in the previous case, sorting the set of these values in increasing order and assigning to them successive probabilities, we get the numerical distribution function for chi square distribution, presented in Figure 3. Carrying out the calculations for the shortest and symmetric coverage interval, we get for example values: 3.839 and 5.062. Both determined intervals differ substantially, by over 30%, and the value of the shortest interval is close to the value of the quantile of chi square distribution for confidence interval 95 %, which is equal to 3.841. A set of values of all 500 coverage intervals was shown in Figure 4.

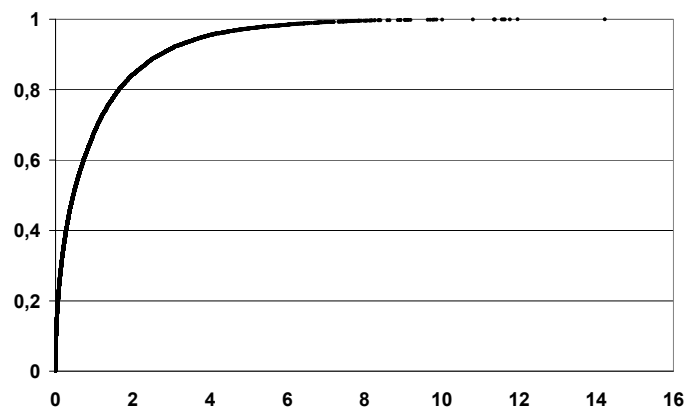


Fig. 3. Numerical distribution function for chi-square distribution with one degree of freedom

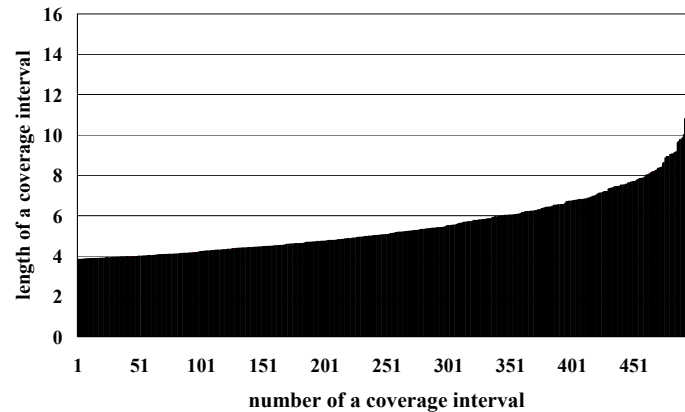


Fig. 4. Numerical coverage intervals for chi-square distribution with one degree of freedom

4. Conclusions

The estimate of a measurand is in practice usually an average value being an expected value of probability distribution. In case of standardised normal distribution, its value equals zero. Around the estimate a coverage interval is formed. For this type of distribution the expected value divides the interval in halves with numerically equal values of expanded uncertainty. The symmetric and shortest coverage intervals are comparable, although due to the computational accuracy of the Monte Carlo method, the shortest interval is usually slightly more narrow than the symmetric interval.

The expected value for χ^2 distribution with one degree of freedom is equal to one. However, this value does not determine the centre of coverage interval, both the shortest and the symmetric. Therefore, the expanded uncertainty cannot in this case be determined, only the boundaries of coverage interval can be determined. We should state, then, whether the values of the limits of this interval were determined for the shortest or for the symmetric one. Such situation can occur if the measurand is defined using a non-linear model.

Expanded uncertainty U , applied generally in metrology as a measure of inaccuracy of measurement result, determines the symmetric dispersion of the measurand value around its estimate. Problems appear when the asymmetric distribution of type chi square or gamma is used. The research results presented in the paper point to the significance of the raised issues, which, however, cannot be widely discussed within the limits of this publication.

References

- [1] International vocabulary of metrology – Basic and general concepts and associated terms (VIM), BIPM, JCGM 200:2008.
- [2] Evaluation of measurement data – Guide to the expression of uncertainty in measurement, BIPM, JCGM 100:2008.
- [3] Otomański P., Szlachta A. The evaluation of expanded uncertainty of measurement result in direct measurement using the LabVIEW environment, Measurement Science Review, Vol. 8, No 6, 2008, 147-150.
- [4] Evaluation of measurement data – Supplement 1 to the “Guide to the expression of uncertainty in measurement” – Propagation of distributions using a Monte Carlo method, BIPM, JCGM 101:2008.

On a Non-Parametric Two-Sample Test of Equality of Location Parameters of Multivariate Populations

F. Rublík

Institute of Measurement Science, Slovak Academy of Sciences, Dúbravská cesta 9,
841 04 Bratislava, Slovakia
Email: umerrubl@savba.sk

***Abstract.** The paper investigates the behaviour of the power of the test, used in a monograph on modern nonparametric methods for testing the equality of location parameters of two multi-dimensional distributions. It is shown by means of simulations that the test has bad sensitivity to the violations of the null hypothesis.*

Keywords: Non-parametric Test, Location Parameter, Rank Statistic

1. Introduction

The two sample setting, used in this paper, is as follows. \mathbf{X} is a random sample of size m from the distribution of the k -dimensional random vector $\xi + \mu_X$, \mathbf{Y} is a random sample of size n from the distribution of the k -dimensional random vector $\xi + \mu_Y$, where ξ are k -dimensional random fluctuations and μ_X, μ_Y are location parameters. Thus

$$\mathbf{X} = (\mathbf{X}_1, \mathbf{X}_2, \dots, \mathbf{X}_m) = \begin{pmatrix} X_{11} & X_{12} & \dots & X_{1m} \\ X_{21} & X_{22} & \dots & X_{2m} \\ \vdots & & & \\ X_{k1} & X_{k2} & \dots & X_{km} \end{pmatrix},$$

$$\mathbf{Y} = (\mathbf{Y}_1, \mathbf{Y}_2, \dots, \mathbf{Y}_n) = \begin{pmatrix} Y_{11} & Y_{12} & \dots & Y_{1n} \\ Y_{21} & Y_{22} & \dots & Y_{2n} \\ \vdots & & & \\ Y_{k1} & Y_{k2} & \dots & Y_{kn} \end{pmatrix},$$

i.e., the observations are k -dimensional column vectors and variables are rows.

2. Subject and Methods

The subject of the paper is testing of the null hypothesis

$$H_0 : \mu_X = \mu_Y \tag{1}$$

of the equality of the location parameters of the two multivariate populations. First we explain the formula for the test statistic, proposed in [2].

Let $j \in \{1, \dots, k\}$ be a fixed index. Combine the recorded values of the j -th variable from \mathbf{X} and \mathbf{Y} and compute their ranks W_{jt} . Thus

$$W_{j1}, W_{j2}, \dots, W_{jN}, \quad N = m + n$$

denotes the vector of midranks of the j -th row of the matrix (\mathbf{X}, \mathbf{Y}) , i.e., the midranks of the j -th variable, and obviously $1 \leq W_{ji} \leq N$. Then

$$W_j = \sum_{t=1}^m W_{jt}, \quad j = 1, \dots, k$$

denotes the sum of ranks of the j -th variable obtained from the first random sample \mathbf{X} . Put

$$W_{sum} = \sum_{j=1}^k W_j, \quad E = \frac{km(N+1)}{2}, \quad S_i = \sum_{j=1}^k W_{ji}, \quad i = 1, \dots, N.$$

Thus S_i denotes the sum of the i -th column of the matrix (W_{ji}) with columns $i = 1, \dots, N$ and rows $j = 1, \dots, k$, i.e., the sum of ranks of the i -th observation. Further, let

$$\bar{S} = \frac{1}{N} \sum_{i=1}^N S_i, \quad \sigma_S^2 = \frac{1}{N} \sum_{i=1}^N (S_i - \bar{S})^2, \quad var = \frac{mn}{N-1} \sigma_S^2. \quad (2)$$

The null hypothesis (1) is on pp. 203-205 of [2] tested by means of the test statistic

$$Z = \frac{W_{sum} - E}{\sqrt{var}} \quad (3)$$

and the test consists in referring the statistic (3) to the standard normal distribution. There are two possibilities of doing this, by the one-sided test (4) or by the two-sided test (5), i.e.,

$$\text{reject } H_0 \text{ if } Z > u_{1-\alpha}, \quad (4)$$

$$\text{reject } H_0 \text{ if } |Z| > u_{1-\alpha/2}, \quad (5)$$

where u_β denotes the β -th quantile of the standard normal $N(0, 1)$ distribution.

The hypothesis (1) can be tested also by means of the Lawley-Hotelling statistic. This statistic is defined in the 2-sample setting by the formulas

$$T = m(\bar{X} - \bar{U})' S^{-1} (\bar{X} - \bar{U}) + n(\bar{Y} - \bar{U})' S^{-1} (\bar{Y} - \bar{U}), \quad \bar{X} = \frac{1}{m} \sum_{i=1}^m \mathbf{X}_i, \quad \bar{Y} = \frac{1}{n} \sum_{i=1}^n \mathbf{Y}_i, \quad (6)$$

$$S = \frac{1}{m+n-2} \left(\sum_{i=1}^m (\mathbf{X}_i - \bar{X})(\mathbf{X}_i - \bar{X})' + \sum_{i=1}^n (\mathbf{Y}_i - \bar{Y})(\mathbf{Y}_i - \bar{Y})' \right), \quad (7)$$

and has the asymptotic chi-square distribution with k degrees of freedom, provided that the null hypothesis (1) holds and the distribution of ξ has a regular covariance matrix. The null hypothesis (1) is rejected if $T > \chi_k^2(1-\alpha)$, where $\chi_k^2(1-\alpha)$ is the $(1-\alpha)$ -th quantile of the chi-square distribution with k degrees of freedom.

In contemporary statistics there is often considered the use of tests not requiring the existence of the covariance matrix, because such testing rules usually do not fail to yield reliable results also in the case of sampling from heavy tailed distributions.

One of such test statistics was presented in [3], but since its computation in the case $m = n = 30$ requires much of the computer time, it is not included into the presented simulations. A simpler test statistic, based on the spatial median, was presented in [6] and studied also in [7].

The spatial median $\hat{\boldsymbol{\mu}} \in R^k$ of the k -dimensional vectors $\mathbf{Z}_1, \mathbf{Z}_2, \dots, \mathbf{Z}_n$ is defined by the equality

$$\sum_{i=1}^n \|\mathbf{Z}_i - \hat{\boldsymbol{\mu}}\| = \min\left\{\sum_{i=1}^n \|\mathbf{Z}_i - \mathbf{M}\|; \mathbf{M} \in R^k\right\}. \quad (8)$$

If these k -dimensional vectors do not lie on any line in R^k and are mutually distinct (which holds for sampling from continuous distribution), then according to [4] their spatial median is uniquely determined and can be computed by means of the results from [9].

Let $\hat{\boldsymbol{\mu}}_{\mathbf{X}}$ be the spatial median of the vectors $\mathbf{X}_1, \dots, \mathbf{X}_m$, $\hat{\boldsymbol{\mu}}_{\mathbf{Y}}$ be the spatial median of $\mathbf{Y}_1, \dots, \mathbf{Y}_n$ and $N = m + n$. Put

$$\bar{\boldsymbol{\mu}} = (m\hat{\boldsymbol{\mu}}_{\mathbf{X}} + n\hat{\boldsymbol{\mu}}_{\mathbf{Y}})/N.$$

Further, let $\hat{\boldsymbol{\mu}} = \hat{\boldsymbol{\mu}}_{\mathbf{Z}}$ denote the spatial median of the pooled random sample $(\mathbf{Z}_1, \dots, \mathbf{Z}_N) = (\mathbf{X}_1, \dots, \mathbf{X}_m, \mathbf{Y}_1, \dots, \mathbf{Y}_n)$ and

$$\hat{\mathbf{D}}_1 = \frac{1}{N} \sum_{i=1}^N \frac{1}{\|\mathbf{Z}_i - \hat{\boldsymbol{\mu}}\|} \left[\mathbf{I}_d - \frac{(\mathbf{Z}_i - \hat{\boldsymbol{\mu}})(\mathbf{Z}_i - \hat{\boldsymbol{\mu}})'}{\|\mathbf{Z}_i - \hat{\boldsymbol{\mu}}\|^2} \right], \quad \hat{\mathbf{D}}_2 = \frac{1}{N} \sum_{i=1}^N \frac{(\mathbf{Z}_i - \hat{\boldsymbol{\mu}})(\mathbf{Z}_i - \hat{\boldsymbol{\mu}})'}{\|\mathbf{Z}_i - \hat{\boldsymbol{\mu}}\|^2},$$

where $\mathbf{I}_d = \text{diag}(1, \dots, 1)$ is the $d \times d$ unit matrix. Let $\hat{\mathbf{V}} = \hat{\mathbf{D}}_1^{-1} \hat{\mathbf{D}}_2 \hat{\mathbf{D}}_1^{-1}$. The test statistic M_1 from [6] is

$$M_1 = m(\hat{\boldsymbol{\mu}}_{\mathbf{X}} - \bar{\boldsymbol{\mu}})' \hat{\mathbf{V}}^{-1} (\hat{\boldsymbol{\mu}}_{\mathbf{X}} - \bar{\boldsymbol{\mu}}) + n(\hat{\boldsymbol{\mu}}_{\mathbf{Y}} - \bar{\boldsymbol{\mu}})' \hat{\mathbf{V}}^{-1} (\hat{\boldsymbol{\mu}}_{\mathbf{Y}} - \bar{\boldsymbol{\mu}}).$$

If the distribution of $\boldsymbol{\xi}$ has a density f with respect to the Lebesgue measure on R^k and f is bounded on every bounded subset of R^k , then according to the results of [6] the rule rejecting H_0 if $M_1 > \chi_k^2(1 - \alpha)$ is the test of (1) at the asymptotic significance level α .

Another test statistic for testing (1) was presented in [8]. As explained on p. 334 of [6], this statistic is in the two-sample setting given by the formula

$$W_1 = \frac{mnk}{N} \left\| \frac{1}{m} \sum_{i=1}^m U(\mathbf{X}_i - \hat{\boldsymbol{\theta}}) - \frac{1}{n} \sum_{j=1}^n U(\mathbf{Y}_j - \hat{\boldsymbol{\theta}}) \right\|^2, \quad (9)$$

where $\hat{\boldsymbol{\theta}}$ is the spatial median of the data (\mathbf{X}, \mathbf{Y}) and $U(\mathbf{Z}) = \mathbf{Z}/\|\mathbf{Z}\|$ if $\|\mathbf{Z}\| > 0$, and $U(\mathbf{Z}) = \mathbf{0}_{k \times 1}$ otherwise. If the random vector $\boldsymbol{\xi}$ has a density with respect to the Lebesgue measure, then according to [8] the rule rejecting H_0 if $W_1 > \chi_k^2(1 - \alpha)$ is the test of (1) at the asymptotic significance level α .

3. Simulation Results

In the following table \hat{P}_Q denotes the simulation results of the probability of rejection of (1) by the test based on the statistic Q , when the sample sizes are $m = 30$ and $n = 30$, respectively. The following estimates were obtained from trials consisting of 5000 simulations, the rejection was carried out at the asymptotic significance level $\alpha = 0.05$. The dimension of the random vector was $k = 3$, the random vector $\boldsymbol{\xi}$ was assumed to have independent components, all of them were either $N(0, 1)$ distributed (Normal case) or all of them had the Cauchy $C(0, 1)$ distribution (Cauchy case). The location parameters are $\boldsymbol{\mu}_{\mathbf{X}} = (0, 0, 0)'$, and $\boldsymbol{\mu}_{\mathbf{Y}} = c(0.1, -0.1, 0.1)'$. Thus when $c = 0$, then the null hypothesis (1) holds. The sampling from the distributions with the values $c = 0, 1, \dots, 7$ was used to demonstrate the behaviour

of the tests when the distance from the null hypothesis is increasing. The notation $\hat{P}_{Z,1S}$ denotes the simulation estimate of the probability of (4), where $\alpha = 0.05$, and $\hat{P}_{Z,2S}$ denotes the simulation estimate of the probability of (5), where $\alpha = 0.05$, both for $m = n = 30$.

		Normal case							
c		0	1	2	3	4	5	6	7
$\hat{P}_{Z,1S}$		0.047	0.028	0.017	0.011	0.007	0.004	0.002	0.000
$\hat{P}_{Z,2S}$		0.047	0.056	0.073	0.097	0.135	0.186	0.249	0.319
\hat{P}_T		0.068	0.102	0.197	0.386	0.609	0.811	0.931	0.982
\hat{P}_{M_1}		0.043	0.067	0.128	0.263	0.454	0.664	0.839	0.938
\hat{P}_{W_1}		0.049	0.074	0.157	0.303	0.523	0.730	0.878	0.958

		Cauchy case							
c		0	1	2	3	4	5	6	7
\hat{P}_T		0.024	0.024	0.027	0.032	0.040	0.051	0.061	0.077
\hat{P}_{M_1}		0.062	0.064	0.085	0.113	0.155	0.205	0.266	0.341
\hat{P}_{W_1}		0.053	0.060	0.077	0.111	0.167	0.244	0.338	0.445

4. Discussion

As far as the tests based on T , M_1 or W_1 are concerned, the overall picture is analogous as in the 3-sample case, investigated in the simulation study of [6]. For distributions having covariance matrix the use of the Lawley-Hotelling test can be expected to yield good result, even though a better agreement of the size of this test with the nominal value will require sample sizes larger than $\min(m, n) = 30$. But if the possibility of observations coming from heavy tailed distributions has to be considered, then the Lawley-Hotelling test cannot be used, because as the results of the simulations show (the Cauchy case), it is insensitive to violations of the null hypothesis in such a case. For heavy tailed distributions from the tests considered in the previous simulations appears to yield mildly moderately best results the test based on W_1 . A disadvantage of the tests based on M_1 or on W_1 is that they are not affine invariant. A test with this property is presented in the forthcoming paper [5]. The simulations show, that in general, both tests (4) and (5) are either insensitive or only weakly sensitive to violations of the null hypothesis (1).

5. Conclusions

Because of their bad performance, the tests (4) and (5), proposed in the monograph [2], should not be used for testing the null hypothesis (1) against the general alternative, that (1) does not hold. It is recommendable to carry out this testing by the tests based on W_1 , M_1 or by the Lawley-Hotelling test.

Acknowledgements

The research was supported by the grant 1/0077/09 from VEGA and by the grant 2/0019/10 from VEGA.

References

- [1] Chaudhuri, P. Multivariate location estimation using extension of R-estimates through U-statistics type approach. *Annals of Statistics*, 20 (1992), 897-519.
- [2] Higgins, J. J.: An Introduction to Modern Statistics. Thomson Books/Cole, Pacific Grove, 2004.
- [3] Hettmansperger, T. P., Möttönen J. and Oja, H. Affine invariant multivariate rank tests for several samples. *Statistica Sinica*, 8(1998), 785-800.
- [4] Milasevic, P. and Ducharme, G. R. Uniqueness of the spatial median. *Annals of Statistics*, 15(1987), 1332-1333.
- [5] Rublík, F. and Somorčík, J. Affine equivariant spatial median and its use in the multivariate multi-sample location problem. *Submitted for publication*.
- [6] Somorčík, J. Tests Using Spatial Median. *Austrian Journal of Statistics*, 35(2006), 331-338.
- [7] Somorčík, J. Performance of some spatial median tests under elliptical symmetry. *Measurement Science Review (online journal)*, 7(2007), Section 1, No. 4, 43-50.
- [8] Um, Y. and Randles, R. H. Nonparametric tests for the multivariate multi-sample location problem. *Statistica Sinica*, 8(1998), 801-812.
- [9] Vardi, Y. and Zhang, C. H. The multivariate L_1 -median and associated data depth. *Proceedings of the National Academy of Sciences of the United States of America*, 97(2000), 1423-1426.

Data Mining – Novel Statistical Method

¹A. Horníková, ²N.M. Durakbasa, ²E. Güclü, ²G. Bas

¹University of Economics, Faculty of Economic Informatics, Dept. of Statistics,
Dolnozemska cesta 1/b, 852 35 Bratislava, Slovakia,

²Vienna University of Technology, Institute for Production Engineering and Laser
Technology, Dept. of Interchangeable Manufacturing and Industrial Metrology,
Karlsplatz 13/3113, 1040 Vienna, Austria
Email: adriana.hornikova@euba.sk

Abstract. *Data Mining (DM) is a new and very dynamic discipline that is oriented on finding new knowledge in databases. DM is predicted to be „one of the most revolutionary developments of the next decade“, according to the online technology magazine ZDNET News. [7] DM is a set of methods originating from practically attained knowledge. They are based though on a thorough statistical basis and machine learning. DM is usually used in following steps: starting with problem definition, tasks allocation, processes description, variables assignment, up to learning and evaluating the ensemble models, all phases should be explained in detail. This paper presents the general principles of data mining methodology applicable to re-calibration intervals to minimize the costs of re-calibration of measurement devices.*

Keywords: Data Mining, Applied Statistics, Clustering, Classification, Association Rules

1. Introduction

It was the beginning of the nineties of last century when scientists started to call this scientific discipline **knowledge discovery in databases or knowledge discovery process**. Knowledge Discovery in Databases (KDD) is the name coined by Gregory Piatetsky-Shapiro in 1989 to describe the process of finding interesting, interpretable, useful and novel data. Later the term of DM has become a synonym for the whole process of knowledge discovery in databases. The major distinguishing characteristic of DM is that it is data driven as opposed to other methods that are often model driven. [1] The evolution of KDD has undergone three distinct phases:

1. first generation systems that have been providing only one DM technique with very weak support for the overall process framework,
2. second generation systems (suites) provided multiple types of integrated data analysis,
3. third generation systems introduced the vertical approach enabling to address specific problems.

In today's understanding is DM an interactive and iterative process of finding knowledge in experimental data sets. It comprises from following steps: problem specification, hypothesis building, data collection, pre-processing of collected data, model building or estimation, results interpretation and summarizing. [10]

2. Philosophy of Data Mining

DM methodology nowadays uses one of these two approaches for obtaining results: predictive or descriptive approach. Predictive approach uses the known variables for prediction of unknown values of other variables. Different approaches are used for different tasks. Descriptive methods use the pattern recognition approach that uses the description process of

experimental data and that can be interpreted according to statistics. Output from the knowledge discovery in databases is the generated new knowledge, usually described in terms of rules, patterns, classification models, associations, trends, statistical analysis, etc.

But what is the actual purpose of DM ? It is the process of making decisions. Decisions in organizations should be based on extensive Data Mining and analytics to model what-if scenarios, forecast the future, and minimize risks. Nowadays we can apply DM in energy consumption predictions, prediction of exchange rates on markets, classification of bank customers or insurance companies customers, analysis of service providers change, reliability analysis for different kinds of machines or their parts, analysis of patients in hospitals, analysis of the consumers' baskets and similar with large data sets. [2, 4]

3. Methodology of Data Mining

To formalize the knowledge discovery process within a common framework introduced was the process model concept or the standardized process model. Roughly DM steps are: to pre-processing raw data, mine the data, and interpret the results. In general there are several standard methodologies currently enabling to use DM.

Once the objective for DM is known, a target data set must be assembled. A data source is a datamart or data warehouse. Pre-processing of raw data involves "cleaning" of data which is the dismissal of noise or missing data. The cleaned data is reduced into feature vectors, usually one vector per observation. Feature vectors are divided into two sets, the "training set" and the "test set" (and the validation set). The training set is used to "train" DM algorithm(s), while the test set is used to verify the accuracy of any patterns found. For mining the data are commonly used four classes of tasks: classification, clustering, regression and association rules. The final step of KDD is to verify the patterns produced by DM algorithms.

Not all patterns found by DM algorithms are necessarily valid (overfitting). Further a number of statistical methods may be used to evaluate algorithms by the lift chart, the ROC (receiver operating characteristic) chart, the profit chart, the Lorentz curve, the K-S assessment chart (to evaluate a combination of two or more of the models one can use to evaluate the ensemble model). If learned patterns do not meet the desired output requirement then it is necessary to re-evaluate, update pre-processing and DM phases.

4. Usage of Data Mining

DM should be a white-box approach with understanding of the algorithm and should be implemented in conjunction with utilized software. There are currently in use several widespread methods for discovering knowledge in databases. The dominating methods are: SEMMA methodology (Sample, Explore, Modify, Model and Assess), 5A methodology (Assess, Access, Analyze, Act and Automate) and CRISP-DM methodology (the Cross Industry Standard Process for Data Mining). [3-4]

SEMMA model's abbreviation stands for Sample (identify input datasets), Explore (explore datasets statistically and graphically), Modify (prepare data for analysis), Model (fit a predictive model) and Assess (compare predictive models). Specialized licensed module of the SAS Company package dedicated to DM is the SAS Enterprise Miner®. Other software for DM tasks is WEKA (Waikato Environment for Knowledge Analysis), Minitab statistical software, Traceis software and many more.

As a result of an European research project was created CRISP-DM methodology. The aim was to create a new framework (standard) on higher level of generalization that would be useful for any DM application. CRISP-DM is an iterative and adaptive process of six basic steps that can be used in differing order when analyzing a DM related problem:

1. research understanding phase or business understanding phase (with several sub-steps: determination of business objectives, assessment of the situation, determination of DM goals and generation of a project plan),
2. data understanding phase (with several sub-steps: collection of initial data, description of data, exploration of data and verification of data quality),
3. data preparation phase (with several sub-steps: selection of data, cleansing of data, construction of data, integration of data and formatting of data subsets),
4. modelling phase (with several sub-steps: selection of modelling techniques, generation of test design, creation of models and assessment of generated models),
5. evaluation phase (with several sub-steps: evaluation of results, process review and determination of the next step) and
6. deployment phase (with several sub-steps: plan deployment, plan monitoring and maintenance, generation of final report and review of process sub-steps).

This methodology can be represented by a circle of DM project having six phases. The order of steps implementation is not fixed, just outputs of one step influence the selection of approaches within the next step. Sometimes it is needed to re-start and re-evaluate the analysis. A circle becomes then a suitable symbol for representing cycles of CRISP-DM methodologies' steps. CRISP-DM methodology is supported by Clementine® DM software suite by SPSS.

5. Re-Calibration Interval Application

The supervision of measuring equipment is an essential quality requirement for modern production especially at the higher demands of micro and nanotechnology. The efficiency of the confirmation can be increased and expenses can be reduced substantially through computer assistance with flexible checking intervals. A special method developed at the Institute for Metrology for this purpose allows increasing of the flexibility level and efficiency of a system for the intelligent management and supervision of measuring devices.

On the basis of preceded calibrations the intervals are to be shortened if necessary, to secure the precision continually. They can be also enlarged, if it from the calibration results clearly emerges, that this measure the trust in the precision does not hurt the measuring and test devices. The system must ensure that the measuring and test equipment will be calibrated according to the determined timetable.

"Optimal Interval" is defined as the one having the total costs at minimum. If the interval is chosen too small, the checking costs goes up, because there are more checking in the equal period than necessarily. If the interval is chosen too large it raises the probability to find the measuring and test equipment as "inadmissible" at the next checking. Poor quality is joined always with a rise of the costs [6]. But how to model and set the optimal intervals ?

The size of it depends on a number of different factors: frequency of utilization, mode of using, behavior of abrasion, consequences at lapses, permissible tolerance range, number of users, status in the calibration chain, etc [5]. Since these elements are not temporally constant, the optimal interval cannot be a constant size either.

For this purpose has been a special method developed, which is based on the artificial intelligence [7]. This method is based on the demand, to consider on the environment conditions of the past as well as of the expected future. This happens exclusively through the application of fuzzy-logic in conjunction with clustering approach (DM based method), which operates also with linguistic variables.

Three input variables shall be enough for defining an output variable, which means that there is a three-dimensional model. The mathematical method namely, fuzzy clustering, fuzzy k-

means clustering, could be suitable. These methods compute the membership function that represents the presence of each observation to a cluster, and a membership score.

Other clustering methods those are more easily utilizable as they are a part of several packages for DM. We have compared several clustering approaches (hierarchical as well as non-hierarchical clustering methodologies) for creating clusters of measurement devices.

6. Conclusions

DM is defined as the process of extracting patterns from data. The authors have applied selected DM methods of a database of re-calibration intervals of measurement devices with the purpose to minimize the re-calibration costs. Adjustable quantity is the length of the re-calibration interval which is seen by the authors as not constant. This method aims a financial efficiency of the re-calibration process.

DM has been in recent years widely used in area of science and engineering, such as bioinformatics, genetics, medicine, education and electrical power engineering. But there is also an ethical horizon of DM. It requires data preparation which can uncover information or patterns which may defeat confidentiality and privacy obligations. A common way to resolve this is through data aggregation. [3]

Acknowledgements

Authors would like to thank the Slovak Research and Development Agency and the OeAD-GmbH/ICM Centre for International Cooperation and Mobility for the financial support of the Slovak-Austrian Bilateral Cooperation project entitled Statistical Analysis in Support of Technical Development and Evaluation of Measurement (SASoTDEM) with number SK-AT-0013-10 within the framework of the Slovak-Austrian Research and Development Cooperation. This contribution was elaborated with the support of the grant agency VEGA in the framework of the projects number 1/0543/10 and 1/0437/08.

References

- [1] Fayyad, Usama; Gregory Piatetsky-Shapiro, and Padhraic Smyth (1996). "From Data Mining to Knowledge Discovery in Databases".
- [2] 17.12.2008 at: <http://www.kdnuggets.com/gpspubs/aimag-kdd-overview-1996-Fayyad.pdf>.
- [3] Cios, K. J., Pedrycz, W., Swiniarski, R. W., Kurgan, L. A.: Data Mining. A Knowledge Discovery Approach. Springer 2007. ISBN 978-0-387-33333-5.
- [4] Terek, M., Labudová, V., Horníková, A.: Híbková analýza údajov. Iura Edition, 2010.
- [5] Osanna, P.H., Durakbasa, N.M.: Prüfmittelüberwachung und –verwaltung im Qualitätsmanagement – leistungsfähig und flexibel durch Rechnereinsatz, Elektrotechnik und Informationstechnik, 4, pp. 207/212, 1998.
- [6] Durakbasa, M.N., Pfeiffermann, G.G.: Computer Aided Confirmation and Management of Inspection, Measuring and Test Equipment in the Quality Management Systems, Proceedings „Measurement ,97“, International Conference on Measurement, pp. 63/66, Smolenice, Slovak Republic, May, 1997
- [7] Zadeh, L.A.: Fuzzy Sets, Information and Control; Vol.8 (1965), S 338/353.
- [8] Myatt, G. J., Johnson, W P.: *Making Sense of Data II. A Practical Guide to Data Visualization, Advanced Data Mining Methods, and Applications*. USA: J. Wiley and Sons, 2009. ISBN 978-0-470-22280-5.
- [9] February 8, 2001 at www.wikipedia.com/datamining
- [10] Lyman, Peter; Hal R. Varian (2003). "How Much Information". Retrieved on 2008-12-17 at <http://www.sims.berkeley.edu/how-much-info-2003>.

A comparison of simultaneous tolerance intervals in a simple linear regression model

¹M. Chvosteková

¹Institute of Measurement Science SAS, Bratislava, Slovakia

Email: chvosta@gmail.com

Abstract. *The derivation of a multiple use confidence interval in the statistical calibration problem can be solved by inverting simultaneous tolerance interval, see Lieberman, Miller, and Hamilton (1967) and Mee, Eberhardt, and Reeve (1991). The simultaneous tolerance intervals in a regression have been recognized and considered in various settings by many authors, but all existing intervals are approximate. We offer numerical comparison of the known methods for constructing simultaneous tolerance intervals for a linear regression. In particular, we compare the Lieberman-Miller method, the Wilson method, the Limam-Thomas method, the modified Wilson method, and the LRTW method based on the estimated of confidence in the specified simple linear regression model.*

Keywords: Linear Regression Model, Tolerance Factor, Simultaneous Tolerance Intervals

1. Introduction

Statistical calibration problem can be accomplished using a simultaneous tolerance intervals (STI), see e.g. [3], [5]. STI in regression are constructed using the vector of observations $Y = (Y_1, \dots, Y_n)^T$ corresponding to n known independent predictors $\mathbf{x}_1, \dots, \mathbf{x}_n$, so that with a confidence level $1 - \alpha$, at least a γ proportion of the future observation $Y(\mathbf{x})$ -distribution is to be contained in the corresponding tolerance interval, simultaneously for all possible values of predictors \mathbf{x} . In simultaneous statistical calibration, sometimes rather called inverse regression, the n pairs (\mathbf{x}_i, Y_i) , $i = 1, \dots, n$ referred to as calibration data are used to construct confidence intervals for a sequence of unobserved independent predictor values $\mathbf{x}_{n+1}, \mathbf{x}_{n+2}, \dots$ corresponding to an infinite sequence of observable variables Y_{n+1}, Y_{n+2}, \dots . Multiple use confidence interval constructed by inverting simultaneous tolerance interval in a linear regression cover the true predictor value with a probability γ and the probability of constructing the interval, based on the same calibration data, is $1 - \alpha$. The simultaneous tolerance intervals in a regression have been recognized and considered in various settings by many authors. Lieberman and Miller (SW) in [2] presented an approximation for the case of a simple linear regression. Further suggested methods for computing STI in a linear regression, the Wilson (W) method in [6], Limam-Thomas (PS) method in [4], modified Wilson (MW) method in [4] and the LRTW method (LRTW) in [1], are based on the general confidence-set (GCS) approach. Mee, Eberhardt, and Reeve in [5] obtained the narrowest tolerance intervals, but they considered the STI for limited range of possible values of predictors. All known STI in a regression are derived using various approximations, there is no procedure satisfying the definition of the STI exactly. We present a numerical comparison of SW, W, PS, MW, and LRTW method. For the specified case of a simple linear regression we state estimates of confidence levels of the method for four combinations of pairs $\alpha = \{0.01, 0.05\}$, $\gamma = \{0.9, 0.95\}$.

2. Simultaneous tolerance intervals in a linear regression model

In this article we study STI for a multiple linear regression. Random vector $\mathbf{Y} = (Y_1, \dots, Y_n)^T$ of n independent observations is represented as

$$\mathbf{Y} = \mathbf{X}\boldsymbol{\beta} + \sigma \mathbf{Z}, \quad (1)$$

where $\mathbf{X} = (\mathbf{x}_1, \dots, \mathbf{x}_n)^T$ is an $n \times q$ ($n > q$) matrix of rank q , with known constant elements. Vector $\boldsymbol{\beta} = (\beta_0, \beta_1, \dots, \beta_{q-1})^T$ and standard deviation $\sigma > 0$ represent unknown parameters of the regression model and \mathbf{Z} is an $n \times 1$ vector of standard normal errors, i.e. $\mathbf{Z} \sim N_n(\mathbf{0}, \mathbf{I}_n)$. Under the assumptions, the least squares estimators of $\boldsymbol{\beta}, \sigma$ are

$$\hat{\boldsymbol{\beta}} = (\mathbf{X}^T \mathbf{X})^{-1} \mathbf{X}^T \mathbf{Y} \quad \text{and} \quad S^2 = \frac{(\mathbf{Y} - \mathbf{X}\hat{\boldsymbol{\beta}})^T (\mathbf{Y} - \mathbf{X}\hat{\boldsymbol{\beta}})}{n - q}. \quad (2)$$

Note that $\hat{\boldsymbol{\beta}} \sim N_q(\boldsymbol{\beta}, \sigma^2 (\mathbf{X}^T \mathbf{X})^{-1})$ and $(n - q)S^2 / \sigma^2 \sim \chi_{n-q}^2$, where χ_{n-q}^2 denotes a central chi-square random variable with $n - q$ degrees of freedom. Random variables $\hat{\boldsymbol{\beta}}$ and S^2 are independent.

A tolerance interval is specified by its *content (coverage)* and *confidence level*, denoted $0 < \gamma < 1$ and $0 < 1 - \alpha < 1$, respectively. In practical applications the values are close to one. A future observation of a response at the predictor $\mathbf{x}^T = (1, x_1, \dots, x_{q-1})^T$ is written as $Y(\mathbf{x}) = \mathbf{x}^T \boldsymbol{\beta} + \sigma Z$, where $Z \sim N(0, 1)$ and $Y(\mathbf{x})$ is assumed to be independent of \mathbf{Y} .

For a fixed predictor \mathbf{x} , a $(\gamma, 1 - \alpha)$ two-sided tolerance interval for a future observation $Y(\mathbf{x})$ is considered in the following (general) form

$$\langle \mathbf{x}^T \hat{\boldsymbol{\beta}} - \lambda(\mathbf{x} | \gamma, 1 - \alpha, \mathbf{X}) S, \mathbf{x}^T \hat{\boldsymbol{\beta}} + \lambda(\mathbf{x} | \gamma, 1 - \alpha, \mathbf{X}) S \rangle, \quad (3)$$

where $\lambda(\mathbf{x} | \gamma, 1 - \alpha, \mathbf{X})$ is a *tolerance factor* for the given content γ , confidence level $1 - \alpha$ and \mathbf{X} , for simplification we will use a shorter notation $\lambda(\mathbf{x})$.

The simultaneous $(\gamma, 1 - \alpha)$ two-sided tolerance intervals of the form (3) in a linear regression model with normally distributed errors are constructed using vectors of observations \mathbf{Y} such that, with the confidence level $1 - \alpha$, at least the proportion γ of the $Y(\mathbf{x}) = \mathbf{x}^T \boldsymbol{\beta} + \sigma Z$ distribution is to be contained in the corresponding interval, simultaneously for all $\mathbf{x} \in \mathbf{R}^q$.

Let $C(\mathbf{x}; \hat{\boldsymbol{\beta}}, S) = P_{Y(\mathbf{x})}(\mathbf{x}^T \hat{\boldsymbol{\beta}} - \lambda(\mathbf{x}) S \leq Y(\mathbf{x}) \leq \mathbf{x}^T \hat{\boldsymbol{\beta}} + \lambda(\mathbf{x}) S | \hat{\boldsymbol{\beta}}, S)$ denote the content for the tolerance interval (3), given $\hat{\boldsymbol{\beta}}$ and S . The tolerance factors for all possible predictor values are determined subject to the content and confidence level requirements

$$P_{\hat{\boldsymbol{\beta}}, S}(C(\mathbf{x}; \hat{\boldsymbol{\beta}}, S) \geq \gamma \quad \forall \mathbf{x} \in \mathbf{R}^{q \times 1}) = 1 - \alpha. \quad (4)$$

The probability $1 - \alpha$ is associated with uncertainty of the outcome of the designed experiment and the probability γ is associated with uncertainty that can be attributed to errors in the future measurements.

Lieberman and Miller in [2] proposed to formulate the tolerance factors for all possible predictor values in a simple form $\lambda(\mathbf{x}) = \lambda^* \delta(\mathbf{x})$, where $\delta(\mathbf{x})$ is the standard error of $\mathbf{x}^T \hat{\boldsymbol{\beta}}$ and they derived the procedure for computing scalar λ^* . The general confidence set (GCS) approach to construction of STI for a linear regression model consists in defining a certain form of the $(1 - \alpha)$ -level pivotal set $G(\mathbf{X})$ for the pivotal quantities

$$\mathbf{b} = \frac{(\hat{\boldsymbol{\beta}} - \boldsymbol{\beta})}{\sigma} \sim N(0, (\mathbf{X}^T \mathbf{X})^{-1}) \quad \text{and} \quad u = \frac{S}{\sigma}, \quad (n-q)u^2 \sim \chi_{n-q}^2. \quad (5)$$

That is, it holds $P((\mathbf{b}, u) \in G(\mathbf{X})) = 1 - \alpha$ and the distributions of \mathbf{b}, u are free of unknown parameters $\boldsymbol{\beta}, \sigma$, dependent only on the design matrix \mathbf{X} . Furthermore, quantities \mathbf{b}, u are independently distributed. The function $\lambda(\mathbf{x})$ that satisfies Eq. 4 based on a set $G(\mathbf{X})$ is determined to satisfy equation

$$\lambda(\mathbf{x}) = \min\{\lambda : C(\mathbf{x}; \mathbf{b}, u) \geq \gamma \mid (\mathbf{b}, u) \in G(\mathbf{X})\}. \quad (6)$$

The pivotal sets proposed in the Wilson [6], the Limam-Thomas [4] and the modified Wilson [4] methods are constructed with approximate confidence $1 - \alpha$, only the pivotal set used in the LRTW method [1] is exact. In addition, the formulas for computing the tolerance factors by the methods were derived using the further approximations, in the Lieberman-Miller [2] and the LRTW methods too. There is no procedure to compute the tolerance factor $\lambda(\mathbf{x})$ satisfying the Eq. 4. In the next section we provide numerical comparison of the mentioned method for the case a simple linear regression, i.e. the future observation at the predictor $\mathbf{x}^T = (1, x)$ is expressed in the form $Y(\mathbf{x}) = \beta_0 + \beta_1 x + \sigma Z$, where β, σ will be specified and $Z \sim N(0, 1)$.

3. Simulations

We compare the estimated confidence levels of STI constructed by the Lieberman-Miller (SW), the Wilson (W), the Limam-Thomas (PS), the modified Wilson (MW), and the LRTW (LRTW) method. The approximate values of the confidences are determined based on the 10 000 simulated samples. For case a simple linear regression the first column of design matrix \mathbf{X} consists of ones and the second consist of possible various constants. In particular, for each sample we obtained the 19-dimensional vectors of observation of normal $N(\mathbf{X}(2, 1.7)^T, 1.5^2 I_n)$ distribution, where the second column of design matrix consists of $n = 19$ values $x_i, i = 1, \dots, 19$ randomly chosen from the range [1, 10]. We computed coverage of the tolerance intervals determined by the SW, the W, the PS, the MW, the LRTW method for each sample at the x values -3.0, -2.9, -2.8, ..., 14.0 as

$$\text{coverage}(\mathbf{x}) = \Phi\left(\frac{\mathbf{x}^T (\hat{\boldsymbol{\beta}} - \boldsymbol{\beta}) + \lambda(\mathbf{x})S}{\sigma}\right) - \Phi\left(\frac{\mathbf{x}^T (\hat{\boldsymbol{\beta}} - \boldsymbol{\beta}) - \lambda(\mathbf{x})S}{\sigma}\right),$$

where $\mathbf{x}^T = (1, x)$, $\hat{\boldsymbol{\beta}}, S$ are estimated from the designed experiment and Φ denotes cumulative distribution function of the standard normal distribution.

Table 1. The estimates of the confidence STI computed by the five methods for the four combinations of the content and the confidence values based on 10000 samples.

	$\alpha = 0.01$		$\alpha = 0.05$	
	$\gamma = 0.9$	$\gamma = 0.95$	$\gamma = 0.9$	$\gamma = 0.95$
SW	0.9989	0.9988	0.9933	0.9938
W	0.9989	0.9998	0.9954	0.9942
PS	0.9985	0.9988	0.9894	0.9896
MW	0.9989	0.9988	0.9877	0.9882
LRTW	0.9973	0.9965	0.9809	0.9814

The percentage of the samples, where coverage was at least γ over the grid of 181 predictor values is the estimate of the confidence. Table 1 contains the numerical results for combinations of $\gamma = \{0.90, 0.95\}$, $\alpha = \{0.05, 0.01\}$.

4. Conclusions

STI are defined to cover simultaneously for all $\mathbf{x} \in \mathbb{R}^q$ at least γ proportion of all corresponding $Y(\mathbf{x})$ -distributions with confidence $1 - \alpha$. In this simulation study, we have checked the coverages over the finite subset of possible predictor values, therefore the confidence levels presented in Table 1 are only approximate. Based on the results, all the known procedures exceed the nominal level, they are conservative. For the same confidence level and different values of the contents the estimates are close, as we expected. In spite of the different value of confidence the estimates are changed minimally for the same content, noticeable differences are for the PS, the MW, the LRTW method in ascending order. STI determined by the LRTW method are the closest to satisfy the specified requirements for the confidence level and the content.

Acknowledgements

The paper was supported by the Slovak Research and Development Agency (APVV), grant SK-AT-0003-08 and by the Scientific Grant Agency of the Slovak Republic (VEGA), grant 1/0077/09 and 2/0019/10.

References

- [1] Chvosteková, M. Determination of Two-sided Tolerance Interval in a Linear Regression Model. *Forum Statisticum Slovacum*, 6 (5): 79 – 84, 2010.
- [2] Lieberman, G. J., Miller, R. G., Jr. Simultaneous Tolerance Intervals in Regression. *Biometrika*, 50 (1/2): 155 – 168, 1963.
- [3] Lieberman, G. J., Miller, R. G., Jr., and Hamilton, M. A. Simultaneous Discrimination Intervals in Regression. *Biometrika*, 54 (1/2), 133– 145, 1967.
- [4] Limam, M. M. T., Thomas, R. Simultaneous Tolerance Intervals for the Linear Regression Model. *Journal of the American Statistical Association*, 83 (403): 801 – 804, 1988.
- [5] Mee R. W., Eberhardt, K. R., Reeve, C. P. Calibration and Simultaneous Tolerance Intervals for Regression. *Technometrics*, 33 (2): 211– 219, 1991.
- [6] Wilson, A. L. An Approach to Simultaneous Tolerance Intervals in Regression. *The Annals of Mathematical Statistics*, 38 (5): 1536 – 1540, 1967.

Accuracy in Analytical Measurements

J. Zakrzewski

Silesian University of Technology, Gliwice, Poland

Email: jan.zakrzewski@polsl.pl

Abstract. The paper presents some essential differences between analytical measurements and measurements of physical quantities. The rules of accuracy presentation are also not the same. Additionally they are incoherent. It creates a great confusion which ought to be overcome by close cooperation of NMI's, accreditation institutions and international organisations.

Keywords: Analytical Measurements, Accuracy Terms, International Documents

1. Introduction

The theory of measurements in a very wide scope, as a method of empirical cognition of the nature, should have a common understanding. In practice however, both laboratory and industrial practice, one has to distinguish between measurements of physical quantities and analytical measurements. The term analytical measurements include biological, chemical and medical measurements. Both categories of measurements mentioned above have been developed separately one to another by use of different methods, procedures and presentation of the results. There are several reasons for it, namely:

1. The amount of analyte in the matrix (probe) is often very small. The measuring procedure must be extremely sensitive and of great resolution.
2. The matrix has unpredictable and unrepeatable contents and forms. The methods of analyte recognition must be sufficiently selective with respect to the variety of matrix.
3. Accessibility of etalons is sometimes limited. The measurements even with the use of Reference Certificated Materials give different results in case of different matrix composition.
4. The results of the analytical measurements are often important juristically and from the moral point of view.

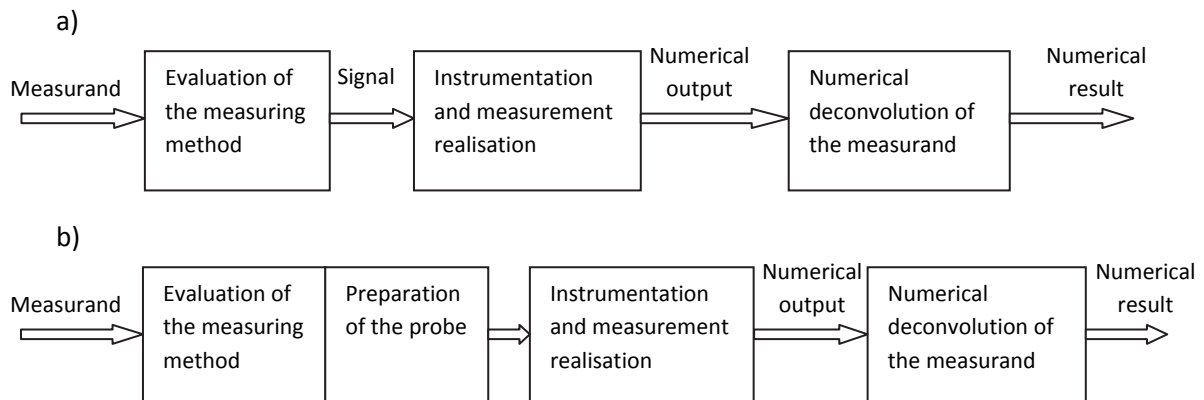


Fig.1. Fundamental parts of measuring chains (a) in physical measurements (b) in analytical measurements (b)

The chain of physical quantities measurement has three main parts presented in Fig.1a. Analytical measurements include an additional part involving preparation of the probe, that depends on the matrix, and often is the most important and most complicated part of the measuring procedure (Fig 1 b).

The methods of the measurement result calculation and presentation specified in GUM [1] are known and commonly respected in practical measurements of physical quantities. They serve as an essential material in laboratory accreditation procedure. In analytical laboratories GUM is treated with dislike or even with aversion. The reason is evident. The specific problems of analytical measurements are in GUM completely neglected. Analytical laboratories have created their own elaborate systems of the proper work including validation and confirmation of the results obtained. The methods of calculating and presenting the results are based on the existing literature and other documents. Unfortunately these documents are incoherent in presentation the metrological terms and their meanings. It leads to numerous problems.

2. Documents Study

Accuracy is an essential term in metrology. According to VIM [2] accuracy is a qualitative term. In many publications and documents however, accuracy is presented as a quantitative measure. The meaning of that measure is not unified and depends on the author. For example in old document [3] accuracy is described as “*A quantity referring to the differences between the mean of a set of results or an individual result and the value which is accepted as true or correct value for the quantity measured*”. But also in a new document [4] we find a definition like “*Closeness of agreement between a quantity value obtained by measurement and the true value of the measurand*”. The quantitative definition of accuracy can be found also in ASTM standards (American Society for Testing and Material). Nowadays qualitative meaning of accuracy is becoming more popular. So, in [5] accuracy is defined as “*Ability of a measuring instrument to give responses close to a true value. Note: In this context accuracy is a qualitative concept*” The idea of “true value” belongs to the past. It exists still in VIM but with a notice underlining its restricted application. Some documents like [6] and [7] don't use the term at all. In [8] True value is replaced by “*target or reference value*”.

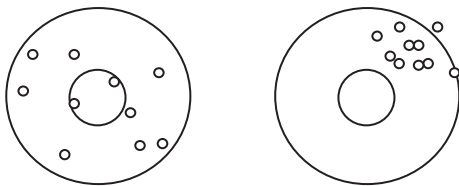


Fig. 2 Presentation of precision and trueness incoherent with GUM codification

Documents published by Eurachem seem to be very important for chemical laboratories. The definition presented in [9] “*The closeness of agreement between a test result and the accepted reference value. Note: The term accuracy, when applied to a set of test results, involves a combination of random components and a common systematic error or bias component*” is hard to understand and different from the one given in GUM.

GUM codification deliberately does not refer the concepts of systematic errors and random errors. Instead of them we can find precision and trueness. The difference between those terms is sometimes explained in the form presented in Fig. 2 as a result of shooting to the

target. It is completely wrong explanation. The hunter sees the target and knows where is the centre but he doesn't succeed. A person executing the measuring procedure don't know the "true value". Only ones knowledge and skills allows to obtain the result near to that value. A better interpretation of Fig. 2 would be, that Fig. 2a presents a situation when uncertainty type A is greater than type B and Fig. 2b, the opposite case.

In order to avoid terms "systematic error" and "random error" unacceptable by GUM, the term "bias" is often used. The definition given by NIST [8] seems to be a good one "*In particular, for a measurement laboratory, bias is a difference between a laboratory's average value (over time) for a test item and the average that would be achieved by the reference laboratory if it undertook the same measurements on the same test item*". Other definitions are less precise and sometimes false. They are also based on the systematic error as in [4] and [10] after ISO 3534-1.

It is worth to notice that in analytical laboratories the word "precision" is used in a form "intermediate precision" with a different meaning, i.e. interlaboratory or externlaboratory reproducibility. In contrast to the procedures used for measurement of physical quantities, chemical laboratories attach a great importance to interlaboratory measurements and to the hierarchy of laboratories. They elaborated some specific kind of evaluation of the measuring results, not used in physical measurements, named recovery. The procedure depends on the adding of the precisely known small amount of analyte to the probe and then measuring the increase of the result. It is a specific method of calibration where the influence of matrix composition is reduced. In [11] recovery is identified with accuracy and a specific relative standard deviation RSD, namely variability coefficient CV is calculated according to the Horvitz equation $CV = 2^{1-0.5 \log c}$ where c is an analyte concentration. That CV (possibly with coefficient equal to 0,67) is used to validate the measuring procedure.

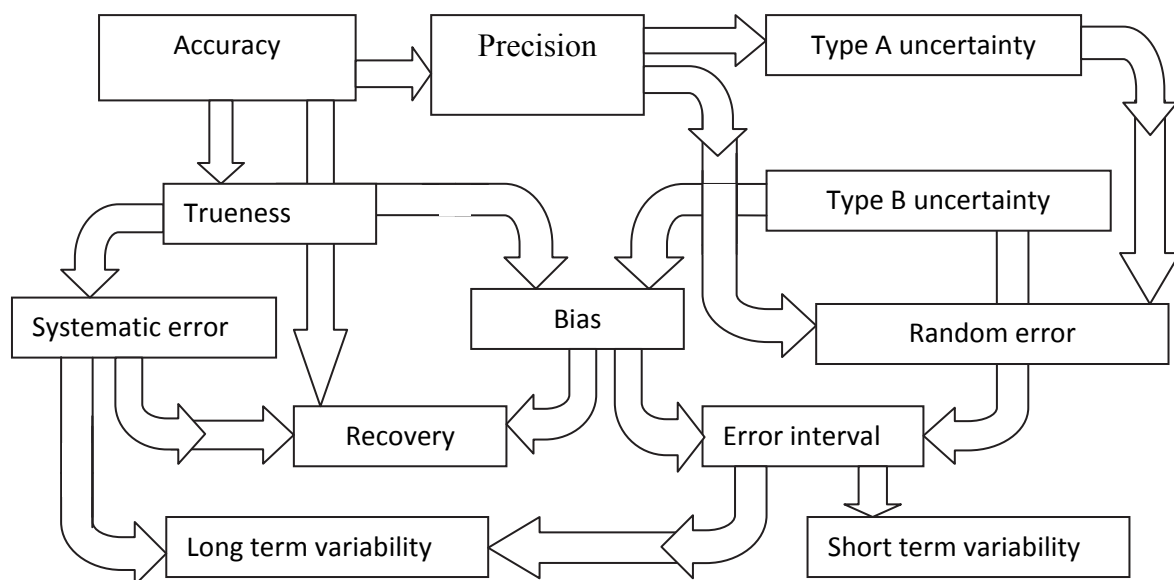


Fig. 3. Relations between essential metrological terms presented in various documents (sic!)

Fig. 3 presents the relations between mentioned above terms according to the documents cited in references and to many others. The lack of coherence is evident, in spite of the fact that majority of documents are the relatively new ones. That situation is highly uncomfortable especially for laboratories striving for accreditation. Even excellent performed validation procedure is not sufficient for accreditation when the results are not calculated and presented in the form required by auditors. The question “which form ought to be used as the obligatory one” is still open.

3. Conclusion

Majority of analytical laboratories; chemical, medical, biological, environmental, etc. work perfectly but the methods they use for presentation their results are not unified. At present, the unification is impossible because of disorder and incoherence of normative documents. There is an urgent need to indicate a set of not contradictory documents and rules dealing with the measurement results presentation and accepted by analytical laboratories with respect to the specific procedures implemented there. It is a challenge for National Measuring Institutes cooperating with Accreditation Centres. The expectation the problem to be solved by international organisations is not realistic. It must be done at the level of national organisations. Globalisation of those directives may be expecting eventually as the next step.

References

- [1] GUM Guide to the Expression of Uncertainty in Measurement (1995).
- [2] International Vocabulary of Metrology ,3-d ed. ISO/IEC Guide 99:2007
- [3] IUPAC Compendium of Chemical Terminology – Golden Book (1985)
- [4] EURACHEM / CITAC Guide. Use of uncertainty information in compliance assessment 1-t ed., (2007)
- [5] EURACHEM / CITAC Guide CG 4 Quantifying Uncertainty in Analytical Measurement. 2-d ed., (2000)
- [6] CITAC / EURACHEM Guide to Quality in Analytical Chemistry An Aid to Accreditation
- [7] EA-4/02 Publication Reference: Expression of the Uncertainty of Measurement in Calibration (1999)
- [8] NIST/SEMATECH e-Handbook of Statistical Methods, <http://www.itl.nist.gov/div898/handbook/eda/eda.htm>
- [9] EURACHEM Guide; The Fitness for Purpose of Analytical Methods. A Laboratory Guide to Method Validation and Related Topics (1998)
- [10] Menditto A., Patriarca M., Magnusson B.: Understanding the meaning of accuracy trueness and precision. Accreditation Quality Assurance, (2007)
- [11] Guidelines on method validation to be performed in support of analytical methods for agrochemical formulations, after document CIPAC 3807, Collaborative International Pesticides Analytical Council, (1985)
- [12] EA-04/10 Publication Reference: Accreditation for Microbiological Laboratories (2002)
- [13] Magnusson B., Näykki T., Hovind H., Krysel M.: Handbook for calculation of measurement uncertainty in environmental laboratories. Nordtest Technical Report 569
- [14] EA- 4/16 Guidelines on the expression of uncertainty in quantitative testing (2003)

Influence of Covariances on Uncertainties of Temperature Measurement by Calibrated SPRT

^{1,2}R. Palenčár, ^{1,2}S. Ďuriš

¹Slovak University of Technology (STU) Bratislava, Slovakia,

²Slovak Institute of Metrology (SMU), Slovakia

Email: rudolf.palencar@stuba.sk, duris@smu.gov.sk

Abstract: This paper is about propagation of uncertainties of realisation of the International Temperature Scale of 1990 (ITS-90) by calibrated standard platinum resistance thermometer (SPRT) at defining temperature points (DFPs) when temperature is directly measured in the calibration laboratory. Analysis of correlations between SPRT resistances from temperature measurements and resistances from measurements at DFPs is introduced.

Keywords: ITS-90, Standard Platinum Resistance Thermometer, Defining Fixed Point, Calibration, Uncertainty

1 Introduction

Uncertainties of measured temperature in calibration laboratory could be directly influenced by correlations between calibration and measurement of temperature. These correlations could be incurred by using the same equipment in calibration and measurement processes. Authors of this paper follow their previous publications [1, 2, 3, 4], where the problematic of influences of covariances in temperature measurement was presented. There was also presented an algebraic method of uncertainty determination based on law for propagation of uncertainties in accordance with GUM [6]. Method of orthogonal polynomials [8 - 11] is also successfully utilized. This approach is published in international document BIPM [5], where the authors cooperated. Algebraic method presented in GUM allows taking into account covariances between resistances for uncertainty determination. Document [5] introduces another approach. Anyway algebraic method could allow doing analysis of correlations and uncertainty determination for different cases as were presented in [5]. As was discussed in [2, 3] under the conditions in [5], both approaches lead to consistent results. In this paper the method is amended by inclusion of correlation influences between SPRT resistances from calibration and measurement of temperature. Method of uncertainty determination taking into account these correlations is introduced.

2 Total Uncertainty of Realisation of Temperature Scale in Calibration Laboratory

ITS-90 defines temperature T in temperature range from 13,8 K to 961,78 °C by means of SPRT calibrated at DFPs. Temperature is defined by reference functions describing dependence of resistance ratio W_r of SPRT (SPRT used also for realisation of ITS-90) on temperature T and deviation functions for corresponding subranges of ITS-90. Resistance ratio of SPRT $W=R/R_{TPW}$ is ratio of resistance R of SPRT at temperature T and resistance R_{TPW} of SPRT at temperature of triple point of water (TPW).

ITS-90 [7] defines inverse reference function for different subranges

$$T = f(W_r) , \tag{1}$$

whereby

$$W_r = W - \Delta W , \tag{2}$$

where

ΔW is deviation from calibration of SPRT and it is function of parameters and W , deviation functions for different subranges is published in [7] ;

W is resistance ratio defined as ratio of SPRT resistance R at temperature T and resistance R_{TPW} at temperature of triple point of water (TPW).

Uncertainty of temperature T is determined by equation

$$u(T) = A_r u(W_r), \quad (3)$$

where $u(W_r)$ is uncertainty of resistance ratio W_r . Sensitivity coefficient A_r is obtained by differentiating of inverse reference function (1) with respect to W_r .

If consider that ΔW is function of parameters of deviation function and W , parameters of deviation function are functions of resistance ratios at defining fixed points (DFPs) W_i and W_{Ti} , resistance ratios are functions of resistances at DFP and if W_{Ti} are known, then in accordance with the law of uncertainty propagation and law of covariances propagation and with respect to eq. (4) is:

$$\begin{aligned} u^2(W_r) = & \frac{1}{R_{TPW}^2} \left[u^2(R) + W^2 u^2(R_{TPW}) + \sum_{i=2}^N A_i^2 \left[u^2(R_i) + W_i^2 u^2(R_{TPW,i}) \right] + \right. \\ & 2 \sum_{i=2}^{N-1} \sum_{j=i+1}^N A_i A_j u(R_i, R_j) + 2 \sum_{i=2}^{N-1} \sum_{j=i+1}^N A_i A_j W_i W_j u(R_{TPW,i}, R_{TPW,j}) - 2 \sum_{i=2}^N \sum_{j=2}^N A_i A_j W_j u(R_i, R_{TPW,j}) - \\ & 2 \sum_{i=2}^N A_i W W_i u(R_{TPW}, R_{TPW,i}) + 2 \sum_{i=2}^N A_i W u(R_{TPW}, R_i) - \\ & \left. 2 \sum_{i=2}^N A_i u(R, R_i) + 2 \sum_{i=2}^N A_i W_i u(R, R_{TPW,i}) - 2 W u(R, R_{TPW}) \right]. \quad (4) \end{aligned}$$

Sensitivity coefficients A_i in eq. (4) are determined by algebraic or numerical approximation (see [5, 8-12]).

Except for $u(R)$, $u(R_{TPW})$, $u(R_{TPW,i})$, $u(R_i)$, $u(R_{TPW}, R_i)$, $u(R_i, R_j)$, $u(R_i, R_{TPW,i})$, $u(R, R_{TPW,i})$, $u(R, R_i)$ and $u(R, R_{TPW})$, all uncertainties and covariances are obtained as the results of the SPRT calibration and temperature measurement, where R_i and $R_{TPW,i}$ are SPRT resistances at DFP_{*i*} or at TPW_{*i*}.

First line of eq. 4) represents the contribution from resistance uncertainties at DFPs in calibration of SPRT and resistance uncertainties from temperature measurement.

Second line of eq. (4) represents contributions of covariances between resistances at DFPs from calibration.

Third line of eq. (4) represents the contribution of covariances between resistance at TPW used by client and resistances at DFPs from calibration.

Fourth line of eq. (4) represents the contribution of covariances between resistance R and resistances at DFPs from calibration and the contribution of covariances between resistance R and resistance at TPW of client.

Eq. (4) was derived in [1, 2] represents influence of correlations between resistance R and resistances at DFPs from calibration and influence of correlations between resistance R and resistance at TPW of client.

When temperature is measured in calibration laboratory and the same TPW cell is used then it can be supposed (in second case approximately) $u(R_{TPW,i}) = u(R_{TPW})$, $u(R_i, R_{TPW,i}) = u(R_i, R_{TPW})$ $u(R_{TPW,i}, R_{TPW,j}) = u(R_{TPW}, R_{TPW,j}) = 1$, $u(R, R_{TPW,i}) = u(R, R_{TPW})$. Then we are getting

$$u^2(W_r) = \frac{1}{R_{TPW}^2} \left[u^2(R) + A_{TPW}^2 u^2(R_{TPW}) + \sum_{i=2}^N A_i^2 u^2(R_i) + \right. \\ \left. 2 \sum_{i=2}^{N-1} \sum_{j=i+1}^N A_i A_j u(R_i, R_j) + 2 \sum_{i=2}^N A_i A_{TPW} u(R_i, R_{TPW}) - \right. \\ \left. 2 \sum_{i=2}^N A_i u(R, R_i) - 2 A_{TPW} u(R, R_{TPW}) \right]. \quad (5)$$

First line of eq. (5) represents the contribution from resistance uncertainties at DFPs in calibration of SPRT and resistance uncertainties from temperature measurement.

Second line of eq. (5) represents contributions of covariances between resistances at DFPs from calibration.

Third line of eq. (5) represents the contribution of covariances between resistance R and resistances at DFPs from calibration.

3 Discussion

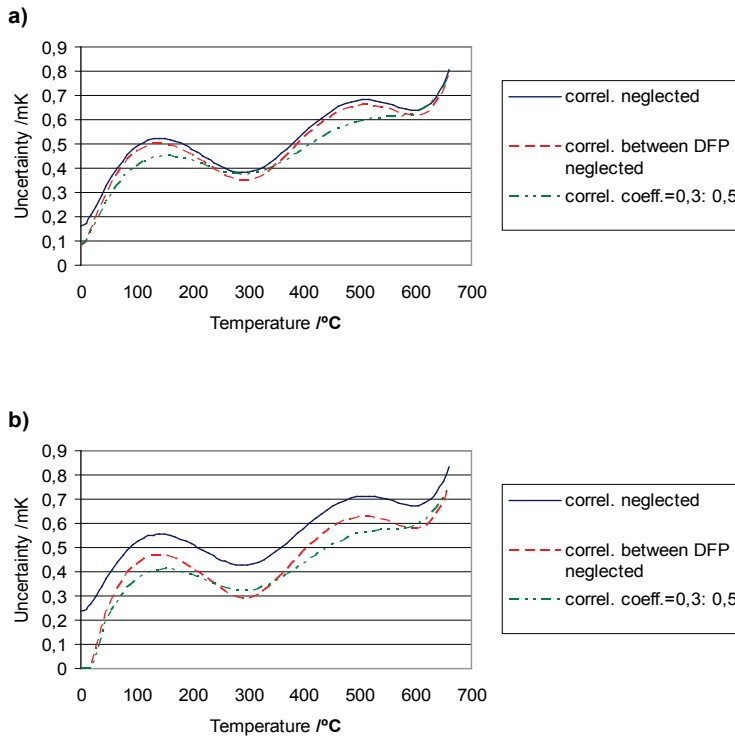


Fig. 1 Propagated uncertainty of SPRT calibration for the water-aluminium subrange, according to the different correlation coefficients between resistances at DFPs when SPRT is used in calibration laboratory. a) $u(R) = 1.10^{-2} \text{ m}\Omega$, $u(R, R_{TPW}) = u(R, R_{TPW}) = 1.10^{-4} \text{ m}\Omega^2$, $r(R_i, R_j) = 0,3$, $u(R_i, R_{TPW}) = 0,5$. b) $u(R) = 2.10^{-2} \text{ m}\Omega$, $u(R, R_{TPW}) = u(R, R_{TPW}) = 4.10^{-4} \text{ m}\Omega^2$, $r(R_i, R_j) = 0,3$, $u(R_i, R_{TPW}) = 0,5$

Correlations between SPRT resistances in temperature measurements and SPRT calibration in calibration laboratory can be caused by some mutual influences on measurements of SPRT resistances. As a result of this is propagation of uncertainty of temperature measurement by resistances correlations.

Influence of correlation between SPRT resistances of temperature measurement and SPRT calibration is presented in Fig. 1. Curves of total uncertainty for following cases are plotted: negligible correlations between SPRT resistances (solid line), consideration of correlations between SPRT resistances in temperature measurement and SPRT calibration, but not between SPRT resistances of calibration at DFPs (dashed line) and consideration of all correlations between SPRT resistances (dot-and-dash line). Uncertainty curve in the whole temperature range for one corresponding $u(R)$ is illustrated in Fig. 1. In reality $u(R)$ is changing with temperature. In Fig. 1 are covariances (for dashed line and dot-and-dash line) $u(R, RTPW) = u(R, Ri) = 4 \cdot 10^{-4} \text{ m}\Omega^2$ in Fig. 1a) and $u(R, RTPW) = u(R, Ri) = 1 \cdot 10^{-4} \text{ m}\Omega^2$ in Fig. 1b).

Correlation measurements of SPRT resistances of temperature measurements and SPRT calibration could decrease uncertainty of temperature measurements in the whole temperature range. Consideration of correlations between SPRT resistances of calibration at DFPs does not need to effect evidently decrease or increase of uncertainty in the whole temperature range. Uncertainties of temperature measurement represent upper limit of uncertainties in the case of negligible correlations between SPRT resistances.

Acknowledgments

Authors thanks for support to Slovak University of Technology (STU) Bratislava, Slovak Institute of Metrology (SMU) and to grant agency APVV grant No. APVV-0096-10, VEGA-grant No. 1/0310/09 a KEGA - grant No. 197-034STU-4/2010.

References

- [1] Duriš, S., Palenčár, R. (2005), *Measurement Science Review*, 5, No.1, s. 15-18. (<http://www.measurement.sk>)
- [2] Duris, S., Palencar, R., Ranostaj, R. (2008) *Measurement Science Review*, 8, No. 1, 5-10. (<http://www.measurement.sk>)
- [3] Duriš, S., Palenčár, R., Ranstaj, J. (2008) *Izmeritel'naja Tehnika*, 44, No. 4, (2008), *Measurement Techniques*, 51, No. 4, 412.
- [4] Palenčár, R., Ďuriš, S., Ranostaj, J. Algebraic Approach for Calculating of Total Uncertainties in SPRT Measurement. In *TEMPMEKO&ISHM 2010*, May 31st – June 4th 2010, Portorož, Slovenia. Ljubljana : University of Ljubljana, MIRS, 2010.
- [5] *Uncertainties in the Realization of the SPRT Sub-ranges of the ITS-90*. Sèvres : BIPM, 2009. (http://www.bipm.fr/en/committees/cc/cct/publications_cc.html)
- [6] ISO *Guide to the Expression of Uncertainty in Measurement*. Geneva : ISO, 1993
- [7] Supplementary Information for the International Temperature Scale of 1990, S`evres, Bureau International des Poids et Mesures, 1990.
- [8] White, D. R. and Saunders P. (2000), *Metrologia*, 37, 285
- [9] White, D. R. (2001), *Metrologia*, 38, 63
- [10] White, D. R. and Saunders, P. (2007), *Meas. Sci. & Tehnol*, 18, 2157
- [11] White, D. R. and Strouse, G. F. (2009), *Metrologia*, 46, 101
- [12] Mayer, C. W. and Ripple, D. C. (2001), *Metrologia*, 43, 327

Estimation of ADC Nonlinearities from the Measurement in Input Voltage Intervals

¹M. Godla, ²L. Michaeli, ³J. Šaliga, ⁴R. Palenčár

^{1,2,3}Department of Electronics and Multimedia Communications, FEI TU of Košice, Slovak Republic

⁴Institute of automation, measurement and applied informatics, SJF STU Bratislava, Slovak Republic

Email: marek.godla@tuke.sk

Abstract. This paper present proposal for fast testing method of AD converters aimed for estimation of INL as the error function and superimposed uncertainty based on two dimensional ADC error model. INL function is being determined by curve fitting of approximation function from the measurement of $INL(k)$ in chosen code bins of the full scale range of ADC under test. Proposed testing method is suitable for approval of final accuracy of assembled data acquisition system.

Keywords: — Analog to Digital Converters (ADC), Curve Fitting, Integral Nonlinearity (INL), Error Function, Uncertainty

1. Introduction

This paper presents a simple experimental method of testing INL characteristics of AD converters which can be performed in laboratories of end user. Test method works with several code bins which are important to approximate of integral nonlinearity as a basic parameter describing deviation in the transfer characteristic.

Integral nonlinearity $INL(k)$ and average code bin width Q' are defined according to [1], [2]. Taking into account Terminal based definitions transient code levels idea and real at both ends are equal $T_{id}(0) = T(0)$ and $T_{id}(2N-1) = T(2N-1)$

The characteristic of a real AD converter could be described by the two dimensional model [1]. INL is being described by the formula

$$INL(k) = LCF INL(k) + HCF INL(k) \quad (3)$$

Where low code frequency component $LCF INL$ represents smothered component of INL function while high code frequency component $HCF INL$ describes deterministic and stochastic effects of ADC nonlinearities. There are various mathematical methods proposed in the literature which approximate $LCF INL(k)$ with sufficient accuracy [4], [5]. The optimal type of approximating function depends on shape resulting error function conditioned by the ADC architecture and utilized technology.

From the metrological point of view, with increasing approximation order the $LCF INL(k)$ convert to the systematic ADC error and remaining $HCF INL(k)$ covers all remaining stochastic error sources. Impact of all those error sources could be described by combined uncertainty.

2. Curve fitting method for approximation of the INL characteristics

The proposed test method is based on the approximation of the ADC error characteristics by a polynomial.

$$INL(k) = a_m k^m + a_{m-1} k^{m-1} + \dots + a_1 k + a_0 \quad (4)$$

The parameters a_0, a_1, \dots, a_m , are estimated using the least mean square (LMS) criteria

$$E = \min \sum_{k=k_1}^{k_n} \left[\text{INL}(k) - (a_m k^m + a_{m-1} k^{m-1} \dots + a_1 k_1 + a_0) \right]^2 \quad (5)$$

The number n of codes ($k_1 \dots k_n$) where the integral nonlinearity $\text{INL}(k)$ have to be measured is lower than all ADC codes, which allows to speed up testing procedure. The transient code levels $T(k)$ in the L interleaved nodes (k_2, k_{n-1}) are measured by standardized testing method [3].

3. Uncertainties and Errors of Measuring of Code Bins

The INL measured in chosen code bins gives information just about systematic error. Uncertainty determines the margin of error of the tested error function by giving a range of values likely to enclose the true value. The combined uncertainty consists from following components in our case.

The first one u_1 represents the testing uncertainty caused by the utilized testing method. It belongs to the uncertainty of type A and could be determined by the repetition of measurement of code bins. We have used 10 measurement for any code bin k . Uncertainty $u_1(k)$ of transient code level testing determines uncertainty of $\text{INL}(k)$ in the nodal code bin.

$$u_1(k) = 3 \sqrt{\frac{1}{l(l-1)} \sum_{i=1}^l (T_i(k) - \overline{T(k)})^2} \quad (6)$$

The total uncertainty of INL estimation in the L nodal points is being determined by the geometrical sum. Uncertainty in nodes $k=0$ and $k=2^N-1$ are zero.

$$u_1 = \sqrt{\left(\frac{1}{L} \left[\sum_{i=1}^L u_1^2(i) + u_1(i) \sum_{\substack{j=1 \\ i \neq j}}^L u_1(j) r_{ij} \right] \right)} \quad (7)$$

where r_{ij} represents the cross correlation between testing results in any nodal point k_n .

The second uncertainty component is determined by the uncertainty of the precise digital voltmeter, which is responsible for traceability of measured code levels. This value could be estimated by the u_2 uncertainty of type B taken from the voltmeter data sheet.

The third component is connected with approximation uncertainty expressed by the approximation mean square error $u_3 = 3 \cdot Q \cdot \sqrt{E}$. This component has no correlation to the other uncertainty components. The uncertainty expressed in the codes must be transformed in voltage.

The total combined uncertainty of testing procedure u_c is being determined by all three contributions. No correlation between them is considered.

$$u_c = 3 \sqrt{\sum_{i=1}^3 u_i^2} \quad (8)$$

Combined uncertainty is an optimal indicator of test confidence. Determination of $\text{INL}(k)$ systematic error is reliable when final uncertainty is lower than maximal value INL_{max} . This figure of merit allows end user to improve its testing procedure in two directions.

The first one is based on the determination of bottlenecks in the proposed method by selection of uncertainty components contributing dominantly to the combined uncertainty. It allows enhancing number of testing attempts, improving the quality of reference voltmeter or increasing order of approximating polynomial.

The second possibility how to achieve satisfying ratio between u_c and INL_{max} is the enhancement of the amount of the testing nodes and order of the polynomial approximation.

Impossibility to achieve required limits of combined uncertainty is a sign that standardized methods has to be applied. As mentioned in paper [6] the suitable error models are dependent on ADC technology.

Besides converter error the digital results at the ADC output are always corrupted by the quantization noise which theoretical value is $u_q = \frac{Q}{\sqrt{12}}$. When the testing combined uncertainty and maximal value of error function are lower than quantization uncertainty it has no sense to perform correction using error function.

4. Experimental Results

Proposed method was tested by two types of ADCs each one representing another internal architecture. First one is 12 bit ADC of type TC7109 A by Microchip based on the double slope integration principle with autozeroing phase. Second tested ADC was 8-bit ADC0804 by Intersil working on the successive approximation principle.

The (Fig. 1.a.) shows results of approximation of the first ADC (TC 7109 A) by the polynomial of 5,10,3-th order when $L=20$ equidistant points in the transfer characteristic were taken for INL estimation. The integral nonlinearity by the standardized method is on (Fig.1.b).

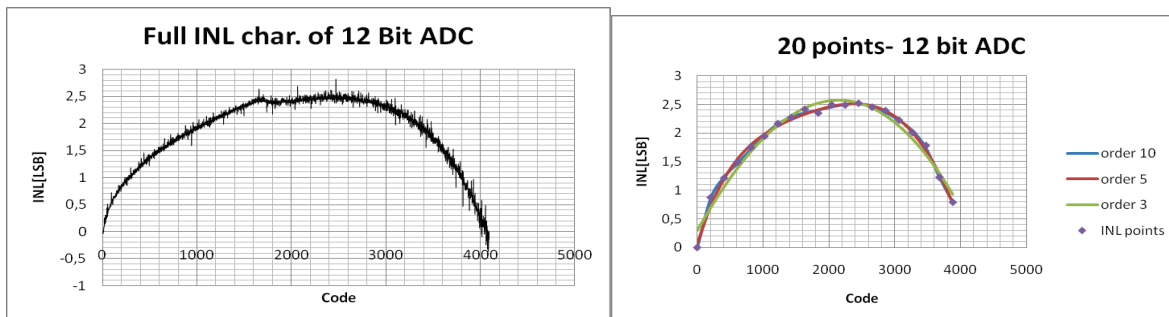


Fig.1.a.) Fig. 1. Measured INL of TC7109 by standardized method b.) approximated function with polynomial of 3,5,10 th order for 20 nodes

The (Fig. 2a). shows results of approximation of ADC0804 with different order. The difference between approximated polynomial and real INL measured by standardized methods is shown on (Fig.2.b). Typical consequence of DAC in the feedback is periodical repetition of the characteristic values of INL over the full scale. The uncertainty components contributions and their impact on combined one are shown on (Tab.1).

Table 1. Final uncertainties for both ADCs with use variety of nodal points

Type of ADC	Nod. points	u_1 [μV]	u_2 [μV]	u_3 [μV]			u_c [μV] 10 pol.
				Order of pol.			
				10	5	3	
8 bit ADC – ADC0804	20	26,893	5,5	4041,87	6097,51	6421,92	12125
	30	19,855		4769,79	6301,83	6735,794	14309,5
	50	23,715		4988,11	6162,17	6423,92	14946,51
12 bit ADC- TC7109	20	18,582		150,517	312,473	671,036	455,27
	30	22,469		99,861	140,156	377,977	307,515
	50	22,404		142,232	176,975	385,502	432,272

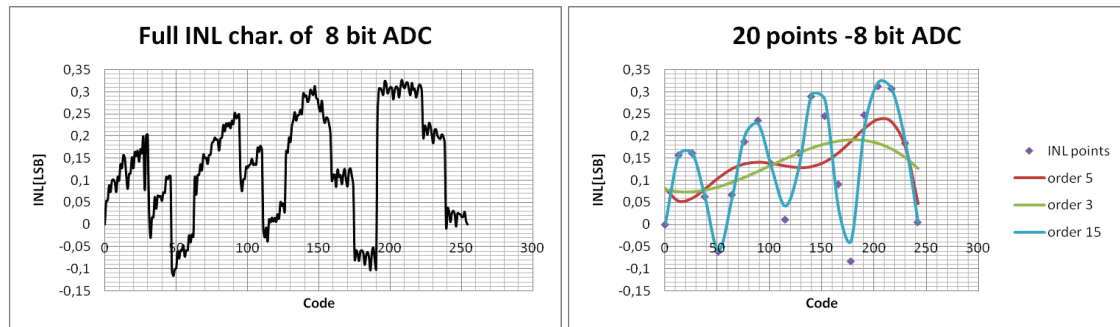


Fig.2a.). Measured INL of ADC0804 by standardized method b.) approximated function with polynomial of 3,5,10 th order for 20 nodes

Conclusions

Experimental results show that approximation of ADCs' INL by a polynomial function on the base of measurement in the reduce amount of measured points of its FSR is a suitable method which can speed up time consuming procedure according to IEEE standards for ADC testing. Increasing resolutions of the produced ADCs increase contribution of analog components to the final error function. Especially, integrated sensor systems could be presented by the generalized analog to digital converter. Testing for the reduced amount of reference physical quantities from the full measuring range is much easier.

Acknowledgment

The work is a part of project supported by the APVV agency APVV-0096-10, VEGA agency (No. 1/0310/09 and 1/0555/11) and KEGA agency (97-034STU-4/2010, 3/7115/09). This publication is the result of the project implementation Development of Centre of Information and Communication Technologies for Knowledge Systems (project number: 26220120030) supported by the Research & Development Operational Programme funded by the ERDF.

References

- [1] Michaeli, L., Michalko, P., Šaliga, J.: Unified ADC nonlinearity error model for SAR ADC /, 2008. In: Measurement. - ISSN 0263-2241. - Vol. 41, no. 2 (2008), p. 198-204. -
- [2] IEEE Standard 1057-1994 for digitizing waveform recorders, Dec. 1994.
- [3] IEEE Standard 1241-2000 for terminology and test methods for analog-to-digital converters, Dec. 2000.
- [4] Janik, Jean-Marie: Estimation of A/D Converter Nonlinearities from Complex Spectrum
- [5] Adamo, F., Attivissimo, F., Giaquinto, N., Kale, I.: Measuring Dynamic Nonlinearity of A/D Converters Via Spectral Methods, Proc of IMEKO IWADC 2003, p.167-170
- [6] Adamo, F., Andria, G., Attivissimo, F., Giaquinto, N.: Linearisation of A/D converters by dither and Chebyshev polynomials, /In: Measurement. - ISSN 0263-2241. - Vol. 35, no. 2 (2004), p. 123-130.
- [7] Stefani, F., Moschitta, A., Macii, D., Carbone, P., Petri, D.: Fast estimation of ADC nonlinearities using Sinewave Histogram Test, In: Measurement. - ISSN 0263-2241. - Vol. 39, no. 3 (2006), p. 232-237.

Time Delay Estimation of Stochastic Signals Using Conditional Averaging

¹A. Kowalczyk, ¹R. Hanus, ¹A. Szlachta

¹Rzeszow University of Technology, Department of Metrology and Diagnostic Systems Rzeszow, Poland

Email: kowadam@prz.edu.pl

Abstract. *The results of the theoretical analysis of selected features of two statistical methods used in time delay estimation (TDE): direct cross-correlation (CCF) and the function of conditional average value of delayed signal (CAV) have been presented in this paper. The model of measured stochastic signals and principle of TDE using CAV and CCF are described in this paper. The relative uncertainty of both functions in extreme point and the relative standard deviations of TDE using CAV and CCF are evaluated and compared. The authors conclude that the method CAV described in this paper has less statistical errors in magnitude and location (time delay) estimation than CCF and can be applied to time delay measurement of random signals.*

Keywords: Time Delay Estimation, Random Signals, Conditional Averaging, Cross-Correlation

1. Introduction

The problem of time delay estimation (*TDE*) is significant in many areas as radar and sonar technology, radioastronomy, location of signal transfer paths or contact-free measurements of transport parameters. Determination of the time delay of stochastic signals received from two or more sensors is commonly carried out with the use of statistical methods. This problem has been thoroughly presented in the literature [1-6], which describes a well-known methods of signals analysis in the time and frequency domains. Among the traditional methods used for stationary signals, the most common one is direct cross-correlation (*CCF*) in the time domain and the phase of cross-spectral power density in the frequency domain [1-3, 7]. The methods based on conditional averaging of signals are relatively new [8-11].

This paper presents the results of comparative research of selected features *CCF* and the method which uses conditional averaging of the delayed signal (*CAV*) [11]. The relatively standard deviations of both functions in extreme points and standard deviations of *TDE* for *CCF* and *CAV* were evaluated and compared. The values of signal-to-noise ratio were determined for the assumed signal models, where the analysed methods had smaller standard deviations of estimation for specific parameters of the analysis.

2. Model of Measurement Signals and Principle of *TDE* Using *CCF* and *CAV*

In the case of many *TDE* applications (i.e. measurements of transport parameters of solids and flows), the relation for signals $x(t)$ and $z(t)$ received from two sensors is usually given by the following formula [1,3]:

$$z(t) = kx(t - \tau_0) + n(t) = y(t) + n(t), \quad (1)$$

where: $x(t)$ is the stationary random signal with a normal probability distribution $N(0, \sigma_x)$, frequency band B and the unilateral spectral power density:

$$G_{xx}(f) = \begin{cases} G & 0 < f \leq B \\ 0 & f > B \end{cases}, \quad (2)$$

k , G are the constant factors; $\tau_0 = d/V$ is the transport delay equal to the quotient of the sensor spacing distance d and the average velocity of object V ; $n(t)$ is the stationary white noise, non-correlated with signal $x(t)$, with the distribution of $N(0, \sigma_n)$. The auto-correlation function of signal $x(t)$ has the following form:

$$R_{xx}(\tau) = GB \left(\frac{\sin 2\pi B \tau}{2\pi B \tau} \right). \quad (3)$$

The direct cross-correlation $R_{xz}(\tau)$ of the signals described by the relation (1) can be expressed by formula [1]:

$$R_{xz}(\tau) = \lim_{T \rightarrow \infty} \frac{1}{T} \int_0^T x(t)z(t+\tau)dt \quad (4)$$

The function (4) achieves the maximum value for $\tau = \tau_0$, so that the delay can be determined as the argument of the main extreme of this function:

$$\tau_0 = \arg \{ \max R_{xz}(\tau) \} = \arg \{ R_{xz}(\tau_0) \}. \quad (5)$$

The expected conditional value of the delayed signal $z(t)$ for the condition $x(t) = x_p$ is defined as follows [11]:

$$A_z(\tau) = A_z \Big|_{x(t)=x_p}(\tau) = \int_{-\infty}^{\infty} z(t+\tau) p(z(t+\tau) | x(t)=x_p) dz(t+\tau), \quad (6)$$

where $p(z(t+\tau) | x(t)=x_p)$ is the conditional probability density for the signal z value at the condition $x = x_p$, x_p – selected threshold value.

A good estimator of the expected conditional value (6) is the arithmetic conditional average value of the delayed signal. In practice, its determination entails detection of non-cross-correlated instant of threshold x_p transition of the original signal $x(t)$, starting the registration of the delayed signal $z(t)$ fragments in those moments and averaging the set of their value.

Peak position of CAV determine the transport delay τ_0 :

$$\tau_0 = \arg \{ \max A_z(\tau) \} = \arg \{ A_z(\tau_0) \}. \quad (7)$$

The principle of time delay estimation based on CCF and CAV is shown in Figure 1.

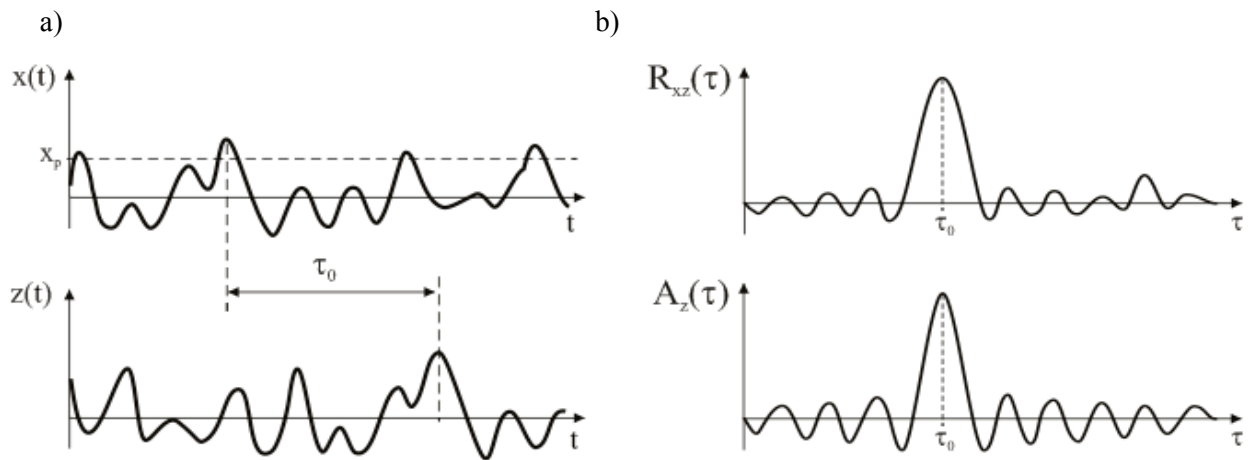


Fig. 1. The principle of time delay estimation using CCF $R_{xz}(\tau)$ and CAV $A_z(\tau)$: a) mutual delayed stochastic signals, b) CCF and CAV functions.

3. Comparison of Statistical Errors of CCF and CAV in Magnitude Estimates

The accuracy of *TDE* depends on gradients and variances of analysing function in the neighbourhood of the maximum. The relative standard uncertainty (relative standard deviation) of *CCF* can be written as [1,12]:

$$u_{rel}[\hat{R}_{xz}(\tau_0)] = \frac{\sigma[\hat{R}_{xz}(\tau_0)]}{R_{xz}(\tau_0)} = \frac{1}{\sqrt{N}} \sqrt{2 + \frac{1}{k^2 SNR}} \quad (8)$$

where N – number of non-correlated samples of signals $x(t)$ and $z(t)$, $SNR = (\sigma_x/\sigma_n)^2$ – signal-to-noise ratio.

The relative standard uncertainty of *CAV* can be presented as [11]:

$$u_{rel}[\hat{A}_z(\tau_0)] = \frac{\sigma[\hat{A}_z(\tau_0)]}{A_z(\tau_0)} = \frac{1}{\sqrt{M}} \frac{\sigma_n}{kX_p} = \frac{1}{k\alpha\sqrt{M \cdot SNR}} \quad (9)$$

where M – number of non-correlated averaged segments of the delayed signal $z(t)$, $\alpha = (x_p/\sigma_x)$ – relative threshold value.

As the result of comparison of (8) and (9) the following expression is obtained:

$$\frac{u_{rel}[\hat{A}_z(\tau_0)]}{u_{rel}[\hat{R}_{xy}(\tau_0)]} = \frac{1}{\alpha} \left[\frac{M}{N} (2k^2 SNR + 1) \right]^{-1/2} \quad (10)$$

Because *CCF* and *CAV* should be determined using non-correlated samples of signals the value M/N can be equal or less than 1. The relation $u_{rel}[\hat{A}_z(\tau_0)]/u_{rel}[\hat{R}_{xy}(\tau_0)] = f(SNR)$ for $M/N = 1$, $k = 1$ and selected values of α is presented in Figure 2. In this case the relative standard uncertainty of *CAV* is always less than for *CCF* if relative threshold value $\alpha \geq 1$ (Fig. 2).

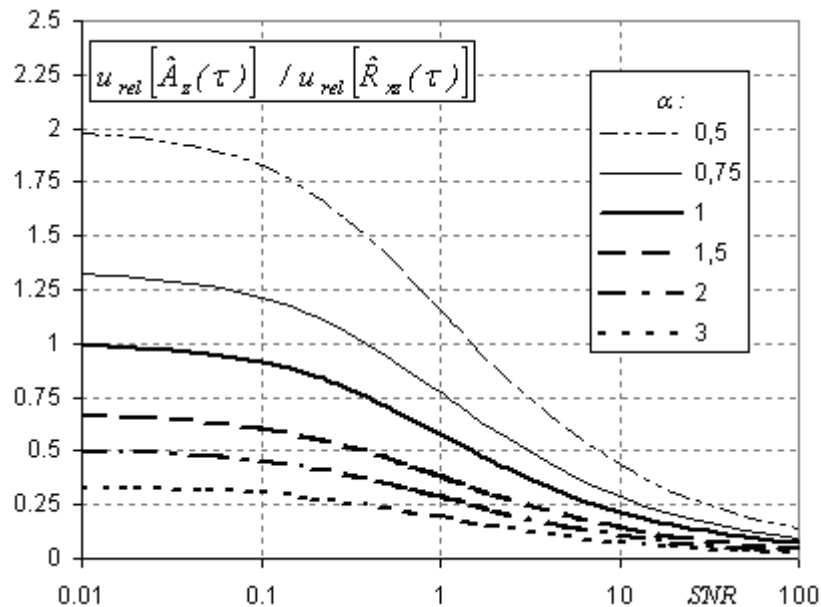


Fig. 2. The relation $u_{rel}[\hat{A}_z(\tau_0)]/u_{rel}[\hat{R}_{xy}(\tau_0)] = f(SNR)$ for $M/N = 1$, $k = 1$ and selected values of α

The results of work [11] shows, that optimum value of relative threshold value α is equal about 2. The dependence $u_{rel}[\hat{A}_z(\tau_0)]/u_{rel}[\hat{R}_{xy}(\tau_0)] = f(SNR)$ for $\alpha = 2$, $k = 1$ and selected values of M/N are presented in Figure 3.

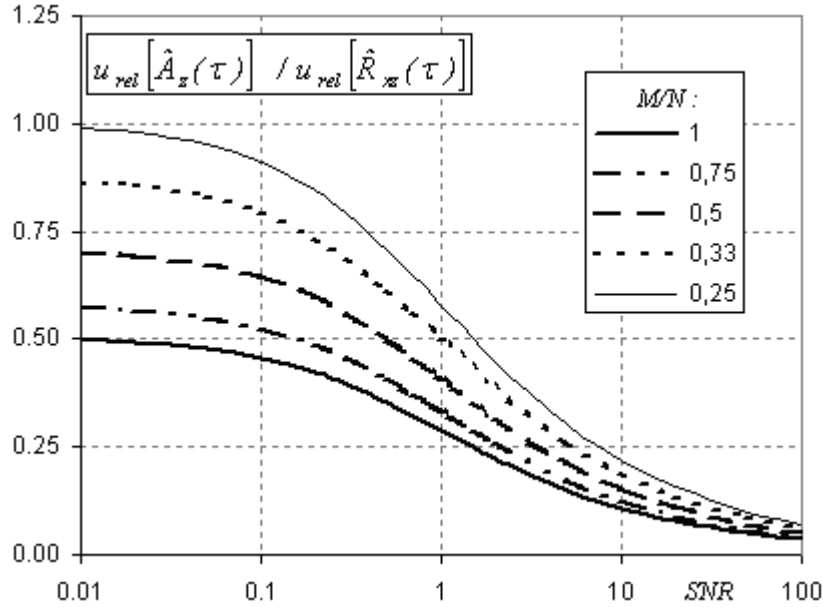


Fig. 3. The relation $u_{rel}[\hat{A}_z(\tau_0)]/u_{rel}[\hat{R}_{xy}(\tau_0)] = f(SNR)$ for $\alpha = 2$, $k = 1$ and selected values of M/N

4. Comparison of Statistical Errors of CCF and CAV in Locations Estimates

The standard deviation of the transport delay τ_0 obtained by CCF based on [1,2] can be evaluated to formula:

$$\begin{aligned} \sigma[\tau_0]_{CCF} &= \frac{1}{\pi B} \sqrt[4]{\frac{3}{4} \left\{ \left(u_{rel}[\hat{R}_{xy}(\tau_0)] \right)^{1/2} \right\}^{1/2}} = \\ &= \frac{1}{\pi B} \sqrt[4]{\frac{3}{4} \left\{ \frac{1}{\sqrt{N}} \left[2 + \frac{1}{k^2 SNR} \right]^{1/2} \right\}^{1/2}} \end{aligned} \quad (11)$$

For CAV can be written, respectively [11]:

$$\sigma[\tau_0]_{CAV} = \frac{1}{\pi B} \sqrt[4]{\frac{3}{4} \sqrt{u_{rel}[\hat{A}_z(\tau_0)]}} = \frac{1}{\pi B} \sqrt[4]{\frac{3}{4} \frac{1}{\sqrt{k\alpha}} (M \cdot SNR)^{-1/4}} \quad (12)$$

The comparison of (11) and (12) equations results the following equation:

$$\frac{\sigma[\tau_0]_{CAV}}{\sigma[\tau_0]_{CCF}} = \frac{1}{\sqrt{\alpha}} \left[\frac{M}{N} (2k^2 SNR + 1) \right]^{-1/4} \quad (13)$$

The relation $\sigma[\tau_0]_{CAV} / \sigma[\tau_0]_{CCF} = f(SNR)$ for $M/N = 1$, $k = 1$ and selected values of α is presented in Fig. 4. The dependence (13) for $\alpha = 2$, $k = 1$ and selected values of M/N are presented in Fig. 5. Similarly to magnitude estimation, standard deviation of transport delay

for *CAV* is less than the corresponding values for *CCF* irrespective of the *SNR* values if relative threshold value $\alpha \geq 2$ and $M/N \geq 0,25$.

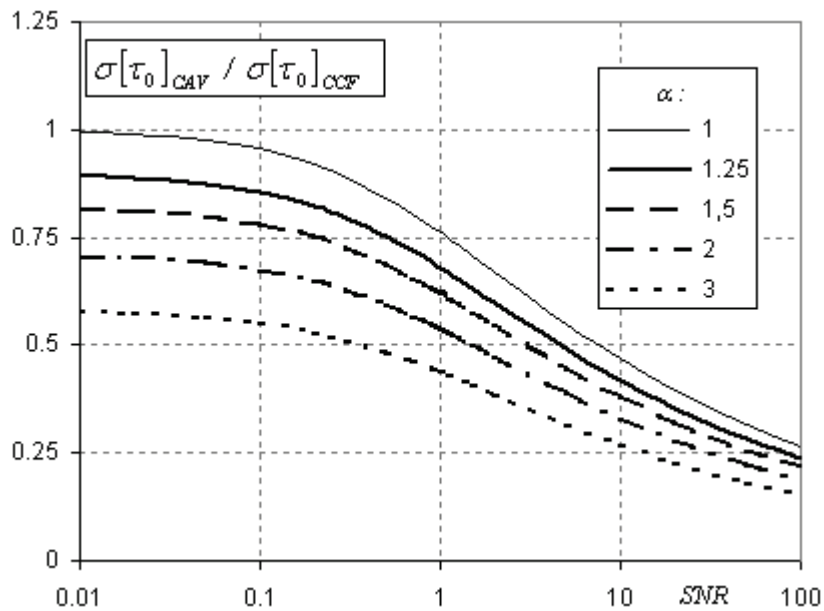


Fig. 4. The relation $\sigma[\tau_0]_{CAV} / \sigma[\tau_0]_{CCF} = f(SNR)$ for $M/N = 1, k = 1$ and selected values of α

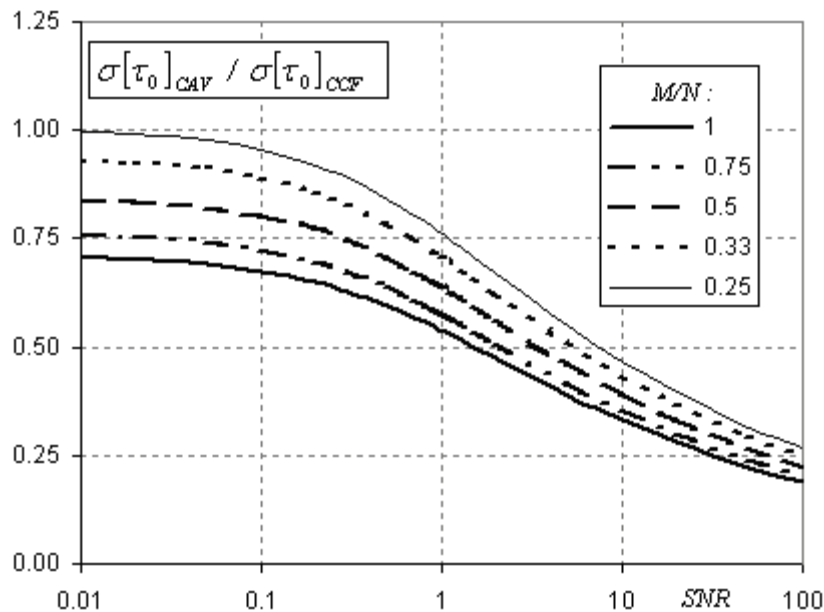


Fig. 5. The relation $\sigma[\tau_0]_{CAV} / \sigma[\tau_0]_{CCF} = f(SNR)$ for $\alpha = 2, k = 1$ and selected values of M/N

5. Conclusions

This work entailed the comparison of statistical errors of the direct cross-correlation and the conditional average value of the delayed signal in magnitude estimation and time delay estimation for the assumed signal models and the given *SNR* values. The theoretical analysis implies that the relative standard uncertainty of the *CAV* at the extreme points is less than the

corresponding standard uncertainty for *CCF* irrespective of the *SNR* values if $\alpha \geq 2$ and N/M is in the range $0,25 \leq N/M \leq 1$.

The standard deviation of transport delay obtained using *CAV* is less than the corresponding values for *CCF* independently of the *SNR* values if the relative threshold value $\alpha \geq 2$ and $0,25 \leq N/M \leq 1$.

The experimental verification of the theoretical analysis presented in this work is currently undergoing further investigation.

Acknowledgements

This work was supported by the Ministry of Science and Higher Education, Poland (grant no. N N505 466038).

References

- [1] J. S. Bendat , A. G. Piersol: *Random data - analysis and measurement procedures*. John Wiley, New York, 2000.
- [2] Bendat J. S., Piersol A. G.: *Engineering applications of correlation and spectral analysis*. John Wiley, New York, 1993.
- [3] M. S. Beck , A. Płaskowski : *Cross-Correlation Flowmeters*. Adam Hilger, Bristol, 1987.
- [4] E. Blok: "Classification and evaluation of discrete subsample time delay estimation algorithms". *Proc. of 14th International Conference on Microwaves, Radar and Wireless Communications*, pp. 764-767, 2002
- [5] C. G. Carter: "Coherence and time delay estimation". *Proceedings of the IEEE*, vol. 75, no. 2, pp. 236-255, 1987
- [6] G. Jacovitti, G. Scarano: "Discrete time technique for time delay estimation". *IEEE Transactions on Signal Processing*, vol. 41, no. 2, pp. 525-533, 1993.
- [7] L. Petryka, R. Hanus, M. Zych: „Statistical signal analysis in the radioisotope two-phase flow measurements”. *Pomiary Automatyka Kontrola*, vol. 54, no. 12, pp. 866-868, 2008. (in Polish)
- [8] A. Kowalczyk: „Regression method of velocity measurement”. *Aparatura Naukowa i Dydaktyczna*, vol. XV, no. 3-4, pp. 34-36, 1989. (in Polish)
- [9] R. Hanus: "Accuracy comparison of some statistic methods of time delay measurements". *Systems Analysis Modelling Simulation*, vol. 40, no. 2, pp. 239-244, 2001.
- [10] R. Hanus, A. Kowalczyk: „Estimators errors analysis of some statistical methods of time delay measurement”. *Pomiary Automatyka Kontrola*, vol. 49, no. 7-8, pp. 8-11, 2003. (in Polish)
- [11] A. Kowalczyk, A. Szlachta: „The application of conditional averaging of signals to obtain the transportation delay”. *Przegląd Elektrotechniczny*, vol. 86, no. 1, pp. 225-228, 2010. (in Polish)
- [12] A. Kowalczyk, R. Hanus, A. Szlachta: "Feature research for the statistical method of time delay estimation based on conditional averaging of the absolute values of delayed signal". *Proc. of Kongres Metrologii 2010, Łódź 6-8. 09. 2010*, pp. 118-119. (in Polish)

Accuracy Verification of Simplified Error Correction Method in Digital Electricity Meters

¹J. Hribik, ¹B. Lojko, ¹P. Fuchs

¹Dept. of Radio Electronics, Faculty of Electrical Engineering and Information Technology, Slovak University of Technology, Ilkovičova 3, 812 19 Bratislava, Slovak Republic

E-mail: jan.hribik@stuba.sk

***Abstract.** There are practically four main error sources in digital sampling electricity meters: errors of analogue input circuits, errors of the sampling process, errors of analogue-to-digital (A/D) conversion and errors of digital calculations. Brief description of correction of these errors is given. Very often it is not possible to make correction of every sample. Then, only the final calculated values are corrected and, thus, additional errors are introduced. MATLAB environment was used to find out the errors of such simplified calculations of the active power and the rms value of the voltage in case of harmonic and nonharmonic voltages and currents.*

Keywords: Digital Electricity Meter, Error Correction, MATLAB

1. Introduction

Basic instruments for the most accurate measurement of electric power and energy are static digital electricity meters. They use digital multiplication of voltage and current samples, [1], [2], received from one A/D converter with multiplexed inputs, [3], or they may use separate A/D converter for each input signal, [4]. The advantages of such instruments are obvious: high accuracy, short- and long-term stability, complex net parameters measurements, possibility of remote automated data processing, auto-calibration, self-test and many other functions resulting from the microprocessor-based digital system possibilities. Nowadays, digital signal processors make it also possible to measure reactive and apparent power, phase shift, power factor and frequency spectra of the power network signals.

Very important characteristic of electricity meters is their accuracy. It depends on the accuracy of analogue input circuits, the accuracy of the sampling process itself, [5], the accuracy of A/D conversion and the accuracy of digital calculations. There are many methods of error correction in digital electricity meters, [6]. Most of these methods use software correction based on calibration process, in which calibration constants are obtained. In the electricity meters usually voltage calibration, current calibration and parasitic phase shift correction are necessary. Every voltage and current range is calibrated separately. Calibration process is usually carried out using harmonic waveforms but there are also attempts to evaluate electricity meters accuracy under nonharmonic conditions [7], [8].

2. Error Correction in Digital Electricity Meters

The measurement errors caused by the analogue input circuits can be simply eliminated in the digital signal processing. The main problem is the stability of the parameters of these analogue parts. The analogue input circuits must be constructed using highly stable components.

The sampling of a real waveform usually approximates the waveform by a staircase or a piecewise linear function. For the sake of calculation simplicity, mainly staircase approximation is used. In symmetrical signals the errors of sampling in one quarter of period are partly compensated in another quarter.

Usually, synchronized or approximately synchronized sampling is used, [5]. Approximately synchronized sampling with starting point in the instant of zero crossing of the sampled signal is the usual case. Better accuracy can be achieved if the sampling starts in the instant of crossing the rms value of the sampled signal, [9]. It is difficult to realize in a three-phase system or if there is a phase shift between the voltage and the current. If the number of samples used in a summation interval is sufficiently high, then the error of sampling is low.

Because of errors caused by time delay between the multiplied voltage and current samples, A/D converter with multiplexed inputs is not used in precise instruments. Low-resolution A/D converters (low number of bits) cause unacceptable quantisation errors. Precise instruments use sigma-delta A/D converters with high resolution (over 16 bits) and high sampling rate (tens kSPS). All the measured quantities are then calculated during one period but, usually, the results are averaged again during longer summation intervals to get higher accuracy.

To find out the error of calculation when only the final calculated values were corrected, simplified calculations of the active power, P , and the rms value of the voltage, V , were compared with the calculations where every sample was corrected, [10], [11], [12], [13]. The selected correction function was a linear function of the type $y = ax + b$, where the constant a represents the gain error and the constant b is the offset error. All the calculations were carried out by MATLAB. In case of **harmonic signals** 1000 samples of the voltage and current per period were calculated using the equations

$$u_i = a_1 V_m \sin\left(\frac{2\pi i}{1000}\right) + b_1 \quad (1)$$

$$i_i = a_2 I_m \sin\left(\frac{2\pi i}{1000}\right) + b_2 \quad (2)$$

where $i = 1, 2, \dots, 1000$. For simplicity, the values V_m and I_m were set to unity.

The following equations show the correct use of the correction function (every sample corrected) (the current calculation is not shown, because it is similar to voltage calculation)

$$V_1 = \sqrt{\frac{1}{N} \sum_{i=1}^N \left(\frac{1}{a_1} v_i - \frac{b_1}{a_1} \right)^2} \quad (3)$$

$$P_1 = \frac{1}{N} \sum_{i=1}^N \left[\left(\frac{1}{a_1} v_i - \frac{b_1}{a_1} \right) \left(\frac{1}{a_2} i_i - \frac{b_2}{a_2} \right) \right] \quad (4)$$

The simplified calculations of the corrected values (the final calculated values corrected) are given by the equations

$$V_2 = \frac{1}{a_1} \sqrt{\frac{1}{N} \sum_{i=1}^N v_i^2 - b_1^2} \quad (5)$$

$$P_2 = \frac{1}{a_1 a_2} \frac{1}{N} \sum_{i=1}^N v_i i_i - \frac{b_1 b_2}{a_1 a_2} \quad (6)$$

The differences of the corresponding values are the calculation errors given by equations

$$\delta_u = \frac{V_2 - V_1}{V_1} \times 100 \quad (7)$$

$$\delta_p = \frac{P_2 - P_1}{P_1} \times 100 \quad (8)$$

The errors δ_u and δ_P were plotted for different values of the coefficients a_1 , a_2 (gain) and b_1 , b_2 (offset). The offset is relative, referenced to the amplitude V_m or I_m . The results show that the relative errors of such simplified calculations are negligible, on the level of calculation errors of MATLAB (approximately 10^{-15}). They are small enough to use simplified calculations instead of much more complicated and time-consuming exact calculations.

To investigate the situation, when the current has a **phase shift** towards the voltage, the current samples were calculated using the equation

$$i_i = a_2 I_m \sin\left(\frac{2\pi i}{1000} + \varphi\right) + b_2 \quad (9)$$

with phase shifts $\varphi = 30^\circ$, 60° (very often used) and 72° ($2\pi/5$ rad). The powers were calculated using equations (4) and (6) and the error δ_P was again calculated using equation (8). The results from MATLAB (for the phase shift $\varphi = 72^\circ$) show that the relative error of such simplified calculation is of the order of tens ppm and is again negligible. But this error increases with increasing phase shift because of the decreasing value of the power factor $\cos\varphi$ and hence, the decreasing value of the calculated power.

In case of **nonharmonic signals** 1024 samples of the voltage and the current per period were calculated in MATLAB using the equations of the desired waveforms. The amplitudes V_m and I_m were set to unity. First, both signals, v_i and i_i , are equal. In this case the rms value differs from the power only in the fact that the rms value is calculated as the square root of the mean value of the sum of samples. The properties of the rms value error are similar as that of the power error, so, the results of the power will be given only.

Very often a half-wave rectified signal is used. Only the first four harmonics were used and the phase shifts $\pi/6$ in the second harmonic, $\pi/5$ in the fourth harmonic and $\pi/7$ in the sixth harmonic were added. The error of such simplified power calculation is relatively high, of the order of tenth %, what is unacceptable for precise instruments. MATLAB calculations show that this error is nearly equal even without phase shifts and with up to ten harmonics used.

Another test signal was the sine wave signal with uniformly distributed random noise superimposed on it. The errors of the simplified power calculation for the noise amplitudes 0 %, 10 % and 20 % of the amplitude of the sine wave signal were in the range ± 10 ppm but they differed for different shapes of the generated noise signal.

The relative errors of the simplified calculations of power for a triangle wave signal with only the first ten harmonics used were on the level of calculation errors (approximately 10^{-15}). Similar errors were achieved for a square wave signal with only the first ten harmonics used.

The calculated relative error of the power for the square wave signal with the added phase shifts $\pi/3$ in the third harmonic and $\pi/5$ in the fifth harmonic was of the order of 1 ppm.

In real conditions, the voltage waveform in a power network is nearly harmonic, but the current waveform is distorted, [14]. Such situation has been also investigated. The MATLAB results show that these errors are a bit lower (from 20 % to 30 %) than corresponding power errors with both, voltage and current signals equally distorted. The only difference is the half-wave rectified signal where these errors are approximately half.

3. Conclusions

Brief description of the four main error sources and the error correction is given. In case if only the final calculated values are corrected, additional errors are introduced. MATLAB environment was used to find out the errors of such simplified calculations of the active power P in case of harmonic and nonharmonic voltages and currents. If both signals are equal, then

these errors are negligible for harmonic signals and for noisy signals. In case of nonharmonic signals the error of the half-wave rectified signal is relatively high, of the order of tenth %. It is caused by nonsymmetry of such signal. From calculations it can be seen that it is not important how much the signal is distorted. Only the symmetry of the signal round some vertical axes is of the great importance. If the voltage waveform is harmonic and the current waveform is distorted, then these errors are a bit lower (from 20 % to 30 %) than corresponding errors with both, voltage and current signals equally distorted. The only difference is the half-wave rectified signal where these errors are approximately half.

Acknowledgements

This work was supported by the Slovak Grant Agency under the project No. AV 4/0012/07 and projekt VEGA No. 2/0107/08.

References

- [1] Kahmann M. Elektrische Energie elektronisch gemessen: Meßgerätetechnik, Prüfmittel, Anwendungen. vde-verlag, Berlin-Offenbach, 1994.
- [2] Webster J. (ed.) Wiley Encyclopedia of Electrical and Electronics Engineering Online. Instrumentation and Measurement. John Wiley & Sons, New York, 1999.
- [3] Schwendtner MF. Digital Measurement System for Electricity Meters. In proceedings of the Conf. „Metering and Tariffs for Energy Supply”, 1996, 190-193.
- [4] K2006 Three-Phase Comparator. Operational Manual. EMH, Brackel – MTE, Zug, 2003.
- [5] Stenbaken DN, Dolev A. High-Accuracy Sampling Wattmeter. *IEEE Transactions on Instrumentation and Measurement*, 41 (6): 974-978, 1992.
- [6] Ďaďo S, Vedral J. Analogue and Digital Measuring Instruments II. Ediční středisko ČVUT, Prague, 1981. (In Czech)
- [7] Gallo D, Landi C, Pasquino N, Polese N. A New Methodological Approach to Quality Assurance of Energy Meters Under Nonsinusoidal Conditions. *IEEE Transactions on Instrumentation and Measurement*, 56 (5): 1694-1702, 2007.
- [8] Cataliotti A, Cosentino V, Lipari A, Nuccio S. On the methodologies for the calibration of static electricity meters in the presence of harmonic distortion. In proceedings of the 17th Symposium IMEKO TC 4, 3rd Symposium IMEKO TC 19 and 15th IWADC Workshop, 2010.
- [9] Michálek R, Gábor P, Lojko B, Fuchs P, Hribik J, Hruškovíc M. Digital Electricity Meter. In proceedings of the 13th International Czech-Slovak Scientific Conference „Radioelektronika 2003”, 2003, 99-102.
- [10] Fuchs P, Michálek R, Gábor P, Lojko B, Hribik J, Hruškovíc M. Digital Electricity Meter. In proceedings of the 4th Internat. Conf. on Measurement „Measurement 2003”, 2003, 411-414.
- [11] Hribik J, Fuchs P, Hruškovíc M, Michálek R, Lojko B. Digital Power Network Parameters Measurement. *Radioengineering*, 14 (2): 19-26, 2005.
- [12] Hribik J, Lojko B, Fuchs P, Hruškovíc M. Error Correction in Digital Electricity Meters. In proceedings of the International Scientific Conference “New Trends in Signal Processing VIII”, 2006, 151-155.
- [13] Hribik J. Digital Measurement of Low-Frequency Electric Power and Energy. Nakladateľstvo STU, Bratislava, 2010. (In Slovak)
- [14] Kaluš E. Ako na meranie striedavých veličín III – zdanlivý a iné výkony. October 2008. <http://hw.cz/teorieapraxe/dokumentace/art2497-ako-na-meranie-striedavych-velicin-iii-zdanlivy-a-ine-vykony.html>

Analyses of Quantization Noise Spectrum for Multiresolution Quantization of Harmonic Signal

M. Kamenský, K. Kováč, G. Valky

Department of Measurement, Faculty of Electrical Engineering and Information Technology, Slovak University of Technology, Ilkovičova 3, 81219 Bratislava, Slovak Republic, +421 2 60291393
Email: miroslav.kamensky@stuba.sk

***Abstract.** An analysis of quantisation noise of multiresolution structure of analog-to digital converters (ADC) is performed. It shows how the noise level as well as the resulting noise spectrum is changing with a level of sampled signal. The theoretical formulas are approved by numerical simulation and experimental measurements performed by PC measuring card emulating two channels ADC structure. The results confirm that resulting quantization noise level is strongly dependent upon the amplitude of measured signal.*

Keywords: Spectrum of Quantization Noise, Multiresolution Quantization

1. Introduction

Time domain spectrum analysis becomes popular technique even in the area of electromagnetic interference (EMI) measurement. It offers time effective alternative to conventional measuring receivers. To ensure necessary high dynamic range at very fast sampling it uses multiresolution structure of sufficiently fast analog-to-digital converters (ADC). After ADCs processing subsystem performs DFT and continuously calculates resulting spectra. Recent systems are able to operate at sampling frequency of 250 MHz [1].

As EMI measurements require high dynamic range at mentioned sampling frequency multiresolution structure of ADCs becomes the main part determining the metrological properties of the system. Multiresolution divides whole input range of system into several intervals. In each interval uniform quantization is used, but the quantization step is different for each interval - multiresolution quantization (MQ). Concept of MQ, realised by lower resolution fast ADCs, allows to improve dynamic range of spectrum measurement but brings specific behaviour of quantization error and quantization noise spectrum. To verify impact of MQ on fidelity of spectrum measurements analysis of spectral properties of quantization noise is presented in the paper for harmonic signal intersecting two intervals of MQ.

2. Multiresolution Structure for Spectrum Measurement

In described system the measured signal is sampled in two or three channels simultaneously. In the Fig. 1 a structure of a multiresolution system is depicted. The input signal is split by a power splitter (PWS) into all channels. Each channel consists of limiter (LM), low-noise amplifier (LNA) and an ADC - usually 8-bit. Using digital signal processing the signal is reconstructed by extracting each sampled value from the ADC where the signal shows the maximum nonclipped value. Principle of MQ offers new quality measurements. But like every new method it requires sufficient analysis of its properties. Coming out of theory of uniform quantization and using simulation we try to point out some problems in spectral behaviour of quantization error in MQ. For simplicity harmonic input signal will be assumed on the input of system which input range is divided by MQ into two intervals.

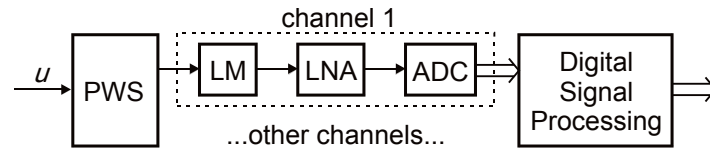


Fig. 1. Block structure of multiresolution quantization in spectral measurements.

3. Quantization Error of Harmonic Input

Consider simple harmonic signal with amplitude U and frequency f_u on the input of a measurement system

$$u(t) = U \sin(2\pi f_u t) \quad (1)$$

For evaluation of overall quantization error root mean square error (RMSE) is suitable. If amplitude U is large compared to quantization step q mean squared error (MSE) approaches good known value of $q^2/12$. But if the ratio U/q is low, better theoretical estimation should be used like in [2]. For assumed zero offset deterministic quantizer input (Eq. 1) and mid-tread quantizer the MSE is

$$MSE = \frac{q^2}{12} + \frac{q^2}{\pi^2} \sum_{k=1}^{\infty} \frac{(-1)^k}{k^2} J_0\left(\frac{k2\pi U}{q}\right) \quad (2)$$

where $J_0(\cdot)$ is the ordinary Bessel function of order zero.

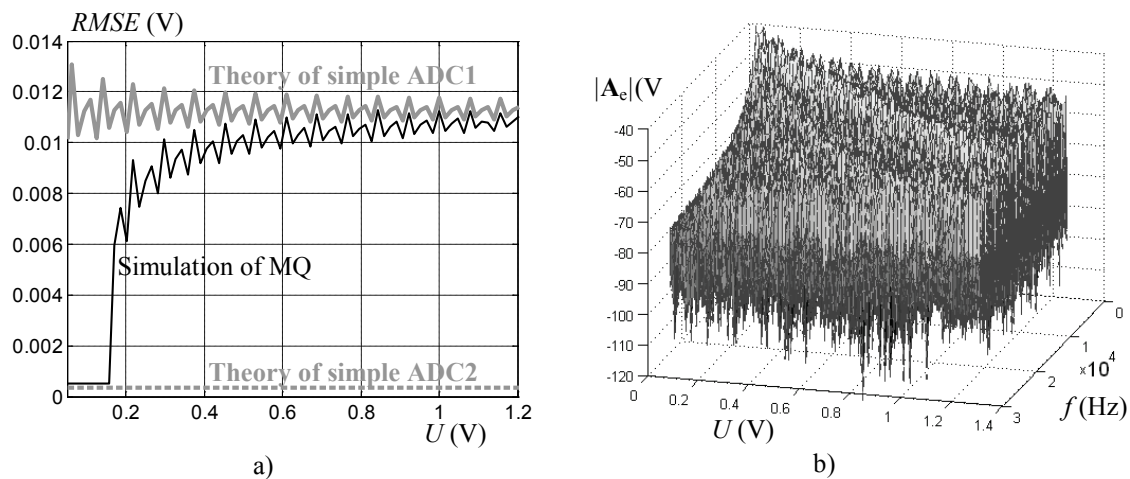


Fig. 2. Dependency of quantization error on harmonic signal amplitude U :
 a) RMSE of multiresolution quantization compared with theoretical error of simple quantization
 b) Simulation spectrum of quantization error for simple quantization

Simulated dependency of theoretical RMSE on signal amplitude is depicted in the Fig.2a. Solid gray line corresponds to 8-bit bipolar ADC (ADC1) with the range of ± 5 V ($q = 0.0391$ V) and dashed gray line to similar ADC (ADC2) with the range 2^5 times smaller (± 0.1563 V, $q = 0.0012$ V) than of the first one. Naturally better accuracy is achieved for lower quantization step q . As could be seen for considered harmonic input the change of overall quantization error is not critical with changing U . For ADC1 oscillations caused by the nature of $J_0(\cdot)$ and by presence of $(-1)^k$ in Eq. 2 are higher for lower U . However for two-channel MQ one may expect RMSE close to the theory of ADC2. This was tested by simulation of harmonic signal (with little noise) for signal frequency $f_u = 100$ Hz, sampling rate 512 time higher and for $N = 4096$ samples. Only for small signal amplitude the quantization noise level of MQ corresponds to better resolution ADC2 as shown in Fig.2a (black line).

Unfortunately there is quite steep slope in the error curve near to the end of ADC2 range. But RMSE dependency does not show in details the impact of error increase to spectrum estimated by Discrete Fourier Transform (DFT). Analysis of quantization noise spectrum should be done to unveil possible spurious spectral components.

If spectrum of quantization error is of interest, the analyses become slightly more complicated. Several approaches are suggested in [3]. Fortunately for a single ADC quite simple approximation is achieved by [4] based on modulation principle. From that power spectral density of quantization noise could be theoretically approximated by

$$S_e(f) = \frac{q^3}{2\pi^3} \sum_{k=1}^{\infty} \frac{1}{k^2} \frac{1}{kU2\pi f_u \sqrt{1 - \left(\frac{qf}{kU2\pi f_u}\right)^2}} \quad \text{for } |f| < 2\pi f_u \frac{U}{q} \quad (3)$$

Amplitude spectrum of quantization error $|A_e|$ could be estimated from S_e . As could be seen from the equation it depends on ratio of signal amplitude to quantization step U/q . In accordance with expectation also for every spectrum component the theoretical error decreases with decreasing q like for total RMSE. But according to Eq. 3 the spectral distribution of quantization error is not flat. Error peaks occur at frequencies (for integer k)

$$f_{p,k} = k \cdot 2\pi \frac{U}{q} f_u \quad (4)$$

Exactly this effect could be observed in the Fig.2b where amplitude spectrum of quantization error $|A_e|$ obtained from simulation of single ADC1 is depicted in dependence on U . One can suspect that after addition of ADC2 the first peak near to $f_{p,1}$ ($f_{p,1} = 1609 U$) can still significantly disturb measurement for signal amplitude just above ADC2 range.

4. Results

The simulations of MQ were realized using parameters from previous section. For some amplitude U of harmonic signal also experiments were added. Data acquisition card was used as a multiresolution quantizer.

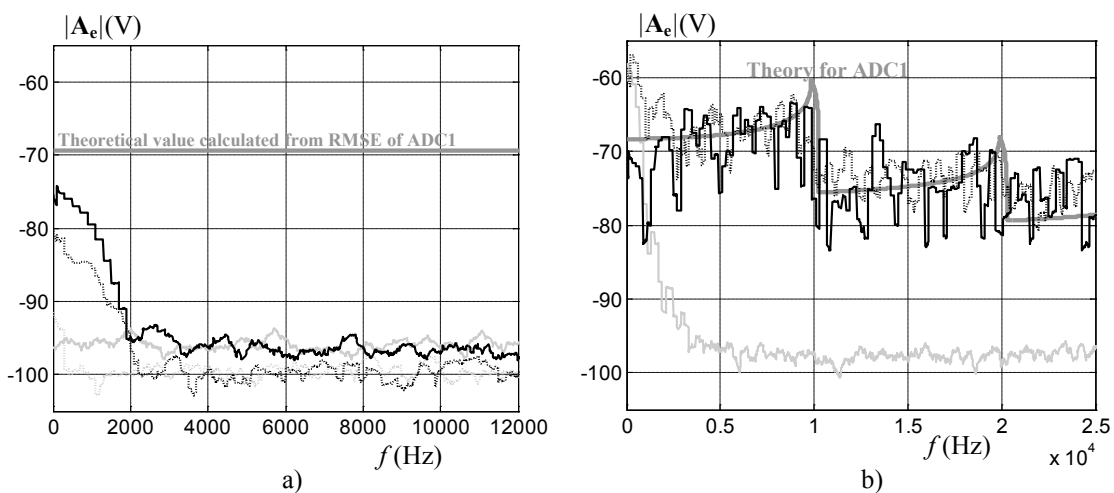


Fig. 3. Spectrum of quantization noise of MQ for several amplitudes U :
 a) Part of spectrum for $U=0.1550$ V (gray) and $U=0.1600$ V (black): simulated—, experimental....
 b) Spectrum for $U=0.1700$ V (light gray) and $U=0.3125$ V (black: simulated—, experimental....)

Smoothed spectrum of quantization error obtained from simulation and experiments is depicted in the Fig. 3a for U near to the end of ADC2 range (0.1563 V). If the amplitude is lower than range ($U = 0.1550$ V) both simulation and experimental spectrum is flat as fine quantization step of ADC2 is used for all samples. Experimental values are even lower than simulated ones because simulated input noise was higher than real. The results are close to theoretical value of -99.24 dB calculated from RMSE of ADC2. But if the amplitude U was increased only by cca 0.3 % extensive increase of 20dB occurred in low-frequency part of spectrum despite lower growth of RMSE (cca 7 dB). The peak of quantization noise can be even stronger if slightly higher amplitude is used. For simulated $U = 0.1700$ V (light gray line in the Fig. 3b) maximal spectral component is more than 10dB above theoretical value of -69.15 dB calculated from RMSE of ADC1. However later the spectrum becomes flatter with rising U approaching theoretical behaviour according to Eq. 3 like results for $U = 0.3125$ V depicted in the Fig. 3b.

5. Conclusions

Two channel of multiresolution structure has been used to analyse spectrum of quantization error for multiresolution quantization (MQ). The theoretically estimated spectrum of quantization noise is not flat as is generally supposed for simplification. It contains increased parts, even peaks at some frequencies, which are not inherent for measured signal but represent spurious components caused by restricted resolution of one stage of multiresolution structure. In some cases this disturbance leads to significant reduction of signal-to-noise ration (SNR) and dynamic range. The difference in distribution of power spectrum of quantization noise could be much higher for MQ than for simple uniform quantization. As presented for harmonic input signal critical input amplitude is just above the range of higher resolution ADC. For two 8-bit ADCs if ratio of ranges is 2^5 a difference between spectral components of quantization noise can reach 40 dB. Hereby a spurious component can exceed theoretical RMSE of the lower resolution ADC by more than 10 dB. So a ratio of maximal to minimal signal amplitude which is distinguishable for analysed MQ could correspond to 13-bit ADC. But SNR still corresponds only to 8-bit resolution.

Acknowledgements

Work presented in this paper was supported by the Slovak Ministry of Education under grant No. 2003SP200280802 and by the Slovak Grant Agency VEGA under grant No. 1/0551/09.

References

- [1] Braun S, Russer P. A Low-Noise Multiresolution High-Dynamic Ultra-Broad-Band Time-Domain EMI Measurement System. *IEEE Transactions on Microwave Theory and Techniques*, 53(11): 3354-3363, 2005.
- [2] Hejn K, Pacut A. Generalized Model of the Quantization Error - A Unified Approach. *IEEE Transactions on Instrumentation and Measurement*, 45(1): 41-44, 1996.
- [3] Widrow B, Kollár I. Quantization Noise. Roundoff Error in Digital Computation, Signal Processing, Control, and Communications. Cambridge University Press, Cambridge, 2008.
- [4] Claasen TACM, Jongepier A. Model for the Power Spectral Density of Quantization Noise. *IEEE Transactions on Acoustics, Speech and Signal Processing*, ASSP-29(4): 914-917, 1981.

Decomposition of Time Series – from Statistical to Linear System Approach

^{1,2}J.Holcik

¹Institute of Measurement Science, Slovak Academy of Sciences, Bratislava, Slovakia

²Institute of Biostatistics and Analyses, Masaryk University, Brno, Czech Republic

Email: umerholc@savba.sk

Abstract. In a field of statistical processing of time series, algorithms used for their decomposition to partial constituent components are ordinarily designed using statistical characteristics of the analysed series. On the other hand, the designed algorithms can be also often characterized by parameters and functions as frequency response, distribution of zeros and poles, impulse response, usually used in case of linear signal processing. The paper describes some classical algorithms for estimation of a time-series drift and analyses their properties using their frequency responses and discusses conditions of their application.

Keywords: Time Series, Decomposition, Moving Average Model, Linear Frequency Filter

1. Introduction

Standard methodology of statistical time series analysis starts by decomposition of a given time series representing realization of a random variable X_i to several constituent components (e.g. [1]). Depending on either additive or multiplicative model it is theoretically

$$X_i = T_i + Z_i + S_i + R_i \quad \text{or} \quad X_i = T_i \cdot Z_i \cdot S_i \cdot R_i, \quad (1)$$

where T_i is a (monotone) function of time called trend, Z_i describes a non-random long term cyclic process, S_i reflects non-random short time periodic seasonal component, and finally R_i is a random noise variable representing all the deviations from the ideal deterministic part of the model. We suppose R_i is a white noise with normal distribution with expectation $E(R_i) = 0$. Sometimes, the variables describing trend T_i and long-term oscillations Z_i are summarized together

$$D_i = T_i + Z_i, \quad (2)$$

and the resulting summarized variable D_i is called drift. The basic task of the time series analysis is to determine and separate deterministic slow components T_i , Z_i , or D_i , and periodical seasonal series S_i from random noise R_i .

2. Algorithms for Drift Estimation

Let us assume an additive model now. If we do not deal with models of trend based on functional approximation then the most often used methods for estimation of the slow drift components are based on moving average (MA) approach.

A MA filter is a type of a finite impulse response filter computing a series of weighted averages of consequential segments of the full data series. For weighted MA filter it is valid that

$$y_i^{\text{MA}} = \sum_{k=i-L1}^{i+L2} w_k X_i \quad (3)$$

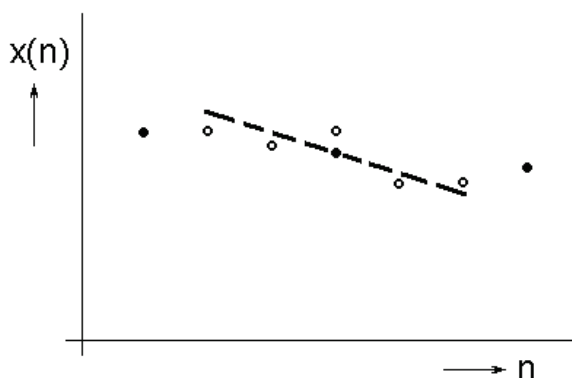
where

$$\sum_{k=i-L1}^{i+L2} w_k = 1 \quad (4)$$

and

$$L = L1 + L2 + 1 \quad (5)$$

defines an order of the MA filter, i.e. length of its impulse response. The coefficients w_k unambiguously defines properties of the filter (in time as well as in frequency domain) and its impact to processed data. If $L1 = L2$ and the sequence of weight coefficient is symmetrical with respect to central sample then the filter does not introduce any phase distortion. That is why odd number of samples in filter impulse response is usually used in this case. Another reason for preferring impulse response with odd samples is its simpler design.



In the field of time series statistical processing two basic approaches are used for design of the filter weight coefficients - algorithms based on smoothing by polynomial functions and filters with exponentially descending weights. The former method usually can take advantage of the above mentioned property of the symmetrical sequence of the MA filter weight coefficients, in case of the latter it is not possible, in principle.

Fig.1 Smoothing of a sequence of five samples by means of a polynomial of the 1st order

3. MA Filters Based on Smoothing by Polynomial Functions

This method (e.g.[2]) is based on an idea that any “reasonable” function can be quite reliably LMS approximated by a polynomial function (Fig.1) of a given order. Then the filtered value is determined as a value of the polynomial function at a position of the substituted sample.

The task necessary to solve before smoothing is to decide which order of the polynomial should be used for the approximation and what the length of the approximated segment is.

Table 1. Weights of MA filters determined by means of polynomial smoothing (partially according to [2])

Length of the segment	Order of the approximating polynomial		
	1 st	2 nd and 3 rd	4 th and 5 th
3	1/3.(1, 1, 1)	(0, 1, 0)	(0, 1, 0)
5	1/5.(1, 1, 1, 1, 1)	1/35.(-3, 12, 17, ...)	(0, 0, 1, ...)
7	1/7.(1, 1, 1, 1, 1, 1, 1)	1/21.(-2,3,6,7,...)	1/231.(5,-30,75,131,...)
9	1/9.(1, 1, 1, 1, 1, 1, 1, 1, 1)	1/231.(-21, 14, 39, 54, 59,...)	1/429.(18,-45,-10,60,120,143,...)

Intuitively, we can say that the higher the order of the polynomial is, the broader the frequency pass-band of the filter is. And the longer the segment is, the narrower the frequency pass-band is. It can be often found in statistical literature that the length of the MA segment should correspond to the period of the seasonal component present in the data series. Generally, it can be true. However, relationship between the length of the segment and period of the seasonal component is not so simple.

Tab.1 depicts weights of filter coefficient for different orders of smoothing polynomials and lengths of smoothed data segments. It can be seen that application of the polynomial of the first order results in filter with rectangular impulse response, computing response as uniformly weighted mean value. Such filters correspond to so called Lynn’s filters [4], very often used filters in biomedical signal and data processing as ECG signals [5].

In statistical time series processing, data representing analysed processes are often sampled with a month sampling period. Such data (biological, financial, ...) usually have a seasonal

component with one year period, it means 12 samples, as well. From the above mentioned recommendation it follows that the length of the filter impulse response should be 12 samples,

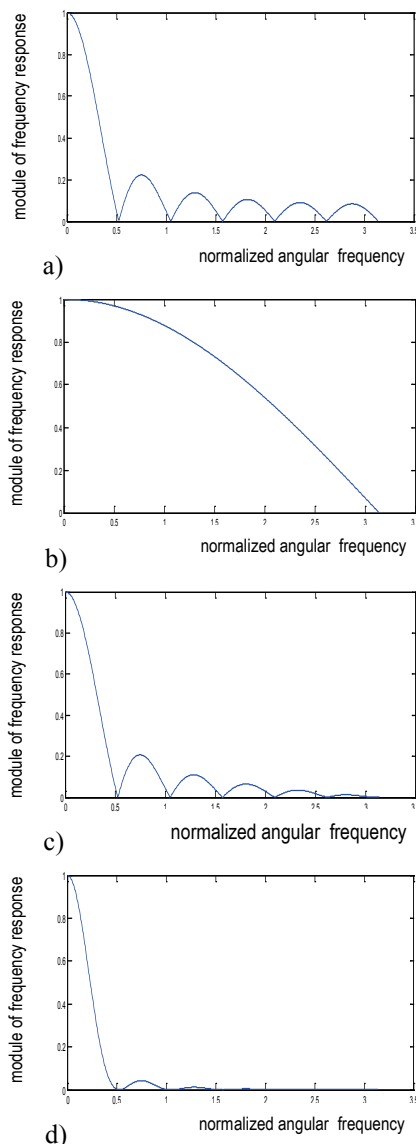


Fig.2 Magnitude frequency responses of the MA filters – a) rectangular impulse response of the length of 12 samples; b) filter with frequency response according to eq.(6); c) filter with frequency response according to eq.(8); d) serial connection of two filters with $H_1(z)$.

seasonal component.

In Fig.3 there are magnitude frequency responses of MA filters based on smoothing data by polynomial of higher orders – the 3rd and 5th order. It is obvious that the higher polynomial order represents broader width of the filter pass-band and on contrary longer length of the filter impulse response (with the same polynomial order) decreases filter cut-off frequency. In all the depicted examples, cut-off frequencies of the filter pass-bands are higher than the fundamental frequency of the seasonal component. It means that the seasonal components have to substantially affect outputs of the filters.

as well. Magnitude frequency response $|H_1(z)|$ of such a filter is depicted in Fig.2a. We can see that zero points of the response are exactly at frequencies that correspond to seasonal period and its integer multiples. Unfortunately, the impulse response has even number of samples and that is why a phase frequency response is not precisely linear, even if the deviations from linearity do not look important. To improve a shape of the phase response of the filter, serial connection of the filter smoothing data with a polynomial of the first order with filter having transfer function defined as

$$H_2(z) = \frac{1}{2}(1 + z^{-1}) \quad (\text{Fig.2b}) \quad (6)$$

Impulse response of the resulting filter is

$$\begin{aligned} g_3(n) &= 1/12. \{1, 1, 1, 1, 1, 1, 1, 1, 1, 1, 1, 1\} \otimes \\ &\quad \otimes \{1/2, 1/2\} = \quad (7) \\ &= 1/12. \{0.5, 1, 1, 1, 1, 1, 1, 1, 1, 1, 1, 1, 0.5\}, \end{aligned}$$

which is the most commonly used filter in statistical decomposition of time series. For its transfer function it is valid that (Fig.2c)

$$\begin{aligned} H_3(z) &= \frac{1}{12}(0.5 + z^{-1} + z^{-2} + z^{-3} + z^{-4} + \\ &\quad + z^{-5} + z^{-6} + z^{-7} + z^{-8} + z^{-9} + \\ &\quad + z^{-10} + z^{-11} + 0.5z^{-12}) \quad (8) \end{aligned}$$

Its zeros remain at the same frequency as zeros of the original filter and attenuation of the side lobes is proportional to that of $H_2(z)$.

To improve attenuation of the higher frequency components (with frequency above the fundamental frequency of the seasonal component) it is possible to use a serial connection of two filters with $H_1(z)$ (Fig.2d).

All the above described filters have zeros at frequencies corresponding to those of periodical seasonal component (integer multiples of $0.52 \text{ rad.sample}^{-1}$). It means that the estimated drift is free of any influence of the

4. Filters with Exponential Weights

Formula defining exponential smoothing filter

$$y_i^{EXP} = (1 - b)x_i + (1 - b)bx_{i-1} + (1 - b)b^2x_{i-2} + (1 - b)b^3x_{i-3} + \dots \quad (9)$$

can be rewritten recursively as

$$y_i^{EXP} = (1 - b)x_i + b[(1 - b)x_{i-1} + (1 - b)bx_{i-2} + (1 - b)b^2x_{i-3} + \dots] = (1 - b)x_i + b.y_{i-1}^{EXP}$$

This difference equation corresponds to a transfer function

$$H_{EXP}(z) = \frac{1 - b}{1 - b.z^{-1}} = \frac{a}{1 - (1 - a).z^{-1}} \quad (10)$$

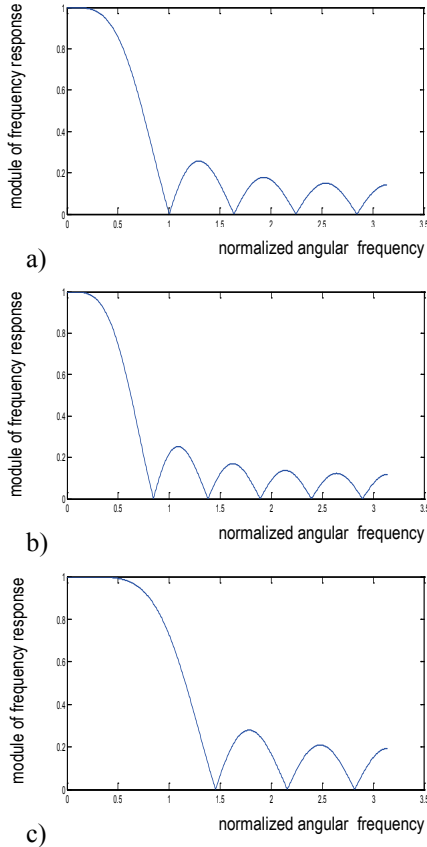


Fig.3 Magnitude frequency responses of filters designed for – a) 3rd order polynomial and 11 sample impulse response; b) 3rd order polynomial and 13 sample impulse response; c) 5th order polynomial and 11 sample impulse response.

where b is so called discount constant and $a = 1 - b$ is a smoothing constant. An example of modular frequency response is in Fig.4. The function is smooth without any zero points. It means that the filter is really not acceptable for processing time series with seasonal component. The width of a pass-band is proportional to the smoothing constant a . The greater the value of the smoothing constant is, the broader is the filter pass-band and the filter is also more stable. It is also necessary to realize that the impulse response is not symmetrical and that is why the phase frequency response of the filter is not linear (Fig.4). That fact can cause a heavy phase distortion in the filtered series.

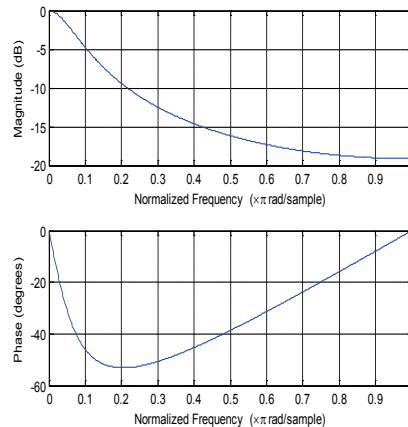


Fig.4 Magnitude and phase frequency response of the filter with exponential weight for smoothing constant $a=0.2$

5. Conclusions

Frequency responses as well as other ways of description properties of linear algorithms designed using statistical characteristics of the analysed time series can and should be used as an adequate tool for verification of assumed properties of the algorithms and their expected effect to the processed data. Unfortunately, it is not the case in statistical approaches to time series processing.

Acknowledgements

This work was partially granted by the research project No. 2/0210/10 of the VEGA Grant Agency in Slovakia.

References

- [1] Falk M. A First Course on Time Series Analysis. Examples with SAS. Chair of Statistics, University of Würzburg, 2006, 240p.
- [2] Cipro T. Financial Econometry. Ekopress, Praha 2008, 538p (in Czech).
- [3] http://en.wikipedia.org/wiki/Moving_average (Feb 25th, 2011)
- [4] Lynn P.A. An Introduction to the Analysis and Processing of Signals. Macmillan, 1989, 277p.
- [5] Holcik J, Kozumplik J. Digital Filtering of ECG Signals. Lékař a technika, 17 (6):114-119,1986 (in Czech).

Choice of Measurement for Phase-Space Analysis: Review of the Actual Findings

A. Krakovská, K. Mezeiová

Institute of Measurement Science, Slovak Academy of Sciences,
Bratislava, Slovak Republic
Email: krakovska@savba.sk

Abstract. *If data are generated by a d -dimensional system, but only one observable is known, Takens' theorem guarantees that reconstruction diffeomorphic to the original dynamics can be build from the single time series in $(2d+1)$ -dimensional phase space. However, some recent results show that, under certain conditions reconstruction in lower dimension is possible, whereby the choice of the variable used for the embedding may be critical. A short review of the latest results and methods regarding transition from single time series to multi-dimensional phase portrait is given. The choice of the lowest possible dimension for the manifold reconstruction and the choice of the variable with the highest observability index are discussed.*

Keywords: Observability, Takens' theorem, Rössler, Lorenz

1. Introduction

Measured data have often a form of scalar time series - sequence of numbers, typically spaced at uniform time intervals. There are two main approaches to time series analysis. The first one views time series as a manifestation of a stochastic process, and works with the traditional statistical tools. The second - younger - approach sees time series as produced by a deterministic dynamical system. The second type of data handling, often called non-linear, originates in physics and the theory of nonlinear dynamical systems. It is not older than 25-30 years and initially its development was quite independent from the established statistical methodology. However, the two schools are still less and less separated. Statisticians discover the power of the state-space idea, while the “dynamicists” realized that taking advantage of rich resources of statistics accelerates further progress in their field.

In 1981 Takens mathematically established that, if we know a single variable of a dynamical system with sufficient accuracy, then it is possible to reconstruct a state portrait, topologically equivalent to the attractor of the original system [1]. Assume that the dynamics has an attractor of box-counting dimension d . According the Takens' delay theorem, the attractor can be embedded (by means of diffeomorphism - one to one, everywhere differentiable with a differentiable inverse) in D -dimensional Euclidean space whereby $D \geq 2d+1$. The theorem has a powerful implication: under certain conditions one single observable is enough for reproducing and studying of complex multi-dimensional underlying dynamics.

Diffeomorphism between the original manifold and its reconstructed image preserves relevant geometrical and dynamical invariants like the dimension of the attractor or the Lyapunov exponents (measure of the sensitivity to initial conditions). It also holds that trajectories which are close in the original state space are also close in the embedding space. This leads to a successful technique of noise reduction and prediction based on the so called method of analogs: in order to predict the next step of the series, take the last point in the reconstructed space, find the nearest point from the past with a known successor, and assume that the current point will make the analogous move.

Experimental researchers unexpectedly got a valuable tool to extract black-box models for complicated systems directly from one or a few measurements. Takens' theorem gave rise to thousands of interesting publications since its statement.

However, some new results suggest that, the investigation of time series based on the multi-dimensional reconstruction can be even more enhanced.

These results and their perspectives will be introduced in the present paper.

2. Review of Methods and Results

The lowest possible dimension for multi-dimensional reconstruction

Let us remind that, if the data are generated by a d -dimensional system, Takens' theorem guarantees that $(2d+1)$ -dimensional embedding is equivalent to the original dynamics.

While this is satisfactory for theoretical work, in practice an embedding of lowest possible dimension is preferred, ideally a d -dimensional embedding. But can we use lower than $(2d+1)$ -dimensional space? Or we may ask: is the condition of $(2d+1)$ -dimensional space sufficient or necessary? As far as almost 30 years after appearance of the Takens' theorem this question has not been theoretically treated. But lately, Cross and Gilmore contributed to the issue, when they analyzed differential mappings of the rotationally equivariant Lorenz dynamical system in some detail [2]. They showed that, while the differential reconstruction based on the x coordinate is an embedding of the attractor in three dimensions, it does not yield an embedding of the entire manifold. The projection of the manifold into \mathbb{R}^3 possesses singularities. However it is possible to embed the manifold into a 3-dimensional twisted submanifold of \mathbb{R}^4 . Then not only diffeomorphism invariants (fractal dimensions, Lyapunov exponents, and so on) but also information about the mechanism responsible for generating chaotic behaviour is preserved. The authors say that the failure to achieve an embedding in \mathbb{R}^3 is related to the different symmetry properties of original and the reconstructed attractor. They showed that the two systems are actually equivalent under topological deformation (isotopic) in \mathbb{R}^4 . Nonisotopic embeddings provide distinct or inequivalent representations of an attractor, as one may not be deformed into another without selfintersection. In a sufficiently high dimension, not greater than $2d+1$ for d -dimensional systems, and 5 for 3-dimensional dynamical systems, all embeddings are equivalent [3]. However, so far little is known about lower than $(2d+1)$ -dimensional embeddings of dynamical systems with $d > 3$.

Choice of variable for reconstruction: univariate case

Theoretically, the variable used for the reconstruction of the attractor can be chosen arbitrarily. In practice, however, some variables seem to be more convenient for analysis than others. For instance, it is much easier to obtain a global model from variable y of the Rössler system than from variable z . When we are facing an unknown system with single known time series, it would be useful to be able to estimate if it is a good variable or not. In other words: we are looking for some index, usually called „observability“ that enables ranking of the observables according to their effectiveness in the reconstruction process.

The concept of observability in control theory is standard and well defined. However, it is a type of “yes or no” measure, that is, the system is evaluated as either observable or not for a given output data series. If a system is observable, it is possible to determine the behaviour of the entire system. If it is not observable, then the output data disallow to estimate (and control) the states of the system completely. To check if a linear system with n states is observable, the rank of the so-called observability matrix is calculated. If it is equal to n , then the n rows are linearly independent, each of the n states of the system is given through linear combinations of the output variables and the system is observable.

As concerns nonlinear systems, the notion of observability is not firmly established yet. Since 1998, Letellier et al. have introduced several measures that rank the variables of the system

according to their observability - assuming that the reconstruction space has the same dimension as the original one [4], [5], [6].

In [5] the authors proposed a definition of observability for nonlinear systems, related to the Jacobian matrix of the coordinate transformation between the original phase space and the differential embedding induced by the given variable. The system is fully observable when the determinant of the Jacobian never vanishes.

In [6] the so-called symbolic observability coefficient has been introduced. The computation of symbolic observability coefficients is based on the so-called fluency matrix of the system, which emphasizes constant and nonconstant elements of the Jacobian matrix, corresponding to linear and nonlinear terms in the vector field of the system. The symbolic observability coefficients are greater than one when the dimension of the reconstructed state space is too large. For some systems the symbolic observability indicates the sufficient dimension to be smaller than provided by the Takens' criterion.

Disadvantage of the above indices is that their estimation is limited to the cases in which the equations of the system are known.

In [7] a procedure is put forward by which it is possible to compare two observables of the same system without the need of the system equations. The proposed time-series approach is based on a recently defined omnidirectional nonlinear correlation functions and it agrees very well with the older indices with respect to observability order of benchmark systems variables. For example, for 3-dimensional chaotic Rössler system the results were in total agreement, indicating that y variable is the best and z is the worst choice for the reconstruction.

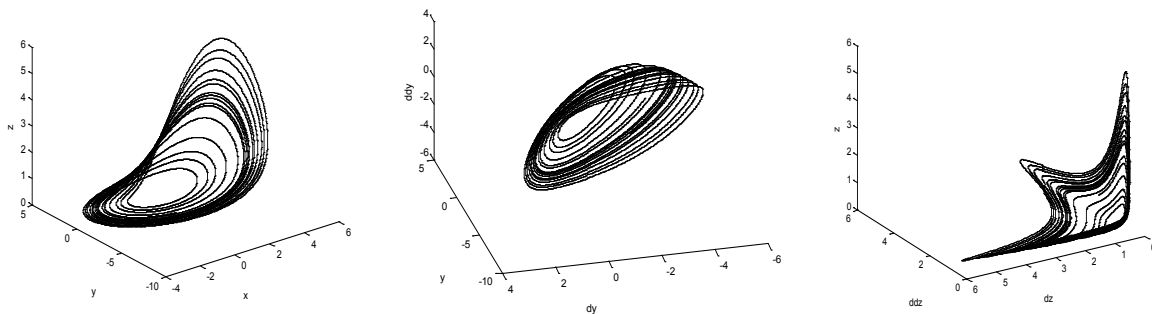


Fig. 1. Attractor of the Rössler system. From right to left: original attractor, reconstruction from y variable and reconstruction from z variable.

Choice of variable for reconstruction: multivariate case

In practice, sometimes more than one physical variable is recorded simultaneously. For example, physiological or economic data are often multivariate.

According to Takens' theorem, one variable suffices for reconstructing a space equivalent to the original phase space - multivariate time series are not required. However, in real world systems, in particular when the dimension of the original phase space is large, there may be advantageous to use more of the measurable variables. As an artificial example Lorenz system can be mentioned. If one variable is used for 3-dimensional reconstruction, the system is not observable. But the combination of x -variable, delayed x -variable and z -variable leads to system that is topologically equivalent to the original [6].

It might seem to be evident that use of more different observables is always preferable to univariate embedding. But it is not true in general. Univariate embeddings are often evenly successful as the best combinations of several measurements.

Moreover, looking for the right multivariate combination is somewhat more complicated than use of a single series, mainly because there is a large choice of possible embeddings. One of a very few tests for optimal choices of observables from a multivariate set is based on

eliminating linear dependence using singular value decomposition. Some observability based test would be very helpful in multivariate analysis.

3. Discussion

The concepts discussed in this paper are of great relevance in phase-space reconstruction problems. We summarized the latest results evidencing that variables of a dynamical system are not equally effective in reconstructing the dynamics from a scalar time series.

On the present we have observability indices available for evaluating the variables in the cases when the system equations are known. Let us use this knowledge as a benchmark and try to find a method how to identify the “good” and “bad” observables in situations, when we are facing an unknown system with one or more scalar time series recorded.

As a first step we can return to the methods that have been used for the estimation of the embedding dimension during past 25-30 years. They are based on step by step expansion of the reconstruction space with simultaneous following of some proper invariants (correlation dimension, largest Lyapunov exponent, predictability, percentage of false nearest neighbours, and so on), which are expected to stay constant after reaching the sufficient embedding dimension. Now, having the benchmark systems of known observability, we can evaluate the worthiness of these methods with accuracy that was not possible before.

Let us begin with false nearest neighbours method (FNN), which is the most popular tool for selection of minimal embedding dimension. The idea of FNN is that if the current embedding dimension d is sufficient to resolve the dynamics, then the images reconstructed in higher dimensions will no longer change considerably. In particular, points which were close in the d -dimensional space should remain close in the $(d+1)$ -dimensional space. But if the embedding dimension is too small, points, which are in reality far apart, may seem as neighbours (consequence of projecting into a smaller space).

As the next presentation shows, the results of the FNN method do not contradict to observability indices, though its ability to detect the best observables is limited.

Acknowledgements

This work was supported by Slovak Grant Agency for Science (grant No 2/0019/10).

References

- [1] Takens F. Detecting Strange Attractors in Turbulence. *Lecture Notes in Mathematics*, 898, 366-381, 1981.
- [2] Cross DJ, Gilmore R. Differential embedding of the Lorenz attractor. *Physical Review*, E 81, 066220-9, 2010.
- [3] Cross DJ, Gilmore R. Representation theory for strange attractors. *Physical Review*, E 80, 056207-6, 2009.
- [4] Letellier C, Maquet J, Le Sceller L, Gouesbet G, Aguirre LA. On the non-equivalence of observables in phase-space reconstructions from recorded time series. *J. Phys. A: Math. Gen.*, 31, 7913–7927, 1998.
- [5] Letellier C, Aguirre LA, Maquet J. How the choice of the observable may influence the analysis of nonlinear dynamical systems. *Communications in Nonlinear Science and Numerical Simulation* 11, 555–576, 2006.
- [6] Letellier C, Aguirre LA. Symbolic observability coefficients for univariate and multivariate analysis. *Physical Review*, E 79, 066210-11, 2009.
- [7] Aguirre LA, Bastos SB, Alves MA, Letellier C. Observability of nonlinear dynamics: Normalized results and a time-series approach. *Chaos* 18, 013123-9, 2008.

Choice of Measurement for Phase-Space Reconstruction: Decision Based on False Nearest Neighbors Method

K. Mezeiová, A. Krakovská

Institute of Measurement Science SAS, Bratislava, Slovak Republic

Email: Kristina.Mezeiova@savba.sk

Abstract. *False nearest neighbors (FNN) method is examined with respect to equivariance of individual observables. The aim is to reveal the most appropriate observable for phase space reconstruction. Results calculated for benchmark systems are compared with symbolic observability degrees. The FNN method resulted in different values of embedding dimensions when calculated for various observables of the same dynamical system. The results roughly corresponded to the symbolic observability degrees; however, in some details disagreed with them.*

Keywords: False Nearest Neighbors Method, Observability, Equivariance of Observables

1. Introduction

According to the Takens' theorem [1] a sufficient embedding dimension to reconstruct a phase space topologically equivalent to the original space is $2m+1$, where m is the dimension of the attractor of the system, and the embedding can be done by delayed coordinates of a single observable. Takens' theorem states the sufficient condition of the embedding dimension, however, for many systems the embedding can be reached in fewer dimensions. The second problem not solved is the fact, that if we have more observables from the same system, they are not equivalent with respect to the phase space reconstruction – for one observable the embedding can be reached in less dimensions than for the another one.

Letellier et. al. [2] extended the theory of observability to nonlinear systems and later proposed the symbolic observability coefficients η , which quantify the level to which the system is observable based on the measurement of some variable. Details of the computation are explained in [2].

What to do in practice when the equations are unknown? The aim of this paper was to compare the method of False nearest neighbors, which is traditionally used to estimate the embedding dimension, with the results of the symbolic observability coefficients.

2. Methods

False nearest neighbors algorithms

False nearest neighbors method [3] is an iterative algorithm which estimates the embedding dimension of the system. In its n^{th} step the phase space is reconstructed into n dimensions by taking the time delayed coordinates of the measured time series: $y_i = x_i, x_{i-\tau}, \dots, x_{i-(n-1)\tau}$, where x is the measured time series and τ is the time delay. In this paper the time delay was set as the first minimum of the mutual information function [4]. For each point $\mathbf{y}(\mathbf{n})$ the distance $R(\mathbf{n})$ to its k^{th} nearest neighbor $\mathbf{y}^k(\mathbf{n})$ is calculated. If $\mathbf{y}^k(\mathbf{n})$ is close to $\mathbf{y}(\mathbf{n})$ not due to the dynamics of the system, but due to a projection of the trajectory from the natural phase space to the lower dimensional space, in the $n+1$ dimensions the distance $R(n+1)$ between these two points becomes large and $\mathbf{y}^k(\mathbf{n})$ is called a false nearest neighbor. Criterion for a

neighbor to be false can be evaluated by the formula: $\sqrt{\frac{R^2(r, n+1) - R^2(r, n)}{R^2(r, n)}} > R_{tol}$, where R_{tol} is some threshold.

There is also a second criterion for the nearest neighbor to be false – if it is not a close point to $\mathbf{y}(\mathbf{n})$. E. g. if the distance $R(\mathbf{n})$ is half the size of the attractor, then the iterated distance $R(\mathbf{n}+1)$ can be maximally $2R(\mathbf{n})$ if $\mathbf{y}(\mathbf{n}+1)$ and $\mathbf{y}^k(\mathbf{n})$ are located at the extremes of the attractor. Such points are considered to be false neighbors and the second formula for the point to be a false neighbor is: $\frac{R(\mathbf{n}+1)}{R_A} > A_{tol}$, where R_A is some attractor's size and A_{tol} is the second threshold.

Here R_A was set to the standard deviation of x .

In each dimension the percentage of the false nearest neighbors is calculated and algorithm terminates when the percentage drops to zero. In this paper the thresholds were adjusted to $R_{tol} = 15$ and $A_{tol} = 2$ and only the first nearest neighbor was taken into account.

Symbolic observability degrees

The symbolic observability degrees η calculated at the dimensions of the dynamical systems were taken from [2].

Systems

Following systems were integrated by the means of the 4th order Runge-Kutta formula with integration step 0.01:

Rössler system:

$$\dot{x} = -y - z, \quad \dot{y} = x + ay, \quad \dot{z} = b + z(x - c),$$

where $[a, b, c]$ are bifurcation parameters; in this study the values were $[0.398, 2, 4]$; initial conditions were $[0, 0, 0.4]$.

Lorenz system:

$$\dot{x} = \sigma(y - x), \quad \dot{y} = Rx - y - xz, \quad \dot{z} = -bz + xz,$$

with the parameters $[\sigma, R, b] = [10, 28, 8/3]$ and the initial conditions $[0.3, 0.3, 0.3]$.

Sprott F system:

$$\dot{x} = y + z, \quad \dot{y} = -x + ay, \quad \dot{z} = -bz + x^2,$$

with the parameters $[a, b] = [0.5, 1]$ and the initial conditions $[0.05, 0.05, 0.05]$.

Hyperchaotic Rössler system:

$$\dot{x} = -y - z, \quad \dot{y} = x + ay - w, \quad \dot{z} = b + xz, \quad \dot{w} = -cz + dw,$$

with parameters $[a, b, c, d] = [0.25, 3, 0.5, 0.05]$ and the initial conditions $[-10, -6, 0, 10.1]$.

3. Results

For the selected dynamical systems the false nearest neighbors method was computed with the time delay set to the minimum of the mutual information function (see Fig. 1). Results and parameters of the calculations of the FNN method as well as the values of the symbolic observability degrees η can be found in Table 1.

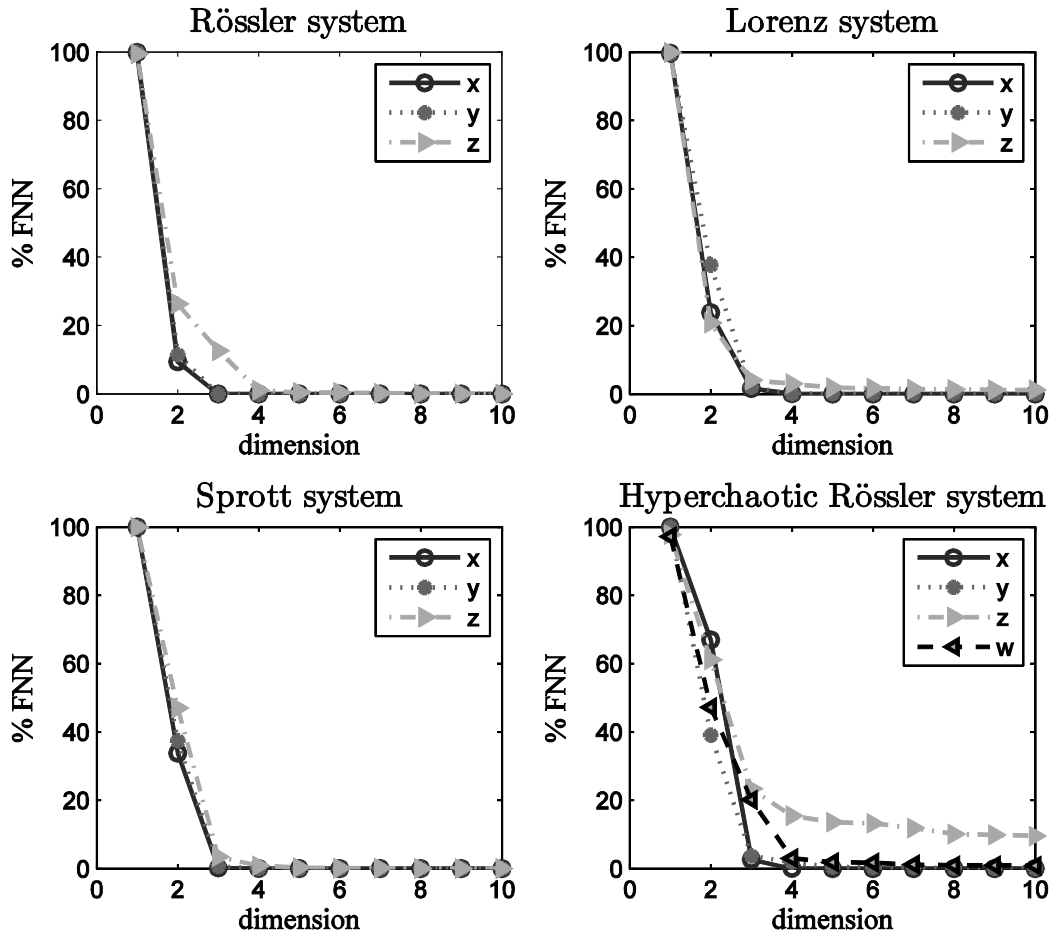


Fig. 1. False nearest neighbors method calculated with the parameters $R_{tol}=15$ and $A_{tol}=2$.

The FNN method can be evaluated in two ways. The result is either the embedding dimension – the dimension at which the percentage of false neighbors approaches zero - or directly the percentage of false neighbors in the dimension, at which also the symbolic observability degrees were calculated.

Both ways implied the same consequences: the FNN method resulted in different values of the embedding dimensions when calculated for various observables from the same dynamical system. The worst observable (with the lowest η) resulted with the highest embedding dimension as well as achieved the highest percentage of false neighbors at the dimension of the dynamical system. However, some details were not in according with the observability coefficients. The FNN algorithm did not distinguish variables with slightly different observability degrees or even resulted with higher embedding dimension for slightly more observable variable.

E.g. for the Rössler system the η values can be sorted from the highest value to the lowest one as $\eta_y > \eta_x > \eta_z$; Rössler system with the value $\eta_y = 1$ is observable in 3 dimensions. The results of FNN for the Rössler system implied that the z observable appeared to be the less appropriate observable for the reconstruction of the phase space with the embedding dimension 5. However, there was no difference between variables x and y, which both resulted in the embedding dimension 3. Similar findings can be written about all benchmark systems.

Table 1. Parameters and results of the FNN method and comparison with the symbolic observability degrees. Min MI – index, at which the first minimum of the mutual information function appeared; $d(\text{FNN} \sim 0)$ – dimension, at which the % of false nearest neighbors approached zero (decreased below 1%, resp.); η – symbolic observability degree; $\% \text{FNN}(d = d_{\text{DS}})$ - % of FNN at the dimension of the original dynamical system

* % FNN did not decrease below 1 % even in the highest dimension calculated

System	Observable	min MI	$d(\text{FNN} \sim 0)$	η	$\% \text{FNN}(d = d_{\text{DS}})$ [%]
Rössler	x	160	3	0.88	0
	y	171	3	1	0
	z	159	5	0.44	12.62
Lorenz	x	24	4	0.89	1.5571
	y	24	4	0.46	2.0185
	z	19	>10*	0.35	4.0493
Sprott	x	187	3	1	0.1317
	y	195	3	1	0.6176
	z	229	4	0.44	3.4729
Hyperchaotic Rössler	x	181	4	0.85	0.03
	y	168	5	0.92	1.89
	z	178	>10*	0.56	15.43
	w	203	8	0.69	3.02

4. Discussion and Conclusion

The results of the FNN method roughly corresponded to the values of the symbolic observability degrees; however, in some details disagreed with them. The FNN algorithm is dependent on the value of the time delay and on the parameter R_{tol} ; the results can differ with various values of these two parameters.

Although the FNN method mirrors to some extent various ability of the variables to reconstruct the phase space, it is not ideal for the choice of the measurement. As the next plan other measures will be examined, e.g. the predictability of the time series based on the reconstructed phase space from different observables.

Acknowledgements

This work was supported by Slovak Grant Agency for Science (grant No 2/0019/10).

References

- [1] Takens F. Detecting strange attractors in fluid turbulence. In Dynamical systems and turbulence. Rand D, Young LS, editors. Springer, Berlin, 1981.
- [2] Letellier C, Aguirre LA. Symbolic observability coefficients for univariate and multivariate analysis. *Physical Review E*, 79: 066210, 2009.
- [3] Kennel MB, Brown R, Abarbanel HDI. Determining embedding dimension for phase-space reconstruction using a geometrical construction. *Physical Review A*, 45(6): 3403-3411, 1992.
- [4] Fraser AM, Swinney HL. Independent coordinates for strange attractors from mutual information. *Physical Review A*, 33(2): 1134-1140, 1986.

Temporal Pooling Method for Rapid HTM Learning Applied to Geometric Object Recognition

^{1,2}S. Štolc, ^{1,2}I. Bajla, ³K. Valentín, ³R. Škoviera

¹ Institute of Measurement Science, Department of Theoretical Methods,
Slovak Academy of Sciences, Bratislava, Slovakia

² Austrian Institute of Technology, GmbH,
Department Safety and Security, Seibersdorf, Austria

³ Faculty of Mathematics, Physics, and Informatics, Department of Applied
Informatics, Comenius University, Bratislava, Slovakia

Abstract: *In the paper, we propose an alternative approach to the temporal pooling of the Hierarchical Temporal Memory (HTM) – a biologically inspired large-scale model of the neocortex. The novel method is compared with the conventional temporal pooling algorithm based on a smooth traversal of training images and their efficiency is demonstrated on a problem of the position, scale, and rotation-invariant recognition of simple geometric objects. Results have shown that the proposed method provides significantly faster convergence to the theoretical maximum classification accuracy than the conventional one.*

Keywords: *Hierarchical Temporal Memory (HTM); Temporal Pooling; Rapid Learning; Image Explorer; Position, Scale, and Rotation-Invariant Pattern Recognition*

1 Introduction

Hierarchical Temporal Memory (HTM), proposed by [1,2] and implemented as the free software package by Numenta, Inc. [3,4], is a recent development of an artificial intelligence network that excels at ambiguous pattern recognition problems. Promising results have been achieved in application of HTM to various pattern recognition/classification problems in machine vision, voice recognition, and other application areas [5,6]. These results usually refer to the situation in which the objects have fixed position and scale within the network's field of view (retina). The application of the HTM network to problems of the position, scale, and rotation-invariant recognition represents another challenging step in a development its functions. For the design of a successful classifier in this class of problems, characteristic by its extreme variability of a potential input, it is crucial to find an appropriate set of features, which are enough robust against expected object transformations. Moreover, it is very important to use an effective training algorithm, requiring neither too large training set nor too long training process.

In the HTM model, a key source of the invariance has been identified with the temporal learning, called the *temporal pooling*. The traditional approach to the temporal pooling [3,4] utilizes pattern sequences, called the *temporal sequences*, which are generated by a smooth traversal (exploration) of training images. This method often suffers from a slow convergence, causing that HTM requires a quite long training process to deliver reasonable results. In the paper, we propose an alternative approach to the temporal pooling that allows for a faster and more efficient training of the HTM networks. To demonstrate this ability, we

conducted experiments with the position, scale, and rotation-invariant recognition of simple geometric objects, such as rectangles, triangles, or circles (represented as smoothed grey scale images) in which the efficiency of the both methods could be quantitatively compared.

2 Description of the HTM model

As proposed in [1,2,3], the HTM network forms a tree-shaped hierarchy of layers consisting of basic operational units called *nodes*. Each HTM node works in two modes – *learning* and *inference*. Within the learning phase the node performs two operations – *spatial pooling* and *temporal pooling*. Once these two steps are finished, the node can be switched to the inference mode. Although each node can be, in principle, trained by a different pattern sequence and contain its own spatial and temporal pooler data, a precondition of a successful position-invariant recognition is the equivalence of nodes at the same level. This, in fact, significantly simplify the whole training process, as only a single node needs to be trained at each network level and all the others share the same learned information.

Spatial pooling

In course of the spatial pooling, input patterns of each trained node are quantized into representative clusters. All clusters are characterized by their quantization center, which altogether form a codebook of spatial patterns approximating the input data. In the Numenta implementation of the spatial pooler, usually some kind of a smooth image explorer is used for collecting representative patterns. Their method depends strongly on an appropriate choice of the quantization parameter *maximum distance*, which specifies the size of the quantization clusters. Such an approach suffers from several weaknesses, which were addressed in [7]. In this study, we applied a different spatial pooling method that does not depend on any other parameters but the codebook capacity. This method randomly selects a required number of image patterns of a given size (e.g., 8x8 pixels) from provided training images and these patterns are afterwards considered as the quantization centers. In order to suppress appearance of irrelevant or empty patterns, the random selection is performed via the Metropolis-Hastings algorithm [8,9]. For running this algorithm, one needs to define two functions, the *pattern likelihood* and *pattern proposal* function. The pattern likelihood is a function of an image pattern X and accounts for assessing its relative relevance. For the purposes of this study, we used the following pattern likelihood function: $L(X) = (E(X^2))^k$, where $E(\cdot)$ is the arithmetic mean over the pattern intensity values, and k is a tunable constant (in our case, $k = 4$ worked very well). The proposed patterns were randomly sampled from the training images with coordinates uniformly distributed over the whole image extent.

Temporal pooling

In the temporal pooling step, the quantization centers are being grouped according to their temporal coherence within the training sequence of patterns. The resulting non-overlapping sets of codebook patterns are called *temporal groups*. The original HTM theory postulated several conditions, which are to be satisfied by any pattern sequence used for training HTM networks. The most crucial one is the condition of a smooth translation of objects within the network's retina, meaning that the position, rotation, scale, or illumination change smoothly

in time¹. Up to now, when dealing with the static images containing no inherent temporal information (unlike video streams), the temporal pooling has been accomplished by means of some sort of a smooth traversal of training images (e.g., along the horizontal lines or a smooth Brownian-like random walk), in course of which a sequence of image patterns is generated. Hereinafter, we refer to this type of the image exploration as the *smooth explorer*. The generated pattern sequence then serve for estimating the temporal statistics reflecting temporal coherences of the codebook patterns. The concept the smooth image exploration, however, can be implemented many different ways, which may end up in significantly different temporal groups in terms of their invariance. Usually the reason is that different temporal pooling approaches may provide differently accurate temporal statistics, though based on the same training data. As the temporal learning is most important factor influencing the invariance provided by HTM, an efficient temporal pooling algorithm is crucial for its functionality. The construction of a novel more efficient temporal pooler was the objective of our research and it will be described in details in Section 3.

Inference

In the inference mode, each HTM node produces a vector of beliefs for all memorized temporal groups, given arbitrary input pattern. The resulting belief vectors are then passed to the next network level, where they serve as inputs for superior HTM nodes. For calculating beliefs over the temporal groups, we applied principle of a strong lateral inhibition called “*winner-take-all*”. According to this system, only one temporal group in a time can be active, meaning that the winning temporal group receives belief of 1 and the rest belief of 0. The active temporal group is always the one, which contains the codebook pattern that is closest (in L_2 sense) to the current input pattern.

Supervised classification

Usually at the very top of the HTM hierarchy, there resides a supervised classifier responsible for assigning predefined object categories (classes) to the concatenated belief vectors coming from HTM nodes on the top most network level. In the papers, one can find HTMs combined with various supervised classifiers, e.g., KNN, SVM, or MLP. In this study, we considered a simple *nearest neighbor* (NN) approach, as our intention was to investigate qualities of two temporal pooling algorithms, regardless of capabilities of any employed supervised classifier. The NN method is most suited for such a task, as its generalization power merely depends on the organization of the input data.

3 Alternative Approach to the Temporal Pooling Providing More Accurate Temporal Statistics

As already suggested, the main drawback of the Numenta-like smooth explorer is its slow convergence to the theoretical maximum classification accuracy. When the problem domain is large, pattern sequences produced by the smooth explorer need to be rather long to capture the

¹ Be aware that such a condition does not imply generation of pattern sequences, which are smooth in the sense of Euclidean metric, i.e., L_2 distance between patterns appearing nearby in a sequence is not necessarily small.

data in its entirety, assuring sufficiently accurate temporal statistics². When processing the training sequence, codebook patterns, which occur nearby in the training sequence (representing a virtual time), generate updates of the structure called the *time adjacency matrix* (TAM)³. In each training step, TAM is increased at the locations corresponding with the co-occurring codebook patterns according to the update function defined as follows [3,4]:

$$U(d) = \begin{cases} TM - d + 1 & \text{if } 0 < d \leq TM, \\ 0 & \text{otherwise,} \end{cases} \quad (3.1)$$

where $d \in \mathbb{N}$ is the temporal distance of the two patterns (i.e., the number of temporal transitions separating given two patterns in the training sequence) and TM is the Numenta parameter *transition memory*, which gives the maximum accepted number of temporal transitions.

To overcome weaknesses of the smooth explorer, we proposed a novel method of the temporal learning, the so-called *pair-wise explorer*. Instead of generating smooth random walks through images, our explorer performs the HTM training using pairs of relevant patterns sampled from a hypothetic infinite random walk, which crosses each image coordinate in each direction. These pairs of patterns are randomly sampled from the training images, so that distances \hat{d} of their coordinates follow the probability distribution $P(\hat{d})$, which is proportional to the update function $U(d)$ (see Eq. (3.1)), given some reasonable conversion between \hat{d} and d (e.g., $d = \lfloor \hat{d} \rfloor$). Each pair of patterns is considered as an extremely short temporal sequence, which produces exactly one TAM update having a constant influence and that ends immediately after processing the second pattern. Afterwards, the training can continue with processing another pair of patterns. The whole training is finished when requested number of TAM updates is performed.

When the temporal learning is over, the requested number of temporal groups is generated using the *agglomerative hierarchical clustering* (AHC). We have achieved good results with the *UPGMA*⁴ linkage and the dissimilarity measure $D_{i,j}$ given as:

$$D_{ij} = \begin{cases} 1 - TAM_{ij} / \sqrt{\max_i(TAM_{ij}) \max_j(TAM_{ij})} & \text{if } i \neq j, \\ 0 & \text{otherwise.} \end{cases} \quad (3.2)$$

4 Classification Experiments with Simple Geometric Objects

In order to demonstrate advantages of the pair-wise explorer over the smooth explorer, we conducted experiments with the position, scale, and rotation-invariant recognition of simple geometric primitives of three classes – circles, triangles, and rectangles. The objects were arbitrarily scaled, rotated and translated within the network's retina of 64x64 pixels. The

² Note that the overtraining effect does not apply to the temporal pooling. The longer training sequence is taken, the more stable and accurate temporal statistics is obtained.

³ TAM is a square matrix, where each row and column corresponds to a single codebook pattern. Thus, each coordinate in TAM has a unique association with a particular pair of codebook patterns. In our experiments, TAM was always updated symmetrically.

⁴ Unweighted Pair Group Method with Arithmetic Mean (UPGMA)

considered HTM network consisted of a single layer of non-overlapping nodes, each looking at the patch of 8×8 pixels. In accordance with the image size and types of used patterns, we set the codebook size to 512, the requested temporal group count to 64, and the transition memory to 4.

The classification accuracy was investigated with respect to two variable parameters. The first observed parameter was the number of training images varied from 10 to 300 per class, whereas the number of testing images was fixed at 300 per class. The second parameter was the number of TAM updates ranging between 1024 and 32768, which specified the length of training for the both temporal pooling methods and an equivalent basis. The classification accuracy was evaluated 10 times independently for each combination of the variable parameters and the average values have been used.

5 Results and Conclusions

In the performed classification experiments, the accuracy of NN classifier in the original space takes the values within the interval $\langle 0.378, 0.701 \rangle$. The classification accuracy for any of two HTM methods with sufficiently long training (i.e., sufficiently high number of TAM updates) increased up to 13.4 % in comparison with NN classifier (see Fig. 1, left). The proposed method of temporal pooling outperforms the conventional one with regard to both investigated parameters (i.e., the number of training images and the number of TAM updates). With the increasing number of TAM updates the difference between the two methods decreases asymptotically. For lower numbers of TAM updates within the interval $\langle 2896, 4096 \rangle$, our method yields the accuracy improvement of 1.104 in comparison with the conventional one. It corresponds to the cases for which the training sequence is quite short in the context of a given problem domain (see Fig. 1, right, and Tab. 1).

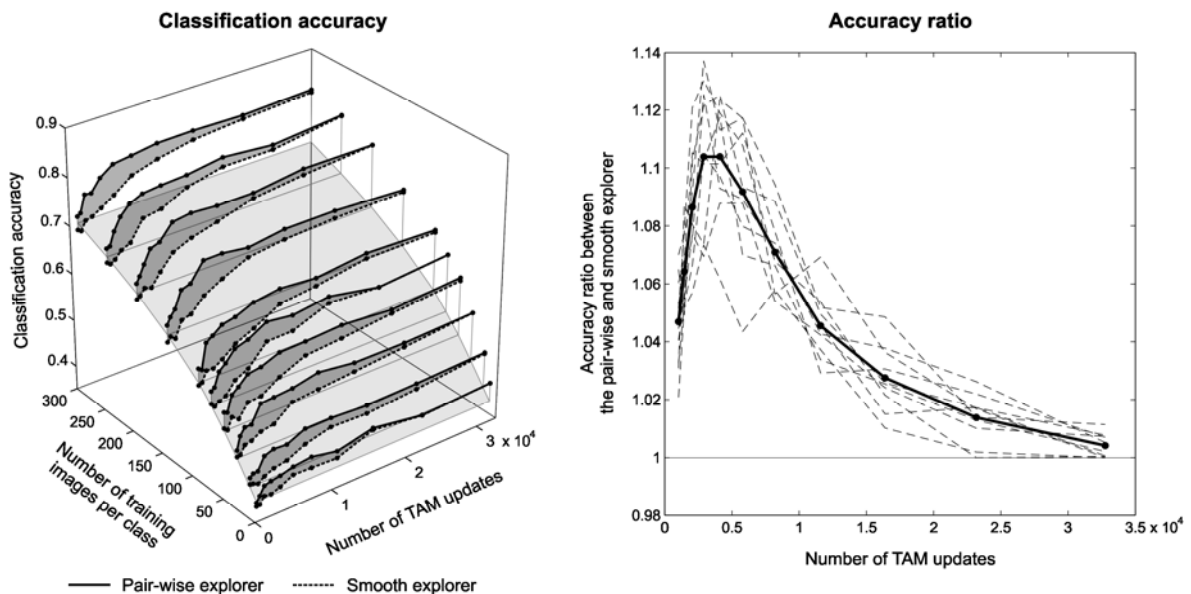


Fig. 1: (Left) The plot demonstrates that the pair-wise method outperforms the Numenta-like smooth method in terms of faster convergence mostly in the range of lower numbers of TAM updates. The gray surface represents the classification accuracy achieved by NN classifier performed in the original data space. (Right) The plot shows the classification accuracy gain of the pair-wise explorer over the smooth explorer.

Tab. 1: The actual values of classification accuracy ratio of the two temporal pooling methods, which have been averaged over variously sized training sets. The maxima of ratio are emphasized.

Number of TAM updates	1024	1448	2048	2896	4096	5793	8192	11585	16384	23170	32768
Mean accuracy ratio	1.047	1.064	1.086	1.104	1.104	1.092	1.071	1.046	1.028	1.014	1.004

The results have shown that, in contrast to the conventional method, the proposed novel temporal pooling method yields significantly faster convergence to the theoretical maximum classification accuracy with respect to both the length of the training sequence and the number of training samples. Therefore we suggest using this method instead of the conventional one, especially when dealing with complex large domain problems.

6 Acknowledgement

This work has been supported by the Slovak Grant Agency for Science (project No. 2/0019/10) and partially by the Foundation of Tatrabanka, through program E-talent for young scientists in the field of applied informatics (project No. 2010et019).

References

- [1] Hawkins, J. and Blakeslee, S. (2004). *On intelligence*. Henry Holt and Company, New York.
- [2] George, D. and Hawkins, J. (2009). Towards a mathematical theory of cortical micro-circuits. *PLoS Computational Biology* 5(10). DOI 10.1371/journal.pcbi.1000532.
- [3] Numenta (2008). Hierarchical Temporal Memory, concepts, theory, and terminology. Document version 1.8.0.
- [4] Numenta (2009). Numenta node algorithms guide, NuPIC 1.7.
- [5] Csapó, A., Baranyi, P., and Tikk, D. (2007). Object categorization using VFA-generated nodemaps and Hierarchical Temporal Memories. In: *5th IEEE Int. Conf. on Computational Cybernetics*, 257–261.
- [6] Sassi, F., Ascari, L., and Cagnoni, S. (2009). Classifying human body acceleration patterns using a Hierarchical Temporal Memory. In: R. Serra & R. Cucchiara, eds. *AI*IA 2009: Emergent Perspectives in Artificial Intelligence*. Berlin, Heidelberg, 496–505.
- [7] Štolc, S. and Bajla, I. (2010). On the optimum architecture of the biologically inspired Hierarchical Temporal Memory model applied to the hand-written digit recognition. *Measurement Science Revue* 10(2), 28–49. DOI 10.2478/v10048-010-0008-4.
- [8] Metropolis, N., et al. (1953). Equations of state calculations by fast computing machines. *Journal of Chemical Physics* 21, 1087–1092.
- [9] Hastings, W. (1970). Monte Carlo sampling methods using Markov chains and their applications. *Biometrika* 57, 97–109.

Comparison of Time Series Decomposition Methods

¹V. Svendova, ^{1,2}J. Holcik

¹Institute of Biostatistics and Analyses, Brno, Czech Republic,

²Institute of Measurement Science, SAS, Bratislava, Slovakia

Email: svendula@mail.muni.cz

Abstract. In this paper we presented some of the classical methods for the decomposition of a time series. We used moving average/median methods for removing trend and combined them with averaging and recursive methods for removing a seasonal component. We applied these methods to medical data of colorectal cancer incidence in the Czech Republic and results were compared using Fisher's g test statistics. Moving median in combination with either of the season removing methods proved to be the most effective method for the cancer incidence data.

Keywords: time series decomposition, moving average, moving median, recursive method, Fisher's g test of periodicity

1. Introduction

There are number of methods for eliminating trend (T), seasonal (S) and random (ε) components of a time series. We applied some of the most used methods and compared suitability of their application on the data we work with, which describes dynamics of monthly incidence of colorectal cancer. We used additive decomposition model, signed as

$$y_t = T_t + S_t + \varepsilon_t \quad (1)$$

2. Subject and Methods

Trend estimation

Trend estimation is based on suppression of seasonal and random fluctuations. Method of centered moving averages, also called filtering, is one of the classical approaches for obtaining trend. Let us denote filter coefficients as a vector:

$$f = (f_{-n}, f_{-n+1}, \dots, f_0, \dots, f_{n-1}, f_n) \quad (2)$$

The trend estimation T_t of a time series y_t by centered moving averages, is computed as

$$T_t = \sum_{i=-n}^n f_i y_{t+i}, \quad \text{where } \sum_{i=-n}^n f_i = 1 \quad (3)$$

Order and values of the filter coefficients depend on character of a series, smoothness requirements and expected period of a seasonal component. The order of a filter is defined by the width of a time series segment which is smoothed by a polynomial or other function. We assume that our monthly data show deterministic trend and are periodic with a period of one year. Therefore the frequency is $1/12 = 0.0833$ [month⁻¹] and a filter needs to be of the length $12k + 1, k \in \mathbb{Z}$ (odd length for practical reasons, see [1]). The longer the filter is, the smoother the trend is going to be.

We compared performance of *simple moving average (SMA)* [1], length of 13:

$$f_{SMA} = \frac{1}{12} \left(\frac{1}{2}, 1, 1, 1, 1, 1, 1, 1, 1, 1, 1, \frac{1}{2} \right), \quad (4)$$

triangle moving average (TMA), length of 25, which represents serial connection of two SMA filters:

$$f_{TMA} = \frac{1}{144} \left(\frac{1}{4}, 1, 2, 3, 4, 5, 6, 7, 8, 9, 10, 11, 11.5, 11, 10, 9, \dots, 3, 2, 1, \frac{1}{4} \right), \quad (5)$$

polynomial moving average (PMA) [1], length of 13:

$$f_{PMA} = \frac{1}{143} (-11, 0, 9, 16, 21, 24, 25, 24, 21, 16, 9, 0, -11) \quad (6)$$

and *moving median (MM)* [1], length of 13:

$$T_t = \text{median}(y_{t-6}, y_{t-5}, \dots, y_t, y_{t+1}, \dots, y_{t+6}) \quad (7)$$

Seasonal estimation

Seasonal components describe periodical changes in a time series. Computer calculations demand to use as easiest methods as possible, so that the results can be misleading. The most common method is *averaging (AV)* [1] which is based on the arithmetic means of individual months ($m = 1, \dots, 12$), calculated over k -periods (years):

$$S_m^{AV} = \frac{1}{k} \sum_{i=0}^k y_{m+iT} \quad (7)$$

where T is a period of the seasonal component (in our case 12 months).

Simplicity of this method is in an assumption of stationarity of the seasonal component.

An alternative method to the above mentioned averaging can be a *recursive method (R)* defined by a difference equation

$$S_m^R = 0.1 y_m + 0.9 S_{m-12}^R, \quad (8)$$

that represents a recursive comb filter with pass-bands at frequencies corresponding to fundamental frequency of a seasonal component and its integer multiples. This method does not assume a stationary character of the seasonal component and responds to instantaneous variations in its frequency content.

Evaluation of the method performance

We used Fisher's exact g test of periodicity [3] for comparison of results of separation of the time series additive components, where

H_0 : series is a Gaussian white noise

H_1 : series contains a deterministic periodic component

with level of significance $\alpha = 0.05$. This test is based on the periodogram spectral estimator and rejects the null hypothesis that the periodogram contains a value significantly larger than the average value.

Fisher's g test statistic (in [3] called *g statistic*) for a series of length n is computed as

$$fisher(n) = \frac{\max_{1 \leq i \leq n} \{pgram_i\}}{\sum_i pgram_i},$$

where $pgram_i$ is an i^{th} value of periodogram of the time series.

Fisher value of a given series was compared with a *fisher* value of Gaussian noise, labelled as *IdealFisher*.

We compared the *fisher* values after the removal of a trend component, as well as after the removal of both the trend and the seasonal component.

3. Results

Data for the experiment were taken from the Czech National Cancer Registry [4]. We constructed the time series of a normalized incidence of a colorectal cancer (monthly values over almost 30 years).

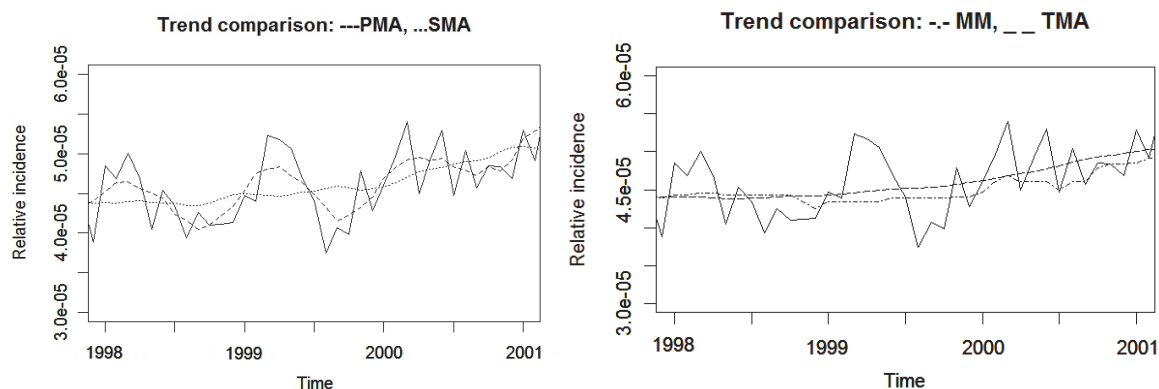


Fig. 1. Comparison of trends: solid line for the original data, dashed for polynomial (PMA), dotted for simple (SMA), longdashed for triangle (TMA) moving average and dotdashed for moving median (MM).

We see (Fig.1) that the triangle method produces significantly smoother trend than the others. Periodograms of the data with removed trend are shown in Fig.2.

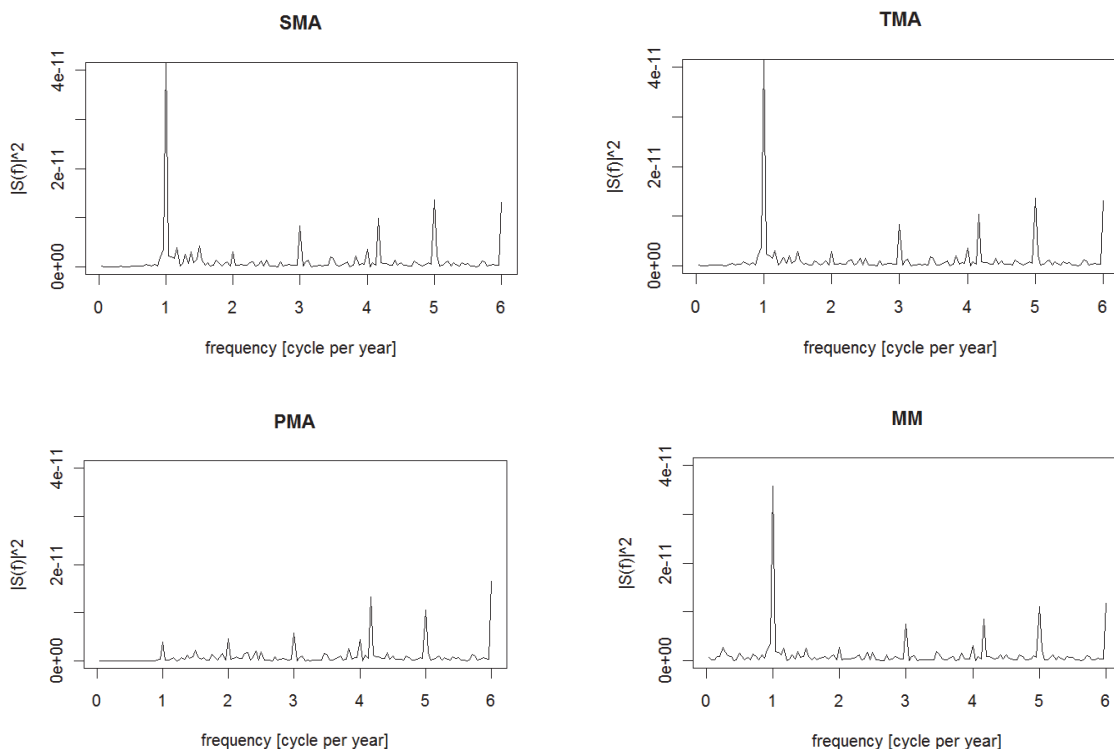


Fig. 2. Periodograms of time series with removed trend.

Table 1. Fisher's statistics for different processing of the time series. 'Season+random' stands for the original data after removing trend by the method in corresponding column (SMA,PMA,TMA,MM); 'random AV' and 'random R' stands for the original data after removing both trend and the seasonal component by AV, and R method, resp. (The closer to IdealFisher the fisher statistics is, the closer is a series to the white noise.) **IdealFisher = 0.038** (for a series of 288 values).

	SMA	PMA	TMA	MM
season+random	0.264	0.121	0.269	0.237
random AV	0.108	0.176	0.117	0.089
random R	0.104	0.164	0.107	0.086

4. Discussion

Due to the transients in computations of a filter responses, the original data were shortened from 372 to 288 values. Fisher's test rejected all null hypothesis on Gaussian noise, which indicates that there is still a significant periodic value in the processed data series after removing trend and seasonal component by the methods described here. This led us to application of the Fisher's statistics from the Fisher's exact g test and comparison *IdealFisher* value with a *fisher* value for the specific time series, as a rate of proximity to the white noise. From the Table 1, it is obvious that the best results (after removing the seasonal component) were obtained by means of moving median method (MM). MM method suppresses influence of outlying values, which seems to be important for our data. PMA filter, while used for removing trend, suppressed also a significant amount of periodic component at its fundamental frequency. This can be seen in Fig. 1, where trend determined by PMA closely matches the original series, as well as from the low value of $|S(f)|^2$ at the frequency $f = 1$ [**cycle per year**] in the periodogram in Fig. 2. We can see (Table 1, method PMA) the value of *fisher* statistics for the 'random R' series higher than that for 'season+random' series. This indicates the fact that application of the R method to the series describing colorectal cancer incidence with no significant seasonal component with a year periodicity, introduces false periodicity instead of removing it. Unfortunately, the seasonal component of the processed data does not satisfy a condition of stationarity. Further, signal to noise ratio for the given type of data is rather low and the number of repetitions of the seasonal component is relatively small. That is why the results obtained by the averaging method appeared even worse than in case of the recursive filter.

Acknowledgements

The research was granted by the project of the Czech Science Foundation No.102/09/H083: "Information Technology in Biomedical Engineering".

References

- [1] Cipra T, Finanční ekonometrie. EKOPRESS,s.r.o., 2008, 257-325.
- [2] Cryer J D, Chan K-S, Time Serie Analysis with applications in R, Springer, 2008.
- [3] Ahdesmaki M, Lahdesmaki H, Yli-Harja O, *Robust Fisher's Test for Periodicity Detection in Noisy Biological Time Series*, 2007
- [4] Klinická onkologie, The Journal of the Czech and Slovak Oncological Societies, Supplement 2007

Bootstrap in Common Mean Estimation – a Case Study

B. Arendacká

Institute of Measurement Science, Slovak Academy of Sciences, Dúbravská cesta 9,
841 04 Bratislava, Slovakia

Email: barendacka@gmail.com

Abstract. *It is known that in small samples the asymptotic variance of a maximum likelihood estimator for the common mean in random effects model underestimates the true variance and leads to too short confidence intervals for the true consensus value. This is illustrated e.g. in Rukhin, Metrologia 46(323-31), 2009. We look at two concrete small sample situations to investigate the possibility of improving the confidence intervals by employing bootstrap.*

Keywords: Bootstrap, Common Mean, Confidence Intervals, Maximum Likelihood

1. Introduction

Estimation of the common mean, determination of its uncertainty and of a confidence interval for its true value are tasks arising in certification of reference materials or in interlaboratory studies, see e.g. [1], [2]. The model used is very often the random effects model allowing for different within-laboratory variances and the estimates of the common mean are various weighted means of the estimates supplied by the different laboratories. Procedures of this kind are discussed at length in [1] and it is stressed that they differ in how their variance is estimated. However, this is of crucial importance and influences in turn the quality of the derived confidence intervals. In situations when there is no simple formula for the variance of a procedure or for the distribution of an (approximate) pivot underlying the construction of confidence intervals, bootstrap (see [3]) is a generic method that may be used to overcome the difficulties. By nature, it is an asymptotic method; however, in reality (when e.g. certifying a reference material) it is not uncommon to have a relatively small number of observations coming from only a few laboratories. In this paper we will study performance of bootstrap confidence intervals for the common mean in two such situations. The model and methods used are described in detail in Section 2. Section 3 summarizes results of our simulation study and Section 4 offers some concluding remarks.

2. Model and Methods

The model used for describing measurements of essentially the same quantity obtained in k laboratories is

$$y_{ij} = \mu + b_i + e_{ij}, \quad i=1, \dots, k > 1, j=1, \dots, n_i > 1 \quad (1)$$

where y_{ij} denotes the j -th observation in the i -th laboratory, μ is the unknown common mean, $b_i \sim N(0, \tau^2)$ is the random effect of the i -th laboratory and $e_{ij} \sim N(0, \sigma_i^2)$ are random errors. All b_i s and e_{ij} s are assumed to be mutually independent, $\tau^2 \geq 0$, $\sigma_i^2 > 0$, $i=1, \dots, k$, are unknown nuisance parameters. The resulting model for the laboratory means $y_i = \sum_j y_{ij}/n_i$ is $y_i \sim N(\mu, \tau^2 + \theta_i^2)$, where $\theta_i^2 = \sigma_i^2/n_i$. An unbiased estimator of θ_i^2 is $u_i^2 = \sum_j (y_{ij} - y_i)^2 / [n_i(n_i - 1)] \sim \theta_i^2 \chi_i^2 / (n_i - 1)$, where χ_i^2 denotes a χ^2 distribution with $n_i - 1$ degrees of freedom.

Estimators for μ of the form $\sum_i w_i y_i$, $\sum_i w_i = 1$ were considered in [1]. We will use two of them: the maximum likelihood (ML) estimator, μ_{ML} , and the DerSimonian-Laird estimator, μ_{DL} . For details on ML estimators of the unknown parameters in model (1) see [4]. Denoting them μ_{ML} ,

$\tau^2_{ML}, \theta^2_{iML}, i=1, \dots, k$, asymptotic considerations lead to the variance of μ_{ML} being estimated as

$$Var_A(\mu_{ML}) = (\sum_i 1/(\tau^2_{ML} + \theta^2_{iML}))^{-1} \quad (2)$$

and the corresponding 95% confidence interval for μ being

$$\mu_{ML} \pm q_{0.975} \sqrt{Var_A(\mu_{ML})}, \quad (3)$$

where $q_{0.975}$ denotes the 97.5th quantile of $N(0,1)$. This interval was found in [1] to be sometimes too short, i.e. its coverage was lower than the nominal level. The interval based on μ_{DL} suggested in [1], which performed quite well in the simulations therein, is of the form

$$\mu_{DL} \pm t_{0.975, k-1} \sqrt{Var_w(\mu_{DL})}, \quad (4)$$

where $t_{0.975, k-1}$ denotes the 97.5th quantile of the t-distribution with $k-1$ degrees of freedom and

$$Var_w(\mu_{DL}) = \sum_i w^2_{iDL} (y_i - \mu_{DL})^2 / (1 - w_{iDL}) \quad (5)$$

where $w_{iDL} = v_{iDL} / \sum_i v_{iDL}$, $v_{iDL} = 1/(\tau^2_{DL} + u_i^2)$ and $\tau^2_{DL} = \max(0, [\sum_i u_i^{-2} (y_i - y_0)^2 - k + 1] / [\sum_i u_i^{-2} - \sum_i u_i^{-4} (\sum_i u_i^{-2})^{-1}])$, $y_0 = \sum_i u_i^{-2} y_i / \sum_i u_i^{-2}$.

Since $\mu_{ML} = \sum_i w_{iML} y_i$, with $w_{iML} = v_{iML} / \sum_i v_{iML}$, $v_{iML} = 1/(\tau^2_{ML} + \theta^2_{iML})$ (see [4]), its variance may be estimated similarly to the variance (5) of μ_{DL} , see also [1], p. 327, so that

$$Var_w(\mu_{ML}) = \sum_i w^2_{iML} (y_i - \mu_{ML})^2 / (1 - w_{iML}). \quad (6)$$

However, what quantile should be used in combination with this estimator to form a confidence interval for μ is not clear. This difficulty can be avoided by employing bootstrap. In this paper we will consider only bootstrap t-intervals, which are suited especially for location parameters, see [3], p. 161. A 95% bootstrap t-interval is derived as follows:

1. Based on y_i 's, u_i^2 's estimate the unknown parameters μ_{est} , τ^2_{est} , $\theta^2_{i est}$, $i=1, \dots, k$ and $Var(\mu_{est})$.
2. Generate N_B bootstrap samples from model (1) with the unknown parameters replaced by their estimates from the step 1.
3. For each of the N_B bootstrap samples, estimate the unknown common mean and its variance, μ_{estB} , $Var(\mu_{estB})$, and compute $T = (\mu_{estB} - \mu_{est}) / \sqrt{Var(\mu_{estB})}$.
4. The interval for μ is $[\mu_{est} - q_{T, 0.975} \sqrt{Var(\mu_{est})}, \mu_{est} - q_{T, 0.025} \sqrt{Var(\mu_{est})}]$, where $q_{T, 0.025}$ ($q_{T, 0.975}$) denotes the 2.5th (97.5th) quantile of the distribution of T (estimated from the N_B values of T).

In our simulation study we considered model (1) with $k=3$, $n_1=10$, $n_2=10$, $n_3=12$, $\mu=0$, $\theta^2_1=2.7$, $\theta^2_2=1.9$, $\theta^2_3=0.5$ (case I) and $\theta^2_3=2.1$ (case II). τ^2 was 0, $0.25*m$, m , $(1+M)/2$, M , $4*M$, $m = \min(\theta^2_i)$, $M = \max(\theta^2_i)$, a choice inspired by [5]. For each scenario, we simulated 1000 sets of observations of (1) and constructed appropriate confidence intervals for μ . Based on these 1000 intervals we estimated the coverage of the respective procedures. We considered interval (4) and its bootstrap version (using μ_{DL} , $Var_w(\mu_{DL})$), interval (3) and its bootstrap version (μ_{ML} , $Var_A(\mu_{ML})$), as well as a bootstrap interval based on μ_{ML} , $Var_w(\mu_{ML})$. For obtaining bootstrap t-intervals $N_B=1500$ was used. Computations were done in R.

τ^2	0	.25m	m	.5(1+M)	M	4M	0	.25m	m	.5(1+M)	M	4M
DL _A	4.08	4.39	4.94	7.30	8.15	14.0	6.01	6.53	8.32	8.07	9.02	14.4
DL _B	5.05	5.65	6.30	9.92	11.7	19.5	6.91	7.66	9.68	9.42	10.8	16.9
ML _{Bw}	4.71	4.95	5.42	7.08	7.92	23.1	6.76	7.13	8.80	8.62	9.62	18.0

Table 1: Median lengths of the simulated 95% confidence intervals in case I (left) and II (right). Notation is the same as in Figure 1.

3. Results

Figure 1 shows simulated probabilities of coverage of the different intervals in the two cases of model (1) as described in the previous Section. We see that the approximate interval (4) based on the DerSimonian-Laird estimator may have lower probability of coverage than the nominal level, especially when the within-laboratory variances are substantially different (case I). It is also clear that the employment of bootstrap improves the performance of the interval. In case of the ML estimator and the associated intervals, interval (3), as expected, does not maintain the desired probability of coverage. Bootstrap results in an improved behaviour of the interval, but a real improvement appears only in combination with the modified estimator of the variance (6). A comparison of the length of the different intervals makes sense only in cases when the nominal confidence level is preserved. In Table 1 we state median lengths obtained in the simulations for 3 of the considered intervals for which the actual probability of coverage was roughly satisfactory. We see that the improvement in the probability of coverage resulting from employing bootstrap in case of interval (4) does not result in a too dramatic increase in the length.

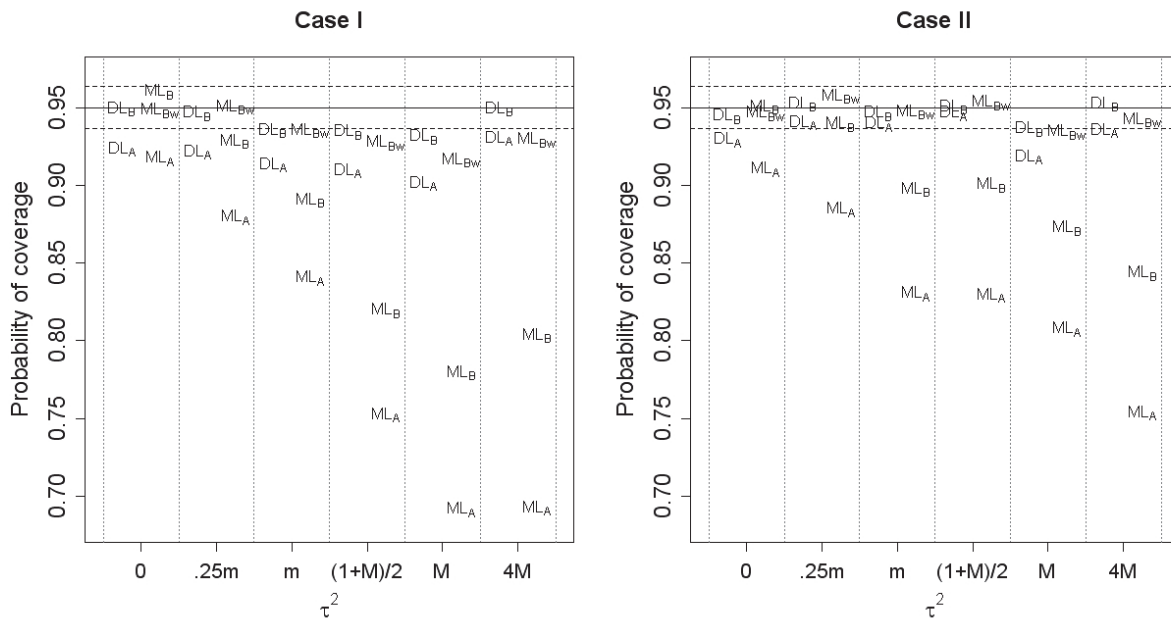


Fig. 1: Simulated probabilities of coverage for the two cases of model (1). DL_A denotes interval (4), DL_B its bootstrap version, ML_A denotes interval (3), ML_B its bootstrap version and ML_{Bw} a bootstrap interval using (6). Shown is the nominal level 0.95 together with limits which the simulated probability of coverage should fall into with probability 0.95 if the true coverage is 95%.

4. Discussion

Even though further investigation is needed to clarify the matter, the studied cases show a potential for an improvement in the probability of coverage of confidence intervals for the common mean in small samples when bootstrap is employed. However, a naive application of bootstrap may not be of help, as can be seen from the case of the ML estimator, when only bootstrap combined with a modified estimator of the variance led to a meaningful increase in the probability of coverage. The assumption for the bootstrap t-intervals to work well is that the quantity $T^* = (\mu_{est} - \mu) / \sqrt{Var(\mu_{est})}$ is an approximate pivot, i.e. its distribution is (approximately) independent of the unknown parameters. In the considered model, this means

independence not only of the parameter of interest, the common mean, but also of the nuisance parameters τ^2 , θ^2_i , $i=1,\dots,k$. For μ_{ML} this condition seems to be better satisfied with (6) than with (2) as can be seen from Figure 2 comparing the distributions of the respective T^* when $\tau^2=0$ and when $\tau^2=10$ in case I considered in our simulations.

Although not reported, we examined also bootstrap percentile intervals (such an interval is formed by the lower and upper quantiles of μ_{estB} estimated from the N_B values of μ_{estB}), but except for the case when $\tau^2=0$ (and sometimes $\tau^2=0.25*m$), the obtained probability of coverage was unsatisfactory.

Currently, further investigation into the performance of bootstrap in combination with weighted means estimators of μ is being undertaken.

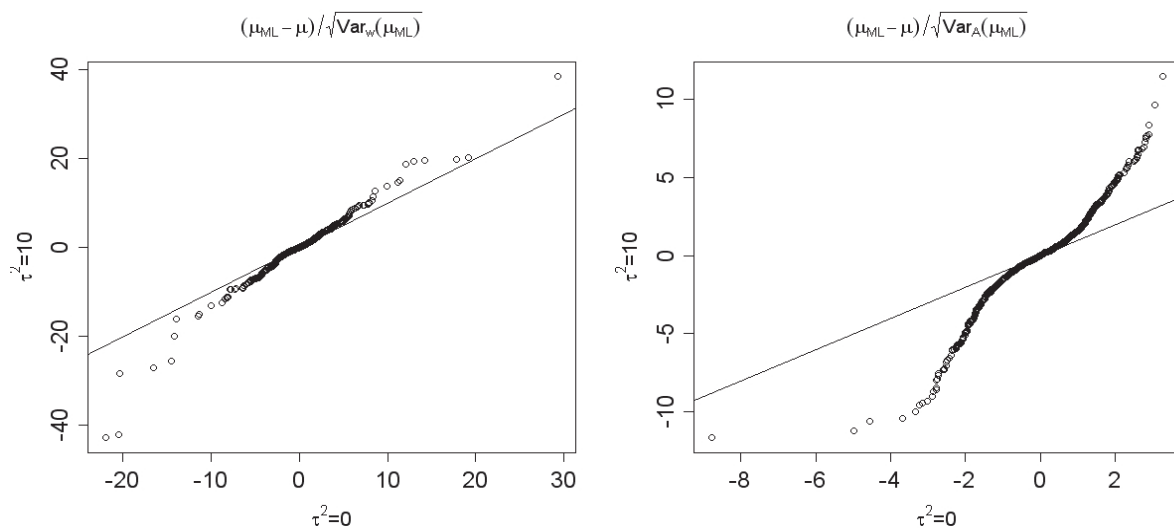


Fig. 2: QQplots comparing the distributions of T^* with (6) (left) and with (2) (right) for two different values of τ^2 in case I of model (1). The closer to the identity line the points lie, the more alike the two distributions

Acknowledgements

The author wishes to thank Dr. Antonio Possolo for an introduction to the topic. The work was initiated during the author's visit to Statistical Engineering Division at NIST and was further supported by the Slovak Research and Development Agency under the contract No. LPP-0388-09, and by the grants VEGA 1/0077/09 and VEGA 2/0019/10.

References

- [1] Rukhin AL. Weighted means statistics in interlaboratory studies. *Metrologia*, 46: 323-331, 2009.
- [2] Rukhin AL, Sedransk N. Statistics in Metrology: interlaboratory key comparisons and interlaboratory studies. *Journal of Data Science*, 5: 393-412, 2007.
- [3] Efron B, Tibshirani RJ. An Introduction to the Bootstrap. Chapman & Hall, Inc., New York, 1993.
- [4] Vangel MG, Rukhin AL. Maximum likelihood analysis for heteroscedastic one-way random effects ANOVA in interlaboratory studies. *Biometrics*, 55: 129-136, 1999.
- [5] Iyer HK, Wang CMJ, Mathew T. Models and confidence intervals for true values in interlaboratory trials. *JASA*, 99: 1060-1071, 2004.

Performance of Likelihood Calibration Method by Gruet from the Posterior Point of View. Simulation Study

K. Hornišová

Institute of measurement science, Slovak academy of sciences, Bratislava, Slovakia

Email: umerhorn@savba.sk

Abstract. Most calibration methods proposed in the literature are of likelihood type, i.e. they guarantee some statement about conditional probabilities $p(Y|X)$ where X is quantity of interest and Y its surrogate. However, more natural would be to investigate posterior properties of calibration methods, i.e. statements about probabilities $p(X|Y)$. Here, posterior behaviour of likelihood calibration method by Gruet will be examined by simulation from joint distributions of (X,Y) with different strength of dependence between X and Y .

Keywords: Calibration, Likelihood vs. Posterior Methods

1. Introduction

The situation when direct measurement of some quantity X is difficult and its values are inferred from measurements of another quantity Y is frequently encountered in many scientific branches. Such inference may make use of some physical law about relationship between X and Y , or of set of paired measurements of (X,Y) , supposedly obtained at the same conditions as unpaired measurements of Y with unknown counterparts of X which we would like to estimate. This second approach is called calibration.

There were many approaches proposed for calibration considered as a solution to a probabilistic problem. Most of them could be named likelihood ones, since they guarantee the validity of some statement about probabilities $p(Y|X)$ – in the calibration task unknown value(s) of X is parameter of interest. But considering the often random nature of both X and Y , it would be more useful to know the posterior properties of calibration method - something about probabilities $p(X|Y)$ – given unpaired measurements of Y (and previously obtained set of paired measurements of (X,Y)), what can be said about unknown corresponding values of X ?

2. Subject and Methods

Here we concentrate only on one calibration method, proposed in (Gruet, 1996), giving (under measured unpaired value(s) of Y) simultaneous interval calibration estimates $B(Y)$ for unknown x . This belongs among likelihood methods, since it guarantees (under suitable conditions) that

$$\liminf_{n \rightarrow \infty} P(P(x \in B(Y) | \{(X_i, Y_i); i=1, \dots, n\}) \geq 1 - \alpha; \forall Y) \geq 1 - \delta.$$

The posterior performance of this method was investigated by simulation in the following way: From the given joint distribution function $H(x,y)=C(F(x),G(y))$, where $C(.,.)$ is a copula and $F(.,) , G(.,)$ are marginal distribution functions of X and Y , respectively, n pairs $(X_1, Y_1), \dots, (X_n, Y_n)$ were generated and (parameters of) simultaneous calibration band $\{(Y, B(Y))\} = \{(Y, x); L(Y) \leq x \leq U(Y)\}$ for given α and δ was computed according to (Gruet, 1996). Then approximation $\hat{\psi}$ of “posterior probability content” of the band, i.e. approximation of

$$\psi := P(\{y; |P(X < L(y)|Y=y) - P(X < U(y)|Y=y)| \geq 1 - \alpha\})$$

was computed. This was repeated N times. The number

$$\Psi := \#\{j=1, \dots, N; \hat{\psi}_j = 1\} / N$$

was finally compared with coverage $1 - \delta$.

Simulations were carried out for the following values of parameters:

$C(u, v) = C_\theta(u, v) = \Phi_\theta(\Phi^{-1}(u), \Phi^{-1}(v))$, i.e. bivariate normal copula described in (Klaassen & Wellner, 1997), where Φ is distribution function of $N(0, 1)$, Φ_θ is distribution function of bivariate normal distribution with zero expectations, unit variances and correlation θ ; $\theta = 0.9$ or 0.99 ; F, G are $Unif(0, 1)$ or $N(0, 1)$; $n = 4, 10, 20, 40, 100, 200$; $\alpha = 0.05$; $\delta = 0.1$; $N = 100$.

Since approach of (Gruet, 1996) makes use of kernel regression, the choice of kernel and particularly of bandwidth can have an influence on calibration. Here we use Epanechnikov kernel and the bandwidth is computed separately for each simulated calibration set by method implemented in `npcdensbw` function of `np` package of R software.

3. Results

The results of simulations rounded to two decimal points are in the table.

n	θ	F	G	Ψ	F	G	Ψ	F	G	Ψ
4	0.9	U(0,1)	U(0,1)	0.94	N(0,1)	N(0,1)	0.97	U(0,1)	N(0,1)	0.65
10		U(0,1)	U(0,1)	0.94	N(0,1)	N(0,1)	0.83	U(0,1)	N(0,1)	0.98
20		U(0,1)	U(0,1)	0.94	N(0,1)	N(0,1)	0.81	U(0,1)	N(0,1)	0.91
40		U(0,1)	U(0,1)	0.8	N(0,1)	N(0,1)	0.74	U(0,1)	N(0,1)	0.56
100		U(0,1)	U(0,1)	0.6	N(0,1)	N(0,1)	0.08	U(0,1)	N(0,1)	0.29
200		U(0,1)	U(0,1)	0.5	N(0,1)	N(0,1)	0	U(0,1)	N(0,1)	0.2

n	F	G	Ψ	θ	F	G	Ψ	F	G	Ψ
4	N(0,1)	U(0,1)	0.91	0.99	U(0,1)	U(0,1)	0.98	N(0,1)	N(0,1)	0.95
10	N(0,1)	U(0,1)	0.78		U(0,1)	U(0,1)	0.98	N(0,1)	N(0,1)	0.92
20	N(0,1)	U(0,1)	0.85		U(0,1)	U(0,1)	0.98	N(0,1)	N(0,1)	0.9
40	N(0,1)	U(0,1)	0.68		U(0,1)	U(0,1)	0.98	N(0,1)	N(0,1)	0.71
100	N(0,1)	U(0,1)	0.68		U(0,1)	U(0,1)	0.98	N(0,1)	N(0,1)	0.37
200	N(0,1)	U(0,1)	0.38		U(0,1)	U(0,1)	0.88	N(0,1)	N(0,1)	0.07

n	F	G	Ψ	F	G	Ψ
4	U(0,1)	N(0,1)	0.89	N(0,1)	U(0,1)	0.86
10	U(0,1)	N(0,1)	0.99	N(0,1)	U(0,1)	0.91
20	U(0,1)	N(0,1)	0.98	N(0,1)	U(0,1)	0.98
40	U(0,1)	N(0,1)	0.86	N(0,1)	U(0,1)	0.89
100	U(0,1)	N(0,1)	0.88	N(0,1)	U(0,1)	0.73
200	U(0,1)	N(0,1)	0.8	N(0,1)	U(0,1)	0.63

4. Discussion and Conclusions

As can be seen from the table, simulation results are coarse and inconclusive. This is in part due to small value of N . It seems that the results are better when dependence between X and Y is stronger, as it could be expected, and also that different margins can affect the calibration results differently, but it is not convincing.

It transpires that the bandwidth is very influential parameter of the method. The bandwidth selection method used here leads to inappropriate results – calibration bands are often very wide and their boundaries are rather insensitive to value of Y . Therefore, it can be suspected that corresponding computed values of Ψ given in the table are unrealistically high.

Suitable and sufficiently universal method of bandwidth selection for calibration method by Gruet has to be found yet. It seems, however, that there are cases when the value of Ψ could be considerably changed by change of bandwidth, but large portion of the calibration band would remain constantly unadvantageously wide regardless of bandwidth.

Acknowledgements

The work has been supported by VEGA grants 1/0077/09 and 2/0019/10.

References

- [1] Gruet M–A. A nonparametric calibration analysis. *Annals of statistics*, 24 (4): 1474-1492, 1996.
- [2] Klaassen CAJ, Wellner JA. Efficient estimation in the bivariate normal copula model: normal margins are least favourable. *Bernoulli*, 3: 55-77, 1997.

The Influence of Increasing Number of Breath Gas Compounds on Binary Classification of Noisy Data

K. Bartošová

Institute of Measurement Science, Slovak Academy of Sciences, Bratislava, Slovakia

Email: katarina.cimermanova@gmail.com

Abstract. Classification of subjects into one of two classes is an important problem. Subject's exhaled breath profile measured by Proton Transfer Reaction Mass Spectrometry (PTR-MS) includes 210 different compounds; assigned to mass to charge ratios m/z . Analyzed breath concentrations include variability of repetitive measurements of subjects, thus we label them as noisy data. For classification we use a robust classification method for noisy data.

In this paper we observe an influence of the number of input compounds on sensitivity and specificity of classification. The order in which the compounds are added is determined by related Youden Indexes.

Keywords: Breath Gas Analysis, Noisy Data, Robust Classification Method, the Youden Index

Introduction

Exhaled breath is a product of inhaled breath and molecules, more specific Volatile Organic Compounds (VOCs), which are released from blood of lung alveolus. Thereto, they are also contributed from cells of upper airways and digestive tract.

In the present time, by development of analytical methods for measuring small quantities of VOCs, we can detect 3481 different compounds in human breath. From them, there are 1753 compounds which have positive alveolar gradient [2]. It means that the concentrations of these compounds are greater in exhaled breath than in inhaled breath. We expect for these compounds that they are endogenous, produced by human body. For this reason the breath analysis is an attractive noninvasive method, without direct intervention to the human body and therefore without a risk for a patient during multiple repetitions.

An ideal analytical method for measurement of small quantities of VOCs in human breath is Proton Transfer Reaction Mass Spectrometry (PTR-MS). PTR-MS is suitable for measuring low concentrations; at particles per billion (ppb) levels. PTR-MS achieves to measure in real time with low detection limit; particles per trillion (ppt) level [1]. The PTR-MS methodology is based on a reaction where the proton H^+ is transferred to VOC from a precursor in drift tube during certain conditions. The precursor, protonated water H_3O^+ , is produced by decomposition of water in primary ion source. After the reaction, new ions $VOCH^+$ are selected based on molecular masses, mass to charge ratio m/z , by electromagnetic field and consecutively quantified by ion multiplier into the quadrupole mass spectrometer. Molecular masses detectable by PTR-MS range from m/z 21 to m/z 230. The compounds measured as m/z are tentatively identified as VOC with strongest representation, e.g. m/z 42 is tentatively identified as acetonitrile.

An analyzed data come from a pilot study prepared at Medical University in Innsbruck during the years 2006 and 2008. The breath samples of volunteers were collected to Tedlar bags during a check-up. For some volunteers more bags were collected. Each bag was measured by PTR-MS at least three times.

The database includes data for 217 volunteers, but of which 173 are non-smokers and 44 smokers. For each subject we obtain only one representative vector of exhaled breath profile computed as a median from medians of repetitive measurements of subject bag profiles. Data obtained like this include variability of repetitive measurements. We label them as noisy data.

Let us have a random vector $\mathbf{X} = (X_1, \dots, X_N)$ where X_j represents random variable of concentrations of the j -th compound and N is the number of all compounds. For each subject i , $i = 1, \dots, n$ where n is the number of all subjects, defined by measured values $\mathbf{x}_i = (x_{i1}, \dots, x_{iN})$ we have categorization to a population y_i : $y_i=1$ if $\mathbf{x}_i \in \omega^{(1)}$ and $y_i=-1$ if $\mathbf{x}_i \in \omega^{(2)}$. Superscripts (1), (2) denote affiliation with the positive group $\omega^{(1)}$ and the negative group $\omega^{(2)}$ of subjects respectively.

Selection of Statistically Significant Breath Gas Compounds

Not all measured compounds are statistically significant for classification of subjects based on observed marks. The selection of compounds could be realized based on related Youden indexes. The Youden index measures effectiveness of a compound for distinguishing subjects with observed mark from those without. This index ranges between 0 and 1. A value close to 1 indicates large effectiveness; usually the compound is considered a biomarker of the observed mark. On the other hand a value close to 0 indicates limited effectiveness [4].

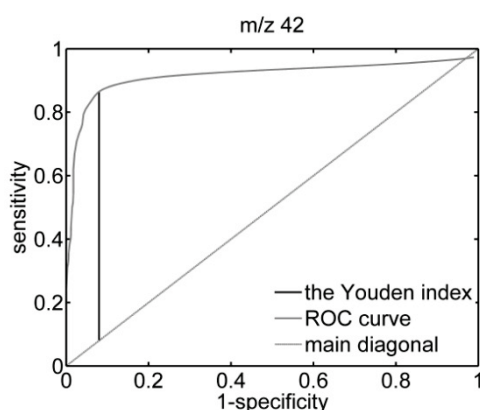


Fig.1. Graphical representation of the Youden index as the maximum vertical distance between the ROC curve and the main diagonal of the graph. The Youden index measures compound effectiveness of classification based on the observed mark.

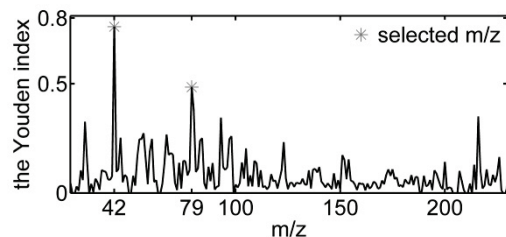


Fig.2. The Youden index for breath compounds measured by PTR-MS with marked selected compounds m/z 42 and m/z 79, tentatively identified as acetonitrile and benzene, for which the Youden index is greater than 0.5.

The Youden index J is a function of sensitivity Se and specificity Sp

$$J = \max_t \{Se(t) + Sp(t) - 1\} \quad (1)$$

for all points t of the measured variable X_j . Sensitivity Se at a point t is defined as the probability of a correct classification of positive subjects

$$Se(t) = P(X^{(1)} > t) = 1 - P(X^{(1)} \leq t) = 1 - F^{(1)}(t)$$

and can be evaluated using distribution function $F^{(1)}$ of the positive group at the point t . Specificity Sp at a point t represents the probability of a correct categorization of negative subjects (subjects without the observed mark)

$$Sp(t) = P(X^{(2)} \leq t) = F^{(2)}(t)$$

and corresponds to a value of the distribution function $F^{(2)}$ of the negative group at the point t .

The Youden index J can be rewritten in the form

$$J(t) = Se(t) + Sp(t) - 1 = F^{(2)}(t) - F^{(1)}(t)$$

$$J\{F^{(2)-1}(p)\} = p - F^{(1)}\{F^{(2)-1}(p)\},$$

where $F^{(2)-1}(p) = t$ is a value of the p -quantile of the distribution function of the negative group, i.e. $F^{(2)}(t) = p$.

Because empirical distribution functions are not continuous the estimate of the Youden index has a very erratic appearance, especially in the case when the group sizes are different. Therefore to estimate this index we use smoothed estimates of cumulative distribution functions obtained with the help of a Gauss kernel function [5]

$$\hat{F}^{(\cdot)}(t) = \frac{1}{n^{(\cdot)}} \sum_{i=1}^{n^{(\cdot)}} \Phi\left(\frac{t - x_i^{(\cdot)}}{h^{(\cdot)}}\right)$$

where h is the band width of the kernel function and Φ is the distribution function of the standard normal distribution $N(0,1)$.

Classification of Noisy Data

Classification of subjects into one of two classes is an important problem. There are some classification methods which classify data into one of two classes, but in a real life situation the observed vectors are corrupted with noise. A solution to this problem is a robust formulation that stems from the Support Vector Machine (SVM) method. The formulation is a convex optimization problem; in particular, it is an instance of the Second Order Cone Programming (SOCP) problem. An ellipsoidal uncertainty model is assumed; it means that the true value, not always the measured value, is some point of the specified ellipsoid. The classification method assumes only the existence of the second order moments [3].

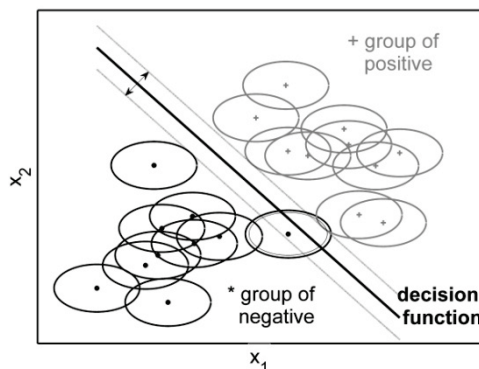


Fig.3. Robust classification method for classification of noisy data, where the optimal linear decision function is found based on specified ellipsoids representing the input data. The optimal decision function is found by the maximization of a margin between two hyperplanes parallel to the decision function with respect to the minimal lost (ellipsoids fallen to other side of the decision function).

Let our classifier be a hyperplane $\langle \mathbf{w}, \mathbf{x} \rangle + b = 0$. Our goal is to find optimal parameters \mathbf{w}, b based on specified input ellipsoids $\mathbf{x} \in B(\mathbf{x}_i, \Sigma_i, \gamma)$, where \mathbf{x}_i and Σ_i are the center and the shape matrix of the i -th input ellipsoids, $i = 1, \dots, n$, where n is the number of all subjects and γ is a noise level $\gamma \geq 0$. When $\gamma = 0$ we assume input data without noise.

This leads to an optimization problem

$$\min_{\mathbf{w}, b, \xi} \sum_{i=1}^n \xi_i$$

$$\text{w.c.} \quad y_i (\langle \mathbf{w}, \mathbf{x}_i \rangle + b) \geq 1 - \xi_i + \gamma_i \|\Sigma_i^{1/2} \mathbf{w}\|$$

$$\|\mathbf{w}\| \leq W$$

$$\xi_i \geq 0$$

where ξ_i are slack parameters of lost. The optional parameter $W \in (0, \infty)$ ensures existence of a solution. When $W = 0$ we lose the control of the parameters of lost. Otherwise, when W is excessively large, $\xi = 0$ and in the case when the data are not linearly separable the solution is not found.

This nonlinear convex optimization problem is solved by interior point method using the Matlab toolbox for optimization over symmetric cones SeDuMi [6]. The decision rule for new subjects characterized by measured values \mathbf{x} is $\hat{y}(\mathbf{x}) = \text{sign}(\langle \mathbf{w}, \mathbf{x} \rangle + b)$.

Simulation study

In the simulation we classified subjects characterized by different number of selected compounds N , where we started from the most statistically significant compound and step by step we added the next compound in the row. Subjects were 100 times divided into a training set and a testing set (3:2). For each step we estimated the Youden index $J = Se + Sp - 1$ from 100 values of sensitivity and specificity of classification of subjects based on the smoking habit

$$\hat{Se} = \frac{TP}{n^{(1)}} = \frac{\#\{i, y_i = \hat{y}_i | y_i = +1\}}{\#\{i, y_i = +1\}} \quad \text{and} \quad \hat{Sp} = \frac{TN}{n^{(2)}} = \frac{\#\{i, y_i = \hat{y}_i | y_i = -1\}}{\#\{i, y_i = -1\}},$$

where TP releases to correct classified subjects from testing set of positive group and TN to correct classified subjects from testing set of negative group. The optional parameters of the robust classification method were chosen from previous studies as $W = 10$ and $\gamma = 0.1$.

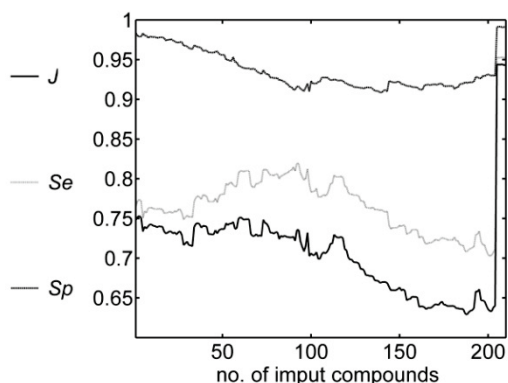


Fig.4. The Youden index J , sensitivity Se and specificity Sp for classification of subjects into the class of smokers or nonsmokers based on different number of breath compounds N which were added based on the effectiveness of classification.

Results

The result of the simulation study is visible in Fig. 4. We see that sensitivity and specificity have inverse progress. While specificity is decreasing to $N=93$, sensitivity (the more important measure for diagnosis) is increasing. Up to $N=93$ the Youden index remains relatively unchanged. After the point $N=93$ the observed measures have opposite character, until the point $N=205$. After this point all observed measures are rapidly increasing.

Discussion

We expected that input data described by more compounds would be better classified to the appropriate classes. In the described classification method we see that the effectiveness of classification is first decreasing. A turning point is appears for higher dimensional data. We think that

the reason is that in this higher dimensional space the classes are better linearly separable.

Conclusions

Unlike traditional classification methods the robust classification method assumes that the input data are corrupted with noise. From the result we see, that this classification method gives better result for input data described by more compounds, in other words the robust classification method is optimal for high dimensional data.

Acknowledgements

The research was supported partly by the Scientific Grant Agency of the Slovak Republic (VEGA), grant 2/0019/10 and 1/0077/09 and by the Slovak Research and Development Agency (APVV), grant SK-AT-0003-08.

References

- [1] Amann, A., et. al. Model Based Determination of Detection Limits for Proton Transfer Reaction Mass Spectrometer. *Measurement Science Review*, 10 (6), 2010, 180-188.
- [2] Bajtarevic, A., et. al. Noninvasive Detection of Lung Cancer by Analysis of Exhaled Breath. *BMC Cancer*, 9 (348), 2009, 1-16.
- [3] Bhattacharyya, Ch. Robust Classification of Noisy Data Using Second Order Cone Programming Approach. *Proceeding of Intelligent Sensing and Information Processing*, 2004, 433-438.
- [4] Fluss, R., et.al. Estimation of the Youden Index and its Associated Cutoff point. *Biometric Journal*, 47, 2005, 458-472.
- [5] Hall, P.G., et. al. Nonparametric Confidence Intervals for Receiver Operating Characteristic Curves. *Biometrika*, 91 (3), 2004, 743-750.
- [6] Sturm, J.F. Using SEDUMI 1.02, a Matlab*toolbox for Optimization over Symmetric Cones, *Optimization Methods and Software*, Vol. 11, 1995, 625-653.

Confidence Interval for the Distance of Two Micro/Nano Structures and Its Applications in Dimensional Metrology

^{1,3,4}G. Wimmer, ²K. Karovič, ²V. Witkovský, ⁵R. Köning

¹Mathematical Institute, Slovak Academy of Sciences, Bratislava, Slovakia

²Institute of Measurement Science, Slovak Academy of Sciences, Bratislava, Slovakia

³Faculty of Natural Sciences, Matej Bel University, Banská Bystrica, Slovakia

⁴Institute of Mathematics and Statistics, Masaryk University, Brno, Czech Republic

⁵Physikalisch-Technische Bundesanstalt (PTB), Braunschweig, Germany

Email: wimmer@mat.savba.sk

Abstract. We propose a method for computing an approximate (Bonferroni type) confidence interval for the distance of two micro- and/or nanostructures considered in dimensional metrology, e.g. grating lines, using data obtained by a length comparator, which allows to determine the coordinates of the edges, the position and the width of the structure from its photometric profile together with the related uncertainty contributions. The implementation is demonstrated using data obtained by the Nanometer Comparator operated at the PTB Braunschweig, Germany.

Keywords: Length Comparator, Dimensional Metrology, Confidence Intervals

1. Introduction

In many applications the positions and/or the distance of two micro- and/or nano-structures on a surface of a material, as e.g. grating lines, have to be determined together with an appropriate evaluation of the respective uncertainties. Today one-dimensional metrology is typically based on measurements obtained by using highly precise length comparators; as e.g. the Nanometer Comparator implemented at PTB Braunschweig, Germany, see [2, 3].

Here we consider the model for a one-dimensional measurement device where the measurement object is moved and the structure localization sensor (the optical interferometer and the photoelectric sensor unit) is kept in a fixed position. The output of the measurement device relates the photoelectric signal of the sensor, $y(x)$, with the position x of the structure on the measurement object, which is placed on a movable slide of the comparator. For illustration, Fig. 1 depicts the levels of the photoelectric signal $y(x)$ as a function of position x of two $4 \mu\text{m}$ wide reflective lines (here denoted as the micro-structures), with nominal distance of $30 \mu\text{m}$, on a line scale.

In Sections 2 and 3 we will derive and illustrate the construction of the Bonferroni's type confidence interval for the distance of two line structures as an alternative to the standard approach to uncertainty evaluation based on expanded uncertainty. Comparison of those two approaches accompanied with a brief discussion will be presented in Section 4.

2. Subject and Methods

A crucial point in the dimensional metrology of line structures is determination of the coordinates of the structure's edges, the central positions and their respective widths. The coordinate of the left edge is defined as such position x_L that $F = y(x_L)$, i.e. the position of the intersection of selected threshold F and the (increasing part of) photoelectric signal $y(x)$.

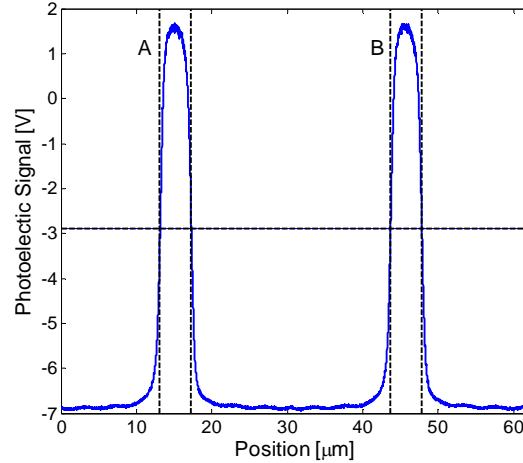


Fig. 1. Photometric profile (signal) of two 4 μm reflex lines A and B with nominal distance of 30 μm . The horizontal dashed line is the threshold F , the vertical dashed lines (from left to right) depicts the positions of the edges Ax_L , Ax_R , Bx_L , and Bx_R .

The coordinate of the right edge x_R is such that $F = y(x_R)$, i.e. the position of the intersection of the threshold F and the (decreasing part of) photoelectric signal $y(x)$. The approximate conservative $(1 - \alpha) \times 100\%$ -confidence interval for the central position and for the edges of the line structures have been considered in [4,5,6]. The suggested method is based on the approximation of the monotonically increasing and/or decreasing sections of the photoelectric signal by linear regression lines.

According to [3-6], the $(1 - \alpha) \times 100\%$ -confidence interval (CI) for the position of the structure left edge x_L , say $\langle x_{L_1}, x_{L_2} \rangle$, is determined by the following relations:

$$x_{L_1} = \frac{M}{N} - \frac{\sqrt{M^2 - NQ}}{N}, \quad x_{L_2} = \frac{M}{N} + \frac{\sqrt{M^2 - NQ}}{N}, \quad (1)$$

where

$$N = 1 - \frac{s_{\hat{b}_L}^2 t_{n_L-2}^2(1 - \alpha/2)}{\hat{b}_L^2}, \quad M = \hat{x}_L + \frac{s_{\hat{a}_L \hat{b}_L} t_{n_L-2}^2(1 - \alpha/2)}{\hat{b}_L^2}, \quad Q = \hat{x}_L^2 + \frac{s_{\hat{a}_L}^2 t_{n_L-2}^2(1 - \alpha/2)}{\hat{b}_L^2}, \quad (2)$$

and

$$\hat{x}_L = \frac{F - \hat{a}_L}{\hat{b}_L} \quad (3)$$

is an estimator of the coordinate of the structure left edge. Here, by \hat{a}_L and \hat{b}_L we denote the estimators of the *left* regression line coefficients (i.e. the intercept and the slope), by $s_{\hat{a}_L}$, $s_{\hat{b}_L}$, and $s_{\hat{a}_L \hat{b}_L}$ we denote the respective standard deviations and the covariance of the estimators, and by $t_{n_L-2}(1 - \alpha/2)$ we denote the $(1 - \alpha/2)$ -quantile (for chosen significance level $\alpha \in (0, 1)$) of the Student's t -distribution with $(n_L - 2)$ degrees of freedom, n_L represents the number of data points used for fitting the left regression line. The detailed derivation of the above expressions, as well as the expression for the standard deviation $s_{\hat{x}_L}$ of the estimator \hat{x}_L defined by the equation (3), can be found in [3-6]. The analogical expressions for the *right* edge of the line structure will be denoted by the index R . From that, we directly get the following probability statements for locations x_L and x_R , respectively:

$$\Pr(x_{L_1} \leq x_L \leq x_{L_2}) = \Pr\left(\frac{x_L}{2} \in \left\langle \frac{x_{L_1}}{2}, \frac{x_{L_2}}{2} \right\rangle\right) = 1 - \alpha, \quad \Pr\left(\frac{x_R}{2} \in \left\langle \frac{x_{R_1}}{2}, \frac{x_{R_2}}{2} \right\rangle\right) = 1 - \alpha. \quad (4)$$

Table 1. Summary results: Evaluation of 12000 photoelectric measurement data pairs.

	A	B		A	B	ABd_L, ABd_R, ABd			
x_{L_1}	13.1594	43.7334				$Bx_{L_1} - Ax_{L_1}$	30.5720		
x_{L_2}	13.1611	43.7351	\hat{x}_L	13.1602	43.7342	$Bx_{L_2} - Ax_{L_2}$	30.5760	$B\hat{x}_L - A\hat{x}_L$	30.5740
95% CI for x_L	0.0017	0.0017	$ks_{\hat{x}_L}$	0.0009	0.0009	95% CI for ABd_L	0.0039	$ks_{(B\hat{x}_L - A\hat{x}_L)}$	0.0013
x_{R_1}	17.2439	47.8232				$Bx_{R_1} - Ax_{R_1}$	30.5774		
x_{R_2}	17.2456	47.8248	\hat{x}_R	17.2448	47.8240	$Bx_{R_2} - Ax_{R_2}$	30.5811	$B\hat{x}_R - A\hat{x}_R$	30.5792
95% CI for x_R	0.0017	0.0015	$ks_{\hat{x}_R}$	0.0009	0.0008	95% CI for ABd_R	0.0037	$ks_{(B\hat{x}_R - A\hat{x}_R)}$	0.0012
x_S									
$(x_{L_1} + x_{R_1})/2$	15.2015	45.7782				$(Bx_{L_1} + Bx_{R_1} - Ax_{L_2} - Ax_{R_2})/2$	30.5745		
$(x_{L_2} + x_{R_2})/2$	15.2035	45.7800	\hat{x}_S	15.2025	45.7791	$(Bx_{L_2} + Bx_{R_2} - Ax_{L_1} - Ax_{R_1})/2$	30.5788	$B\hat{x}_S - A\hat{x}_S$	30.5766
95% CI for x_S	0.0020	0.0019	$ks_{\hat{x}_S}$	0.0007	0.0006	95% CI for ABd	0.0043	$ks_{(B\hat{x}_S - A\hat{x}_S)}$	0.0009
w									
$x_{R_1} - x_{L_2}$	4.0826	4.0879							
$x_{R_2} - x_{L_1}$	4.0865	4.0916	\hat{w}	4.0845	4.0898				
95% CI for w	0.0039	0.0021	$ks_{\hat{w}}$	0.0013	0.0012				

We define the centre of the structure as $x_S = (x_L + x_R)/2$ and its width as $w = x_R - x_L$, with their estimators $\hat{x}_S = (\hat{x}_L + \hat{x}_R)/2$ and $\hat{w} = \hat{x}_R - \hat{x}_L$. Their standard deviations are denoted by $s_{\hat{x}_S}$ and $s_{\hat{w}}$, respectively. By using the Bonferroni's inequality and the equation (4) we get

$$\Pr\left(x_S \in \left\langle \frac{x_{L_1} + x_{R_1}}{2}, \frac{x_{L_2} + x_{R_2}}{2} \right\rangle\right) \geq 1 - 2\alpha, \quad (5)$$

and

$$\Pr(w \in \langle x_{R_1} - x_{L_2}, x_{R_2} - x_{L_1} \rangle) \geq 1 - 2\alpha. \quad (6)$$

Now we are interested in the dimensional relations of two line structures. Let us consider the line structures, say A and B , as illustrated in Fig. 1. The related variables, as defined above, will be symbolically denoted by the left-hand sided indices A and B , respectively. The distance of the edges of two line structures A and B is defined as $ABd_L = Bx_L - Ax_L$, (for left edges), and as $ABd_R = Bx_R - Ax_R$ (right edges), and finally the distance of two line structures is $ABd = Bx_S - Ax_S$. Again, by using the Bonferroni's inequality and equations (4-6) we get

$$\Pr(ABd_L \in \langle Bx_{L_1} - Ax_{L_2}, Bx_{L_2} - Ax_{L_1} \rangle) \geq 1 - 2\alpha, \quad (7)$$

$$\Pr(ABd_R \in \langle Bx_{R_1} - Ax_{R_2}, Bx_{R_2} - Ax_{R_1} \rangle) \geq 1 - 2\alpha, \quad (8)$$

and finally,

$$\Pr\left(ABd \in \left\langle \frac{Bx_{L_1} + Bx_{R_1} - Ax_{L_2} - Ax_{R_2}}{2}, \frac{Bx_{L_2} + Bx_{R_2} - Ax_{L_1} - Ax_{R_1}}{2} \right\rangle\right) \geq 1 - 4\alpha. \quad (9)$$

3. Results

As an illustration of the suggested confidence intervals for the coordinates of structure's edges, their central positions, their respective widths, and their distances we present evaluation of 12000 photoelectric data pairs from two 4 μm wide reflective lines (the line structures), with nominal distance of 30 μm , on a line scale obtained by the Nanometer

Comparator implemented at PTB Braunschweig, Germany, see Fig. 1. The summary of the results are presented in Table 1. For comparison, the expanded uncertainties (with the coverage factor $k = 1.96$) are also given.

4. Discussion

In this contribution we have proposed a method for computing an approximate (Bonferroni type) confidence interval for the distance of two micro- and/or nanostructures considered in dimensional metrology, e.g. grating lines, using data obtained by the length comparator. The usually used confidence interval (see e.g. GUM [1]) for the distance $_{AB}d = {}_Bx_S - {}_Ax_S$, with its length given as $2k s_{(B\hat{x}_S - A\hat{x}_S)}$ (and for the coverage factor $k = 1.96$), is shorter than the suggested Bonferroni type confidence interval, however, as the estimator $_{AB}\hat{d} = {}_B\hat{x}_S - {}_A\hat{x}_S$ is not normally distributed, it does not ensure the stated nominal confidence level (here 95%). On the other hand, the Bonferroni type confidence interval ensures the stated confidence level. The statistical properties of the suggested confidence intervals, especially their coverage probabilities for different experimental setups, are subjects for further investigations.

Acknowledgements

The work was partially supported by the Slovak Research and Development Agency, grants VV-0096-10 and SK-AT-0003-08, by the Scientific Grant Agency of the Ministry of Education of the Slovak Republic and the Slovak Academy of Sciences, grants VEGA 1/0077/09, 2/0019/10, and 2/0201/10, and by the Ministry of Education, Youth and Sports of Czech Republic, LC06024.

References

- [1] GUM 1995 with minor corrections. Evaluation of measurement data — Guide to the expression of uncertainty in measurement. BIPM-IEC-ISO-OIML, JCGM 100:2008.
- [2] Köning R, Flügge J and Bosse H. A method for the in situ determination of Abbe errors and their correction. *Measurement Science and Technology*, 18, 476–481, 2007, doi:10.1088/0957-0233/18/2/S21.
- [3] Köning R., Karovič K., Wimmer G., Witkovský V.: Estimating the uncertainty of the straight line fit algorithm used to determine the position and the width of a graduation line. NanoScale 2010, 9th Seminar on Quantitative Microscopy (QM) and 5th Seminar on Nanoscale Calibration Standards and Methods Dimensional and related measurements in the micro- and nanometre range, 2010.
- [4] Wimmer G., Karovič K. Interval Estimators of the centre and width of a two-dimensional microstructure. *Measurement Science Review*, Volume 9 (4): 90-92, 2009, 10.2478/v10048-009-0015-5.
- [5] Wimmer G., Karovič K. Determining the confidence interval for the center and width of a structure in fitting measured data by the regression line. In Tyšler M, Maňka J and Witkovský V. Eds.: MEASUREMENT 2009, Proceedings of the 7th International Conference, Smolenice, 45-48, 2009.
- [6] Köning R., Karovič K., Wimmer G., Witkovský V.: Estimating the uncertainty contributions of the standard algorithm used to determine the position and the width of a graduation line. *Measurement Science and Technology*, 2011, (Submitted).

Application of Cluster Analysis on Antenna Factor Measurements Data

¹M. Kollár, ²K. Kováč

¹Seibersdorf Laboratories GmbH, RF-Engineering, A-2444 Seibersdorf
Austria, Email matej.kollar@seibersdorf-laboratories.at

²Department of Measurement, Faculty of Electrical Engineering and Information
Technology, Ilkovičova 3, 81219 Bratislava, Slovak Republic

Abstract. *Clustering is a method of partitioning set of observations into subsets (clusters) in a way that observations within individual subsets are similar in some sense. Antenna calibration is a method for obtaining antenna factor for specific antenna. Antenna factor is then used to determine the actual radiation emission level in various measurements where the antenna is involved. This paper deals with cluster analysis of antenna factor data for various antenna models and different calibration methods and parameters. As the cluster analysis is extremely data specific, related problems are discussed. The application of several clustering methods to the antenna factor data has been explored. The evaluation of the obtained results is presented.*

Keywords: Antenna Calibration, Antenna Factor, Data Clustering

1. Introduction

Calibration of the antennas is a very important type of measurement which enables today industry to perform various radiation emission and immunity tests on electronic devices. The purpose of the antenna calibration procedure is to obtain antenna factor data that can be used for correction of the received radiation emission level. When calibrating an antenna, there are plenty of effects which influence resulting antenna factor e.g. manufacturing properties, errors caused by a measurement system, errors originating from the antenna setup, and measurement errors inherent in the method. All these form the actual appearance of the calibration data. When various measurements are displayed in one chart they tend to create natural groups (clusters), see Fig.1. Being able to recognize these groups, one may extract valuable information, about the data generation process. It is possible to say, if the data measured with a specific antenna diverts from the others of the same model, the antenna or measurement is likely to be invalid and further verification has to be conducted.

2. Subject and Methods

Clustering is a method of unsupervised learning, and a common technique for statistical data analysis used in many fields, including machine learning, data mining, pattern recognition, image analysis, information retrieval, and bioinformatics. Antenna factor data can be viewed as values of a function of frequency, and thus our problem can be seen as functional clustering. For this purpose we have selected two well-known clustering approaches.

1. Hierarchical clustering finds successive clusters using previously established clusters. These algorithms are either agglomerative ("bottom-up") or divisive ("top-down"). Agglomerative algorithms begin with each element as a separate cluster and merge them into successively larger clusters. Divisive algorithms begin with the whole set and proceed to divide it into successively smaller clusters.

2. Partitional algorithms typically determine all clusters at once, but can also be used as divisive algorithms in the hierarchical clustering.

An important step in clustering is to select an appropriate distance/dissimilarity measure for the given problem (e.g., Euclidean, City-block, Chebyshev). The choice of a particular dissimilarity measure may significantly affect the actual shapes of the resulting clusters.

Antenna calibration data are characteristic by non-uniform sampling in the frequency domain. This is caused by different frequency steps used for different frequency ranges. E.g. in the range between 1 and 100MHz the data are acquired with 1MHz step. On the other hand, in the range between 100MHz and 200MHz the frequency step is 5MHz. In our experiments we consider the calibration curves as vectors and use the Euclidean distance that has proved to be a proper distance measure. It progressively places a greater weight on measurement points which are further apart, and thus it appropriately determines dissimilar measurements.

Next, the agglomerative hierarchical and k-means++ clustering algorithms were applied to our data. In the first step of the agglomerative hierarchical clustering, all the elements are considered as individual clusters. Afterwards, they are sequentially paired according to the selected distance measure and linkage criterion [1], until there are no clusters to be merged. In our analysis, the complete linkage has been used.

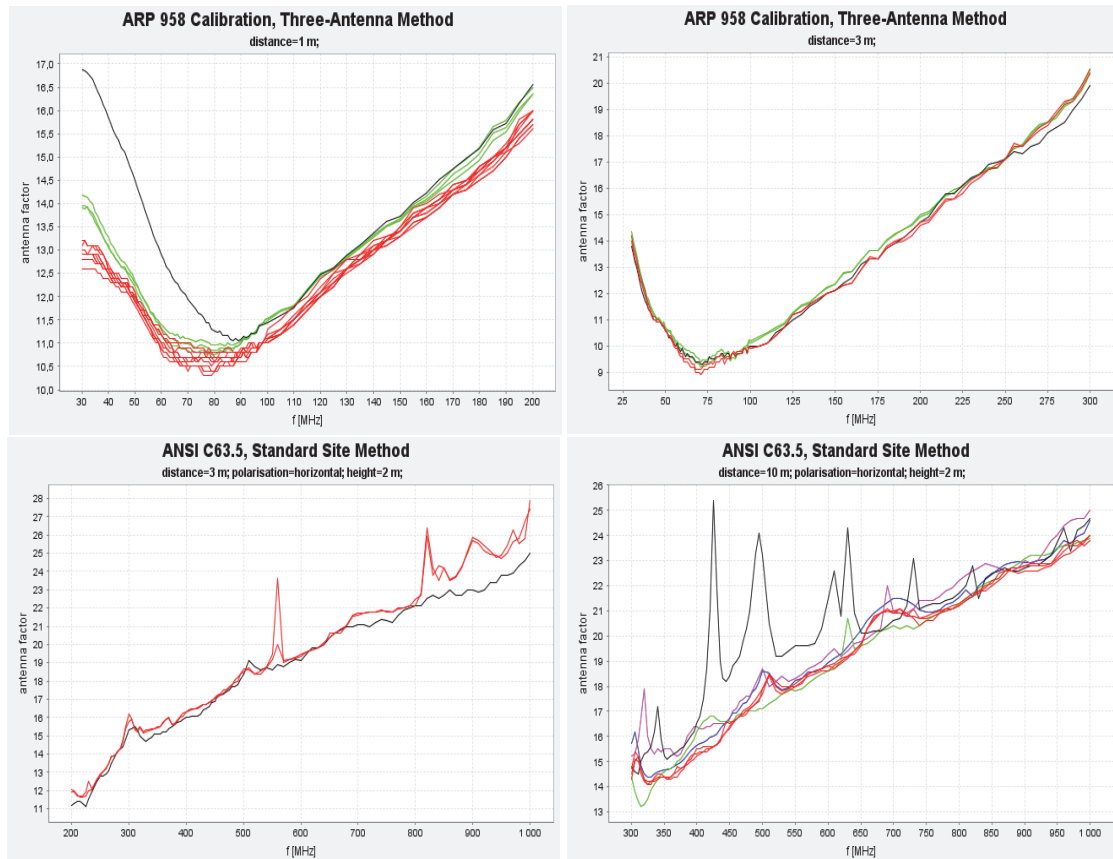


Fig. 1. Result of the cluster analysis applied to the antenna factor measurements. Individual clusters are drawn in different colours.

At the beginning of k-means clustering, a set of randomly chosen data points are set as k initial cluster centers (centroids). In the next step, all data points are assigned to the nearest centroids. Afterwards, new cluster centers are computed. This process is repeated until cluster

centers arrive at the stable positions or maximum number of iterations is reached. This method does not guarantee that the final clusters always contain the same elements and therefore the k-means++ [2] algorithm was used. This modification of the original algorithm determines the initial cluster centers in such a way that previous property is satisfied.

Data for clustering were selected from a set of calibrations performed according to ANSI C63.5 [3] and ARP 958 [4]. In Fig.1 some of the clustering results for different measurement distances (1m, 3m, 10m) are depicted. One can see that the given set of data contains correct calibration data, as well as false antenna calibrations. Using the Euclidean distance measure, there was no difference in performance between both clustering methods.

The crucial property of the both clustering algorithms is that they require the desired number of clusters is defined prior to the execution of the algorithm. If the number of clusters is not explicitly known, one needs to estimate this number empirically from the data. This is a problem on its own for which a number of techniques can be employed. Some of them are as follows: entropy-based partitioning of dendrogram [5], information theoretic approach [6], Silhouette [7], v -fold cross-validation [8]. The common problem of these methods is that they are more suited for large datasets which is not the case of the antenna calibration data. Furthermore, some of them involve algebraic matrix operations, which fail due to singularities and violated assumptions when applied to unsuitable data.

The principle of determining the number of clusters in arbitrary dataset is to define a criterion function that measures the clustering quality of any partition of the data. Then the problem is to find such a partition of data that minimizes this criterion function [9]. If the dataset to be clustered contains a reasonable number of elements, it is possible to run clustering algorithm iteratively for various numbers of clusters starting with one to a size of the dataset and stopping the algorithm when the minimum value of the criterion function is reached.

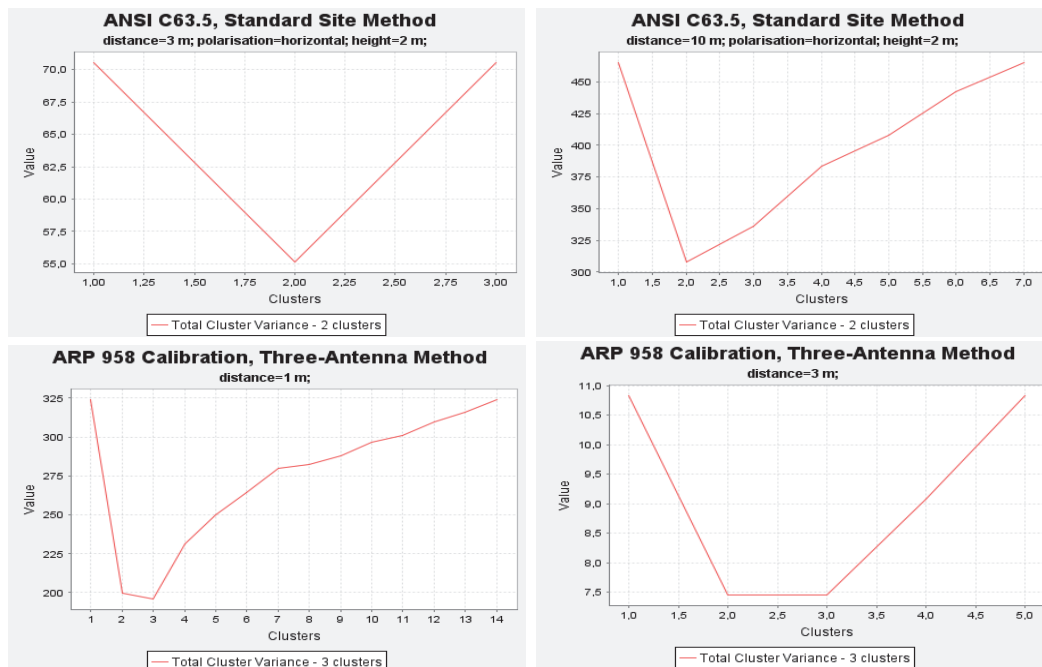


Fig. 2. The actual shapes of the total cluster variance criterion functions applied to different datasets. The minimum gives the estimate on the number of clusters.

3. Results

Examining various criterion functions, the total cluster variance S_T delivered the most acceptable results. In our case the total cluster variance is defined by the sum of between cluster variance S_B and within cluster variance S_W .

$$S_T = S_B + S_W$$

The resulting criterion functions, calculated for the dataset are depicted in Fig.1, are shown in Fig.2. In the case of ANSI C63.5 10m distance dataset only 2 instead 5 clusters were determined.

4. Discussion

The application of the agglomerative hierarchical, as well as the k-means clustering was successful for partitioning of the measured data of the antenna factor. In determination of the number of clusters in the dataset, we used the total variance criterion function in combination with the agglomerative hierarchical clustering.

In general, the cluster analysis appeared to be a complex application-specific problem. The standard clustering algorithms performed well on the antenna factor measurements. One can expect that the same situation may apply also to other similar data. In determination of the number of clusters, a difficult question has arisen, what is the real number of clusters? Usually it is being resolved by an expert opinion which explicitly assigns particular data elements to predefined groups. Although a promising automatic method for determination of the number of clusters for antenna factor data has been identified, it has to be verified on larger datasets.

References

- [1] "The CLUSTER Procedure: Clustering Methods". SAS/STAT 9.2 Users Guide. SAS Institute.
- [2] Arthur, D. and Vassilvitskii, S. (2007). "k-means++: the advantages of careful seeding". Proceedings of the eighteenth annual ACM-SIAM symposium on Discrete algorithms: 1027–1035.
- [3] ANSI C63.5-1988; American National Standard for Electromagnetic Compatibility - Radiated Emission Measurements in Electromagnetic Interference (EMI) Control - Calibration of Antennas (9 kHz to 40 Ghz).
- [4] SAE ARP 958; SAE Aerospace Recommended Practice a Standard Method for Checkout and Calibration of Electromagnetic Interference Measurement Antennas
- [5] Casado et al. (1997). "An objective method for partitioning dendrograms based on entropy parameters". Plant Ecology Volume 131, Number 2, Springer Netherlands, pp. 193-197.
- [6] Catherine A. Sugar and Gareth M. James (2003). "Finding the number of clusters in a data set: An information theoretic approach". Journal of the American Statistical Association 98 (January), pp. 750–763.
- [7] Peter J. Rousseeuw (1987). "Silhouettes: a Graphical Aid to the Interpretation and Validation of Cluster Analysis". Computational and Applied Mathematics 20: 53–65.
- [8] Geisser, Seymour (1993). Predictive Inference. New York: Chapman and Hall.
- [9] R. O. Duda, P. E. Hart, and D. G. Stork, Pattern Classification, New York: John Wiley & Sons, 2001, Unsupervised Learning and Clustering, pp. 29-37a

The Positional Deviation in Two Numerically Controlled Axes

¹E. Kureková, ²M. Halaj, ³R. Palenčár, ⁴T. Loebli

^{1, 3, 4} Slovak University of Technology, Faculty of Mechanical Engineering,
Institute of Automation, Measurement and Applied Informatics, Bratislava, Slovakia,

²Slovak Institute of Metrology, Bratislava, Slovakia,

E-mail: eva.kurekova@stuba.sk

Abstract. Nowadays many modern production machines require positioning in thousandths of millimeter. Therefore a big attention must be paid to prepare positioning software that drives individual axes of the production machine with minimized deviations between the desired position and actually reached position – the so called positional deviation must be minimized. This goal requires a new methodology that enables estimation of the positional deviation in any point in a plane or in a space respectively, together with calculation of the uncertainty of such estimate. Such a methodology can be incorporated into a machine axis positioning system in the form of corrections enhancing positioning possibilities of individual axes. Such compensation can further improve the positional accuracy of machine tools.

Keywords: Numerically Controlled Axis, Positional Deviation, Measurement Uncertainty

1. Introduction

The quality of the numerically controlled axis has a big influence on quality of final manufactures. Qualitative parameters of final product that are affected by numerically controlled axis can be traced down to surface quality and dimensional accuracy of the final product. Namely dimensional accuracy is widely influenced by the positioning accuracy of the numerically controlled axis. Therefore it is of the utmost importance to enhance the positioning accuracy of the numerically controlled axis.

The international standard ISO 230-2:2006 [1] is aimed at the precision of machine tools linear axes. The problem is that this standard does not provide solutions for creating a continuous compensation line over the whole length of a numerically controlled axis. To create suitable line one should use another approach being more mathematically complicated. With this approach it is possible to create compensation line that could be implemented into control system, thus decreasing the positional deviation of the linear axes.

2. Evaluation According to the Standard

Testing of the positional deviation of the numerically controlled axis (either rotary or longitudinal) is ruled by the international standard ISO 230-2:2006. This standard provides guide for design of the test, testing conditions and also describes evaluation procedure for processing the measured data. In general, the testing procedure is based on repeated measurements of the actual position of the tested axis in several discrete points (target positions), distributed equally along the axis travel. The measuring cycle must be used for the measurement, as measured data are processed after completing this cycle.

Measurements according to the standard require several conditions that should be met before the measurements starts. The surrounding temperature of 20 °C and fully operational condition of the machine under test represent the main desired parameters. All types of corrective mechanisms in the control program of the axis shall be activated [1, 2].

3. Measurement model in two axes

Measurement according to the standard doesn't describe calculation of uncertainty and positional deviation in any point of axis travel. Positional deviation according to the standard can be evaluated only in discrete measured points (Fig. 1). It is not available in the form of a continuous function. Standard predicts that positional deviation is linear in between measured points that is not always true and cannot be simply stated. Regression analysis seems to be more useful in this case, providing the user with a continuous function of positional deviation [3, 4, 5].

If we want to obtain the estimates of the positional deviations also in other points than the measurement ones, we must approximate course of estimates (Fig. 2).

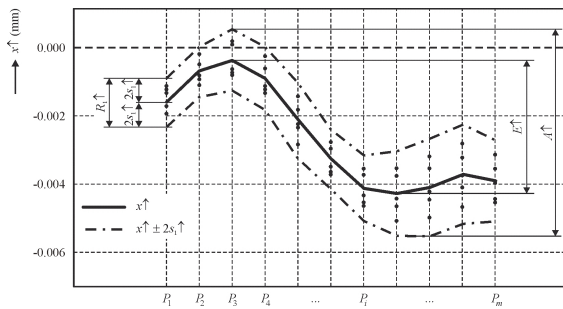


Fig. 1. Evaluation result according to the standard ISO 230-2:2006 Fig. 1

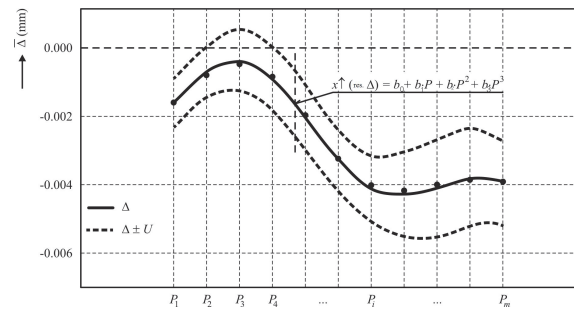


Fig. 2. Regression curve in x-axis together with uncertainties

The basic model without interactions for a regression plane (two-dimensional case) gets the form

$$\Delta = b_0 + b_1 \cdot P + b_2 \cdot P^2 + \dots + b_n \cdot P^n + b_{n+1} \cdot R + \dots + b_{n+k} \cdot R^k + e \quad (1)$$

where

$b_i, i = 1, \dots, n+k$ – unknown parameters of the polynomial function,

e – overall sum of random errors,

P – coordinate of a measured point in the 1st axis,

R – coordinate of a measured point in the 2nd axis,

Δ – the overall positional deviation.

For estimate of parameters of the regress surface \hat{b} with use of least squares method and when considering the weighs of individual measurements with dependence on their uncertainty, following expression in matrix form is valid:

$$\hat{b} = (X^T U^{-1} (\Delta) X)^{-1} X^T U^{-1} (\Delta) \Delta \quad (2)$$

where

$U(\Delta)$ – is a variance-covariance matrix of a random vector Δ , having the form:

$$U(\Delta) = \begin{pmatrix} u^2(\Delta_1) & u(\Delta_1, \Delta_2) & u(\Delta_1, \Delta_3) & \dots & u(\Delta_1, \Delta_m) \\ u(\Delta_2, \Delta_1) & u^2(\Delta_2) & u(\Delta_2, \Delta_3) & \dots & u(\Delta_2, \Delta_m) \\ \vdots & \vdots & \vdots & \vdots & \vdots \\ \cdot & \cdot & \cdot & \cdot & u(\Delta_{m-1}, \Delta_m) \\ u(\Delta_m, \Delta_1) & \cdot & \cdot & u(\Delta_m, \Delta_{m-1}) & u^2(\Delta_m) \end{pmatrix} \quad (3)$$

where

$u(\Delta_1), u(\Delta_2), \dots, u(\Delta_m)$ – are uncertainties of individual positional deviations.

$u(\Delta_1, \Delta_2)$ is the covariance between positional deviations in position Δ_1 and position Δ_2 ,
 ...

$u(\Delta_{m-1}, \Delta_m)$ is the covariance between positional deviations in position Δ_{m-1} and position Δ_m .

Uncertainties and covariances of the matrix (3) are obtained upon the uncertainties analysis during the experiment. Both elements evaluated by the type A method and by the type B method are present.

4. Practical Results

A result of this analysis is a regression plane which represents positional deviations and uncertainty of positioning in any point of plane. Such a plane can be used as an input parameter for correction of linear axes positioning.

Theoretical results were adapted to a three-axis machine tool produced by Microstep, Ltd. Measurements were carried out at two axes of the machine. Each axis was measured in tree different positions of another axis. The overall positioning deviation in a single point of a plane is obtained by vector superposition of deviations of the two axes while individual components of vector are represented by deviation of individual axes (see Fig. 3). It means that two regress planes should be prepared for x axis – regress plane for approach from right (see Fig. 4) as well as a regress plane for approach from left (see Fig. 5). The same applies for the second axis.

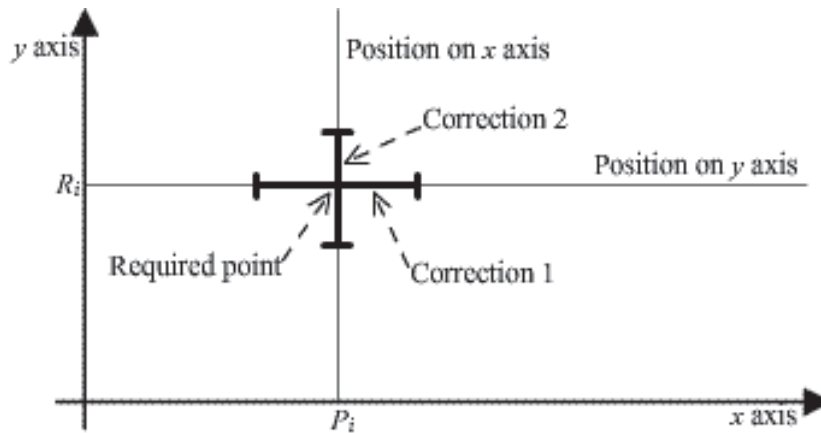


Fig. 3. Sketch of a desired point and necessary corrections

The equation describing the regress plane for the x axis and for approach from right is calculated according to (2) and has a form of

$$\begin{aligned} \Delta = & -10,949 + 0,3569P - 0,8497 \cdot 10^{-3} P^2 + 0,0013 \cdot 10^{-3} P^3 - 1,0939 \cdot 10^{-9} P^4 + \\ & + 5,1413 \cdot 10^{-13} P^5 - 1,2536 \cdot 10^{-16} P^6 + 1,2355 \cdot 10^{-20} P^7 + 0,0422R - \\ & - 0,0206 \cdot 10^{-3} R^2 \end{aligned} \quad (4)$$

while the equation of regress plane for approach from left has a form of

$$\begin{aligned} \Delta = & -11,538 + 0,3618P - 0,88858 \cdot 10^{-3} P^2 + 0,0014 \cdot 10^{-3} P^3 - 1,2008 \cdot 10^{-9} P^4 + \\ & + 5,7354 \cdot 10^{-13} P^5 - 1,4148 \cdot 10^{-16} P^6 + 1,406 \cdot 10^{-20} P^7 + 0,0368R - \\ & - 0,0144 \cdot 10^{-3} R^2 \end{aligned} \quad (5)$$

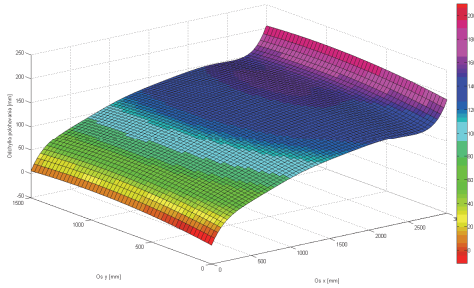


Fig. 4. Regress plane for x axis, approach from left

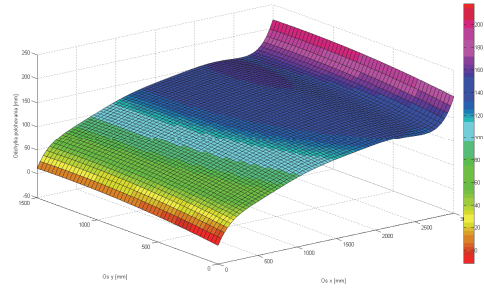


Fig. 5. Regress plane for x axis, approach from right

5. Conclusions

The international standard ISO 230-2:2006 provides scheme for calculation of positional deviation of the numerically controlled axis only in several discrete points. The procedure presented in this paper enables to estimate the positional deviation in any point of plane, no matter whether rotational or longitudinal axes are considered. Moreover it provides the estimate of the positional deviation with the respective uncertainty of such estimate. This gives the designer or programmer of the machine control system the information about behavior of the machine in any point of the axis travel. Thus appropriate corrections can be included into the control program or the adequate design corrections can be performed in the design of the machine.

Acknowledgements

The research work described in the paper was performed by a financial support of the Slovak Scientific Agency (VEGA), grant No. 1/0310/09.

References

- [1] ISO 230-2: 2006. Test code for machine tools – Part 2: Determination of accuracy and repeatability of positioning of numerically controlled axes.
- [2] STN 20 0300-31 Measuring of geometrical precision of machine tools. Measuring method for measuring of positional accuracy - Meranie geometrickej presnosti obrábacích strojov. Metódy merania presnosti polohovania.
- [3] V. Chudý, R. Palenčár, E. Kureková and M. Halaj, Technical quantities measurement - Meranie technických veličín. STU in Bratislava, Bratislava, 1999.
- [4] R. Palenčár, P. Gros, M. Halaj, Evaluation of the positional deviation of numerically controlled axes. *Strojnícky časopis*, Vol. 57, n° 1: 1-12, 2006.
- [5] J. Anděl, Statistical methods. - Statistické metody. Praha, Matfyzpress 1998.
- [6] Shih-Ming, Wang - Han-Jen, Yu – H.ung Wei, Liao: A new high-efficiency error compensation system for CNC multi-axis machine tools. In: *Int J Adv Manuf Technol* 28 s. 518-526, 2006.

Measurement of Physical Quantities

Dimensional Micro- and Nanometrology at PTB

**R. Köning, J. Flügge, D. Hüser, W. Haessler-Grohne, H.U. Danzebrink, G. Dai,
U. Brand, V. Nesterov, S. Bütefisch, G. Ehret, M. Wurm, B. Bodermann, E.
Buhr, H. Bosse**

Physikalisch-Technische Bundesanstalt (PTB), Bundesallee 100,38116 Braunschweig,
Email: rainer.koenig@ptb.de

Abstract. *In this contribution we will provide an overview of the current state and the actually ongoing developments in the field of dimensional micro- and nanometrology at PTB. That is, we will report on the methods and instruments developed, applied and that are in development for high precision, traceable measurements in these important areas of dimensional metrology.*

Keywords: Dimensional Metrology, Nanometrology, Micrometrology, Traceability

1. Introduction

The control of the geometrical dimensions in the industrial production of single components and whole systems demands appropriate measurement techniques. The related measurement instruments have to be chosen according to different criteria like throughput, robustness, price, 3D-capability, in-line ability, measurement range, required resolution and accuracy. Meanwhile, dimensional features in the area of micro- and microsystem technology can be characterized and controlled during production on the basis of traceable measurement results in the same way as in conventional manufacturing process control. In nanotechnology the desired properties of the product often depend much stronger on the geometrical dimensions or even appear as a consequence of the reduced dimensions and therefore even tighter specifications have to be met. Here the progress made in the available measurement equipment over the last two decades has just enabled this field of technology.

Dimensional metrology instruments aiming at the smallest measurement uncertainties achievable have to comply with two fundamental requirements. Firstly a well-designed and well-characterized positioning system, which provides a relative movement of the measurement object with its functional dimensional features of interest with respect to the probing system of the measurement instrument, is mandatory. Secondly, a sound physical model of the interaction of the probing system with the dimensional features of the sample should be available and applied in the evaluation of the measurement results. This is particularly important if the size of the features comes close to the resolution limit of the probing system. The measurement of some geometrical properties, for example the diameter of nanoparticles, is simply impossible without considering the probe sample interaction.

We will show examples of different probing methods in this paper, namely tactile, opto-tactile, optical and electron beam methods and discuss challenges for future developments in micro- and nanometrology.

2. Micrometrology

In micrometrology the dimensions of measurement objects are usually in the range of some 100 μm to some mm. Typically the required measurement uncertainties of the dimensional features are in the range of 0.1 μm or below. Several metrology institutes developed, built and meanwhile operate suitable reference measurement systems for dimensional characterization

of microcomponents and microsystems [1-3]. Optimized probe systems adapted to these small objects, which were required have been developed as well. Here the reduction and a better control of the probing force had to be established. The contributions of the PTB also were threefold, namely development of a reference micro-CMM [1], the development of improved probing systems [4-8] and the development of a micro- and nanoforce measurement facility [9,10].

Micro- and Nanoforce facility

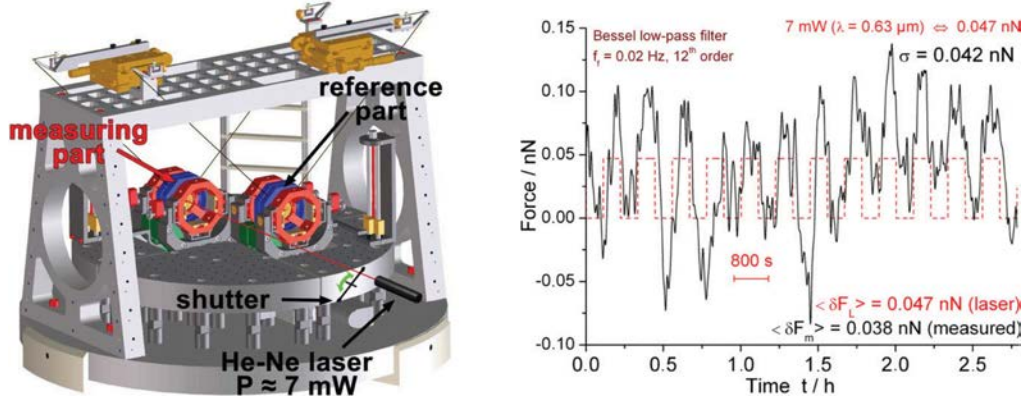


Fig. 1. Schematic of the Micro- and Nanoforce measurement facility (left) and the measured force caused by an incident laser beam

The necessary reduction of the probe size and the probing force required to measure the dimensions of microstructures sufficiently accurate possessed a real challenge. In order to be able to measure these forces as well as the stiffness of AFM cantilevers a Micro- and Nanonewton measurement facility has been built [9,10], which has a measurement range from 10 μN to 1 nN with a resolution of 1 pN. It is based on the measurement of the displacement of a disc pendulum and uses electrostatic stiffness reduction and force compensation. In addition an identical reference pendulum is employed for the compensation of thermal and seismic noise. It is shown in Fig. 1 together with the measurement results of the force acting in case a laser beam ($\lambda = 633\text{nm}$) with an optical power of 7 mW hits the measurement disc.

Microprobe developments

Historically an opto-tactile probe was first developed and also transferred to industry as a 2D measurement probe [4]. It basically consists of a fiber ball probe with diameters down to 15 μm which is illuminated by the fibre and whose position is measured with a CCD camera. This system recently was enhanced to provide full 3D probing capability by analysis of the speckle pattern of a fibre ball if it is illuminated by a coherent light source [5].

In addition a 3D tactile microprobe was developed in cooperation with the Institute for Microtechnology at the TU Braunschweig. Here the deformation of a so-called silicon boss membrane is measured by means of integrated piezoresistive transducers [6]. The deformation of the membrane is caused by deflections of a microprobe fixed to the centre part of the membrane (boss). This 3D sensor allows to measure forces as well as displacements and different probe configurations were reported (ball diameter, shaft length, boss type). Both types of probe are used in the μCMM (see below). A third development of a probe system which is also suitable for characterization of microcomponents is an assembled cantilever probe (ACP) [7]. Here two AFM-cantilevers are glued together so that they form approxi-



Fig 2. Microprobe systems developed and used at the PTB for characterization of microcomponents. Left: opto-tactile 3D probe; middle: Si boss membrane 3D microprobe (with Euro Cent coin for size comparison); right: ACP probe (assembled cantilever probe).

mately a right angle (see fig. 2), so that the deflection of the 1st, vertical cantilever can be transferred to the 2nd, horizontal cantilever and detected by a conventional AFM head. The ACP probes have been used successfully to measure the form of sidewalls of micro gears [7]. Fig. 2 shows the three described microprobe systems, which all allow to measure the dimensional features of interest on the accessible surface areas of microcomponents.

For the characterization of object features which are normally inaccessible for tactile probes or which are completely hidden within the measurement object, like e.g. inclusions, x-ray based industrial computed tomography (CT) techniques are increasingly used. The PTB has contributed to this metrology area by development of suitable standards and by basic investigations with respect to the traceability of the CT measurement results [11] and will continue to investigate the application of CT techniques also in the field of micrometrology.

Reference Micro Coordinate Measuring Machine

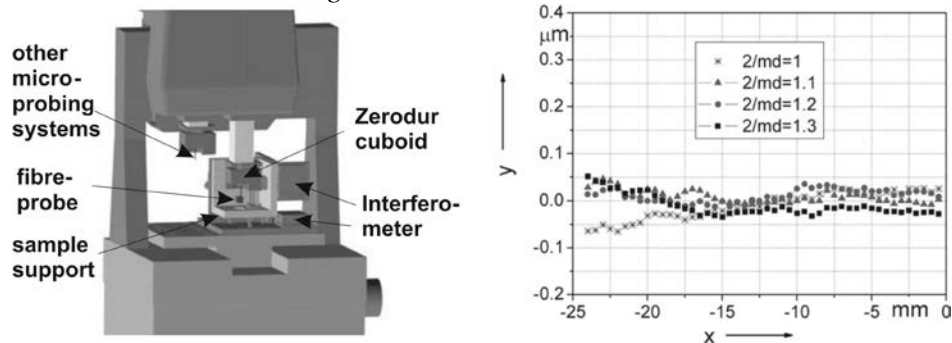


Fig. 3. Schematic of the μ CMM (left) and typical repeatability of a flatness measurement (md: distance of the measurement trace the of fibre probe from the upper edge of the optical flat)

The μ CMM is based on a commercially available coordinate measuring machine with improved air bearings and high resolution Zerodur scales using an opto-tactile fibre probe for the localization of microstructures. It has been equipped with a metrology frame, which contains six laser interferometers for high-precision position and guiding deviation measurements, a Zerodur cuboid carrying the mirror surfaces for the laser interferometers to which the fibre probe is fixed, and an invar support for the measuring objects to which the reference mirrors of the interferometers are fixed. This led to a reduced measurement volume of 24 mm x 34 mm x 35 mm. The orthogonality and flatness deviations of the Zerodur measuring surfaces have been measured and taken into account in the equation of motion of

the probing sphere. Therefore the μ CMM is capable of providing directly traceable measurements. As a first performance test, the flatness of an optical flat has been measured with the fibre probe. Measuring-depth-dependent and probing-force-dependent shifts of the probing position were observed. In order to reduce the scattering of the probing points, 77 data sets were taken and averaged for the measurement of one coordinate point. This has led to measuring times of several hours for one plane and to strong thermal drifts. A typical repeatability of this type of measurements is shown in the diagram of figure 3. The expanded measurement uncertainty is 236 nm. If the drift contribution is omitted 61 nm are obtained so that the uncertainty can be considerably reduced by a reduction of the measurement time.

In addition a F25, a μ CMM made by Zeiss was investigated. It offers a much larger range of 130 mm x 130 mm x 100 mm, which also leads to an increase of the achievable measurement uncertainty. It closes the gap in the measurement capabilities of the large CMMs and the μ CMMs. Zeiss specifies an uncertainty of about $(0.4 + L/666) \mu\text{m}$, where L is in mm. Recent investigations at PTB on calibration objects like a special Zerodur ball plate have shown, that measurement uncertainties in the range of 50 nm for the ball positions could be achieved under optimum circumstances with this type of μ CMM.

The transition from micro- to nanometrology is smooth. There are objects with outer dimensions in the mm range with either nanosized features of interest or with very small dimensional tolerances, which need to be characterized precisely. In order to deal with this challenge, a metrological large range scanning probe microscope (LR-SPM) was developed at the PTB [12] which allows to use the full positioning range of 25 mm x 25 mm x 5 mm of the so-called Nano Positioning and Nano Measuring Machine [12] for traceable dimensional measurements with a nominal resolution of 0.1 nm. The motion control, data acquisition and data evaluation software of this instrument has recently been enhanced by integration of the CMM software Quindos. Therefore it can now be applied to precisely calibrate 3D reference objects for micro-coordinate metrology. Figure 3 shows on the left side a set of two spheres in a nominal distance of 3 mm with 1 mm radius each and an example of the repeatability of distance calibrations, which was obtained by the LR-SPM using the Si boss membrane probe shown before [6]. Also shown in the same figure on the right side is an SEM image of a precision micropyramid with landmark type test structures, which was produced by focussed ion beam figuring techniques. Such a micropyramid structure can be calibrated by instruments like e.g. the metrological LR-SPM and can then be used as a 3D calibration artefact for other types of SPMs or SEMs [13].

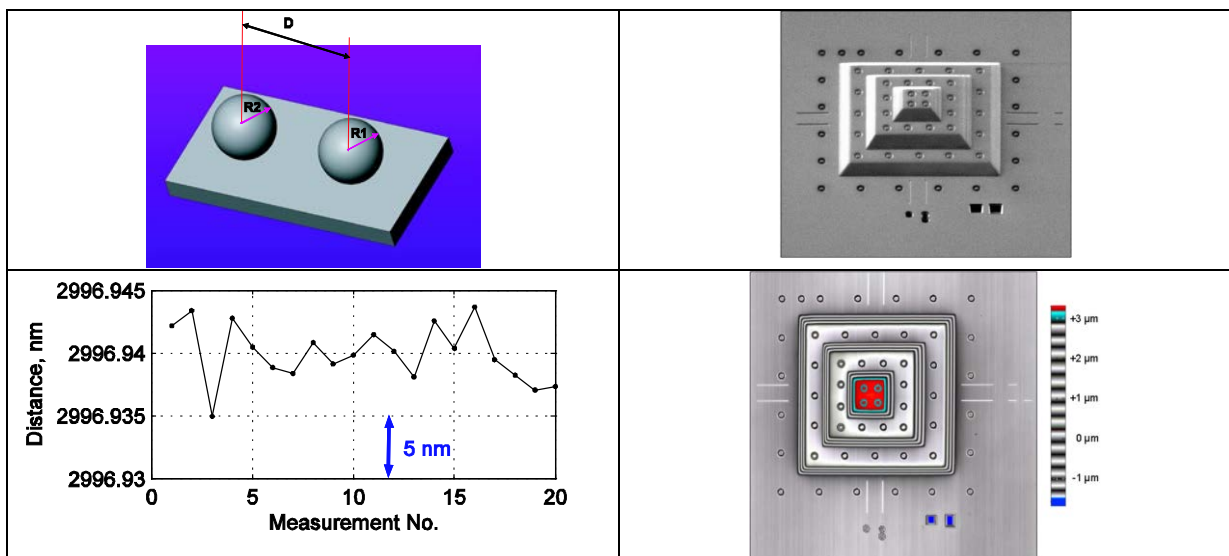


Fig. 4. Left: Test object of 2 small spheres in 3 mm nominal distance with 1 mm radius each and repeatability of the distance measurement results as obtained by the metrological LR-SPM of the PTB. Right: SEM (top) and SPM image (34 μm scan range) of a micropyramid which is used as a 3D microscope calibration artefact.

Nanometrology

Nanotechnology usually utilizes size-dependent phenomena that enable novel applications [14], which usually start to appear at feature sizes smaller than 100 nm. It requires the understanding and control of matter and processes at the nanoscale, below 100 nanometres in one or more dimensions. In order to be able to control the related processes, appropriate measurement techniques with an adequate spatial resolution have to be developed and employed. Here we will provide an overview of the measurement capabilities of the PTB in dimensional nanometrology.

As already mentioned in the preceding section there are also microstructures whose dimensional properties, like height, width and distance, have to be measured with uncertainties in the nanometer range. Probably the highest requirements occur in surface metrology. Here the “high resolution topo scan” (HRTS) [15], a 2-dimensional surface profiler, developed at the PTB, started to operate lately. For one-dimensional traceable length calibrations of line scales, photomasks and incremental encoders on substrates up to 600 mm with uncertainties down to a few nm only, the PTB is operating a special vacuum interference comparator, the so-called “Nanometer Comparator” [16,17]. The length of gauge blocks with suitable surface quality can be measured with even lower uncertainty [18]. Such samples are used to determine the thermal expansion coefficients and the compressibility and to investigate the stability of materials. The accurate knowledge of these material parameters, including their uncertainties, is a necessary prerequisite for measurements of larger parts with measurement uncertainties in the single nanometer range. Small angle measuring devices are key components in deflectometer set-ups which are used for high precision flatness and synchrotron mirror metrology [19]. They have also to be used for the characterization of the angle deviation of the scan apparatus, which are required for a reliable determination of the Abbe error contribution to the measurement uncertainty. Such measurements require high precision angle calibrations. Therefore investigations are ongoing to improve the measurement performance of electronic autocollimators and their calibration procedures [20].

Optical methods

Optical microscopy is despite its rather low resolution still widely in use in nanotechnology. Progress in the technology of available light sources, in the design of optical materials, elements and their production, the efficiency of the image detectors (CCD-cameras as well as photo diodes and photomultipliers) lead together with the increase of the image data acquisition and processing capabilities to a steady increase of their performance. The PTB already participates in these developments for a long time. High resolution optical UV microscopes operating at a wavelength of 365 nm are already in use for quite a while in the line width and photo mask calibration service.

Fig. 5 shows a schematic of the new deep UV transmission microscope [21], which is currently being set up and which is especially designed for line width (critical dimensions or CD) measurements of micro- and nanostructures. The optical resolution is about 100 nm. The main application will be CD metrology of photo masks used in optical lithography. The high lateral resolution will be obtained by using of 193 nm excimer laser radiation for illumination in conjunction with a high-aperture objective (NA= 0.9) of highest quality (Strehl ratio 0.99)

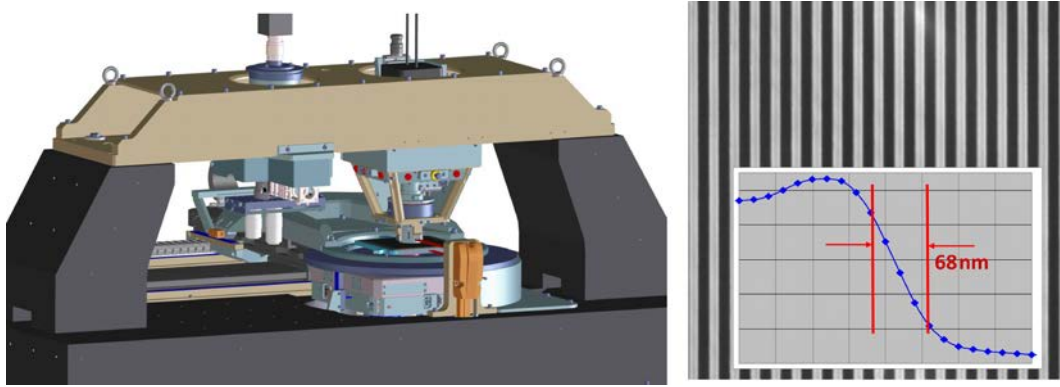


Fig. 5. Schematic of the new 193 nm microscope and first performance data

The illumination and imaging system will provide various imaging modes, ranging from ordinary brightfield to specially structured illumination schemes. Traceability will be accomplished through an integrated laser interferometer. The mechanical set-up is characterized by an ultra-stable bridge construction on a granite base and has been designed with special emphasis on realizing a positioning stability in the nanometer range. The projected (2σ) measurement uncertainty for line width measurements on photomasks (chromium on quartz) is only 10 nm.

Another trend is the use of non-imaging methods for the measurements of nanostructures. Figure 6 shows the basic operation principle and the realization of the new DUV scatterometer of the PTB [22]. This versatile setup allows reflectometric, diffractometric and ellipsometric measurements of a wide range of different samples and various wavelengths ranging from 840 nm down to 193 nm.

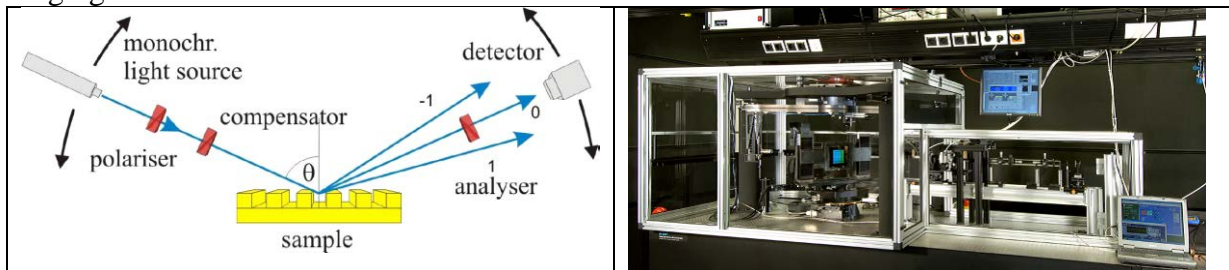


Fig. 6. Basic operation principle and realization of the new PTB DUV scatterometer.

The optical diffraction pattern of grating structures does not only contain information about the mean pitch, but also about other dimensional features of interest of the grating structures like the height, top CD or bottom CD and sidewall angle. To extract information on these structure parameters from measured optical diffraction pattern, one has to solve the inverse scattering problem. Therefore it is necessary to rigorously model the interaction of light with a 3D structure geometry, for which PTB uses Maxwell solvers either based on the rigorous coupled wave analysis method (RCWA) or a finite element method (FEM) [23]. Such simulations are also required for the aforementioned line width measurements by means of optical microscopy. Due to the mathematical complexity of this particular task, the PTB closely cooperates with institutes of applied mathematics [24].

The wavelength used at the PTB scatterometers for the characterization of nanograting structures ranges from the VIS over DUV (193 nm) to EUV (13 nm). The latter wavelength range is available at the Berlin synchrotron storage rings BESSY II and the new PTB Metrology Light Source (MLS) [25].

In the recent international comparison on 2D gratings called Nano 5 [26], the PTB has participated with a diffractometer ($\lambda=496$ nm, 476 nm and 266 nm) set-up and with the LR-SPM. The measurement results of both instruments on the two comparison standards with nominal pitches of 300 nm and 1000 nm were in good agreement with the comparison reference values. Standard uncertainties of the PTB results e.g. for the mean x-pitch of the 300 nm 2D grating sample were 12 pm for the diffractometer and 5.6 pm for the LR-SPM. In contrary to the diffraction methods the LR-SPM also provides information on the local pitch variation of the sample. Another international comparison on optical diffraction measurements of 1D gratings also showed a good agreement of results between the four participating national metrology institutes [27].

Scanning electron microscopy

In the preceding section the importance of appropriate physical models for the simulation of the measurement signal and for the extraction of the measurand out of this signal was emphasized. These are necessary prerequisites for traceable measurements as well as for the accurate determination of the accompanying measurement uncertainties of these precision measurements. In electron beam based metrology, especially in scanning electron microscopy (SEM) the situation is similar, although the primary SEM beam spot offers a much higher resolution of down to 1 nm only.

However, the primary electrons initiate a series of elastic and inelastic scattering events in the solid state material which effectively reduce the achievable spatial resolution. For the simulation of these scattering events and for the generation of secondary and backscattered electrons which are detected for SEM image signal generation, the PTB uses its self-developed Monte Carlo based simulation programs [28].

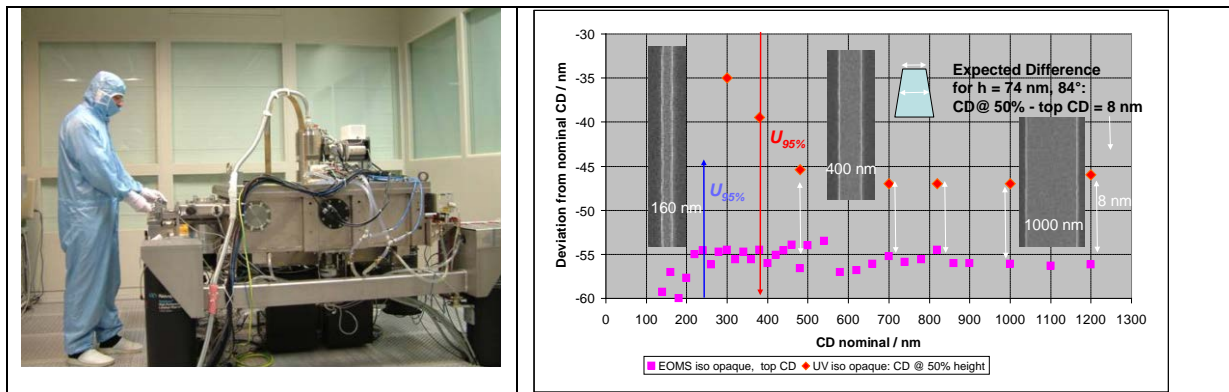


Fig. 7. The Electron Optical Metrology System in the PTB clean room centre and results of CD calibrations by the EOMS (top CD) and UV transmission microscopy (CD at 50 % height of the line features [29]).

On the basis of these simulation programs, the PTB has developed special edge detection algorithms, which are used for traceable SEM line width metrology. One example is an exponential fit operator for determination of the top width of a line which is based on the electron diffusion characteristics of secondary electrons emitted in the vicinity of edges of line structures. Figure 7 shows a photo of the Electron Optical Metrology System (EOMS) which is used for SEM measurements on larger planar objects together with the results of a comparison measurement with UV transmission microscopy on different line features on a chrome on quartz mask [29]. Another application of SEM modeling and measurement of increasing importance, that has been pursued by the PTB, is the traceable characterization of the size and shape of nanoparticles [30]. Here the PTB also collaborates with partners from academia, other national metrology institutes and industry in an EU-funded project.

Scanning Probe Microscopy

Scanning probe microscopy (SPM) has also an important role in high resolution characterization as well as in the creation and manipulation of nanostructures and nanoobjects. The PTB is involved in the field of scanning probe based dimensional metrology since it emerged.

The first metrology instruments were home-built scanning tunnelling microscopes (STMs) with a capacitive based position feedback employed to overcome the insufficient properties of the piezoelectric materials used to provide the scan motion. The capacitive displacement sensors were calibrated by means of heterodyne interferometry [31,32]. Both, a scanning sample design as well as a scanning probe design were implemented. However, STM measurements can only be performed at well conducting samples and, due to the very small tip sample distance, with very low speed. Therefore the scanning force detection scheme was adapted as soon as it became available [33]. The use of scanning optical near field microscopes was also investigated [34]. Due to the difficulties in the interpretation of the images and the lack of high quality commercially available probes these activities were abandoned. The plans to obtain well defined position standards by producing nanostructures coupled to the surface lattice using SPM based nanolithography were also dismissed due to missing knowledge of the fundamentals of the structure formation process [35]. Also an ultra-precision interference comparator that used two scanning tunnelling microscopes as surface probes [36] was implemented. The instrument was supposed to measure gauge blocks but the measurement uncertainties achieved were far behind those of the optical gauge block interferometers [18] and therefore this approach was not followed further. In addition, in a collaboration with the TU Ilmenau, interferometers were integrated in the AFM Veritekt (built by former company Carl Zeiss Jena) to set up a traceable metrology AFM [37]. Other instrument developments were the successful adaptation and upgrade of the Nano Measuring Machine NMM (from SIOS Messtechnik GmbH) to the metrological LR-SPM already mentioned, the development of a large sample AFM (Nanostation 300, development performed in cooperation with former company S.I.S.) for measuring photomasks [38], the integration of home built STM and AFM with the combined optical and X-ray interferometer (COXI) [39,40] and the AFM designed to study tip-sample interactions [41]. In addition a number of commercial instruments are in use. Currently an AFM with a short scan range ($5\ \mu\text{m} \times 5\ \mu\text{m} \times 5\ \mu\text{m}$) is being set up. It comprises of a novel type of CMOS sensor based and FPGA processed interferometers. This AFM is intended for highly accurate measurements of nanostructures like nanoparticles and lithography features in the range below $1\ \mu\text{m}$. A discussion of the metrological design and functional principle of the interferometers is to be published in [42].

Both the LR-SPM and the Nanostation 300 have the capability to probe in full 3D

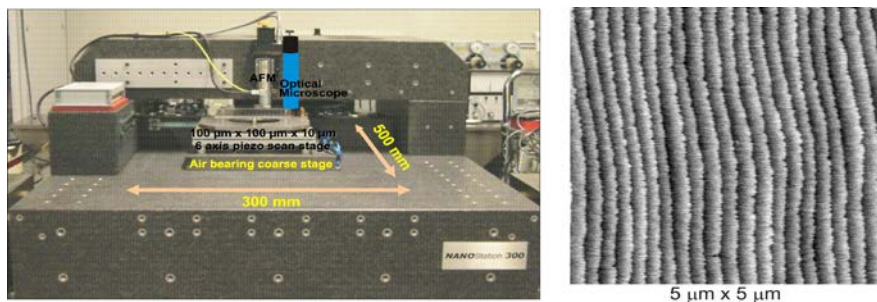


Fig. 8. Nanostation 300 and an AFM image of a silicon surface with the monoatomic steps resolved.

vectorially. The limitation of raster scanning along two horizontal axes with equidistant sampling points has been overcome offering a method to image sidewalls of structure with a high aspect ratio. This is a prerequisite in accurate linewidth metrology. Figure 8 shows a picture of the Nanostation 300 and an AFM image in which the monoatomic steps of the imaged silicon surface are resolved. An absolute position error of 2 to 3 μm over the whole motion range of 300 mm by 550 mm of the coarse positioning, air bearing stage allows to position areas to be investigated underneath the AFM scan head sufficiently well so that the position error can easily be corrected by adjusting the offsets of the AFM scan range. It should be noted that before an AFM scan starts the stage is set down and the air bearings are turned off to eliminate their contribution to the noise. In this way, as shown in figure 8, the instrument is able to resolve monoatomic steps on a silicon surface (step height approx. 0.3 nm) using a tube scanner in the normal scan mode.

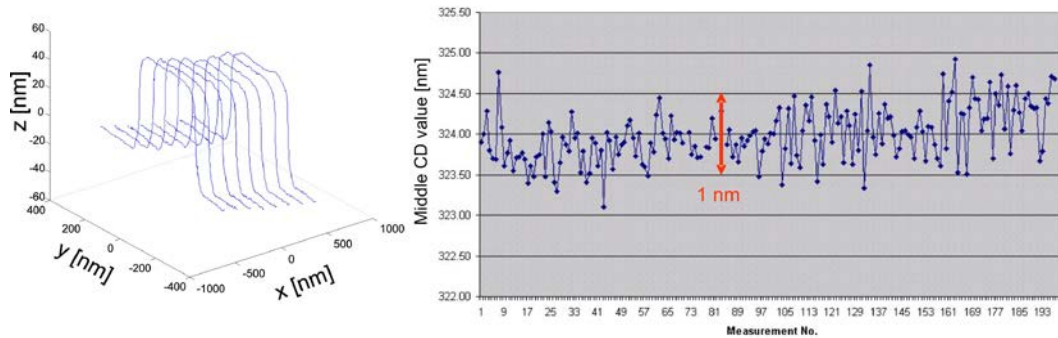


Fig. 9. Left scan profiles of a line structure. Right: Results of repeated line width measurements.

In the conventional mode an AFM scans the surface line-by-line, while the tip remains in the interaction regime all the time and the controller tries to keep the force interaction constant. In the new mode of this instrument single points are probed: the tip is approached until the interaction force reaches a predefined threshold and several readings of all 3 position axes of the scanner as well as readings of the interaction signals are taken. The tip is retracted after each point and moved to the next position, which may be located in arbitrary distance. For each probing point, the signal values are averaged. A sequence of such probing points is taken to obtain profiles of a line structure from which the line width (critical dimension CD) is evaluated. In the left diagram of Fig. 9 repeated profiles of a line structure are shown. Details of the sidewalls have been resolved. In the right diagram results of 200 line width measurements obtained from repeated scans are shown. The results exhibit a scatter below 2 nm and show only, if at all, a small trend towards larger line width values, which indicates that the tip shape is preserved. In the case of tip wear of boot shaped tips, the line width values would decrease.

The line profile data of the left diagram allows to retrieve the important details of the line structure, like the side wall angle, corner roundings and footings and the height, which are required as input parameters for the simulation of the optical and electron-optical images and optical scattering and diffraction signals. Therefore the AFM complements these methods.

While the geometrical influence of the tip geometry can be treated adequately [43,44] the simulation of the image formation process has just been started. It seems that the models of the physical tip-sample interaction need to be refined considerably although the results presented at the recent nanoscale conference are very promising [45]. It should be mentioned here that these results still need to be transferred from ultrahigh vacuum to ambient conditions. The PTB has also started investigations here, which have been documented in [46,47]. The results show already that the physical tip-sample interaction, and therefore the

image signal of the AFM, changes drastically at steep sidewalls.

Conclusion

The PTB has a strong commitment to both, dimensional micro- and nanotechnology. To be able to perform dimensional measurements at the highest level of accuracy requires specialized and often especially developed instruments and a complete understanding of measurement signals including the interaction of probe and sample. The assumption that this interaction does not vary during the course of the measurement is no longer justified.

References

- [1] Brand U, Kirchoff J. A micro-CMM with metrology frame for low uncertainty measurements *Measurement Science and Technology* 16: 2489-2497, 2005.
- [2] Küng A, Meli F, Thalmann R. Ultraprecision micro-CMM using a low force 3D touch probe *Measurement Science and Technology* 18(1):319-327, 2007
- [3] Van Seggelen J K, Rosielle P C J N, Schellekens, P H J. Design of a 3-D CMM with elasticall guided z-axis and x-y-axis with less than 2 mm Abbe offset. In proceedings of 3rd Euspen conference, 2002, 29-32
- [4] Ji G, Schwenke H, Trapet E. Opto-tactile sensor for measuring small structures on coordinate measuring machines. In Proceeding of the annual meeting of the American Society for Precision Engineering, 1998, 25-28.
- [5] Neuschaefer-Rube U, Wissmann M. *PTB-Mitteilungen* 117(4):390–396, 2007 (in German)
- [6] Dai G, Bütefisch S, Pohlenz F, Danzebrink H U. A high precision micro/nano CMM using piezoresistive tactile probes. *Measurement Science and Technology* 20: 084001-084010, 2009
- [7] Dai G, Wolf H, Weinmann T, Xu M, Pohlenz F, Danzebrink H U. Nanoscale surface measurements at sidewalls of nano- and micro-structures. *Measurement Science and Technology* 18: 334-341, 2007.
- [8] Nesterov V, Brand U. Modelling and investigation of the mechanical and electrical characteristics of the silicon 3D-boss microprobe for force and deflection measurements. *J. Micromech. Microengineering* 16: 1116–1127, 2006
- [9] Nesterov V. Facility and methods for the measurement of micro and nano forces in the range below 10^{-5} N with a resolution of 10^{-12} N (development concept). *Measurement Science and Technology* 18: 360-366, 2007.
- [10] Nesterov V, Mueller M, Frumin L, Brand U. A new facility to realize a nanonewton force standard based on electrostatic methods. *Metrologia* 46:277-282, 2009
- [11] Bartscher C M, Hilpert U, Goebbels J, Weidemann G. Enhancement and Proof of Accuracy of Industrial Computed Tomography(CT) Measurements. *CIRP Annals-Manufacturing Technology* 56(1):495 -498, 2007
- [12] Dai G, Pohlenz F, Danzebrink H.U, Xu M, Hasche K, Wilkening G. Metrological large range scanning probe microscope. *Review of Scientific. Instruments* 75:962–969, 2004
- [13] Ritter M, Dziomba T, Kranzmann A, Koenders L. A landmark-based 3D calibration strategy for SPM *Measurement Science and Technology* 18 (2): 404 – 414, 2007
- [14] <http://www.iso.org> and links to the scope of ISO TC 229 on ‘Nanotechnology’

- [15] Thomsen-Schmidt P. Characterization of a traceable profiler instrument for areal roughness measurements. In Proceedings of Nanoscale 2010, to be published in special issue of Measurement Science and Technology.
- [16] Köning R, Flügge J, Bosse H. Recent activities at PTB nanometer comparator In Proceedings of the Conference on Recent Developments in Traceable Dimensional Measurements, 2003, SPIE, Vol. 5190, 391-399
- [17] Köning R, Flügge J, Bosse H. Achievement of sub nanometer reproducibility with the Nanometer Comparator. In Proceedings of the Advanced Lithography Conference, 2007, SPIE 6518, 65183F-1 - 65183F-8
- [18] Schödel, R, Abou-Zeid, A. PTB's precision interferometer for high accuracy characterization of thermal expansion properties of low expansion materials, In: Nanoscale calibration standards and methods: dimensional and related measurements in the micro- and nanometer range, Wilkening, G. and Koenders, L., eds.; ISBN 3-527-40502-X; ISBN 978-3-527-40502-2, pp. 500 - 514 (2005)
- [19] Geckeler R D. Optimal use of pentaprisms in highly accurate deflectometric scanning. *Measurement Science and Technology* 18(1): 115-125, 2007.
- [20] Just A, Krause M, Probst R, Wittekopf R. Calibration of high-resolution electronic autocollimators against an angle comparator. *Metrologia* 40:288-294, 2003.
- [21] Ehret G, Pilarski F, Bergmann D, Bodermann B, Buhr E. A new high-aperture 193 nm microscope for the traceable dimensional characterization of micro- and nanostructures *Measurement Science and Technology* 20(6):084010-084020, 2009
- [22] Wurm M, Pilarski F, Bodermann B. A new flexible scatterometer for critical dimension metrology. *Review of Scientific Instruments* 81: 023701- 023709, 2010
- [23] Bodermann, B, Ehret G. Comparison of different approaches for modelling microscope images on the basis of rigorous diffraction calculation. In, Proceedings of SPIE 5858, 2005, 09-1 - 09-12
- [24] Gross H, Model R, Bär M, Wurm M, Bodermann B, Rathsfeld. A Mathematical Modeling of indirect measurements in scatterometry *Measurement* 39 (9): 782–794, 2006.
- [25] Scholze F, Laubis C; Ulm G, Dersch U; Pomplun J, Burger S.; Schmidt F. In Proc. of Advanced Lithography Conference, 2008, SPIE 6921, 69213R-1 - 69213R-11.
- [26] Garnaes J, Dirscherl K. NANO5-2D-Grating-Final report, *Metrologia* 45:04003, 2008.
- [27] Decker J E, Buhr E, Diener A, Eves B, Kueng A, Meli F, Pekelsky J R, Pan S-P, Yao B-C. Report on an international comparison on one-dimensional (1D) grating pitch *Metrologia* 46: 04001, 2009
- [28] Frase C. G. Haessler-Grohne W. Use of Monte Carlo models in the development and validation of CD operators. *Surface and Interface Analysis* 37(11):11, 942 – 950, 2005
- [29] Richter J, Heins T, Liebe R, Bodermann B, Diener A, Bergmann D, Frase C G, Bosse H. Calibration of CD mask standards for the 65 nm node:CoG and MoSi. In Proceedings of the 23rd European Mask & Lithography Conference. 2007, SPIE 6533, 6533-53
- [30] Buhr E, Senftleben N, Klein T, Bergmann D, Gnieser D, Frase C G, Bosse H. Characterization of nanoparticles by scanning electron microscopy in transmission mode. *Measurement Science and Technology* 20:084025 (9p), 2009
- [31] Zhao X. Scanning Probe Microscopes with High resolution capacitive transducers PTB Report, PTB-F-32, ISBN 3-89701-207-3, 1998

- [32] Jusko O, Zhao X, Wolff H, Wilkening G. Design and three dimensional calibration of a measuring scanning tunneling microscope. *Review of Scientific Instruments* 65(8):2514-2518, 1994
- [33] B. Barbato, K. Carneiro, J. Garnæs, G. Gori, G. Hughes, C. Jensen, J.F. Jørgensen, O. Jusko, Livi, H. McQuoid, L. Nielsen, G.B. Picotto, G. Wilkening. Scanning Tunneling Microscopy Methods for Roughness and Micro Hardness Measurements. Synthesis Report on BCR project 3423/2/0/284/4/92-BCR-DK(30), (1994)
- [34] Danzebrink, H. U, Nahfeldmikroskopischer Sensor mit interner Signalwandlung. PTB report, PTB-F-27, ISBN 3-89439-830-8
- [35] Köning R, Jusko O, Koenders L, Schlachetzki. A Systematic Investigation of Nanostructuring by STM. *Journal of Vacuum Science and Technology* B14: 48 -53, 1996
- [36] Koenders L, Harms C H, Waltereit E, Wilkening G. An ultra-precision interference comparator for dimensional measurements using two tunnelling microscopes as probes. *Measurement Science and Technology* 14(6):943-952, 2003
- [37] Hasche K, Herrmann K, Mirande W, Pohlenz F, Seemann R. Development of Scanning Force Microscopy with Subnanometric Capability. In Proceedings of 4th seminar of quantitative microscopy, 2000, PTB report (PTB-F-39), 219-225
- [38] Discherl K, Cerkas S, Bosse H, Fuß H A. The Nanostation 300 – Development of an SPM for large objects, unpublished
- [39] Yacoot A, Kuetgens U, Koenders L, Weimann T. A combined scanning tunnelling microscope and x-ray interferometer. *Measurement Science and Technology* 12(8):1660-1665, 2001
- [40] Yacoot A, Koenders L. From nanometre to millimetre: a feasibility study of the combination of scanning probe microscopy and combined optical and x-ray interferometry. *Measurement Science and Technology* 14(8):N59-N63, 2003
- [41] Yacoot A, Koenders L, Wolff H. An atomic force microscope for the study of the effect of tip sample interaction on dimensional metrology. *Measurement Science and Technology* 18 350–9
- [42] Strube S, Molnar G, Danzebrink H-U. Compact FPGA based multi-axial interferometer for simultaneous tilt and distance measurement in the sub-nanometre range. In Proceedings of Nanoscale 2010, to be published in a special issue of Measurement Science and Technology.
- [43] Villarrubia J S. Algorithms for scanned probe microscope image simulation, surface reconstruction and tip estimation. *Journal of Research of the National Institute of Standards and Technology* 102:245-254, 1997
- [44] Williams P, Williams P M, Shakesheff K M, Davies M C, Jackson D E, Roberts C J and Tendler S J B. Blind reconstruction of scanning probe image data. *J. Vac. Sci. Technol. B* 14:1577–62, 1996a
- [45] Sugimoto Y, Pou P, Abe M, Jellinek P, Perez R, Morita S, Custance O. Chemical identification of individual surface atoms by atomic force microscopy. *Nature* 446(1):64-67, 2007
- [46] Yacoot A, Koenders L. Aspects of scanning force microscope probes and their effects on dimensional measurements. *Applied Physics* 41(8):103001-103047, 2008
- [47] Hüser-Espig D, Haessler Grohne W, Dai G, Bosse H. Investigation of cantilever response of NC-AFM in measuring true 3D structures. In proceedings of Nanoscale 2010 to be published in a special issue of Measurement Science and Technology

Analysis of Magnetic Fields on the Surface of Grain Oriented Electrical Steel

¹A. J. Moses, ¹P. I. Anderson, ¹N. Chukwuchekwa, ¹J. P. Hall, ¹P. I. Williams and ¹X. T. Xu

¹Wolfson Centre for Magnetics, School of Engineering, Cardiff University, Cardiff, UK

Email: Mosesaj@cf.ac.uk

Abstract. *Magnetic properties of grain oriented electrical steel are often measured using well established surface field sensors. Use of magnetic domain observation, magnetic force microscopy (MFM) and Barkhausen noise measurement for studying magnetic properties and microstructure is demonstrated. It is shown that uncertainty over the region in which Barkhausen noise is detected needs clarification. It is further shown that different domain observation techniques appear to identify different types of micro structural features and that uniaxial magnetic field sensors may not reveal the total loss occurring in the steel. The origin of unusual MFM images is discussed.*

Keywords: Electrical Steels, Magnetic Domains, Barkhausen Noise, Magnetic Losses, Magnetic Force Microscopy, Magnetic Field Detectors

1. Introduction

Grain oriented electrical steel (GOSI) is a key component of electrical machine cores. It is produced in thin strip form, typically 0.30 mm thick following a complex sequence of rolling and heat treatment schedules together with application of electrical insulating coatings [1]. The steel comprises large grains (up to around 100 mm² surface area) with a strong {110}<001> texture. When laminations are magnetised at power frequencies along their rolling directions, as in transformer cores operating in electrical power systems, magnetic losses occur during domain wall motion [2]. Such losses are responsible for up to 10% of all electrical energy generated [3]. More knowledge based measurement and interpretation of losses is necessary to quantify metallurgical and processing parameters which control the losses.

The underpinning dependence on composition, internal stress, thickness, impurities, grain size and texture cannot be fully quantified without a deeper knowledge of magnetisation processes. Two measurable physical features closely associated with the loss process are magnetic domain motion and Magnetic Barkhausen emission (MBE). Although an IEC standard for loss measurement for commercial grading of GOSI is well established [4], its use as a research tool for investigating loss mechanisms is limited. Other methods based on surface magnetic field sensors are commonly used for localised loss evaluation. Magnetic domain observation (MDO) and magnetic force microscopy (MFM) are useful tools for surface magnetic field characterisation. Domain images obtained from the commonly used Bitter technique and the Kerr magneto optic (KMO) effect are presented to show how these techniques can imply the presence of different domain structures. It is shown that a better understanding of MBE measurements is needed to develop quantitative relations between microstructure and magnetic properties.

2. Anomaly of loss measurement using surface sensors

The energy loss in a sheet of GOSI under ac magnetisation is dependent on the tangential component of surface magnetic field (H) and spatial rate of change of flux density along the magnetising direction (dB/dt). Sensors are commonly used to measure H and dB/dt along the magnetising direction but transverse components of B and H are present in GOSI as illustrated in Fig.1. On application of an external field H_a , magnetisation within individual grains remains predominantly parallel to their $[001]$ directions. Demagnetising effects within grains results in a localised field distribution which is the resultant of H_a and the demagnetising field whereby H in each grain is not parallel to the rolling direction [5]. Ignoring this, as is the case in localised measurement and IEC testing, leads to loss underestimations of up to 10 % [6].

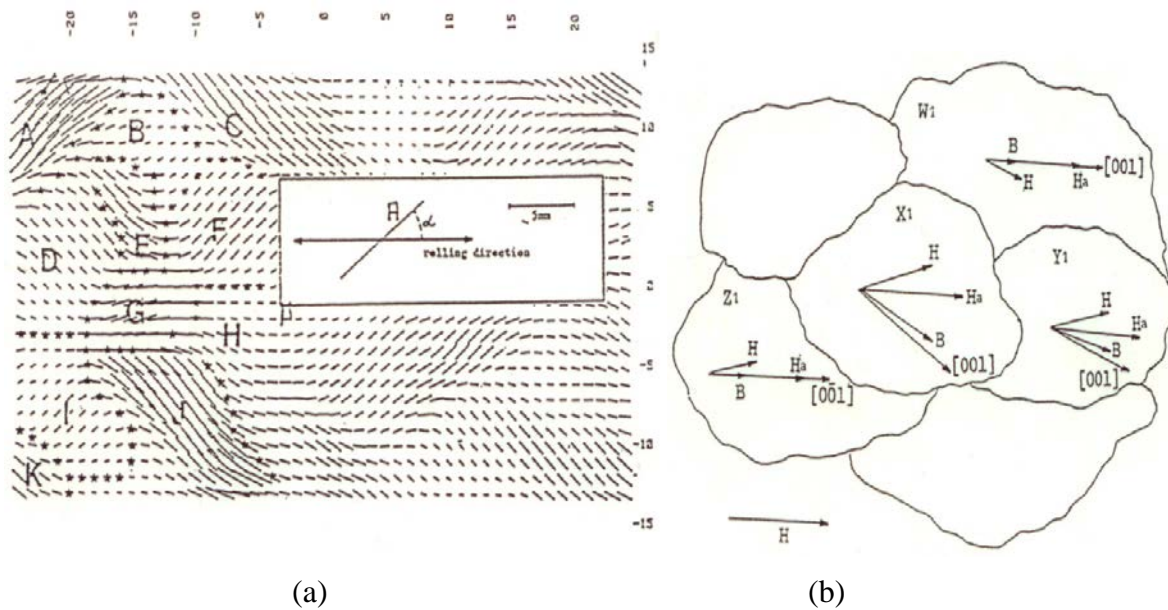


Fig. 1. (a) Measured field pattern on a GOSI surface showing location of grains and transverse components of H , (b) Schematic representation of effect of demagnetising field in misoriented grains.

3. Interpretation of domain observations

It is important to study the effect of grain boundaries on the localised domain pattern in order to understand loss processes. Figure 2 shows static domains, separated by 180° walls, observed on the same GOSI surface using KMO and a modified Bitter pattern technique [7]. A low angle grain boundary cannot be seen using the KMO method. Although the true magnetic structure is identical for each observation technique, the Bitter technique detects surface stray field whereas KMO senses the surface magnetization component and in this case they yield different domain patterns. Under AC conditions, KMO does reveal the presence of the grain boundary due to domain wall refinement and nucleation. Static images are often used to deduce loss processes so it is important to anticipate the phenomenon.

Few surface observations on GOSI have been reported using the MFM because its resolution is often too high for investigating the predominant 180° walls. An attempt was made to see if the grain boundary in Fig 2 (a) could be observed by the MFM but its presence is not obvious in the image shown in Figure 3. On close inspection a fine *finger print* pattern is present on either side of the region where the boundary is located. The cause of this pattern is not yet known. It may be simply an aberration of the MFM measurement method or image processing

although it was not found on samples of non-magnetic material. If it is magnetic in origin, it could lead to an additional source of MBN although the curved nature of the pattern is not expected in steel.

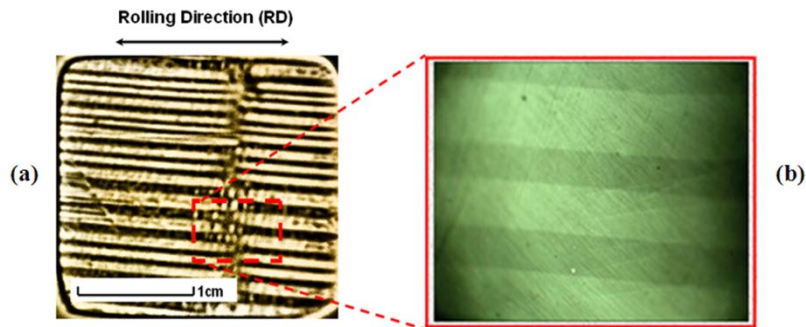


Fig. 2. Static domains observed on a 25 mm x 25 mm GOSI surface (a) Image obtained using a modified Bitter technique (b) magnified KMO image over the dashed box area.

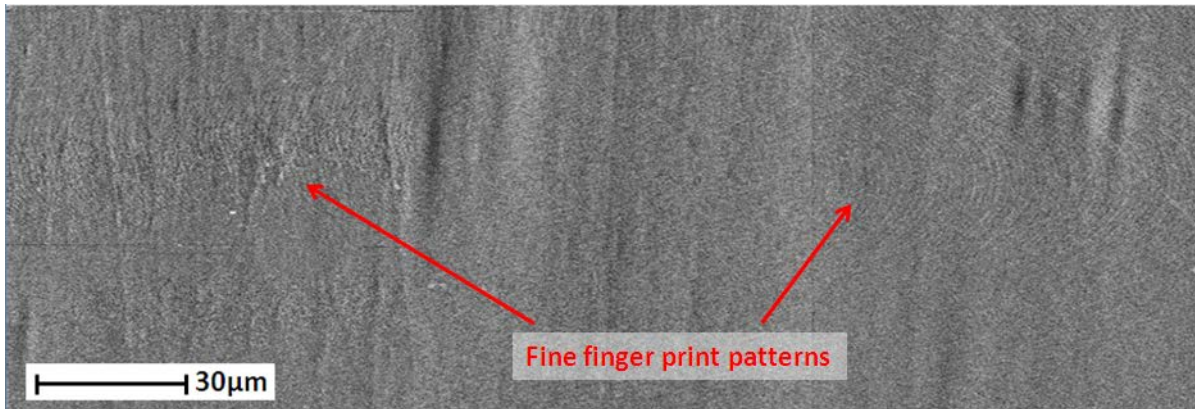


Fig. 3. MFM image over a 270 μm (horizontal) by 90 μm (vertical) region showing finger print patterns (vertically directed grain boundary across central region is not apparent).

The MBN referred to above can be measured in many ways [8]. The detected Barkhausen noise voltage pulses are due to emissions occurring when moving domain walls pass through material inhomogeneities close to the surface of the steel. MBN, at 50 Hz excitation, has been measured using the system shown in Figure 4 (a). Figure 4 (b) shows regions of high and low rms MBN in GOSI detected by scanning a 1000 turn, 2 mm diameter ferrite probe over the surface. No correlation with grain or domain structures is apparent. Further measurements show that, above around 0.2 T, the MBN is higher in well oriented GOSI than in the conventional steel but this reverses at low flux density. This is thought to be because domain wall motion in both at low fields is jerky and produces relatively more Barkhausen jumps whose cumulative effect is higher in amplitude in less well oriented material because the domain wall pinning effect of the greater number of grain boundaries is not so influential [9].

4. Conclusions

MDO, MFM and MBN measurements, combined with localise loss measurement are powerful tools for investigating relationships between microstructure and magnetic properties of GOSI. However, both loss measurement using surface field sensors and MDO using static KMO must be interpreted cautiously. If unexplained, MFM patterns are magnetic in origin they might help identify links between MBN and magnetic properties of GOSI. The regions

over which MBN emissions are detected need to be quantified in order to help correlate localised MBN measurements with grain structure.

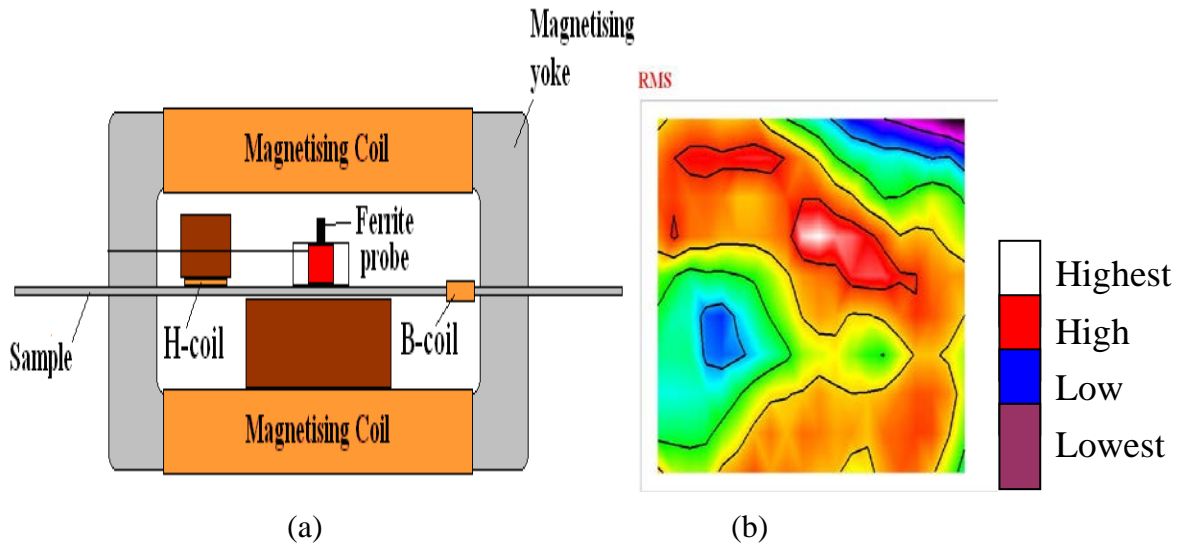


Fig. 4. (a) Schematic of MBN measurement system (b) MBN profile over a 20 mm by 35 mm GOSI surface.

Acknowledgements

Two authors N. Chukwuchekwa and X. Xu are grateful to the EPSRC and Cogent Power Ltd respectively for sponsorship of their PhD projects related to this investigation.

References

- [1] Littman M F. Grain-oriented silicon steel sheets. *JMMM*. 26 (1-3) 1-10 1982.
- [2] Nozawa T, Mizogami M, Mogi H, Matsuo Y. Magnetic properties and dynamic domain behavior in grain-oriented 3% Si-Fe. *IEEE Trans. Mag.* 32 (2) 572-589 1996.
- [3] Moses A J. Opportunities for exploitation of magnetic materials in an energy conscious world. *Interdisciplinary Science Review*. 27 (2) 100-113 2002.
- [4] International Electrotechnical Commission. IEC 404-2: (3) 1996.
- [5] Moses A J. Detection and importance of magnetic surface fields on steels. *Grain Boundaries: their characterisation and Influence on Properties* (Ed. I R Harries and I P Jones). IOM Communications Book 743 187-196 2000.
- [6] Moses A J, Konadu S N and Zurek S. Losses due to the transverse component of flux density in grain oriented electrical steels. *J. Optoelectronics and Ad. Mats.*, 1110-1114 2008.
- [7] Xu X T, Moses A J, Hall J P, Williams P I and Jenkins K. A comparison of magnetic domain images using a modified bitter pattern technique and the Kerr method on grain oriented electrical steel. Submitted to *IEEE Trans. Mag.* Jan. 2011.
- [8] Moses A J, Patel H V and Williams P I. Challenges in quantifying Barkhausen noise in electrical steels, *Electromagnetic Non-destructive Evaluation* (S Takahashi and H Kikucki Eds, IOS Press. 178-185 2007.
- [9] Chukwuchekwa N, Moses A J and Anderson P I. Barkhausen noise in grain-oriented 3% Si-Fe at 50 Hz. *J. Elec. Eng.* 61 7/s 69-72 2010.

Validation of CLIC Re-Adjustment System Based on Eccentric Cam Movers – One Degree of Freedom Mock-Up

¹J. Kemppinen, ¹H. Mainaud Durand, ¹F. Lackner

¹European Organisation for Nuclear Research, Geneva, Switzerland

Email: Juha.Kemppinen@cern.ch

Abstract. *Compact Linear Collider (CLIC) is a 48 km long linear accelerator currently studied at CERN. It is a high luminosity electron-positron collider with an energy range of 0.5-3 TeV. CLIC is based on a two-beam technology in which a high current drive beam transfers RF power to the main beam accelerating structures. The main beam is steered with quadrupole magnets. To reach CLIC target luminosity, the main beam quadrupoles have to be actively pre-aligned within 17 μm in 5 degrees of freedom and actively stabilised at 1 nm in vertical above 1 Hz. To reach the pre-alignment requirement as well as the rigidity required by nano-stabilisation, a system based on eccentric cam movers is proposed for the re-adjustment of the main beam quadrupoles. Validation of the technique to the stringent CLIC requirements was started with tests in one degree of freedom on an eccentric cam mover. This paper describes the dedicated mock-up as well as the tests and measurements carried out with it. Finally, the test results are presented.*

Keywords: CLIC, Main Beam Quadrupole, Eccentric Cam Mover, Alignment

1. Introduction

CLIC main beam (MB) will be steered using approximately 4000 quadrupole magnets which are divided into four types. Quadrupole length varies between 420 mm and 1915 mm depending on the type. To reach the design luminosity of $2.3\text{-}5.9 \cdot 10^{34} \text{ cm}^{-2}\text{s}^{-1}$, the CLIC main beam has to be stabilised to 1 nm in vertical and 40 nm in horizontal direction above 1 Hz [1]. This will be performed by a nano-stabilisation system which requires high stiffness from the re-adjustment system on top of which it will be installed. In order to implement beam based alignment and beam based feedback, the MB quadrupole magnets and their associated beam position monitors (BPM) will have to be pre-aligned with a precision and accuracy of 14 μm rms in 5 degrees of freedom (d.o.f.).

A system based on eccentric cam movers was chosen for the CLIC MB quadrupole re-adjustment. Cam mover based alignment systems are already in use in several accelerators and synchrotrons and with less stringent requirements. Cam movers provide both good resolution and high stiffness [2]. Each assembly consists of 5 cam movers which are used to manipulate a magnet within 5 d.o.f. It is a 3 point support contact with 4 interfaces with respect to the basement.

2. One degree of freedom tests

Validation of the CLIC MB quadrupole re-adjustment system based on eccentric cam movers was started with tests in 1 d.o.f. The cam mover used in the first tests is based on the design used at the SLS [3]. The entire assembly was further developed by minimizing clearances and implementing state of the art components (gearbox etc.). This section will present the 1 d.o.f. mock-up and the repeatability tests carried out using it.

One degree of freedom mock-up

Figure 1 (a) presents the 1 d.o.f. mock-up described in [4]. The cam mover (A) is installed under a cam follower plate (B). The plate is attached to rigid walls with four low friction

linear guidings (C). The guidings limit the plate's motion to one degree of freedom (z in figure 1 (a)). The plate (B) weighs 35 kg. An additional weight of 100 kg is mounted on top of the plate.

The goal of the 1 d.o.f. mock-up is to test the cam mover's repeatability. For this, the upper plate's vertical position is measured using capacitive Dimensional Offset Measurement Systems (DOMS) with below $0.1 \mu\text{m}$ resolution [5]. The DOMS are shown by arrows (D) in figure 1 (a).

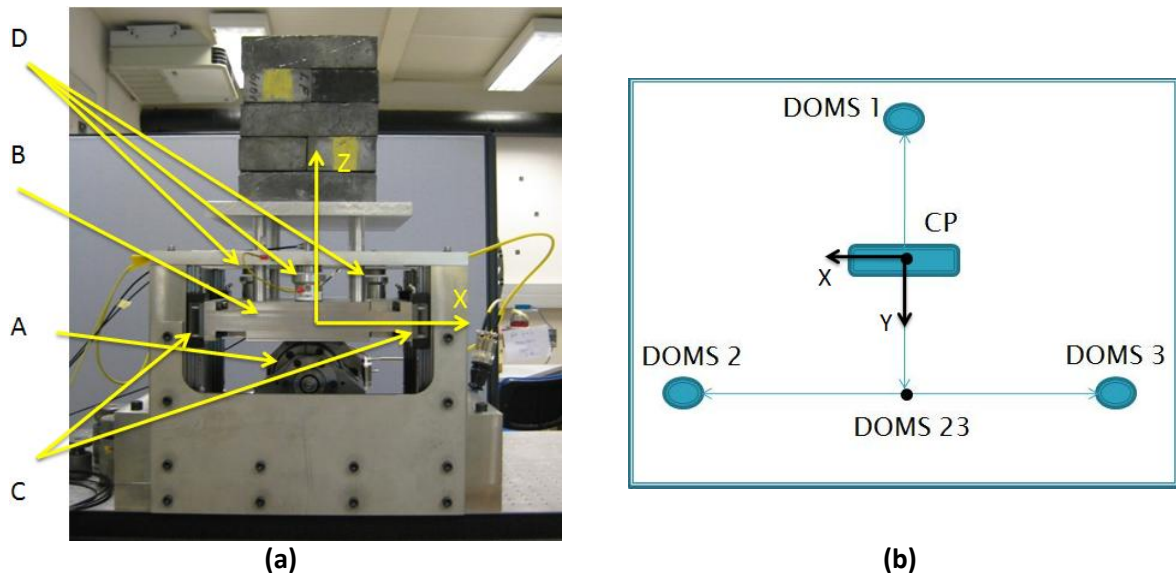


Fig. 1. (a) Side view of the one degree of freedom mock-up. (b) Top view of the DOMS sensors measuring the upper plate's z -position viewed from above. CP is the contact plane between the cam mover and the upper plate.

Figure 1 (b) shows the setup to measure the upper plate's z -position. Three DOMS were used instead of one to have redundancy and to measure the inclination of the upper plate. The vertical position of the contact plane (CP in figure 1 (b)) between the cam mover and the upper plate can be calculated based on the DOMS readings.

Test methods

A cylindrical enclosure (housing) acts as the mechanical interface between the cam mover and the cam follower. In the case of the 1 d.o.f. mock-up, the upper plate (B in figure 1 (a)) acts as the cam follower. Linear movement of the housing is realized by rotating an eccentric cam shaft which is mounted inside the housing. A bearing is installed between the cam shaft and the housing.

Two different types of bearings were tested; spherical roller bearing and cylindrical roller follower. In addition, two types of housings were tested; again with cylindrical and spherical outer surfaces. Both housings have induction hardened surfaces. Three different configurations were built using these bearing and housing types and tested in the 1 d.o.f. mock-up.

Table 1 is showing the three tested configurations. Bearing references are listed in the table in addition to bearing and housing types. Configuration 1 consists of a spherical roller bearing and a cylindrical housing. Configurations 2 and 3 both have a roller follower bearing. The only difference between the bearings used in configurations 2 and 3 is the outer ring. It is cylindrical in configuration 2 and crowned in configuration 3. The housing is cylindrical in configuration 2 and spherical in configuration 3.

Table 1. Configurations tested in the 1 d.o.f. mock-up.

Configuration No.	Bearing type	Bearing reference	Housing type
1	Spherical roller bearing	SKF 22209 E	Cylindrical
2	Roller follower	IKO NAST 45 ZZUU	Cylindrical
3	Roller follower	IKO NAST 45 ZZUUR	Spherical

For each configuration, preparatory tests were carried out to find the the best parameters for the repeatability test. The optimized parameters were: the number of data acquisitions after each sequence, the number of test drives in a test series, the settling time after a sequence and before data acquisition and the stepper motor reference speed.

A test series was performed based on the optimised parameters to find out the cam mover repeatability within the whole stroke of 10 mm. In the beginning of the test, the cam follower plate was at its upper dead center. One test drive consisted of two parts. First, the plate was driven from the upper dead center to the lower dead center ($\pi/2$ evolution) and vice versa in the further iteration. The cam mover was stopped 20 times per $\pi/2$ evolution for measurements. This procedure was repeated 10 times. The mean values and root mean square errors (RMSE) were calculated between corresponding measurement points of all the 10 test drives of the test series.

The cam mover's range in vertical motion (stroke) is 10 mm. This translates through the planetary gear and the worm gear to nine million micro steps of the stepper motor. The repeatability test series was repeated with a reduced stroke of the cam mover. One million steps were omitted from both ends of the stroke.

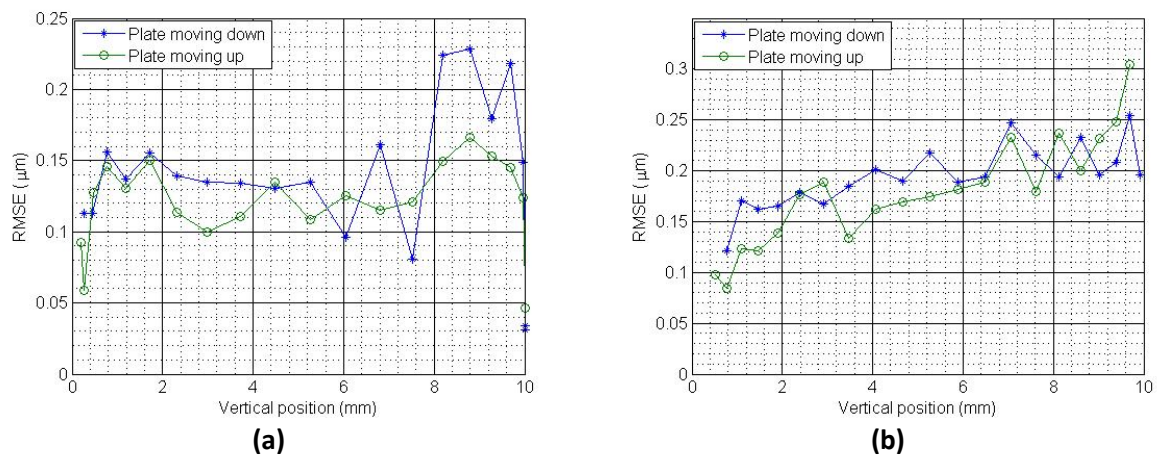


Fig. 2. Repeatability as a function of measured vertical position of the cam follower plate using configuration 1 in the 1 d.o.f. mock-up. The range is (a) the full stroke of 9 million steps, (b) between 1 and 8 million steps from the upmost position.

3. Results

The results of the repeatability tests of configuration 3 are shown in figure 2. Figure 2 (a) presents the full stroke of nine million steps and 2 (b) presents the reduced stroke. As can be seen in figure 2, the cam mover's repeatability in 1 d.o.f. with this configuration was below $0.3 \mu\text{m}$ within the whole range.

Configuration 3 had best repeatability with full stroke. The full stroke repeatability was below $1.0 \mu\text{m}$ and $0.4 \mu\text{m}$ for configurations 1 and 2 respectively.

Configuration 2 had the best repeatability, below 0.2 μm , with reduced stroke. For configuration 1, the repeatability was below 0.35 μm and for configuration 3 below 0.3 μm . Configurations 1 and 2 had better repeatability with the reduced stroke than with the full one. For configuration 3, the results were better with full stroke than with partial stroke.

4. Discussion and conclusions

The CLIC main beam quadrupoles have to be pre-aligned within 14 μm in 5 d.o.f. A system based on eccentric cam movers is proposed for the re-adjustment. The system's validation process was started with repeatability tests in 1 d.o.f.

The cam mover was tested with three different bearing and housing configurations in 1 d.o.f. The repeatability of all of the three configurations was below 1.0 μm . The roller follower had better repeatability than the spherical roller bearing with both outer rings and housings. With reduced stroke, the differences between the configurations were negligible.

Clearances inside the spherical roller bearing allow small lateral movement whereas the roller follower blocks it. The 1 d.o.f. mock-up diminishes efficiently movements in x- and y-directions. Therefore all of the effects of the clearances might not have been visible in the 1 d.o.f. test results.

A 5 d.o.f. mock-up will be built for the validation of the sub-micrometric resolution cam mover system. The cam mover design has been further improved from the one used in the 1 d.o.f. mock-up. The structure is now more rigid, clearances between parts are smaller, worm gear and stepper motor have been changed and there is a zero backlash bearing reducer instead of a planetary gear. Both bearing types will be tested also in 5 d.o.f.

In addition to positioning precision, the re-adjustment system has to provide a rigid support for the MB quadrupoles. The system's eigenfrequency should be as high as possible. This has been taken into consideration in the cam mover design optimization process. The validation of the 5 d.o.f. concept will show if a further iteration in the re-adjustment system design will be required.

References

- [1] Artoos K, Capatina O, Collette C, Guinchard M, Hauviller C, Lackner F, Pflugstner J, Schmickler H, Sylte M. Study of the stabilization to the nanometer level of mechanical vibrations of the CLIC main beam quadrupoles. In proceedings of the 23rd Particle Accelerator Conference, 2009, TH5RFP080
- [2] Mainaud Durand H, Touzé T, Griffet S, Kemppinen J, Lackner F. CLIC active pre-alignment system: proposal for CDR and program for TDR. In proceedings of the 11th International Workshop on Accelerator Alignment, 2010.
- [3] Schlott V, Kramert R, Rohrer M, Streun A, Wiegand P, Zelenika S. Dynamic alignment at SLS. In proceedings of the 7th European Particle Accelerator Conference, 2000, 693-695.
- [4] Lackner F, Artoos K, Collette C, Mainaud Durant H, Hauviller C, Kemppinen J, Leuxe R. Development of an eccentric CAM based active pre-alignment system for the CLIC main beam quadrupole magnet. In proceedings of the 6th International Conference on Mechanical Engineering Design of Synchrotron Radiation Equipment and Instrumentation, 2010.
- [5] Herty A. Micron precision calibration methods for alignment sensors in particle accelerators. Master's Thesis. Nottingham Trent University, Nottingham, 2009.

Cube Model Approach in Simulating of Magnetite Nanoparticles Behaviour in External Magnetic Fields

O. Strbak, D. Gogola, I. Frollo

Institute of Measurement Science SAS, Bratislava, Slovakia

Email: oliver.strbak@savba.sk

Abstract. Iron ‘overloading’ can lead to various health complications, such as diabetes, cirrhosis, and heart disease. Moreover, biogenic iron oxides nanoparticles, found in human brain tissue are connected to neurodegenerative processes. MRI represents potential tool in non-invasive body-iron quantification, because iron strongly affects the MRI signal. However, iron oxides nanoparticles are with respect to behaviour in external magnetic fields, generally approximate to a ‘Sphere’ model. This can lead to incorrect evaluation. Here, we introduce a more realistic ‘Cube’ model, with two approaches: (i) cell unit (CU), and (ii) bulk, with almost identical results.

Keywords: Magnetite Nanoparticles, Cube Model, MRI, Body-Iron Evaluation

1. Introduction

Recently, biogenic iron oxides (magnetite) nanoparticles have been found in several animal species, including humans [1]. Biological magnetite is produced by genetically-controlled biochemical process, and in animal species plays a crucial role in geomagnetic navigation [2]. Its role in humans is still unclear, but elevated levels of magnetite particles are associated with neurodegenerative disorders [3]. However, an “iron overloading” can lead to various other complications, such as diabetes, cirrhosis, and heart disease [4]. Therefore, the proper quantification method of body-iron is crucial in diagnostics. Iron strongly affects relaxation times of protons during MRI and causes such a contrast enhancement of examined tissue. It predestines the MRI to become a completely non-invasive body-iron diagnostic method. Because body-iron is usually in a form of iron oxides, we have chosen magnetite nanoparticles as a model system. However, magnetite nanoparticles are in external magnetic fields generally approximated to a sphere with radius $\approx 10^{-7}$ m and magnetic moment $\approx 2 \times 10^{-15}$ Am² [5]. Here, we introduce practically more intuitive and accurate ‘Cube’ model method with two approaches: (i) cell unit (CU), and (ii) bulk.

2. Subject and Methods

Sphere model approximation represents magnetite nanoparticles as the sphere with radius $\approx 10^{-7}$ m and magnetic moment $\approx 2 \times 10^{-15}$ Am². We introduce ‘Cube’ model method with two approaches: (i) cell unit (CU), and (ii) bulk. Because of biological origin of biogenic magnetite nanoparticles, we take into consideration only single-domain particles with (cube) dimension $a_{\text{mag}} = 4 - 500$ nm [6].

In ‘CU’ approach, a magnetic moment of particle is derived from cell unit (CU) shape and size of the particle. Magnetite CU is made from 8 formula units (FU) and belongs to isometric – hexoctahedral crystal system (space group Fd3m) with cell dimensions $a_{\text{CU}} = 0.83958$ nm and volume $V_{\text{CU}} = 5.9182 \times 10^{-28}$ m³. Magnetic moment for particle was calculated as follows:

$$\bar{\mu}_{\text{mag(CU)}} = N_{\text{CU}} \bar{\mu}_{\text{CU}} = \frac{V_{\text{mag}}}{V_{\text{CU}}} 8 \bar{\mu}_{\text{FU}} = 34.64 \frac{V_{\text{mag}}}{V_{\text{CU}}} \mu_{\text{B}} \quad (1)$$

where N_{CU} is the number of CU in particle and $\mu_{FU} = 4.33 \mu_B$ [7], where μ_B is the Bohr magneton.

In ‘Bulk’ approach, the magnetic moment is derived from equation

$$\bar{\mu}_{mag(Bulk)} = M_{sat(Bulk)} m_{mag} = M_{sat(Bulk)} \frac{V_{mag}}{V_{CU}} m_{CU} = M_{sat(Bulk)} \frac{8a^3 Mr(Fe_3O_4) m_u}{V_{CU}} \quad (2)$$

where $M_{sat(Bulk)}$ is the saturation magnetization (for magnetite $M_{sat(Bulk)} \approx 90 \text{ Am}^{-2} \text{ kg}^{-1}$), m_{mag} is the mass of one magnetite nanoparticle with cube dimension a , M_r is a molecular weight of magnetite, and m_u is an atomic mass constant.

We determined nanoparticle magnetization \mathbf{M}_{mag} (which is size and temperature dependent) in magnetic field \mathbf{B} applying Langevin function:

$$\bar{M}_{mag}(a, T) = M_{sat} m_{mag} [\coth(x) - 1/x] \quad (3)$$

where m_{mag} is the mass of magnetite particle and $x = \mu_{mag} \mathbf{B} / k_B T$. The values of saturation magnetization M_{sat} for magnetite nanoparticles were determined experimentally (for $a = 4; 11.5; 47.7; 150 \text{ nm} \rightarrow M_{sat} = 31.8; 60.1; 65.4; 75.6 \text{ Am}^2 \text{ kg}^{-1}$ at $T = 300 \text{ K}$ [8]).

3. Results and discussion

In **Figure 1** is shown comparison of models for nanoparticles magnetic moment calculation. Cube models approaches represent our proposed method and sphere model represents general approximation. Stability of information, saved in preservation of particle’s magnetic moment direction is shown in **Figure 2**.

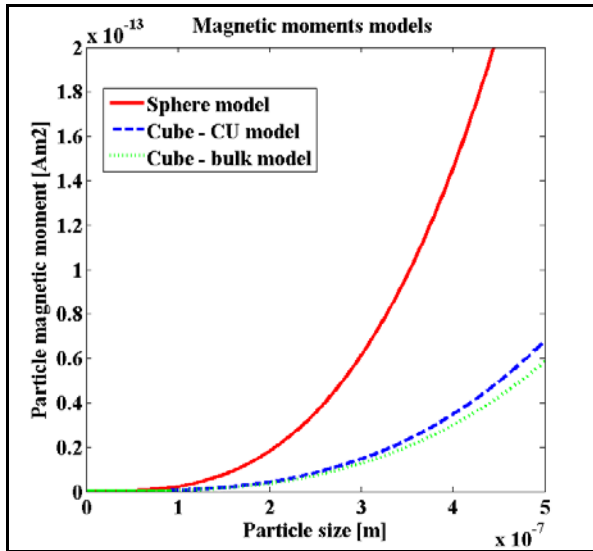


Fig. 1. Comparison of magnetic moment values in magnetite nanoparticles, for generally used ‘Sphere’ model and our proposed ‘Cube’ model with cell unit (CU) and bulk approaches. Magnetic moments for “Sphere model are calculated in the same manner than for “Cube model”, but with a_{mag} as a radius.

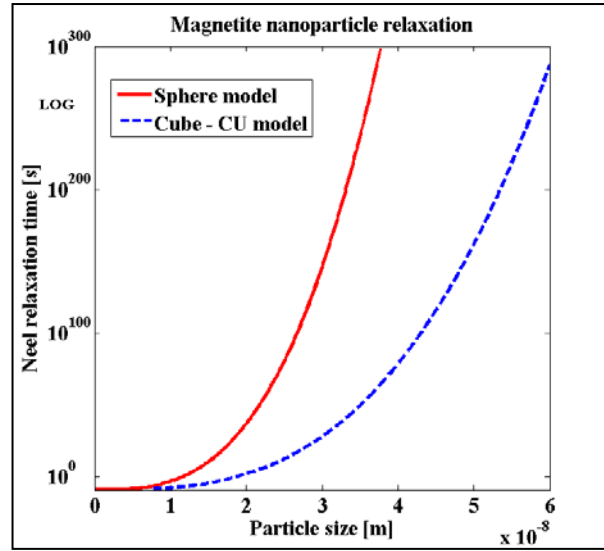


Fig. 2. Néel relaxation times for magnetite nanoparticles depending on size of particles ($\tau_0 \approx 10^{-9} \text{ s}$, $K = 13.5 \text{ kJm}^{-3}$). Y axis is in LOG scale. It is evident that magnetite nanoparticles are suitable as information storage medium. We compare our ‘Cube model’ approach and “Sphere model’ approach.

Magnetization of magnetite nanoparticles for different sizes, and in strong magnetic fields, is shown in **Figure 3a-d**. It is obvious, that for high magnetic fields the differences between models are insignificant. However, for low magnetic fields the differences are important and

using an incorrect model can lead to wrong conclusions. This is demonstrated in **Figure 4**, where is shown Geomagnetic-field rotational work dependence on size of particle. Magnetic field of the Earth varies form $\approx 30 \mu\text{T}$ to $\approx 60 \mu\text{T}$ (for our latitude $\approx 50 \mu\text{T}$).

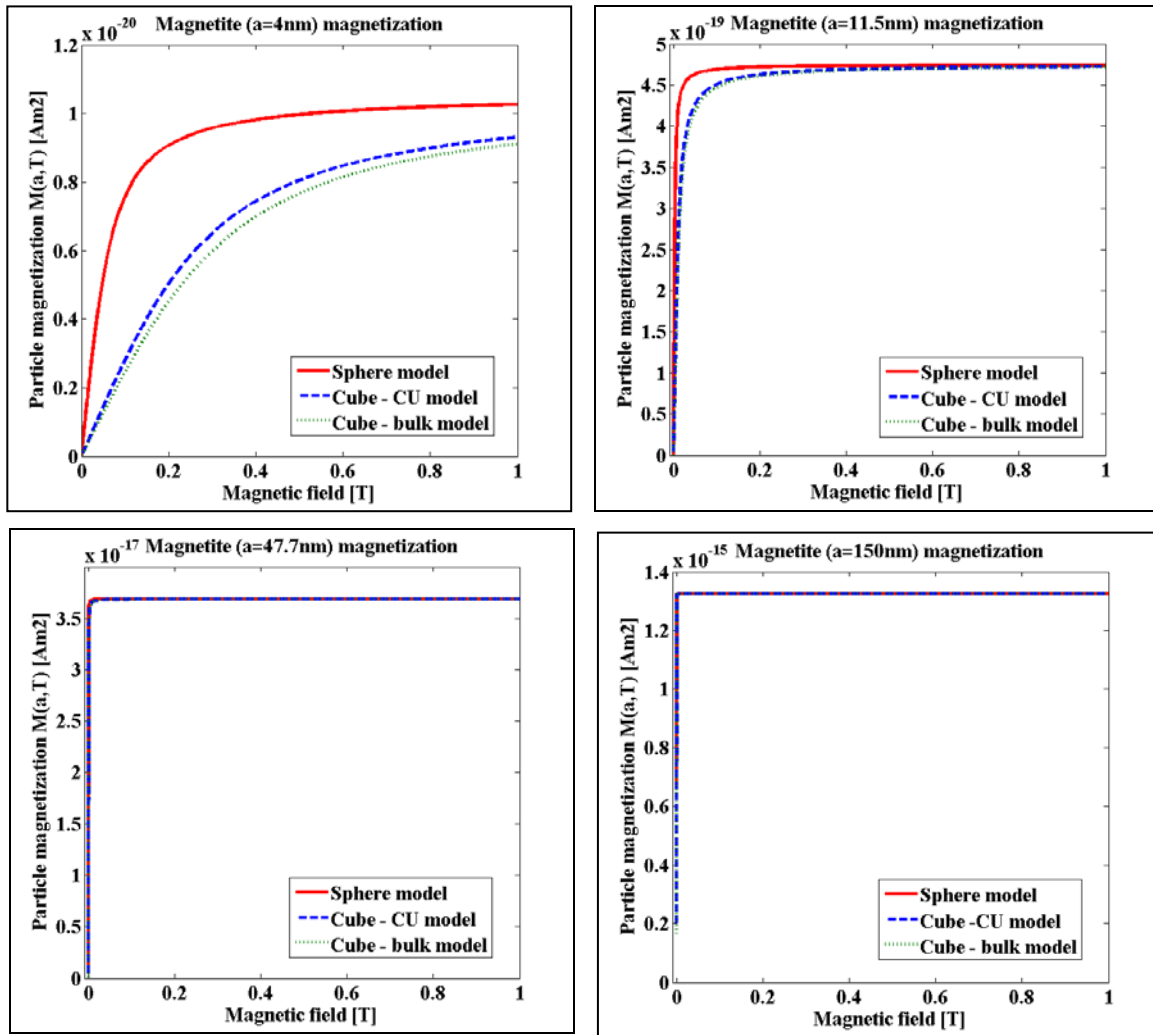


Fig. 3. Comparison of magnetite nanoparticles magnetization values for generally used 'Sphere' model and our proposed 'Cube' model with cell unit (CU) and bulk approaches, in magnetite nanoparticles with different sizes: (a) 4 nm, (b) 11.5 nm, (c) 47.7 nm, and (d) 150 nm.

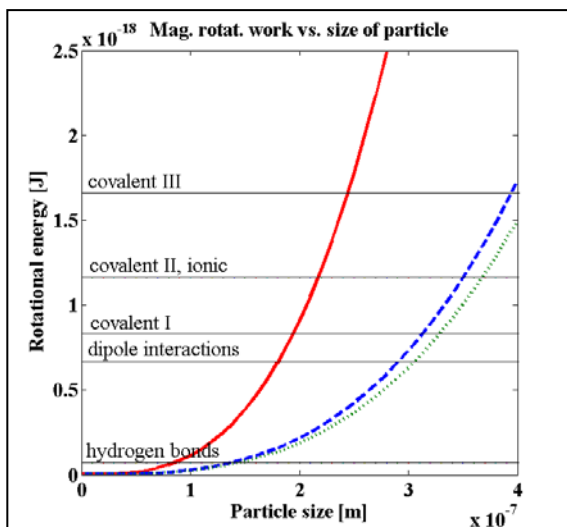


Fig. 4. Magnetic rotational work vs. size of magnetite nanoparticle (for range 0 – 400 nm) in magnetic field of the Earth. Comparison of 'Sphere' model and our 'Cube' model with cell unit and bulk approach. Horizontal lines represent maximum level in typical biochemical bond energy. As seen, energies associated with rotational work of geomagnetic field on the magnetite nanoparticles correlate with energies of biochemical interactions. Calculated for $\theta = \pi/2$.

4. Conclusions

We showed, that for strong magnetic field ($>1\text{T}$) and larger particles ($>50\text{nm}$), the magnetization of magnetite nanoparticles is almost identical for ‘Sphere’ and ‘Cube’ model approach. However, for smaller particles (ferritin-like), the differences are quite distinct, and the use of incorrect model can lead to incorrect MRI body-iron evaluation. There are also big differences between models in determination of magnetic moments for particles bigger than 100 nm. Cube model represents more realistic approach and apart from body-iron evaluation can be helpful in determination of contrast agent efficiency, evaluation of electromagnetic hazard, or other issues related to iron oxides nanoparticles.

Acknowledgements

This work was supported by Slovak Scientific Grant Agency in the framework of Project ‘VEGA 2/0090/11’ and The State program ŠPVV no. 2003SP200280203.

References

- [1] Kirschvink JL, Kobayashi-Kirschvink A and Woodford BJ. Magnetite biomineralization in the human brain. *Proceedings National Academy of Sciences USA* **89** 7683-7687 1992.
- [2] Kirschvink JL and Hagadorn JW. A grand unified theory of biomineralization. In Bauerlein E edition, *The biomineralization of Nano- and Micro- Structures*, Wiley-VCH Verlag GmbH, Weinheim, Germany, 2000, (pp 139-150).
- [3] Pankhurst QA, Hautot D, Khan N and Dobson J. Increased levels of magnetic iron compounds in Alzheimer’s disease. *Journal of Alzheimer’s Disease* **13** 49-52 2008.
- [4] Jensen PD. Evaluation of iron overload. *British Journal of Haematology* **124** 697-711 2004.
- [5] Vaughan TE and Weaver JC. Energetic constraints on the creation of cell membrane pore by magnetic particles. *Biophysical Journal* **71** 616-622 1996.
- [6] Schultheiss-Grassi P, Weissiken R and Dobson J. TEM investigations of biogenic magnetite extracted from human hippocampus. *Biochimica and Biophysica Acta* **1426** 212-216 1999.
- [7] Huang DJ et al. Spin and orbital magnetic moments of Fe_3O_4 . *Physical Review Letters* **93**(7) 077204 2004.
- [8] Goya G, Berquo T, Fonseca F and Morales M. Static and dynamic magnetic properties of spherical magnetite nanoparticles. *Journal of Applied Physics* **94**(5) 3520-3528 2003.

SFS heterostructures prepared by focused-ion-beam technique

¹V. Štrbík, ¹Š. Beňačka, ¹V. Šmatko, ¹Š. Gaži, ¹Š. Chromik, ¹A. Dujavová,
¹I. Vávra, ²P. Vrabček

¹Institute of Electrical Engineering, Slovak Academy of Sciences, Bratislava, Slovakia

²Slovak Institute of Metrology, Bratislava, Slovakia

Email: elekstrb@savba.sk

Abstract. We present initial investigation of the superconductor-ferromagnet-superconductor (SFS) heterostructures of nanometer dimensions prepared by gallium focused ion beam (FIB) technology. The SFS heterostructures were realized using high-T_c superconducting YBa₂Cu₃O_x and ferromagnetic La_{0.67}Sr_{0.33}MnO₃ thin films. SFS weak link junctions require dimensions of weak link connection in a range of nanometer size realizable by FIB patterning. Presented results show that FIB offers suitable procedure for realization of nanometer size devices but some degradation of ferromagnetic and superconducting properties was observed. The solution of this problem will be solved in the next stage of our investigations.

Keywords: Superconductor-Manganite Junctions, Proximity Effect, Magnetic Domain Wall

1. Introduction

Superconductor-ferromagnet (SF) bilayer and SFS trilayer heterostructures, in a form of weak links or Josephson junctions, are very attractive objects for the study of mutual interplay between superconductivity and ferromagnetism [1]. In addition, their potential applications are very promising in cryoelectronic or superconducting spintronic circuits [2] (e.g. qubits, 0-, pi-junctions, spin valves, etc.). However, utilization of high-T_c superconductors (HTS) in these fields was until now not successful due to their very small coherence length. In case of SFS junction with high-T_c cuprate superconductor YBa₂Cu₃O_x (YBCO) one appear manganites as convenient ferromagnetic (F) materials, e.g. La_{0.67}Sr_{0.33}MnO₃ (LSMO) - ferromagnetic perovskite half metal, which may be totally spin polarized in one spin direction. YBCO/LSMO heterostructures, prepared on single crystal MgO or SrTiO₃ substrates, are able to create high quality thin films and SF interfaces necessary for the study of physical properties. Generally, electron transport through interface between superconductor and normal (N) or F metal in close proximity with S, is mediated by Andreev reflection, the process in which an electron with energy smaller than the energy gap of S, is reflected as hole preserving in N (F) phase coherence of Cooper pairs (CP) over some distance from the interface. There are essential differences between the proximity effect in SN and SF structures due to different coherence lengths ζ_N and ζ_F which characterize the penetration depth of CP in N (F) material. Fortunately, in addition to the short coherence length ζ_F ($\sim 1-2\text{nm}$) $\ll \zeta_N$ there was discovered long range proximity effect (LRPE) in FS structures, in case if inhomogeneous magnetization in the vicinity of SF interface is present [3]. LRPE is consequence of such inhomogeneity (e.g. domain wall, spin active interface) which generates a triplet spin CP [4], with amplitude comparable to the singlet one, containing phase correlations between electrons with the same spin projections ($\uparrow\uparrow$), on the coherence length ζ_{FL} . The penetration depth in case of LRPE should be of the order ζ_N as in the case of singlet spin CP into a normal metal. The realisation of high quality high-T_c SF or SFS structures manifesting LRPE is complicated task. The magnetic inhomogeneity, in the so called *series geometry*, must be localized immediately at the SF interface what is experimentally extremely difficult, otherwise the triplet current amplitude is negligible small. Recently, it was analysed

[5] that, in comparison with the *serial geometry*, amplitude of triplet current component may be in the so called *lateral geometry* (Fig. 1) enhanced by a factor l_d/d , where l_d is the domain wall width and d is the thickness of F thin film. In this paper we report on first approaches to prepare and study the properties of YBCO/LSMO/YBCO nanometer heterostructures, using technology of gallium focused ion beam (FIB) patterning, to find out whether this technology is suitable tool for realization of superconductor weak link structures.

2. Experimental

The dc magnetron sputtering was used for in situ growing the bilayer heterostructure $\text{YBa}_2\text{Cu}_3\text{O}_x$ (YBCO) and $\text{La}_{0.67}\text{Sr}_{0.33}\text{MnO}_3$ (LSMO) on single crystal MgO (100) substrate. The single LSMO thin films showed transition to the metallic ferromagnetic state at about 200K and their resistivity ρ was in the range of $\rho \approx 10^{-3} \text{ } \Omega\text{cm}$ at liquid nitrogen temperature [6]. Thickness of LSMO layers was in the range 20-50 nm where the LSMO thin film is still ferromagnetic. The LSMO crystallizes as pseudocubic perovskite, it has a fully spin-polarized conduction band and bulk material exhibits ferromagnetic transition around room temperature. The YBCO films were deposited applying high pressure on-axis dc magnetron sputtering carried out at oxygen pressure 300 Pa, substrate temperature $T_s = 810 \text{ } ^\circ\text{C}$, and dc power 200 W, with a deposition rate of 1 nm/min [7]. The thickness of the YBCO superconducting films was about 150 nm. Patterning of the basic bilayer structures, for four points measuring of transport properties, was carried out by optical photolithography and wet (1% H_3PO_4) or Ar ion beam (300 eV, 20 mA/cm²) etching, with substrate cooled to temperature minus 20 °C. Subsequently Ga^{+3} focused ion beam patterning was applied (Quanta 3D 200i) to receive the convenient *lateral geometry* (Fig. 1).

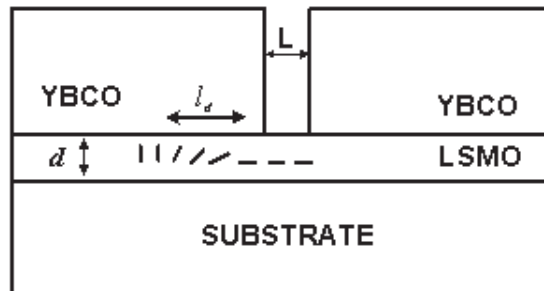


Fig. 1. *Lateral geometry* of the SFS microstrip structure. Magnetic inhomogeneity in LSMO of thickness d is intended to be realized by domain wall of width l_d . The two YBCO electrodes are separated by the length L , as shown.

3. Results and discussion

Zero resistance critical temperature T_{C0} of single c-axis oriented YBCO films, deposited directly on single crystal MgO substrate, was typically somewhat below 90 K, critical current density at 77 K $j_c(77 \text{ K}) \approx 3 \times 10^6 \text{ A/cm}^2$ and a FWHM for the rocking curves of the (005) YBCO peak of 0.2°. Small decrease of T_{C0} and $j_c(77 \text{ K})$ is due to lattice mismatch between YBCO and MgO. Zero resistance critical temperature of the YBCO/LSMO bilayers was above 80 K, in the presented sample $T_{C0} = 87.5 \text{ K}$. In Fig. 2 we show SEM picture of YBCO/LSMO microstrip ($5 \times 0.5 \text{ } \mu\text{m}^2$) prepared by Ar ion beam etching. Subsequently the sample was transferred in Quanta 3D 200i and the gap of length L in the YBCO film was realized by FIB etching. In addition the FIB etching was used for smoothing the microstrip edges. The resistance vs. temperature (R-T) dependence of the YBCO/LSMO microstrip bilayer indicates small decrease of T_{C0} to 85 K due to the gallium ions irradiation. In the

following step, to realize *lateral geometry* of the SFS structure (Fig. 1), it was crucial to remove YBCO (without removing the LSMO very thin film) as a narrow lateral gap of length L (Fig. 2, inset). This is the most critical step of the sample preparation, because during the sample irradiation adjusted on the 30 keV Ga^{+3} ions, the properties of superconductor and manganite films can be influenced.

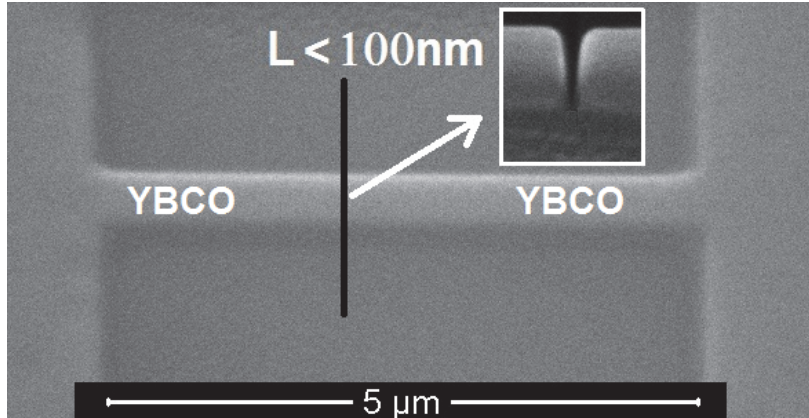


Fig. 2. SFS structure realized as YBCO/LSMO/YBCO junction of *lateral geometry*. The inset shows gap in YBCO thin film of length $L \approx 70\text{-}80$ nm created by FIB etching of YBCO in YBCO/LSMO microstrip.

After this procedure T_{C0} of SFS structure was decreased to ~ 45 K and current-voltage characteristics (IVC) at various temperatures were measured (Fig. 3).

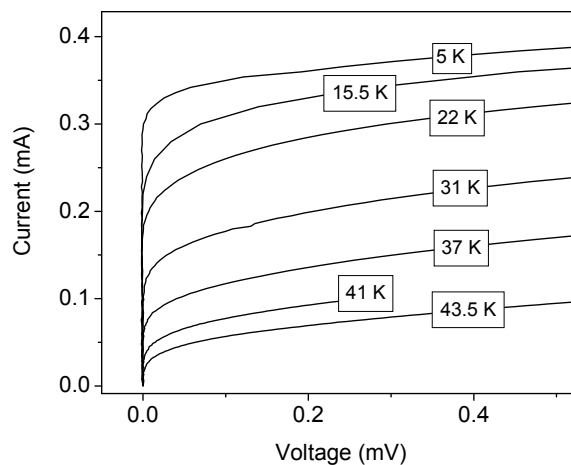


Fig. 3. The current-voltage characteristics of SFS structure at various temperatures.

The IVC exhibit superconducting properties of the SFS junction but the part of IVC at $V > 0$ did not correspond to weak link RSJ model. The quasi-linear critical current vs. temperature, $I_C(T)$ dependence, is frequently indicated in SNS weak link junctions [8]. Moreover, we observed only very weak dependence of the critical current on external magnetic field. Therefore, we suppose so far that in the gap of the SFS structure remains very thin residual YBCO film with above indicated critical current. After further application of additional FIB etching we did not observe superconducting properties of the sample, for that reason we conclude that YBCO was completely removed and the LRPE was not observed due to large length L of the gap, or the inhomogeneous magnetization near the SF interface was not realized. These conclusions confirm typical LSMO R-T dependence measured on the SFS structure. At the same time we observed small shift in LSMO resistance maximum to lower temperature, as a result of FIB application during the YBCO film cutting.

4. Conclusions

The realization of high quality superconducting weak links or Josephson junctions based on high-T_c superconductors is at present very difficult task. Some achievements are expected using advanced microcircuit technologies (e.g. FIB) for preparation of nanometer dimension SNS or SFS structures. SFS heterostructures, in addition offer opportunity of new physical effects, LRPE, as well as new modes of operation in cryoelectronic or superconducting spintronic circuits. In the paper we present preliminary results on the high-T_c superconducting SFS structure in the so-called lateral geometry [5]. In the YBCO/LSMO bilayer the top YBCO layer was disconnected by narrow ($L \approx 70\text{-}80\text{ nm}$) lateral gap in the YBCO microstrip using focused ion beam (FIB) patterning. Results show that FIB offers suitable procedure for realization of nanometer size devices but problems of films degradation by FIB irradiation have to be solved. Another separate problem, generation of LRPE in SFS structure, is connected with creating of local magnetic inhomogeneity in the ferromagnetic half metal LSMO film. Solution of these problems is the aim of our following investigations.

Acknowledgements

The research within EURAMET joint research project leading to these results has received funding in part from the European Community's Seventh Framework Program, ERA-NET Plus, under Grant Agreement No. 217257 (JoSy) and Slovak Scientific Grant Agency VEGA, contract Nos. 2/0144/10 and 2/0164/11. This publication is the result of the project implementation: Centre of Excellence for New Technologies in Electrical Engineering, ITMS code 26240120019, supported by the Research & Development Operational Programme funded by the ERDF.

References

- [1] Bergeret FS, Volkov AF, Efetov KB. Odd triplet superconductivity and related phenomena in superconductor-ferromagnet structures, *Reviews of Modern Physics*, 77: 1321-1373, 2005.
- [2] Tao YC, Hu JG. Superconducting spintronics: spin-polarized transport in superconducting junctions with ferromagnetic semiconducting contact, *Journal of Applied Physics*, 107: 041101-041101-13, 2010.
- [3] Buzdin AI. Proximity effects in superconductor-ferromagnetic heterostructures, *Reviews of Modern Physics*, 77: 935-976, 2005.
- [4] Golubov AA, Kupriyanov My, Ilichev E. The current phase relation in Josephson junctions, *Reviews of Modern Physics*, 77: 411-469, 2005.
- [5] Kupferschmidt JN, Brouwer PW. Enhanced triplet Andreev reflection off a domain wall in a lateral geometry, *Physical Review B*, 80: 214537-214537-5, 2009.
- [6] Španková M, Chromik Š, Vávra I, Sedláčková K, Lobotka P, Lucas S, Stanček S. Epitaxial LSMO films grown on MgO single crystalline substrates, *Applied Surface Science*, 253: 7599-7603, 2007.
- [7] Oszi Zs, Benacka S, Strbik V, Chromik S, Spankova M, Kostic I, Kleja P. Properties of YBa₂Cu₃O_x and Bi₂Sr₂CaCu₂O_x thin film microstrips patterned by argon ion beam, *Thin Solid Films*, 433: 359-362, 2003.
- [8] Delin KA, Kleinsasser AW. Stationary properties of high-critical-temperature proximity effect Josephson junctions, *Superconductor Science and Technology*, 9: 227-269, 1996.

X-Ray Microtomography and Its Use for Non-destructive Characterisation of Materials

¹M. Hain, ²M. Nosko, ²F. Simančík, ²T. Dvorák, ²R. Florek

¹Institute of Measurement Science Slovak Academy of Sciences, Bratislava, Slovakia

²Institute of Materials and Machine Mechanics Slovak Academy of Sciences,
Bratislava, Slovakia

Email: Miroslav.Hain@savba.sk

***Abstract.** The aim of the paper is to describe use of X-ray microtomography for non-destructive characterisation of materials. The microtomography method is used for visualisation of the internal structure of composite and porous materials, identifying of inhomogeneities of porous materials after their pressure infiltration with metals, and quality control of porous structure of aluminium foam after the die casting. The paper will refer also to other potential uses of microtomography in material research.*

Keywords: X-Ray, Microtomography, Non-Destructive Testing, Defect, Metal Foam

1. Introduction

X-ray radiation was discovered in r. 1895 by the German physicist W.C. Röntgen. It is electromagnetic radiation in the wavelength range from 10 nm to 0.01 nm and its outstanding feature is - similarly to the gamma radiation and cosmic rays - the high penetration ability through materials. This property of X-ray radiation can be effectively used for the non-destructive visualisation of internal structures of objects and crack detection in materials, allowing the expansion of X-ray imaging methods in the materials research, and also in industry applications. Since the discovery of X-ray radiation the two-dimensional imaging methods were intensively developed. These 2D methods often provide valuable information about the internal structure of objects under test, but really a new quality in the information obtained using X-rays appeared with the discovery of computed tomography CT [1]. This imaging method enables the visualisation of internal 3D structures and brings a new quality in non-destructive testing. Further progress in the development of X-ray tomographic imaging methods is based on the principle of X-ray shadow microscopy [2]. This imaging method is called X-ray microtomography and brings significant increase in CT resolution.

In this article we will address specific possibilities of using of X-ray microtomography, particularly quality control of ceramic plates after pressure infiltration with lead and observation of internal structure of foam materials. 3D microtomography can also be used to observe the distribution of particles or fibers in composites, or even to monitor abuses in mechanical stress [4]. X-ray tomography has been proven as a good tool for non-destructive quality control of welds and solders joints of all types.

2. Method of X-ray microtomography measurement

X-ray microtomography measurement is composed of two basic steps – acquisition of projections and volume reconstruction. The first step – acquisition of projections is schematically illustrated in Fig. 1. In this phase the object under test is stepwise turned around the rotation axis at a small selected angle (e.g. 15 °) and so called X-ray projections are measured. Projections are X-ray absorption images, which are created on two-dimensional detector after transition of beams through the object. The object is at standard conditions of

measurement rotated totally at 360° . During this one turn the selected number of projections is captured. In the case when the angle of rotation is $15'$, the number of projections is 1440.

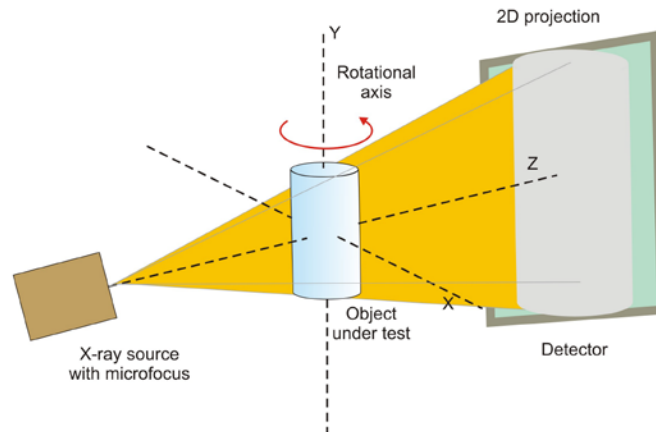


Fig.1 Acquisition of projections – first step of microtomographic measurement

During the acquisition of projections it is extremely important to ensure the high mechanical stability of the object - both dimensional stability and position of the object in a coordinate system of the microtomograph are important. The rate of the stability during the measurement can be assessed by a comparison of the first and the last projections measured at angles 0° and 360° . In the case of small changes of a position or size of the object (most often due to temperature drift), they can be corrected using special software; whereas in the case of major changes it is necessary to repeat the acquisition of projections. After obtaining all necessary projections the second phase starts: volume image reconstruction. It is a set of mathematical operations that are based on the so called inverse Radon transform, when from the group of measured projections the 3D image of an object is reconstructed. This phase of evaluation is extremely challenging to computing power and can be in the case of large voxel volumes very time-consuming, even when using a powerful computer cluster.



Fig.2 Laboratory of X-ray microtomography with Nanotom 180

In the framework of the project CEKOMAT a microtomographic laboratory with a device Nanotom 180 [3] was established (Fig. 2). Nanotom is equipped with nanofocusing X-ray tube, maximal accelerating voltage 180 kV and output power 15 W. X-ray detector has a resolution of 2300×2300 pixels, and the dimension of one pixel is 50×50 micrometers. These parameters allow the voxel resolution in reconstructed images down to $0.5 \mu\text{m}$. The maximum transverse dimension of the measured object is limited to 120 mm and height up to 150 mm, then the voxel resolution is around $50 \mu\text{m}$.

3. Results

Microtomographic methods were used for quality control of ceramic plates to detect internal defects before and after pressure infiltration with lead. Observations were in this case focused at the detection of cracks inside the ceramic plates and other defects prior to infiltration (Fig.3).

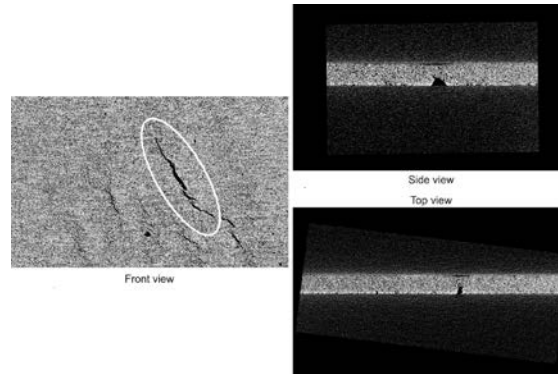


Fig.3 The crack inside the ceramic plate prior to pressure infiltration of plate with lead visualised by X-ray microtomography

The microtomography observations after infiltration (Fig. 4) provide visualisation of big pores filled with lead.

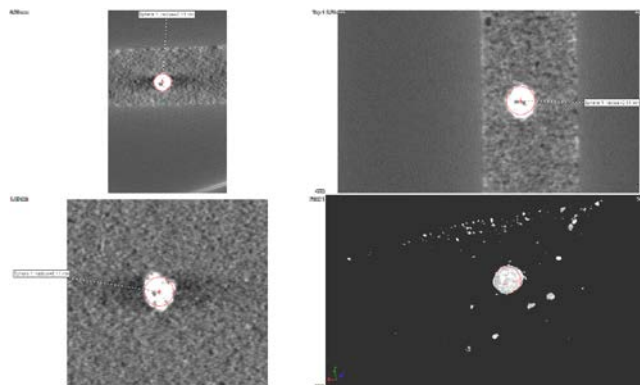


Fig.4 The ceramic plate after pressure infiltration with lead - a big lead-filled pore (white area) was visualised by X-ray microtomography method.

X-ray microtomographic methods were also used for inspection of the internal structure of porous material - detecting of porosity distribution and structural parameters (pore size, orientation, degree of circularity, etc.) after a die casting. Method allows fast and non-destructive visualisation of the inner structure of aluminum foam (Fig. 5a) and following analysis can provide comprehensive data on porosity, pore size distribution in volume, their orientation, shape, etc. Previously, the tests were made by a destructive way and always only one particular section could be analysed and therefore the informative capability of the results, comparing to this new microtomographic method, was very limited. Moreover, it was difficult to prepare slices and transfer them into digital form suitable for analysis.

On the Fig.6a defects in the structure of aluminum foam after die casting are shown. The principle of the die casting was presented at the conference Metfoam 2007 [5] and the conference Euromat 2009 [6]. Areas, which were not transformed completely during the process of foaming to the aluminum foam, are visible as darker spots. Fig. 6b shows the X-ray image of a properly foamed sample of the aluminum foam.

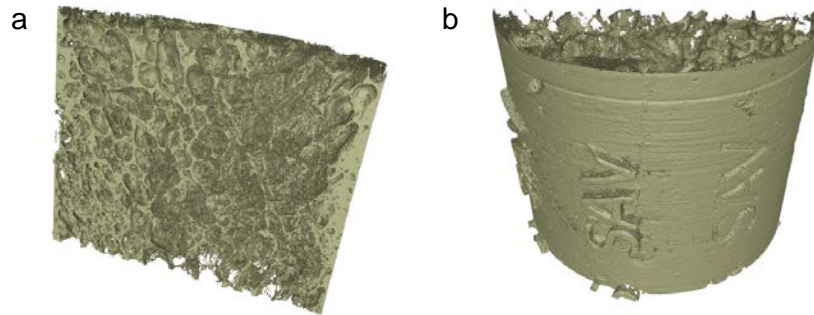


Fig.5 Reconstructed 3D image of an aluminum foam: (a) the internal structure (b) the outer surface

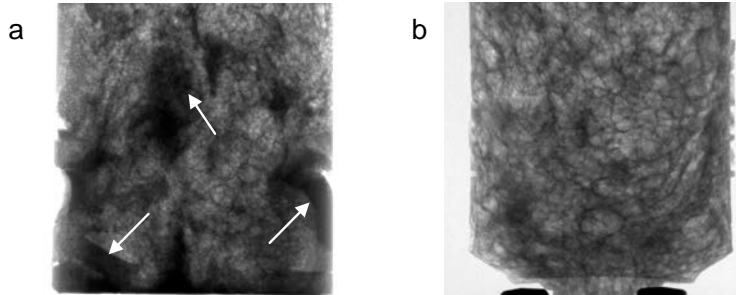


Fig.6 X-ray image of an aluminum foam: (a) non-foamed areas, (b) properly foamed sample.

4. Discussion and Conclusions

The paper presents the basic principle of X-ray microtomography method and examples of its use. The utilisation of this method in the non-destructive testing of ceramic disc before and after pressure infiltration with lead has been reported. Moreover, it was presented as the microtomography can be used for non-destructive reconstruction and visualisation of aluminum foam structures aimed at the monitoring of the porosity distribution and detection of non-foamed places in the internal structure.

Acknowledgements

This paper was created by the realisation of the project “CEKOMAT”, ITMS No. 26240120006 based on the support of Operational Program Research and Development financially supported by European Regional Development Fund. This work was also supported by the Slovak Research and Development Agency under contract APVV No. 0736-07 "LOWCOSTFOAM" and by a grant from Scientific Grant Agency - VEGA 2/0201/10.

References

- [1] Kak A C, Slaney M. Principles of Computerized Tomographic Imaging. IEEE Press., New York, 1988.
- [2] Cosslet V E, Nixon W C. X-ray Shadow Microscope. Nature, 168: 24 -25, 1951.
- [3] <http://www.ge-mcs.com/en/radiography-x-ray/ct-computed-tomography/nanotom-s.html>
- [4] Maire E. Three-dimensional microstructural information from diffraction and tomography of synchrotron X-rays, GEMPPM INSA, Lyon.
- [5] Simančík F, Florek R, Tobolka P, Nosko M. Rapid Prototyping for Complex 3-D Parts of Aluminium Foams. In proceedings of Metfoam, 2009.
- [6] Nosko M, Simančík F, Florek R, Tobolka P. New manufacturing route for cheaper aluminium foam. In proceedings of Euromat, 2009.

Comparison and Use of Hg Porosimetry and X-ray Computed Microtomography in Durability Tests of Sandstone on the Charles bridge in Prague

¹K. Kovářová, ²R. Ševčík, ³M. Chmelíková, ⁴M. Bednarik, ⁴R. Holzer

¹Department of Geotechnics, Faculty of Civil Engineering, Czech Technical University, Prague, Czech Republic

²Institute of Measurement Science, Slovak Academy of Science, Bratislava, Slovakia

³Department of Hydrogeology, Faculty of Natural Sciences, Comenius University, Bratislava, Slovakia

⁴Department of Engineering Geology, Faculty of Natural Sciences, Comenius University, Bratislava, Slovakia

Email: katerina.kovarova@fsv.cvut.cz

Abstract. Sandstones were often used as dominant building material in medieval Prague. Weathering processes lead to deterioration of these dimension stones and to changes in their durability. The range of the deterioration depends on petrography, including internal structure, mineral composition and cementation type, and also changes initiated. The stone's properties are negatively influenced especially during the winter frost period. A special weathering simulation program was developed to enable study the durability of sandstone in Prague winter climatic conditions. The Kocbeře cretaceous sandstone used for the last reconstruction of the Charles bridge in Prague was tested during this experiment. Changes developing in the internal structure were determined by Hg porosimetry and X-ray computed microtomography. The relationship between uniaxial compressive strength and porosity were studied during this experiment. The uniaxial compressive strength decreased with decreasing total open porosity measured by Hg porosimetry while total porosity measured by X-ray computed microtomography stayed constant. It was possible to determine the residual porosity based on the comparison of outputs of these two methods. It was ascertained that the decrease of uniaxial compressive strength is accompanied by growth of the volume of closed pores. This ascertainment contributed to the understanding of this non-typical phenomenon.

Keywords: Hg Porosimetry, X-Ray Computed Microtomography, Sandstone Weathering

1. Introduction

Sandstones were often used as a dominant building material in medieval Prague. The action of weathering processes leads to their deterioration and to the loss of their original physical and mechanical properties, i.e. to the changes of their durability. Sandstones are consolidated clastic sedimentary rocks mainly formed of quartz grains with addition of feldspars and stone chips. The grains are joined by cement of different character.

Intergranular spaces influence the porosity, presence and transport of the water inside the rock. This is one of the most important factors controlling the weathering process. Presence of water in the pore system affects the cohesion of grains if its state changes [1]. When water freezes, it increases in volume of approximately 9% [2]. This can cause large pressure and additionally the changes in the pore structure [1]. Ice then shrinks as the temperature decreases about 0.4% going from 0°C to - 45°C.

2. Subject and Methods

Experimental material and procedure

The cube samples (5 x 5 x 5 cm) of Kocbeře cretaceous sandstone were treated by exposition in the climatic chamber. Based on the meteorological data measured in Prague during winter periods in years 1999 - 2008, the weathering simulation program was developed to simulate Prague winter climatic conditions. According to the statistical analysis, the program consists of 56 cycles with the temperature range from - 14°C up to 14°C. The samples were soaked in distilled water for 24 hours before the beginning and after each 14 freeze/thaw cycles of the simulation program [3]. The samples were tested before and after climatic treatment to check the level of deterioration process.

Durability assessment

Stone durability can be assessed based on strength and pore structure properties. For example, stones with high compressive strength tend to be more durable. The uniaxial compressive strength test is used to determine the maximum value of stress attained before failure [4]. The samples were tested according to ČSN EN 1926 [5].

The porosity is very frequently used as an estimator for durability evaluation. Porosity is defined as a ratio of the volume of voids to total volume of stone, expressed as a percentage. More specifically, connected porosity is related to the flow of weathering agents and decay processes [4].

Hg porosimetry

Mercury porosimetry is based on the premise that a non-wetting liquid intrudes capillaries under pressure and pore size distribution is therefore determined from the volume of intruded mercury at each pressure increment. The percentage value of the open porosity is then determined by the total intruded volume. Hg porosimetry has a limit to determine pore diameter smaller than ca. 3.5 nm. The porosimeters Pascal 140 and 240 were used.

X-ray computed microtomography

The method of X-ray computed tomography belongs to non-destructive tests method, which was used to obtain the information about open and closed porosity as well. This method enables to evaluate pores larger than 5000 nm. Small cylinder's samples with the diameter 1 cm and the height 1.5 cm were prepared from untreated and treated sandstone. Samples were measured by X-ray microCT phoenix|x-ray nanoton180 at 90 kV, 100 μA with timing 2 s and 2880 projections. Voxel size was 5 μm.

The porosity was estimated in subsurface layer to the depth of 1 cm in both methods of porosity determination. The 3-D reconstruction and cross-section of untreated sandstone is shown in Fig. 1.

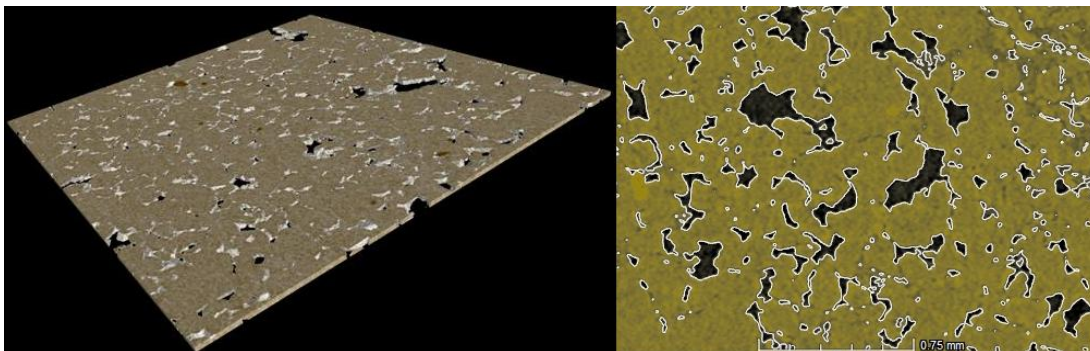


Fig. 1. 3-D reconstruction and cross-section of untreated sandstone.

3. Results

As showed the results of mercury porosimetry, the total open porosity decreased by 26 % and the specific volume of pores larger than 4000 nm decreased by 6.35 % after the treatment in the climatic chambre. The pores larger than 4000 nm create 75.25% portion of all pores by untreated sandstone and 70.47 % portion of all pores by treated sandstone. These values correspond to the total open porosity, which is 13.18 % in the first case and 9.12 % in the second case (Table 1).

Table 1. The values of total open porosity and for the portion of pores with the diameter larger than 4000 nm using mercury porosimetry (including standard deviation - in brackets).

	K _n - untreated samples	K IV - treated samples	Change (%)
Total open porosity (%)	17.51 (0.28)	12.95 (0.34)	- 26.08
Portion of pores > 4000 nm (%)	75.25 (0.42)	70.47 (1.97)	- 6.35
Total open porosity of pores > 4000 nm (%)	13.18 (0.14)	9.12 (0.01)	- 30.82

The total porosity was obtained by both samples using the X-ray computed microtomography. The total porosity of untreated samples is 15.61 % and treated samples 16.93 %. Results show the change by 8.48 %. It is possible to calculate the residual porosity with the diameter larger than ca. 4000 nm using data of Hg porosimetry. The results are presented in the following table (Table 2).

Table 2. The values of total porosity and residual porosity of pores larger than 4000 nm using X-ray computed microtomography (including standard deviation - in brackets).

	K _n - untreated samples	K IV - treated samples	Change (%)
Total porosity of pores > 4000 nm (%)	15.61 (1.74)	16.93 (1.84)	+ 8.48
Residual porosity of pores > 4000 nm (%)	2.43	7.82	+ 321.81

After the simulation program the uniaxial compressive strength decreased by 12.21 %.

4. Discussion

Cnudde *et al.* [6] demonstrates that mercury porosimetry generally gives higher total porosity values than the X-ray computed microtomography. This phenomenon could be caused due to the used technique, which allowed the detection of pores with diameter larger than 10 µm. In our case the detection limit was 5 µm.

In our experiment, the results of mercury porosimetry showed decrease of total open porosity of treated samples but according to the results obtained by the X-ray microtomography the total porosity (including open and closed pores) increased. After the conversion of data obtained by Hg porosimetry, the percentage of residual porosity was obtained.

The residual porosity consists of closed pores and such pores, whose identification and determination of their size distribution was impossible due to the "ink bottle" effect, which is

a typical limitation of mercury porosimetry [6, 7]. It means, that measuring of the true pore size distribution is distorted due to detection of the diameter of the throat entrance.

Although the X-ray computed microtomography enables to determine the pores with diameter larger than 5000 nm and Hg porosimetry enables the detection of pores with the diameter larger than 3.5 nm, use of X-ray microtomography clarified the non-typical change of porosity with increasing number of freeze/thaw cycles measured by Hg porosimetry. According to Fitzner [7] pore size distribution changes toward coarser pore size during freezing tests and the uniaxial compressive strength decreases with increasing porosity, however the results of our investigation are opposite. The decrease of uniaxial compressive strength with decreasing porosity measured via Hg porosimetry can be explained by the presence of the "invisible" closed pores.

Supporting chemical analysis didn't show the presence of any newly formed phases in pore space so it is obvious that the changes of porosity and of pore space properties are the result of frost action.

5. Conclusions

The X-ray computed microtomography enables to determine the residual porosity, what is not possible to define using mercury porosimetry. The limitation of the X-ray computed microtomography is the detection of pores with larger diameter than 5 μm .

In conclusion, the X-ray computed microtomography is useful non-destructive method for the description of pore space and it may clarify many other phenomena.

Acknowledgements

This research has been supported by Czech grants of CTU No. SGS10/027/OHK1/1T/11 and MŠMT No. MSM 6840770005 and Slovak grant VEGA No. 2/0201/10.

References

- [1] Winkler EM. Stone in architecture. Properties, Durability. Springer-Verlag, Berlin, 1997.
- [2] Johannesson B. Dimensional and ice content changes of hardened concrete at different freezing and thawing temperatures. *Cement & Concrete Composites*, 32: 73-83, 2010.
- [3] Kovářová K. Influence of weathering processes on sandstones – Simulation of Prague winter climatic conditions. In proceedings of III International Interdisciplinary Technical Conference of Young Scientists, 2010, 311-314.
- [4] Benavente D, García del Cura MA, Fort R, Ordóñez S. Durability estimation of porous building stones from pore structure and strength. *Engineering geology*, 74: 113-127, 2004.
- [5] ČSN EN 1926 (72 1142) Natural stone test methods - Determination of uniaxial compressive strength, 2007.
- [6] Cnudde V, Cwirzen A, Masschaele B, Jacobs PJS. Porosity and microstructure characterization of building stones and concretes. *Engineering geology*, 103: 76-83, 2009.
- [7] Fitzner B. Porosity properties of naturally or artificially weathered sandstones. In proceedings of VIth International congress on deterioration and conservation of stone, 1988, 236-245.

Measurement and Calculation of Relaxation Time T_2 and Diffusion of Gel Electrolytes Based on the NaClO_4 Inorganic Salt During Polymerization by NMR Method with Focusing on ^{23}Na and ^1H Nuclei

^{1,2}R. Kořínek, ^{1,2}K. Bartušek, ³J. Vondrák, ³M. Musil

¹ Institute of Scientific Instruments of the ASCR, v.v.i., Královopolská 147, 612 64 Brno, CZE,

² Department of Theoretical and Experimental Electrical Engineering FEEC BUT, Kolejní 4, 612 00 Brno, CZE

³ Department of Electrotechnology FEEC BUT, Technická 10, 602 00 Brno, CZE

Email: radim.korinek@gmail.com

Abstract. In the article, the measurement and following calculation of relaxation time T_2 of gel electrolytes based on the NaClO_4 inorganic salt and measurement of diffusion coefficients are described. The measurement is focused on ^1H and ^{23}Na nuclei. The value of relaxation time T_2 is obtained by approximation of the measured FID (Free Induction Decay) signal with two exponentials using a genetic algorithm. To measure relaxation time T_2 , the Hahn echo was used. To measure diffusion, the PFG-SE method (Pulsed Field Gradient Spin) was used. The change of relaxation times and diffusion coefficients during polymerization time indicate a change in the internal structure and chemical composition of gel electrolytes based on NaClO_4 .

Keywords: T_2 Relaxation, Diffusion, NMR, Measurement

1. Introduction

Nuclear magnetic resonance spectroscopy is one of the ways to examine the properties of conducting gels based on the NaClO_4 inorganic salt during polymerization. For batteries with liquid electrolyte, a key challenge is to replace the liquid electrolyte with solid electrolyte. The main disadvantage of liquid electrolyte batteries is the risk of mechanical damage to the packaging equipment leading to spillage or evaporation of the solvent. As a solvent, commonly flammable or toxic organic compounds (acetonitrile, N, N-dimethylformamide, dimethoxyethane, etc.) are frequently used [1]. In this paper, basic methods for measuring the properties of gel structure during polymerization, particularly relaxation times T_2 and diffusion coefficients, are introduced. We can obtain these parameters using the MR pulse sequences. We measured two sets of samples. To measure relaxation time T_2 , the Hahn echo was used. To measure diffusion coefficients, the PFG-SE method (Pulsed Field Gradient Spin Echo) was used. All points of the FID signal are measured within the Hahn echo time. Consequently, it is necessary to approximate the FID signal by two exponential functions to obtain the T_2 time. Consequently, we assume the existence of two time constants T_2 . For approximation, the genetic algorithm was chosen because it is a global optimization method. The algorithm is explained in the article.

2. Methods

Third-generation gel electrolytes combine three components: a) polymer networks of suitable composition, b) aprotic solvent, and c) organic salts to ensure conductivity (Li or Ni). For the experiments, gel electrolytes with conductivity based on sodium ions ^+Na were selected [2].

To measure the diffusion coefficients, the PFG-SE method as mentioned in the introduction was used. The PFG-SE sequence is shown in Figure 1 [2]. To measure relaxation time T_2 , the Hahn echo as mentioned in the introduction was applied.

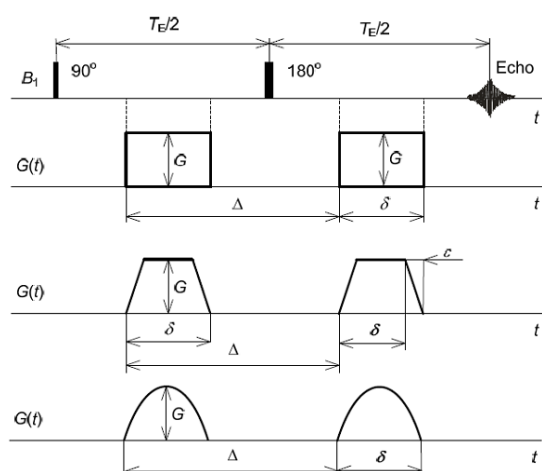


Fig. 1. The PFG-SE sequence and different shapes of diffusion gradients [2][3].

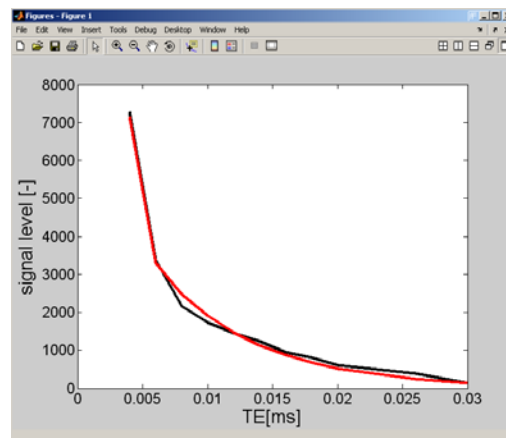


Fig. 2. Approximation of the measured data with two exponentials using a genetic algorithm. (^{23}Na nuclei, 1st set of gels, 1st samp., polymerization time = 0 min)

Genetic algorithm

All points of the FID signal are measured within the time of the Hahn echo course. Now we need to approximate these points by means of a suitable function. There exist a large number of optimization algorithms seeking the criterion function minimum. For example, the Trust-Region Methods for Nonlinear Minimization algorithm, which is contained in the MATLAB lsqcurvefit function, has proved to be effective. The advantage of this algorithm is its speed as well as the comparatively high success rate in the process of seeking the global minimum of our criterion function. From the user perspective, the disadvantage connected with the application of lsqcurvefit pertains mainly to the sophisticated setting of the optimization parameter and the necessity to have a MATLAB optimization toolbox [4]. Therefore, a genetic algorithm was used. An example of the approximation is shown in Figure 2. The main advantage is the ability to set the minimum and maximum values that we seek. However, the main disadvantage of this algorithm is the large computation time. The same genetic algorithm is used in [5]. All points of the FID signal are approximated by this function:

$$M(T_E) = M_{0a} \cdot e^{-\frac{T_E}{T_{2a}}} + M_{0b} \cdot e^{-\frac{T_E}{T_{2b}}}, \quad (1)$$

where M_{0a} , M_{0b} , T_{2a} , T_{2b} are the searched values. The characteristics of the genetic algorithm are described in great detail in [5].

3. Experiment

The experiment was carried out on the NMR tomograph (4.7T/75mm) at the Institute of Scientific Instruments in Brno. The resonant frequency of ^1H nuclei is 200 MHz, and in ^{23}Na it is 51 MHz. The course of the experiment is consistent with the procedure described in [6]. The extension of procedure used to date consists in the fact that we measured *two* sets of gels based on the NaClO_4 inorganic salt. Furthermore, the measurement is extended to the measurement of diffusion. In the following table (Table 1) we can see individual composition

of the gels. NaClO_4 in PC (propylene) make a liquid electrolyte. After mixing with MMA (methyl methacrylic acid, 99%), EDMA (networking factor) and BEE (UV polymerization Initiator), gel electrolyte is gradually created by UV radiation (total time of polymerization for several hours)[6].

Table 1. 1st & 2nd set of measured samples

	1 st samp.	2 nd samp.	3 rd samp.	4 th samp.	5 th samp.	1 st samp.	2 nd samp.	3 rd samp.	4 th samp.	5 th samp.
	1 st set of gels					2 nd set of gels				
total volume of gel – V[ml]	12	12	12	12	12	6	6	6	6	6
PC [ml]	4,4	4,292	4,184	4,076	11,41	2,2	2,146	2,092	2,038	5,705
NaClO_4 [g]	0	0,270	0,538	0,808	1,470	0	0,135	0,269	0,404	0,735
MMA [ml]	7,657	7,657	7,657	7,657	-	3,828	3,828	3,828	3,828	-
EDMA [μl]	43	43	43	43	-	21,5	21,5	21,5	21,5	-
BEE [g]	0,17	0,17	0,17	0,17	-	0,085	0,085	0,085	0,085	-

4. Results

In the first set (Table 1) we are interested in T_2 relaxation of ^1H and ^{23}Na nuclei. In Figure 3 we can see the progress of relaxation T_{2a} and T_{2b} for ^1H nuclei. The progress for ^{23}Na nuclei is shown in Figure 4. Figure 5 observes the progress of diffusion in the second set of samples.

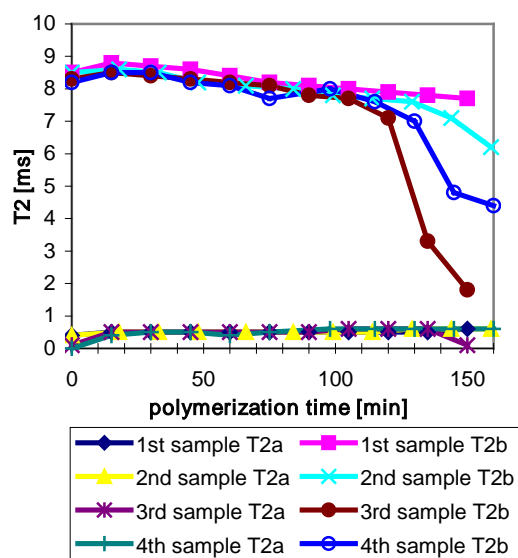


Fig. 3. T_2 relaxation during the polymerization for ^1H nuclei. 1st - 4th samples: 1st set of gels.

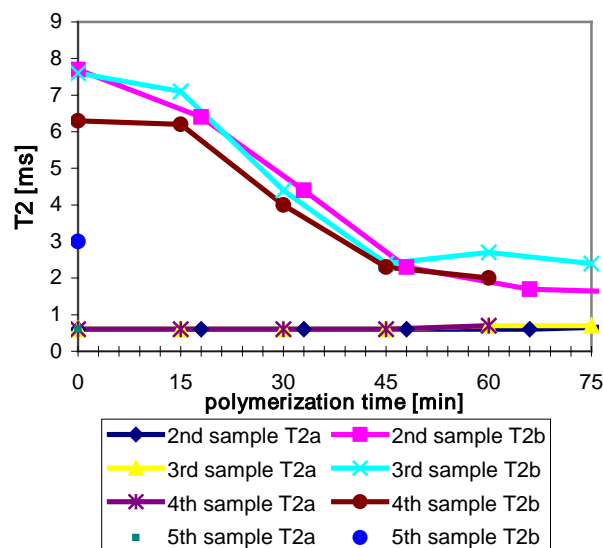


Fig. 4. T_2 relaxation during the polymerization for ^{23}Na nuclei. 1st - 4th samples: 1st set of gels.

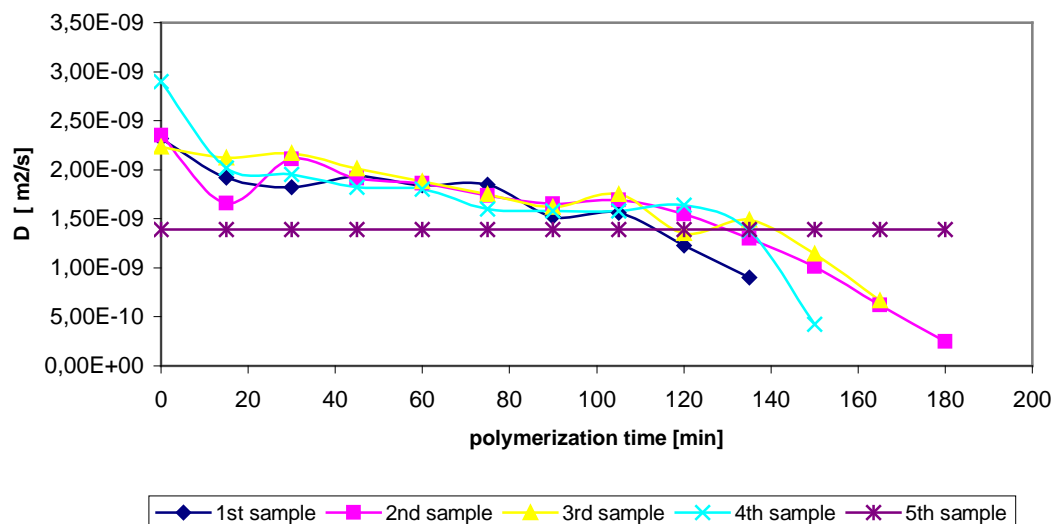


Fig. 5. The dependence of diffusion changes during polymerization for ^1H nuclei. 1st.- 5th. sample: 2nd set of gels.

5. Conclusion

The change in the structure of polymer gels during polymerization is characterized by T_2 relaxation. The decrease of relaxation time T_{2b} of gel with various concentrations is the same. These two aspects characterize the binding ^{23}Na nuclei in the gel. The second relaxation time T_{2a} is independent of the polymerization time. The measurement results will contribute to the study of changes in the structure of gel electrolytes.

Acknowledgements

The work described in the paper was financially supported by the research project of the Czech Science Foundation, Grants No. P102/10/2091, and the project MŠMT CZ.1.05/2.1.00/01.0017 (ED0017/01/01).

References

- [1] REITER, J., VONDRÁK, J., VELICKÁ J., MIČKA, Z. Nové elektrolyty nejen pro chemické zdroje elektrické energie. *Chem. Listy* 2006/100, s. 133-139.
- [2] BARTUŠEK, K. Speciální metody měření difúzních koeficientu metodami nukleární rezonance. VUTIUM, 2007, 21 s. ISBN 978-80-214-3379-3.
- [3] KOŘÍNEK, R., VONDRÁK, J., K., BARTUŠEK, K. Relaxation Time Study of Gel Electrolytes During Polymerization by MR Methods, *ECS Transaction*, (2011) (in press).
- [4] BARTUSEK, K., KUBASEK, R., FIALA, P. Determination of Pre-emphasis Constants for Eddy Current Reduction. *Measurement Science and Technology*, Volume 21, Issue 10, pp. 105601 (2010).
- [5] GOLDBERG D.E., Genetic algorithms in search, optimization and machine learning, Addison-Wesley, New York, (1989).
- [6] KOŘÍNEK, R.; VONDRÁK, J.; BARTUŠEK, K.; MRNKA, M. Study of gel electrolytes properties by MR methods. In *Advanced Batteries Accumulators and Fuel Cells 11th ABAF*. Brno: 2010. s. 43-47. ISBN: 978-80-214-4148-4.

High Precision Production Metrology for Quality Improvement in Biomedical Applications

¹M. N. Durakbasa, ¹P. H. Osanna,
²B. Sagbas, ³A. Hornikova

¹Vienna University of Technology,
Department of Interchangeable Manufacturing and Industrial Metrology,
Karlsplatz 13/3113 1040 Wien, Austria,
durakbasa@mail.ift.tuwien.ac.at

²Yildiz Technical University, Mechanical Engineering Department
Materials Science & Manufacturing Technologies Division
34349 Besiktas, Istanbul, Türkiye,
bsagbas@gmail.com

³University of Economics in Bratislava, Faculty of Informatics Economics,
Department of Statistics,
Dolnozemska cesta 1/b, 852 35 Bratislava, Slovakia
adriana.hornikova@euba.sk

Abstract. *Rapid development in biomedical techniques demands the application of modern computerized measurement techniques and utilization of measuring devices with new technologies. Especially computer aided co-ordinate measuring technique can be applied to evaluate the shape of non technical structures, such as human limbs or joints with high accuracy. Measurement results create the basis for the improvement and optimization of future work in biomedical techniques and related areas. There are lots of important characteristics which describe the implant quality, desired from a successful implant. Besides defining macroscopic structure like material and shape an implant should reach defined microscopic structure such as the chemical, physical, mechanical, and topographic characteristics of the implant surface. These different characteristics describe the effect activity of the attached cells that are in close proximity to the medical implant surface.*

By using initially developed measurement techniques for engineering applications the clinicians could be able to characterise biomedical surfaces to assist in their maintenance, modification, optimisation and trauma repair. With development of robust measurement tools and best practice protocols it will be possible to quantify the appropriate metrology so that it will be possible to provide a quality assurance feedback to the clinicians to assure good practice, functional achievement and long service life of the restoration, implantation object.

Keywords: *Quality Assurance, Medical Implant, Co-Ordinate Metrology, Surface Measurement, Hip Joint, Wear Out*

1. Introduction

There exists rapid development in biomedical technique and this demands the application of modern computerized measurement technique and measuring devices. Especially computer aided co-ordinate measuring technique and 3D digitizing systems can be applied to evaluate the shape of non technical structures as there are human limbs or joints with high accuracy. The results of such measurements give for example the basis for the improvement and optimization of future work in biomedical technique.

In the last years the sophisticated 3D measurement technique has attained an important role in the industrial measurement technology. By the rapid evolution and the commitment of computer-aided coordinate measuring instruments it became possible to control the quality of the industrial products more precisely.

Increasing demand for quality and reliability on the one hand and competition with cost consciousness on the other hand are contradictory requirements in today's production engineering. This issue must be also considered from the point of view of international standards dealing with quality management and quality assurance [1, 2].

In addition to this development, an increasingly important factor, the protection of environment must be taken into consideration, too [3].

2. 3D Measurement and Analysis of Non-Technical Structures

Technical instruments can carry out accurate and reproducible movements only with the utilization of nearly exact and highly accurate predefined elements, like references and standards. Implying an analogy conclusion that human kinematics works on a common basis of exact regulations which are currently unknown. Artificial limbs, joints and their linkage would work better if we would have more accurate information about original human parts (Figure 1).

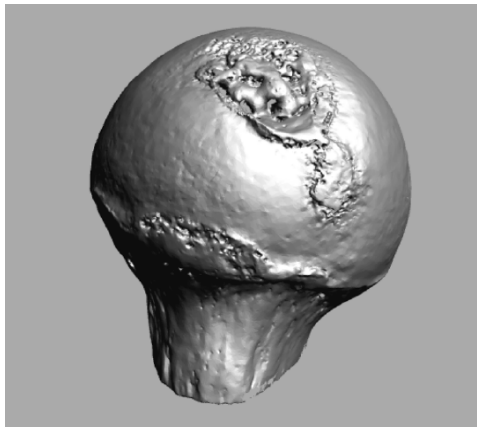


Fig. 1. Evaluation of measuring results of a human hip joint head using white light scanner.

Depending on whether macro-geometry or micro-geometry is of measurement interest in the analysis of workpieces' surfaces, a distinction is made between form errors of different order, both in the technical literature and relevant standards (Figure 2).

It is common technical practice to collectively consider the short wave geometric deviations of the third or higher order as surface roughness characteristic on the basis of worldwide understood and internationally established parameters. As far as geometrical deviations of form and positions are concerned the increased use of co-ordinate metrology has improved common technical knowledge [4].

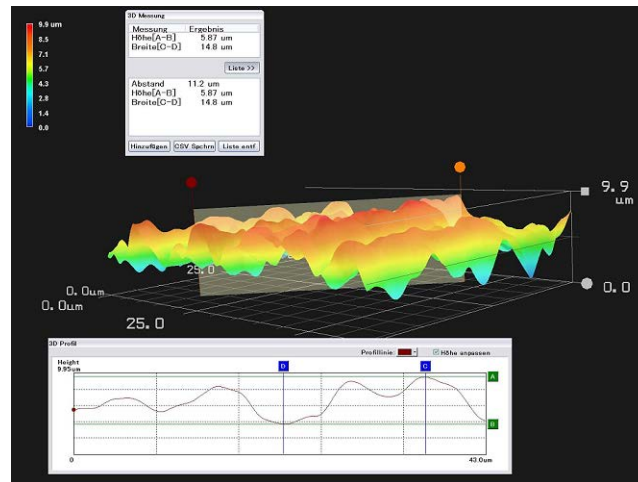


Fig. 2. 3D topographical analysis of a hip joint implant using digital microscopy system

In the case of it is necessary to choose a measuring device, this is done based on reasons of possible deviations of dimension and form measurement plan. Only with three-dimensional co-ordinate measuring machines (CMMs) it is possible to measure deviations in dimensions, forms and positions with high accuracy while using only one measuring device. Furthermore, it can be shown that accurate CMMs can be used to evaluate workpiece micro-geometry, like artificial sole modeling human foot, artificial teeth, hip joint heads, different kind of prostheses [5].

3. Coordinate Metrology for Measurement of Non-Technical Objects

Computer aided co-ordinate measuring technique can be applied to measure and evaluate with high accuracy shapes of non technical objects as human limbs or joints. Measurement results can create and widen the basis for the improvement and optimization of future work in the area of biomedical techniques. At the time being co-ordinate metrology is a very important tool for solving various problems in production metrology especially in the case of high flexibility and high accuracy are demanded.

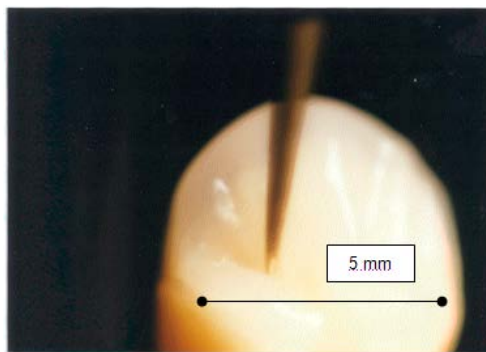


Fig. 3. Measurement of an Artificial Tooth for Implantation.

Measurement problems are handled with sufficiently high accuracy using co-ordinate metrology. The measured specimen is in figure 3 an artificial tooth from human teeth prosthesis. Due to sharp bends and curvature of the surface of artificial tooth its form can be measured as a free form surface using a very small probe, e.g. with a stylus radius of 0,04 mm.

The form of a biomedical surface can be evaluated from measured data when the form measurement is carried out by using CMM in scanning mode. CMM works here only as measuring system and digitizer. This example illustrates that co-ordinate metrology can be used to obtain exact numerical information about dimensions, forms and shapes and connections within biomechanics.

4. Data Evaluation and Applications

It is presupposed that artificial human joints must be constructed according to defined geometric kinematical regularities otherwise it would not be possible that these parts will stay in correct function during whole lifetime. They should last for decades [6, 7]. These regularities and natural motion laws are preconceived by men within technical motion systems and must be testified stepwise individually for each joint and later prosthesis.

Artificial limbs for hip joints are in general, constructed having the shape of spheres although in orthopedics literature is written that this is only an approximation [8-10]. Authors draw here the general conclusion that there exist deviations from the shape of a ball, but they do not see any further effects on the joint.

Stress distributions judgments of a hip implant are being used to study component fracture and permanent deformation, interface loosening, and remodeling process due to wearout. Stresses depend on joint loading and geometry, material properties and interface conditions, and thus are influenced by implant design, choice of materials, and fixation techniques. The importance of listed parameters can be evaluated by analytical and experimental techniques and combined.

Materials used in current total endoprotheses (TEPs) include metal alloys from such as iron, cobalt, and titanium based systems; and polymers such as polyethylene; and carbons; and ceramics. The evolution and application of these materials have established an extensive base of knowledge of short- and long-term compatibility.

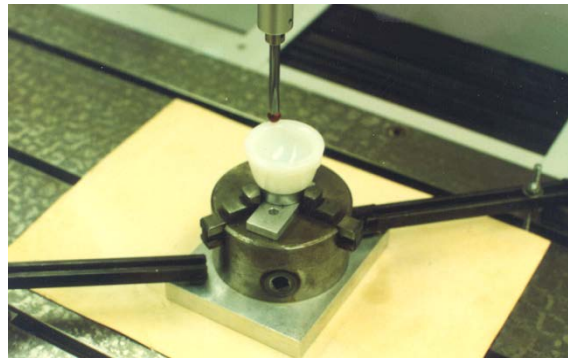


Fig. 4. Measurement process on polyethylene prosthesis using a CMM in scanning mode

The selection of materials depends upon physical, geometrical, mechanical, and chemical properties related to compatibility. Various form properties measurement of wornout prostheses, material friction on these objects and the wearout itself provide us with information and knowledge to establish complete series of quantitative correlations applicable later within clinical practice.

Figure 4 shows how a polyethylene prosthesis form can be measured when the form measurement is carried out by using CMM in the scanning mode. CMM only works as the measuring system and digitizer. The evaluation is done by transferring data to an evaluation computer and using evaluating program for calculation and optimization.

Comparison of nominal data and measured data of socket joint for implanted and worn out prostheses are a good example of application. The calculation for both the socket joint of implanted and worn out prosthesis will be carried out by using the best fit criteria.

The numerical evaluation of measured data and comparison with the nominal geometry of the socket joint form allows for measurement analysis and creates the basis for the improvement of the implementation of ball and socket joints (Figure 5).

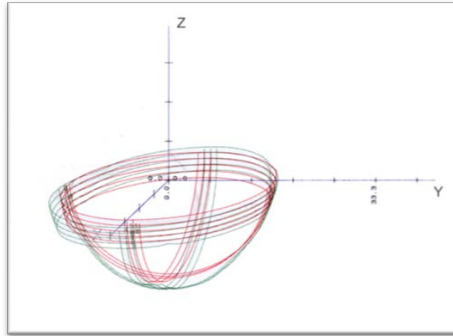


Fig. 5. Comparison of nominal data and measuring data of socket joint of implanted and worn out prostheses.

To achieve acceptable functional performance it has been shown in bio-implants that the surface quality and its adherence to form is the major feature. In hip joints for example poor surface topography has been responsible for most of the early failures in service. In addition product cleanliness is an important issue and the research project will maintain the practices that are defined and essential to ensure that infections to patients do not result from any aspect of measurement of part creation that is undertaken. As example Figure 6 shows the measurement results taken from the surface of an endo prosthesis for the femoral head of a human hip joint. The used measuring instrument is a digital microscope and the results show clearly a scratch that occurred during production of this endo prosthesis that may cause problems with the biocompatibility when already implanted.

Stress analyses can add to an understanding of the complex structure by quantifying and interrelating parameters and natural phenomena. Moreover, finite element methods can be used to predict on a relative basis the mechanical performance of different devices.

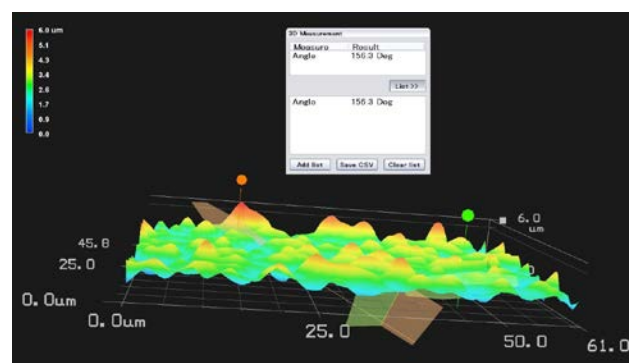


Fig. 6. Measurement taken from the surface of an endo prosthesis for the femoral head of a human hip joint CoCrMo

Finally, stress analyses can provide guidelines to assess consequences of design choices and surgical compromises. For instance, the relative contribution of parameters such as cement layer thickness, stem stiffness, stem length, and stem cross-sectional shape have been established and quantified.

5. Conclusions

In the paper is described an extensive measurement of non technical objects, here implants of various kinds, especially hip joints as well as dental implants carried out using the co-ordinate metrology with tactile probing methodology and non-contact approach using laser scanner for feature measurement.

This can create the standard method for a great variety of different and especially complex tasks for workpiece measurement. Results of various measurement and measurement evaluation can help to start, develop and enhance basis for the improvement and optimization of biomedical techniques for the future.

References

- [1] EN ISO 9001: 2008: Quality management systems – Requirements. 2008.
- [2] EN ISO 13485: 2003 (AC:2009) Medical devices - Quality management systems - Requirements for regulatory purposes.
- [3] EN ISO 14001: 2004 Environmental management systems - Specification with guidance for use.
- [4] Aeby C, Die Sphaeroidgelenke der Extremitätengürtel. Z. Rat.III, XVII, 1863.
- [5] Schmid F, Über die Form und Mechanik des Hüftgelenkes. Inang.-Diss. Bern. Z. Chri., 1874.
- [6] Durakbasa M. N, Koordinatenmesstechnik für Biomedizinische Anwendungen; e&i, 117 (2000), 4; S. 269 – 272.
- [7] Osanna P. H, Durakbasa M. N, Concept for Computer Aided Non-contact Laser Roughness Evaluation of Engineering Surfaces; in: "Laser Metrology Applied to Science, Industry and Everyday Life - LM-2002", (2002), ISBN: 0-8194-4686-6; S. 708 – 714.
- [8] Braune W, Fischer O, Die Bewegung des Kniegelenkes nach einer neuen Methode am lebenden Menschen gemessen. Abhandl. Math. Phys. Class.Königl. Sächs. Ges. Wissensch. 17/2, 1891.
- [9] Bullough P. G, Goodfellow J.W, Greenwald, A. S, O'Conner J.J.: Incongruent Surfaces in the human joint. Nature 217: 1290, 1968.
- [10] Greenwald A. S.: Biomechanics of the hip. Saunders, Philadelphia, 1990.

Metrological Self-Check of Platinum Resistance Thermometer

Yu. Baksheeva, K. Sapozhnikova, R. Taymanov

D.I.Mendeleyev Institute for Metrology (VNIIM), St.Petersburg, Russia

Email: k.v.s@vniim.ru

***Abstract.** The procedure for developing a sensor with metrological self-checking is shown by the example of a platinum resistance thermometer (PRT). The efficiency of the method suggested is grounded by results of the theoretical analysis and experimentally confirmed by the example of the PRTs with a sensing element of the “strain free design”. The sensors developed enable to carry out checks of their metrological serviceability and correction of measurement results directly in the process of operation.*

Keywords: Metrological Self-check, Platinum Resistance Thermometer, Measurement Reliability

1. Introduction

To provide the reliability of measurements results obtained from temperature sensors as well as to decrease costs of the metrological maintenance of these sensors, it is necessary to automate the metrological serviceability check of the sensors in the process of their operation. The well-known decisions [1]-[6] have some significant disadvantages.

The most promising solution of the problem indicated is the self-check of sensors (metrological self-check) [7], [8]. The metrological self-check can be implemented in two forms: a direct metrological self-check using an embedded measuring instrument of a higher accuracy and metrological diagnostic self-check realized without application of means of such a kind. The metrological diagnostic self-check is accomplished on the basis of evaluating a deviation of the parameter characterizing a critical uncertainty component from an accepted reference value of this parameter. By the critical uncertainty component they imply a dominating uncertainty component or that tending to rise quickly.

In the paper the procedure for developing a sensor with metrological diagnostic self-check is illustrated by the example of a platinum resistance thermometer (PRT).

2. Theoretical grounds of the method applied

The development of a PRT with the self-check was carried out on the basis of a sensing element (SE) of the well-known “strain free” design suitable for performing experimental researches. The SE includes a ceramic tube with longitudinal holes, where the spirals of platinum wires filled up with ceramic powder are located. The tube is hermetically sealed. Leading-out wires are soldered to the ends of the spirals [9]. The technology of manufacturing the sensors of such a type contains a noticeable part of manual operations. To control the quality of each operation is extremely difficult. The character of the processes generating an increase of the PRT uncertainty, irrespective of the design and technology of manufacturing, significantly changes depending on a working temperature range.

If one sums up the known data [9]-[11] and others, then within the working temperature range up to $T_{max} < (0,25 - 0,30)T_m$, where T_{max} is its upper limit and T_m is the melting point of platinum (which corresponds to $T_{max} \approx (450 - 500)^\circ\text{C}$), the main processes affecting the change of the PRT uncertainty in the process of operation can be divided into two main groups.

The first group includes the processes leading to destruction of a thin surface layer of conductors and variation of its conductive properties with regard to all SEs of the sensors:

- surface oxidation;
- sublimation of surface substances;
- contamination of the surface layer by the diffusion of oxides and mixtures;
- mechanical damage of the surface, and so on.

Under the influence of the uncertainty sources, which refer to the first group, in the course of time the specific resistance of the surface layer begins to exceed significantly the specific resistance of a conductor material. This can be represented as a certain equivalent decrease of an area of the cross-section of the platinum wire, which correspondingly increases its resistance. Other processes (which are not connected with the destruction of the surface layer) leading to an unexpected change of resistance of some SEs refer to the second group:

- consequences of the technological spoilage, which have not been detected in the production process (a change of contact resistance caused by low-quality welding or soldering, origination of mechanical strains and deformations as a result of heating or cooling of a SE in case of its poor fixation, and so on);
- variation of those parameters of the sensor elements, which are external with respect to the SE spirals (drop of the specific resistance of the sealing layer, increase of its gas- and/or humidity permeability, e.g., due to cracking, etc.).

The influence of the processes, which refer to the second group, on the sensor uncertainty to a great extent depends on the accepted design and technology of manufacturing the PRTs, as well as on the efficiency of the quality control of the production process. When the processes of the first group dominate, a critical uncertainty component is the deviation of the platinum wire resistance, which is caused by variation of the properties of the wire surface layer.

In [12] it is proposed to use the redundancy for realizing the function of metrological diagnostic self-check, i.e., to make a SE of two or a number of parts differently sensitive to factors influencing on the growth of the critical uncertainty component.

To realize the function of metrological diagnostic self-check in the process of operation, the diagnostic function (DF) β that depends on the values of signals coming from various parts of the SE is calculated. For example, β is equal to the ratio of the wire resistance values.

At the stage of the original calibration of the temperature sensor, which corresponds to the start of operation, a nominal value β_0 of the DF is determined. A relative deviation $\delta\beta$ of the DF from the nominal value is rigidly connected with the sensor uncertainty. In the process of operation the check of the metrological serviceability is performed by determining $\delta\beta$ at a temperature measured and comparing it with a permissible relative deviation.

When the value $\delta\beta$ exceeds the permissible limits or approaches to such a limit, it is necessary to perform an unscheduled calibration of the sensor even if the specified interval has not come to its end. When the specified calibration interval comes to the end and $\delta\beta$ does not exceed a permissible value, then this fact can become an argument for significant increasing the corresponding interval and using the sensor further.

In the general case (for various designs of the PRT), it is necessary to provide a different ratio of the cross-section area to the perimeter of the cross-section of the SE parts.

In each part of the SE the destruction rate (rate of resistance variation) of the conductor surface layer weakly depends on the geometrical parameters of the conductors themselves,

and the depth of the destructed layer is small as compared to linear dimensions of the conductor cross-section. For the version of the SE including two parts made of the wires of various diameters

$$\delta\beta = \left| \frac{\beta - \beta_0}{\beta_0} \right| \approx 4a \left| \frac{d_1 - d_2}{d_1 d_2} \right|, \quad (1)$$

where

a assumed thickness of the surface layer subjected to the destruction;

d_1 and d_2 wire diameters.

Provided the relationship between the $\delta\beta$ value and uncertainty δT of the temperature measurement is known, then, using a value of $\delta\beta$ determined experimentally, it is possible to introduce a corresponding correction into a measurement result.

3. Experimental Results

For preliminary evaluation of the efficiency of the considered metrological self-check method, there were carried out experimental investigations of the SE prototypes. This was done in the mode of a forced load, “heating up to 600°C - cooling“, with a cycle time of 70 – 80 hours. The prototypes contained a SE consisting of two spirals (each having a resistance of 100 Ohm) which were made of a platinum wire of 50 and 30 μm in diameter. In each cycle the resistance of each spiral was measured at temperature of 0, 450 and 600 °C determined with a reference thermometer. Then the values of β , $\delta\beta$ and resistance deviation (increment) ΔR for each spiral were calculated.

Before the experiments a preliminary annealing of the SEs was done at temperature of 800°C to stabilize the SE characteristics. After that, they were calibrated with uncertainty of $\pm 0.2^\circ\text{C}$. It was noticed that during the first cycles of the forced load the process of annealing was still in progress, its rate being different due to the fact that cold-hardening of the wires differed in diameter was not the same. Therefore, the characteristics obtained after annealing of both two spirals were taken as the calibration characteristics. A “zero” value was assigned to the corresponding cycle; the resistance increments ΔR for each cycle being determined with respect to the resistance value measured in the “zero” cycle. On the basis of the data obtained, the DF values β_0 for the “zero” cycle were calculated, and for the subsequent cycles the DF relative deviation $\delta\beta$ and relative uncertainty δT of temperature measurements were determined. The characteristic dependencies are illustrated in Fig.1a and 1b.

The type of these dependencies confirms that the SEs are predominantly influenced by the processes relating to the first group. However, in some prototypes among those investigated, there have been fixed up metrological defects caused by the processes of the second group.

The experiment performed has shown that the metrological self-check method enables a cumulative uncertainty to be evaluated and metrological defect to be revealed. However, the development of the sensor with two spirals of the wire of different diameters requires introducing some changes into the design and technology of the sensor. The PRT design with the metrological self-check should provide for the closeness of original resistance values of SE wires and closeness of the design parameters (values of a pitch, length and diameter of spirals). These conditions can be jointly satisfied if the first SE part is made of a single conductor and the second part contains several conductors connected in parallel. The analysis has shown that the optimal number of conductors in the SE part made of a thinner wire is 2. To increase mechanical strength and rigidity of this spiral, it is useful to make it of twisted wires connected in parallel.

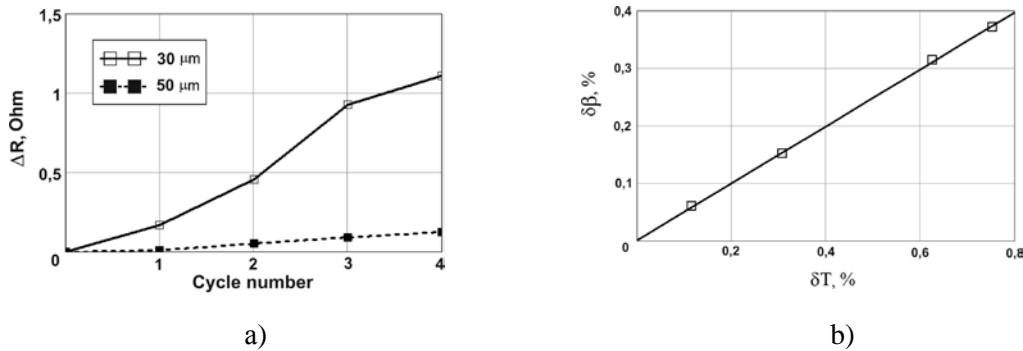


Fig.1. The characteristic dependencies obtained in the experiment at temperature of 450°C

- a) Dependence of the resistance increment in the SE parts on the cycle number;
 b) Dependence of the relative DF deviation on the relative uncertainty of temperature measurements

4. Conclusion

A temperature sensor with metrological self-check can be implemented on the basis of the technologies applied in industry. Its advantages are:

- automatic check of the measurement information reliability in the process of operation and opportunity of automatic correction of uncertainties;
- availability of diagnostic information that allows the calibration to be realized according to a technical condition;
- possibility to increase by many times the calibration interval.

References

1. Hashemian H. M. Sensor Performance and Reliability. ISA, USA, 2005.
2. http://www.omega.com/pptst/TC-K-NPT_RTD-NPT.html
3. <http://www.tesey.com>
4. <http://npk-etalon.ru/>
5. <http://www.electrotherm.de>
6. Oleynik B. N., Sumerin V. M., et al. Temperature Measurement Using Thermonoise Thermometers, *Measurements, Control, Automation*, 1 (45): 22-29 1983.
7. Taymanov R., Sapozhnikova K. Metrological Self-Check and Evolution of Metrology, *Measurement*, 7 (43): 869-877, 2010.
8. GOST R 8.673-2009. Intelligent Sensors and Intelligent Measuring Systems. Basic Terms and Definitions.
9. Samsonov G.V., Kitz A.I., Kuzenia O.A., Lakh V.I., et al., Sensors for Measuring Temperature in Industry, Naukova Dumka, Kyev, 1972.
10. Berry R. J., Oxidation, Stability and Insulation Characteristics of Rosemount Standard Platinum Resistance Thermometers, *Temperature, Its Measurement and Control in Science and Industry*, AIP, New York, 5: 753-761, 1982.
11. Li X., Zhao M., and Chen D., A Study on the Stability of Standard Platinum Resistance Thermometer in the Temperature Range from 0°C through 720°C. <http://www.hartscientific.com>
12. RU2321829 G01 D 3/00. Gorokhov L. P., Sapozhnikova K. V. and Taymanov R. E., Mode of Control of Metrological Condition of Measuring Converter of Non-electric Value and Installation for its Execution, Bulletin, 10, 2008.

Measurements of ASTRA Satellite Signal Parameters

I. Bačić, K. Malarić

University of Zagreb, Faculty of Electrical Engineering and Computing
Department of Wireless Communication, Zagreb, Croatia

Email: iva.bacic@fer.hr

Abstract. *In this work, after a basic theoretical background on the ASTRA satellite constellation and their satellite signal and channels, our model for measuring the satellite signal reception in our laboratory is presented. The satellite signal was received with a parabolic antenna, led over an LNB converter and satellite in-line amplifier to a digital satellite receiver and a television set. The strength of satellite receiver's input signal was measured with a spectrum analyzer. The communication channel width was analyzed.*

Keywords: *ASTRA, Satellite Link, Satellite Signal Reception, Measuring Peak Power Signal Strength, Communication Channel Width, Intermodulation Products*

1. Introduction

Planned broadcasting directly to home TV receivers takes place in the Ku band. These services are known as direct broadcasting satellite services. ASTRA is one of the major TV satellite services in Europe and is located at the 19.2° east orbital position downlinking in the 10.7 – 12.70 GHz range [1]. Their satellites have a geostationary orbit, meaning that they are at the height of 36000 km and have a 24 hour period. Output power of the travelling wave tube is $P = 63$ W and the loss of the downlink may be calculated as follows:

$$L(\text{dB}) = 20 \log_{10} \left(\frac{4\pi d}{\lambda} \right), \quad (1)$$

where λ is the wave length [m] and d [m] represents the path length from satellite to earth station where the earth station receives the signal via a parabolic antenna [2]. The diameter D [m] of the parabolic reflector defines an antenna gain:

$$G = \eta \left(\frac{\pi D}{\lambda} \right)^2, \quad G(\text{dB}) = 10 \log_{10} G, \quad (2)$$

where η is the aperture efficiency (and usually has the value $\eta = 0.7$).

The parabolic antenna received the signal from a satellite transponder. In laboratory after measuring parameters of received signal, relation between the symbol and code rate and the channel width, as well as the signal strength at the satellite receiver was tested.

2. Measuring setup

Figure 1 shows a setup for measuring the satellite signal from satellite service provider, ASTRA. The outdoor unit consists of a parabolic antenna feeding directly into a low-noise block downconverter (LNB). Used parabolic reflector has the diameter of $D = 0.9$ m. In Croatia this is the usual diameter for parabolic antennas according to the ASTRA recommendations for good signal reception [1].

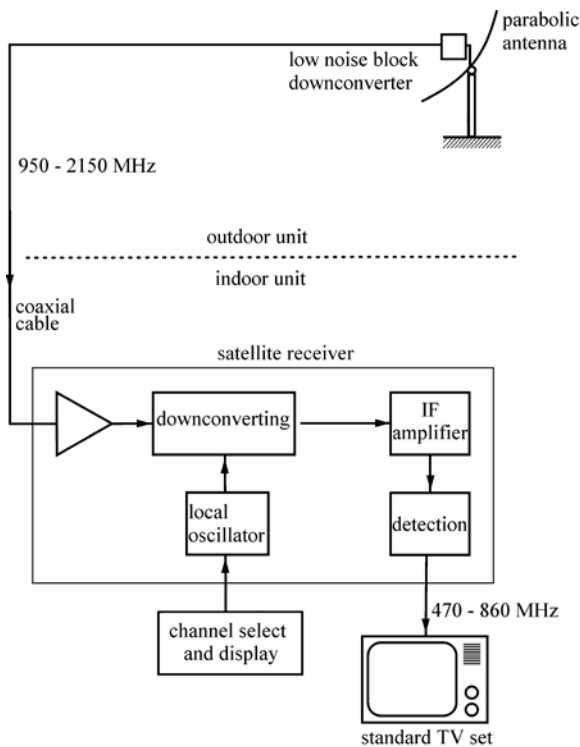


Fig. 1. Setup scheme for measuring the satellite signal from the ASTRA satellite service provider.



Fig. 2. Setup realisation for measuring the satellite signal.

From satellite receiver the signal was led to Microelectronics inc. LNB converter. The LNB amplifies the received signal by 55 dB and converts it to a lower frequency range. The frequency conversion is performed by mixing the received signal at the LNB input with the frequency produced by a local oscillator with frequencies of $f_{LO} = 10.6$ or 9.75 GHz. The LNB converts the satellite signal's frequency to 950-2150 MHz. This converter has a noise figure of 0.6 dB, where noise figure is defined as the ratio of the amount of noise in the output to the amount in the input. Therefore a coaxial cable can be used as feeder to the indoor unit. This way the signal travels with much less attenuation and more signal is left at the satellite receiver end of the cable [3].

The LNB's output signal is led to the indoor unit where it is amplified via a coaxial satellite in-line amplifier and brought to the satellite receiver. The line amplifier is useful since a long cable run of about 30 m was used and an excessive loss of 2 dB in the lead to the receiver is expected. Amplifier's specifications are given in Table 1. and receiver's specifications are in Table 2.

Measuring instrument set up is given in Fig. 2. Spectrum analyzer was used for measuring the peak power signal strength at receiver. To ensure that the

Table 1. Satellite in-line amplifier performance specifications.

Performance specifications	
Passband	950 – 2250 MHz
Gain	20 dB
Impedance	75 Ω
Noise figure	5 dB
Output strength	max.105 dB/μV

Table 2. Satellite receiver specifications.

Quadro DR-9000FTA satellite receiver performance specifications	
RF input frequency range	950 – 2150 MHz
RF input power levels	-65 to -25 dB
IF output frequency	55 MHz
RF output frequency range	470 – 860 MHz
Video output impedance	75 Ω

spectrum analyzer was able to identify the signal from background noise, the input

attenuation was set to 10 dB. The span, specifying the range between the start and stop frequencies that has to be monitored was set to 5 or 10 MHz. The resolution bandwidth, that determines how close the frequency components in the signal spectrum can be and still be displayed as distinct components, was set to 3 MHz. For each channel the carrier frequency, f_{ch} was calculated since the information of the sent signal's frequencies at transponder f_t , was visible in the configuration menu of the used television set [2]:

$$f_{ch} = f_t - f_{LO}. \quad (3)$$

On spectrum analyzer's monitor the signal strength peak value was detected for each channel. Next step was to find the channel bandwidth, i.e. the frequency interval where signal strength is no lower than 3 dBm from measured peak power signal strength.

Satellite signal reception was measured in five different channels. The signal frequencies at the satellite transponder and satellite receiver, as well as the symbol and code rates are given in Table 3. The measured peak power signal strength at the satellite receiver's input and the measured channel width are also listed in Table 3.

Figure 3 is a representative figure showing measurement results from channel with signal frequency $f_t = 11934$ MHz at the satellite transponder and the signal frequency $f_c = 1334$ MHz at the satellite receiver. On spectrum analyzer the peak power signal strength at the receiver's input was measured, $P_{LNB} = -55.4$ dBm. By moving to the left and right of the P_{LNB} , the channel width is defined and measured: $B = 27.4$ MHz.

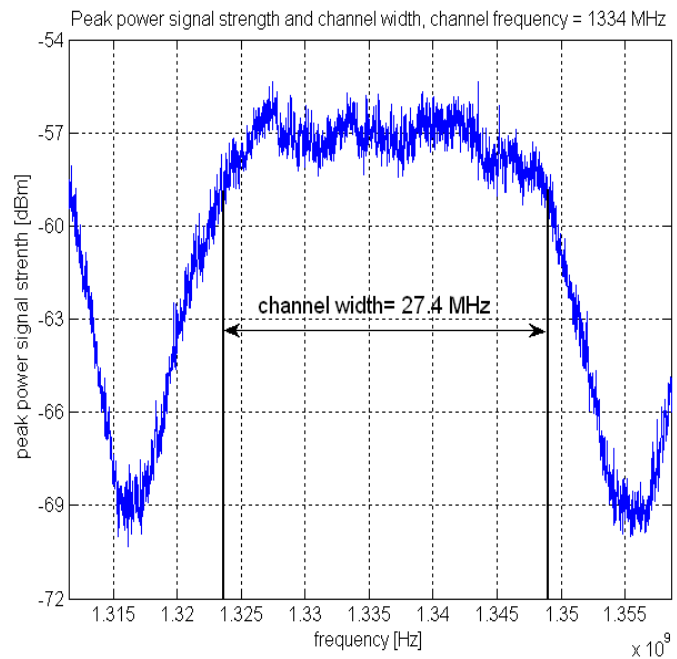


Fig. 3. Signal at $f_{ch} = 1334$ MHz (transponder frequency $f_t = 11934$ MHz).

Table 3. Measured channel parameters.

Signal frequency at transponder	Signal frequency at receiver	Symbol rate	Code rate	Measured peak power signal strength at receiver	Measured channel width
$f_t = 11934$ MHz	$f_{ch} = 1334$ MHz	$R = 27500$	$3/4$	$P_{LNB} = -55.4$ dBm	$B = 27.4$ MHz
$f_t = 11836$ MHz	$f_{ch} = 1236$ MHz	$R = 27500$	$3/4$	$P_{LNB} = -52.0$ dBm	$B = 24.6$ MHz
$f_t = 11778$ MHz	$f_{ch} = 1178$ MHz	$R = 27500$	$3/4$	$P_{LNB} = -52.9$ dBm	$B = 24.9$ MHz
$f_t = 11538$ MHz	$f_{ch} = 1788$ MHz	$R = 22000$	$5/6$	$P_{LNB} = -57.3$ dBm	$B = 21.4$ MHz
$f_t = 11509$ MHz	$f_{ch} = 1759$ MHz	$R = 22000$	$5/6$	$P_{LNB} = -56.9$ dBm	$B = 21.2$ MHz

These steps were repeated for each channel and peak power signal strength at the satellite receiver, as well as the channel bandwidth were measured (Table 3, Figure 3-5).

3. Discussion and conclusion

Analyzing Table 3, when sending and receiving the message with higher symbol rate ($R = 27500$), the power of the in-line amplifier input signal is higher than with lower symbol rate ($R = 22000$). On the other hand, when a higher code rate ($5/6$) is used, compared to a lower code rate ($3/4$), the power of the signal strength is lower. Higher symbol rate ($R = 27500$) and lower code rate ($3/4$) showed a wider channel width of approximately $B = 27$ MHz and $B = 25$ MHz. When the message was sent with a lower symbol and a higher code rate ($R = 22000$, $5/6$), according to our measurement results in Table 3, the channel width was $B = 21$ MHz.

During measuring of channels with frequencies $f_{ch} = 1788$ MHz and $f_{ch} = 1759$ MHz (corresponding frequencies at transponder are $f_t = 11538$ MHz and $f_t = 11509$ MHz), an effect called the intermodulation distortion or product could be observed. Intermodulation distortion occurs when the non-linearity of a device or system with multiple input frequencies causes undesired outputs at other frequencies [4]. In satellite communication this means that signals in one channel can cause interference with adjacent channels. The detected intermodulation products are given in Fig. 5. The next step in our research is to determine source of unwanted interference in order to avoid these effects.

References

- [1] http://www.ses-astra.com/tv-guide/lineup/markets/ALL192_all.htm
- [2] Šimunić D, Malarić K, Zrno D, Škokić S. Mikrovalne komunikacije, upute za laboratorijske vježbe. Faculty of electrical engineering and computing, University of Zagreb, 31-36, 2004.
- [3] Roddy D. Satellite Communication. 4th Edition. The McGraw-Hill Companies Inc, 2006, 239-245.

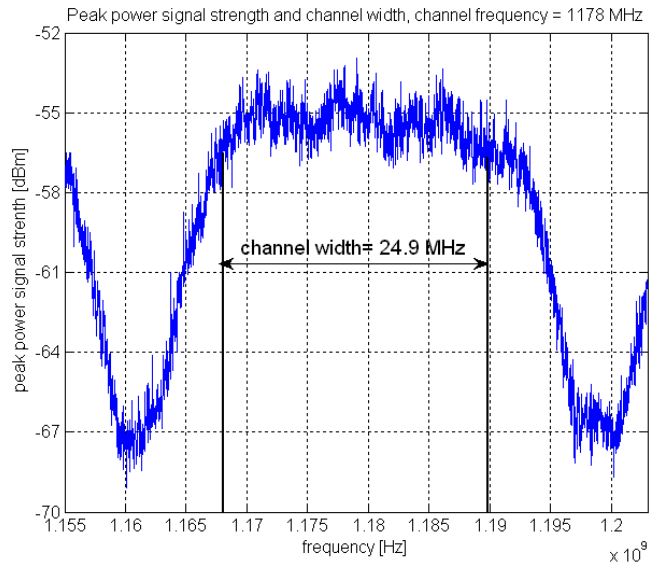


Fig. 4 Signal at $f_{ch} = 1178$ MHz (transponder frequency $f_t = 11778$ MHz).

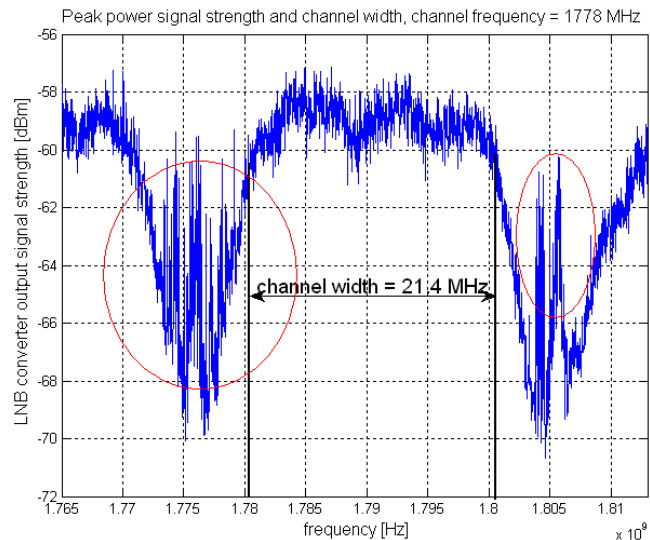


Fig.5. Signal at $f_{ch} = 1778$ MHz (transponder frequency $f_t = 11538$ MHz) with intermodulation products (circled).

- [4] Maury Microwave Corporation. Theory of intermodulation distortion Measurement (IMD). Ontario, California, 1999, <http://www.maurymw.com>.

Bedřichov Tunnel – Continual Automated Measurement of Physical Quantities

^{1,2}R. Špánek, ^{1,2}P. Tyl, ¹M. Hernych, ¹M. Hokr, ¹P. Svoboda, ²M. Řimnáč,
²J. Štuller

¹TU Liberec, Liberec, Czech Republic,

²Institute of Computer Sciences, Academy of Sciences of the Czech Republic, Prague,
Czech Republic

Email: {roman.spanek, pavel.tyl, milos.hernych, milan.hokr,
premysl.svoboda}@tul.cz
{rimnacm, stuller}@cs.cas.cz

Abstract. *The paper presents a solution for continual measurement of physical quantities proposed for Bedřichov tunnel site situated in granite massif in Jizera Mountains. The solution consists of a set of sensors placed at important points in the tunnel as well as on the surface, which are connected by wired RS 485 line or by wireless communication. The communication chain contains also GPRS module for the transfer of measured data to a dedicated server.*

Keywords: Remote Continual Automated Measurement

1. Introduction

One of the issues of the nuclear power engineering is the storage of used radioactive material. Current standard solution accepted in most countries all over the world is a geological disposal – a repository several hundred meters deep, in stable rock, providing isolation properties. Granite massifs are studied as a possible host environment.

The research in some countries is based on underground laboratories like Aspo in Sweden and Grimsel in Switzerland built fully or partly for research purposes. In the Czech Republic we use existing underground constructions – an example is the Bedřichov waterworks tunnel (**Fig. 1**) (Jizera Mts. approx. 120 km North from Prague), an industrial analogue with a lot of options how to observe a long-term response of the rock massif to the excavation [1]. Similar to the laboratories abroad, the research site is related to generic properties of the host rock and exploration methods and it is not the place considered for real repository. Several institutions have participated in the research since 2003.

One of the main issues is how to monitor various physical quantities without a need for manual measurement in the tunnel (formerly within interval of 14 days). Between quantities being currently monitored belong flowrate in water springs (inflow to the tunnel), temperature (both water and rock massif), pH, conductivity, redox potential, fracture displacements and seismic activity [2]. One of the requirements is a possibility to add new sensors on the fly. The data from sensors must be accessible 24 hours a day, 365 days in a year.



Fig. 1: Situation in the tunnel with combined blasted or bored parts [1]

2. Building Infrastructure and Sensor Placement

At the beginning there was no infrastructure in the tunnel available. The first step was to build wired infrastructure consisting of RS485 (12-24 V). The wired line was built up to 890 meters from the tunnel entrance and the remaining length of tunnel will be covered by wireless or laser communication technology, as building wired infrastructure was shown to be very expensive. In **Fig. 2** you can see the tunnel situation and examples of sensors installed.

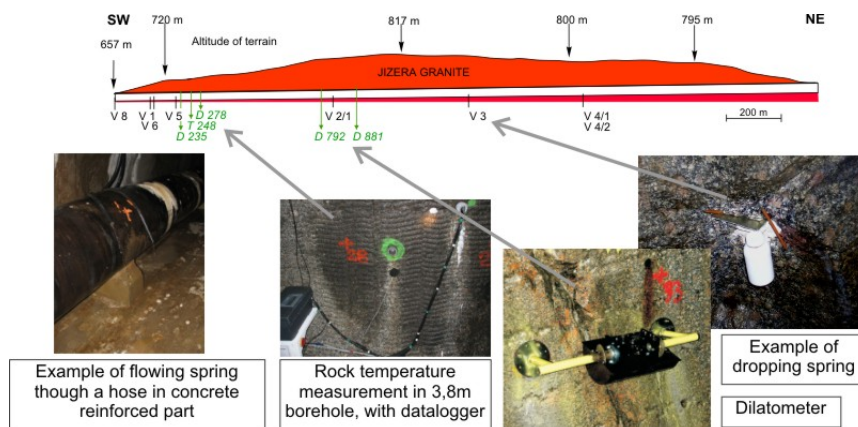


Fig. 2: Scheme of the tunnel and sensor placement

3. Data Gathering and Transmission to Persistent Storage

Proposed communication network (see **Fig. 3**) consists of sensors placed in the tunnel communicating with a microchip module at the tunnel entrance, which is responsible for data transmission over wireless line (currently GPRS) to a dedicated database server. Measured data are stored in a structured way in a relational database. Database scheme was wittingly proposed in Boyce-Codd normal form, which ensures no data redundancies coming from functional dependencies. No redundancy is important as it simplifies (in some cases allows) various queries on stored data (like fetch all temperatures within predefined time period, fetch inflow from the whole tunnel, etc.).

The first version of communication network relied on the fact that microchip module is able to reconstruct measured data coming directly from sensors based on their internal format into a structure that corresponds to the database schema. Java application (see **Fig. 3**) running on the server was intended to communicate with the dedicated database server and to reconstruct data from simple communication protocol defined over TCP/IP. Experiments revealed that

such configuration is not appropriate, as some sensors used in the tunnel cannot send all data needed by database structure (a sensor placement, unique identifier of sensors, etc.) and such missing data has to be calculated/inferred based on sensors metadata stored in the database. Unfortunately calculations/inferences are too complex to be done by microchip module (omitting the fact that the microchip ought to communicate with a database server when accessing sensor metadata).

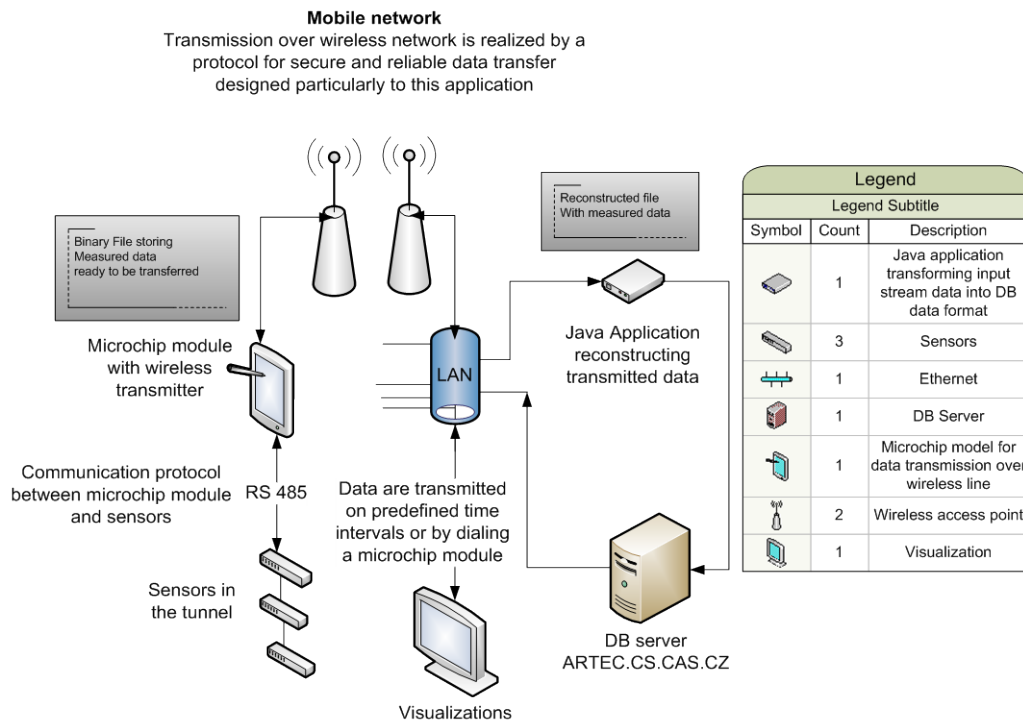


Fig. 3: Communication Network

Consequently, in the second version the communication network was redesigned. The need for calculations/inferences comes from the fact that some sensors are very different from each other (in terms of data structures storing measured data) and therefore it is impossible to cover all of them by a functionality included directly in a Java application (we will call it RemoteDataReceiver). The proposed solution makes use of plug-ins (so called DLLs). For each sensor in the tunnel, there must exist a plug-in being responsible for reconstructing data to a form acceptable by the database. Plug-ins are loaded on fly from predefined directory, so it is easy to implement functionality of a new sensor. Another issue identified is the fact, that debugging plug-ins may be very hard, as the microchip module installed in the tunnel sends all data to just one IP address. In order to overcome this issue, a simulation of tunnel traffic is included in RemoteDataReceiver. It allows to send randomly generated data to arbitrary IP address (localhost for instance) and to debug a plug-in in “offline” mode (by offline is meant a situation where there is no traffic coming from the tunnel and input data are generated artificially). Moreover, the currently developed version of the RemoteDataReceiver allows forwarding traffic coming from the tunnel to arbitrary IP address(es).

4. Conclusions

The communication network proposed for Bedřichov tunnel, excavated in granite massif, provides online measurement of physical quantities. Several new sensors have been designed to achieve desired measurement; the diversity of measured quantities requires combination of

different sensor types and manufacturers. Especially the commercially available intelligent sensors often use digital output with closed (unknown) communication protocol; moreover they do not include all data required by a database scheme, so it was necessary to propose a slightly modified version of the communication network.

Storing measured data in relational database is also possible, but with respect to a proper database schema engineering. From our experiments it comes out that Boyce-Codd normal form is appropriate as lower normal forms do not prevent inconsistencies. Storing data in improper database relation or storing unstructured data results in inability to extend set of acceptable queries, impossibility to reuse stored data, etc.

Our experiments further showed that automated measurement of physical quantities in adverse conditions of underground tunnel requires building of reliable communication network, that can be based on existing technologies, but with stress on industrial technologies (like RS 485 bus) rather than technologies commonly available for laboratories (LAN network).

Moreover, supporting communication by dedicated microchip communication device is also possible, but such device should be used only for forwarding measured data to higher level application that ought to be responsible for all calculations/transformations.

Acknowledgements

This work was realized under the state subsidy of the Czech Republic within the research and development project "Advanced Remediation Technologies and Processes Centre" 1M0554 - Programme of Research Centres supported by Ministry of Education, within the research project FR-TI1/362 supported by Ministry of Industry and Trade and by the student grant SGS 2011/7821 "Interactive Mechatronics Systems Using the Cybernetics Principles"

Further the support from Radioactive Waste Repository Authority is acknowledged, contract nr. 2009/012/Mi. Authors thank to "Severočeské vodovody a kanalizace", the tunnel operator, for providing access to the tunnel for the research.

References

- [1] KLOMÍNSKÝ, J. et al. (2008): Study of fracture network dynamics of granitoids in water-supply tunnels in Jizera mountains period 2006-2008. Czech geological survey 171 p. (In Czech)
- [2] Klomínský, J. Woller, F. (Eds.) 2010: Geological studies in the Bedřichov water supply tunnel. Technical report 02/2010, SÚRAO(RAWRA).

Performance Measurements of Laboratory IEEE 802.11 b, g WEP Point-to-Point Links

^{1,2} J. Pacheco de Carvalho, ^{2,3} H. Veiga, ² C. Pacheco, ^{2,3} N. Marques, ^{1,2,4} A. Reis

¹Departamento de Física, ²U. de Detecção Remota, ³Centro de Informática,
Universidade da Beira Interior, Rua Marquês d'Ávila e Bolama,
6201-001 Covilhã, Portugal

⁴Departamento de Electrónica e Telecomunicações / Instituto de Telecomunicações,
Universidade de Aveiro, 3810 Aveiro, Portugal
Email: pacheco@ubi.pt

Abstract. *The importance of wireless communications has been growing. Performance is a most relevant issue, resulting in more reliable and efficient communications. Security is crucially important. Laboratory measurements are made about several performance aspects of Wi-Fi (IEEE 802.11 b, g) WEP point-to-point links. A contribution is given to performance evaluation of this technology under WEP encryption, using WRT54GL wireless routers from Linksys. Detailed results are presented and discussed, namely at OSI levels 4 and 7, from TCP, UDP and FTP experiments: TCP throughput, jitter, percentage datagram loss and FTP transfer rate data.*

Keywords: WLAN, Wi-Fi, WEP Point-to-Point Links, Wireless Network Laboratory Performance

1. Introduction

Electromagnetic waves in several frequency ranges, propagating in the air, have been decisively important for the development of wireless communications e.g. Wi-Fi and FSO, microwave and laser based technologies, respectively.

The importance and utilization of Wi-Fi have been growing for complementing traditional wired networks. Wi-Fi has been used both in ad hoc mode and infrastructure mode. In this case an access point, AP, permits communications of Wi-Fi devices with a wired based LAN, through a switch/router. Thus a WLAN, based on the AP, is formed. Wi-Fi has reached the personal home, forming a WPAN, where personal devices communicate. Point-to-point and point-to-multipoint setups are used both indoors and outdoors, with specific directional and omnidirectional antennas. Wi-Fi uses microwaves in the 2.4 and 5 GHz frequency bands and IEEE 802.11a, 802.11b, 802.11g and 802.11n standards [1]. Nominal transfer rates up to 11 (802.11b), 54 (802.11 a, g) and 600 Mbps (802.11n) are permitted. CSMA/CA is the medium access control. Wireless communications, wave propagation [2,3] and WLAN practical implementations [4] have been studied. Detailed information is available about the 802.11 architecture, where an optimum factor of 0.42 was presented for 11 Mbps point-to-point links [5]. Wi-Fi (802.11b) performance measurements are available for crowded indoor environments [6].

Performance has been a fundamentally important issue, giving more reliable and efficient communications. In comparison to traditional applications, new telematic applications are specially sensitive to performances. Requirements have been pointed out, such as: 1-10 ms jitter and 1-10 Mbps throughput for video on demand/moving images; jitter less than 1 ms and 0.1-1 Mbps throughputs for Hi Fi stereo audio [7].

Wi-Fi security is very important, as microwave radio signals travel can be easily captured. WEP is a security method for providing authentication. In spite of presenting weaknesses, it is still widely used in Wi-Fi networks for security reasons. In WEP, the communicating devices use the same shared key to encrypt and decrypt radio signals.

Several measurements have been made for 2.4 and 5 GHz Wi-Fi open links [8,9], as well as very high speed FSO [10]. In the present work new Wi-Fi (IEEE 802.11 b,g) results arise, using WEP, through OSI levels 4 and 7. Performance is evaluated in laboratory measurements of WEP point-to-point links, using available equipments.

The rest of the paper is structured as follows: Chapter 2 presents the experimental details i.e. the measurement setup and procedure. Results and discussion are presented in Chapter 3. Conclusions are drawn in Chapter 4.

2. Subject and Method

The measurements used Linksys WRT54GL wireless routers [11] and other equipments [8]. The wireless mode was bridged access point, point-to-point. Interference free communication channels were used for the links. 128 bits WEP encryption was activated. Data were collected under far-field conditions. No power levels above 30 mW (15 dBm) were required as the access points were close.

The laboratory setup is shown in Fig. 1. TCP and UDP experiments at OSI level 4, were as mentioned in [10], permitting network performance results to be recorded. For a TCP connection, TCP throughput was obtained. For a UDP connection with a given bandwidth parameter, UDP throughput, jitter and percentage loss of datagrams were obtained. One PC, with IP 192.168.0.2 was the Iperf server and the other, with IP 192.168.0.6, was the Iperf client. Jitter was continuously computed by the server, as specified by RTP in RFC 1889 [12]. This scheme was also used for FTP measurements, using FTP server and client applications [8]. Batch command files were written to enable the TCP, UDP and FTP tests. The results were obtained through remote control via switch and written as data files to the client PC disk.

3. Results and Discussion

The APs were configured, for each standard IEEE 802.11 b, g, with typical fixed transfer rates. For every fixed transfer rate, data were obtained for comparison of the laboratory performance of the links, measured namely at OSI levels 4 and 7 using the setup of Fig. 1. At OSI level 1, SNR values and noise levels N were recorded, as shown in Fig. 2. For each standard and every nominal fixed transfer rate, an average TCP throughput was determined. This value was used as the bandwidth parameter for every corresponding UDP test, giving average jitter and average percentage datagram loss. The main results, which were reasonably steady versus time, are shown in Figs. 2-3. In Fig. 2, polynomial fits were made to the TCP throughput data. The best TCP throughput performance was found for 802.11g (average values of 14.3 \pm 0.4 and 2.9 \pm 0.1 Mbps for 802.11g and 802.11b, respectively). A fairly good agreement was found with the data obtained for open links [8]. In Figs. 2 and 3, the data points representing jitter and percentage datagram loss were joined by smoothed lines. It was found that, on average, the best jitter performances are for 802.11 g both for WEP and open links. On average, for both standards, the best jitter performances were found for open links. Concerning percentage datagram loss data (1.3 % on average) no significant sensitivities were found, within the experimental errors, either to standard or link type.

At OSI level 7 we measured FTP transfer rates versus nominal transfer rates for both standards, as in [8]. The data are shown in Fig. 3, including polynomial fits. The results show the same trends found for TCP throughput.

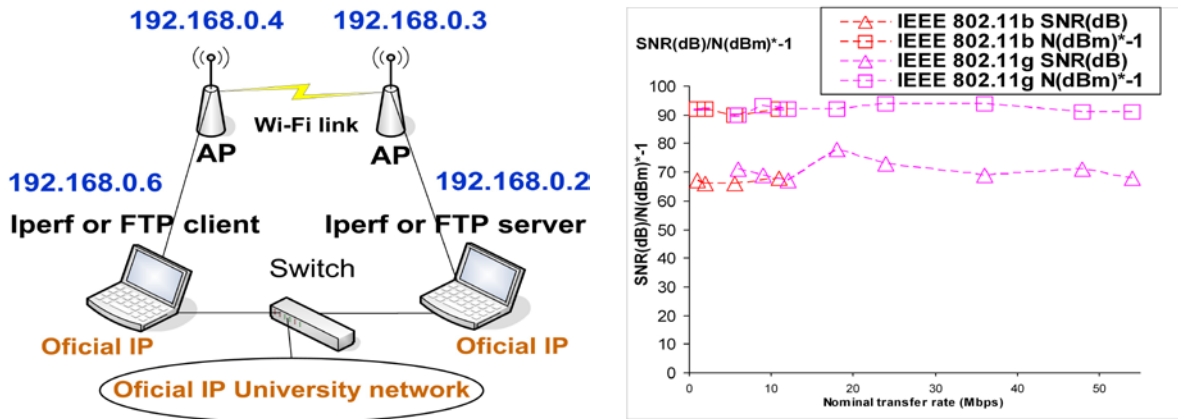


Fig. 1. Wi-Fi laboratory setup scheme and typical SNR (dB) and N (dBm).

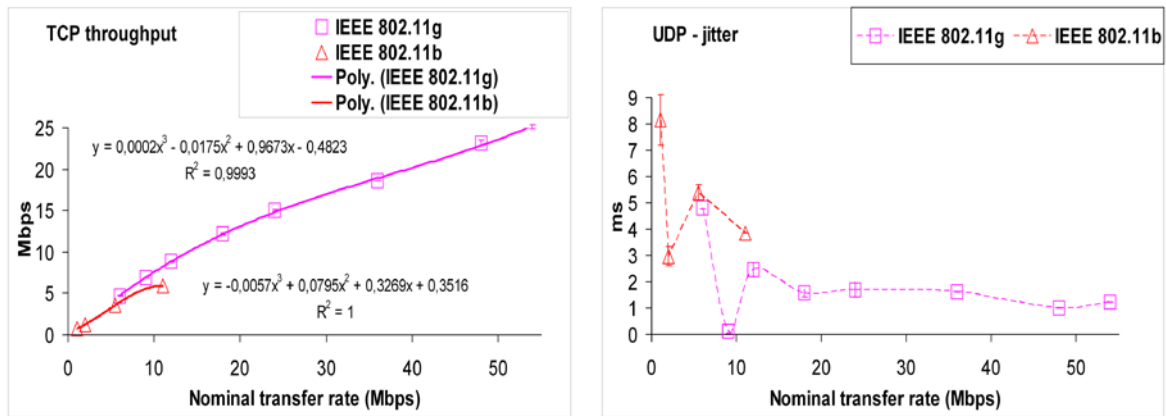


Fig. 2. TCP throughput and UDP jitter results, versus technology (IEEE 802.11 b,g).

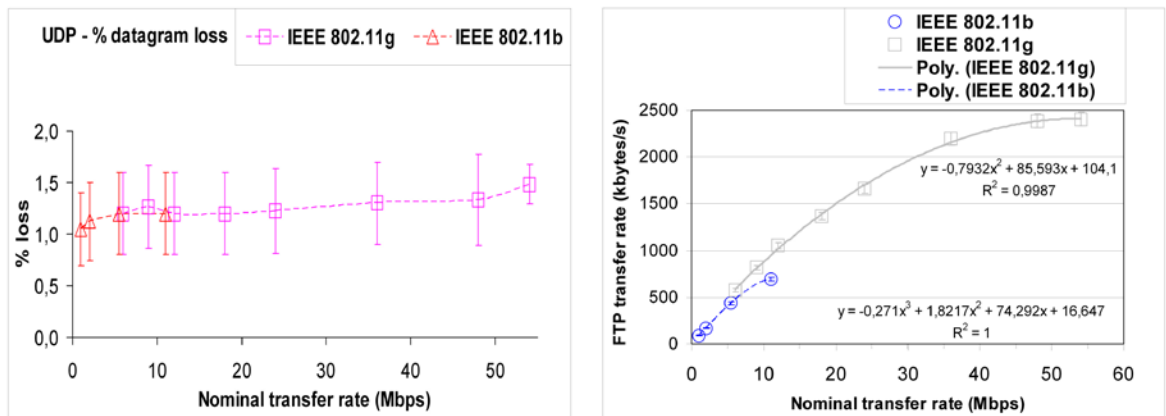


Fig. 3. Results of UDP percentage datagram loss and FTP transfer rate, versus technology (IEEE 802.11 b,g).

4. Conclusions

A laboratory setup was planned and implemented that permitted systematic performance measurements of available wireless equipments (WRT54GL from Linksys) for Wi-Fi (IEEE

802.11b, g) in WEP point-to-point links. TCP, UDP and FTP results were obtained and compared for each standard. The best TCP throughputs were found for 802.11g. A fairly good agreement was found for the 802.11 b, g data both for WEP and open links. For jitter, it was found that, on average, the best performance was for 802.11 g for both link types. On average, for both standards, the best jitter performances were found for open links. For percentage datagram loss, no significant sensitivities were found, within the experimental errors, either to standard or link type. FTP results show the same trends found for TCP throughput. Additional performance measurements either started or are planned using several equipments and security settings, not only in laboratory but also in outdoor environments involving, mainly, medium range links.

Acknowledgements

Supports from Universidade da Beira Interior and FCT (Fundação para a Ciência e a Tecnologia)/POCI2010 (Programa Operacional Ciência e Inovação) are acknowledged.

References

- [1] Web site <http://standards.ieee.org>
- [2] Mark JW, Zhuang W. Wireless Communications and Networking. Prentice-Hall, Inc., Upper Saddle River, NJ, 2003.
- [3] Rappaport TS. Wireless Communications Principles and Practice, 2nd ed., Prentice-Hall, Inc., Upper Saddle River, NJ, 2002.
- [4] Bruce III WR, Gilster R. Wireless LANs End to End, Hungry Minds, Inc., NY, 2002.
- [5] Schwartz M. Mobile Wireless Communications, Cambridge University Press, 2005.
- [6] Sarkar N, Sowerby K. High Performance Measurements in the Crowded Office Environment: a Case Study. In Proc. ICCT'06-International Conference on Communication Technology, Guilin, China, 27-30 November 2006, 1-4.
- [7] Monteiro E, Boavida F. Engineering of Informatics Networks, 4th ed., FCA-Editor of Informatics Ld., Lisbon, 2000.
- [8] Pacheco de Carvalho J, Gomes P, Veiga H, Pacheco C, Marques N, Reis A. Measurements of Performance in Laboratory IEEE 802.11 b, g Point-to-Point Links. In Proc. Measurement 2009 – 7th International Conference on Measurement, Smolenice Castle, Slovakia, May 20-23, 2009, 182-185.
- [9] Pacheco de Carvalho JAR, Veiga H, Gomes PAJ, Ribeiro Pacheco CF, Marques N, Reis AD. Wi-Fi Point-to-Point Links- Performance Aspects of IEEE 802.11 a,b,g Laboratory Links. In Electronic Engineering and Computing Technology, Series: Lecture Notes in Electrical Engineering, Sio-Iong Ao, Gelman L, Editors. Springer, Netherlands, 2010, Vol. 60, 507-514.
- [10] Pacheco de Carvalho JAR, Marques N, Veiga H, Ribeiro Pacheco CF, Reis AD. Experimental Performance Evaluation of a Gbps FSO Link: a Case Study. In Proc. WINSYS 2010- International Conference on Wireless Information Networks and Systems, Athens, Greece, July 26-28, 2010, 123-128.
- [11] Web site <http://www.linksys.com>
- [12] Network Working Group, “RFC 1889-RTP: A Transport Protocol for Real Time Applications”, <http://www.rfc-archive.org>

High Magnetic Field Sensing by the Help of Semiconductor Resonator

L. Laurinavičius

Department of Electrical Engineering Vilnius Gediminas Technical University
Saulėtekio av.11, LT-2040 Vilnius, Lithuania
Email: lagnel4@gmail.com

Abstract. *The effects of dimensional resonance of magnetoplasmic waves in semiconductors were investigated. It was demonstrated that these effects could be used to measure the high magnetic fields. Possible ways to design contactless magnetic field sensors operating at cryogenic temperature, such as that of liquid nitrogen are discussed. It has been shown that for high field sensors a low gap semiconductor material of high carrier mobility μ is needed.*

Keywords: Semiconductors, Helicon Waves, Dimensional Resonator, Magnetic Field, Sensor

1. Introduction

Magnetic sensors can be classified according to low, medium, or high-field sensing range and operating temperatures. High field or bias field sensors detects fields that are larger than the Earth's field [1]. Conventional sensors can detect a physical property (pressure, temperature and other) directly but magnetic sensors detect changes in magnetic fields and from them derive information on physical properties. The output signal of these sensors requires some signal processing for translation into the desired parameter. Mine high-field sensors technologies are magnetoresistance, Hall and GMR (giant magnetoresistance) effects. Some of sensors, such as magnetoresistors, are capable of measuring fields up to several teslas, others, such as GMR devices, can detect fields smaller than the Earth's field [2]. Sometimes in the practice high pulsed magnetic fields with amplitudes up to 50 T can be generated at room or cryogenic temperatures. The existing magnetic field measurement methods are applicable in case of known magnetic field direction and the accuracy of such methods is low when the direction of magnetic field is not determined in advance or it is changing during experiment [3]. Possible ways to design contactless magnetic field sensors operating at room or cryogenic temperatures, such as that of liquid nitrogen will be discussed.

2. Physical background of investigation

If semiconductor specimen is placed in external magnetic field (Fig.1), microwaves can propagate in semiconductor along the direction of magnetic induction B . The propagation of magnetoplasma wave may be detected from the characteristic equation [4].

$$c^2 \frac{k^2}{\omega^2} \equiv \varepsilon_{\pm}' + i\varepsilon_{\pm}'' = \varepsilon_L \left(1 - \frac{\omega_p}{\omega[(\omega \pm \omega_c) + i\nu]} \right), \quad (1)$$

where k is wave vector, ω is frequency, ε_{\pm} is complex permittivity, ε_L is lattice constant of semiconductor, $\omega_c = eB/m^{\otimes}$ is cyclotron frequency, $\omega_p = \left(\frac{e^2 N}{m^{\otimes} \varepsilon_0 \varepsilon_L} \right)^{1/2}$ is plasmas frequency, $\nu = 1/\tau$ is frequency of carrier's collisions.

The conditions when magnetoplasma helicon waves can propagate in magnetic material are as followings:

$$\omega \pm \omega_c \gg \nu; \quad \omega_c \gg \omega; \quad \omega_c \tau \equiv \mu B \gg 1. \quad (2)$$

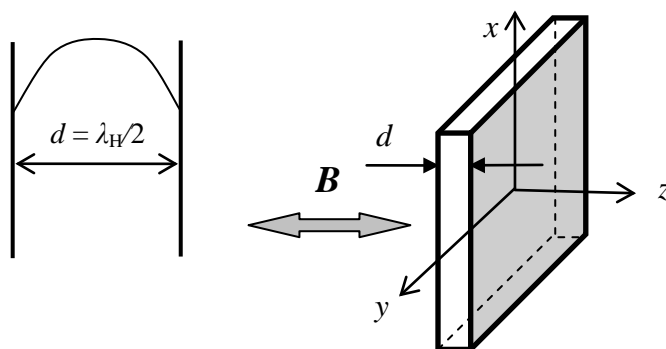


Fig.1. Semiconductor specimen is placed in external magnetic field B .

The length λ_H of helicon waves is determined by equation [5]

$$\lambda_H / 2 = \pi / k' = \frac{c}{\omega} \frac{1}{\sqrt{\epsilon'}} = \frac{c}{\omega} \left(\frac{\epsilon_0 \omega B}{eN} \right)^{1/2}. \quad (3)$$

It means that it is possible to determine the density of free charge carriers N by observation of dimensional resonances of magnetoplasma microwaves in magnetic materials. When mine (half – length) resonance is observed, the value of density N is determined by simple equation

$$N = \frac{A \cdot B}{d^2 \cdot f_R}, \quad (4)$$

where B is magnetic induction, f_R is exciting frequency ($d = \lambda_H/2$), d is thickness of the specimen and $A = \text{const}$.

Physical background of the operation of magnetic field sensor is based on the effect of the dimensional resonance of magnetoplasma waves in known semiconductor plate (charge carriers N) placed in the static magnetic field.

3. Experimental results

The technical possibility to realize the magnetic field (B) sensor by the help of high frequency Hall effect in semiconductors was proposed by author [6]. A current-carrying InSb semiconductor plate is kept in a magnetic field and has two electrodes. The Hall voltage increases with applied field to several teslas. The temperature dependence of the voltage is governed by the temperature dependence of the carrier mobility μ . Different semiconductor materials and different doping levels result in trade-offs between sensitivity and temperature dependence of sensor.

The main objective of the present paper is to show that it is possible to determine the magnetic induction B by observation of dimensional resonances of magnetoplasma microwaves in semiconductors. Thus, it is possible to create a non-contacting field sensor which design is shown in Fig. 2. A non-contacting high field sensor may be developed by applying two perpendicular coils to a semiconductor plate of finite dimensionality. Then, by

satisfying the conditions of helicon origination (2) we may obtain coupling of coils of a resonant character.

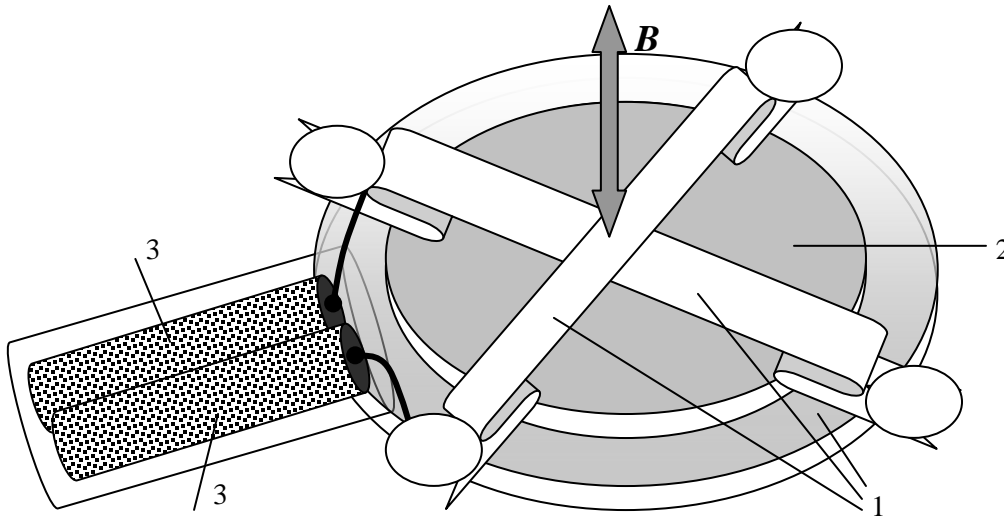


Fig. 2. A semiconductor sample (gyrotropic filling - helicon resonator) is placed into d.c. magnetic field B and a.c. microwave field b : 1 – microstrip lines; 2 – semiconductor layer; 3 – coaxial lines.

The magnetic induction B can be easily calculated from typical amplitude frequency response in Fig. 3:

$$B = 1,28 \cdot 10^{-25} N \cdot f_R \cdot d^2. \quad (5)$$

A simplified block diagram of high magnetic field meter is shown in Fig. 4. A semiconductor plate (magnetic sensor) 1 is put in magnetic field generated by axial solenoids 2. High frequency generator 3 is connected with exciting microstrip line (coil) 4. The helicon wave is excited in local area of a semiconductor plate. Propagating across semiconductor plate helicon wave is indicated by receiving micro-strip line (coil) 5, situated perpendicular to exciting. A receiving signal is registered by recorder 6. Described magnetoplasma magnetic field meter has also a high frequency detector 7, cryogenic system and signal analyser which are not shown.

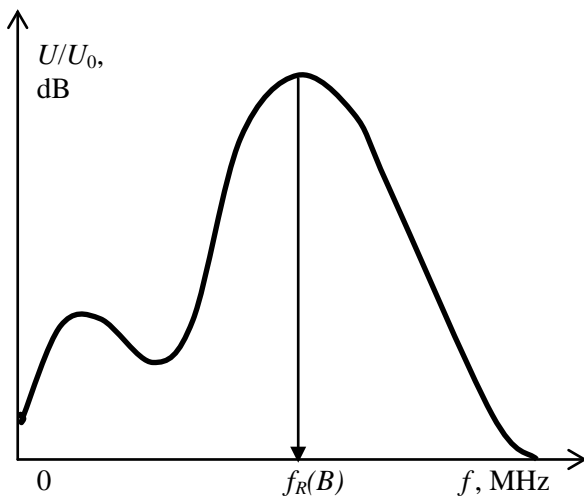


Fig. 3. A typical amplitude frequency response.

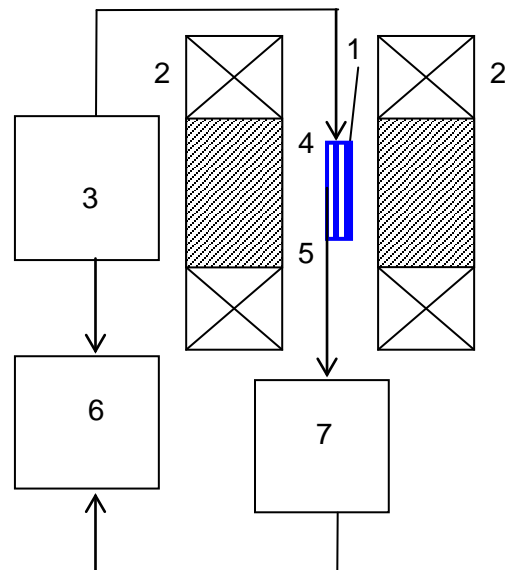


Fig. 4. Block diagram of high magnetic field meter

For the magnetic fields less than 2T, the most suitable semiconductor material is alloy $\text{Cd}_x\text{Hg}_{1-x}\text{Te}$ or Te-doped $n\text{-InSb}$ of high carrier mobility and high carrier density $N > 0,8 \cdot 10^{23} \text{ m}^{-3}$. At cryogenic and at room temperatures $f_R(B_R)$ dependence is linear (Fig. 5).

4. Conclusions

The measurements of magnetic induction by the help of helicon waves in semiconductors could be provided in contactless mode. Practically all semiconductor materials can be put into practice if the high magnetic field (~ 20 Tesla) is available. Magnetic field sensing by the help of semiconductor helicon resonator can be used at cryogenic temperatures as well. The measurement results are in compliance with data obtained by the use of different field sensing methods (technologies).

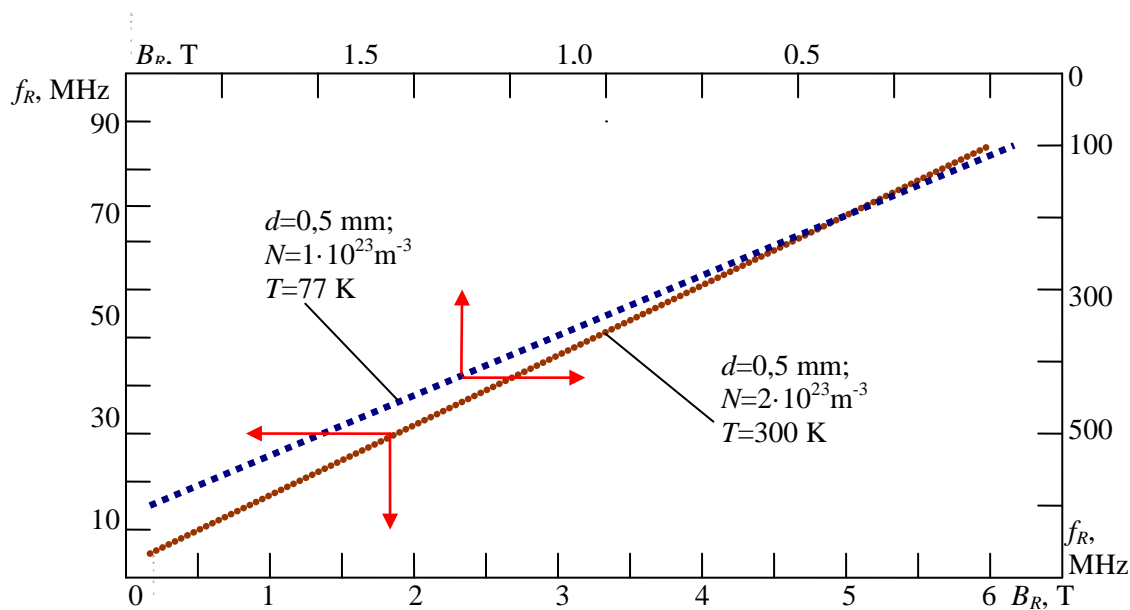


Fig. 5. High frequency f_R dependence from magnetic induction B_R at room and at liquid nitrogen temperatures.

References

- [1] Lenz. J.E. A Review of Magnetic Sensors. Proc IEEE, June 1990. Vol. 78, No 6. P. 973-989.
- [2] Michael J. Caruso, Tamara Bratland, C. H. Smith, and Robert Schneider. A New Perspective on Magnetic Field Sensing. Sensors Magazine. December 1998. Vol. 15, No. 12. P. 34-46.
- [3] Bartkevičius S. et al. Data Processing of Manganite Sensors Array for Measurements of Non-Homogeneous Pulsed Magnetic Field. Electronics and Electrical Engineering. 2006. No. 4(68). P. 69-72.
- [4] Palik E. D., Furdina J. K. Infrared and Microwave Magnetoplasma Effects in Semiconductors. Report on Progress in Physics. V. 33. 1970. P. 1195 - 1322.
- [5] Jankauskas Z., Laurinavičius L. Magnetic and Electric Excitation of Magnetoplasmic Waves. Electronics and Electrical Engineering. 2002. No 2(37). P. 32-34.
- [6] Laurinavičius L. et al. Strong Magnetic Field Sensor. U.S.S.R. Patent 1584676 A1, April 8, 1990.

Advantages of Direct Field Approach in Application to Magnetic Hysteresis Measurements

O. Stupakov

Institute of Physics of the Academy of Science of Czech Republic, v.v.i.,
Na Slovance 2, 18221 Prague, Czech Republic
Email: stupak@fzu.cz, Web: www.fzu.cz/~stupak

Abstract. *Advantages of method of direct field determination were illustrated for two industrial cases of magnetic hysteresis measurements: a standard single sheet tester and an attached single-yoke coercimeter. A vertical array of three Hall sensors was used to measure the tangential field profile above the sample surface. The sample surface field was determined by a linear extrapolation of this measured field profile to the sample face. The direct field parameters were compared with the corresponding data obtained classically using the magnetization current. It was shown that the direct field approach gives more realistic data with excellent correlation to the reference values. Moreover, the method provides stable magnetic output even in the case of magnetically open circuits, which affords new opportunities for practical applications.*

Keywords: *Direct Field Measurements, Magnetically Open Samples, Magnetic Hysteresis*

1. Introduction

Magnetic measurements are based on determination of the ferromagnetic material magnetization as a function of the sample magnetic field. Inductive measurement method uses a time varied magnetic field to magnetize the sample (varied magnetization current/voltage is applied to the magnetization winding). At this condition, it is not a problem to detect the magnetization waveform precisely: according to the Faraday's law, the induced voltage in a search (induction/pick-up) coil wound around the sample cross-section is proportional to the time rate of change of the magnetic flux, $U_{ind} = -n \cdot d\Phi/dt = -nS \cdot dB/dt$, where n is number of the induction windings, Φ is magnetic flux, S is sample cross-section, and B is magnetic induction [1]. The complications can only arise for the dc measurements of tiny samples. In such a case, a modern fluxmeter is needed for accurate analog integration of the weak induction signal and elimination of a floating zero offset.

However, it is not a trivial task to determine the sample magnetic field precisely, which is probably the main actual problem in the field of magnetic measurements. The difficulties are connected with small sample sizes and huge field gradients at the sample surface. The problem was historically solved by a technical way: the sample magnetic field H_i was evaluated to be proportional to the magnetization current I , $H_i = NI/l$, where N is number of the magnetizing windings, and l is effective magnetic path. This requires the robust pseudo-closed magnetic circuits, such as a standard Epstein frame and a single sheet tester (SST), which minimizes the error of current field approach to a reasonable extent of 3-5 % [1].

Therefore, our attention was focused on the method of direct field determination. Measurements of tangential surface fields with a sensor, which can be usually placed at minimal distance to the sample face of about 1-2 mm, are not stable due to the huge gradients of subsurface field. This problem was solved by application of an extrapolation technique and a special shielding approach as shown in the following section [2], [3]. This work illustrates

the advantages of our measurement approach in application to two industrial setups: the standard double-yoke SST and the mobile single-yoke coercimeter. The direct field data expectedly provide excellent result repeatability and reasonable values of magnetic parameter.

2. Single sheet tester

Magnetic property of electrical steels determines their industrial quality. The classical SST setup A was slightly modified for direct field measurements (see setup B in Fig. 1). A vertical array of three Hall sensors was used to measure the sample tangential surface fields. Temperature-stable and 5 mV/G sensitive chips A1321ELHLT-T from Allegro MicroSystems Inc were used. A recently introduced “shielding” approach was used for suppression of the field gradient: two soft magnetic sheets from laminated FeSi steel force the magnetic leakage flux to flow through the sample [3]. The sample surface field was determined by a linear extrapolation of the measured field profile to the sample face [2]. Setup C presents the same Helmholtz type solenoid without the closing yokes (fully open magnetic circuit). The measurements were performed with 50 Hz sinusoidal driving voltage.

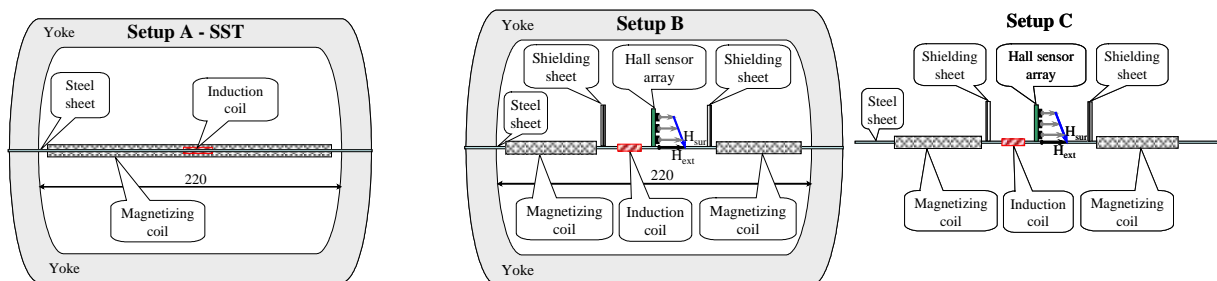


Fig. 1. Schemes of the used measurement setups.

The main advantage of the direct field method is that it provides the same stable results even with the open magnetic circuit, which is not possible with the current field method due to the huge demagnetization factor (see Fig. 2a). This is a very important finding, which gives new opportunities for practical application in on-line magnetic testing systems. Moreover, the direct field data have good linear correlation with the standard SST values (see Fig. 2b) [4].

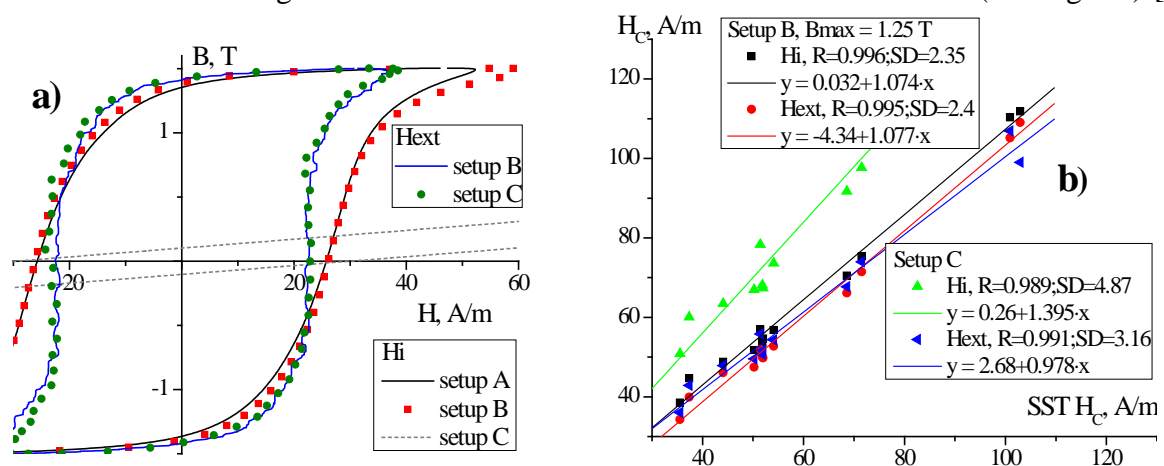


Fig. 2. (a) Typical hysteresis loops of oriented steel, measured at $B_{max} = 1.5$ T by the different setups with the current H_i and the extrapolation H_{ext} methods of field determination. (b) Correlations of the hysteresis coercive force H_c , obtained with the same field approaches at the magnetically closed and open setups B and C, with the standard SST data for the series of non-oriented steels measured at $B_{max} = 1.25$ T. The correlation factor R and the standard deviation SD of the linear fits are shown in the graph labels.

3. Coercimeter

This mobile single-yoke device has been utilized in former USSR since the end of 1930s for coercimetric local control. Magnetization winding is placed on the small attached yoke; and the main drawback of this device is instability of the magnetization conditions with respect to uncontrollable yoke-sample contact [2]. Therefore, it can provide the stable result only for the coercive force value, which is independent of the demagnetization factor induced by the gap between the yoke and the sample [5].

For further improvement, we equipped the single yoke carrying the magnetization coil with the Hall sensor array and the two shielding plates as shown in Fig. 1 [3]. For precise measurement, the induction coil should be wound around homogeneously magnetized sample cross-section, which limits its application potential [2]. For the contactless measurement, a Barkhausen noise technique with a surface-mounting coil can be utilized [6].

Differences between the current and the extrapolation field methods are illustrated for the coercive field and the remanent induction values in Figs. 3 and 4. The measurements were done for plastically pre-deformed low-carbon steel [6]. Fig. 3 presents the data for the samples of 70x70x3 mm measured in a relatively stable configuration by a single Fe–Si yoke of 70 mm width with inner and outer pole distances of 40 and 90 mm. The samples were quasi-statically magnetized with frequency of 0.2 Hz and induction amplitude of 1.7 T. All magnetic parameters have large scattering in a Lüders band region up to 5 % of strain, where the sample microstructure is not settled. Fig. 4 presents the magnetic anisotropy data with respect to the strain direction. Before these measurements with induction amplitude of 1.35 T, the samples were machined to discs of 60 mm diameter to minimize a shape-induced measurement error [2]. The data were fitted well by a cosine square function, which is the simplest form of anisotropy energy [1], [6]. The error bars present the standard error of four identical tests.

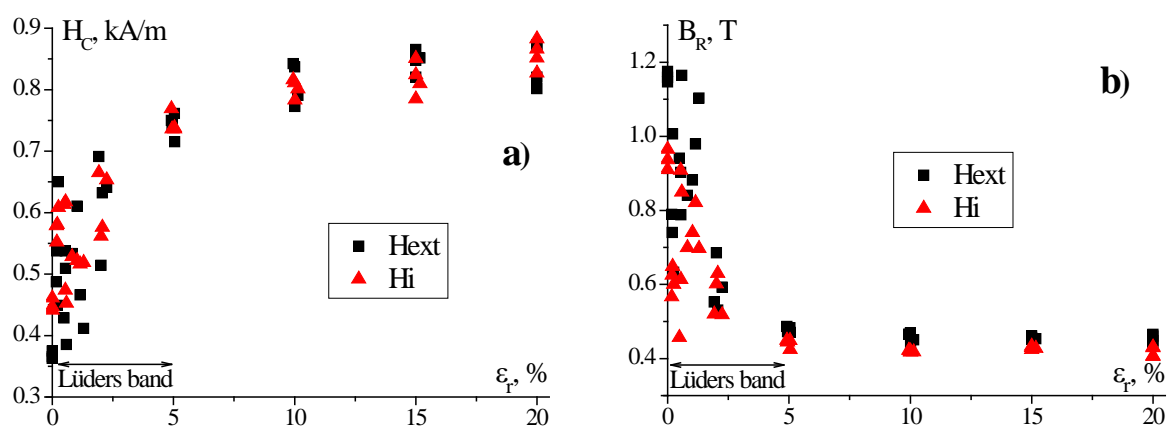


Fig. 3. Dependence of coercive force, H_c , (a) and remanent induction, B_r , (b) on residual strain for the current H_i and the extrapolation H_{ext} field methods.

It is well seen that both methods of field determination provide qualitatively similar results, however, there are serious quantitative distinctions. For magnetically hard deformed samples ($\epsilon = 10\text{--}20\%$) the methods give close values; but for the unstrained ($\epsilon = 0\%$) and the perpendicularly magnetized samples ($\varphi \sim 90^\circ$), the difference is considerable, especially for the remanence values, due to higher demagnetization component (see Figs. 3 and 4b). Moreover, the coercive force obtained by the extrapolation field method determines the easy magnetization axis $\varphi = 90^\circ$ precisely, whereas the corresponding current field values show a shift of about six degree (see Fig. 4a). Quantitative correlation is worse for the measurements

of magnetic anisotropy because of mistakes induced by the disk sample shape [6]. However, the extrapolation field data are more sensitive with the magnetization angle (see Fig. 4).

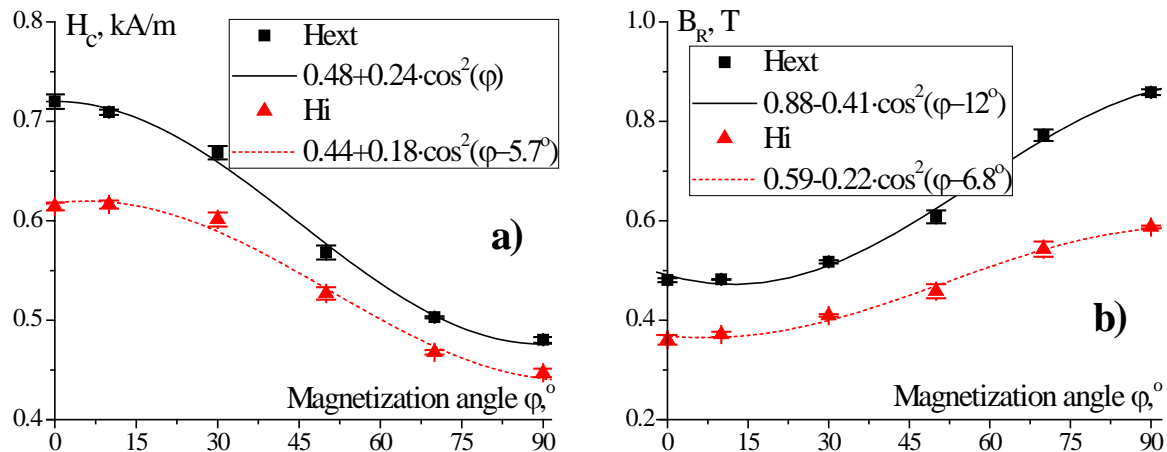


Fig. 4. Dependence of coercive force, H_c , (a) and remanent induction, B_r , (b) on magnetization angle for the current H_i and the extrapolation H_{ext} field methods measured for the 5% strained sample ($\varphi = 0$ is the stress direction).

4. Conclusions

It was experimentally proved that physically-based direct field measurements provide stable and reliable results even for the open magnetic circuits, which can not be done with the simple and standard current field method. This is the important outcome, which can change the main principles of the industrial testing techniques. The disadvantage of the proposed method is a comparative complication of the magnetic setup, especially in the case of mobile coercimeter.

Acknowledgements

The author appreciates the financial support of the Czech Science Foundation (GACR) under the postdoctoral project no. 102/09/P108 and of Academy of Sciences of the Czech Republic under the project AVOZ10100520.

References

- [1] Bozorth RM. Ferromagnetism. IEEE Press, New York, 2003, 842-855.
- [2] Stupakov O. Investigation of applicability of extrapolation method for sample field determination in single-yoke measuring setup. *Journal of Magnetism and Magnetic Materials*, 307: 279-287, 2006.
- [3] Perevertov O. Increase of precision of surface magnetic field measurements by magnetic shielding. *Measurement Science and Technology*, 20: 055107, 2009.
- [4] Stupakov O. Measurement of non-oriented steels with field control. *Journal of Electrical Engineering*, 61 (7/s): 2010.
- [5] Bida GV, Nichipuruk AP. Coercive force measurements in nondestructive testing. *Russian Journal of Nondestructive Testing*, 36: 707-727, 2000.
- [6] Stupakov O, Uchimoto T, Takagi T. Magnetic anisotropy of plastically deformed low-carbon steel. *Journal of Physics D: Applied Physics*, 43: 195003-1-7, 2010.

Static Magnetic Field Instability and Its Inhomogeneity Distribution Mapping in NMR

P. Andris, I. Frollo

Institute of Measurement Science, Slovak Academy of Sciences,
Dúbravská cesta 9, 841 04 Bratislava, Slovak Republic
Email: peter.andris@savba.sk

Abstract. *Instability of the static magnetic field of an NMR scanner can distort measured maps of its inhomogeneity distribution. The research described in the paper was aimed at finding a method of correction influences of the instability. Measured maps of the static magnetic field inhomogeneity distribution were processed using an optimization method and recalculated to the initial value of the static magnetic field. The resulting inhomogeneity maps were measured using two methods and compared with very good results.*

Keywords: *Static Magnetic Field, Inhomogeneity, Optimization, Phase of NMR Data, Spectral Line Position of Water*

1. Introduction

Mapping inhomogeneity distribution of the static magnetic field of an NMR scanner can be used for setting the magnet. Intentionally caused inhomogeneity can be an initial value for calculation of some physical parameter. There are many methods of mapping the static magnetic field distribution in NMR. The research described in the paper is a continuation of the research described in Ref. [1]. The maps of the static magnetic field are distorted by drifting the magnetic field frequently and the ratio processing can not give proper results. Purpose of the paper is to present a new method of processing such maps. Phases of the both NMR data matrices are modified using addition of the phase values which serve as variables for the subsequent optimization of the magnetic field level. The values acquired after the optimization recalculates the both source matrices to the initial same magnetic field. It ensures reliable unwrapping the resulting phase as a source for the magnetic field distribution calculation. It is assumed that the optimized matrices are determined for the ratio processing and the magnetic field drift has not caused a more complex distortion.

2. Subject and Methods

Static magnetic field distribution can be measured in more ways. Measuring from the phase of the NMR data is quick and simple. Nevertheless for accurate results some rules must be adhered. In the previous work [1] there was showed that double measurement using an NMR measuring sequence sensitive to inhomogeneities e.g. the gradient echo (GRE) with different values of the time echo (TE) can remove most of significant distortions. Nevertheless if the initial phases do not have suitable values (e.g. due to parasitic phase shifts caused by drifting the field during the measurement) unwrapping of the resulting phase need not be perfect. Therefore the new method was developed to correct the parasitic phase shifts. Each of the both initial matrices measured with different TE after the Fourier transform is multiplied by exponential term with variables $\varphi_{1,shift}$ and $\varphi_{2,shift}$ representing correcting phase shift. Then an object function is created depending on the both variables. Possible object function can be derived from the root mean square as

$$f(\varphi_{1shift}, \varphi_{2shift}) = \sqrt{\frac{1}{k} \cdot \sum_{\mathbf{r}_j \in ROI} (\Delta B(\mathbf{r}_j))^2}, \quad (1)$$

where \mathbf{r}_j are position vectors of voxels from the region of interest (ROI), $j \in \langle 1, k \rangle$.

Magnetic field distribution is given by

$$\Delta B(\mathbf{r}) = \frac{\varphi_1 - \varphi_2 + \varphi_{1sh} - \varphi_{2sh} + \varphi_{1shift} - \varphi_{2shift}}{\gamma \Delta TE} = \frac{1}{\gamma \Delta TE} \cdot \text{Arg} \left(\frac{\mathbf{I}_1}{\mathbf{I}_2} \right) + \frac{\varphi_{1shift} - \varphi_{2shift}}{\gamma \Delta TE}, \quad (2)$$

where γ is the gyromagnetic ratio and $\mathbf{I}_1, \mathbf{I}_2$ are complex matrices of measured and Fourier transformed NMR data. ΔTE is difference between the both echo times. Magnetic field distribution can also be measured and calculated from the position of the spectral line of water [2]. The considered method is based on repeated measurements with increasing TE. Voxel signal of such measurement can be considered as sampled FID signal with sampling interval ΔTE . Spectrum of FID signal is a line one (if not distorted) corresponding to the static magnetic field inhomogeneity in the considered voxel. In the conditions of the drifting static magnetic field all measured matrices of NMR data first must be recalculated to the same magnetic field. The matrices are again multiplied by exponential terms realizing phase shifting variables. The ratio processing of 5 measured and Fourier transformed matrices yields 4 matrices for optimization. They should be equal. Therefore the object function is given by

$$\begin{aligned} f(\varphi_{1shift}, \varphi_{2shift}, \varphi_{3shift}, \varphi_{4shift}, \varphi_{5shift}) = & \\ & \sqrt{\frac{1}{k} \cdot \sum_{\mathbf{r}_j \in ROI} (\Delta B_1(\mathbf{r}_j) - \Delta B_2(\mathbf{r}_j))^2} + \sqrt{\frac{1}{k} \cdot \sum_{\mathbf{r}_j \in ROI} (\Delta B_1(\mathbf{r}_j) - \Delta B_3(\mathbf{r}_j))^2} + \\ & + \sqrt{\frac{1}{k} \cdot \sum_{\mathbf{r}_j \in ROI} (\Delta B_1(\mathbf{r}_j) - \Delta B_4(\mathbf{r}_j))^2} + \sqrt{\frac{1}{k} \cdot \sum_{\mathbf{r}_j \in ROI} (\Delta B_2(\mathbf{r}_j) - \Delta B_3(\mathbf{r}_j))^2} + \\ & + \sqrt{\frac{1}{k} \cdot \sum_{\mathbf{r}_j \in ROI} (\Delta B_2(\mathbf{r}_j) - \Delta B_4(\mathbf{r}_j))^2} + \sqrt{\frac{1}{k} \cdot \sum_{\mathbf{r}_j \in ROI} (\Delta B_3(\mathbf{r}_j) - \Delta B_4(\mathbf{r}_j))^2}. \end{aligned} \quad (3)$$

Magnetic field distributions can be calculated using the ratio processing as

$$\begin{aligned} \Delta B_1(\mathbf{r}) &= \frac{\varphi_1 - \varphi_2 + \varphi_{1sh} - \varphi_{2sh} + \varphi_{1shift} - \varphi_{2shift}}{\gamma \Delta TE} = \frac{1}{\gamma \Delta TE} \cdot \text{Arg} \left(\frac{\mathbf{I}_1}{\mathbf{I}_2} \right) + \frac{\varphi_{1shift} - \varphi_{2shift}}{\gamma \Delta TE}, \\ \Delta B_2(\mathbf{r}) &= \frac{\varphi_2 - \varphi_3 + \varphi_{2sh} - \varphi_{3sh} + \varphi_{2shift} - \varphi_{3shift}}{\gamma \Delta TE} = \frac{1}{\gamma \Delta TE} \cdot \text{Arg} \left(\frac{\mathbf{I}_2}{\mathbf{I}_3} \right) + \frac{\varphi_{2shift} - \varphi_{3shift}}{\gamma \Delta TE}, \\ \Delta B_3(\mathbf{r}) &= \frac{\varphi_3 - \varphi_4 + \varphi_{3sh} - \varphi_{4sh} + \varphi_{3shift} - \varphi_{4shift}}{\gamma \Delta TE} = \frac{1}{\gamma \Delta TE} \cdot \text{Arg} \left(\frac{\mathbf{I}_3}{\mathbf{I}_4} \right) + \frac{\varphi_{3shift} - \varphi_{4shift}}{\gamma \Delta TE}, \\ \Delta B_4(\mathbf{r}) &= \frac{\varphi_4 - \varphi_5 + \varphi_{4sh} - \varphi_{5sh} + \varphi_{4shift} - \varphi_{5shift}}{\gamma \Delta TE} = \frac{1}{\gamma \Delta TE} \cdot \text{Arg} \left(\frac{\mathbf{I}_4}{\mathbf{I}_5} \right) + \frac{\varphi_{4shift} - \varphi_{5shift}}{\gamma \Delta TE}. \end{aligned} \quad (4)$$

3. Results

Verification experiments were performed on the Opera NMR scanner with permanent magnet of 0.18 T (Esaote Group, Genova, Italy). The GRE sequence was applied to ball-shaped phantom filled with the water solution of 5 mM of NiCl_2 and 55 mM of NaCl. Diameter of

the phantom was 140 mm. During the first experiment transversal slice was depicted two times with two values of TE, $\Delta TE = 2$ ms. Parameters of the measurement: the slice thickness 5 mm, FOV = 200 mm \times 200 mm, the resolution was 256 pixels \times 256 pixels, number of averages 6, the repetition time TR = 500 ms. The both matrices of measured data were processed using the equations (1), (2). The processing yielded magnetic fields map depicted in Fig. 1. The map acquired without optimization is also depicted in Fig. 1.

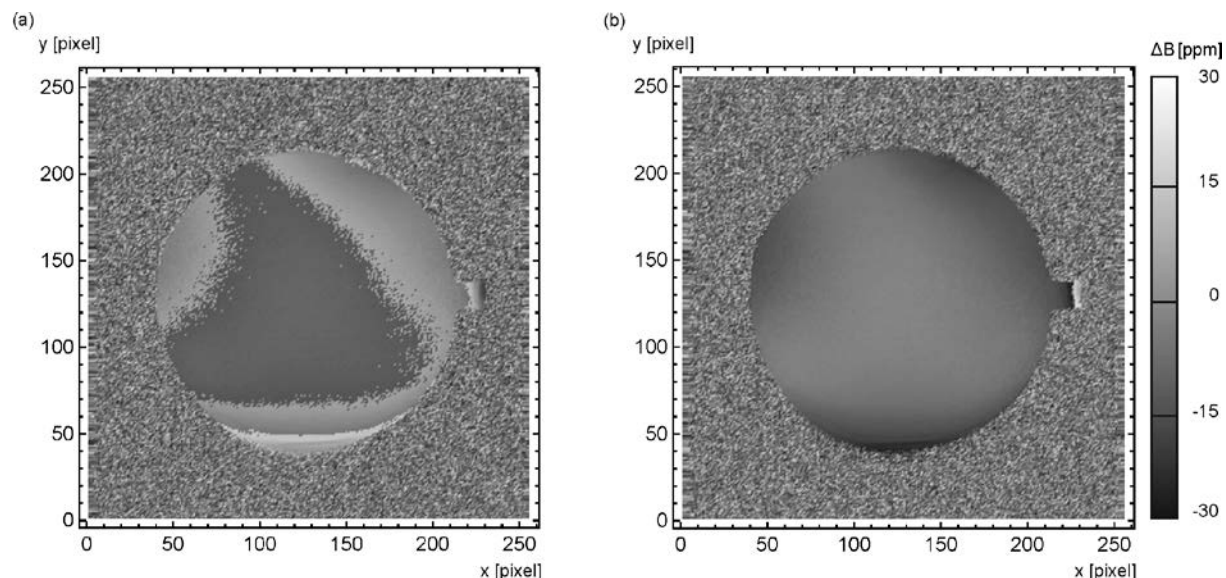


Fig. 1. Figure of the static magnetic field map (a) without the optimization and (b) after the optimization. Improving the unwrapping thanks to the optimization is evident.

During the second experiment the same phantom was measured under the same conditions 5 times with increasing TE, $\Delta TE = 2$ ms.

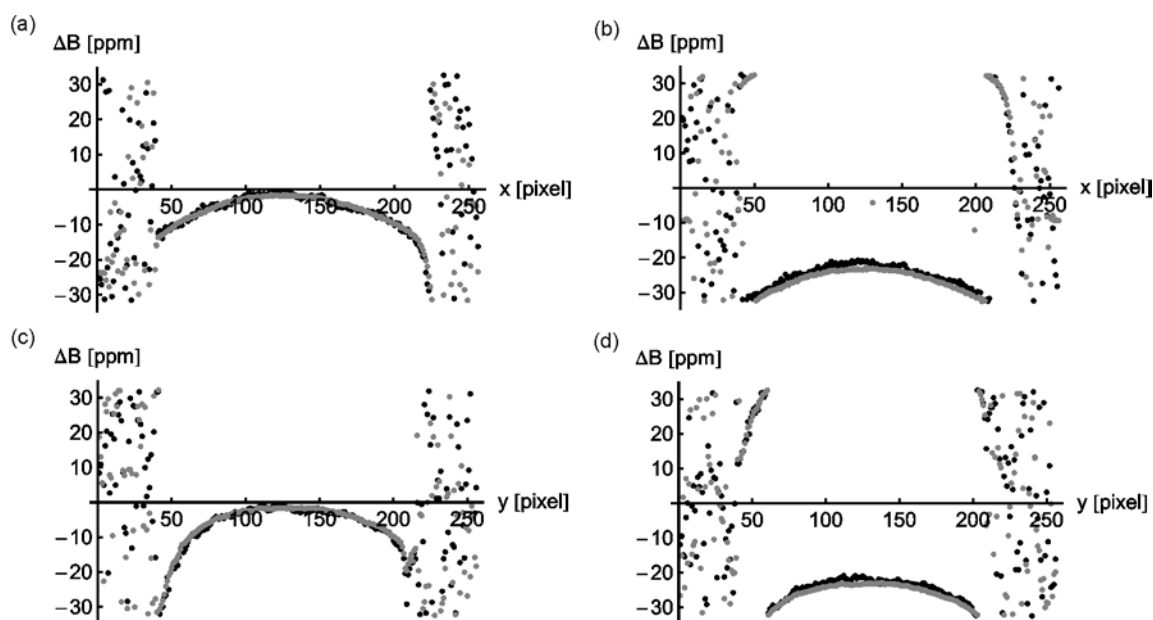


Fig. 2. Verification of the results from the optimized measurement with five matrices. The row (a) and the column (c) from the middle of the sample phantom prove the total agreement between the both manners of measurements. The black points were calculated from the phases and the grey points from the spectral lines of water positions. Figures (b) and (d) depict the same situation before optimization. The unwrapping is correct but the level of the magnetic field is too low therefore aliasing distorted the data. The whole maps of the magnetic field distribution are very similar to those in the figure 1.

The data were optimized using the equations (3), (4) and the static magnetic field map was calculated from the phase using the ratio processing and from the position of the spectral line of water. The FID signal for the position of the spectral line calculation was determined by 5 samples. It is not sufficient for successful processing therefore an interpolation using the zero filling method was used. The both results were compared in the Fig. 2. Figures (b) and (d) depict comparison of the middle row and column for the both methods without the optimization. The black points were calculated from the phase, the grey points were determined from the position of the spectral line of water using the zero filling interpolation. Imperfect unwrapping is evident again. Figures (a) and (c) compare the same row and column after the optimization. The improvement is evident.

4. Discussion

The map of the magnetic field acquired from the position of the spectral line of water was calculated only from 5 samples. To improve resolution the technique of zero filling was used. The whole number of the data matrices was increased by adding 301 zero matrices to get interpolated resolution of 0.2 ppm. The position was then determined as a simple maximum of the spectral curve. Spectral curves should be of line shape but more frequently they are in many ways distorted. Therefore more sophisticated manners of determining the position of the spectral line are used, e.g. average of the both values at the half-level of the spectral curve. Such results have also features of interpolation and the zero filling is not necessary or can be reduced to less number of zero matrices. All calculations were performed using the program package Mathematica (Wolfram Research Inc., Champaign IL).

5. Conclusions

The described method is intended for scanners with lower stability of the static magnetic field or for more long-time measurements. Important component of the method is proper object function. Object function for a specific experiment can have also a specific form therefore this is more a group of methods. Looking for more sophisticated techniques of determining the position of the spectral line of water and interpolations are problems for possible future works. More details on the described method can be found in Ref. [3].

Acknowledgements

The research was sponsored by the Grant Agency of the Slovak Academy of Sciences, grant number 2/0090/11 and the State program ŠPVV no 2003SP200280203.

References

- [1] Andris P, Frollo I. Simple and accurate unwrapping phase of MR data. *Measurement* 42: 737-741, 2009.
- [2] Weis J, Frollo I, Budinsky L. Magnetic field distribution measurement by modified FLASH method. *Zeitschrift für Naturforschung A* 44: 1151-1154, 1989.
- [3] Andris P, Frollo I. Optimized measurement of magnetic field maps using nuclear magnetic resonance (NMR) *Measurement Science and Technology*, in press - accepted (2011).

Experimental and Theoretical Study of Effects in Power Distribution Net

M. Truhlář, M. Košek, A. Richter

Faculty of Mechatronics, Technical University of Liberec, Liberec, Czech Republic
Email: martin.truhlar@tul.cz

Abstract. *Magnetic field is responsible for many disturbing effects in the power distribution nets. Its calculation is complicated by the skin-effect and eddy currents. A formula was derived for the current density distribution in conductor of rectangular cross section. In order to verify it, the magnetic field was measured. Preliminary experiments confirmed the formula qualitatively. For better verification the experimental accuracy should be improved, which is realizable by relatively simple means.*

Keywords: *AC Magnetic Field, Skin-effect, Low Magnetic Field Measurement, Eddy Currents*

1. Introduction

Strong currents flow in distribution points that can lead to high forces between conductors, especially when transition effects take a place. In order to estimate the forces, magnetic field produced by the conductors must be known. It can be calculated from currents in conductors, but the calculation must be verified experimentally, at least in the initial stage.

Because of high currents, distribution points use conductors of large cross section. Due to the skin effect, the current density is not uniform in them even at low technical frequencies. In this simple case the current distribution in analytical form can be derived and calculated simply. Unfortunately, the solution is in unusual complex symbolic form. Its understanding is more difficult and its improper use can lead to serious errors. Therefore, the experimental verification of results is necessary. Since the current density inside conductor cannot be measured, its theoretical distribution should be verified by excited magnetic field. It is the second, theoretical, reason for the magnetic field precise measurement.

2. Subject and Methods

We consider a massive conductor of rectangular cross section of dimensions $2a$ and $2b$ in plane XY and current in the direction of Z axis. The following formula was derived for current density¹ $\hat{i}(x, y)$ simply supposing constant current density i_o on the conductor surface [1]

$$\hat{i}(x, y) = i_o \left[-\frac{\cosh(\hat{\delta}x)\cosh(\hat{\delta}y)}{\cosh(\hat{\delta}a)\cosh(\hat{\delta}b)} + \frac{\cosh(\hat{\delta}x)}{2\cosh(\hat{\delta}a)} + \frac{\cosh(\hat{\delta}y)}{2\cosh(\hat{\delta}b)} \right]. \quad (1)$$

The attenuation coefficient $\hat{\delta}$ is given by the formula

$$\hat{\delta} = (1 + j) \sqrt{\frac{\omega\mu\gamma}{2}}, \quad (2)$$

where

$\omega = 2\pi f$ is angular frequency and f is frequency,
 μ is absolute permeability of the conductor material,
 γ is electrical conductivity of the conductor.

¹ Complex numbers are denoted by a hat above symbol. Imaginary unit symbol is j .

Three massive conductors, modeling the key part of distribution net, are fed by the three phase system. Apparatus used for the complete study is in Fig. 1 together with its block scheme. The skin-effect is studied by changing the frequency in the range from 15 Hz to 1.2 kHz. The current in conductor varies from about 1500 A to about 250 A. The vector of AC magnetic flux density is measured along a selected line (over the conductors) by a 3D Hall probe. The probe position is controlled by a computer and all the waveforms are stored in its memory.

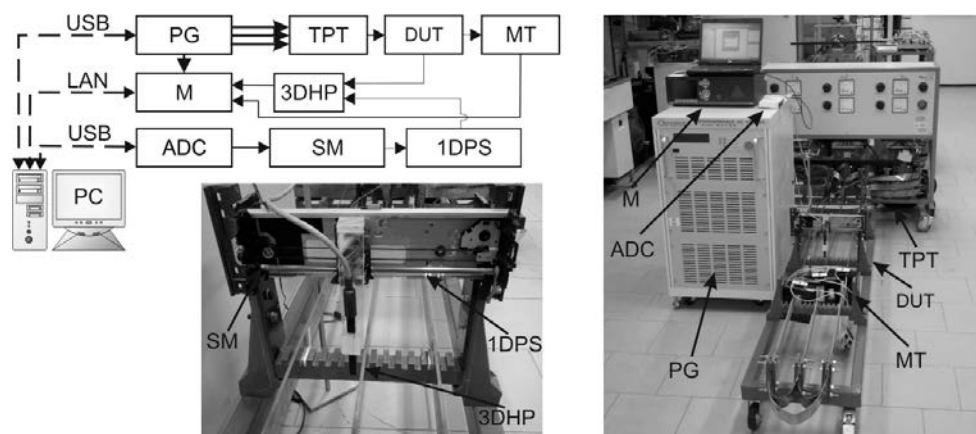


Fig. 1. Apparatus for complete power net study. Legend: PG – Power generator Chroma 61704, M – General purpose meter Norma 5000, ADC – Analogue to digital converter NiDaq, TPT – Three-phase transformer, 3DHP – 3D Hall probe, SM – Step motor, DUT – Massive conductors, MT – Measuring transformers, 1DPS – 1D positioning system, PC – Personal computer.

Preliminary experiments in three phase system revealed that the effect of eddy currents is dominant at all frequencies. In order to study the skin-effect, one phase system was used. Only the central conductor was fed and the current flows back by outside conductors.

Irrespective of high currents in conductors the magnetic flux density generated by them is low and noise is present. There are several methods of noise reduction. As the best one the method of FFT (Fast Fourier Transform) was found. Its application is in Fig. 2. Several waveforms were extracted from the probe output and their spectrum was computed by the FFT, see Fig. 2a. Then the actual waveform was reconstructed from the dominant harmonics (and DC component). Both the waveform and experimental points are in Fig. 2b.

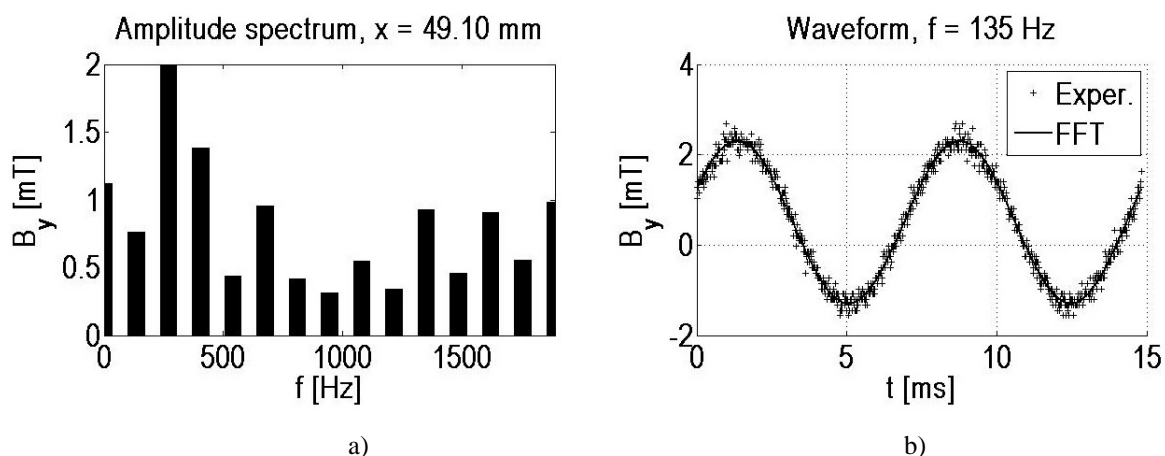


Fig. 2. Waveform reconstruction. a) FFT spectrum of 2 selected periods. The DC component and the second harmonics are 50 times higher in reality. b) Measured points and waveform reconstructed from both the DC component and the second harmonics.

This approach was applied to all the probe positions. Since the eddy currents are proportional to the current (and magnetic flux density) derivative, the time moment for calculations was selected at the maximum of reconstructed waveform. Then eddy currents are in principle avoided.

The magnetic field, as a check of skin-effect, was calculated numerically for both the constant current density and the varying current density according to formula (1) in MATLAB. The speed of calculation is relatively fast, since an analytical formula exists for a straight thin conductor, which is presented in literature [2], for instance. Then the numeric integration is performed only in the conductor cross section.

3. Results

Only preliminary experimental results dealing with the magnetic field measurement by apparatus described in part 2 are presented here. Both the component of magnetic flux density was measured above the conductors and close to them according to Fig. 3. The first realized probe movement, using printing system from old printers, was limited to about 210 mm.

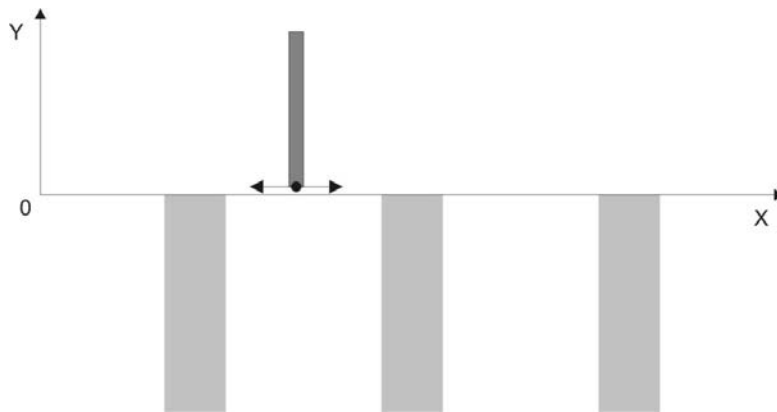


Fig. 3. Probe movement above the conductors (cross section) and coordinate system.

At low frequency of 45 Hz both the magnetic flux density components are in Fig. 4. The skin-effect does not take a place practically and the agreement between theory and experiment is good. If the frequency increases about 10 times, the skin-effect is evident for B_y component, as it is shown in Fig. 5b. In both the figures, the preliminary experiment is limited to the measurement in area near the central conductor.

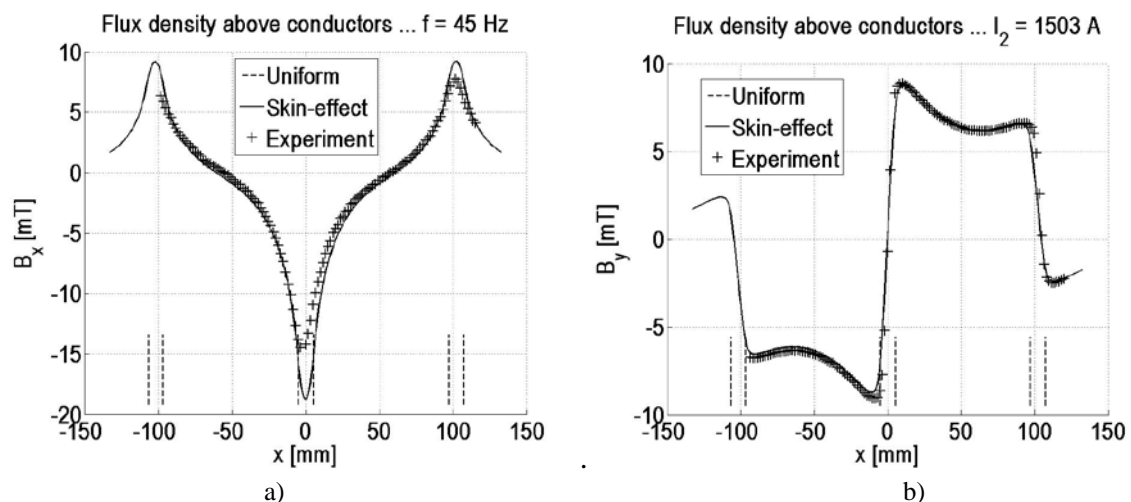


Fig. 4. Components of magnetic flux density at low frequency of 45 Hz and high current of 1500 A.

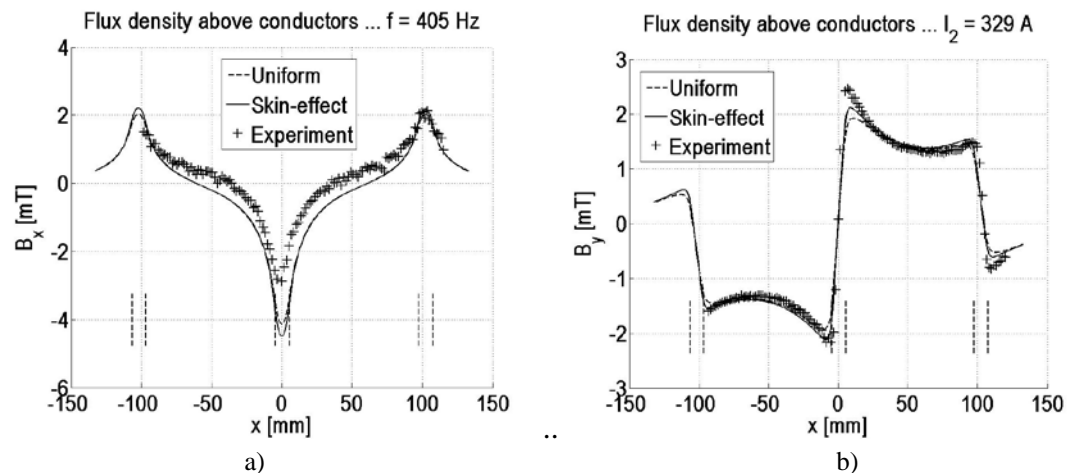


Fig. 5. Components of magnetic flux density for higher frequency of 405 Hz and decreased current of 330 A.

In the case of higher frequency the current decreases about 5 times, the magnetic field is lower and measurement errors are visible, especially for the x component. The serious current decrease is a feature of commercial instrument.

4. Discussion

We have shown that the skin-effect can be studied by relatively simple means – measurement of magnetic field near the massive conductors. At low frequency a good agreement between theory and experiment was found. Systematic error for the x component in Fig. 4a is due to the incorrect probe calibration, probably.

At about 10 times higher frequency the skin-effect takes a place theoretically. The difference is not high, however, and its maximum is at conductor edges. Experiment confirms qualitatively the skin-effect for the B_y component in Fig. 5b. The experimental points are not symmetrical however. As for the x component, the errors are too high, to allow any judging.

Main problem for quantitative verification of skin-effect formula (1) is in the low magnetic field that is difficult to measure precisely. The current cannot be increased by given source. The solution is to increase the probe sensitivity and accuracy. As it is shown in Ref. [3] the improvement is practically realizable and the skin-effect formula verification can be made.

Acknowledgements

This work was supported by the student grant SGS 2010/7821, Interactive mechatronic systems in technical cybernetics, and the fund of Czech Science Foundation GAČR, grant No. 102/08/H081.

References

- [1] Kosek M., Truhlar M., Richter A. Magnetic field of massive conductor at low frequency. In proceedings of conference Computational Problems in Electrical Engineering, CPEE 2010, 2010, 12. Full paper will be published in Electrical Review.
- [2] Frollo I., Andris P., Pribil J., Vojtisek I., Holubekova Z., Dermek T. Magnetic field measurement of a planar coil using magnetic resonance imaging method. In proceedings of the 7th International Conference Measurement 2009, 2009, 238–240.
- [3] Novak M., Slavik L., Kosek M., Truhlar M. Precise measurement of low magnetic field. In proceedings of the 8th International Conference Measurement 2011 (this issue).

Online Measurement of the Penetration Depth in Arc Welding

¹P.P.L. Regtien, ²I.M.P. van Wieringen

¹Measurement Science Consultancy, Hengelo, The Netherlands

²Penweld, Holten, The Netherlands

Email: paul@regtien.net

Abstract. *A measurement method is presented for automatic arc welding systems. In particular it is applicable in situations where no access to the back side of the material is possible, for instance pipes. The method is based on the oscillations of the welding pool, when subjected to a high current trigger pulse. The spectrum of the response to this pulse contains information about the penetration depth of the weld pool in the material, and can be retrieved from the arc voltage. Experimental results are in agreement with the theory, and demonstrate the feasibility of the method for industrial practice.*

Keywords: Arc Welding, Weld Pool Oscillation, Orbital Welding

1. Introduction

Arc welding is based on the creation of an electric arc between an electrode and the material to melt. The quality of the welded joint is determined largely by the weld pool geometry during the welding process, metallurgical properties of the weld material and the geometry of the materials to be welded. In order to obtain adequate strength in a welded joint, it is necessary to achieve proper weld penetration. Too little penetration results in an incomplete adhesion between the metal parts throughout the thickness of the joint, and too much penetration may produce a weak joint of the base metal with the surrounding material.

Therefore, it is important to develop techniques to analyze and sense the level of penetration during arc welding and develop control systems for automatic welding. Inspection methods that do not require access to the backside are ultrasonic sensing, surface temperature, trace element method, arc voltage variation due to surface sagging and weld pool oscillation sensing. The latter technique is described in more detail in the next sections.

2. Principle of weld pool penetration measurement

The measuring method is based on the relation between the arc voltage and the distance between the electrode and the surface of the weld pool. This distance changes with the shape of the weld pool, the latter being determined by forces acting on the pool and material flow within the pool ([1]). The basic idea of penetration depth measurement is pool oscillation. During welding, the weld pool is brought into oscillation by applying high current pulses with a short pulse time, in the order of tens of ms. The oscillation modulates the distance between the pool surface and the electrode, and hence the arc voltage at constant current. Fig. 1 shows a typical response on a trigger pulse of about 300 A, at a particular penetration depth.

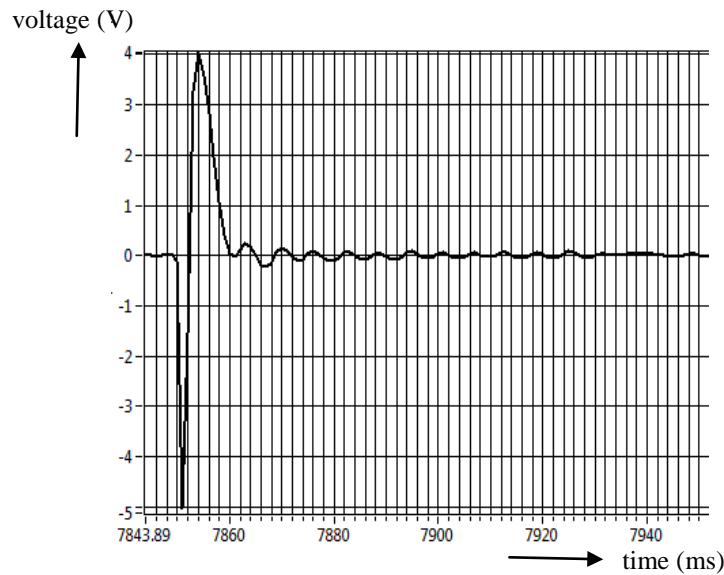


Fig. 1. Typical response of the arc voltage on a high current trigger pulse

The pulses are repeated every 0.5 to 1 s, providing information about the weld pool depth during welding. The oscillation frequency shortly after this trigger pulse is determined by the shape and depth of the weld pool as well as the material properties, see Fig.2 [2].

Mode	Top view	Side view	frequency
Mode 1			$f = 5.84 \left(\frac{\gamma}{\rho} \right)^{\frac{1}{2}} D^{-\frac{3}{2}}$
Mode 2			$f = 3.37 \left(\frac{\gamma}{\rho} \right)^{\frac{1}{2}} D^{-\frac{3}{2}}$
Mode 3			$f = \frac{1.08}{D} \left(\frac{\gamma}{\rho h} \right)^{\frac{1}{2}}$

Fig. 2. Typical response of the arc voltage on a high current trigger pulse

In this figure, γ is the surface tension in N.m^{-1} , ρ the metal density in kg.m^{-3} , D the diameter of the weld pool in mm and h is the weld pool depth in mm.

When the weld pool has just reached the bottom of the material (denoted by full penetration), the oscillation mode of the liquid metal changes from mode 1 or 2 to mode 3, which is reflected in a change in frequency spectrum of the arc voltage right after the trigger pulse, as can be seen in Fig. 3 illustrating schematically this process [3].

3. Experiments

A series of experiments on a flat plate is executed to verify the theory and to investigate the applicability in industrial practice. The arc voltage is measured by a differential amplifier, band-pass filtered and further processed by a Labview programme. For the time being the FFT is performed offline, after having completed a welding experiment. We report here about just a single experiment, with major welding parameters: base current 65 A, pulse current 350 A, pulse width 1 ms, shielding gas: argon, material: steel 304, plate thickness 3 mm. The

distance between the plate and the electrode is set at 1.5 mm. The spectra of the arc voltage are shown in Fig. 4, at three instances of the process.

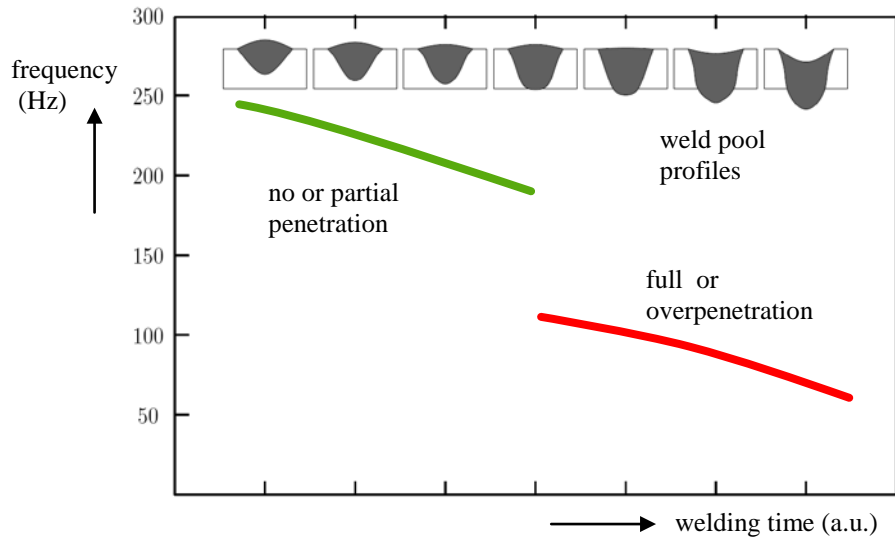


Fig. 3. Principal frequency components versus penetration (theoretical).

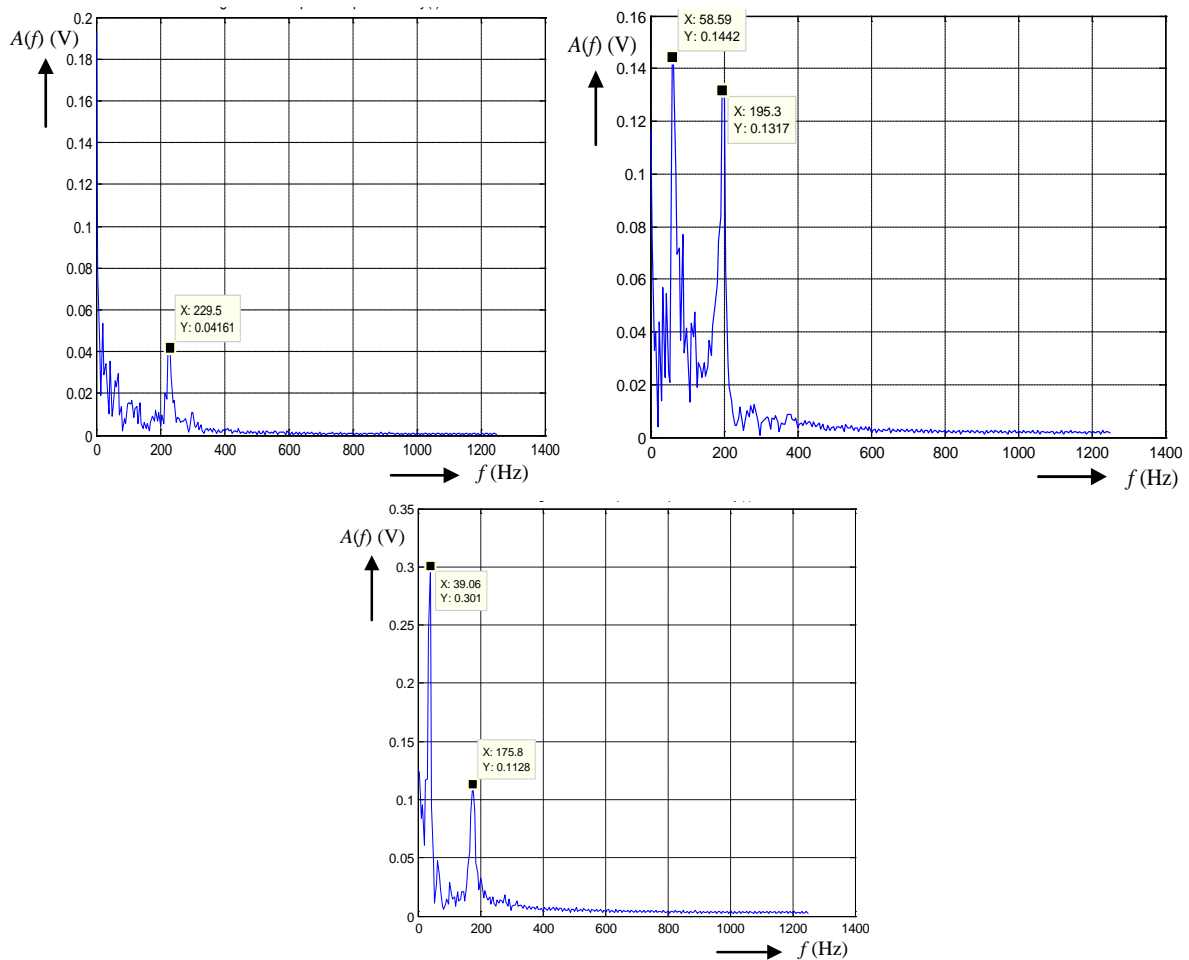


Fig. 4. Arc voltage spectrum after the 1st, 10th and 18th trigger pulse

The time window for the FFT starts just after the high peak in the response shown in Fig. 1, and has a width of about 50 s. The three pictures in Fig. 4 show three penetration stages. The

first has a main peak at a relatively high frequency, in this case around 200 Hz, corresponding with partial penetration. The second one shows two peaks, around 200 and 50 Hz respectively. In the third picture the 50 Hz component dominates the spectrum. At the 10th pulse, where both frequencies are present, there is a transition from partial to full penetration, which corresponds to an optimal weld. The frequencies are in agreement with values reported in literature ([2,4]).

Fig. 5 shows the welding result of the welding experiment described in Fig. 4, corresponding to the situation after the 18th pulse. From this picture we see that full penetration has been reached indeed, and no overpenetration occurred.

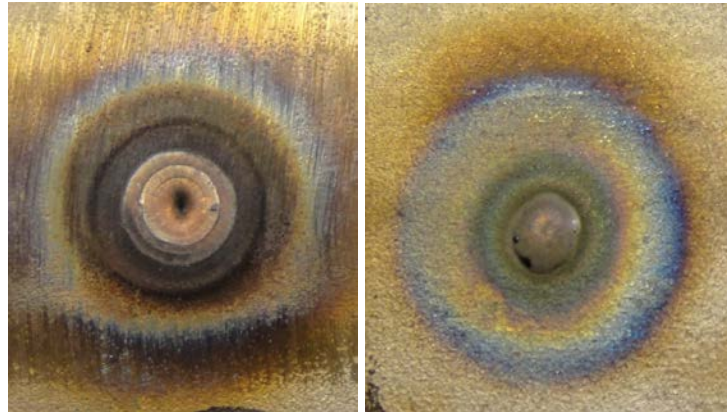


Fig. 5. Front (left) and back (right) side of the welding

4. Conclusions and further work

Many more experiments have been carried out, with different parameters of the trigger pulse, different materials and both fixed and moving electrodes. These experiments have demonstrated the feasibility to measure the moment of full penetration in a TIG welding process without the need of any additional sensors, just by analyzing the frequency spectrum of the arc voltage. This information can be used in a control system to automatically keep the penetration depth at an optimal value, irrespective of electrode distance, welding speed, material thickness and other variations.

Further research aims at the optimization of the control system and extension of the applicability to orbital welding of pipes, where online monitoring of the weld quality inside the pipe itself is impossible.

References

- [1] Kou S. and Sun D.K., "Fluid Flow and Weld Penetration in Stationary Arc Welds", *Metallurgical and Materials Transaction A*, 16(1), pp 203-213, 1985
- [2] Yudodibroto R.B.Y.B, "Liquid Metal Oscillation and Arc Behavior During Welding", *Pd.D Thesis, Delft University of Technology, The Netherlands, 2010*
- [3] Patent pending
- [4] Aendenroomer T., "Weld Pool Oscillation for Penetration sensing and Control", *Ph.D. Thesis, Delft University of Technology, The Netherlands, 1996*

A New Circuit Approach to Predict Discharge Currents for Air Discharges of ESD Generators

¹I. Mori, ²O. Fujiwara, ³H. Garbe

¹Suzuka National College of Technology, Suzuka, Japan,

²Nagoya Institute of Technology, Nagoya, Japan

³Leibniz Universität Hannover, Hanover, Germany

Email: i-mori@info.suzuka-ct.ac.jp

Abstract. To predict discharge current waveforms for air discharges of electrostatic discharge (ESD) generators (ESD-guns) used in an IEC immunity test against human ESD, an equivalent circuit modelling for air discharges of ESD-guns is proposed. To simulate spark discharges, two typical spark resistance formulae (Rompe-Weizel's and Toepler's) are applied to the modelling, which consists of a spark voltage source derived from a spark resistance formula, the output impedance of an ESD-gun, and an injecting-point impedance of equipment under test (EUT). For validation, discharge current waveforms for air discharges onto an IEC calibration target in lieu of EUT are calculated to compare with measured waveforms. As a result, it is found that the calculated discharge current waveforms derived from both spark resistance formulae approximately agree with the measured ones, and that Rompe-Weizel's and Toepler's formulae can better predict their rising slopes and tails, respectively.

Keywords: Air Discharge, Discharge Current Waveform, ESD-Gun, Equivalent Circuit Modelling, Spark Resistance Formulae

1. Introduction

The transient electromagnetic (EM) fields due to electrostatic discharge (ESD) events have broadband frequency spectra reached in GHz region, which cause serious EMC problems [1-2]. From this perspective, an immunity test against ESD is being specified by the International Electrotechnical Commission (IEC) as the IEC 61000-4-2 [3]. In the standard, an immunity test against ESD events from a charged human body is being prescribed. To simulate the discharge currents from a charged human body, commercially available ESD generators (ESD-guns) are used. The IEC prescribes two types of discharges, or air and contact discharges of ESD-guns. From the viewpoint of reproducibility of the discharge current waveforms, the IEC recommends contact discharges without sparks, while air discharges accompanying sparks should be more faithful to real ESD phenomenon. To evaluate the severity of the immunity test, the authors previously measured discharge currents for both discharges of an ESD-gun onto an IEC calibration target, and showed that below 1 kV air discharges can provide a severer and reproducible immunity test [4]. Regarding the air discharges, however, the characteristics of discharge current waveforms are not yet fully grasped.

In this study, an equivalent circuit modelling is shown to predict the discharge currents for air discharges of ESD-guns. Two typical spark resistance formulae [5][6] are applied as a voltage source which simulates a spark between the tip electrode of the ESD-gun and the discharge target. For validation, calculated discharge current waveforms are compared with measured ones for air discharges onto an IEC calibration target.

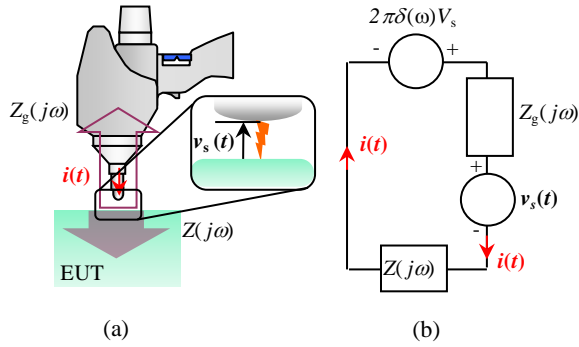


Fig. 1. Schematic diagram (a) and representation of equivalent circuit modeling (b) for air discharges of ESD-gun onto EUT.

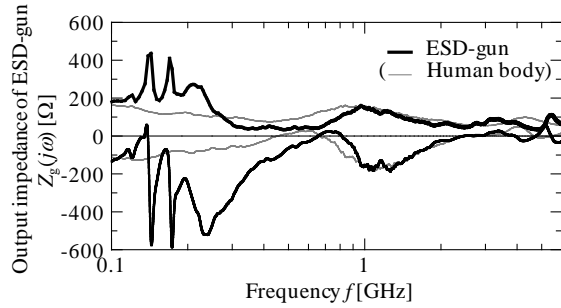


Fig. 2. Measured frequency characteristics of output impedance of ESD-gun.

2. Equivalent circuit modeling

Fig. 1 (a) shows a schematic diagram for air discharges of an ESD-gun onto EUT. Here, $i(t)$ is a current injected onto EUT, $v_s(t)$ is a time-dependent spark voltage, $Z_g(j\omega)$ is the output impedance or internal impedance of an ESD-gun with a charge voltage of 0 V seen from tip electrode, and $Z(j\omega)$ is the injecting-point impedance looking into a contact point of EUT. If a spark fully grows due to the charge accumulated in a stray capacitance between the tip electrode and the EUT, a spark voltage can be derived in a closed form from a spark resistance formula. Rompe-Weizel's and Toepler's spark resistance formulae provide the following time-dependent spark voltages at the atmospheric pressure:

$$v_s(t) = \frac{V_s}{\sqrt{1 + \exp\left\{\frac{1}{2}\left(\frac{V_s}{\alpha\delta}\right)^2(t-t_0)\right\}}} \quad (1)$$

and

$$v_s(t) = \frac{V_s}{1 + \exp\left\{\frac{V_s}{\beta\delta}(t-t_0)\right\}} \quad , \quad (2)$$

respectively. Here, V_s [V] is a charge voltage of the ESD-gun, α and β are the spark constant ($\alpha \square 67$ [V·s^{0.5}/m], $\beta \square 3.7 \times 10^{-3}$ [V·s/m]), δ [m] is a spark gap length between the tip electrode of an ESD-gun and EUT [6].

Fig.1 (b) shows an equivalent circuit modelling for air discharges of ESD-guns. The circuit consists of a time-domain voltage source $v_s(t)$ simulating a spark, a frequency-domain charge voltage source which represents the Fourier transform of charge voltage V_s of an ESD-gun or $2\pi\delta(\omega)V_s$, $Z_g(j\omega)$ and $Z(j\omega)$. The discharge current $i(t)$ is derived from the figure as

$$\begin{aligned} i(t) &= \frac{1}{2\pi} \int_{-\infty}^{+\infty} \frac{2\pi\delta(\omega)V_s - F[v_s(t)]}{Z_g(j\omega) + Z(j\omega)} e^{j\omega t} d\omega = \frac{V_s}{Z_g(0) + Z(0)} - \frac{1}{2\pi} \int_{-\infty}^{+\infty} \frac{F[v_s(t)]}{Z_g(j\omega) + Z(j\omega)} e^{j\omega t} d\omega \\ &= \frac{V_s}{Z_g(0) + Z(0)} - \frac{1}{2\pi} \int_{-\infty}^t \int_{-\infty}^{+\infty} \frac{F\left[\frac{dv_s}{dt}\right]}{Z_g(j\omega) + Z(j\omega)} e^{j\omega t} d\omega dt. \end{aligned} \quad (3)$$

Here, $F[]$ indicates the Fourier transform. $Z_g(j\omega)$ is obtained from measuring the reflection coefficient S_{11} with a network analyzer (an example is shown in Fig. 2 with a human body impedance when a human holds the tip electrode for air dischargers in his hand [7]).

3. Result and discussion

Figs. 3 (a) and 3 (b) show examples of calculated discharge voltage waveforms from Rompe-Weizel's spark resistance formula (Eq. 1) and Toepler's one (Eq. 2), respectively. The charge voltage is 1 kV. In the figures of the discharge current waveforms, the waveforms measured with a 12-GHz digital oscilloscope are also shown with thick solid lines [4]. As a discharge target, we used a commercially available calibration target or a current detector (Schaffner: MD102). The discharge current waveforms injected into the target were observed as voltage waveforms appearing across a 50- Ω termination load of the digital oscilloscope. Thin solid lines indicate discharge current waveforms calculated from Eq. 3. We chose spark gap length δ so that the peak currents match the measured waveforms ($\delta = 78$ [μm] for Rompe-Weizel's,

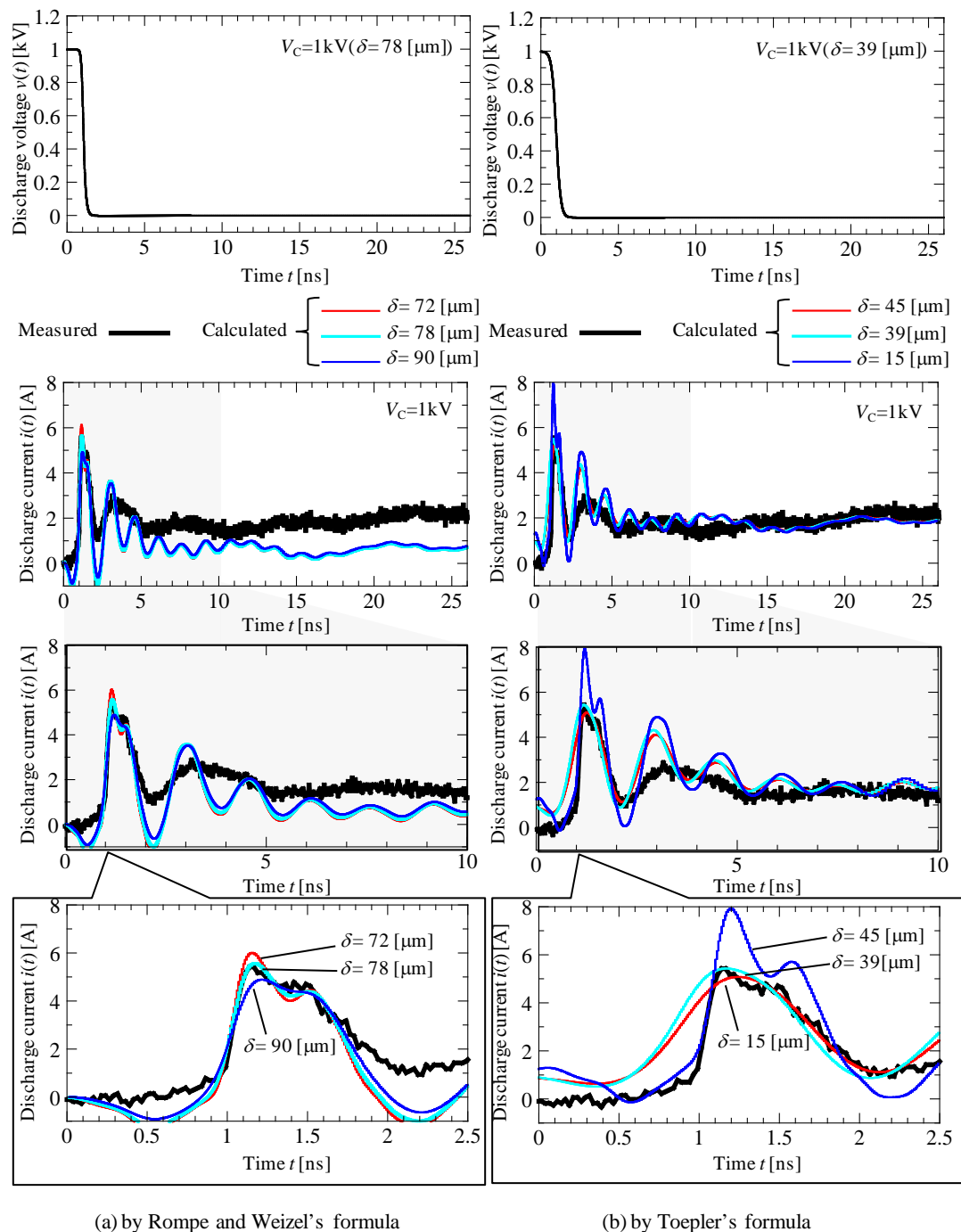


Fig. 3. Examples of discharge voltage and current waveforms calculated by spark resistance formulae, Rompe and Weizel (a) and Toepler (b).

and $\delta = 39$ [μm] for Toepler's, respectively). The lower figure is an enlarged view of the calculated waveforms. In our measurement set-up, the spark gaps δ cannot be measured directly and therefore the values were determined as the calculated waveforms agree with the measured ones.

Regarding Rompe-Weizel's, when the length of 78 [μm] is chosen as the spark gap δ , the calculated waveform agrees well with the measured one especially for its rising slope. As a reference, examples of $\delta = 72$ and 90 [μm] are also plotted. Regarding Toepler's, on the other hand, the length of 39 [μm] chosen as the spark gap δ provides good agreement between the calculated and measured waveforms especially for their tails. As a reference, examples of $\delta = 15$ and 45 μm are also plotted.

4. Conclusion

An equivalent circuit modelling for air discharges of an ESD-gun was proposed, which includes a time-dependent spark voltage source derived from Rompe-Weizel's formula or Toepler's one. The modelling was validated by comparing the calculated waveforms with the measured ones onto the IEC calibration target. As a result, we found that the calculated discharge current waveforms for air discharges agree with measured ones. It was also found that Rompe-Weizel's and Toepler's formulae can better predict rising slopes and tails of the waveforms, respectively.

Our future task is to confirm the feasibility of the circuit modelling for air discharges of ESD-gun with different charge voltages especially low charge voltages below 1 kV.

Acknowledgements

This work was supported by JSPS KAKENHI 21760301.

References

- [1] Fotis G.P, Gonos I.F, Stahopoulos I.A. Measurement of the electric field radiated by electrostatic discharges. *Measurement Science and Technology*, 17(6): 1292-1298, 2006.
- [2] Jobava J, Pommerenke D, Karkashadze D, Schubitzidze P, Zaridze R, Frei S, Aidam M. Computer simulation of ESD from voluminous objects compared to transient fields of humans. *IEEE Transactions on Electromagnetic Compatibility*, 42(1): 54-64, 2000.
- [3] IEC. IEC 61000-4-2 Electromagnetic Compatibility (EMC) – Part4-2: Testing and measurement techniques –Electrostatic discharge immunity test. Edition 2.0, 2008.
- [4] Mori I, Fujiwara O. Severity evaluation of the IEC immunity test against ESD based on wideband measurement of discharge current waveforms. *IEEJ Transactions on Fundamentals and Materials*, 130(5): 457-461, 2010 (in Japanese).
- [5] Fujiwara O. An analytical approach to model indirect effect caused by electrostatic discharge. *IEICE Transactions on Communications*, E79-B(4): 483-489, 1996.
- [6] Taka Y, Fujiwara O. Verification of spark-resistance formulae for micro-gap ESD. *IEICE Transactions on Communications*, E93-B(7): 1801-1806, 2010.
- [7] Mori I, Taka Y, Fujiwara O. Wideband measurement of discharge current caused by air discharge through hand-held metal piece from charged human-body. *IEEJ Transactions on Fundamentals and Materials*, 126(9): 902-908, 2006 (in Japanese).

Uncertainty Analysis of Model for Cuboid Shape Samples Applied on Thermophysical Measurement of Stone Porous Material

¹V. Boháč, ²P. Dieška, ¹Ľ. Kubičár, ¹V. Vretenár

¹Institute of Physics, Slovak Academy of Sciences, Bratislava, Slovakia,

²Department of Physics, FEI - STU, Ilkovičova 3, Bratislava, Slovakia

Email: bohac@savba.sk

Abstract. A new model for the sample of square cross section having cuboids geometry including the effect of heat loss from the surface of the sample was tested using the theory of sensitivity coefficients. Theoretical calculation of model uncertainty is presented. Results of the uncertainty analysis set out range of experimental conditions under which the model is valid and the uncertainty of estimated parameters is optimal. The sensitivity coefficients serve to derive the formulas for calculation of analytical error propagation for non-stochastic dynamic measurements. Result shows limitations relating to a restricted range of validity. The analysis improve the accuracy of measurements. Model was used for data evaluation of thermophysical parameters measured on the sandstone from locality Pravčická brána. Evaluation procedure was tested on experimental data measured under different experimental conditions. In conclusion, the discussion of the experiment optimization is presented.

Keywords: Pulse Transient Method, Sensitivity Coefficient Analysis, Thermophysical Property

1. Introduction

Thermophysical parameters, e.g. thermal diffusivity, specific heat and thermal conductivity reflect thermodynamical state of the material structure. This state changes with the consideration of the atomic structure arrangement, arrangement of crystalline components and consideration on material defects created in time that are responsible for further development of structure change or degradation. Thermodynamical state should be a measure of the quality, stability and durability of material in regarding to industrial use. Process of material deterioration of stones or their state and quality comparing its basic or initial state should be monitored by continuous measurements (monitoring) of thermophysical properties too. Pulse Transient Technique that belongs to a group of dynamic methods for measurement of thermophysical parameters can be used for the quality control in material testing.

The problems connected with deficiency in a large amount of testing material cause some problems in data evaluation as an ideal model assumes already infinitively large specimen or cylinders. The finite geometry of the specimen cause additional effects that harm the accuracy of measurement. The particular contributions to uncertainty comes form additional effects caused by differences in ideal and real sample geometry. The main effects are the heat losses from the sample surface; the heat capacity of the heat source and technically the heat pulse of certain duration that is not ideal Dirac function. In this paper we discuss the given problem for cuboid shape samples.

2. Subject and Methods

Principle of the Pulse transient method

In principle the planar heat source generates the heat pulse. A temperature response to the heat pulse is recorded by thermocouple placed at distance h from the heat source (Fig. 1). In an ideal case of unlimited sample size the temperature response is described by function

$$T(h,t) = \frac{2 \cdot Q}{c \rho \sqrt{\kappa}} \left[\sqrt{t} \cdot i \Phi^* \left(\frac{h}{2\sqrt{\kappa t}} \right) - \sqrt{t-t_0} \cdot i \Phi^* \left(\frac{h}{2\sqrt{\kappa(t-t_0)}} \right) \right] \quad (1)$$

For the maximum of the temperature response there were derived simple formulas for evaluation $\kappa = h^2/2t_m \cdot f_\kappa$, $c = Q/\sqrt{2\pi e \rho h T_m} \cdot f_c$ and $\lambda = \kappa \cdot c \cdot \rho$ [1]. This we call one point evaluation procedure. Description of used variables one can find in [1, 3 and 4].

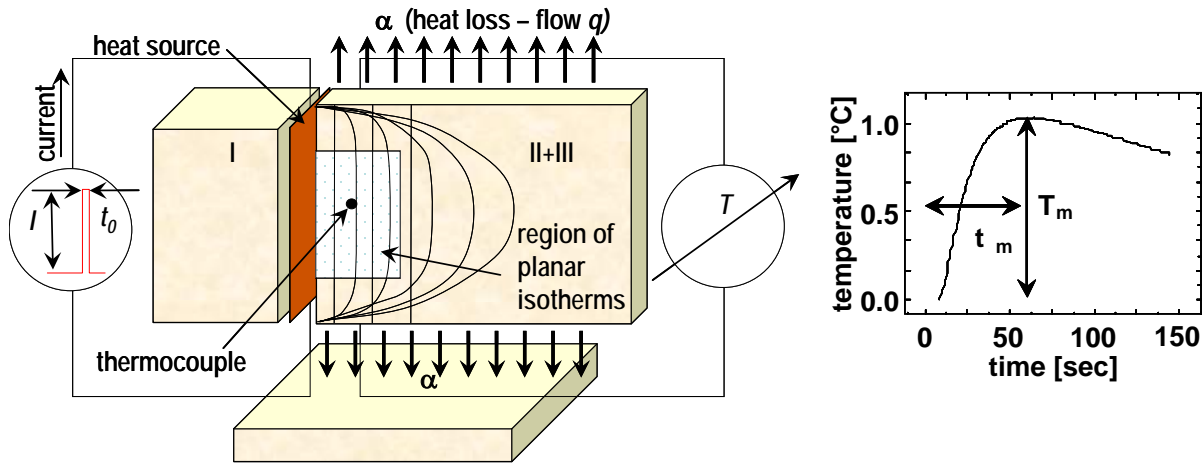


Fig. 1. Wiring diagram and the sample set. In between three parts of a sample set a planar heat source and thermocouple are inserted. In the sample cut it is illustrated a problem with deformed temperature equipotentials. Non influenced temperature equipotentials are planar and are depicted in a white region for shorter times of measurements or lower thicknesses. They are deformed later in time, especially for bigger thicknesses of materials. An example of temperature response in on the right.

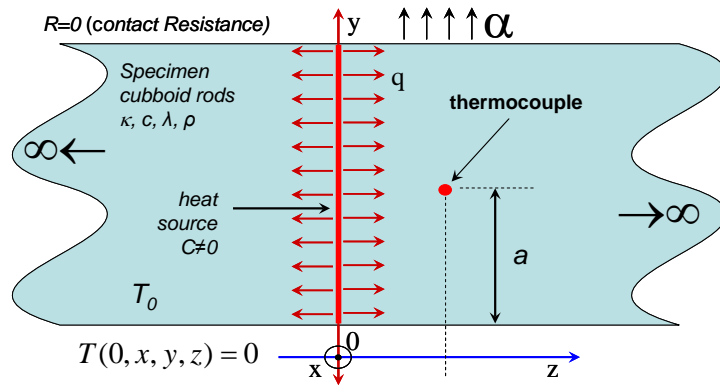


Fig. 2. Initial and boundary conditions for the model. κ , c , λ and ρ are thermal diffusivity, specific heat, thermal conductivity and density of material. T_0 is stabilizes initial temperature of sample.

Mechanism of deformation of planar temperature equipotentials by heat losses effect is drawn on Fig. 1. This effect is evident for specimens having bigger thicknesses or using longer times of the measurements. For this case it was derived a model for cuboid geometry that accounting a heat transfer coefficient α . The solution of temperature response under initial and boundary conditions drawn in Fig. 2. for basic heat equation is the following:

$$T(t, x, y, z) = T_0 \frac{w}{2} \sum_{n=1}^{\infty} \sum_{m=1}^{\infty} \frac{b_n b_m}{v_{nm}} F(u, v_{nm}) \varphi_n \left(\frac{x}{a} \right) \varphi_m \left(\frac{y}{a} \right) \quad (2)$$

where variables are

$$\varphi_n(s) = \sqrt{\frac{2\beta}{\beta + \sin^2 \mu_n}} \cos(\mu_n s), \quad F_n(u, v) = e^{-2uv} \Phi^*(u-v) - e^{2uv} \Phi^*(u+v), \quad T_0 = \frac{qa}{\lambda}, \quad \beta = \frac{a\alpha}{\lambda},$$

$$u = \frac{z}{\sqrt{\lambda kt}}, \quad w = \frac{\sqrt{kt}}{a}, \quad v_{mm} = w\sqrt{\mu_n^2 + \mu_m^2}, \quad b_n = \varphi_n(0) \frac{\sin(\mu_n)}{\mu_n} \text{ and } T \text{ temperature, } t \text{ time, } z \text{ axial}$$

space coordinate, x, y transversal space coordinates, $2a$ transversal size of the sample, q heat flow density at source, λ thermal conductivity, k thermal diffusivity, α heat transfer coefficient for sample – ambient interface, $\Phi^*(u)$ is the complementary error function, μ_n are the roots of equation $\beta \cos \mu - \mu \sin \mu = 0$.

Theoretical calculation of model uncertainty

This type of uncertainty arising from different sources and includes errors in the data, parameter estimation procedure and model structures. They are all propagated through the model for uncertainty analysis and their relative importance is quantified via sensitivity analysis. This type of uncertainty should be supposed as systematic error. The uncertainty analysis was developed in respect with experimental data set $\{t_n, T_n\}_{n=1}^N$, where N is the number of measurements. Model temperature function $T_{model} = f(t, a, b)$ represents temperature response in time that depend on constants $b = \{b_j\}_{j=1}^{N_b}$ in model are determined by different independent measurements and dependent random variables represented by set of free parameters $a = \{a_i\}_{i=1}^{N_a}$ that are evaluated by fitting procedure. We used least square optimization to search for $\min \left\{ \sum_{n=1}^N [T_n - f_n(a, b)]^2 \right\}$, where $f_n(a, b) = f(t_n, a, b)$, t_n is deterministic parameter, $b, \{T_n\}_{n=1}^N$ are independent random variables. The least square optimization gives the system of non-linear equations that based on sensitivity coefficients (Fig. 3.).

$$\sum_{n=1}^N (T_n - f_n) \frac{\partial f_n}{\partial a_i} = 0, \quad i = 1, 2, \dots, N_a \quad (3)$$

Uncertainty of the model is given by formula $u(a_i)^2 \sim \langle (a_i - \langle a_i \rangle)^2 \rangle = \langle (\Delta a_i)^2 \rangle \sim \langle (da_i)^2 \rangle$.

Differentiating equation (3) we obtain system of equations (correlation matrix)

$$\sum_{i=1}^{N_a} A_{ki} da_i = \sum_{n=1}^N dT_n \frac{\partial f_n}{\partial a_k} + \sum_{j=1}^{N_b} B_{kj} db_j, \quad k = 1, 2, \dots, N_a \quad (4)$$

for which we estimated uncertainty contribution of any particular measurement of involved parameters like T or b. Then for relative uncertainties we can write the equation

$$u_r(a_k)^2 = C_{kT}^2 \frac{u(T)^2}{a_k^2} + \sum_{j=1}^{N_b} v_{kj}^2 u_r(b_j)^2 \quad (5)$$

3. Results

Experimental data measured in RTB1.02 chamber with temperature stability of 0.01 K are plotted in Fig. 4. Data under the air and vacuum atmosphere were obtained in the temperature range from -22 up to 70°C. Temperature responses were measured for the pulse width of 3 and 6 seconds. The total time of the recording was up to 370 seconds. Two temperature models were used for data evaluation. First model consider final pulse width and evaluation procedure based on formulas derived for maximum of the temperature response published in several papers [3, 4]. The second one uses fitting procedure and model assuming cuboid

samples having squared cross section and heat losses from the sample surface (Eq. 1.). The sandstone specimen set was carved in a form of cuboids having finite length. The dimensions of parts I and III were 50x50x30 part II 50x50x10mm. The volume density was 1738.7 kg m⁻³. Porosity measured by weighting dry and water saturated specimen was 27.5%.

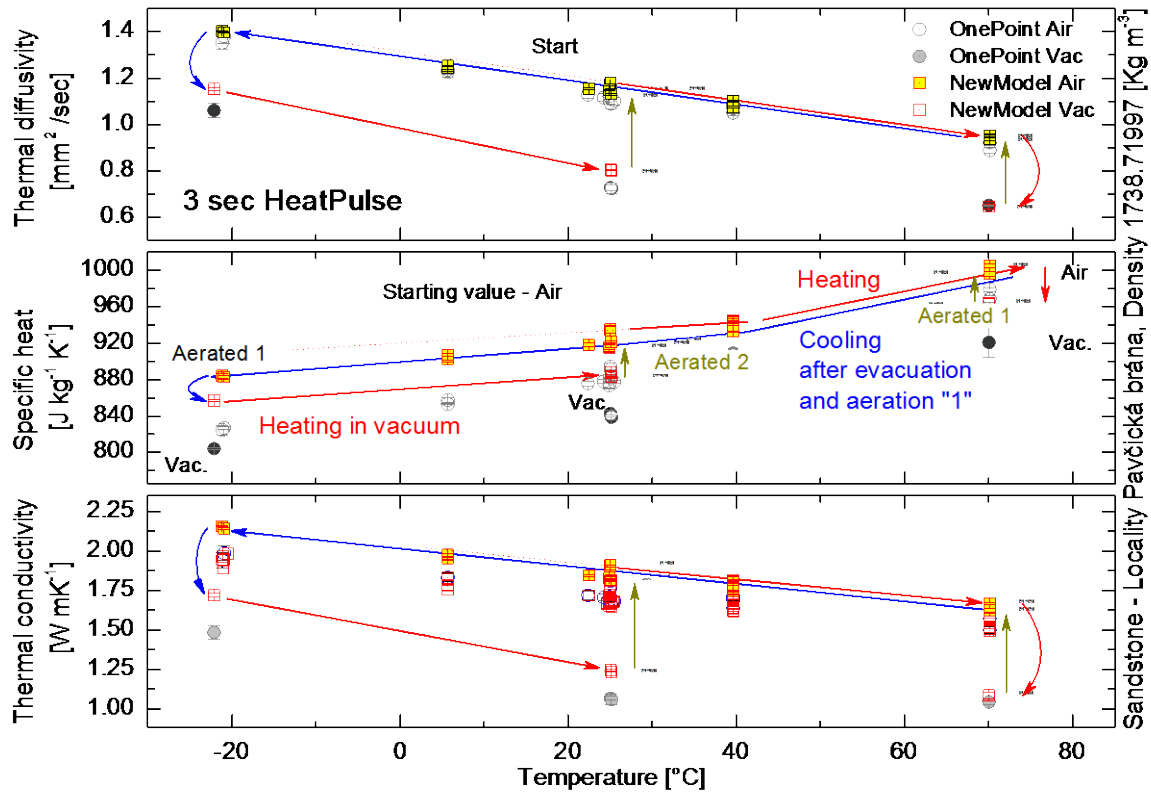


Fig. 3. Thermophysical parameters estimated by model fitting. The temperature history as well as vacuum treatment follows the arrows denoting heating and cooling regime. The shifted temperature dependency of evacuated data follows the measurements performed under the air atmosphere. Annealing and the vacuum treatment causes lowering of all thermophysical parameters due to removing of remanent water from pores and structure of sandstone (compare red and blue arrows of first heating and cooling).

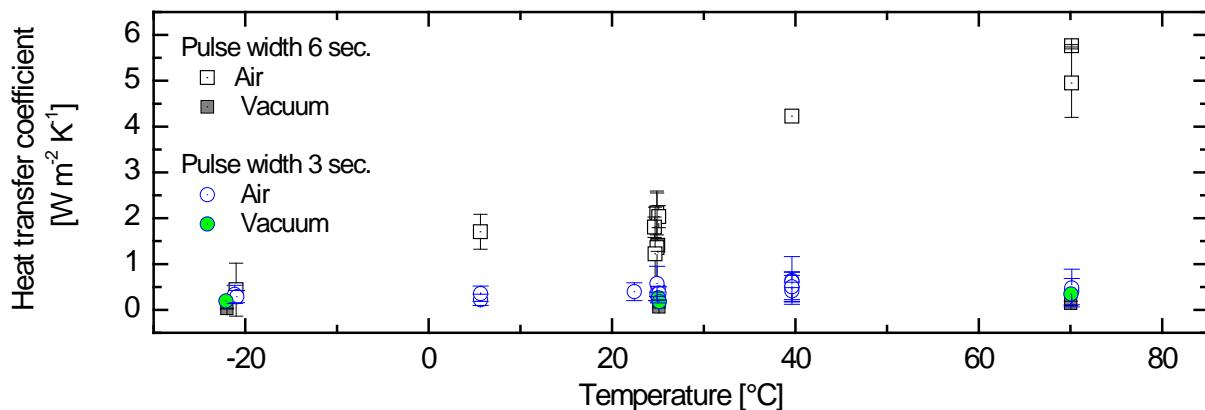


Fig. 4. Heat transfer coefficients calculated by fitting procedure for 3 and 6 second of pulse duration as well as for air and vacuum conditions. The low values are for 3 seconds of pulse duration as well as for data measured under the vacuum. This is the consequence of sensitivity for this parameter only for bigger thicknesses of material or higher times of measurement of temperature response. The positive temperature dependence of this parameter is evident for 6 seconds pulse width. The heat transfer coefficient from the sample surface to the surrounding is temperature dependent.

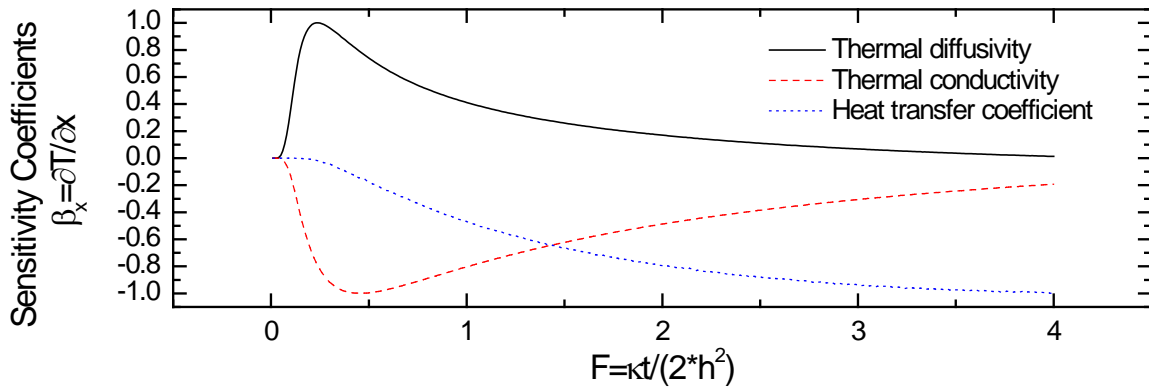


Fig. 5. Normalized sensitivity coefficients derived from temperature function given by Eq. 1. $\beta_p = \partial T / \partial p$ where p denotes free parameter in model, e.g. thermal diffusivity, thermal conductivity and heat transfer coefficient. The normalized sensitivity coefficients in Fig. 5. were calculated for values of thermophysical parameters like those one measured in experimental part and are give in Fig. 3. Optimized region for data evaluation is up to value of $2F$ in dimensionless time

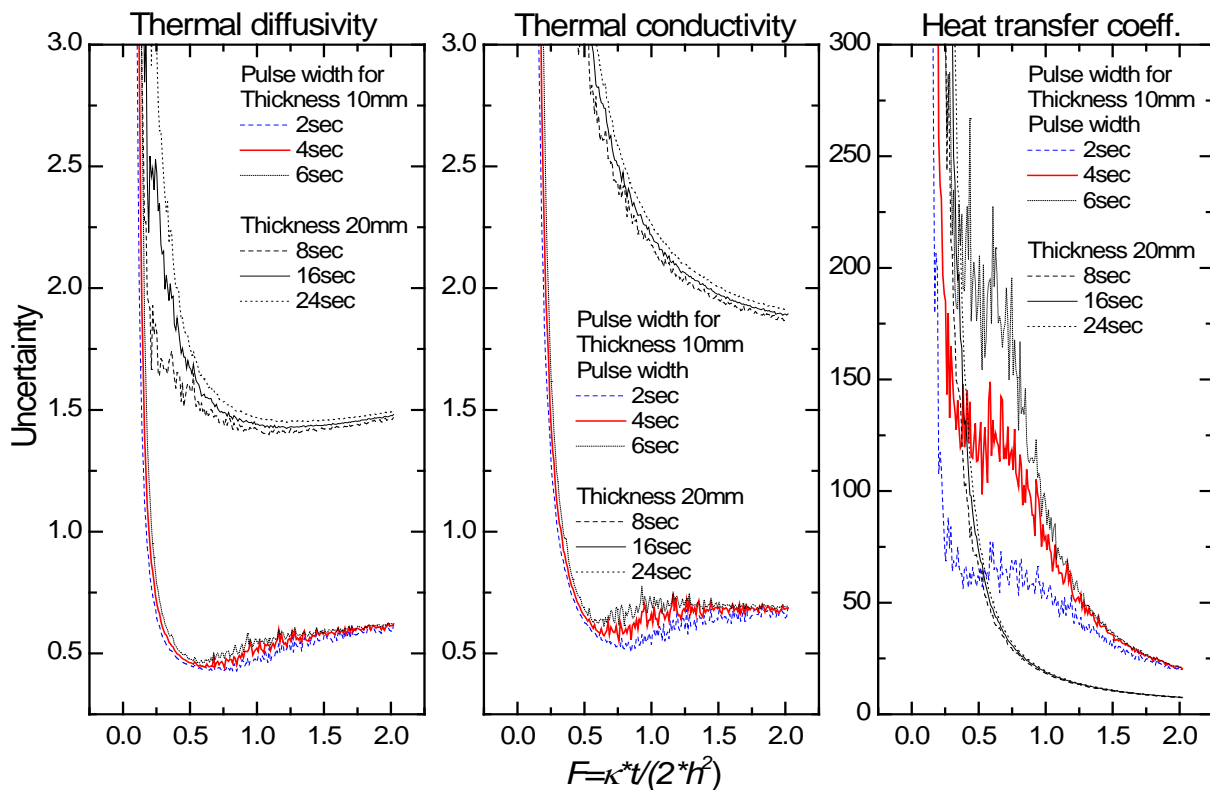


Fig. 6. Uncertainty analysis for sample thickness of 10mm at 2, 4 and 6 seconds of pulse width and thickness 20mm for 8, 16 and 24 seconds of pulse duration. The maximum of temperature response is at $0.5 F$. This concludes the discussion on the total time of transient record measurement.

Measured thermophysical parameters of porous sandstone depend on quality of material and the moisture content in pores. Temperature dependency of transport parameters (thermal diffusivity and thermal conductivity) are of negative slope, while the specific heat have positive slope in a give temperature range from -22 up to 70°C (Fig. 4). Differences in all parameters after evacuation and aeration were caused by drying process in vacuum as well as at the elevated temperatures. The calculated values of heat transfer coefficients are in Fig. 4.

Analysis of uncertainty (Fig. 6.) was calculated for fixed number of points in evaluation time interval, variable time step and fixed time window that begin at $t=0$ sec. Each data point represents different length of the time interval but the number of points in each interval is the same to preserve statistical weight of the calculation results. Fig.6 illustrates the correlation of uncertainties and the time of the measurement as well as the thickness of the sample. It explains why the heat transfer coefficient is possible to evaluate only from data measured at longer times (6 sec. pulse width data at Fig. 5.). The reason is that the sensitivity for this parameter is higher for longer times of measurements. Heat loss effect starts to influence the measurement at higher times and at higher thicknesses of material. Uncertainty of estimation of the heat transfer coefficient is decreasing with increasing thickness of the sample as well as with increasing time of the measurement. The similar situation we found at uncertainty calculations for thermal diffusivity and thermal conductivity. Their values are decreasing with time and after getting maximum of the temperature response at $0.5F$, e.g. about 42 seconds in real time axes it starts to slightly increase. This means that there is no reason for the increase of the measurement time higher than $1.5 \div 2F$ (280÷370sec. for this sandstone material).

4. Conclusions

The thermophysical properties of sandstone were investigated by pulse transient method for dry state. The data were evaluated by procedures of one point evaluation and by fitting by new model for cuboid samples that accounts heat losses from the sample surface.

The uncertainty analysis of the new model was analyzed in the Fig. 5 and Fig. 6. Data illustrates the sensitivity on the heat transfer coefficient in regarding the time of the measurement as well as geometry of the specimen. This parameter affects the measurement with increasing time of the measurement or at higher thicknesses of the sample. The heat transfer coefficient is not possible to estimate unambiguously for lower times of measurement. The values measured in vacuum are practically the same over all temperature range and also for the data measured for shorter pulse width (3sec.).

Acknowledgements

The data used for the analysis were obtained thanks to support of the grant VEGA 02/161/08. Presented analysis was elaborated in preparing stage for project APVV-0641-10 Study of rocks properties and investigation of structural and textural characteristic in correlation with thermophysical and physico-mechanical properties that starts in may 2011.

References

- [1] Kubičár Ľ, 1990, *Pulse Method of Measuring Basic Thermophysical Parameters*. in Comprehensive Analytical Chemistry Vol. XII Thermal Analysis Part E Ed Svehla G, Amsterdam, Oxford, New York, Tokyo: Elsevier, pp 350.
- [2] Beck, J.V.;Arnold, Kenneth J., *Parameter Estimation in Engineering and Science*, ISBN: 9780471061182, Better World Books (Mishawaka, IN, U.S.A.) John Wiley & Sons, 1977
- [3] Boháč V., Kubičár Ľ., Vretenár V., *Investigation of heat transport in porous materials by pulse transient method*, HIGH TEMP-HIGH PRESS. 2003/2004, Vol. 35/36, pp 67-74
- [4] Boháč V, Dieška P, Kubičár Ľ. *The Heat Loss Effect at the Measurements by Transient Pulse Method*, MEASUREMENT SCIENCE REVIEW, Volume 7, Section 3, No. 2, 2007 pp 24-27

Synchrotron X-ray Diffraction Study of the Crystallization Process in the As-Prepared Amorphous Fe–Mo–Cu–B System

¹M. Pavúk, ^{1,2}M. Miglierini

¹Department of Nuclear Physics and Technology, Slovak University of Technology,
Ilkovičova 3, 812 19 Bratislava, Slovakia,

²Centre for Nanomaterial Research, Šlechtitelů 11, 783 71 Olomouc, Czech Republic
Email: milan.pavuk@stuba.sk

Abstract. The crystallization of amorphous $Fe_{79}Mo_8Cu_1B_{12}$ alloy was studied *in situ* using X-ray diffraction of synchrotron radiation. Both sides of the ribbon shaped samples were investigated. The onset temperature of crystallization, the volume fraction of primary crystalline phase, and the speed of the development of structural transformation were determined from analysis of the shape of diffraction maximum located at the position of the main *bcc*-Fe reflection. The surfaces of the ribbon showed the differences in these parameters.

Keywords: Synchrotron, X-ray Diffraction, In Situ, Crystallization, Amorphous Alloy

1. Introduction

Today, there is an opportunity to study structural transformations *in situ* using intense beams of synchrotron radiation. Ideal materials for such studies are amorphous Fe–*M*–B alloys, where *M* denotes a transition metal. They are produced by rapid solidification from the melt and serve as precursors for the production of nanocrystalline alloys commercially known as NANOPERM [1]. Nanocrystalline state is achieved by annealing the amorphous precursors at optimal temperature. The temperature must be higher than the onset temperature of the first stage of crystallization so that the formation of nanocrystallites in amorphous matrix may occur. The temperature should not reach the second stage of crystallization which is accompanied by formation of borides and larger grains which deteriorate soft magnetic properties. In the optimal structural state the alloy consists of nanocrystalline *bcc*-Fe phase with grain size about 20 nm and residual amorphous matrix.

The aim of this work was to study quantitatively the evolution of primary crystalline phase at each side of the ribbon during crystallization of amorphous $Fe_{79}Mo_8Cu_1B_{12}$ alloy. To achieve this goal highly intense beams of synchrotron radiation were employed. The diffraction patterns were recorded by a two-dimensional detector.

2. Subject and Methods

Amorphous $Fe_{79}Mo_8Cu_1B_{12}$ alloy was prepared by planar flow casting technique. The casting operation was carried out in air. The result of this process is a metallic glass in the form of ribbon. The ribbon is 20–22 μm thick and 10 mm wide. The chemical composition of the glassy alloy was checked by emission spectrometry with inductively coupled plasma. To prepare samples for experiments the ribbon was cut into approximately 2 cm long pieces using ceramic scissors.

Structural transformations during heating with a rate of 10°C/min were recorded by diffraction of synchrotron radiation with the energy of 7 keV ($\lambda = 0.177$ nm) at the KMC-2 beamline at the BESSY synchrotron radiation facility in Berlin (Germany). Radiation diffracted into the region around the main (110) reflection of *bcc*-Fe phase was registered by

two-dimensional area detector HI-STAR (Bruker AXS, USA). Acquisition of the data was performed every 10 seconds. The position of detector was fixed during temperature run. Angular resolution in diffraction patterns is $0.03^\circ 2\theta$. For quantitative analysis of X-ray diffraction patterns the PeakFit 3.0 (Jandel Scientific, CA) software was used.

Arrangement of the diffraction experiment was as follows: The sample in the original amorphous state was fixed by hold down clamps to tantalum plate which was firmly screwed to the Boralectric[®] heater (Tectra GmbH, Germany). The whole system was covered with a hemispherical beryllium window (the so-called dome) which allowed vacuum annealing of the investigated sample and also an undisturbed passage of synchrotron radiation. The pressure inside the furnace was lower than 10^{-3} Pa. There were three type K thermocouples used to monitor the temperature inside the furnace. One was connected to the heated plate, the second one to the Ta plate, and the last was in direct contact with the sample. We have used one of the clamps to secure the thermocouple and maintain a good contact with the sample.

An evacuated cone, which minimized scattering of radiation in the air, was attached in front of the detector. It was covered with a polymer foil and extended up to the proximity of the beryllium dome.

The sample was continuously heated up to the temperature of 800°C . The temperature increase was linear with a ramp of $10^\circ\text{C}/\text{min}$. After reaching 800°C , the sample was annealed for 2.7 minutes. After that time the heating was turned off and the temperature inside the furnace started to drop spontaneously. The time-to-temperature profile was set using a programmable Eurotherm 2604 (Eurotherm Limited, UK) temperature controller.

With respect to the different surfaces of the ribbon we will use the following denotation. The side of the ribbon, which was in contact with the quenching wheel during the production – optically matte, will be denoted as the wheel side. The side of the ribbon, which was exposed to the surrounding atmosphere in the production process – optically glossy, will be denoted as the air side.

3. Results

During heating 2-D diffraction patterns were acquired which were subsequently integrated over all χ angles. The obtained profiles were arranged into 3-D images depending on temperature. The obtained 3-D mappings from both sides of the ribbon are presented in Fig. 1. Both 3-D records show gradual formation of the (110) reflection which corresponds to a *bcc* phase with increasing temperature. In the second stage of crystallization, the creation of cubic Fe_{23}B_6 phase and subsequently the tetragonal Mo_2FeB_2 phase can be observed.

Using diffraction of synchrotron radiation we were able to trace the onset temperature of primary crystallization T_{x1} *in situ* in each specimen. Individual temperatures T_{x1} were determined to be of 410°C and 392°C for the air and the wheel side, respectively.

Relative volume fraction of crystalline *bcc*-Fe phase was determined from the reflection of the main diffraction line (110). A typical X-ray diffraction pattern of partially crystalline $\text{Fe}_{79}\text{Mo}_8\text{Cu}_1\text{B}_{12}$ sample is illustrated in Fig. 2. It also shows the decomposition of the main diffraction line into its corresponding components, i.e. relative contributions originating from crystalline phase and amorphous rest. For determination of the envelope of the narrow reflection, Lorentzian and Gaussian line profiles were used. The amorphous phase was described by Voigt line profile. The relative area of the profiles is proportional to the relative fraction of each phase.

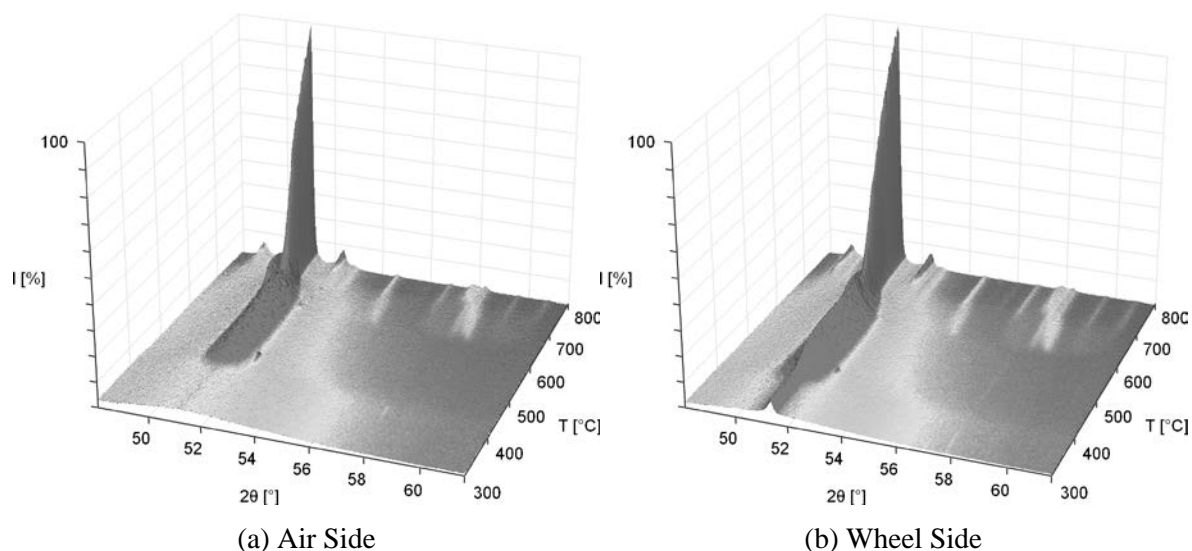


Fig. 1. Diffractograms of the $\text{Fe}_{79}\text{Mo}_8\text{Cu}_1\text{B}_{12}$ alloy measured *in situ* during linear heating with the rate of $10^\circ\text{C}/\text{min}$ and arranged into three-dimensional record: (a) the air side of the ribbon, (b) the wheel side of the ribbon.

From the quantitative analysis of 1-D diffraction patterns of the as-quenched $\text{Fe}_{79}\text{Mo}_8\text{Cu}_1\text{B}_{12}$ alloy it was found that a considerable amount of crystalline *bcc*-Fe(Mo) phase occupying 8.2% of the total volume is located at the wheel side of the ribbon. During casting, this side of the ribbon is expected to have better conditions for solidification of the melt (mainly due to higher cooling rate). However, this phenomenon occurs at the opposite side as we have expected. Contribution of the crystalline phase at the air surface of the ribbon is as low as 0.6 vol.%. The hypothesis is proposed that heat removal was sufficient but the alloy was still located at the boundary of glass forming ability as a consequence of low concentration of boron. Therefore additional factors which can initiate the crystallization began to manifest. These include defects or impurities at the wheel side of the ribbon which can act as base of heterogeneous embryos.

Besides *bcc*-Fe(Mo) nanocrystals, traces of tetragonal Mo_2FeB_2 phase were unveiled in the amorphous matrix of the as-quenched alloy. Indications of this phase are visible as bright spots of incomplete Debye rings in 2-D patterns. Quantification of its contribution from 1-D pattern would be difficult, but considering a high scattering factor of Mo_2FeB_2 phase we can clearly say that its contribution to the amount of other present phases (*bcc*-Fe(Mo) and mainly the amorphous rest) is at this point negligible.

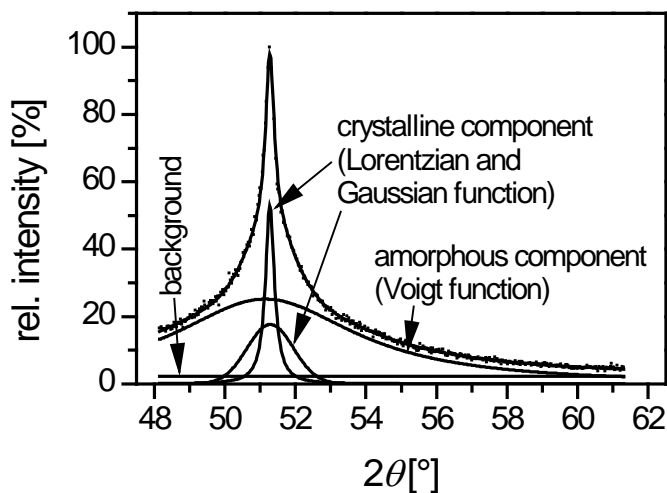


Fig. 2. X-ray diffractogram of the wheel side of the $\text{Fe}_{79}\text{Mo}_8\text{Cu}_1\text{B}_{12}$ ribbon and its decomposition into corresponding components. It was measured *in situ* at a temperature of 410°C .

Quantitative assessment of the evolution of the crystalline *bcc*-Fe(Mo) phase in the Fe₇₉Mo₈Cu₁B₁₂ alloy is shown in Fig. 3. After the onset of primary crystallization at 392°C, we observe a linear increase in relative volume fraction of crystalline *bcc*-Fe(Mo) phase with the slope of 0.64 vol.%/°C on the wheel surface of the Fe₇₉Mo₈Cu₁B₁₂ ribbon. It should be noted that this surface had already some quenched-in Fe-rich nanocrystals with *bcc* structure in initial stages of structural transformation. On the air surface, the onset temperature of crystallization is located at 410°C and evolution of the principal crystalline *bcc* phase is more rapid with the slope of 1.17 vol.%/°C. At the temperature of 590°C the alloy studied exhibit about 52% of the volume fraction of the crystalline phase.

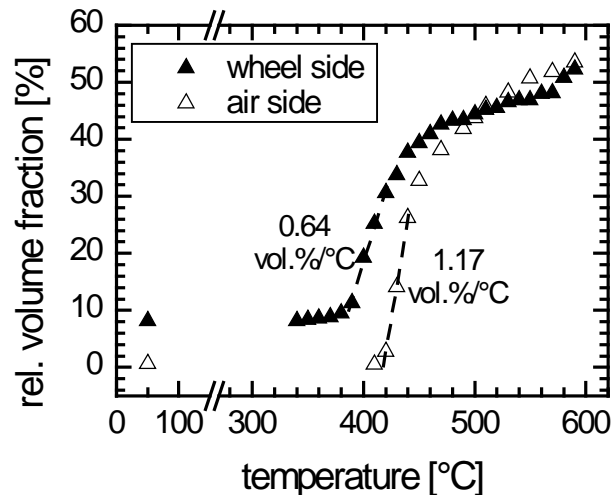


Fig. 3. Temperature evolution of the relative volume fraction of the crystalline *bcc*-Fe(Mo) phase in the Fe₇₉Mo₈Cu₁B₁₂ alloy.

4. Discussion

This work was focused on structural transformations which are taking place in NANOPERM-type alloy with the composition of Fe₇₉Mo₈Cu₁B₁₂ during thermal treatment. Attention was focused mainly on investigation of surface layers utilizing rarely used analytical technique such as *in situ* temperature scans of diffraction of synchrotron radiation.

Analysis of X-ray diffraction results obtained from Fe₇₉Mo₈Cu₁B₁₂ alloy in the as-quenched state has shown that significant amount of crystalline *bcc*-Fe(Mo) phase (~8 vol.%) is located at the wheel side of the ribbon. In addition, the crystallization starts earlier at this side of the studied ribbon.

Acknowledgements

The authors express their thanks to Dr. I. Zizak for his assistance in operating the KMC-2 end station and to Dr. D. Janičkovič for preparation of the amorphous ribbon. This work was supported by the grants VEGA 2/0192/10, SK-PL-0013-09 and MSM6198959218.

References

- [1] Suzuki K, Kataoka N, Inoue A, Makino A, Masumoto T. High saturation magnetization and soft magnetic properties of *bcc* Fe-Zr-B alloys with ultrafine grain structure, *Materials Transactions, JIM*, 31 (8): 743-746, 1990.

Development of a Scatterometer for Spatial Distribution Measurements of Reflected and Transmitted Light from Diffuse Surfaces

^{1,3}E.Kawate, ^{1,2}M.Hain

¹AIST, 1-1-1, Central 2, Umezono, Tsukuba, Ibaraki 305-8568, Japan

²Institute of Measurement Science, Slovak Academy of Sciences, Bratislava, Slovakia

³TRAS, Inc., 725-28 Shimohirooka, Tsukuba, Ibaraki 305-0042, Japan

E-mail address: e.kawate@aist.go.jp

Abstract. *A new device is comprised of two ellipsoidal mirrors of revolution and an optical detection system. It enables the absolute measurements of the reflectance and transmittance and the spatial distribution measurements of light scattering from almost all materials. The optical detection system is developed to measure total photo-intensity using a photodiode and to capture the imaging data using a CCD camera. This results in faster, more complete and often more accurate measurements than can be achieved with traditional goniometric methods and integrated sphere methods. The absolute total integrated reflectance and transmittance of well-known samples were measured and the spatial distribution of light scattering from a diffraction grating was captured and evaluated.*

Keywords: STAR GEM, CCD Camera, Fish-Eye Lens, Absolute Diffuse Reflectance

1. Introduction

Scattering measurements provide us with material characterization based on scatter for metals, plastics, paper, textiles and also with surface treatment characterization based on scatter for cleaners, polishes, paints, coatings. Not only TIR/TIT (Total Integrated Reflectance/Transmittance) but also BRDF/BTDF (Bi-directional Reflection/Transmission Distribution Function) are mainly measured in the scattering measurements. Traditionally BRDF/BTDF measurements are performed using goniometric systems, which involve tilting and rotating a sample or detector about the sample center in order to measure the BRDF/BTDF at selected points on the sphere around the sample, but these systems are relatively slow, potentially requiring hours to measure the sample.[1] Nominally TIR/TIT measurements are made by integrating the BRDF/BTDF over a portion of the sphere around the sample, but actually they are measured using an integrating sphere. Although the measurement using the integrating sphere is fast, it is made only at a designed angle of incidence and the measurement of the spatial distribution can't be made.

Almost all devices for the measurements of reflectance and transmittance have not been designed to scrutinize spectra measured by the devices themselves. A way of the scrutinization of the spectra is to measure both reflectance and transmittance spectra with the same accuracy at the same time and to compare the spectra with the law of energy conversation. Thus the accuracy of the measured spectra can be estimated. We have already completed this scrutinization method for the measurements of reflectance and transmittance of specular samples using a STAR GEM[®] (Scatter, Transmission and Absolute Reflection measurements using a Geminated Ellipsoid Mirror) and the method is called a self-diagnosis [2] of measured spectra.

Because reflection and transmission around us are diffusive with a few exceptions like mirrors and windows, the spatial distribution of the scattered light as well as absolute reflectance (transmittance) is important. Our goal is to develop a STAR GEM type 3, which allows high-precise absolute reflectance (transmittance) measurements based on the spatial distribution measurements of the scattered light using a CCD camera.

2. Structure of a STAR GEM type 3

Until the early 1980s a hemi-ellipsoidal mirror had been studied as a scatterometer.[1] A fatal flaw is inter-reflections between a sample and a detector, which are located at two focuses, through the intermediation of the ellipsoidal mirror. When the reflectance of a sample becomes higher, this inter-reflection becomes larger. For example, Sullivan and Allen [1] estimated the size of the inter-reflection error by employing an averaging sphere at the detector focus. For an actual sample reflectance of 0.70, inter-reflections would cause the reflectance to be measured as 0.77.

A STAR GEM is comprised of two ellipsoidal mirrors of revolution and an optical detection system. The previous STAR GEM intended to measure both reflectance and transmittance of specular samples is composed of two belt-shape ellipsoidal mirrors. The belt-shape ellipsoidal mirror in Fig. 1(a) was fabricated by cutting an ellipsoid along two planes at the same distance from an equatorial plane and also along a plane perpendicular a rotation axis through one focus. A sample is placed at a common focus and two rotating mirrors are placed at two remaining focuses. Because the light source and detector are placed outside the ellipsoidal mirrors, the inter-reflection becomes negligible.

In the scatterometer the sample and optical detection system must be placed at the common focus and third focus, respectively, and are facing toward the ellipsoidal mirror. These setups are the same as those in the previous scatterometer with the hemi-ellipsoidal mirror. In order to reduce the inter-reflection, two kinds of ellipsoids were prepared, a quarter ellipsoid in Fig. 1(b) and an octantal ellipsoid in Fig. 1(c). The quarter was fabricated by cutting an ellipsoid along the equatorial plane and also along a plane perpendicular the axis through one focus, so that a volume ratio of the quarter to a whole ellipsoid is larger than quarter but a solid angle of the quarter looked by the sample is π steradians. The octant was cut the quarter in half and a solid angle is $\pi/2$ steradians.

An example of a scatterometer using the belt-shape (E1) and quarter (E2) ellipsoidal mirrors is shown in Fig. 2 and Fig. 3, where a common focus (F0), a focus (F1) of the E1 mirror and a focus (F2) of the E2 mirror are aligned. A sample is placed at F0, a plane rotation mirror (RM1) is placed at F1 and the optical detection system is placed at F2. The reason why the belt-shape was chosen as an incoming ellipsoid is to make the absolute measurements of both reflectance and transmittance using a modified symmetry X method. The second reason is to reduce the inter-reflection with decreasing the E1 mirror area. The third is to change an incident angle to the sample by the rotation of the RM1 mirror.

The symmetry X method [3] was invented to measure absolute reflectance of a specular sample. When two optical paths measuring reflection from the sample agree everywhere with two optical paths measuring background without the sample, the optical loss at all optical components is completely compensated by the calculation of the geometric means of four light intensities. Consequently, the absolute reflectance of the sample can be obtained.

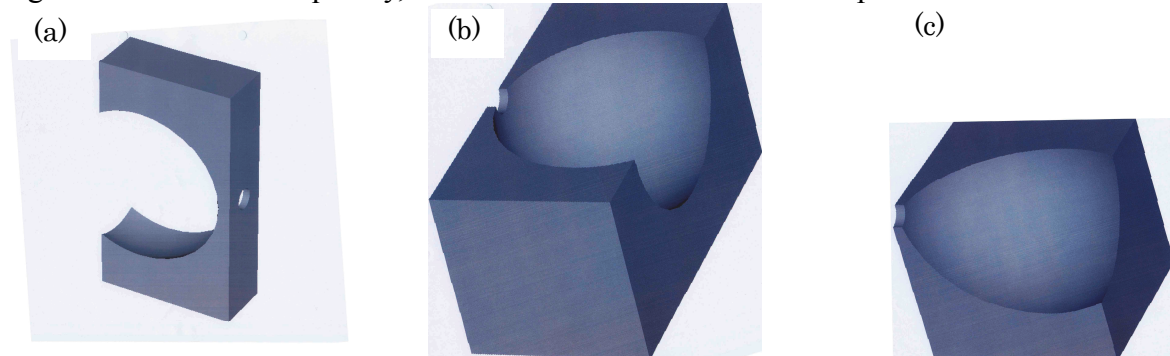


Fig. 1(a), (b), (c) A belt-shape, a quarter, and an octantal ellipsoidal mirrors, respectively.

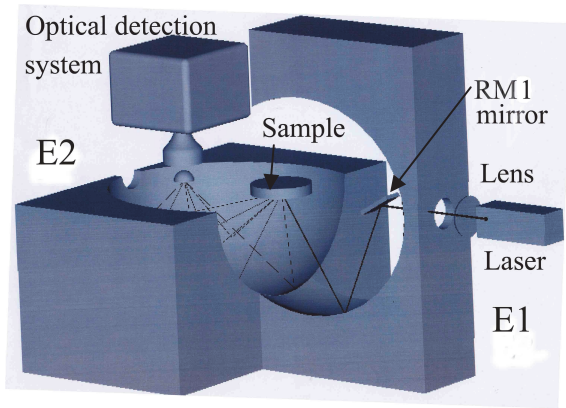


Fig. 2 STAR GEM type 3

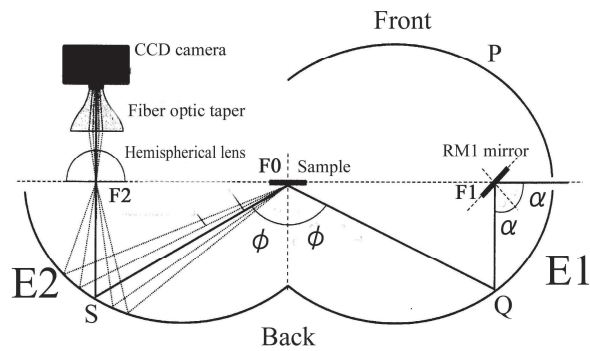


Fig. 3 Sectional drawing of STAR GEM type 3. Reflection measurement mode (RBB)

The modified symmetry X method is explained as follows. In Fig.3 the E1 mirror and RM1 mirror can be rotated independently around the axis of the ellipsoid and around the axis perpendicular the equatorial plane, respectively. Upper and lower sides of the scatterometer are named Front and Back, respectively. For the background measurement the RM1 mirror looks at the upper side, one optical path is a sequential line of F1-P-F0-S-F2 denoted by BFB. The other path is a sequential line of F1-Q-F0-S-F2 by BBB, when the E1 mirror is rotated by 180 degrees. For the reflection measurement the RM1 mirror looks at the lower side and the sample is placed at F0 and light reflected from the diffuse sample spreads around S, one optical path is a sequential line of F1-Q-F0-around S-F2 denoted by RBB. The other path is a sequential line of F1-P-F0-around S-F2 by RFB, when the E1 mirror is rotated by 180 degrees. Thus two reflection paths of RBB and RFB agree everywhere with two background paths of BFB and BBB, if the sample is specular. If the sample is diffuse, two paths of RBB and RFB agree partially with two paths of BFB and BBB.

The optical detection system at F2 is composed of a hemispherical lens, a fiber optic taper and a photo-detector such as a CCD camera and a photodiode. The hemispherical lens at F2 has a function of a fish-eye lens. The diameter and refractive index of the lens made of S-LAH79 (Ohara) are 10mm and 2.003, respectively. The focal plate obtained from the ray tracing is a curved surface and coincides with a large aperture of the fiber optic taper as shown in Fig.4. Its small aperture also coincides with an image sensor of the CCD camera. The angular resolution of the system is determined by the number of pixels on the image sensor and is about 0.5 degrees (0.0003 steradians). The weak point of the system is that the image at a surrounding area is compressed too much.

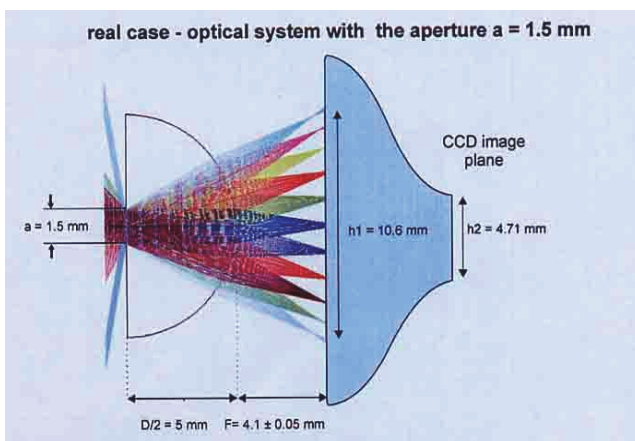


Fig. 4 Focal plate of a hemispherical lens

Red curve: with a hemispherical lens
Black curve: without a hemispherical lens

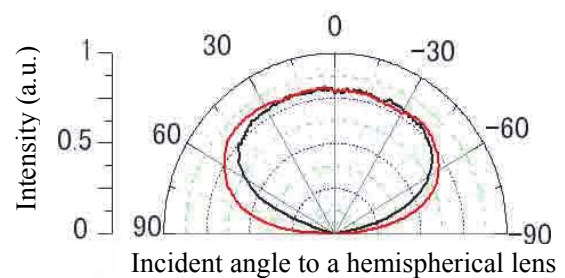


Fig. 5 Efficiency of a hemispherical lens

3. Results and Discussions

A light source was a He-Ne laser of 633 nm. The effect of the hemispherical lens was studied. The optical detection system was only a hemispherical lens and a Si photodiode, which is located at the focal plate. A beam was scanned along a semicircle of the quarter by rotating the E1 mirror with a fixed RM1 mirror. In Fig. 5 red curve was obtained with the hemispherical lens and black curve without it. Using the hemispherical lens the visual angle is larger by 30 degrees. Our optical detection system works well as a fish-eye lens.

The absolute reflectance (R) and transmittance (T) measurements of several samples were made according to the modified symmetry X method. The samples were a specular quartz plate, a spectralon as a perfect diffuse material, and two kinds of a frosted quartz of #240 and #1,500 as a partial diffuse material. In Fig 6 open circles, open squares and open triangles are T , R and absorptance ($A=1-R-T$) of the specular quartz, respectively, and solid squares are R of the spectralon. In the range of a small angle of incidence A is almost zero, which is an expected value of the pure quartz and R of the spectralon is almost 0.5, which is also an expected value, because the quarter is looking at π steradians. In Fig. 7 T , R , and A of the frosted quartz are shown. In this case A is not zero but 0.1, because the spatial distribution of light scattering from the frosted samples is not isotropic.

Figures 8 (a) and (b) are the spatial distribution measurements of an irradiation beam and of light scattering from a diffraction grating, respectively. The full width at half maximum is 0.003 steradians from Fig. 8 (a). This value is the angular resolution of our STAR GEM type3.

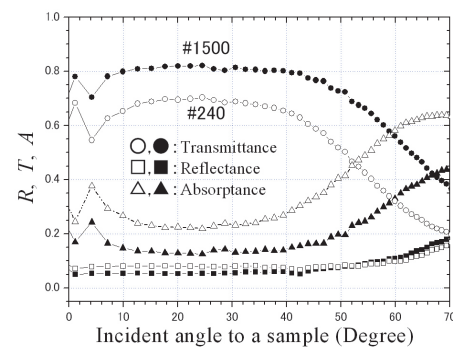
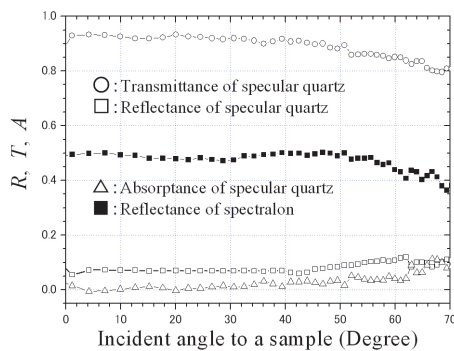


Fig. 6 R , T and A of a specular quartz and spectralon Fig. 7 R , T and A of a frosted quartz of #240 and #1,500

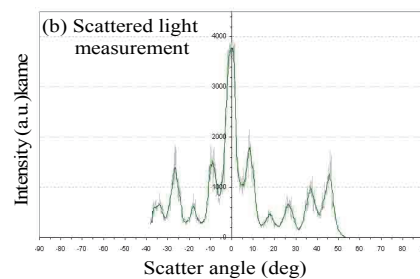
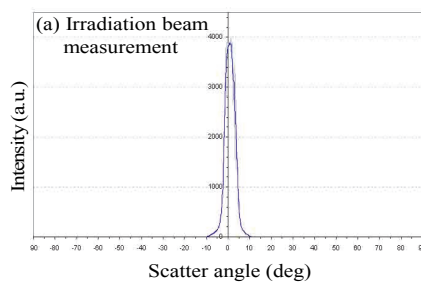


Fig. 8(a), (b) Spatial distributions of an irradiation beam and of light scattering from a grating, respectively

4. Conclusions

A new device, which is comprised of two ellipsoidal mirrors, a hemispherical lens, a fiber optic taper and a CCD camera, has been developed. Absolute reflectance and spatial distribution from diffuse surfaces were measured successfully.

References

- [1] Workman J. and Springsteen A.W., APPLIED SPECTROSCOPY, ACCADEMIC PRESS, San Diego, 1997.
- [2] Kawate E. An optical accessory for absolute reflection and transmission measurements in the wavelength region from 0.24 μm to 25 μm . In proceedings of SPIE, vol. 7065, 2008, 70650M-1-70650M-11
- [3] Kawate E, Symmetry X system and method for absolute measurements of reflectance and transmittance of specular samples, Appl. Opt. vol.42, 5064-5072 (2003)

High Precision Algorithms for Shadow Inspection of 3D Objects in Partially Coherent Light

^{1, 2, 3} Yu.V. Chugui, ^{1, 3} E.S. Senchenko

¹ Technological Design Institute of Scientific Instrument Engineering SB RAS,

² Novosibirsk State University,

³ Novosibirsk State Technical University,
Novosibirsk, Russia

Email: chugui@tdisie.nsc.ru

Abstract. *The peculiarities of 3D object's image formation in a diffraction-limited system using quasi-monochromatic source with finite angular width are presented. The algorithms to determine the geometric parameters of the 3D objects by shadow optical method inspection are proposed. The theoretical results obtained have been experimentally verified.*

Keywords: *3D Diffraction, Shadow Method, Dimensional Inspection, Partially Coherent Source*

1. Introduction

The shadow systems due to their high precision and operation speed as well as broad measurement range are widely used among optical means of noncontact dimensional inspection in industry [1]. The essence of the measurement shadow method consists in finding of the position of object's true boundary. It allows us to determine its different geometrical dimensions, including width, length, holes diameter, etc. In case of flat objects (zero thickness), the true boundary is determined using shadow image thresholding, either at 25 % of light intensity illuminating the object (coherent illumination) or at 50% of intensity (noncoherent illumination) [2]. Under inspection of the extended objects in coherent light the threshold shift takes place [3], which is proportional to Fresnel zone.

Because of known difficulties occurring under the use of coherent illumination (first of all, speckle noises) the more perspective is the partially coherent illumination for inspected 3D objects using, for instance, small-size LED.

The peculiarities of 3D object images formation in a diffraction-limited system under their illumination by partially coherent light are examined. The methods for analytical determination of shift of 3D object image shadow boundary and its correction depending on the object thickness and the optical system parameters are proposed. These algorithms allow us to considerably increase the measurement precision of 3D objects by the shadow method.

2. The Shadow Measurements for 3D Objects in Partially Coherent Light

The optical scheme of the system to realize the shadow inspection method for 3D objects can be seen in Fig. 1a. Source 1 with angular sizes $2\theta_s$ is illuminating 3D object 3 as an extended (thick) edge with width d through objective of lens 2. Projection lenses 4 and 6 are forming its shadow image on photodetector matrix 7. Aperture diaphragm 5 with angular sizes $2\theta_{ap}$ is situated at focal distance f from the lens. The image profile of the 3D object's edge can be seen in Fig. 1b.

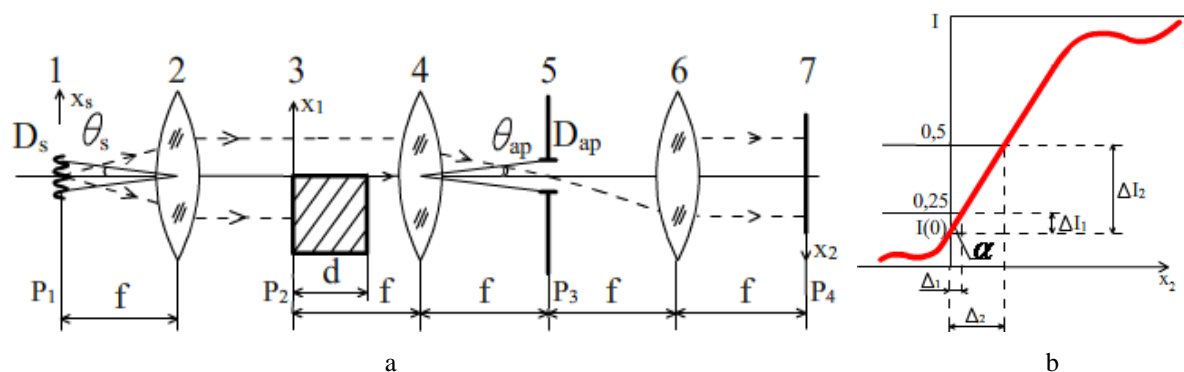


Fig. 1. Formation of 3D object's image in a diffraction-limited system: optical scheme (a); image profile of the 3D object's edge (b).

The value of threshold $I_{thr} = I(0)$ depends on many parameters, including angular size of the light source and the aperture diaphragm, as well as the object's volumetricity. In case of flat objects ($d=0$) illuminated by coherent light the threshold is equal to $I_{thr}^{(1)} = 0,25$ ($\theta_s \rightarrow 0 \text{ rad}$), and by noncoherent light the threshold equals $I_{thr}^{(2)} = 0,5$ ($\theta_s \rightarrow \pi/2 \text{ rad}$). Under partially coherent illumination the threshold becomes within the limits of $0,25 < I_{thr} < 0,5$ ($0 \text{ rad} < \theta_s < \pi/2 \text{ rad}$) [2].

The influences of 3D object extension on the structure of the field in its image is determined by the ratio of critical diffraction angle $\theta_{cr} = \sqrt{\lambda/d}$ (under which the volume effects become significant) to the angular aperture size $2\theta_{ap}$ [3] (λ is wavelength). If at $\theta_{cr} \gg \theta_{ap}$ the weak volume effects occur, so at $\theta_{cr} \ll \theta_{ap}$ their effects are sufficiently significant. For further calculations one has limited by weak volume effects taking place in practical applications.

3. Algorithms for High Precision Determination of 3D Object's Boundaries

Two algorithms to determine the position of the geometric boundary of thick (extended) edge which plane perfectly absorption surface coincides with optical axis ($x_1=0$) have been developed. The first one is based on the use of threshold $I_{thr} = I(0)$ (Fig. 1b) that takes into account the angular source size $2\theta_s$ and object's thickness d . For calculation we used the constructive theory of image formation for extended objects with sharp shadow projection [3]. One has shown that normalized light intensity in the thick edge image in point $x_2=0$ that coincides with boundary geometric position, under $\theta_s \ll \theta_{ap}$ is equal to:

$$I_{thr} = I(0) = \frac{1}{4} + \frac{1}{3\pi^2} \frac{\theta_s^2}{\theta_{ap}^2} - \frac{\theta_{ap}}{\sqrt{2\pi}\theta_{cr}}. \quad (1)$$

It is seen that value $I(0)$ is determined by the three components. The first corresponds to the case when a flat object is being illuminated with point axial light source (coherent illumination). The second one refers to the influence of the final angular source size that is quadric and results in increase of $I(0)$. At last the third component is determined by the object volumetricity with decreases the threshold of $I(0)$. Thus, at given parameters of d and θ_{ap} one has had an opportunity, by choosing the angular source size $2\theta_s$, to compensate the

effect of the object's volumetricity on the change of light intensity at the point of geometric position of the thick edge boundary ($x_2 = 0$).

Computer modeling has allowed obtaining the dependency of the level of threshold on the light source diameter (Fig. 2). According to the obtained results (Eq. 1) the threshold levels for the thick and flat edges illuminated by light source of different size are differed by the third component. Under $\theta_s = \theta_{ap}$ threshold level jump is observed. The theoretical results as well as computer modeling ones are in good agreement.

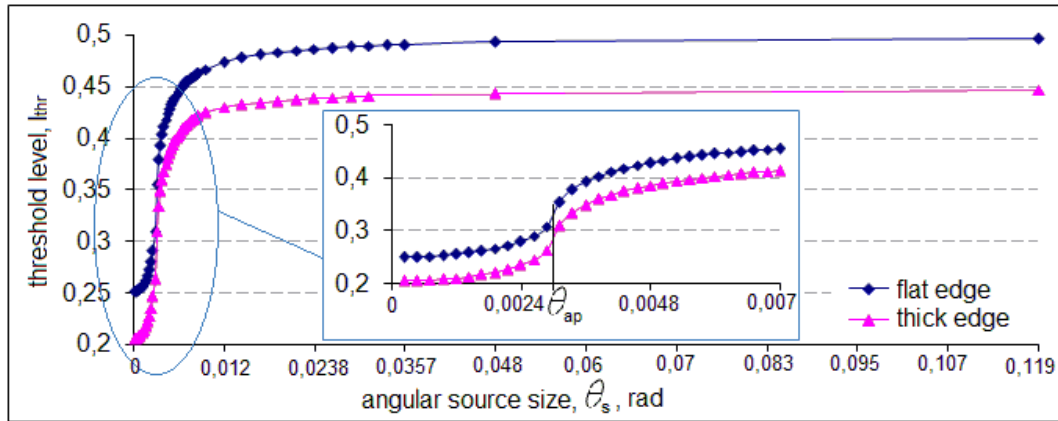


Fig. 2. The threshold level for shadow image vs. the light source diameter.

The second algorithm developed envisages the determination of the position of the 3D edge's boundary using the two standard thresholds: $I_{thr}^{(1)} = 0,5$ and $I_{thr}^{(2)} = 0,25$. It is important that high precise determination of the boundaries requires introduction of two corrections Δ_1 and Δ_2 that are determined by the following (Fig. 1b):

$$\Delta_1 = \frac{0,5 - I(0)}{I'(0)} = \frac{\Delta I_1}{tg \alpha}, \quad \Delta_2 = \frac{0,25 - I(0)}{I'(0)} = \frac{\Delta I_2}{tg \alpha}, \quad (2)$$

where $tg \alpha = I'(0)$ is the slope angle of the 3D edge's image profile under selected level. In this case one has to know the value of $I'(0)$. It's established that at $\theta_s \ll \theta_{ap}$

$$I'(0) = \frac{2\theta_{ap}}{\lambda} + \frac{4}{\sqrt{2\pi}\lambda\theta_{cr}} \left(\frac{1}{3}\theta_s^2 - \theta_{ap}^2 \right) \quad (3)$$

Taking into account the Eq. 3, the Eq. 2 for corrections Δ_1 and Δ_2 is as follows:

$$\Delta_1 = \frac{\lambda}{\theta_{ap}} \left[0,25 + \frac{3}{2\sqrt{2\pi}} \frac{\theta_{ap}}{\theta_{cr}} - \frac{1}{3\pi^2} \frac{\theta_s^2}{\theta_{ap}^2} \right], \quad \Delta_2 = \frac{\lambda}{\theta_{ap}} \left[\frac{3}{2\sqrt{2\pi}} \frac{\theta_{ap}}{\theta_{cr}} - \frac{1}{3\pi^2} \frac{\theta_s^2}{\theta_{ap}^2} \right] \quad (4)$$

It is seen that the values of the corrections depend on the angular aperture size, the angular light source size and the critical angle. The corrections can be minimized through choice of the parameters system due to the different signs of the components in the Eq. 4.

4. Experimental Results and Discussion

The theoretical results obtained have been experimentally verified. The scheme of experimental optical system is presented in Fig. 1a. As light source 1 one used LED with effective wavelength $\lambda = 628$ nm and spectral width $\Delta\lambda = 15$ nm. Necessary angular light

source size was set using a diaphragm. The homogeneity illumination of the inspected object is reached by mat diffuser. The extended object 3 was projected by lenses 4 and 6 on photodetector camera with 2210×3002 pixel matrix (size of the pixel was $3.5 \mu\text{m}$). The angular size of aperture diaphragm 5 had been set on the assumption that $\theta_{ap} > \theta_s$.

In experiments we used ceramic isolations rings with thickness of 0.8-80 mm, outer diameter of 28 – 80 mm and inner diameter of 23 – 62 mm as the extended objects. The position of thick edge was determined at level $I_{thr}^{(1)} = 0,5$.

It has been experimentally established and confirmed theoretically the influence of the object's thickness and of the optical system parameters on the image position profile. For example, when measuring thicknesses of the three-dimensional edge is varied from 2 to 10 mm, the position boundary shift was $4,77 \mu\text{m}$. The results of the experiment and computer modeling are presented in Fig. 3, which shows the dependence of ring edge's shift from the thickness.

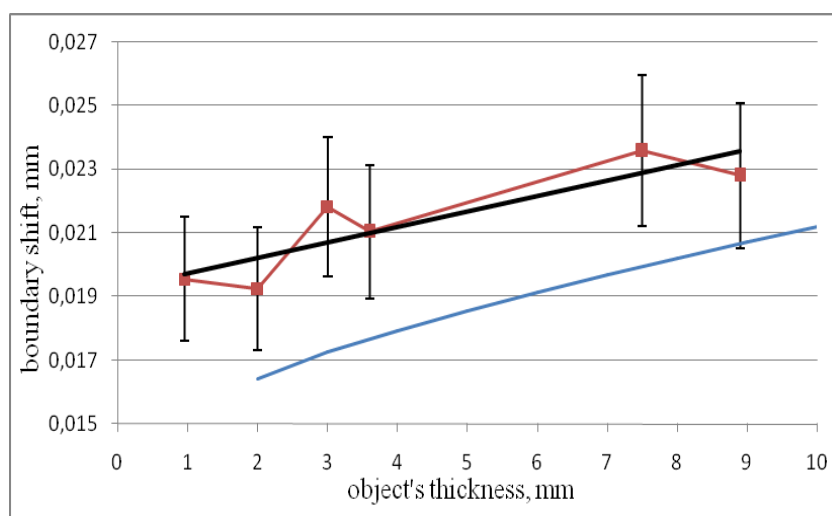


Fig. 3. Shift of the position of 3D object's edge vs. the object's thickness: jugged line – experimental data; thick line – averaged experimental curve; the curve below – calculation data.

One can see that deviation of the experimental and theoretical data in average has not exceeded a few microns that can be explained by non accuracy precision in calibration of the initial objects (instrument error was about $2 \mu\text{m}$).

Using the second algorithm one has been able to decrease the systematic error of the inspection system by 10 times: from $20 \mu\text{m}$ to $2 \mu\text{m}$.

5. Conclusion

We have studied the peculiarities of image formation for 3D object as a thick edge with sharp shadow projection illuminated by partially coherent light applied to dimensional inspection. The developed algorithms for processing the measurement information allow one by choosing the angular light source size to increase significantly the precision of 3D objects geometrical parameters measurement. The results obtained can be used for development of precision measurement systems for 3D objects inspection with sharp shadow projection.

References

- [1] Webster JG. The Measurement, Instrumentation, and Sensors Handbook. CRC Press LLC, Boca Raton, 1999.
- [2] Goodman JW. Introduction to Fourier Optics. McGraw-Hill, New York, 1968.
- [3] Chugui YuV., Sokolov VA. High-frequency filtered images of an optically thick edge. Journal of Optical Society of America, A 15 (3): 611-621, 1998.

Automatic Optoelectronic System for Inspection of Wire Wear Using High-Speed Image Analysis

**V.E. Kalikin, A.G. Verkhogliad, S.V. Kalichkin,
S.N. Makarov, V.S. Bazin, S.G. Savkov**

Technological Design Institute of Scientific Instrument Engineering SB RAS,
Novosibirsk, Russian Federation
Email: kalikin@tdisie.nsc.ru

***Abstract.** Advanced automated optoelectronic system for contact wire wear inspection on the go using a structured light method is presented. The algorithm of the video stream analysis and approaches to its implementation using high-performance electronic equipment are given. The automated system described has allowed measuring wear parameters with 10 mm interval at the inspection wagon velocity of 60 km per hour. The root-mean-square error for the measurements of the remaining height and contact plot constitutes 0.15 and 1.5 mm². The system also can be utilized to inspect public transportation network and to measure the geometric parameters of cables and tubes being fabricated with rolling technique.*

Keywords: Contact Wire, Wear Measurement, Structured Light Method, High Speed Real-Time Image Processing

1. Introduction

To ensure the safety in industry, transport and nuclear power system, it is required to inspect the geometry of distant industrial articles. Particularly, safety of railroad transportation takes continuous inspection of the geometric parameters of wearing constructions, especially a contact wire wear and defects of a railroad network. A number of automated systems [1-3] utilized by the industry that detect the wear on the go using the noncontact method are put into operation on Italian, Germany and Japanese railroads. At the present time there is no functional automated system in Russia, which meets construction features and operational conditions of our railroads. In this article we are presenting a problem of contact wire flaw detection, significantly improved method for wire wear calculation and fast automated system for real rail applications.

During long operation period the contact wire can be subjected to some geometrical defects that require their timely detection and removal. Unworn-out contact wire (Fig. 1a) and possible geometrical defects are shown in Fig. 1 b, c, d. The standard defect is decreasing of the cross-section area due to the friction against a current collector that result in increase of the specific resistance and may cause a wire break (Fig. 1b). In this case the wear is characterized by the two key parameters (Fig. 1b): the width of the wear contact area (w) and the wear depth (D).

The system to be developed must meet the following requirements: 1) noncontact principle of measurement; 2) simultaneous flaw detection of up to 4 wires in a catenary suspension; 3) the measurement error must not exceed 0.2 mm; 4) the measurement space interval of at least 10 mm at inspection wagon velocity of 60 km/h.

There are many methods and systems for inspection of geometric parameters of industrial articles under their fabrication or operation [4]. The shadow method [5] being the simplest and widely applied cannot provide flaw detection of contact wires due to the construction features of wire networks.

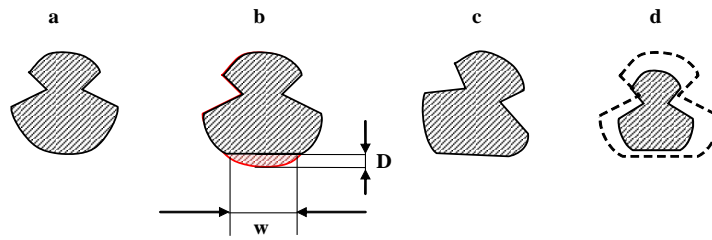


Fig. 1. A contact wire profile and its flaws: an unworn wire (a); a standard defect (b); a “turn” defect (c); “neck” defect (d).

Currently the majority of the automated optoelectronic systems in use are based on so-called a contact pad measurement method [1, 2]. The significant disadvantage of this method is informational limitation of the regular signal received. Being high-performance these systems [3] are not capable to detect and correctly determine such defects as a ‘turn’ or a “neck” defect and cannot process a big set (up to four) of contact wires in one catenary suspension system.

A part of the above-mentioned problems can be solved using the structural light method [6]. As for the problems of transferring and processing of large video information flows as well as the measurement of wire residual height with sufficient accuracy under the high wear values, they has not been solved for the present time.

2. Optical Layout and Electronic Components

The optical layout of the measurement unit is displayed in Fig. 2. The pulse mode of the laser provides high brightness of the radiation scattered on the surface of the contact wire that has significantly increased the S/N ratio of the image. The small exposure time (from 5 to 20 μ s) allows us to filter a significant part of background noise. Thus, the images obtained could be segmented into connected regions for subsequent processing. The images of unworn and worn wires, taken at frequencies of \sim 1000 Hz with structured light method, are displayed in Fig. 3.

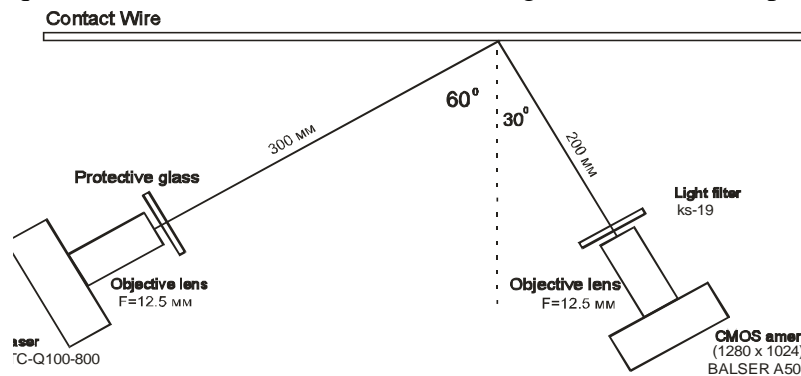


Fig. 2. Optical layout of contact wire wear inspection system.

The A504k camera includes the following benefits: a rugged housing designed for use in industrial environments, 500 frames per second at one megapixel resolution, area of interest (AOI) scanning allows higher frame rates. Matrox Odyssey Xpro+ is a scalable, vision processor board. It has a processing section and supports an optional frame grabber module for image acquisition. Video processor mainly unloads connected pixel area processing from CPU. The laser illuminator source has to provide a given value of radiation-intensity distribution for every point of the observational volume, and the registration unit has to

provide a contrast image with constant magnification for each point of the volume. The inspection productivity of the new system developed is limited by the impulse frequency of the laser, which is connected to the frame grabber of the video processor via a synchronization circuit and no longer limited by other elements as in [6]. Using camera with laser pulse timing generator with the same frame size we reach performance peak with 1000 frames per second.

3. Fast Image Processing

The first step of the image processing is indication of the informative sections of an image i.e. those that contain the image of the cross section of the wire illuminated by the laser beam. Such sections reveal themselves as connected pixel areas with quite a number of pixels. To simplify the search the areas are being traced in the frame sequences while the measurements are carried out. We assume a shape of contact wire to be constant in range of laser beam width. So it is enough for us to calculate the centers of mass by the brightness for every vertical column of pixels, converting the radiation intensity shape in a line. Doing that one should take into account the geometric distortion caused by the fact, that wire illumination angle and wire acquisition angle are not equal [6].

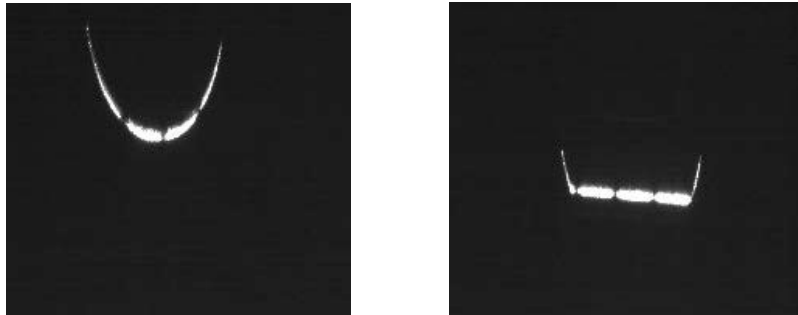


Fig. 3. Real nonprocessed (raw) image of contact wire under structured light for unworn wire (left) and worn wire (right) cases.

Processing the curve, represented by the centers of mass detected one determines the profile of the contact wire cross section. To do that one selects using algorithmic analysis, the centers that mark unworn sections of the wire surface. Within the sections the cross section of the wire has round shape. It allows us to calculate the center of the cross-section outline as the center of a circle with the similar set of points using statistic methods.

In more details the computational procedure could be described as the following: a) one searches for all possible combinations (A_i, B_k) , where A_i is running through all the points of the first group, and B_k - of the second (see Fig. 4); b) for each cross section one finds circle's center $C_{i,k}$ with known radius R containing the both points; c) one calculates standard deviation $d_{i,k}$ for all the points of the both groups from the circle as it has been determined previously; d) after determining all possible combinations one searches a center of a cross section according to the following formula: $C = (\sum_{i,k} C_{i,k} * \frac{1}{d_{i,k}}) / (\sum_{i,k} \frac{1}{d_{i,k}})$ i.e., one determines the center of mass for previously determined points $C_{i,k}$ with weight function $\frac{1}{d_{i,k}}$.

It is supposed that the size of a cross section and its allowable wear height are determined for each contact wire mark and are set initially. The groups of the centers of mass and the results

of cross-section profile determination are displayed in Fig. 4. The video processor also computes the array of the vertical centers of the connected components. The wire cross-sections recognized together with the information on spatial location and wear of a contact wire are placed into a special database. The data allow one to reconstruct the history of inspection sessions and to control performance quality of the system at the critical points of the contact network inspected.



Fig. 4. Groups of mass centers inside square marks used for determination the center of a cross section (left) and real system (right) dismantled from inspection wagon after series of tests.

System has been tested on the «Seyatel» train station. Measurement system was fixed on the current collector of inspection wagon moving with 60 km per hour speed along a track section contains 2 contact wires in catenary suspension. The root-mean-square error for the measurements of the remaining height and contact pad constitutes 0.15 and 1.5 mm² correspondently.

4. Conclusion

We have presented an advanced automated optoelectronic system for fast contact wire wear inspection. The algorithm of the video stream analysis and the variant of its implementation using high-performance electronic equipment were developed.

The automated system described has allowed measuring wear parameters with 10 mm interval at the inspection wagon velocity of 60 km per hour. The system also can be utilized to inspect contact wire wear in public transportation network and to measure the geometric parameters of cables and tubes being fabricated with rolling technique.

References

- [1] Kusumi S et al. Quarterly Report of RTRI. 2000, 4: 169-172.
- [2] Richter U, Schneider R. Eisenbahningenieur. 2001, 6: 18-23.
- [3] Nagasawa H, et al. Quarterly Report of RTRI. 2000, 3: 117-119.
- [4] Weckenmann A and Nalbantic K. Measurement of Conformity and Wear of Cutting Tool Inserts. Proceedings of SPIE, 2002, 4900 (1): 541-547.
- [5] Gromolin OG, Kuchinskii KI, Ladygin VI and Yunoshev SP. Control System of Industrial Product Geometrical Parameters on the Basis of the Shadow Image Analysis. *Journal Pattern Recognition and Image Analysis*, 9 (1): 141-142, 1999.
- [6] Bazin VS, Chugui YuV, Kalichkin SV, Kalikin VE, Makarov SN, Verkhogliad AG, and Vykhristyuk IA. Optical-Remote Inspection of Live Contact Wire Cross-Sections in a Train's Electro-Supply Network. *Measurement Science and Technology*, 18 (6): 1773-1778, 2007.

Using a Structured LED Linear Light Instead of a Laser Line Generator for High Measurement Tasks

¹M. Rückwardt, ¹A. Göpfert, ¹M. Schellhorn, ¹S. Holder, ¹G. Linß, ²S. Kienast

¹Ilmenau University of Technology (Faculty for Mechanical Engineering, Department Quality Assurance), Ilmenau, Germany,

²Steinbeis-Transferzentrum Qualitätssicherung und Bildverarbeitung, Ilmenau, Germany

Email: matthias.rueckwardt@tu-ilmrnau.de

Abstract. *Measurement tasks are often solved by using the triangulation principle for getting the structure and the surface of the object under test. For this purpose a laser line or even a laser multi line generator is used normally. Though the laser generator is limited having regard to its power, high costs and especially if there are speckles on the object under test.*

Other structured linear light sources are possible to use, if the linear light has got a define width, brightness and sharpness. Due to theirs fast development the LED seems to be a feasibility.

For this several researches were done at the department quality assurance in Ilmenau for getting the three dimensional coordinates of the ground of a groove by using a structured LED linear light. This is done in a first step by extensive computer-aided simulations and the solutions are given here.

Keywords: Linear Light, Structured LED Light, Detection of 3D Surfaces, Triangulation

1. The Triangulation principle for 3D measuring

Triangulation is a method for distance and surface measurements, using mostly a laser as the light source [1]. If the send out beam is a point only the distance can be measured. But if the beam is structured to a more complex geometric shape, like a line at least, also surfaces can be measured.

In a typical case, the laser beam illuminates the object under test in the distance of which from the laser device is going to be measured. Diffuse or specular reflections from that point are monitored with a detector which is mounted in a known distance from the laser beam. This is done in such a way that the laser source, the object and the detector form a triangle. At the detector, normally a CCD camera, the position of the linear light on the chip and its composition reveals the direction of the incoming light, i.e., the angle between the laser beam and the returning light, from which the distance and the surface of the object can be calculated [1].

Laser lines are primarily characterized by their length and their working distance, with other parameters becoming relevant depending on the measuring task. The measurement resolution is given by the line width, which can be limited by speckle. A sufficient depth of focus has to be taken into account when measuring objects of variable height [2].

This is exactly the measuring task for getting the ground of a groove, i.e. of a spectacle frame like in Fig.1. The transparent plastic frame on the left side of Fig.1 has got speckles and hence the width can not be detected clearly. Beside high reflective metal also transparent objects under test causes a lot of speckles, due to the fact that the laser beam is not only reflected at the surface furthermore also on different particles in the transparent plastics like dust, bubbles or flaws.

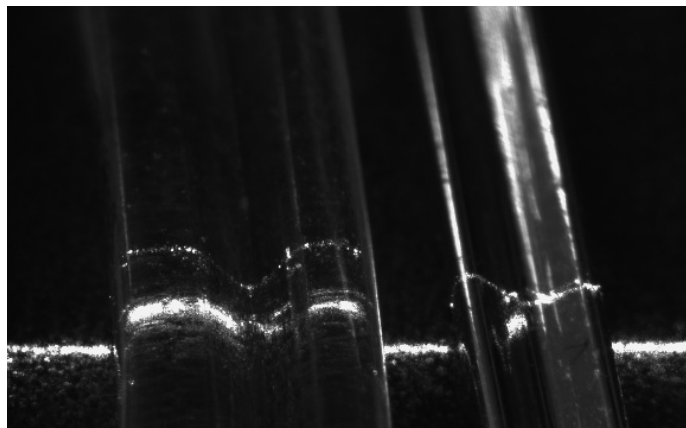


Fig. 1. A plastic and a metal frame with its groove, illuminated with a laser line generator (from left to right).

2. Advantages of structured LED light sources compared to laser line generators

The main disadvantage of laser line generator is the incidence of speckle. Because of the coherence of the laser light there can be interference pattern on the surface of the object under test. This has got a huge influence on sharpness of the contour and homogeneity of the linear line. The speckle pattern depends on the surface and material under test. An exact measuring is not possible especially by high reflective metal and polish surfaces.

On the other hand laser diodes are very expensive compared to a LED. There is not only an unbalance at the acquisition cost for both systems, also protection measures have to be demanded often during operation. Even the power dissipation and thus the heating are higher for laser than for LED light sources, see also table 1. For this reason a laser based 3D object recognition system is inappropriate for several measuring tasks.

There again an enormous offer of different LEDs is on the market. The diversity of power, spectral color, structural shape and so on allows a solution to nearly all measuring tasks. In some cases this is possible only by changing the source of light, the LED. So the main advantages of LED light sources are the huge range of spectral colors and the ten times higher illumination power.

Table 1. Typical Properties of LEDs and Laser diodes [3].

property	LED	Laser diode
Wave length	NIR, red, yellow, green, blue, UV, white	NIR, red, blue, UV
Power (typical)	500mW	visible: 50mW
Spatial coherence	highly multi-mode	single transversal modus (speckle)
Time coherence	incoherent ($\Delta\lambda > 10$ nm)	coherent ($\Delta\lambda < 0,1$ nm) (speckle)
Dimming	linear	not linear, Laser Threshold
Modulation	MHz	GHz

But the illumination is shared in all directions, like in Fig. 2 on the left side. So high power LED for measuring tasks need an attachment optic (Fig. 2 on the right side) for building a powerful point light source.

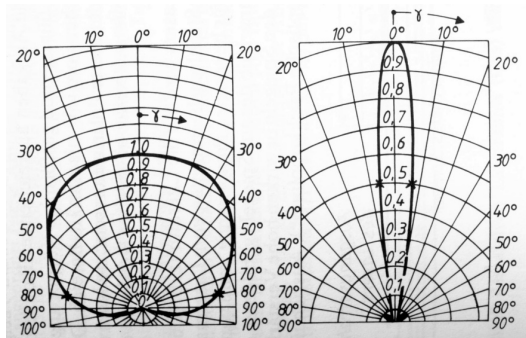


Fig. 2. Light emission of a LED without and with attachment optic [3].

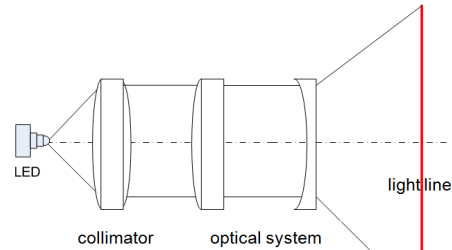


Fig. 3. Basic set up to generate a light line.

3. Creation of a structured linear light

One premise a point light source is already mentioned. The other is: beams have to be parallel and bundled before they can be modelled by optical systems with apertures, splits and lenses. Also the scattered radiation has to be reduced with apertures. In the field of technical optic the elementary way to build a collimator is a biconvex lens [3].

There are different basic set ups to generate a light line, see also Fig 3:

- projection of a split
- beam moulding with a cylindrical lens
- beam moulding with a parabolic reflector
- a combination of them

The plurality of assembling out of the set ups depends a measuring task with a clear special aim. The object under test is the groove of a spectacle frame, which depends the following list of specification (see Table 2) to measure it.

Table 2. Criteria for groove measuring and realised criteria

Criterion	Specification	realised criteria
light source	LED white coloured	LED Vishay (TLCR5100-white)
width	$\leq 500 \mu\text{m}$	336 μm
length	10 mm	9,4 mm
depth of focus	$\geq 5 \text{ mm}$	6 mm
illuminance	0,1 lm/mm^2	0,03 lm/mm^2
low cost	< 350 €	145 €
working distance	< 50 mm	40 mm

With these parameters different solutions were simulated with the optical program ZEMAX. The best results were simulated (see also Table 2) for the measuring task by the following assembling:

An optical system build out of a split and a cylindrical lens for generation the linear light, like in Fig. 4 and 5.

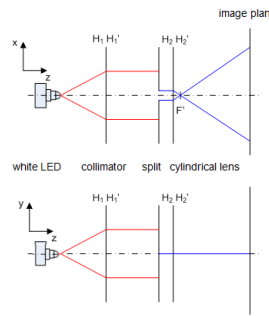


Fig. 4. Beam rum with split and cylindrical lens.

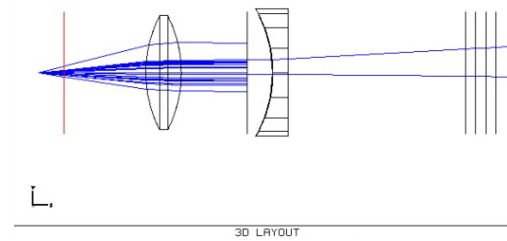


Fig. 5. ZEMAX 3D Layout.

The split has got a width of 300 μm and a length of 12 mm and projects the linear light on the image plane. Its width is constant over the whole depth of focus, like in Fig 6. The cylindrical lens is used to the beam expansion (see Fig. 7) and due to this the illuminance is reduced to larger working distance, like in Fig. 8. An example of the Simulation is given in Fig. 9.

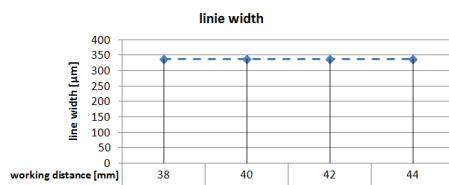


Fig. 6. Line width.

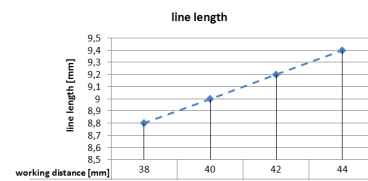


Fig. 7. Line length.

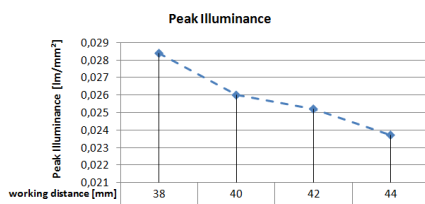


Fig. 8. Peak illuminance.

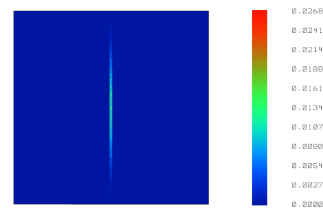


Fig. 9. False Color DV – line width 336 μm .

4. Results

This study shows, that it is theoretical possible to use a structured LED linear light instead of a Laser line generator for high measurement tasks, here brought out of detecting the ground of the frame groove. The best results are achieved with an optical system out of a split and a cylindrical lens.

Acknowledgements

This work is funded by the Federal Ministry of Economics and Technology Germany within the framework of the InnoNET program.

References

- [1] Dorsch R. G. et al. Laser triangulation: fundamental uncertainty in distance measurement, Appl. Opt. 33 (7), 1306 (1994).
- [2] Schäfter + Kirchhoff GmbH http://www.sukhamburg.de/download/laser_lg_e.pdf (13.02.2011).
- [3] Kienast S. Untersuchung, Auslegung und praktische Erprobung eines LED-Multilinenlichts – Strukturierte Beleuchtung zur 3D-Objektvermessung, Ilmenau, diploma thesis, 2009.

Smartphones, Cloud Computing and Apps - Green Game Changers for Measurement Science and Education

D. Hofmann, P.-G. Dittrich, E. Düntsch

Technologie- und Innovationspark Jena GmbH - SpectroNet, 07745 Jena, Germany,
Email: dietrich-hofmann@t-online.de

***Abstract.** Aim of the paper is to show innovative game changers for measurement science and education, instrumentation and training. Smartphones, cloud computing and apps open new opportunities for measurement science and education. Smartphones are in principle powerful computers. Cloud computing is the innovative technical infrastructure for knowledge acquisition, transfer and application. It is convenient, reliable and affordable. Apps are a new kind of software modules for direct specialized applications. They are reducing the complexity of universal software packages and facilitate an application for everyone. Personalized web competence matrices are new tools for mobile scientific work and education in real-time.*

***Keywords:** Smartphones, Cloud Computing, Apps, Measurement Science, Measurement Education, Instrumentation, Training, Green Measurement*

1. Introduction

Aim of the paper is to show innovative game changers for measurement science and education, instrumentation and training. Smartphones, cloud computing and apps open new opportunities for measurement science and education. Smartphones are in principle powerful computers. Cloud computing is the innovative technical infrastructure for knowledge acquisition, transfer and application. It is convenient, reliable and affordable. Apps are a new kind of software modules for direct specialized applications. They are reducing the complexity of universal software packages and facilitate an application for everyone. Personalized web competence matrices are new tools for mobile scientific work and education in real-time.

2. State of the Art in Computers

Days before yesterday standard computers have been main frames and process computers. They have been big, expensive and functionally poor. The next era was characterized by desktop and laptop computers. With laptops the era of mobile and outdoor applications have been started, although to a certain extend inconvenient and expensive. Today the functionality of laptops is equipped in the dimensions of smartphones (Fig. 1.). Smartphones are commodities with a huge dissemination worldwide. Big numbers of smartpads are at the dawn.

3. State of the Art in Computing and Applications

Cloud computing is currently one of the most significant topics of the further development of information and communication technologies for producers and customers. Cloud computing is an innovative challenge for digital products and services. Till now only the top of the iceberg is seen. During the last years, mobile smartphones became commodities for cloud computing and apps. Their biggest advantages are convenience, reliability and affordability (Fig. 2.). Apps are innovative tools to reduce the complexity of bigger software packages. The worldwide mobile availability of smartphone, the ease in dealing with cloud computing and apps and the worldwide possibility of cashless payment for apps is an enormous drive for the development of permanently new or improved software apps in any fields.

4. Fundamental Tasks of Measurement Science and Education

The competent handling of digital information and communication media becomes a fundamental role in everyday life. Particularly encouraging is the innovative role of the internet for measurement science and education. Fundamental tasks of measurement science are to discover new relationships in measurements and to generalize new knowledge for measurements. Fundamental tasks of measurement education are to educate young specialists for measurements and to re-qualify measurement people at work and at home (Fig. 3.). The promotion of measurement science and education via internet is an innovative means for convenient, reliable and affordable collaborations to share standpoints, to harmonize issues and to unify doctrines [1].

5. Innovative Capabilities of Measurement Instrumentation and Training

The innovative capabilities of measurement instrumentation are characterized by measurement value acquisition and processing with smartphones. Also especially in mobile measurement education and training powerful smartphones are the enabler of innovative capabilities (Fig. 4.). The practical training gets innovative boundary conditions for more freedom in volume, time and place concerning exercises with real measuring tools or with their simulators. The instrumentation and training can be supported by see see & click manuals (SSC-manuals) with complete user guiding and a guaranteed success for the measurement procedure [2].

6. Personalized Web Competence Matrices for Science and Education

Smartphones and cloud computing are modern enabler for real-time transfer and personalized traceability of scientific publications, lectures, podcasts, webinars, trailers and videos (Fig. 5. and Fig. 6.). Personalized web competence matrices are the very beginning of a new understanding of collaboration in measurement science and education in a more “green” way – convenient, reliable and affordable – every time and everywhere – and in an increasing number of automatic translated languages [3].

7. Conclusions

Aim of the paper was to demonstrate, that smartphones, cloud computing and apps are modern enabler for mobile real-time transfer of measurement information, for personalized collaboration and for easy traceability of scientific publications, lectures, podcasts, webinars, trailers and videos. They are fundamental game changers for measurement science and education, instrumentation and training in an innovative “green” way.

References

- [1] <http://www.spectronet.de>
- [2] http://spectronet.de/de/akademie/qualifizierung-training---steinbeis--transfe_gcarq6pi.htm
- [3] <http://www.greenvision.spectronet.de>



Fig. 1. Evolution of computers

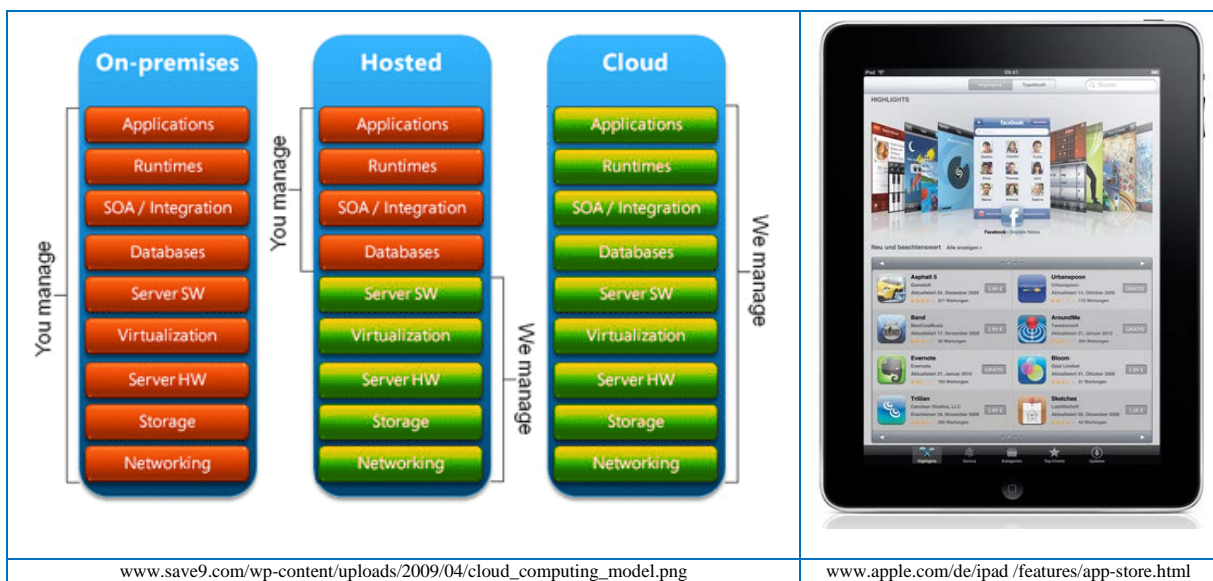


Fig. 2. From on-premises computing to cloud computing and apps.



Fig. 3. Fundamental tasks of measurement science and education.

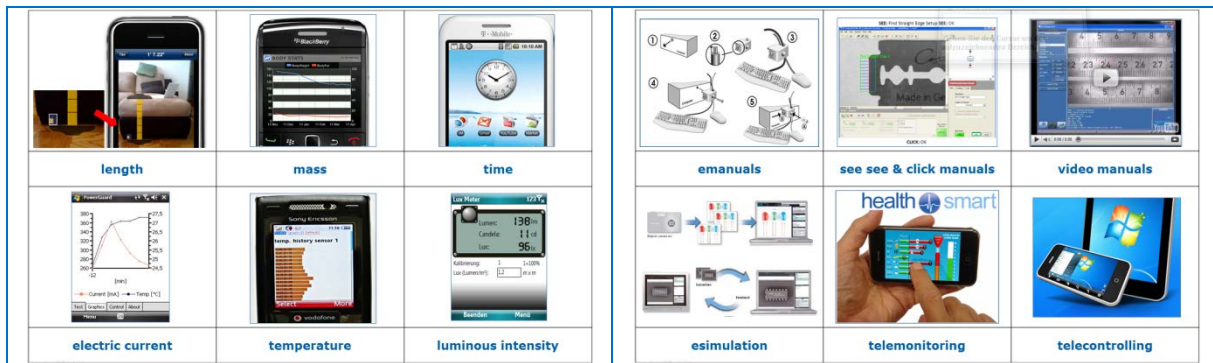


Fig. 4. Innovative capabilities of measurement instrumentation and training.

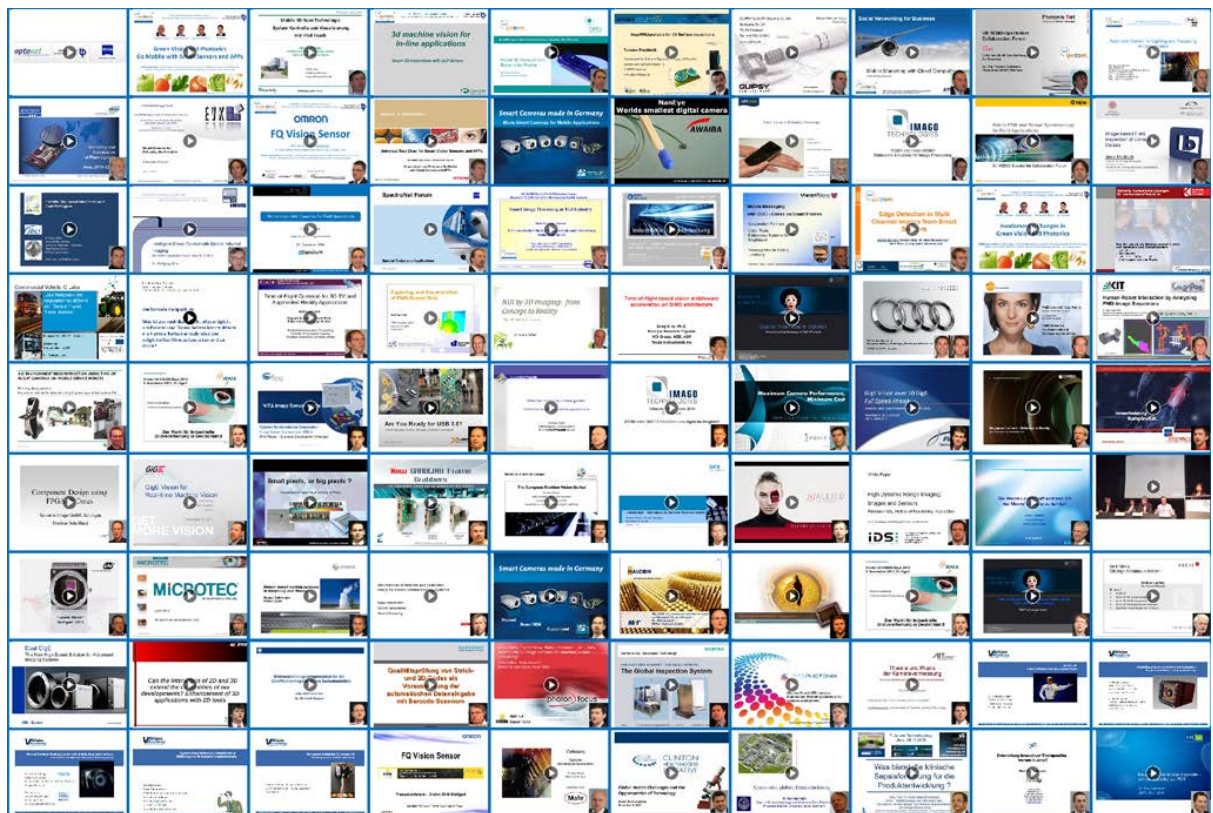


Fig. 5. Personalized web competence matrices for science and education.

Lecture	Webinar	Hands-on Training
SPIE/IS&T Symposium	NEMO-Tag des BMWi	STEMMER-IMAGING
Dr. Bernice E. Rogowitz	RD Dr. Dieter Belter	Dipl.-Ing. Lars Fermum

Fig. 6. Details of web lectures, webinars and hands-on trainings.

Modeling and Measuring of the Changes of the Magnetic Field Next to Non-Ferromagnetic Substances for Magnetic Susceptibility Calculation

¹P. Marcon, ^{1,2}K. Bartusek, ¹M. Cap

¹Brno University of Technology, DTEEE, Brno, Czech Republic,

²Institute of Scientific Instruments of the ASCR, Brno, Czech Republic

Email: xmarco00@stud.feec.vutbr.cz

Abstract. This article is focused on the principles of the magnetic susceptibility measurement of the non-ferromagnetic substances using NMR tomography. Magnetic susceptibility is calculated from changes of the magnetic field close to the cylinder shaped specimen. COMSOL program was used for modeling experiment results. Consequently, model results were compared to MR tomograph measured data. Changes of the magnetic field in space of xy cut of the specimen were integrated in both cases. Before integrating of the magnetic field changes was necessary to filter, unwrap and detect accurate position of the specimen. Magnetic susceptibility calculated from measured data is in comparison to theoretical value, as well as model value, slightly different. Difference of those values is lower than 5%. Due to the used model and measurement were extended principles of the NMR method for magnetic susceptibility measurement.

Keywords: COMSOL, Non-ferromagnetic, NMR, Magnetic Susceptibility

1. Introduction

Magnetic susceptibility is the physical quantity describing material properties in the external magnetic field. Magnetic susceptibility is defined as ratio between magnetization \mathbf{M} of the material in the magnetic field and the field intensity \mathbf{H} :

$$\mathbf{M} = \chi_m \mathbf{H}. \quad (1)$$

All materials can be classified by value of magnetic susceptibility into three groups. This article is focused on the non-ferromagnetic (paramagnetic and diamagnetic) materials. These materials have defined magnetic susceptibility in range $-1 < \chi_m \ll 1$.

Non-ferromagnetic substation placed in homogeneous magnetic field B_0 react with this field and create the local changes of the magnetic field close to the specimen. Changes of the magnetic field depend on the magnetic susceptibility of used material. NMR method of measurement magnetic susceptibility is based right on measurement of these changes [1] and [2]. Next paragraphs show calculating of the magnetic susceptibility from distribution of the magnetic field around the specimen in COMSON environment. Consequently, value of the magnetic susceptibility is calculated from the measured data and compared with theoretical and from the model calculated value.

2. Subject and Methods

Model and real specimen used the same space configuration of the sample as is shown in Fig.1. Cubic space (40x40x40 mm) filled by a deionised water has magnetic susceptibility $\chi_{m1} = -13 \cdot 10^{-6}$, labeled by number (1) in Fig. 1. In the center of this space is placed the sample of mentioned materials with different magnetic susceptibility χ_m . The samples are

cylindrical 10 mm in length and 4 mm in diameter, labeled by number (2) in Fig. 1. Sample materials was used aluminum ($\chi_{mAl} = 2.2 \cdot 10^{-5}$) and copper ($\chi_{mCu} = -9.2 \cdot 10^{-6}$). No. (3) is the cutting plane (xy plane) placed in the center of the cylinder. In this article is always used this plane.

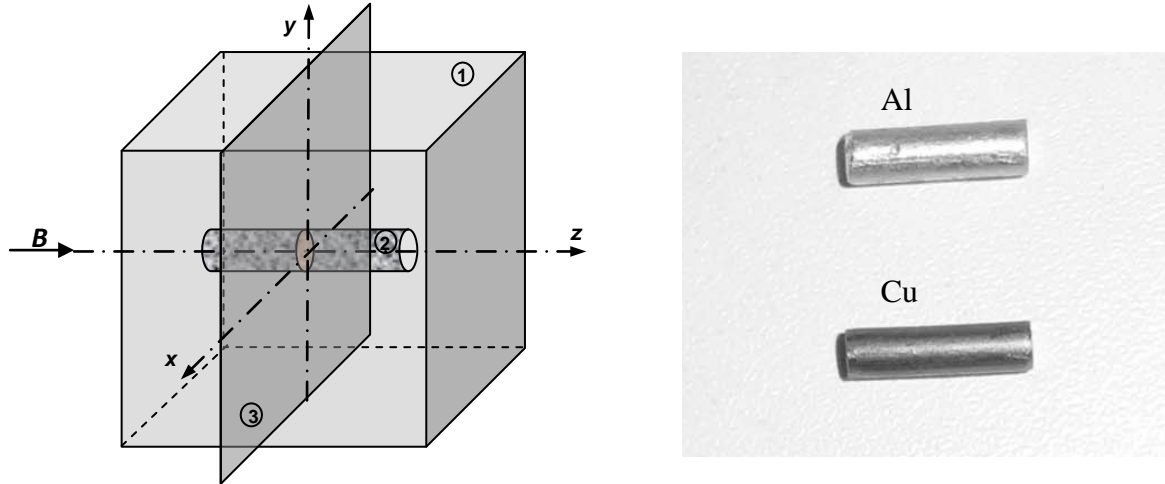


Fig. 1. Left - Configuration of the modeled system, cube filled by an air with sample. Right – copper and aluminum cylinders.

Modeling of the changes of the magnetic field close to the specimen in COMSOL environment
 COMSOL environment was used for calculating of the magnetic field distribution. Created configuration (in Fig. 1) use mesh of the final elements. Equations for the electromagnetic field are used for calculation of the magnetic field distribution. In the same way was calculated reaction magnetic field ΔB , as

$$\Delta B = B - B_0. \quad (2)$$

In article [3] is used equation for calculation of the magnetic field form the 1D cut. We extend this equation for 2D space use, xy plane in the center of the cylinder (No. (3) in Fig. 1). Integral of the reaction field ΔB_w round the cylinder divided by space of the cylinder cut $S_{cylinder}$ give as differential magnetic susceptibility

$$\Delta\chi = -\frac{\iint \Delta B_w \cdot dx dy}{S_{cylinder} \cdot B_0}. \quad (3)$$

Calculation of the magnetic susceptibility from data measured by MR tomograph

As a measurement method we chose Gradient echo (GE) method. GE is very sensitive to inhomogenities of the static magnetic field, what can be useful for susceptibility measurement. By this method measured image is phase coded image $\Delta\varphi$ used for reaction field ΔB calculation by the following equation:

$$\Delta B = \frac{\Delta\varphi}{\gamma \cdot T_E}, \quad (4)$$

where T_E is time to echo. More about GE you can see in [4], [5].

In Fig. 2 is shown how are the MR data processed. First of all are the data convert by the FFT from k -space to the $2D$ spatial function of intensities. Next step is image filtering, correcting of the image and phase unwrapping. As an input for Eq. 4 and for reaction field, calculation is used this unwrapped image. Only one image from whole set is used for magnetic susceptibility calculation as was mentioned above. Cylinder position in the image is marked by detection algorithm and whole space of the cylinder is set to zero. From resulting image we can easily calculate the ΔB_w integral and establish this value to Eq. 3 for magnetic susceptibility calculation.

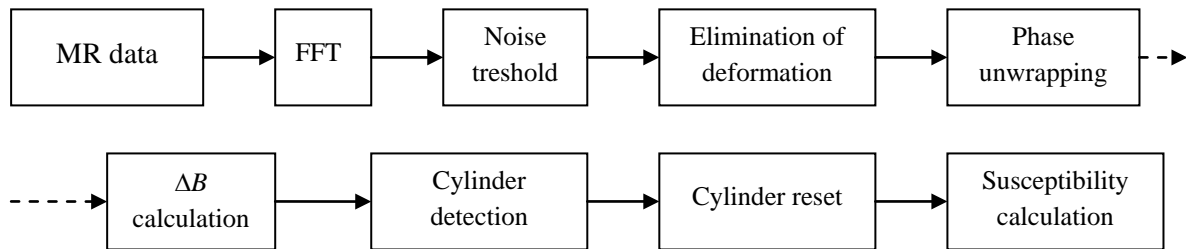


Fig. 2. Block diagram of the process of magnetic susceptibility calculation from MR data.

3. Results

Reaction field distribution ΔB_w in the measured MR image is shown in Fig. 3. Measured data are processed by algorithm from Fig. 2. Result of this algorithm is matrix 80×75 px. Magnetic field changes are shown in Fig. 3, on the left 2D, on the right the 3D image of distribution of the reaction field.

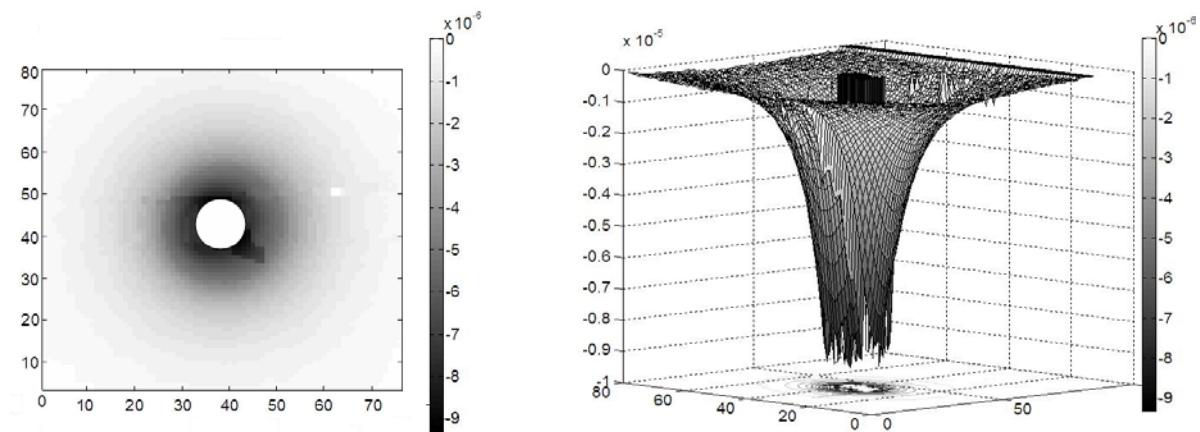


Fig. 3. Reaction field ΔB_w in xy plane in the center of the aluminum cylinder. On the left 2D, on the right the 3D image of distribution of the measured reaction field.

Summary of the results are presented in Table 1. Middle column are values obtained from COMSOL model, right column are values calculated from MR measurement. Measurement was provided on a MR tomograph at the Institute of Scientific Instruments, Academy of Sciences of the Czech Republic (ISI ASCR). The MR tomograph dispose of static field flux density $B_0 = 4,7$ T, nuclei resonance frequency is 200 MHz.

Table 1. Tables Values of the magnetic susceptibility for aluminum and copper cylinders calculated from model and MR data.

Material	$\chi_{\text{model}} [x 10^{-6}]$	$\chi_{\text{NMR}} [x 10^{-6}]$
Aluminum	21,484	21,713
Copper	-8,940	-9,401

4. Discussion and Conclusions

The results are compared with sample properties published in literature. The causal agent is the measurement of magnetic susceptibility in static magnetic field $B_0 = 4,7 \text{ T}$ and the material saturation. Magnetic susceptibility is published in literature as $\chi_{\text{Al}} = 22 \cdot 10^{-6}$ for aluminum and as $\chi_{\text{Cu}} = -9 \cdot 10^{-6}$ for copper. Due to calculation of the magnetic susceptibility from COMSOL model we verified that the Eq. 3 give us right results. How you can see in Table 1 the difference between the value calculated from model and the value calculated from measured data is very small. This difference is caused by size of the mesh of the model. Deviation of the obtained magnetic susceptibilities did not exceed 4,5%. Reached accuracy of this method makes it very suitable for magnetic susceptibility measurement of the non-ferromagnetic materials. Future research of this method holds possible ways for improvement of these method possibilities.

Acknowledgements

The research described in the paper was financially supported by research plan No. P102/11/0318 and MŠMT CZ.1.05/2.1.00/01.0017 (ED0017/01/01).

References

- [1] Wang ZJ, Li S, Haselgrove JC. Magnetic Resonance Imaging Measurement of Volume Magnetic Susceptibility Using a Boundary Condition. *Journal of Magnetic Resonance*, 140: 477-481, 1999.
- [2] Bartušek K, Dokoupil Z, Gescheidtova E. Mapping of magnetic field around small coils using the magnetic resonance method. *Measurement Science and Technology*, 18: 2223 – 2230, 2007.
- [3] Bartusek K, Cap M, Marcon P, Mikulka J, Magnetic susceptibility modeling using ANSYS, *PIERS Proceedings*, 2011.
- [4] Bartusek K, Dokoupil Z, Gescheidtova E. Magnetic field mapping around metal implants using an asymmetric spin-echo MRI sequence. *Measurement Science and Technology*, 17 (12): 3293-3301, 2006.
- [5] Vladingerbroek MT, Den Boer JA. Magnetic resonance imaging. Springer-Verlag, Heidelberg (Germany), 1999.

Properties of Magnetoinductive Resonator Array for MRI Application

K. Bartusek, D. Nesor, P. Drexler, P. Fiala

Department of Theoretical and Experimental Electrical Engineering,
Brno University of Technology, Brno, Czech Republic,

Email: bartusek@feec.vutbr.cz

Abstract. *A method for partial resonant frequencies measurement of the magnetoinductive array is described. The method utilizes a return loss measurement of a coil probe and it allows to verify the mutual adjustment of the resonant frequencies. The effective permeability evaluation of the array is presented and results of numerical analysis are shown. Numerical analysis results are compared to the experimental results. It was found that at the resonant frequency the signal from the resonator array is suppressed due to the very low real part of the permeability.*

Keywords: Periodical Structure, Resonator Array, Nuclear Magnetic Resonance

1. Introduction

A possibility of manipulation of magnetic field distribution in magnetic resonance (MR) systems has been shown in recent works [1]. Some approaches consider this phenomenon as a subwavelength imaging which can be observed with metamaterial slabs. In contrast to classical metamaterial imaging concept, which utilizes double negative synthetic material, an exploitation of metamaterial slab with only negative permeability or only a negative permittivity is possible. The typical characteristic of metamaterials structures is the dimension relation between the metamaterial slab components and the wavelength of the wave which is to carry through the slab. The dimensions of metamaterial components are much smaller than the wavelength of the interest. In spite of this dimension disproportion the metamaterial structures show response at these wavelengths. Regarding to these dimension relations it can be found that the metamaterial structure-wave interaction is in the realm of quasi-static fields. This phenomenon allows consider only electric or magnetic part for imaging purposes. In the case of magnetic imaging a progress has been made by Freire and Marques [2].

The main goal of manipulation of magnetic field distribution in MR systems is to increase the received MR signal which is a response to radiofrequency sample excitation. The preliminary concept of the magnetoinductive structure for experimental MR system has been proposed and built [3]. The lens components – a capacitance loaded ring resonators - are based on non-ferromagnetic materials. In spite of their insignificant response in the DC magnetic field, they exhibit magnetic response around a certain resonant frequency. The resonant frequency has to be close to the frequency of the excitation RF pulse. By suitable configuration of the components the imaging effect is expected and the device behaves like a magnetic RF field concentrator. In previous work [3] the theoretical approach to resonator arrays design has been presented. There has been presented some issues of the resonators fabrication and component selections. One of the goals is to achieve mutual resonant frequencies adjustment. The results have shown the need for careful resonators assembly. The suggested points of the design have been taken into the account in the next resonator arrays fabrication. The results of resonant frequencies measurement of improved resonator array will be presented in the paper. The partial resonant frequencies are examined by means of coil probe return loss measurement. In order to obtain a notion of resonator array behaviour two analysis steps has been performed. The first analysis step, a numerical simulation, gives an idea about the

frequency dependence of array's effective permeability. The second analysis step consists in MR system measurement of field distribution in array vicinity.

2. Measurement of arrays partial resonant frequencies

The total frequency characteristic of the array consists of the superposition of partial resonant curves of each resonator, which are mutually coupled. Measurement of resonant frequency of magnetoinductive (MI) resonator array has been described in [3]. For the measurement of the single resonator resonant curve a method utilizing a small coil probe, directional coupler, frequency generator and spectrum analyzer has been proposed, see Fig. 1 (left part). The analyzer with built-in tracking generator and directional coupler has been used and the return loss of the small loop probe has been measured, Fig. 1 (middle part). The example of loop probe return loss is shown in the right part of Fig. 1 as a remarkable drop with dip level above 7 dB.



Fig. 1. Setup for resonant curve of single resonator measurement (left), the loop probe detail (middle) and an example of measured characteristic (right).

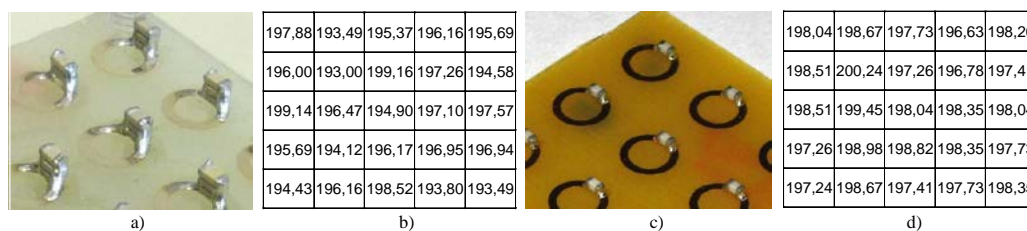


Fig. 2. Early MI array detail a) and its map of resonant frequencies in MHz b), new MI array detail c) and its map of resonant frequencies in MHz d).

3. Numerical analysis

As has been noted the resonator array shows a magnetic response around certain resonant frequency. Hence, the frequency dependence of array permeability exhibits typical resonant characteristic. In order to characterize the properties of the array the effective magnetic permeability may be used. To obtain an idea about the effective permeability characteristic a finite element method numerical analysis by means of Comsol system has been performed. The simulated structure consist of 3x3 array of resonators with outer diameter of 5 mm, inner diameter of 3 mm, thickness of 35 μm and ring spacing of 18 mm. The substrate with thickness of 2 mm has a dielectric constant of 4,5. The perfect electrical conductor (PEC) has been used as the ring. The capacitance of the resonators has been modeled in such a way, that to every finite element of the ring has been assigned a dielectric constant with suitable value. The total capacitance of the ring model was equal to the lumped capacitance 112 pF.

The structure has been excited by planar wave with a magnetic component H_y perpendicular to the array which is in plane xy . Following general wave equation has been solved:

$$\nabla \times \mu_r^{-1} (\nabla \times \mathbf{E}) - k_0^2 \left(\varepsilon_r - \frac{j\sigma}{\omega \varepsilon_0} \right) \cdot \mathbf{E} = 0, \quad \nabla \times \mu_r^{-1} (\nabla \times \mathbf{H}) - k_0^2 \left(\varepsilon_r - \frac{j\sigma}{\omega \varepsilon_0} \right) \cdot \mathbf{H} = 0. \quad (1)$$

where μ_r is relative permeability, \mathbf{E} is electric field intensity vector, k_0 is vacuum wave number, ε_r is relative permittivity, σ is conductivity, ω is wave angular frequency and \mathbf{H} is magnetic field intensity vector. Considering the material relation $\mathbf{B} = \mu_r \mu_0 \mathbf{H}$, we can derive from the magnetic flux relation on the array surface a relation:

$$\iint_{\Omega} \mathbf{B} d\mathbf{S} = \mu_r \mu_0 \iint_{\Omega} \mathbf{H} d\mathbf{S}, \quad (2)$$

where Ω is a integration area specified as a array surface a $d\mathbf{S}$ is vector surface element. When we consider a wave magnetic field component H_y perpendicular to the array surface we can derive from (2) an relation for effective permeability μ_{eff} of the array:

$$\mu_{\text{eff}} = \left(\iint_{\Omega} B_y d\mathbf{S} \right) / \left(\mu_0 \iint_{\Omega} H_y d\mathbf{S} \right), \quad (3)$$

where H_y is an excitation magnetic field intensity and B_y is an magnetic flux density on the array surface. The resultant frequency characteristic of the effective magnetic permeability is shown in Fig. 3. In Fig. 3a) is a real part of the effective magnetic permeability μ'_{eff} , in Fig. 3b) is an imaginary part of the effective magnetic permeability μ''_{eff} . Around the resonant frequency of the array a smaller frequency step has been used also and the analysis repeated. Fig. 3c) shows a decomposition of the total characteristic on partial resonances. Since identical parameters of the resonators have been used, this effect is probably caused by mutual resonator coupling and finite element size, which has been used.

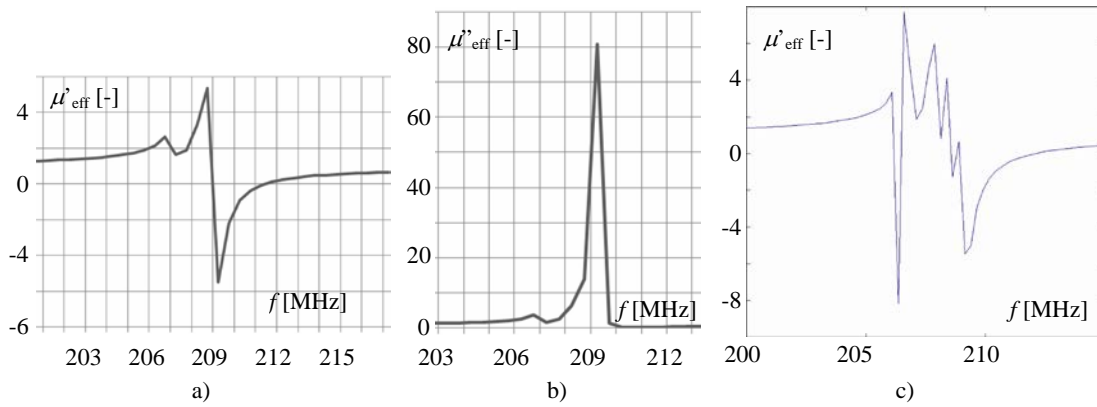


Fig. 3. Computed real part of the effective magnetic permeability μ'_{eff} a), imaginary part of the effective magnetic permeability μ''_{eff} b), detail of real part of the effective magnetic permeability μ'_{eff} computed with finer frequency step c).

4. Impact of the array on field distribution in MR cavity

Since the resonator array structure, which has been built (Fig. 2c)) exhibits a magnetic response on frequency close to the excitation frequency of the intended MR system, verification of the array's impact on field distribution has been proposed.

Result of numerical analysis in section 3 shows that at the resonant frequency of the array the real part of the effective permeability approaches to zero, while the imaginary part rises. This fact should cause the $\pi/2$ phase shift of the induced field in compare to the excitation field. Since the response detection of the specimen is evaluated regarding the initial phase, it may

seem that for the close space around the resonator no response signal is present. The induced in-phase field of the resonators will be suppressed. For the verification of array's impact on the MR response an image acquisitions of water phantom with resonator array has been performed. The array has been placed in the box with water. The plane of the array was parallel to the water surface, in plane xz . A transverse slice xy crossing the middle resonator has been acquired. The slice thickness was 2 mm. The magnitude image is shown in Fig. 4a). Fig. 4b) shows a field map which magnitude is related to magnitude of excitation field B_1 . From Fig. 4b) is obvious that the response of the specimen is strongly suppressed around the resonators. A possible influence of the capacitor susceptibility may be observed as areas with increased magnitude, which is shown in detail in Fig. 4c).

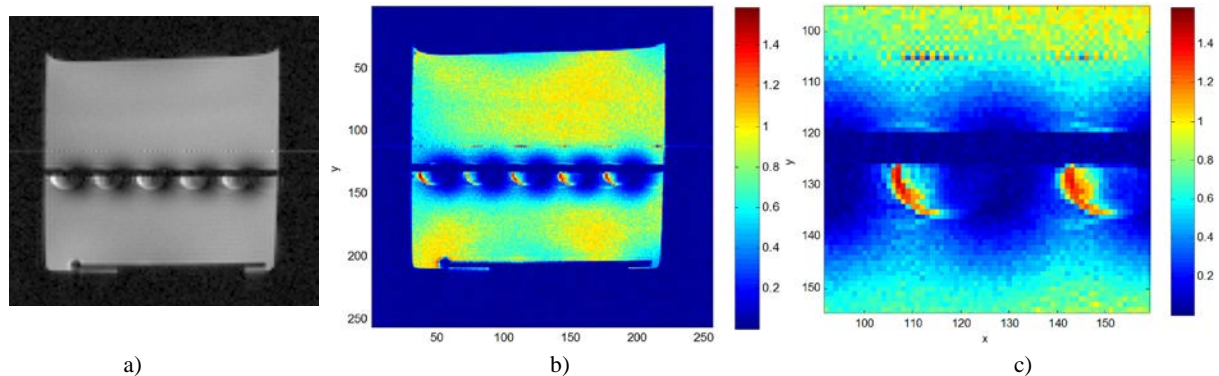


Fig. 4. Images of slice of array-water phantom configuration - magnitude image a), field map b), field map detail c).

5. Conclusions

It might be concluded that the results of experimental verification of resonator array's impact on the field distribution in MR cavity coincide with the numerical analysis results. The detected real part of the specimen response is strongly suppressed around the resonators. This evidences that the array's partial resonant frequencies were set very close to the excitation frequency of the MR system. To achieve a possibility of MR signal improvement and imaging properties of the array the resonator frequencies should be set close to the excitation frequency, which is going to be a matter of further research.

Acknowledgements

The paper was supported by the project GA102/09/0314, project CZ.1.05/2.1.00/01.0017 (ED0017/01/01), project MSM 0021630513 and project of the BUT GA FEKT-S-10-13.

References

- [1] Wiltshire, M. C. K., Hajnal, J. V., Pendry, J. B., Edwards, D. J., Stevens, C. J. Metamaterial endoscope for magnetic field transfer: near field imaging with magnetic wires, *Optic Express*, vol. 11, no. 7, 2003.
- [2] Freire, M. J., Marques, R. Near-field imaging in the megahertz range by strongly coupled magnetoinductive surfaces: Experiment and ab initio analysis, *Journal of Applied Physics*, vol. 100, no. 6, 2006.
- [3] Bartusek, K., Drexler, P., Fiala, P., Kadlec, R., Kubasek R. Magnetoinductive lens for experimental mid-field MR tomograph. In *proceedins of Progress In Electromagnetics Research Symposium PIERS 2010*, pp.943-946, USA: Cambridge, 2010.

Dependence of NMR Spin Echo Form on Liquid Flow Structures

N.K. Andreev, A.S. Malatsion

Kazan State Power Engineering University, Krasnosel'skaya Str., 51,
420066, Kazan, Russia

Email: ngeikandreev@gmail.com

Abstract. *The influence of the flow structure on a NMR spin echo form is discussed. The form of spin echo signals is considered for flow under acoustic pressure (acoustic flow) without any magnetic field gradient and for laminar and turbulent flow in the presence of a magnetic field gradient. The reason for discussion this theme is caused by the influence of the echo form on measurement errors in flow velocity measurements. Spin echo signals can have in some cases from one to four peaks. It is known that intensive acoustic waves can induce in a liquid high pressure and produce two symmetrical circular streams flowing in opposite directions at frequencies $\pm \Delta\omega$. These circular streams cause the kinematic frequency shift from resonance at ω_0 and, consequently, produce corresponding time shifts $\mp \Delta t$ of the echo peaks from the central position at $t = 2\tau$. Unexpected time shift to higher times $t > 4\tau_1$ of the position of the second echo peaks is also discussed and explained by presence of spiral trajectories of flowing liquid particles.*

Keywords: *NMR, Spin Echo Form, Flowing Liquid, Structure, Acoustic Flow, Frequency Shift*

1. Introduction

Various properties of flowing liquids can be studied by using NMR spin echo technique in the presence of a constant or pulse field gradient along the direction of flow [1].

It is known that a flow structure can change with increasing of velocity and Reynolds number. The basic theory [2, 3] gives good description for the form of spin echo signals in the laminar flow region. Some researchers [2, 3, 4] have observed the "anomalous" spin echo signals in turbulent flows, but they did not obtain any good explanation about the form of the signals. The form of an echo signal has great importance in flow velocity measurements because it influences on the measurement errors. Here the short explanation of the results of the papers will be proposed. The reason for discussion this theme is caused by the influence of the echo form on measurement errors in flow velocity measurements.

2. Subject and Methods

Four peaks of spin echo signals in NMR flow measurements

Flow measurements are usually carried out by using spin echo or Carr-Purcell-Meiboom-Gill (CPMG) pulse sequences. Usually first and odd number echo amplitudes are measured in the Carr-Purcell-Meiboom-Gill sequence with rf phase sensitive detection. The stimulated spin echo pulse sequence is also used frequently for flow measurements of high viscous liquids.

Four peaks in the spin echo signal have been observed and the phenomenon explained by Volkov *et al* [3]. For simplicity authors have considered the case when the length L of a transmitter coil of a NMR spectrometer is much greater than the length of a receiver coil l . According to the publication [3], the complex amplitude of a stimulated spin echo signal for flowing at a velocity v liquid can be described by

$$S(a,t) = A(T_1, T_2, D, t) K(g_0, l, t) \int_{-\infty}^{\infty} f(v) \exp(ia v) dv, \quad (1)$$

where $A(T_1, T_2, D, t)$ is a function describing relaxation and diffusion damping of an NMR signal, T_1 and T_2 are relaxation times, D is a diffusion coefficient, g_0 and g_p are the amplitudes of constant and pulse magnetic field gradients.

$$K(g_0, l, t) = \frac{\sin[0.5\gamma g_0 l(t - \tau_1 - \tau_2)]}{0.5\gamma g_0 l(t - \tau_1 - \tau_2)}, \quad (2)$$

$$a = \gamma g_0 \left[\frac{t^2}{2} - t(\tau_1 + \tau_2) + \frac{\tau_1^2 + \tau_2^2}{2} \right] + \gamma g_p \Delta \delta, \quad (3)$$

τ_1 and τ_2 are time intervals between the first and second and the first and third 90° rf pulses, respectively. The formula (2) represents an echo form in the absence of the relaxation and diffusion for an immobile cylinder sample. The amplitude of a spin echo represents itself the oscillating function of time. The form of an echo has usually three peaks for diode detection. The formula (3) describes the total effect of the constant g_0 and g_p gradients on the phase shift of a spin echo signal. Δ and δ are a time interval between the gradient pulses and width of these pulses.

The phase of a spin moving with a velocity V at a moment $2\tau_1$ is $\varphi = \gamma g_0 V \tau_1^2$ for a steady gradient and $\varphi = \gamma g_p V \delta \Delta$ for a pulse gradient. In case of laminar flow of viscous liquid in the round pipe, a profile of velocities can be described by a parabola $V = 2V_0 \left(1 - r^2 / R^2\right)$, where V_0 is an average velocity, R is a pipe radius. After integrating accounting the distribution of the velocities in the pipe, the amplitudes of echo signals are described by

$$R_x(t) = \frac{\sin 2\gamma V_0 (g\tau_1^2 + g_1 \delta \Delta)}{2\gamma V_0 (g\tau_1^2 + g_1 \delta \Delta)}. \quad (4)$$

Therefore, laminar flow results in a $(\sin x)/x$ behavior and the doubled frequency of oscillation of the echoes compared to a cosine behavior and oscillations for plug flow. But the spin echo changes its form near the zeroes of the function (4). The reason is that the signal function (1) is the product of the functions (2) and (4). As a result the spin echo form obtains an additional minimum at its center and has four peaks in this case [3].

Splitted echo signals at the presence of ultrasonic irradiation

The splitted (two-maxima) echo signals have been observed at the presence of ultrasonic irradiation of the water sample containing some amount of paramagnetic salt by Zverev *et al* [4]. The time positions of the peaks were shifted from the usual position at $t = 2\tau_1$ by a small values $\mp \Delta t$. The geometry of the experiment was as follows (Fig.1). The test-tube containing a solution of paramagnetic salt has been irradiated by the strong ultrasonic waves along the long axis of the sample. The tube was placed between the poles of the electromagnet and NMR signals were observed in the homogeneous magnetic field. No gradients of the magnetic field were used. But two symmetrical circle streams flowing in the opposite directions have been seen at the photography made at one side of the tube.

Splitted and shifted to higher times spin echo signals

Koji Fukuda and Akira Hirai [2] have performed pulsed NMR experiments of Carr-Purcell-Meiboom-Gill type on water flowing through a circular pipe. The flow patterns studied were Poiseuille (laminar) flows and turbulent flows. Near the critical Reynolds number the spin echo peaks were noisy and began split into two peaks. They obtained an unexpected time shift

to higher times $t > 4\tau_1$ of the position of the second echo peak with the field gradient vector along the pipe, in the case of turbulent flow. As the Reynolds number became larger than its critical number, the shift of the peak became larger.

3. Results

As to the paper of Zverev *et al.* [4], the explanation of the spin echo splitting is in the structure of the water stream in the test tube. It is known that the acoustic pumping causes the water flow. It is the phenomenon of so called ‘‘Acoustic Flow’’ or ‘Acoustic Wind’ [5]. The acoustic flow can be described by the equation

$$\frac{\partial \mathbf{v}}{\partial t} + (\mathbf{v} \nabla) \mathbf{v} - \frac{\eta}{\rho} \Delta \mathbf{v} = -\frac{\nabla P}{\rho} + F, \quad (5)$$

where P , ρ are the pressure and density of a fluid, η is the viscosity coefficient, F is the force of the acoustic radiation acting on the unit mass of a fluid and causing the flow at a velocity \mathbf{v} . For the acoustic radiation amplitude A in the direction x , the force equals to

$$F \approx \alpha A^2 \exp(-2\alpha x), \quad (6)$$

where α is the damping coefficient.

In the experiment discussed, the acoustic radiation is focused in the central region of the test-pipe. The streams of water flow move initially along the long axis of the test pipe then are reflected from the bottom of the test-pipe to return along the inner wall of the test-pipe. The volume picture of the streams looks as a ring torus (Fig.1).

Thus there are two circular flows in the region of the central plane perpendicular to direction of the resonance magnetic field which have resonance frequencies $\omega_0 \pm \omega_r$. These flows give two signals of the spin echo shifted symmetrically relative to the position of the echo maximum for immobile water.

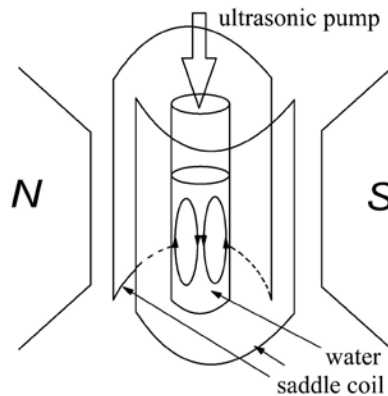


Figure 1. Scheme of the experiment [4].

It is known from the work of Vecheruchin *et al* [6], that circular motion can induce the kinematic shift of the NMR. The spin induction signal for this case can be calculated by

$$U(t) = -kB(x, y)^2 \exp\left(-\frac{t}{T_2}\right) \frac{\partial}{\partial t} \int_V \cos\left\{\left[\gamma B_0 + \mathbf{v}(x, y) / \sqrt{x^2 + y^2}\right] t\right\} dV. \quad (7)$$

The peculiarity of the equation (7) consists of the additional addendum $\mathbf{v}(x, y) / \sqrt{x^2 + y^2} = \Delta\omega$ which was called ‘‘the kinematic shift of the NMR’’. Here $\mathbf{v}(x, y)$ is

the distribution function of the velocity in a sample. Therefore the echo signal must have two peaks shifted from the resonance frequency $\omega = \gamma B_0 \pm \Delta\omega$ at the moments $t = 2\tau \mp \Delta t$.

The observation of the splitted and displaced spin echo signals at $t = 4\tau$ [2] can be also explained by the kinematic shift. Indeed, the echo signals at $t = 4\tau$ cannot be affected by the flow. But they may be affected by the diffusion. The turbulent flow is described sometimes as the macroscopic diffusion. The macroscopic diffusion under consideration has the peculiarity that it contains a spiral motion. The spiral motion can be represented as a sum of a circular motion at a frequency ω_c and straightforward motion. The circular motion gives the observed kinematic shift of the frequency. The growth of the displacement of the second echo with the velocity and Reynolds number is the result of the growth of ω_c .

4. Discussion and conclusion

Thus it was shown here that the form of the spin echo signals is stipulated by the structure of the flow and the time at which this echo signal is detected. Usually one “high” peak and two small peaks on two sides of the first peak can be observed according to the $(\sin x)/x$ form of the spin echo.

Four peaks can be observed for the unfortunate case when the echo maximum is in the vicinity of time of the minimum of the dependence of the echo amplitude on $\tau_1 + \tau_2$ for the stimulated echo pulse sequence.

The splitted (two-peak) echo signals can be observed for the turbulent flow with the vortexes moving in opposite directions. The displacement of the second echo maximum toward higher times can be caused by spiral motion. Such signals can be explained by the kinematic frequency shift caused by the circular part of motion of flowing particles.

To minimize errors stipulated by echo forms, measurements of the flow velocity should be performed by using integral echo amplitudes instead of simple echo amplitudes.

References

- [1] Hope TA, Herfkens RJ. Imaging of the thoracic aorta with time-resolved three-dimensional phase-contrast MRI: a review. *Semin Thorac Cardiovasc Surg.* 2008 Winter;20(4):358-64.
- [2] Fukuda K., Hirai A. A pulsed NMR study on the flow of fluid. - *J. Phys. Soc. Japan*, 47:1999-2006, 1979.
- [3] Volkov V.Ya., Bashirov F.I., Zaripov M.M. Primeneniye metodiki stimulirovannogo echa k izucheniyu techenia zhidkostey (Stimulated echo technique applied to liquid flow measurements, in Russian), in *Nekotoryyy voprosy fiziki zhidkosti (Some problems of the liquid physics)* – Kazan, RF: Kazan State Pedagogical Institute, 6: 89-99, 1976.
- [4] Zverev S.B. Zvukovyjye efekty v zhidkostyakh s magnitnymi jadrami (Sound effects in fluids containing magnetic nuclear, in Russian), in *Kogerentnyje metody v akusticheskikh i opticheskikh izmereniyakh (Coherent methods in acoustical and optical measurements)*. Vladivostok: Center of the Academy of Sciences of the USSR Edition, 88-90, 1981.
- [5] The Physical Encyclopedic Glossary (in Russian), Moscow: Soviet Encyclopedia, 1983, p.15.
- [6] Vecherukhin N.M. and Melnikov A.V. Nuclear magnetic resonance converters of velocity to frequency, *Applied Magnetic Resonance*, 22: 483-486, 2002.

Generation of Homogeneous EM Field for EMC Test Purposes

A. Krammer, R. Hart'anský

Department of Measurement, Faculty of Electrical Engineering and Information
Technology STU in Bratislava, Ilkovičova 3, 812 19 Bratislava, Slovakia

Email: anton.krammer@stuba.sk

Abstract. *This paper describes the problem of homogeneous electromagnetic field generation in consideration of an understanding of non-homogeneous performance creation of electromagnetic field propagation in real environment. One of the possible solutions how to get a homogeneous field is using of a stripline. The properties of stripline are numerically modeled and consequently measured in dependence of its input and output impedance. Based on obtained results a recommendation, which load impedances should be used to get the largest frequency range of the stripline and also the best field homogeneity in it, is prepared.*

Keywords: *Homogeneous Field, Electromagnetic Compatibility, Stripline*

1. Introduction

In EMC area it is necessary to generate electromagnetic (EM) field with given intensity and in given volume [1]. This requirement is known as the homogeneity of the EM field. If EM field is obtained by radiation of the elementary radiator, the field distribution and also its homogeneity depends on many factors, for example a frequency of radiation, a distance from the radiation source, homogeneity of the environment etc. It means that we can ensure homogeneity of the field only if EM field propagates in homogeneous isotropic and infinite environment [2].

Two possible solutions exist to generate the field with necessary requirements. Electromagnetic wave may be excited and propagated in the environment, which properties are similar to the infinite area. It is possible to ensure only in homogeneous environment without any reflections. Next, we may use special elements – equipment in which traveling wave is excited. The wave propagates in a special line, where no reflection creates and geometry is arranged to get the field with known value and distribution in every point of it. Such a special line is stripline, on which this paper is focused.

2. Infinite area with conducting floor

A behavior of the wave in infinite area with conductive plane is analyzed. Consider elementary source of EM field situated over the conductive floor in point O, as it shown in Fig. 1. The EM wave propagates to every point of the analyzed area directly and also by reflection from the conductive plane. Intensity of the direct wave may be obtained [3]:

$$E(r) = \frac{ILk^2 \sin \Theta}{8\pi^2 f \varepsilon r} e^{-jkr} \quad (1)$$

where I is a feeding current of the elementary radiator, L its length, k is a wave number, f frequency of the current and ε permittivity of the environment. The length of direct wave trajectory in dependence of deflection x' is given by equation:

$$Z_a = \sqrt{(Z_p)^2 + (x')^2} \quad (2)$$

and length of reflected wave trajectory is given by sum of two components Z_{b1} and Z_{b2} , given by:

$$Z_{b1} = \frac{X_R}{(2X_R + x')} \sqrt{(Z_P)^2 + (2X_R + x')^2} \quad (3)$$

$$Z_{b2} = \frac{(X_R + x')}{(2X_R + x')} \sqrt{(Z_P)^2 + (2X_R + x')^2} \quad (4)$$

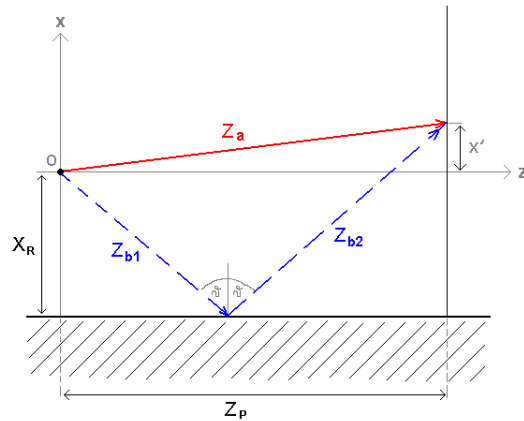


Fig. 1. Propagation of direct and reflected wave

Calculation of intensity of electric component of EM field in an observation point (distance from the radiator 10 m and 1.5 m over the ground plane) was performed at frequency 1GHz. According to (1), (2), (3), (4) a distribution of the intensity of electric field in dependence on deflection x' is calculated. Obtained distribution of the field, if only direct wave is considered, in proportion to its maximal value is shown in Fig. 2. The situation is completely different if also reflected wave is considered. Such a situation is shown in Fig. 3, where the distribution of electric component of the EM field is displayed in percents of the maximal value. As it can be seen in Fig. 3, the intensity of electric field varies from 1% to 100 % of maximal value. Such a distribution is inconvenient in term of field homogeneity. It means that only one reflection from the conductive plane (floor) can decline an experiment and disable to get homogeneous field. It is necessary to reduce possible reflections from the conductive plane using absorber materials to achieve proper field homogeneity [4].

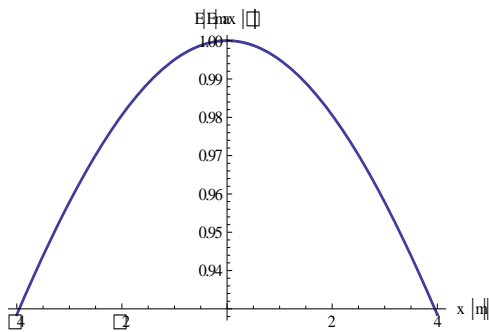


Fig. 2. Distribution of E for direct wave

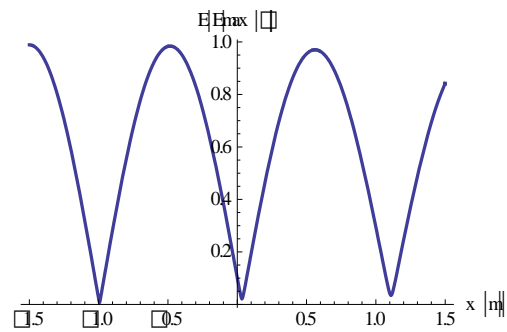


Fig. 3. Distribution of E for direct and reflected wave

3. Use of special elements to obtain homogeneous field – stripline

Another possibility how to obtain a homogeneous field for EMC purposes is using of a stripline. It consists of two strips with constant wave impedance. A traveling wave propagates through these strips. Electric field between the strips is homogenous and depends only on the distance between the strips and amplitude of the exciting rf voltage [5]. Mechanical arrangement of the stripline is shown in Fig. 4. The size of its parallel sheets is 30 x 30 cm and a distance between these strips also 30 cm. It is easy to determine characteristics of stripline in term of its field homogeneity or amplitude-frequency characteristics because it represents just a modification of two parallel plates. According to [6] the field homogeneity shall be fulfilled in 50 % of the stripline cross-section minimally. To use stripline for EMC purposes it is necessary to examine this fact for given stripline. A geometric arrangement of the stripline was modeled in FEKO, which is based on method of moments. Hence, it can

calculate a current distribution along the strips and also the electric field distribution consequently. The result of the numerical simulation for frequency 50 MHz is shown in Fig. 5, where electric field is expressed in dB units. As it can be seen the entire area is practically homogenous except for marginal parts of the examined area.

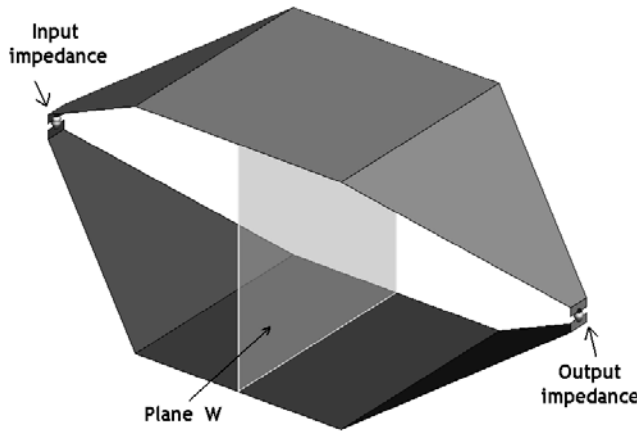


Fig. 4. Arrangement of stripline

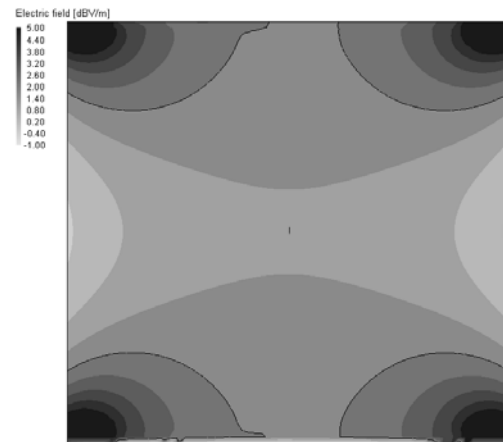


Fig. 5. Distribution of EM field in plane W

Another results shows in Fig. 6 the dependence of homogeneity rate on frequency for three parameters of a tolerance (± 3 dB, ± 2 dB and ± 1 dB) and terminal impedances of stripline 200Ω . If a ± 3 dB tolerance were chosen (common tolerance for EMC measurements [1]) the homogeneity is ensured for 94 % of area minimally. Also if more strict tolerance is chosen, for example at ± 1 dB tolerance it is possible to use more than 71 % of area. Such results confirm the possibility of the stripline use in EMC area [6].

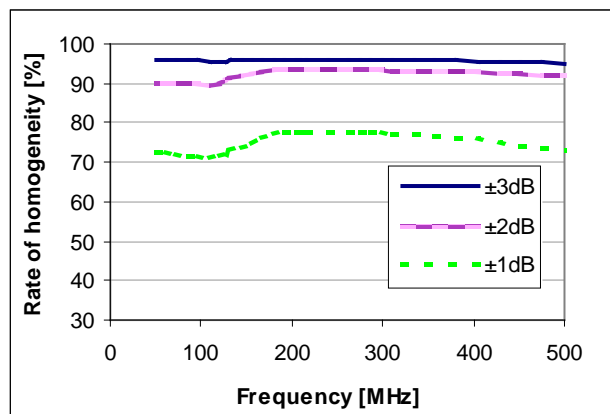


Fig. 6. Dependency of homogeneity rate in stripline on frequency

As it was mentioned the stripline consists of two parallel plates. Hence, aligned amplitude-frequency characteristic may be assumed according to [5]. The real characteristic was analyzed as a dependence of input as well as output impedance. This was expressed as a dependence of a variation of average value of the electric field E_{AVG} on frequency, shown in Fig. 7. Value of E_{AVG} was calculated as an arithmetic mean of electric field intensity values in $X \times Y$ points of cross-section W (see Fig. 4):

$$E_{AVG} (dB) = 20 \cdot \log \left(\frac{\frac{1}{X \cdot Y} \sum_{i=1}^X \sum_{j=1}^Y E_{ij} (V/m)}{1V/m} \right) \quad (5)$$

As it can be seen in Fig. 7 the amplitude-frequency characteristic of the stripline is evidently dependent on frequency. In analyzed frequency range 50 MHz to 500 MHz an undulation of the characteristics are until 15 dB. Such an undulation is unexpected in regard to [5]. Therefore we tried to minimize the undulation of the characteristic by change of the input Z_{IN} and load (output) Z_{OUT} impedance. A dispersion of standard deviation of E_{AVG} is examined in dependence of various combinations of the impedances. This dependence is shown in Fig. 8

for some of impedance combinations. A goal of this analysis was to find such a values of Z_{IN} a Z_{OUT} that value of the standard deviation is minimal. There are suitable values of impedances that can minimize the undulation of amplitude-frequency characteristic, as it is shown in Fig. 8. In our case of $Z_{IN} = 200\Omega$, if $Z_{OUT} = 110\Omega$ the minimal standard deviation of E_{AVG} is only 5 dB.

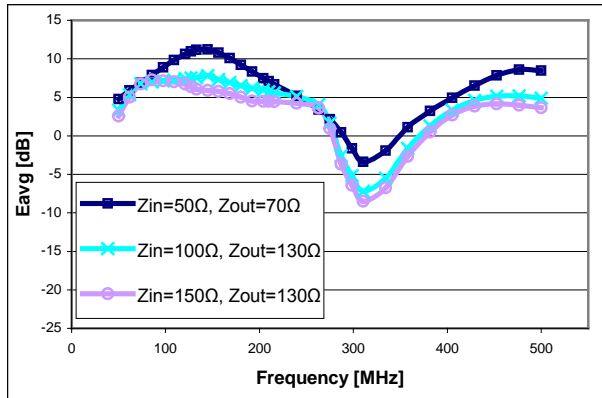


Fig. 7. Dependence of E_{AVG} on frequency with parameters Z_{IN} and Z_{OUT}

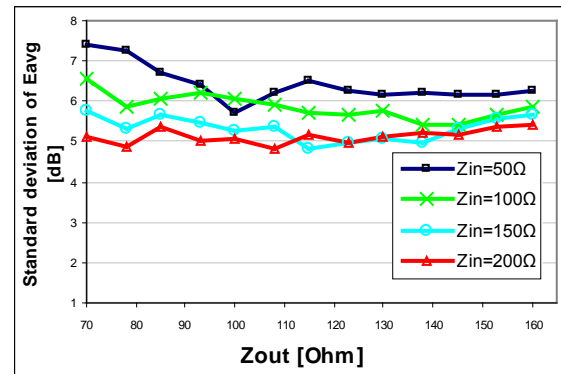


Fig. 8. Dependence of standard deviation of E_{AVG} on Z_{OUT} with parameter Z_{IN}

4. Conclusion

In this paper the problem of homogenous EM field generation for EMC purposes was analyzed. Obtained results concerning to field homogeneity in the stripline are evidently better than it is published in available EMC standards [6]. However, the amplitude-frequency characteristics of the stripline are not so straight as it was expected [5]. Using various combinations of input and output impedances, the undulation can be minimized only to 5dB in frequency range from 50 MHz to 500 MHz using input impedance $Z_{IN} = 200\Omega$ and output impedance $Z_{OUT} = 110\Omega$.

Acknowledgement

This work was supported in part by grant project VEGA 2/0006/10 and VEGA 1/0551/09.

References

- [1] EN 61000-4-3:2006 Electromagnetic compatibility (EMC). Part 4-3: Testing and measurement techniques - Radiated, radio-frequency, electromagnetic field immunity test.
- [2] Goedbloed J. Electromagnetic compatibility. Kluwer Technische Boeken B.V. 1990.
- [3] Vavra Š, Turán J. Antenna and propagation of electromagnetic wave. Alfa, Bratislava, 1989.
- [4] Bittera M, Smieško V, Kováč K. Modeling of Ferrite Lined Semi-Anechoic Chambers. In: EMD 2006. XVI International Conference on Electromagnetic Disturbances. Kaunas, Lithuania, 27-29.9.2006. - Kaunas, Technical University, 2006.
- [5] Johnk C.T.A. Engineering electromagnetic fields and waves. John Wiley & Sons, New York, 1988.
- [6] IEC 801-3 Electromagnetic compatibility for industrial-process measurement and control equipment, Part 3: Radiated electromagnetic field requirements.

Reproducibility of Long Cable Test-Setup of EMC Measurements

J. Hallon, M. Bittera, R. Hart'anský, K. Kováč, V. Smieško

Dept. of Measurement, Slovak University of Technology, Ilkovičova 3, 812 19 Bratislava, Slovak Republic

jozef.hallon@stuba.sk, mikulas.bittera@stuba.sk, rene.hartansky@stuba.sk,
karol.kovac@stuba.sk, viktor.smiesko@stuba.sk

Abstract. This paper deals with an analysis of influence of geometrical arrangement of cables at immunity test against rf electromagnetic field. The effect of a length of the single-wire cable shortened into a bundle upon frequency dependence of induced current, which flows through the wire, is analyzed using numerical simulations. Results obtained by numerical simulations are verified by measurement of real electrical structure.

Keywords: Immunity Testing, Transmission Lines, Influence of Electromagnetic Field, Nondestructive Shortening of Single-Wire Line

1. Introduction

Many of electrical systems contain cablings, which ensure their contact with a surrounding environment. The arrangement of such a cabling is a determining factor of a validity of electromagnetic compatibility (EMC) tests. One of EMC tests, which may be affected by cabling arrangement, is test of immunity against rf electromagnetic (EM) field [1]. A methodology of the test, according to the standard, requires an assurance of homogeneity of EM field within test area and a compliance with specified configuration of a test site.

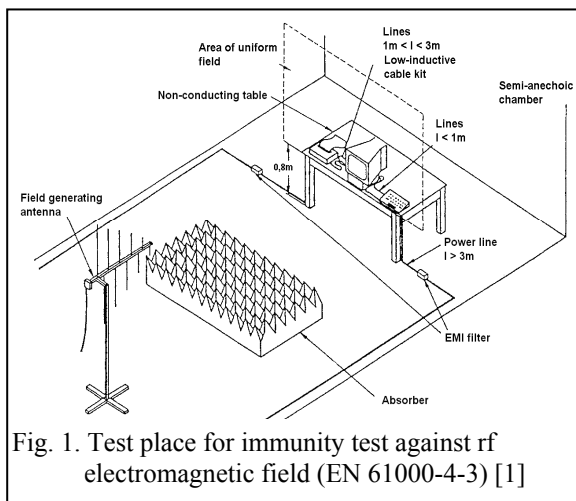


Fig. 1. Test place for immunity test against rf electromagnetic field (EN 61000-4-3) [1]

A configuration of test place for a table-top equipment under test (EUT) represents a basic arrangement of the test place. A problem occurs if equipment's cabling, which is arranged freely on the test table, does not have the specified length of 1 m and it is not possible to shorten it simply to that length. In the case of cables with length between 1 and 3 m, the standard [1] specifies nondestructive shortening into the bundle. This bundle should consist from unbounded loops [2], [3].

A change of geometrical arrangement of the EUT's cabling causes a change of its electrical properties. If this change is significant, the induced currents at the ends of the cable, which is situated in EM field, will be dependant on current cabling configuration. Such situation should not happen according to recommended technical standard. A signification of this effect is given by the fact that almost no external cabling of EUT has necessary length of 1 m. Nondestructive shortening of illuminated cable lengths belongs to frequently performed activities of test engineers. The aim of this paper is qualify a signification of this effect.

2. Creation of test configuration model

The cabling of EUT was replaced by transmission line (TML) to simplify a model. Effect of the EM field to TML was a topic of several works [4], [5]. Their aim was analytical determination of currents flowing through impedances of the cable interfaces. In case of analysis of more complicated shapes of TML, it is more suitable to use the numerical

simulation methods. The numerical simulator FEKO, based on method of moments, was used in our analysis.

The situation, that really occurs by TML irradiated by EM field, may be analyzed using common mode (CM) model of the line. The disturbing common mode voltage is generated between wires of the cabling and conducting reference plane. Coupling between cabling and

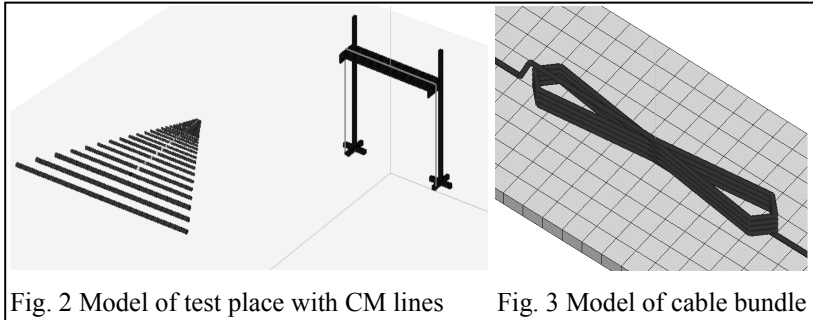


Fig. 2 Model of test place with CM lines

Fig. 3 Model of cable bundle

reference plane is accomplished via cable terminating impedances or via parasitic impedances between them. The latter is dominant in case of tested devices with large cablings.

Single-wire cable long 1m situated in 80 cm height over

the plane was considered in our analysis. This cable was terminated by $50\ \Omega$ impedances to the reference plane and was irradiated by plane EM wave. Such a simple model of the test place may be extended to more complex one, which describes better a behavior of the real system. Then some other parts should be added into the model. Those could be supporting elements from dielectric materials and also dielectric insulation of the wire. The model of log-periodic dipole array is used to simulate the real field source truly.

Only the ground plane was included into the model of anechoic-shielded chamber. Omission of absorbers, which are during the test situated between the antenna and EUT, within the model deteriorated a homogeneity of EM field in vertical direction due to reflections from the ground plane. However, the irradiated cables were in constant height over the plane, so an absence of the absorbers is acceptable. The transmitting antenna was excited by a voltage levels, which ensured EM field according to standard requirements [6]. The model created in FEKO simulator is shown in Fig. 2.

In case of longer cables, which are shortened to 1 m length by nondestructive shortening, the model shall contain also the cable bundles (Fig. 3).

3. Measurement setup

A complex system for testing immunity of EUT against rf field was used to verify obtained results of previous analysis. Stabilized power supply BK 127 was used as EUT. It is a simple regulated analogue voltage source based on integrated circuit $\mu A723$ and realized without considering EMC properties. The complex testing system allows measuring of EUT output voltage during the test, so it is possible to measure frequency dependences of output voltages of the tested power supply on disturbing EM field. Also dependences of absolute additional error may be calculated from the measured values of output voltage.

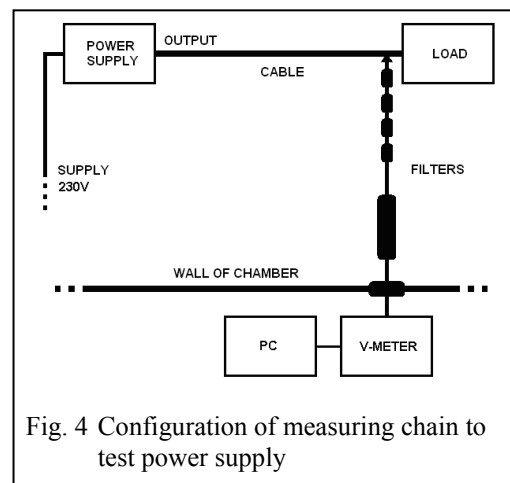


Fig. 4 Configuration of measuring chain to test power supply

A configuration of measuring place is shown in Fig. 4. The EM field was generated according to the standard EN 61000-4-3 [1]. The tested power supply was placed on a wooden board 80 cm over the ground plane. Output cables of voltage source were shortened by the bundle and were situated on the table perpendicularly to EM wave propagation direction. The cables

were terminated by resistive load. Measuring cable was connected into the load to monitoring the output voltage. Additional filters, which ensure rf isolation from the tested source, were added to the measuring cable and this cable was connected to a voltmeter, situated outside the chamber. Measured data acquisition from the voltmeter as well as generating of required EM field was controlled by a computer.

4. Simulated and measured results

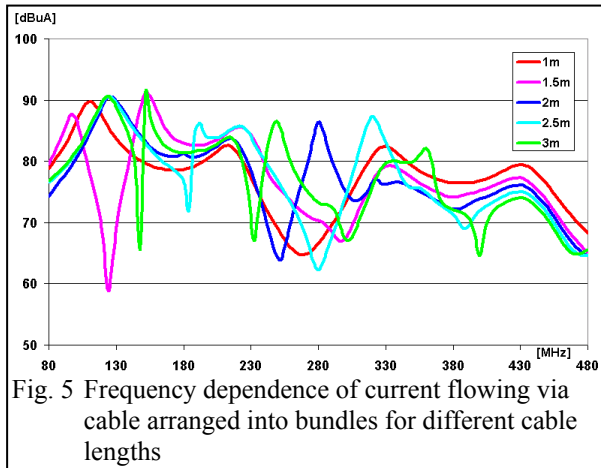


Fig. 5 Frequency dependence of current flowing via cable arranged into bundles for different cable lengths

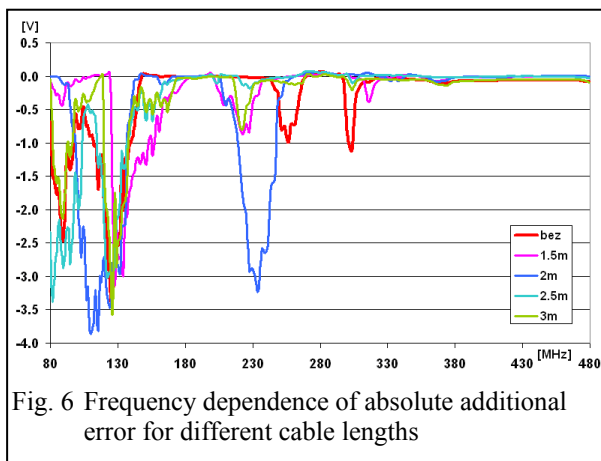


Fig. 6 Frequency dependence of absolute additional error for different cable lengths

Similarly, if same test was realized using the real measurement of the power supply, the maximal error of the output voltage (for different lengths of the cable) varies from 3.14 to 3.86 V, if nominal value of the supply voltage was 10 V (see Fig. 6).

Analysis of bundle positions: The similar three-meter long cable shortened using the cable bundle was used as in previous case. The bundle position was changed. At first it was situated at the center of a horizontal part of the cable, then in near end (from a view of the induced current) and finally in the far end of the cable horizontal part.

Analysis of cable length effect: A model of cable bundles was used as a consideration of shortened cable with length of 1.5, 2, 2.5 or 3 m to the length of 1 m. Longer cables were arranged into more bundle loops with constant geometrical parameters. The length of the bundle loops was 250 mm, their diameter of bending 10 mm, diameter of the wire was 1 mm and a distance between the loops was 2 mm. The cable bundle was situated at the center of the cable. Such cable was irradiated by horizontally polarized log-periodic antenna and the intensity of EM field in the place, where the tested cable was situated, was 10 V/m.

Frequency dependences of induced current for shortened cables of different lengths, which were obtained using numerical simulations, are shown in Fig. 5. Even if maximal values of the induced current are very similar (maximal difference is less than 1.5 dB), an use of bundles increases a probability of high current zone appearance (the frequency dependence has three or four current peaks). Hence it may influence the test validity.

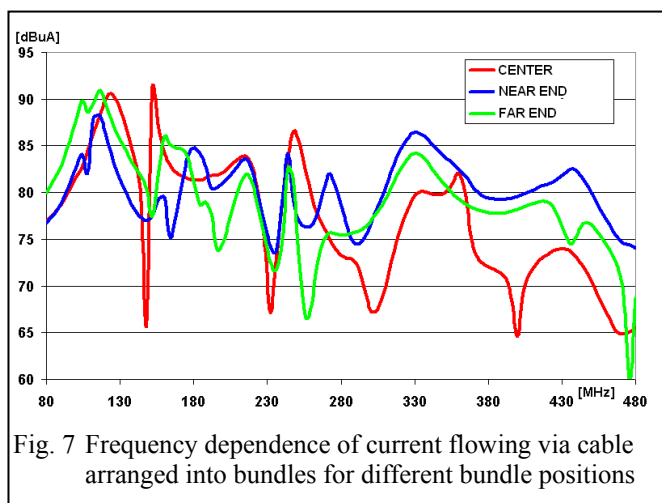


Fig. 7 Frequency dependence of current flowing via cable arranged into bundles for different bundle positions

In Fig. 7, one can see simulated frequency dependences of induced current on the cables shortened using the cable bundle for different position of the bundle in a horizontal part of the cable. Maximal values of the current differ no more than 3 dB. Moreover, the various shape of frequency dependences, similarly to the previous analysis, shows evidence of an influence of the cable bundle position upon the induced current value.

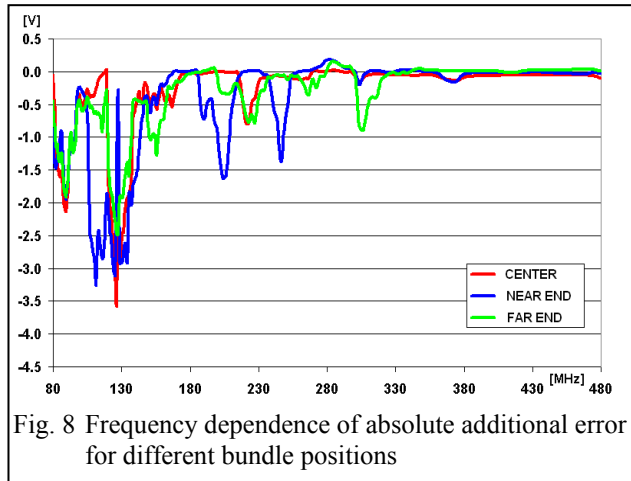


Fig. 8 Frequency dependence of absolute additional error for different bundle positions

Also an experiment with changing the bundle positions was performed with output cable of the power supply. Maximal absolute errors are in interval from 2.49 to 3.53 V. Evident change of shape of the frequency dependence may be seen in Fig. 8 as well as the change of the maximal error of the power supply output voltage.

5. Conclusions

The standard EN 61000-4-3 allows shortening of cables with length from 1 to 3 m into the bundles. However, as it was shown in this paper, such bundles affect the shape of the frequency dependence of induced current due to their position and arrangement. Even if differences between maximal values of the currents are not so evident (maximally 3 dB), frequencies of such maxims change and also there are more local maxims of the induced current in the analyzed frequency range. It may affect validity and also reproducibility of the immunity test. Therefore it is advisable to avoid such a cable shortening in an EMC testing practice.

Acknowledgements

Work presented in this paper was supported by the Slovak Ministry of Education under grant No. 2003SP200280802 and by the Slovak Grant Agency VEGA under grant No. 1/0551/09.

References

- [1] EN 61000-4-3:2006 Electromagnetic compatibility (EMC) - Part 4-3: Testing and measurement techniques - Radiated, radio-frequency, electromagnetic field immunity test.
- [2] Kováč K, Hallon J, Bittera M. Influence of Non-Destructive Shortening of Long Cables upon Repeatability of EMC Immunity Tests. In proceedings of the 19th International Symposium and Exhibition. Wroclaw, 2008, 338-341.
- [3] Van Wershoven L. The effect of cable geometry on the reproducibility of EMC measurements. In proceedings of the IEEE EMC Symposium. Seattle, 1999, vol.2, 780 – 785.
- [4] Paul CR. Analysis of Multiconductor Transmission Lines. New York: Wiley Interscience, 1994.
- [5] Omid M, Kami Y, Hayakawa M. Field Coupling to Nonuniform and Uniform Transmission Lines. *IEEE Transactions on EMC*, vol. 39, no. 3, 1997, 201 - 211.
- [6] Hallon J. Specialty of EMC measurements of large systems. PhD. Theses, Slovak University of Technology in Bratislava, Faculty of Electrical Engineering and Information Technology, Bratislava, 2010.

The Iterative Method of Parameters and Centre of Radial Distortion Estimation

R. Ravas, L. Syrová, J. Grman

Department of Measurement, Faculty of Electrical Engineering and Information Technology, Ilkovičova 3, 812 19 Bratislava, Slovakia,
Email: rudolf.ravas@stuba.sk

Abstract. Correction of radial distortion of the image is a very important process during the calibration of non-metric camera intrinsic parameters. The paper treats the topic of estimation of coefficients and the centre of radial distortion of the image. A new method of coefficients and coordinates of the centre of radial distortion estimation in the image is presented. It is based on the iterative correction of coordinates of selected points on the distorted straight lines. It does not require a parametric expression of distorted lines. It is presented verification of method properties on simulated and real images.

Keywords: Radial Distortion, Image Correction, Straight Line

1. Introduction

During measurement of spatial coordinates of scene interest points by the use of non-metric cameras it is necessary to establish camera model parameters. Model of the camera describes relation of spatial coordinates of scanned point to the coordinates of its image in the camera image plane. Model is established by intrinsic and extrinsic camera parameters. Extrinsic camera parameters express the relationship between coordinates of the point in the space in world coordinate system and coordinates of the same point in camera coordinate system. Relationship between camera and world coordinates of the spatial point is defined by the translation vector and rotation matrix expressing the position and rotation of camera to the world coordinate system. Intrinsic camera parameters are parameters of the model describing relationship between position of the point in the space with coordinates expressed in the coordinate system of the camera and position of the image of the same point expressed in the image coordinate system [1]. Model describes the mechanism of distortion of image point position caused by the imperfection of camera lens as well. The now widely recognized significant source of distortion caused by the camera optics is radial distortion of the image [2] described by model [3]

$$r_d = r(1 + \alpha_2 r^2 + \alpha_4 r^4 + \dots) \quad (1)$$

where

r is distance of the point in ideal undistorted image to the centre of distortion

r_d is the distance of the point in the radial distorted image to the centre of distortion

α_i are coefficients of radial distortion of the image

There are mainly used models with the second, maximal the fourth order of polynomial in published papers [3]. Existing methods of radial distortion correction can be divided into two groups of approaches to the solution. The first approach (multiple view method) uses the correspondence of images of the scene point in multiple images using constrains among images to correct distortion of their position in images. The second approach characterizes methods using only one image [4]. Methods using one image are usually based on the fact that at the perspective projection (assumption in many models) the ideal image of the straight

line in space is straight line. The strategy of methods based on this assumption is based on the detection of potential images of the straight line whose models are quadratic curves well approximating images of lines deformed according model (1). The individual methods differentiate by the ways of approximation of the line images, number of parameters and modification of the model (1) and whether they would calculate centre of radial distortion or whether they would identify centre of radial distortion to the principal point of the image [5]. Method presented in this paper considers the possibility that the centre of distortion and the principal point are not the same. This fact is emphasized in many papers [4], [6]. The submitted method does not require to parameterize distorted image of the straight line.

2. Subject and Methods

Let's suppose to have K sets of images p_{ki} of selected points with coordinates (x_{ki}, y_{ki}) that are in the distorted image. Images of p_{ki} should lie on the straight line L_k in ideal undistorted image. Model (1) is replaced by models considering unequal distortion along the coordinate axes of the image that can be for each point p_{ki} expressed by

$$r_{xki} = \frac{r_{dki}}{(1 + \beta_{x2} r_{dki}^2 + \beta_{x4} r_{dki}^4)} \quad r_{yki} = \frac{r_{dki}}{(1 + \beta_{y2} r_{dki}^2 + \beta_{y4} r_{dki}^4)} \quad (2)$$

where

r_{xki} , r_{yki} are relative coordinates of point p_{ki} to the centre $C=(c_{dx}, c_{dy})$ of radial distortion in undistorted image

r_{dki} is the distance of the image point to the centre of radial distortion in distorted image

β_{x2} , β_{x4} , β_{y2} , β_{y4} are coefficients of the inverse radial distortion along axes x , y

Coordinates (x_{cki}, y_{cki}) of points p_{cki} in undistorted image corresponding to the points p_{ki} can be expressed by

$$x_{cki} = r_{xki} + c_{dx} \quad y_{cki} = r_{yki} + c_{dy} \quad (3)$$

As the equation of the straight line L_k isn't known we use straight line $l_k(x, y)$ that approximates all points p_{cki}

$$l_k(x, y) = a_k x + b_k y + c_k = 0 \quad \sqrt{a_k^2 + b_k^2} = 1 \quad (4)$$

Square of perpendicular distance of point p_{cki} to the straight line (4) will be

$$d_{cki}^2 = l_k^2(x_{cki}, y_{cki}) = (a_k x_{cki} + b_k y_{cki} + c_k)^2 \quad (5)$$

In case of ideal undistorted image sum of distances (5) of all points p_{cki} equals to zero. All corrected points lie on the straight lines (3). We don't know neither corrected coordinates (3) at the start of solution or equations of approximating lines (4). Therefore correction of radial distortion of the image is based on the iterative improvement of values of unknown parameters such as the centre of radial distortion $C=(c_{dx}, c_{dy})$ and parameters β_{x2} , β_{x4} , β_{y2} , β_{y4} are calculated. As the objective is to minimize cost function of 6 parameters $\omega=[c_{dx}, c_{dy}, \beta_{x2}, \beta_{x4}, \beta_{y2}, \beta_{y4}]^T$ defined by

$$J(\omega) = \min_{\omega} \sum_{k=1}^K \sum_{i=1}^{n_k} (l_k(x_{kic}, y_{kic}))^2 \quad (6)$$

where n_k is number of points corresponding to the k -th line. In j -th step of iteration are calculated partially corrected values of points p_{ckij} coordinates for parameter ω_j . From their parameters of $l_{kj}(x, y)$ are calculated by the use of farthest points of subset of points corresponding to L_k . Then the value of cost function (6) can be calculated. Values of ω_{j+1} for

the next step of iteration will be established from the values of parameters near the previous value. Such a value of parameter will be chosen for that value of cost function (6) is less than the value of this function for ω_j .

3. Results

In order to verify the accuracy of the proposed methods simulation experiments and real images of chessboard captured by CCD camera have been used. In both experiments ideal images of points arranged in a grid were examined. Images of grid points in ideal case lie on related vertical and horizontal lines. The ability to correct distorted coordinates of points according to model (2) was in simulations investigated in such a way that corrected coordinates were close to the coordinates of points of ideal undistorted image. Criteria published in [3] have been used to quantify successfulness of correction. Criteria such ARE (Average Residual Error) and MRE (Maximum Residual Error) for deviation of corrected distorted (x_{ci}, y_{ci}) to ideal image points (x_{li}, y_{li}) and quantities corresponding to the criterion (6) of optimisation such as the mean AREL and maximum MREL deviation from the approximating line were.

$$ARE = \frac{1}{N} \sum_{i=1}^N \sqrt{(x_{ci} - x_{li})^2 + (y_{ci} - y_{li})^2} \quad (7)$$

$$MRE = \max_i \sqrt{(x_{ci} - x_{li})^2 + (y_{ci} - y_{li})^2} \quad (8)$$

Criteria AREL and MREL are defined by

$$AREL = \frac{1}{K} \sum_{k=1}^K \frac{1}{n_k} \sum_{i=1}^{n_k} \sqrt{(l_k(x_{kic}, y_{kic}))^2} \quad (9)$$

$$MREL = \max_{i,k} \sqrt{(l_k(x_{kic}, y_{kic}))^2} \quad (10)$$

Table 1. Values of criterion of optimisation and errors for three simulation experiments and correction of the image of planar calibration object in the form of chessboard captured by CCD camera.

Sample	$J(\omega)$	MRE	ARE	MREL	AREL
Sim 1.	0.0044	0.0918	0.0083	0.0204	0.0013
Sim 2.	186.35	10.0469	0.6216	3.1859	0.2786
Sim 3.	0.0873	1.0167	0.0717	0.1060	0.0060
Real	11.7522	-	-	0.7461	0.0429

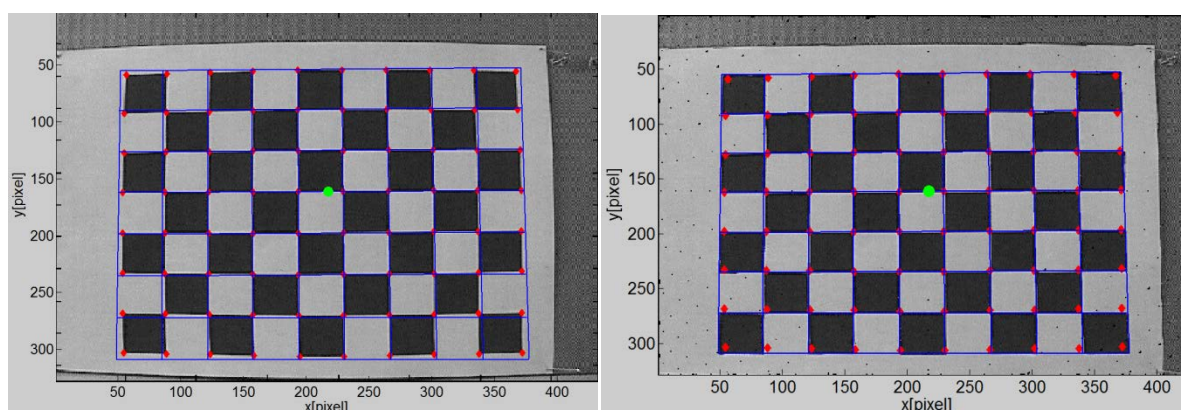


Fig. 1. Distorted and corrected image of the chessboard planar calibration object.

In the table 1 values of mentioned quantities for grid 7x7 points for 3 chosen simulation experiments and correction of real image are presented. In the first experiment image was

distorted symmetrically in both directions of the image, in the second and the third the distortion was different in horizontal and vertical direction with parameters in the table. The results of the second experiment are quantified by the described errors in case when symmetrical model of distortion for the correction was used and in the third case when the model thinking different distortion in horizontal and vertical direction was used. Images captured with CCD camera Mitsubishi CCD-400E (fig.1) have been used in experiments with real images. In ideal case there are corner points of chessboard as elements of vertical and horizontal straight lines on the chessboard. Corner points were extracted by Harris corner detector that can calculate coordinates of corner points with sub-pixel resolution. Module from the program [5] has been used to extract corner points. Positions of extracted points are in both images distinguished by the symbol “diamond”. Position of the radial distortion can be seen by the symbol “circle”. Numerical values of errors are in table 1.

4. Discussion

Experiments, some of which were presented in this paper, showed good properties of proposed method of correction of errors due to the image radial distortion. Optimization of non-linear criterion functions brings the risk of instability, or non-correct convergence of solution. In this case, stability and convergence of the solution is provided by the use of points standardized distances to the centre of distortion by the constant greater than the maximum distance of the corrected point to the principal point and choosing the initial value of the centre of radial distortion near the principal point. Variability of choice of initial value of the centre of distortion and of standardization constant didn't influence the convergence of solution. Initial values of radial distortion coefficients were always set to zero. Criteria AREL and MREL appear to be suitable for assessing the quality of correction in case for that coordinates of points in ideal undistorted image are unknown.

Acknowledgements

We gratefully acknowledge that the results presented here were solved as partial goals of the research task VEGA No. 1/0490/10.

References

- [1] Devernay F, Faugeras O. Straight lines have to be straight, *Machine Vision and Applications*, 13: 14–24, 2001.
- [2] Yusoff F, Rahmat R, Sulaiman MN, Shaharom MH, Majid HSA. Establishing the straightness of a line for radial distortion correction through conic fitting, *IJCSNS International Journal of Computer Science and Network Security*, 9 (5): 286 – 293, 2009.
- [3] Bräuer-Burchardt Ch. A simple new method for precise lens distortion correction of low cost camera systems, C.E. Rasmussen et al. (Eds.): DAGM 2004, LNCS 3175, pp. 570–577, 2004.
- [4] Wang A, Qiu T, Shao L. A simple method of radial distortion correction with centre of distortion estimation. *J Math Imaging Vis*, 35: 165–172, 2009.
- [5] Bouguet JY. Camera calibration toolbox for matlab®. http://www.vision.caltech.edu/bouguetj/calib_doc/. (last updated July 9th, 2010).
- [6] Hartley R, Kang SB. Parameter-free radial distortion correction with center of distortion estimation. *IEEE Transactions on Pattern Analysis and Machine Intelligence*, 29 (8): 1309-1321, 2007.
- [7] Bailey DG. A new approach to lens distortion correction. Proceedings Image and Vision Computing New Zealand 2002, 2002, 59-64.

Round Window Membrane Vibration Measured by Laser Doppler Vibrometer

¹M. Kwacz, ²M. Mrowka, ²J. Wysocki

¹Institute of Micromechanics and Photonics WUT, Warsaw, Poland,

²Institute of Physiology and Pathology of Hearing, Warsaw/Kajetany, Poland

email: m.kwacz@mchtr.pw.edu.pl

Abstract. *The paper describes the results of non-contact measurements of the human ear round window (RW) membrane vibration parameters using the scanning Laser Doppler Vibrometer (LDV) in freshly harvested human cadaver temporal bone specimens – a procedure conducted for the first time in Poland. A PSV 400 Scanning Laser Vibrometer system (Polytec, Waldbronn, Germany) was used in the research. The paper presents amplitude-frequency and phase-frequency characteristics of the RW membrane vibrations in an anatomically correct specimen (in its physiological conditions) and in the same specimen after teflon piston stapes prosthesis implantation. The characteristics were measured in a 400Hz – 10000Hz frequency range with a 90 dB sound pressure level applied to the external auditory canal. It was indicated that measurements of the round window membrane vibrations may be a tool for evaluating hearing results of surgical ossicular chain reconstruction, especially in case of otosclerosis surgery.*

Keywords: *Round Window, Vibration, Laser Doppler Vibrometry, Mechanics of Hearing Organ*

1. Introduction

The process of conducting sound waves from the external auditory canal to the structures of the inner ear is a complex mechanical process, in which air conduction (AC) plays the determining role. In the AC process the sound waves entering the auricula are directed through the external auditory canal and contact the surface of the tympanic membrane causing it to vibrate. That vibrations are passed on through the ossicular chain (malleus, incus and stapes). The vibrating stapes footplate located in the oval window (OW) niche of the bony cochlea and attached by the annular ligament cause perilymph, filling the inner ear, to vibrate. Because the perilymph is incompressible, fluctuations of the stapes cause the round window membrane interaction.

It is assumed that the amplitude of the vibrations of the stapes and the volume of the vibrating fluid neighboring the OW are a measure of the input impedance of the cochlea [1-3]. It has been empirically shown, that for frequencies below 2000 Hz the volume of the vibrating fluid neighboring the OW is the same as next to the RW, where the vibrations take place in anti-phase [4,5]. Hence, in order to determine the degree of stimulation of the cochlea in a low-frequency range (up to 2000 Hz), the volume of the vibrating fluid by the RW or the vibration amplitude of the RW membrane can be used. This is especially crucial in a situation in which the real stimulation of the cochlea is difficult to predict, e.g., after implanting various types of prostheses which transmit vibration energy to the cochlea instead of the immobilized stapes footplate (stapedotomy or stapedectomy procedures). In case the manner of cochlea stimulation changes, the aforementioned stimulation can be examined by measuring the vibrations of the RW membrane maintained in physiological condition.

2. Subject and Methods

The research was conducted in-vitro with the use of appropriately prepared fresh human temporal bone specimens obtained postmortem. Source literature [6,7] reveals, that the functioning of auditory structures in a short time postmortem specimens is the same as their functioning in physiological condition, providing that the following three requirements are met: (i) the temporal bone specimens are harvested from human cadavers within 48 hours after death, (ii) specimens are secured against drying and stored without being frozen in a temperature of approx. 5°C, until the time of measurements, (iii) the measurements are taken in a 1 to 6 day period after death. The research was conducted at the ICHS Physiology and Pathology of Hearing Institute in Kajetany, Poland and consisted of measuring the amplitude and phase of RW membrane vibrations in a frequency function (400 Hz – 10 kHz) with the sound pressure entering into the external auditory meatus at 90 dB. The amplitude-frequency and the phase-frequency characteristics were defined according to the experimental results, depending on the ossicular chain state. The measuring system was assembled on the basis of a commercially available SLDV PSV 400 scanning laser vibrometer produced by Polytec GmbH, Waldbronn, Germany. A detailed description of the measuring system as well as its parameters is supplied in “The Measurement System for Experimental Investigation of Middle Ear Mechanics” [in this Proceedings] and the view of part of the test stand is shown in Figure 1(a).

In order to prevent individual physiological differences among individual specimens from having impact on the results, the experiment was conducted in two stages: (1) stage I – measurements taken in a physiological specimen (the ossicular chain and tympanic membrane were left intact, the middle and inner ear structures were properly hydrated and the tympanic cavity properly ventilated), (2) stage II – vibration measurements in the same specimen after implanting a stapes prosthesis (retail 0.47-mm-diameter Teflon piston stapes prosthesis was used, fastened appropriately to the long crus of the incus by a platinum ribbon).

3. Results

Results of original empirical research into the parameters of the human ear round window (RW) membrane vibration in four physiologically fresh temporal bone specimens, conducted in accordance with the laser Doppler vibrometry method were obtained for air conduction at a calibrated sound intensity level of 90 dB and with frequencies ranging from 400 Hz up to 10 kHz in the external auditory canal. The characteristics of the RW membrane vibrations were determined based on measurements of displacement in measurement grid nodes. The amplitude-frequency characteristics of specimen Preparat 1 before and after stapes prosthesis implantation for targets located on the surface of the RW membrane are shown on Figure 1.

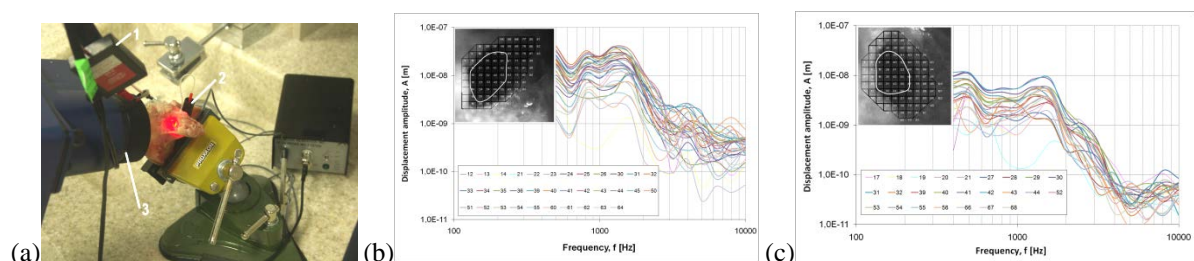


Fig. 1. (a) Photo of part of the test stand. 1 – loudspeaker ER2, 2 – probe microphone ER-7C, 3 – scanning laser head OFV-505, (b) Magnitude of the displacement amplitude of 34 measurement points on the RW membrane – stage I (physiological), (c) Magnitude of the displacement amplitude of 25 measurement points on the RW membrane – stage II (implanted). The results are from specimen Preparat 1 stimulated with an AC when the sound pressure is 90 dB SPL in the external auditory canal.

The displacement amplitude for all measurement points in low-frequency range (0.5–2 kHz) is 10-15 times greater than in the high frequency range (2–10 kHz). Characteristic resonant frequencies of the middle ear are noticeable. The decrease in displacement amplitude of vibrations for frequencies above 2 kHz is related with different vibration phases in each measurement points on the RW membrane. An example 3D visualization of the vibration pattern of the RW membrane for one temporal bone specimens at 1 kHz, 2 kHz, 4 kHz and 8 kHz and 90 dB SPL in the external auditory canal is shown on Figure 2.

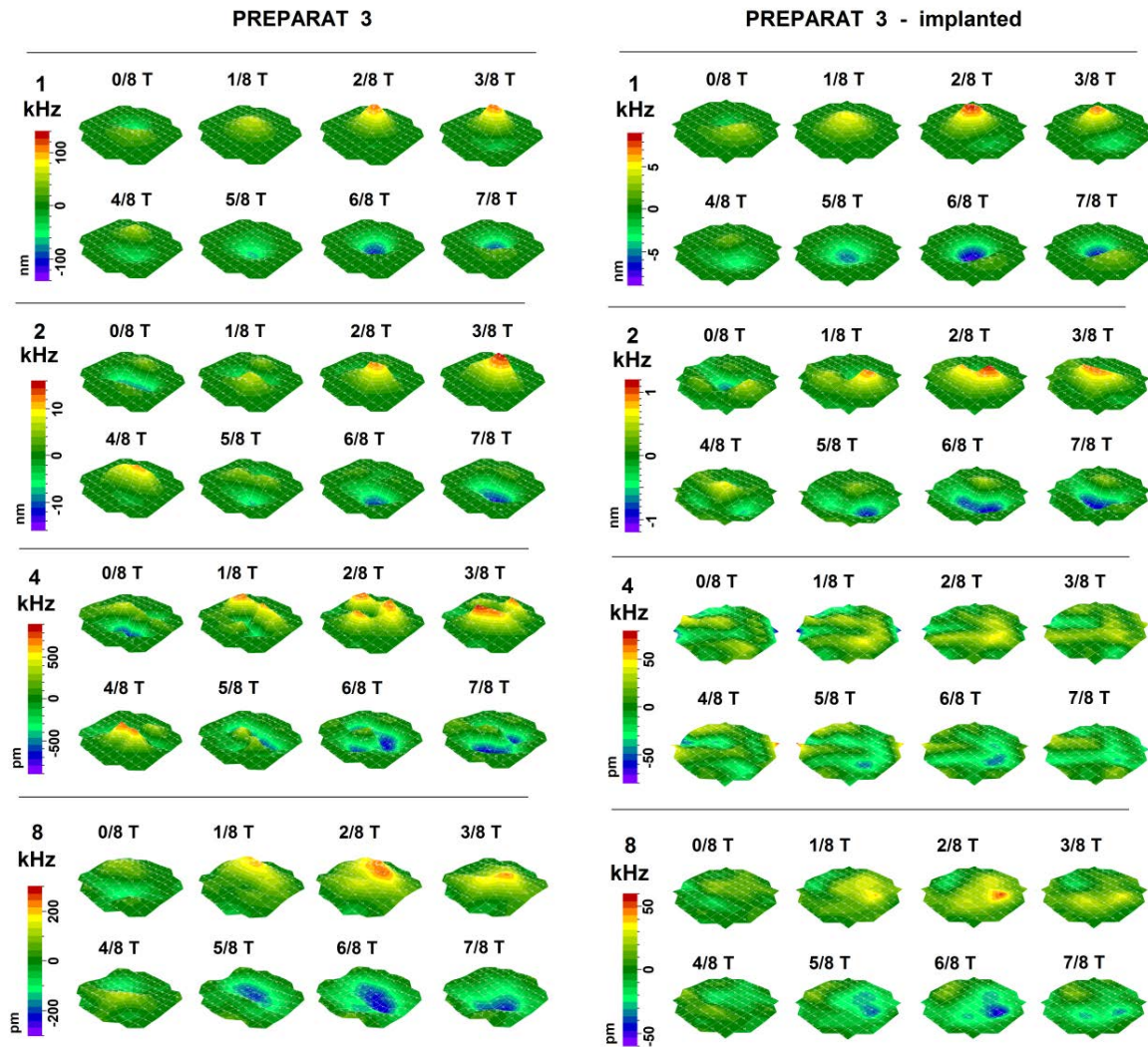


Fig. 2. The vibration pattern (3D visualization) of the RW membrane in specimen number 3 before and after Teflon piston prosthesis implantation. Visualization shows as eight pictures of period for various frequencies: 1, 2, 4 and 8 kHz. The results are shown for AC stimulation with a sound pressure level of 90 dB SPL in the external auditory canal. T – the period of vibration ($T = 2\pi/f$).

4. Discussion

The measurement results for the human ear RW membrane vibrations in four fresh cadaver temporal bone specimens for air conduction at 90 dB SPL in the external auditory canal showed that the maximum displacement amplitude for 1 kHz frequency in the central area of the RW membrane averaged 25 nm, whereas for 2 kHz, 4 kHz and 8 kHz frequencies it averaged 10 nm, 1.6 nm and 0.6 nm, respectively. The dispersion of the maximum vibration

amplitude was related with different shapes and sizes of the RW membrane in each specimen, which is a characteristic trait of biological objects demonstrating individual variability. Based on detailed iso-amplitude chart analysis it was found, that the vibrations of measurement points spread across the entire surface of the RW membrane for all examined specimens in low-frequency ranges were single-phase vibrations. Above 1250 Hz – 2000 Hz frequencies, the phase of vibration for points placed in various parts of the RW membrane was different.

Analysis of the measurements results revealed, that the vibration amplitude of the RW membrane after stapes Teflon piston prosthesis implantation, in comparison with the vibration amplitude in a physiological specimen was reduced several times. Therefore one can assume, that as a result of conducting a standard implanting procedure, a significant change in biomechanical parameters of the middle ear conductive apparatus takes place, which causes a significant changes in the input impedance of the cochlea and a significant decrease in perilymph stimulation levels. The result of a decrease in stimulation of the perilymph in post-implantation condition, in comparison with its physiological condition, in case of otologic surgery conducted in-vivo, could be the incomplete closure of the air-bone gap resulting in hearing outcomes showing signs of conductive hearing loss.

5. Conclusions

Results of conducted empirical research, shows the character of vibrations of the RW membrane in fresh human temporal bone specimens in their physiological condition. The obtained characteristics form a basis for differentiating hearing results achieved after surgical ossicular chain reconstruction. Findings presented in this paper will be of practical use in the development of a new type of stapes prosthesis.

Acknowledgements

The authors would like to thank the IPPH Director, Professor Henryk Skarzynski for granting permission to use facilities at the ICHS Head and Neck Clinical Anatomy Laboratory in Kajetany in order to conduct the research, prof. John J. Rosowski from Harvard-MIT, prof. Sunil Puria from Stanford University, dr Joe Sim and dr Michail Chatzichalis from the ORL-Clinic, University Hospital in Zurich, for their valuable advice and tips regarding preparation methods of temporal bone specimens used for experimentation.

Research was funded by the Research Project Nr N N518 377637.

References

- [1] Puria S, Peake W, Rosowski J. Sound-pressure measurements in the cochlear vestibule of human-cadaver ears. *J Acoust Soc Am*, 101 (5): 2754-2770, 1997.
- [2] Aibara R, Welsh J, Puria S, Goode R. Human middle-ear sound transfer function and cochlear input impedance. *Hearing Research*, 152 (1-2): 100-109, 2001.
- [3] Merchant S, Ravicz M, Rosowski J. Acoustic input impedance of the stapes and cochlea in human temporal bones. *Hearing Research*, 97 (1-2): 30-45, 1996.
- [4] Kringlebotn M. The equality of volume displacement in the inner ear windows. *J Acoust Soc Am*, 98: 192-196, 1995.
- [5] Stenfelt S, Hato N, Goode R. Fluid volume displacement at the oval and round windows with air and bone conduction stimulation. *J Acoust Soc Am*, 115: 797-812, 2004.
- [6] Rosowski J, Davis P, Merchant S, Donahue K, Coltrera M. Cadaver Middle Ears as Models for Living Ears: Comparison of Middle Ear Input Immitance, *Ann Otol Rhinol Laryngol*, 99: 403-412, 1990.

Analysis of Possible Short Length Measurement Using Energy Sucking of Electromagnetic Field

L. Marsalka, R. Hartansky

Dept. of Measurement, Slovak University of Technology, Ilkovicova 3, 812 19

Bratislava, Slovakia

Email: lukas.marsalka@stuba.sk

Abstract. *The paper deals with taking advantage of electromagnetic field energy sucking to measure very short distances, for example in microstructures. A mechanism of two wire structures, which are situated in the vicinity, effect, a variation of their mutual and input impedances and the influence of one segment's length to frequency dependence of other are described.*

Keywords: *Short Distance Measurement, Electromagnetic Field Energy, Mutual Impedance*

1. Introduction

Nowadays multi-discipline project using state of art technologies from various fields gain ground, whereby synergic effect is achieved in many cases. One of such a field is theoretical design and experimental realization of micro-electromechanical components, or elements, which may work as autonomous unit performing simply function. In our case, it is a measurement of extremely short distances necessary for control of micro-objects [1]. A process of gripping shall be integrated with a process of actuator control and a process of measurement of distance between the gripper's arms. Some limitations exist in the gripper's dimensions and micro-movement of the arms. An use of tensometers or utilization of magnetostriction or electrostriction properties are limited at such dimensions [2].

Another complication occurs in information transmission between the gripper and external control unit. Based on these considerations, an idea to use one of physical characteristic of the microstructure to ensure rf electromagnetic energy for signal transmission and for the measurement of arms distance. If the position of arms affects an incident electromagnetic field that some of field parameter (magnitude, phase or frequency) contains information about the distance between the arms, it would be an ideal case of measurement. At first it is necessary to focus on the antenna theory and to create an equivalent rf model of the structure, which is situated in electromagnetic field, to verify such a hypothesis.

2. Coupling between wire structures in electromagnetic field

Consider an electromagnetic field, which is generated by a wire structure – half-wave dipole 1. The dipole's length is $2h$, so it has a resonance at frequency f given by:

$$f = \frac{c}{4h} \quad (1)$$

where c is speed of light. The input current of the dipole depends on its input impedance, which value is changing according to [3]:

$$Z_m = -\frac{1}{I_m^2} \int_{-h}^h I_z(\rho = a, z = z') E_z(\rho = a, z = z') dz' \quad (2)$$

As it can be seen from (2), the input impedance varies with the change of a current distribution $I_z(\rho=a, z=z')$ and a z component of electric field $E_z(\rho=a, z=z')$, or more simply

with frequency. So, input current also varies with the frequency of a signal. Put another dipole, with same dimensions as dipole 1 has, into the vicinity of the dipole 1, as it can be seen in Fig. 1.

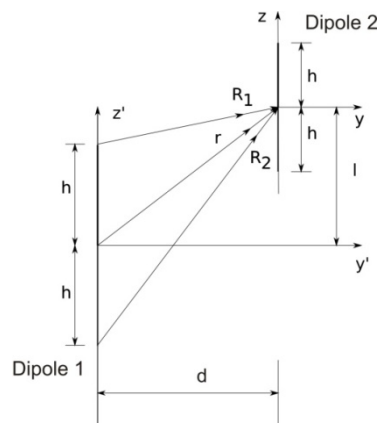


Fig. 1. Mutual impedance between two dipoles

The dipoles start to interact. This interaction causes an origin of mutual impedance between dipole 1 and dipole 2:

$$Z_{21i} = -\frac{1}{I_{1i}I_{2i}} \int_{-h}^h I_2(z') E_{z21}(z') dz' \quad (3)$$

where $E_{z21}(z)$ is the field created by dipole 1, which affects the dipole 2. Also the input impedance of dipole 1 and input current of this dipole are changing due to mutual impedance Z_{21i} origin. One may say that the change of current of the incidence dipole indicates presence of the dipole 2. As it can be seen from (3) the mutual impedance is changing with current distribution of the dipole 2 and the current distribution is changing with dimensions of the dipole 2 [3]. It means that the input current flowing into the dipole 1 contains not only information about a vicinity of some conducting object but also about its dimensions.

3. Numerical modeling of wire structures

It is necessary to solve equations (2) and (3) to verify the mentioned consideration. Formulation of current $I_z(z)$ of dipole 1 or dipole 2 represents the most problematic part of the

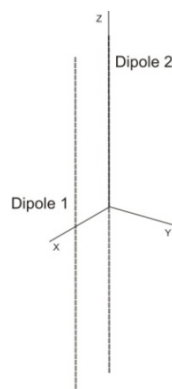


Fig. 2. Model of two dipoles in FEKO simulator.

solution. This formulation is linked to solution of Maxwell's equations, or wave equation in form of integral Pocklington's equation. A general solution of Pocklington's equation does not exist [3]. Therefore numerical solution was chosen. The best method to solve hereof the problem is method of moments (MoM), which solves such kind of equations with sufficient

accuracy. There exist also many commercial software products which have implemented the MoM. The simulation model of two wire structures in simulator FEKO are shown in Fig. 2.

The dipole 1 is situated in z-axis and it is supplied by rf voltage in frequency range from 700MHz to 1.2 GHz. Level of a input power P_{12} of the dipole 1 is changing with the frequency of input signal. The input power is maximal at resonant frequency. If the dipole 2 is approached the dipole 1, the variation of input power P_{12} may be observed (see Fig. 3).

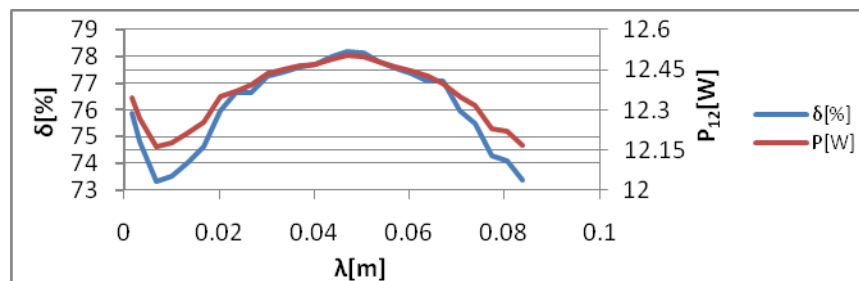


Fig. 3. Dependence of input power on the distance between two dipoles at resonance

The distance between dipoles is expressed as a ratio of the distance to resonant wavelength of the dipole 1 in Fig. 3. The input power of the dipole 1 is equal to $P_{11}=7.017\text{W}$ if no other dipole is in its vicinity. If power P_{11} is chosen as a reference value, we may obtain the relative change of input power of dipole 1 regarding to the distance from dipole 2:

$$\delta(\%) = \frac{P_{12} - P_{11}}{P_{11}} \quad (3)$$

A graphical description of the mentioned change is in Fig. 3. It may be seen that the input power changes its value maximally up to 78% over the value P_{11} due to presence of other dipole.

In respect of results shown in Fig. 3, one may say that the input power of the dipole 1 is affected by conducting object in its vicinity. The object – dipole 2 has the same length than the dipole 1th both were in resonance.

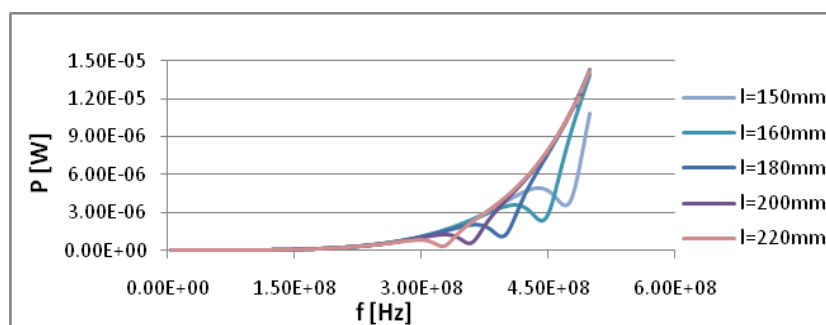


Fig. 4. Frequency dependence of input power on length of conducting object

In next our research was focused on investigation of the influence of dipole 2 of various lengths on a behavior of input power of the dipole 1. It means that it is necessary to observe sensitivity of power P_{12} on length of the dipole 2. The model of simulation is similar to the previous one in Fig. 2. The difference between models is that the dipole 1 is electrically short in respect of a wave. Its length is $2h_1=146\text{mm}$. The dipole 2 has length of h_2 , which is varied during the simulation process. Distance between the dipoles is constant $d=10\text{mm}$.

As it can be seen in Fig. 4, input power of the electrically small dipole – excited dipole – tends to arise exponentially with increasing frequency. If some conducting object is situated at

its vicinity, e.g. influencing dipole, this such tendency of input power is changed, such a characteristic has a local minimum. If length of the dipole's arm is $h_2 = 150\text{mm}$ such maximum appears at frequency of 465 MHz, if the length is $h_2 = 220\text{mm}$ maximum is at 319 MHz. Frequency of the characteristic's local minimum depends on dimensions of the influencing dipole, or on its resonant length. Considering a resonance at dipole's physical length:

$$2h = \frac{\lambda}{2} \quad (4)$$

it is a half-wave dipole. Then, the resonance appears at frequency:

$$f = \frac{c}{\lambda} = \frac{c}{4h} \quad (5)$$

Where $4h$ is double physical length of influencing dipole. Resonant frequency of influencing dipole with arm's length $h_2 = 150\text{mm}$ is $f_r = 499\text{MHz}$ and with $h_2 = 220\text{mm}$ it is $f_r = 340\text{MHz}$. Similar results has been obtained by numerical simulation. The difference between calculated and simulated values are caused by real thickness of the dipole. In such cases the resonance appears at lower frequencies than it is achieved (reciprocal value of half of the wavelength) [3].

Swell of a curve of electrically small dipole's input power appears at frequencies equivalent to half-wave lengths of conducting object - influencing dipole – also to its physical length. Generalizing this consideration, it is possible to measure the object's length by means of an energy generating electromagnetic field in vicinity of the electrical dipole.

4. Conclusion

Analytic model as well as numerical simulation confirmed change of the input power of the excited dipole due to effect of near conducting object. A magnitude of such a change depends on the distance between the dipoles and a frequency of this change depends on the dimensions of the object. This paper shows an interlacing between dimensions (length) of the object and an overshoot of input power of the excited dipole at specific frequency. Such a phenomenon may be utilized as perspective method of distance measurement of conducting object in electromagnetic field. The method transforms directly a length to frequency, which may be easily and accurately measured. Sensitivity of such the method on variation of length of near conducting object (for example arms of the microstructure) depends on the equation (5). Such a change can be till hundreds of MHz if we consider dimensions of the microstructures.

Acknowledgements

This work was supported in part by Ministry of Education of the Slovak Republic under grant 2003SP200280202 and by grant project VEGA 2/0006/10.

References

- [1] Binka J, Hricko J. Compliant Mechanisms Exploited as Micro-Grippers in State-of-the-Art in Mechatronics, Volume II. Simulation Research Press, Alphen aan den Rijn, 2010.
- [2] Durina P, Stefecka M, Roch T, Noskovic J, Trgala M, Pidik A, Kostic I, Konecnicova A, Matay L, Kus P, Plecenik A. Patterning of Nanometer Structures by Using Direct-Write e-beam Lithography for the Sensor Development in proceeding ASDAM 2010, 2010, 89-92
- [3] Balanis C. A. Antenna Theory Analysis and Design. John Wiley & Sons, New York, 1982, 1997.

Measuring Low Magnetic Field in Electromagnetic Flow Meter

M. Novák, L. Slavík, M. Košek, M. Truhlář

Faculty of Mechatronics, Technical University of Liberec, Liberec, Czech Republic

Email: miroslav.novak@tul.cz

Abstract. Space distribution of low magnetic field amounting to 1 mT can be measured in detail using a commercial 3D probe with a modified control circuit. The probe was calibrated carefully using a known field from Helmholtz coils. The 3D positioning system enables the measurement of the field distribution. The apparatus was used for measuring the magnetic field of the electromagnetic flow meter. Additional experiments confirmed high reproducibility of results for repeated probe movement. The magnetic field was calculated numerically by the application of Biot-Savart Law for simplified model of magnetic excitation. The agreement between experiment and theory is good, provided that production inaccuracies and limitations of the model geometry are taken into account.

Keywords: 3D Hall Probe, Probe Calibration, Low Magnetic Field, Flow Meter.

1. Introduction

Magnetic field interactions are used in many technical areas, for instance strong field in small area are necessary for contactless force action and spatially extended field performs forces on charged moving particles in electromagnetic flow meter [1]. In the design and analysis of such devices the magnetic field should be known. As the structure of the devices is complicated, approximated models are used and calculations are made numerically. Therefore, the experimental verification of the models is necessary.

Commercial 3D Hall probes are available, but they are designed for strong magnetic fields [2]. Their use for the correct low field measuring needs reconstruction of the circuit, careful calibration, special data processing and several other precautions. The solution of these questions is a subject of this paper.

2. Subject and Methods

The main problem is to increase the commercial probe sensitivity while its relative accuracy remains unchanged. If the magnetic field is absent, the output voltage is about half of the supply voltage, i.e. 2.5 V. The change of magnetic flux density by 1 mT results in about 0.15 mV output voltage. The quantization error of a standard 16 bit ADC is 25 % in this case. Therefore, high accuracy of the output meter is necessary for accurate low field measurements.

The solution is to use a stable voltage standard for reference voltage, which can be derived from power supply, and measure the voltage difference between probe output and voltage standard. An additional amplifier further increases the probe sensitivity.

In order to ensure accuracy, the new probe control circuit should be calibrated for several values of low magnetic flux density. Linear calibration formula contains sensitivity and offset. The sensitivity can be simply determined by the use of Helmholtz coils, the offset needs an area of zero magnetic field, which can be achieved by a massive ferromagnetic shielding. Another method is to eliminate all other disturbing fields. Earth magnetic field can even significantly distort the results.

Since the space measurement is proposed, it must be fully automated, because of big number of points. Basic block scheme and photographs of apparatus are in Fig. 1. Computer-controlled space positioning system is used for moving the probe. The probe data are digitalized, noise and unwanted signals are rejected (or reduced) digitally and then all the important data are stored in the computer memory for further processing.

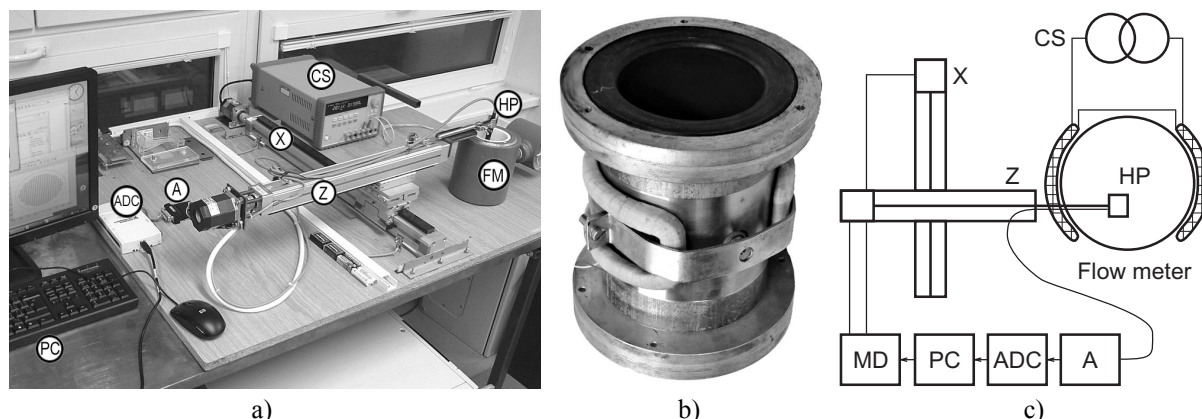


Fig. 1. a) Realized apparatus, b) Flow meter coil detail, c) Block scheme. Legend: FM follow meter, CS current source, Z and X feed axes, HP Hall probe, A signal conditioning, ADC analogue to digital converter, PC personal computer, MD motor driver.

For the magnetic field calculation, the numeric integration derived from the Biot Savart Law is used. The main problem is to design a good model of exciting currents, since the flow meter exciting coil has a 3D shape that is difficult for exact description. Approximate model uses straight lines and circle arcs for individual conductors. The resulting magnetic field is their superposition. Surface as well as volume currents may be used in principle. A similar approach is presented in the literature [3].

3. Results

For the probe calibration, simple Helmholtz coils were used. Their field uniformity in the central part that was obtained by the numeric integration can be seen in Fig. 2, which shows main and parasitic components. The parameter is the distance from coil axis. The rectangle shows area where the deviation is less than 1 %. The probe sensitivity, obtained by the use of several exciting currents and calculated by the least square method, is $142 \mu\text{T/mV}$.

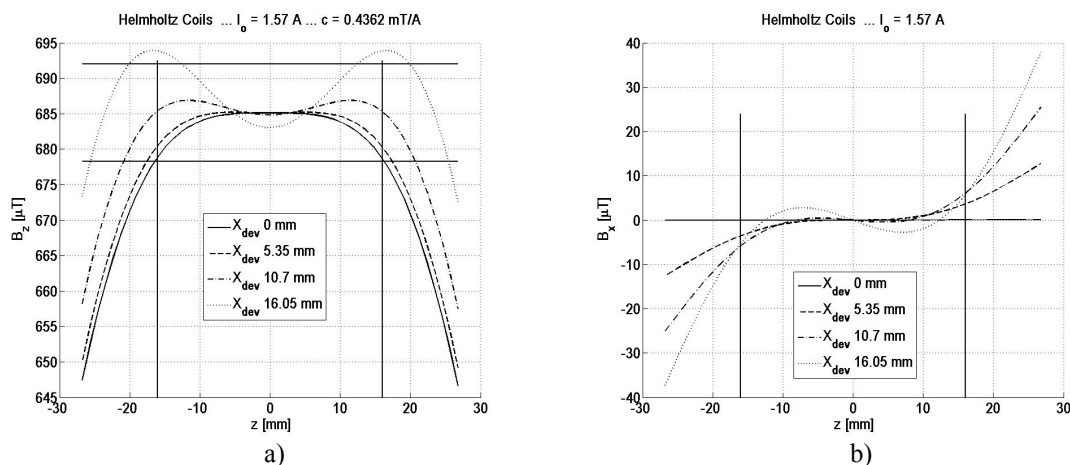


Fig. 2. Magnetic field in the central part of Helmholtz coils. a) Main component B_z , b) Parasitic component B_x . Area of 1% flux density uniformity is shown in picture a).

The apparatus was tested on a commercial flow meter. DC regime was used, although AC excitation is typical. The probe accuracy was estimated through repeated measurements. The relative error depends on the measured flux density. Typical relative errors are in Table 1. Flux density higher than about 0.1 mT can be measured with good accuracy, which is better by one order as compared to standard probes.

Table 1. 3D Hall probe relative error from repeated measurements of low values of magnetic flux density

B_{mean} [μT]	2000	500	200	100	30
δB [%]	0.2	1.5	3	5	15

Theoretical calculations were carried out by MATLAB. The coil was modeled either by one centre conductor or spatially distributed conductors using parallel computing to increase the speed. Since the differences were small, only the results obtained from the simpler model will be presented in this study. Correlations with the model improved if the magnetization of ferromagnetic parts of the flow meter was taken into account through modeling them by line bounded currents. A comparison with theory is shown in Fig. 3. The flux density along the flow meter Y axis, i.e. the axis of coils, is shown in Fig. 4. Data in Fig. 4 are taken along a circle with diameter 32 mm close to the winding in plane perpendicular to the axial axis. The agreement is good. Experimental points exhibit small, but visible, asymmetry.

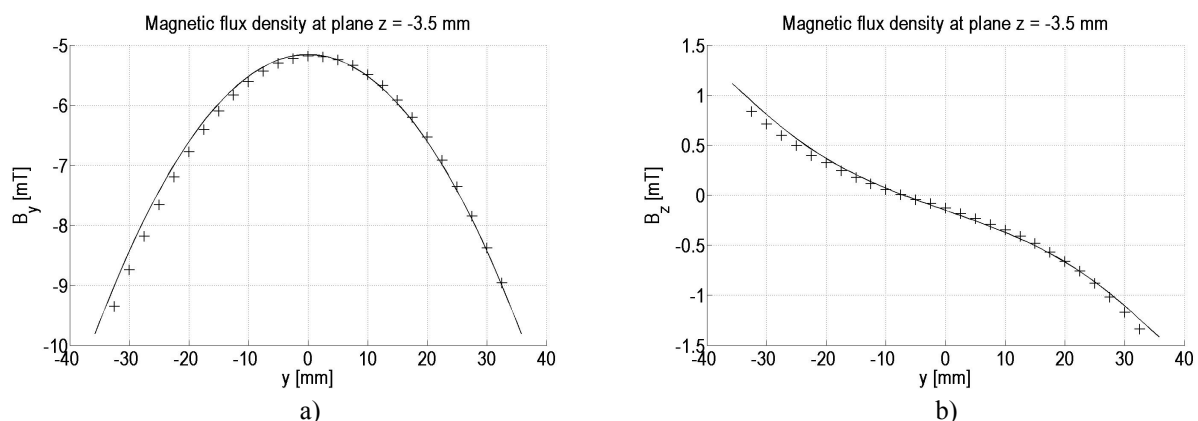


Fig. 3. Comparison between experiment and theory on Y axis (symmetry axis of exciting coils). a) Main component B_y , b) Parasitic component B_z .

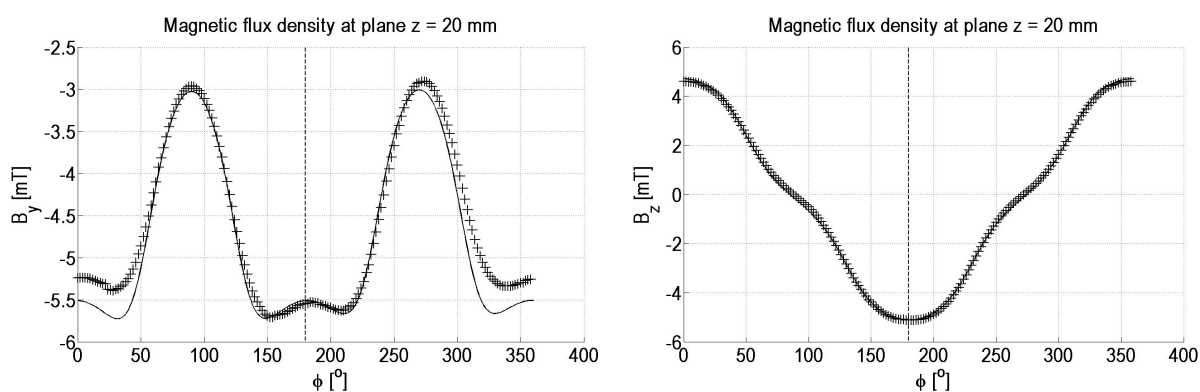


Fig. 4. Comparison between experiment and theory on a circle in general plane normal to axial axis. a) Main component B_y , b) Parasitic component B_z .

Good technical agreement between theory and experiment makes the flow meter numerical analysis possible. Flux density is almost uniform in the flow meter tube (Fig. 5a), but not outside the tube. However, Hall force in the tube area (Fig. 5b) is well-defined.

4. Discussion

We have shown that the commercial Hall probe designed for applications in the range of 2 T, can be efficiently used for measuring low magnetic field amounting to 1 mT with new control circuit. The relative error is usually less than 3 %. Fully-automated measurement needs a space probe positioning apparatus, error in the coordinates is about 0.5 mm. Therefore, the measurement of space distribution of magnetic field is relative precise.

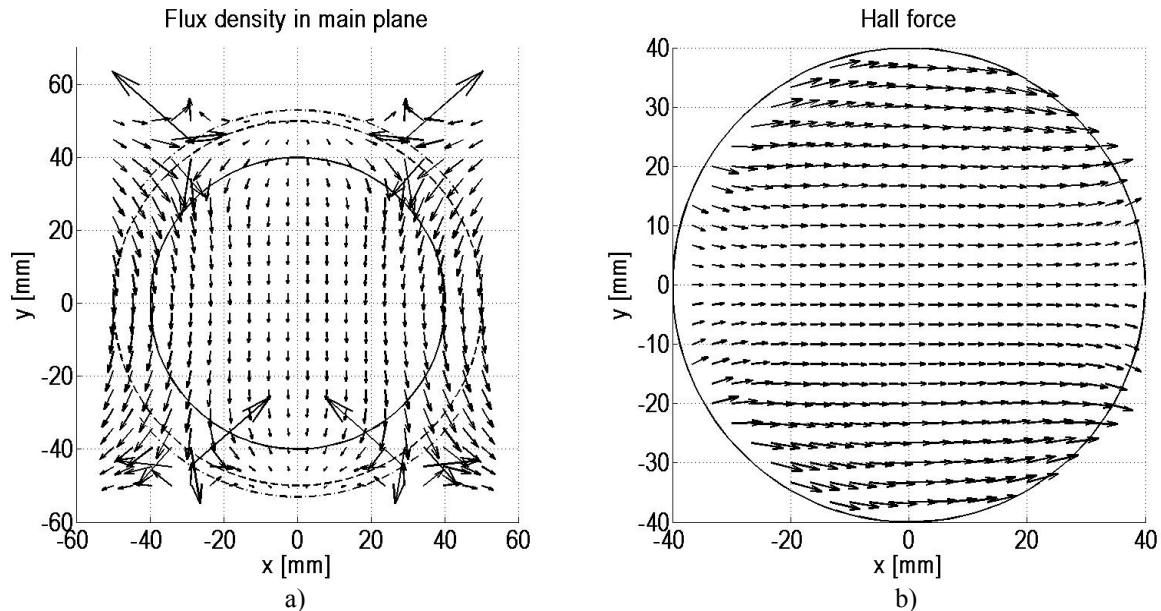


Fig. 5. Flow meter analysis in central plane. a) Flux density vectors. The coil equivalent turn is shown as dot-and-dash arcs outside the external circle. b) Hall force in the inner tube.

The preliminary comparison with theory, using a very simple model, is in a good agreement from the technical point of view. It can be further improved both in theory and experiment. In theory, more precise 3D geometry should be used in flow meter model. In experiment, the coordinates must be corrected for positions of individual sensors of the 3D probe. Then the symmetry of measured points is improved. The remaining experimental asymmetry is then only caused by production errors. Since magnetic field distribution is a key part of flow meter, calculations have shown that the flow meter is well designed; Hall force is almost uniform in its central plane.

Acknowledgement

This work was supported by student grant SGS 2011/7821 Interactive Mechatronics Systems Using the Cybernetics Principles.

References

- [1] Shercliff J.A. The theory of electromagnetic flow-measurement. Cambridge Science Classics – Cambridge University Press, Cambridge, 2009.
- [2] Mikolanda T., Kosek M., Richter A. 3D magnetic field measurement, visualization and modelling. In proceedings of the 7th International Conference Measurement 2009, 2007, 306–309.
- [3] Andris P., Weis J., Frolo I. Magnetic field of saddle-shaped coil. In proceedings of the 7th International Conference Measurement 2009, 2007, 436–439.

Model of Electromechanical Valve in the Anti-lock Braking System

M. Okrouhlý, J. Novák

Czech Technical University in Prague, Prague, Czech Republic

Email: okroumil@fel.cvut.cz

***Abstract.** The current trends in vehicle diagnostics tend to decrease production costs, whereas the same or even higher user safety and comfort level has to be assured. One option is using the centralized diagnostics, which doesn't increase the production costs and still gives precision to the detection of an actual fault. The centralized diagnostics is an alternative to the today online diagnostic solutions. It is based on diagnostic models of every single part of the vehicle in which a properly as well as a faulty behaviour can be simulated. In this paper, the electromechanical valve of anti-lock braking system is described and modelled in detail. In order to proceed with the centralized diagnose of the anti-lock braking system of the vehicle, good understanding of the anti-lock braking system valve is necessary. A physical analysis, mathematical description and a general model of the valve was carried out. In the Conclusions, the signal measured on a real valve was compared with a signal created in the simulated environment on the model of the same valve. The output of the model exactly follows the real performance of the electromechanical valve.*

Keywords: Anti-lock Braking System, Electromechanical Valve, Simulink Model in Matlab

1. Introduction

The safety and reliability in the automobile industry has been discussed since the very first car was produced. The reliability of the braking systems is also discussed in [1]. Current vehicle diagnostics is based on the decentralized concept, which detects consequences of a fault. For modern methods of decentralized vehicle diagnostics, see [2] and **Error! Reference source not found.**

The concept of centralized online diagnostics, developed at our university, is based on measuring of signals at central point of the power supply network in the vehicle. In order to recognize the signals while trying to detect a fault, a deep knowledge of all the performance relevant parts of the vehicle (parts working properly as well as the faulty ones) is required. Diagnostic models of the performance relevant parts are used for this purpose. Thus the method can be applied on the braking system and primarily on the anti-lock braking system. The terms “centralized diagnostics” and “decentralized diagnostics” are explained in [4].

Hence, the suggested method of centralized concept is based on advanced mathematical algorithms. The application of these algorithms can reveal faults even before they really occur. Some of the algorithms used in the automotive industry are described in [5]. The method of centralized diagnostics utilizes measuring of supply currents on the given wiring in the vehicle, so that the additional costs of installation during the final implementation of the system in the vehicle are noticeably decreased. (The purchase costs are the crucial element for implementing this method. The trend of minimizing the production costs is apparent in [6].) Nevertheless, to identify faults in the whole vehicle from one central point, it is necessary to have a deep understanding of all its parts.

The anti-lock braking system consists of a few performance relevant parts. This paper deals with one of such parts: the electromechanical valve within the anti-lock braking system control unit. Considering that the method uses the power supply of the vehicle for the diagnostics, it is essential to understand supply current pulses during switching the single

parts in the control unit of the anti-lock braking system. This topic is also discussed in [7] and [8]. Thus the electromechanical valve model focuses on the accurate simulation of current consumption in the correct as well as the fault states.

2. Subject and Methods

The general model of the electromechanical valve consists of two parts: the electrical and the mechanical one.

The electrical part of the valve

The electrical part of the valve can be described as a serial circuit consisting of a coil with variable inductance and a resistor. For the schematic of this circuit, refer to Fig. 1. It can also be expressed by the equation No 1. The inductance value depends on the position of the movable plunger. The resistance value models the sum of the loss in windings, the metal part of the magnetic circuit and the air part of the magnetic circuit, which also depends on the position of the plunger.

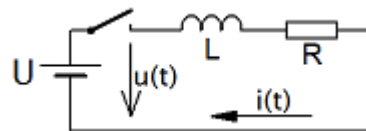


Fig. 1. Equivalent serial circuit coil.

$$\frac{di(t)}{dt} = \frac{1}{L(x)}u(t) - \frac{1}{L(x)}i(t)R(x) \quad (1)$$

where

- $i(t)$ current in the circuit
- $L(x)$ inductance
- $R(x)$ resistance
- $u(t)$ voltage

Every electrical circuit has also capacitance. In this case it was left out, because it is only usable at frequency levels closer to resonance. In this case, the resonant frequency is several orders higher than the maximal measured frequency (max. 1 kHz). The maximal measured frequency was defined by the step response of the valve.

The mechanical part of the valve

The mechanical part of the valve can be (simplified) understood as a mechanical oscillator, see Fig. 2. The oscillator is described by equation No. 2. In order to respect a real situation in an electrical valve, it is necessary to add range limits of some physical values in the resulting model (Fig. 3).

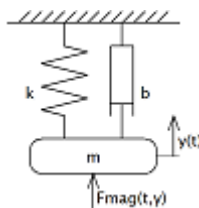


Fig. 2. Mechanical oscillator.

$$m \frac{d^2 y(t)}{dt^2} + b \frac{dy(t)}{dt} + ky(t) + F_{mag}(t, y) = 0 \quad (2)$$

where

- y(t) position of the movable part
- F_{mag}(..) electromagnetic force
- m weight of the movable part
- k spring stiffness
- b damping coefficient

Electromagnetic force is a product of the square of the coil current and of the magnetic constant (equation 3), which here depends on the position of the movable part. This dependence is the result of the change of magnetic resistance during the motion of the plunger, see equation 4.

$$F_{mag}(t, x) = i^2(t) * k_{mag}(x), \quad k_{mag}(x) = \frac{N^2}{2 \mu_0 S (R_{m1}(x) + R_{m2})^2} \quad (3) (4)$$

where

- i(t) coil current
- k_{mag}(x) magnetic constant
- N number of turns
- μ₀ permeability of vacuum
- S cross-section
- R_{m1}(x) magnetic resistance of air
- R_{m2} magnetic resistance of steel

3. Results

By connecting the models of the electrical and mechanical parts, including limits of the real system, we get the final model of the valve, see Fig. 3. The model was calibrated using constants measured on the electromechanical valve of the anti-lock braking system control unit VW 6Q0 614 117/Bosch 0 256 222 006.

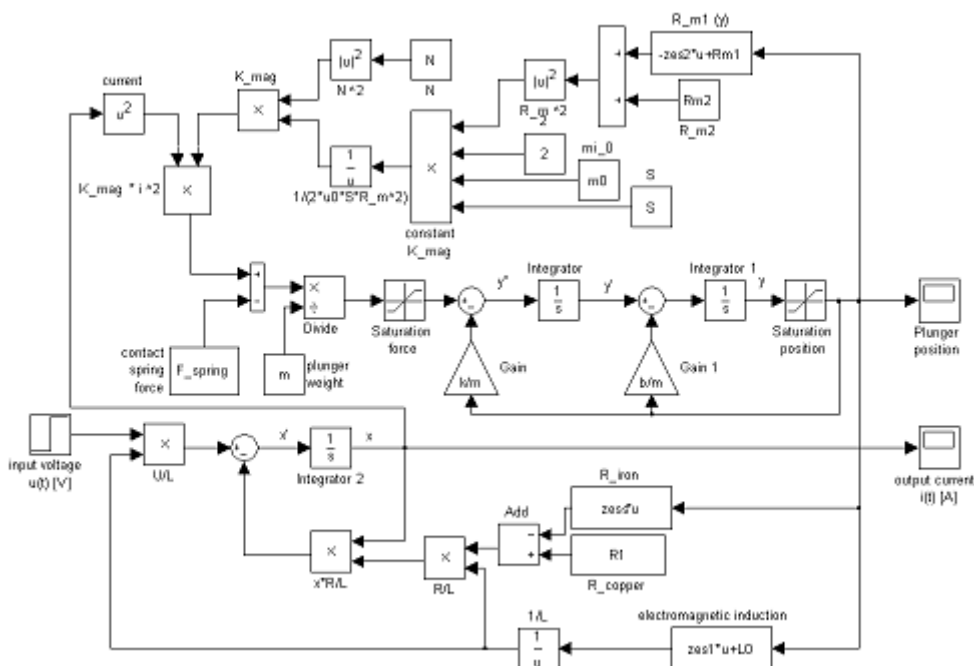


Fig. 3. Final model of the valve

Results comparison

For comparison of current consumption of the real valve and the model, see Fig. 4.

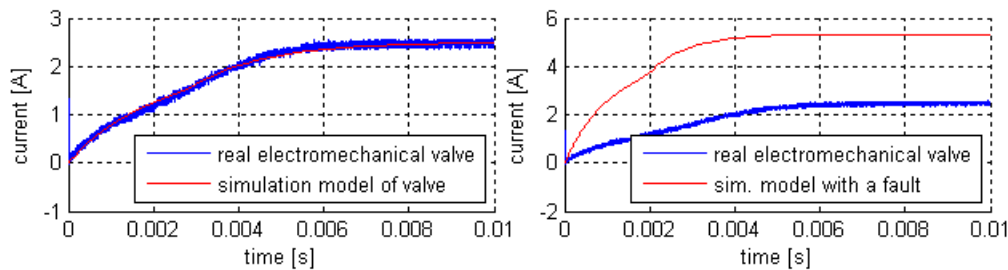


Fig. 4. Real valve compared with the model (left - a properly working valve, right - model with a half of the turns short-circuited)

4. Conclusions

Based on the results stated above it is obvious that the model well approximates the real valve. The deviations of the model from the real system were caused by measuring inaccuracy of some constants and especially by unknown dependence between the position of the plunger and the real inductance of the coil and the position of the plunger towards the losses in the magnetic circuit. Linear characteristics was used which intercuts the measured lateral points.

Acknowledgements

This work was supported by Josef Bozek Research Centre of Engine and Automotive Engineering, project No. 1M0568, Grant Agency of the Czech Technical University in Prague, grant No. SGS10/207/OHK3/2T/13, Czech Science Foundation, grant No. GD102/09/H082.

References

- [1] Börner M, Straky H, Weispfenning T, Isermann R. Model based fault detection of vehicle suspension and hydraulic brake systems. *Mechatronics*, 12 (8): 999-1010, 2002.
- [2] Crossman J, Guo H, Murphey Y, Cardillo J. Automotive signal fault diagnostics - part I: signal fault analysis, signal segmentation, feature extraction and quasi-optimal feature selection. *Vehicular Technology, IEEE Transactions on*, 52 (4): 1063-1075, 2003.
- [3] Murphey Y, Crossman J, Chen Z, Cardillo J. Automotive fault diagnosis - part II: a distributed agent diagnostic system. *Vehicular Technology, IEEE Transactions on*, 52 (4): 1076-1098, 2003.
- [4] Jezdik P, Novak J. Centralised diagnostics of electronic and electric equipment in vehicles, engine lighting equipment testing. *Computing - International Scientific Journal of Computing*, 7: 30-34, 2008.
- [5] Gusikhin O, Rychtycky N, Filev D. Intelligent systems in the automotive industry: applications and trends. *Knowledge and Information Systems*, 12 (2): 47-168, 2007.
- [6] O'Connor A. Tata Nano—world's cheapest new car is unveiled in India. *The Times*, 11: 2008.
- [7] Mills V, Samuel B, Wagner J. Modeling and analysis of automotive antilock brake systems subject to vehicle payload shifting. *Vehicle System Dynamics*, 37 (4): 283-310, 2002.
- [8] Qi X, Song J, Wang H. Influence of hydraulic ABS parameters on solenoid valve dynamic response and braking effect. *SAE paper*, 1: 1590, 2005.

New Approaches to the Improvement in Efficiency of Dimensional Measurements on Multi-Sensor Coordinate Measuring Machines

¹M. Vogel, ¹K. Weissensee, ¹G. Linss

¹Ilmenau University of Technology, Ilmenau, Germany,

Email: michael.vogel@tu-ilmenau.de

Abstract. Efficient dimensional measurements on multi-sensor coordinate measuring machines require optimised inspection plans. From the industrial management point of view the optimisation of the inspection plan is aimed at the minimisation of total measurement costs. That is connected with the minimisation of measurement times based on the optimisation of measurement ways and points in consideration of the tolerance-uncertainty-ratio. Therefore, the selection of an adequate sensor, capable of measuring the inspection feature within its specification, is of extreme importance.

Within this paper different approaches to efficient multi-sensor coordinate measurements based on optimised inspection plans are presented.

Keywords: Uncertainty, Monte-Carlo-Method, Coordinate Measurements, Cost of Measurement, Sensor Travel Time

1. Introduction

For the measurement of geometrical features coordinate measuring machines (CMMs) with different tactile and visual sensors are widely used and important due to their large scope of application and their flexibility in the measurement of different workpieces. Within the inspection planning all parameters for the measurement are defined e. g. the selection and characterisation of sensors and the measurement strategies. The selection of an adequate sensor results from multifarious points of view e. g. geometrical properties and surface characteristics of the unit under test and tolerance limits. Also the measurement uncertainty or subsequent disputed user risks and costs resulting from this are decisive for the inspection planning. The improvement in efficiency of measurements on CMMs could result on the one hand from the increasing automation of perspective processes, for example the essential estimation of the measurement uncertainty, and on the other hand from optimisation of measurement procedures.

2. Model for efficient dimensional measurements

Increasing the benefit of a company always goes ahead with lowering costs. In case of measuring parts with multi-sensor CMMs [1] costs of a measurement can be calculated with

$$K_M = t_M \times (k_P + k_{KMG})$$

with K_M is the costs of the measurement, t_M is the time for the measurement, k_P is the cost rate for employees and k_{KMG} the cost rate for the machine. The time for the measurement results from

$$t_M = t_{Ein} + t_K + t_{KS} + t_A + n \times \left(\sum_{j=1}^k \sum_{i=1}^m t_{ij} + \frac{s_{Verf}}{v_{Verf}} + t_{TW} + t_U \right)$$

where is t_{Ein} the warm up time of the machine, t_K the time for the calibration of the machine,

t_{KS} the time for creating the coordinate system and t_A the time for mounting the test piece. To this the sum of t_{ij} , the time for measuring objects $i=1, \dots, m$ with the sensor $j=1, \dots, k$, plus the time for positioning, represented by the distance between measuring objects s_{Verf} divided by the speed for the positioning v_{Verf} , added by t_{TW} , which is the time for changing the sensor, and t_U , the time for changing the test piece, if more than one is measured. This sum is multiplied by n , which is the number of pieces.

To minimize the time of the measurement the time for detection of a measurement feature and the travel time of the sensor between the features has to be optimized. While travel time is connected with the order of the features the time for the detection highly influences the measurement uncertainty and with that also the proceeds caused by the measurement [1],[2].

3. Minimization of the travel time of the sensor

Calculating an exact solution for the best order of measurement features will cause run time problems if the number of features rises above 10. This is why heuristic methods can be used. To simulate the intuitive behavior of the operator the model of Nearest Neighbor is used as reference in this paper. The model starts with a starting point and integrates the closest point into the route (Fig. 1 a). Especially at the end of the route this model delivers wide ranges to travel.

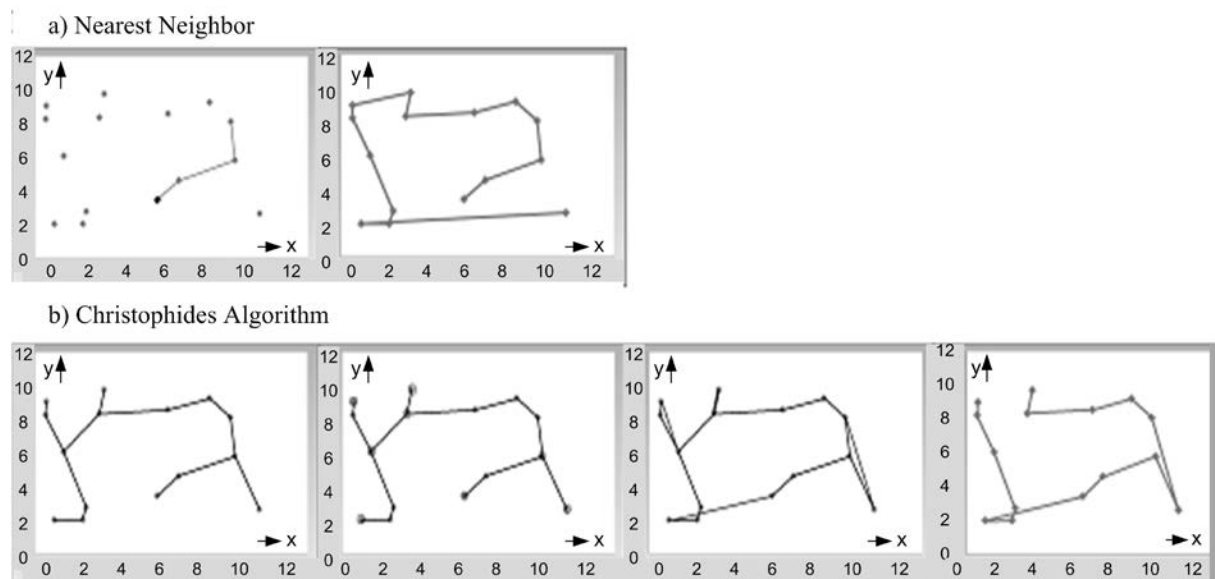


Fig. 1. Comparison of Nearest Neighbor method vs Christophides Algorithm.

A heuristic model to optimize travel distances is the *Christophides Algorithm* (Fig. 1 b). The algorithm works in four steps:

1. Creating a minimal spanning tree
2. Find a minimal perfect matching
3. Integrate points with odd number of neighbors
4. Create an Euler tour

As a result of this method the travel distance could be minimized about 14%.

4. New approach to the efficient GUM-conform uncertainty estimation

The proposed method lays the foundations for the automated indication of a complete measurement result consisting of the best estimate and the GUM-conform expanded measurement uncertainty [3] for coordinate measurements with visual sensors. The digital image of the unit under test is the prerequisite of measurements with visual sensors and represents all available information. Therefore, the newly developed method is based on knowledge about the quality of the image, which represents the measuring scene (Fig. 2 a). Significant image information in combination with measurement results of supplemental experiments in preliminary investigations, saved in the knowledge database (Fig. 2 c), is applied for the estimation of the measurement uncertainty. During the detection of a coordinate point actual quality parameters (Fig. 2 a) are determined and the model for uncertainty estimation is adequately adapted. Due to the non-linear fitting algorithms, characteristic for dimensional measurements, numerical methodologies especially the Monte-Carlo-Method [4] is used for uncertainty propagation.

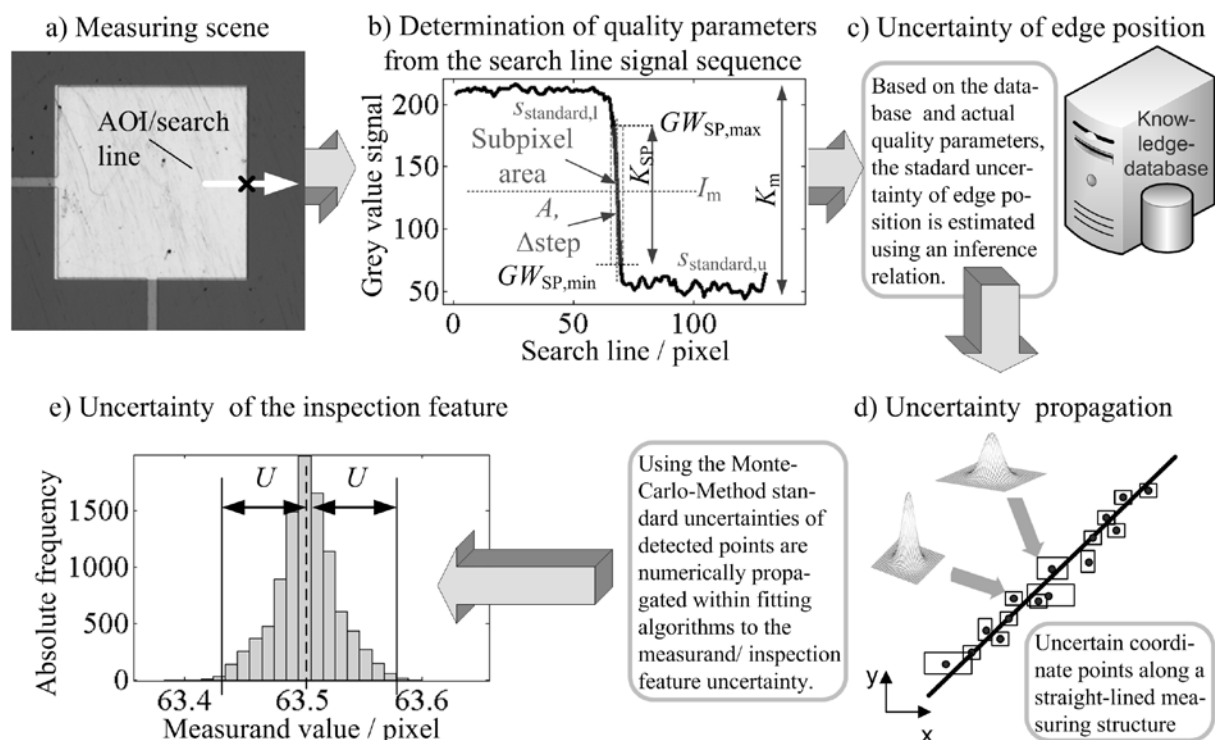


Fig. 2. Methodology for efficient uncertainty estimation of CMM-measurements using visual sensors [5], [6].

It could be shown, that the novel approach (Fig. 2) gives estimates of measurement uncertainty which are practicable and widely-agreed with experimental effected uncertainty declarations. The estimated measurement uncertainty by this means enables the user the evaluation of the reliability of the indicated measurand and the comparability of several measurements without the realisation of extensive supplemental experiments or calibrated workpieces, such as e. g. required in [7].

5. Conclusions

The proposed approaches lay the foundations for efficient measurements on multi-sensor CMMs. It could be shown, that the novel methods are essential prerequisites to bring forward the automation of perspective processes associated with the inspection planning. Thus, the measuring courses of action and the measuring results can be compared directly on different CMMs. All approaches, presented in this paper, have to be combined in one comprehensive system. Therefore, prospective research activities at the department of quality assurance at Ilmenau University of Technology will deal with knowledge-based simulation to create optimised inspection plans.

Acknowledgements

The presented work is the result of the close interdisciplinary research within the SFB 622 funded by the German Research Foundation (DFG), and the research program “Innoprofile” which is funded by the BMBF (Federal Ministry of Research and Education).

References

- [1] Vogel M, Ebinger N, Rosenberger M, Linß G: A novel strategy for cost-efficient measurements with coordinate measurement machines. *Journal of Physics: Conference Series* 238 (2010) 012038.
- [2] Zinner C: Ein Beitrag zu Verteilungsmodellen und deren Einfluss auf die Auswahl von technisch und wirtschaftlich geeigneten Prüfmitteln zur Sicherung der Qualität. Technische Universität Ilmenau, Dissertation, 2005.
- [3] JCGM 100:2008. Evaluation of measurement data — Guide to the Expression of Uncertainty in Measurement (GUM).
- [4] JCGM 101:2008. Evaluation of measurement data — Supplement 1 to the GUM — Propagation of distributions using a Monte Carlo method.
- [5] WO 2009/121333 A1. Method for Determining the Measuring Uncertainty of Coordinates in Geometric Measurement. PCT date of publication November, 25, 2009.
- [6] Weissensee K, Kühn O, Linss, G. Knowledge-based uncertainty estimation of dimensional measurements using visual sensors, *Journal of Physics* 238 (2010) 012023.
- [7] ISO/TS 15530-3:2004. Geometrical Product Specifications (GPS) — Coordinate measuring machines (CMM): Technique for determining the uncertainty of measurement — Part 3: Use of calibrated workpieces or standards.

Measurements of Optical Parameters of γ -Mo₂N/Si(100) Thin Films

^{1,2}E.S. Senchenko, ³V.V. Atuchin, ³T. Khasanov
³V.A. Kochubey, ³L.D. Pokrovsky

¹ Technological Design Institute of Scientific Instrument Engineering SB RAS,

² Novosibirsk State Technical University,

³ Institute of Semiconductor Physics SB RAS,

Novosibirsk, Russia

Email: chugui@tdisie.nsc.ru

Abstract. Molybdenum nitride films γ -Mo₂N/Si have been fabricated with reactive magnetron sputtering in (N₂ + Ar) gas mixture. Phase composition of the films has been defined with RHEED. Refractive index and extinction coefficient of γ -Mo₂N have been evaluated with laser ellipsometry at $\lambda = 632.8$ and 488.0 nm. Upper limit of γ -Mo₂N film thickness measurable with laser ellipsometry has been found as ~ 80 nm.

Keywords: Laser Ellipsometry, Molybdenum Nitride, Thin Film, Optical Parameter

1. Introduction

Molybdenum nitride thin films exhibit high electrical conductivity and chemical stability and are promising candidate for using as Cu diffusion barrier and electrodes in microelectronics [1, 2]. Besides this, molybdenum nitrides show excellent hardness, catalytic ability and superconductivity effects. Different methods have been tested for fabrication of molybdenum nitride layers, including atomic layer deposition, ion assisted deposition, pulsed laser deposition, heavy nitrogen-ion implantation, chemical vapor deposition and nitriding Mo metal at high temperature. In comparison with other methods, reactive sputtering deposition seems be among most effective for transition metal oxide or nitride film fabrication because chemical and phase composition of the film is strongly dependent on the Ar-O₂-N₂ gas composition and deposition conditions. This technique is of special interest due to applicability to large-area substrates and good compatibility with electronic industrial technologies. As to reactive magnetron sputtering method, high quality films can be created even at relatively low substrate temperature because of plasma stimulation of ion interaction with substrate surface. The dependence of phase composition, mechanical and electrical properties of molybdenum nitride films on the $l = p(\text{N}_2)/[p(\text{Ar}) + p(\text{N}_2)]$ ratio and substrate temperature used in reactive sputtering deposition have been observed in several studies. At the same time, top surface structural characteristics are less studied while crystallinity and phase composition of molybdenum nitride films is a function of substrate temperature and nitrogen partial pressure. There is no information reported on optical properties of molybdenum nitrides though ellipsometry was mentioned as a method used for the film thickness control. Evidently, single wavelength ellipsometry is suitable and sensitive method for precise thin film thickness control and determination of physical parameters of nanometric films and bulk crystals [3].

This investigation presents the results of molybdenum nitride thin film fabrication by reactive magnetron sputtering deposition. The reactive gas mixture will be optimized to get γ -Mo₂N phase as main component of the film. Refractive index and extinction coefficient of γ -Mo₂N/Si film will be measured with laser null ellipsometry.

2. Experimental Methods

The molybdenum nitride films were deposited on Si (100) substrates by reactive dc magnetron sputtering of molybdenum metal (99.8%) target. The sputtering chamber was evacuated up to $\sim 5 \times 10^{-6}$ Torr prior to film-deposition and the working pressure was maintained at $\sim 1 \times 10^{-3}$ Torr with ($N_2 + Ar$) reactive gas mixture. The magnetron power was fixed at $W = 160$ W. The substrate temperature was selected to be in the range of $T = 375$ - 580°C . Higher substrate temperatures were not used because partial nitrogen loss from molybdenum nitride was earlier detected at $T \sim 800^\circ\text{C}$. After the deposition the molybdenum nitride film was slowly cooled to room in reactive gas mixture inside the deposition chamber. Structural characteristics of the films were evaluated with reflection high energy electron diffraction (RHEED) under electron energy 50 keV. Optical parameters of the films were defined with laser ellipsometers LEF-2 and LEF-3M ($\lambda = 632.8$ and 488.0 nm). Ten molybdenum nitride film samples were fabricated at different T and l from the ranges $375 < T < 580^\circ\text{C}$ and $31.8 < l < 100\%$ and tested with RHEED for crystallinity and phase composition. Two most representative samples fabricated at $T = 375^\circ\text{C}$ and $l = 31.8\%$ (sample 1) and $T = 425^\circ\text{C}$ and $l = 100\%$ (sample 2) were measured with laser ellipsometry.

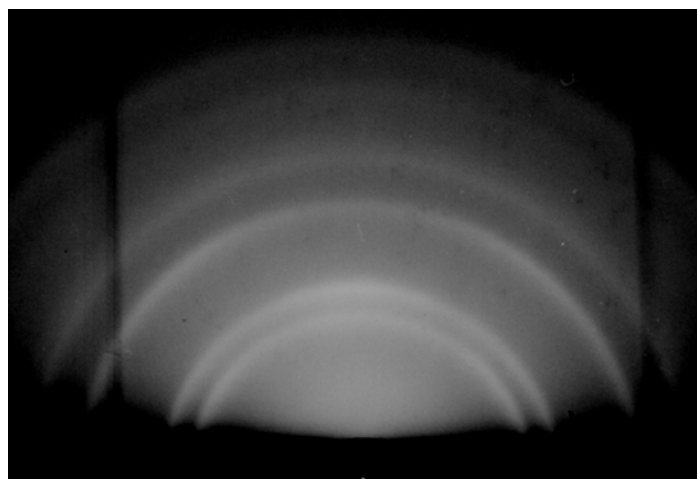


Fig. 1. RHEED pattern of $\gamma\text{-Mo}_2\text{N}$ film deposited at $W = 160$ W, $T = 425^\circ\text{C}$ and $l = 100\%$ (sample 2).

3. Results and Discussion

RHEED observation shows a superposition of polycrystalline and amorphous phases for all deposition conditions. In Fig.1 the RHEED pattern is shown for the film fabricated at low T and l . As it is evident, the intensity of halo related to amorphous phase is relatively low and electron diffraction by small polycrystalline grains is dominant. The polycrystalline phase is identified as $\gamma\text{-Mo}_2\text{N}$ (PDF 25-1366). For the comparison, in Fig.1 the RHEED pattern is demonstrated for the film created at higher T in pure nitrogen gas. In this film the amorphous component is dominating. Residual crystalline phase is identified as $\gamma\text{-Mo}_2\text{N}$. As it appears, increasing of substrate temperature and higher nitrogen flow should be stimulating factors for molybdenum – nitrogen chemical bond formation. Under higher T and l the nucleation is so active that atomic ordering on the film surface is not finished and amorphous state is conserved. Earlier, crystallinity of $\gamma\text{-Mo}_2\text{N}$ have been confirmed by X-ray diffraction (XRD) and transmission electron microscopy (TEM) for the films deposited by reactive magnetron sputtering at $T = 120$ - 500°C in different experiments. To decrease plasma action, in our magnetron set up as high target-substrate distance as $L = 20$ mm was used that ensure

minimum plasma heating of substrate surface. Under the conditions, crystalline $\gamma\text{-Mo}_2\text{N}$ phase is dominant at $T = 375\text{-}425^\circ\text{C}$ and amorphous component is prevailing at $T = 540\text{-}580^\circ\text{C}$. In the range $425 < T < 540^\circ\text{C}$ the intensities of crystalline and amorphous components in RHEED patterns are similar.

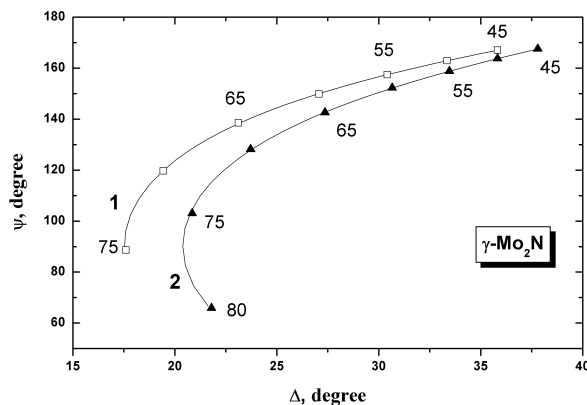


Fig. 2. Dependence of Ψ on Δ calculated with φ as a parameter for $\gamma\text{-Mo}_2\text{N}/\text{Si}$ samples 1 and 2 ($\lambda = 632.8$ nm). Points show the experimental results measured at different φ with a step of 5° .

Ellipsometric parameters Ψ and Δ are defined by

$$\rho = R_p / R_s = \tan\Psi \exp(i\Delta). \quad (1)$$

where ρ - is a complex reflection coefficient, R_p and R_s - are Fresnel coefficients for p and s lightwave polarization. In the experiment the parameters Ψ and Δ were measured for several values of angle of incidence φ . Then, it has been found that equation (1) is fulfilled with measured Ψ and Δ only in the framework of model of semi-infinite optical medium. This means that lightwave reflection is insensitive to the interface and substrate parameters and $\gamma\text{-Mo}_2\text{N}/\text{Si}$ films fabricated in our experiment can be considered as optically thick. Ellipsometric parameters were measured for two samples. Optical constants calculated for these samples using model of semi-infinite optical medium are presented in Table 1. Fidelity of this reflection model for our samples has been confirmed by calculation of $\Psi(\varphi)$ and $\Delta(\varphi)$ functions shown in Fig. 2. Optical parameters of $\gamma\text{-Mo}_2\text{N}$ are evidently dependent on technological conditions of film deposition and higher n and k are found for the film fabricated at lower nitrogen partial pressure and lower substrate temperature. It is interesting that negative dispersion has been observed for optical constants of $\gamma\text{-Mo}_2\text{N}$ over the spectral range $\lambda = 632.8\text{-}488.0$ nm.

Table 1. Optical constants of $\gamma\text{-Mo}_2\text{N}$ films.

Sample	n	k	λ , nm
1	3.287	2.690	632.8
	2.680	2.481	488.0
2	3.020	1.970	632.8
	2.550	1.713	488.0

Laser ellipsometry is a nondestructive method of thin film thickness control. As to $\gamma\text{-Mo}_2\text{N}/\text{Si}$ system, the range of film thickness h measurable by ellipsometry with reasonable possible

error is limited by high optical absorption. The dependence of Ψ on Δ calculated for different h values is shown in Fig. 3. It is evident that γ -Mo₂N film thickness can be measured at $\lambda = 632.8$ nm within the range $0 < h < 85$ nm. This range is in a good relation with the limit $h \sim 80$ nm critical for ellipsometric control as reported for molybdenum nitride films created with atomic layer deposition.

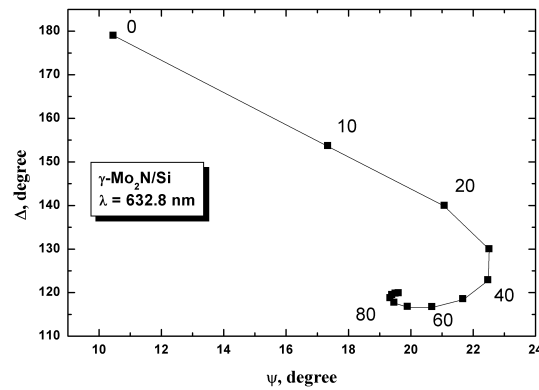


Fig. 3. Dependence of Δ on Ψ calculated for $\varphi = 70^\circ$ with γ -Mo₂N/Si film thickness as a parameter ($\lambda = 632.8$ nm). Optical constants of sample 2 were taken for the estimations. Film thickness values are given in nanometers.

4. Conclusion

The γ -Mo₂N films are fabricated with reactive magnetron sputtering of molybdenum metal target. Micromorphology and crystallographic properties of deposited layer were observed with SEM and RHEED methods. These give a basis for selection of adequate ellipsometric model and define the optical constants of γ -Mo₂N. Negative dispersion of refractive index and extinction coefficient of γ -Mo₂N has been found in visible spectral range.

References

- [1] Chuang Jui-Chang, Tu Shuo-Lun, Chen Mao-Chieh. Sputter-deposited Mo and reactively sputter-deposited Mo-N films as barrier layers against Cu diffusion. *Thin Solid Films*, 346: 299-306, 1999.
- [2] Alén P, Ritala M, Arstila K, Keinonen J, Leskelä M. Atomic layer deposition of molybdenum nitride thin films for Cu metallizations. *Journal of Electrochemical Society*, 152: G361-G366, 2005.
- [3] Atuchin VV, Hasanov T, Kesler VG, Kokh AE, Pokrovsky LD. Amorphization and chemical modification of β -BaB₂O₄ surface by polishing. *Optical Materials*, 23: 385-392, 2003.

Prospects of a Fully Scalable Stabilized LED-Source for Illumination of Measuring Systems

A. Göpfert, R. Fütterer, M. Rückwardt, M. Rosenberger, M. Schellhorn, G. Linß

Technical University of Ilmenau, Ilmenau, Germany,

Email andre.goepfert@tu-ilmenau.de

Abstract. Fluorescence and Raman spectroscopy require ultraviolet lighting. For this light emitting diodes (LEDs) offer a durable, low maintenance lighting source. Through the availability of LEDs for the UV-spectrum, replacement for the current xenon-flash-lamp technology may be at hand. The intent of this paper is the high frequency control of LEDs in the megahertz spectrum. Prevailing flash-controllers for LEDs were assessed. Due to the inadequate parameters of available flash-controllers, two LED control-circuits were designed, prototypes built, and measurements were taken. For the evaluation of the optical output signal a detection circuit was constructed. Furthermore the LED's temperature dependant properties were examined. These observations lead to the conclusion that a temperature control is needed for the LED. With the help of a Peltier cooler the LEDs temperature was stabilized and hence the wavelength and intensity of the emitted UV-Light was made reproducible.

Keywords: Ultraviolet LED, UV Flash, Spectroscopy, Regulator Controller, Photodiode, Photo Diode, Current to Voltage Converter, Peltier-Element

Introduction

With Fluorescence-spectroscopy it is possible to identify special components and concentration. Find the existence of an active ingredient in medicaments as example. In chemical analytics more often markers with fluorescence characteristics are used. For this an illumination with a constant characteristic of amplitude and wavelength is needed. In this case LED with a peak-wavelength in a UV-band was used. If specified substances will be irradiated with this wavelength they radiate in a characteristic way.

Requirement for detection of small colour differences a nearly constant non-oscillating wavelength of the light source. Special at LED-light sources the temperature has a high influence. Because of this the temperature of the LED has to be constant independent of ambient temperature, output power, installed location and mounting orientation. This is very important to achieve constant measurement results anytime. The influences are shown in Figure 1.

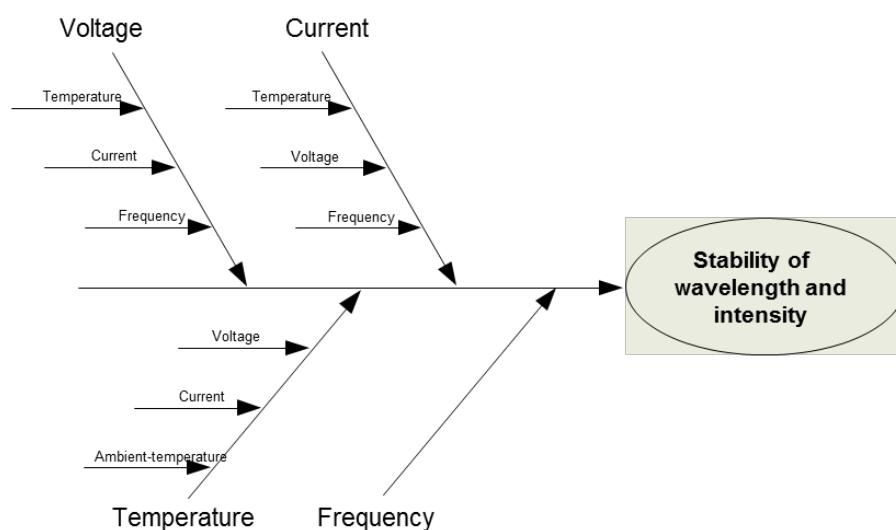


Figure 1: It seems very complex in first, as every parameter affects another parameter. [9]

After this description in a qualitative way, it is interesting which effects are quantitative. This should be on an example. This should be an UV-LED from Nichia with a peak-wavelength of 365nm and an output of 1W in continuous mode.

How can be seen every parameter is connected to ambient temperature. On the one hand there are problems to create a stable system. On the other hand it is possible to create a variable system. You can adjust and control all parameters. You can control the peak wavelength or power output. As example for a longer lifetime of the LED or more power output you can actuate the system in a lower temperature. The options of a full variable system are enormous.

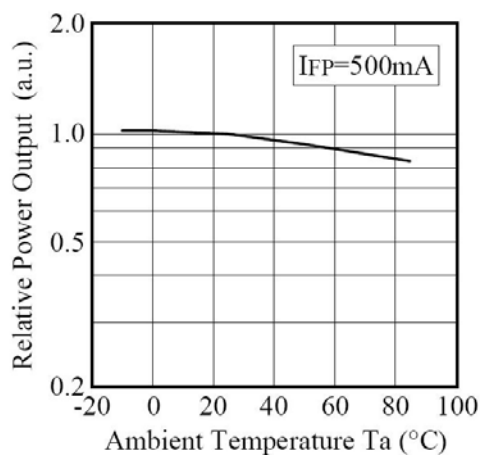


Figure 2: interconnection of power-output and temperature at LED Nichia NCSU033AT [10]

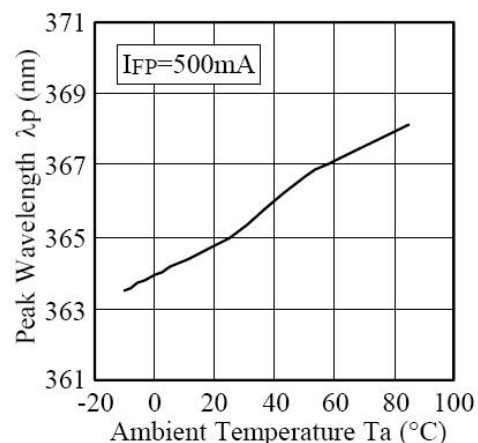


Figure 3: interconnection of peak-wavelength and temperature at LED Nichia NCSU033AT [10]

Solving and implementation

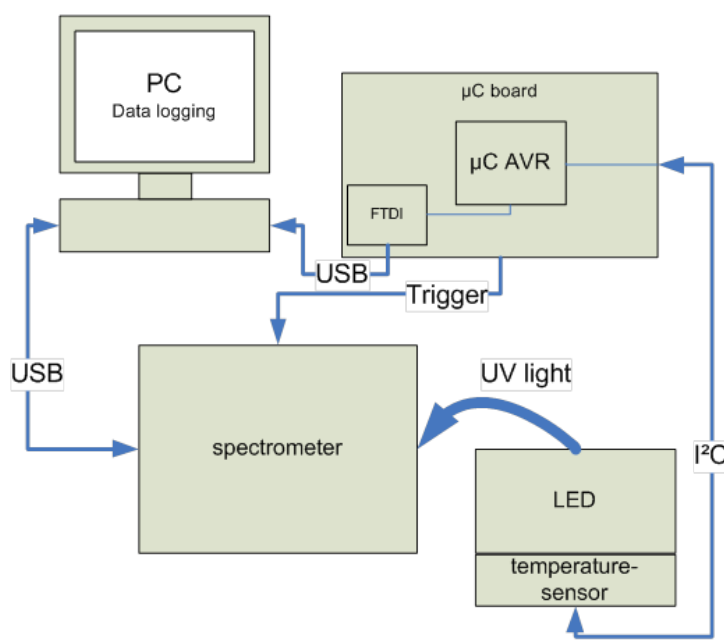


Figure 4: schematic composition of LED and control units [9]

To create such a system many several parts are needed. You need LED a controller board, a temperature sensor, a trigger generator for non-continuous mode, a photodiode to detect the frequency and power of the power output and at last an active cooling system. To measure the wavelength you will need a spectrometer. To control the several parts you need several adjustable voltage and current supplies. The best performance is to adjust everything from the controller board. In real you need also a pc for spectrometer.

In practical tests, the whole system was built and a test plan was created. The plan can be seen in figure 5. With the results of the test plan it was easy to create reference points for every parameter. So the controller can adjust every designated situation of the system.

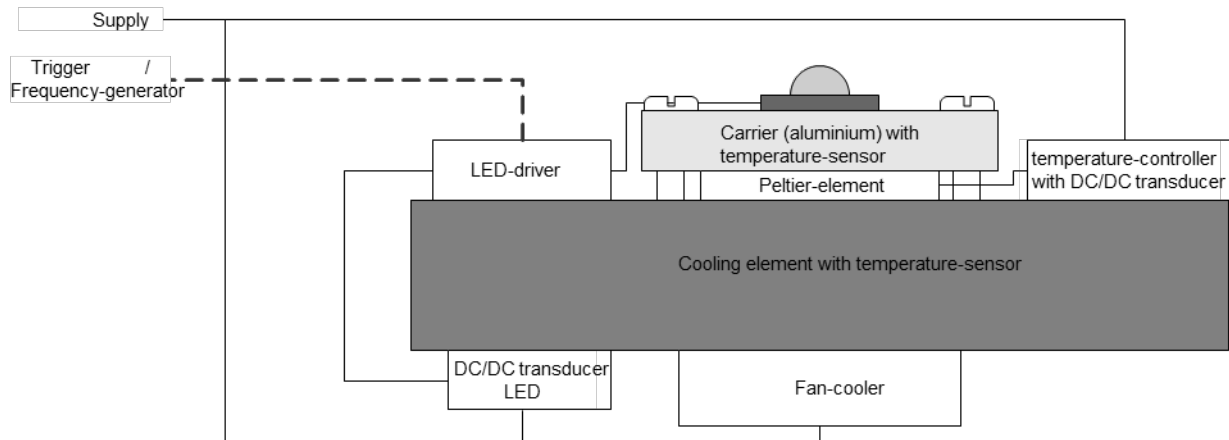


Figure 5: overview of the whole implemented system to adjust a LED

After the calibration of the whole system and his parameters, the important parameter wavelength is adjustable. As seen in figure 6. Here you can see the result of another UV-LED. There is he black plotted calibration curve and the magenta line with the results of measuring the wavelength.

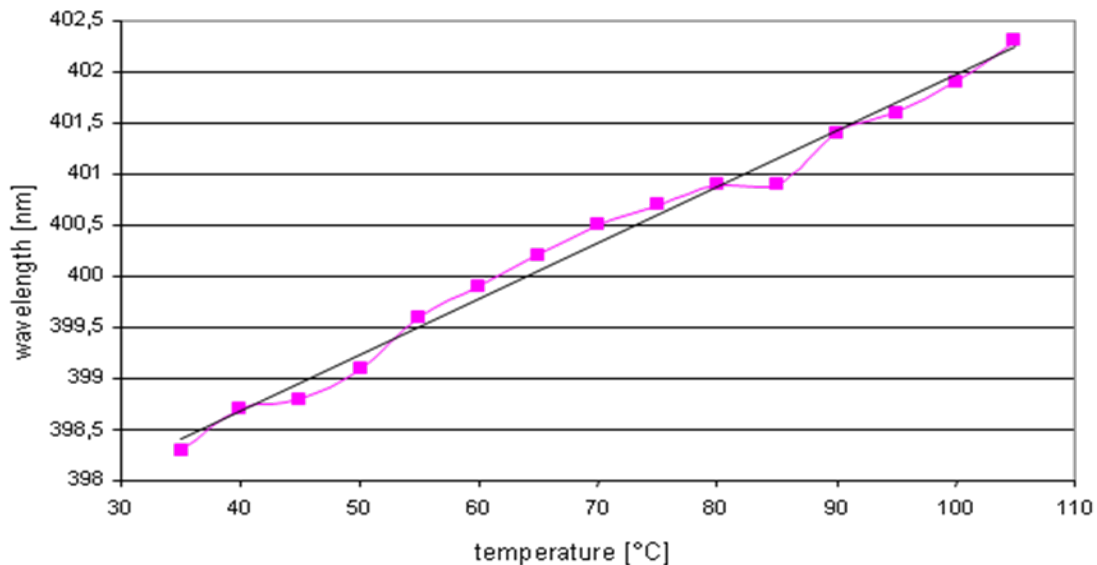


Figure 6: interconnection of wavelength and adjusted temperature of a LED

Results

In result of this project it was shown that is it able to create illumination a system for fluorescence-spectroscopy. The designed system is adjustable in several parameters. It was created, built and start running a high frequency illumination system for UV-LED. This illumination-system contains a high current LED-Driver for up to 20MHz strobe. In another analysis the interconnection of power output and temperature was detected. This is even a huge factor for fluorescence-spectroscopy.

For a stabilized system an active temperature-control-system was created. It contains a peltier-element, a cooler, temperature sensors and a controller. To minimize the power loss dc/dc-converter were used. Losing by pre-resistance components even is avoided.

For optical analysis of the created strobe mode a circuit with photodiodes and amplifier was used. So it was possible to interpret the strobe length and intensity.

At all a scalable system was created, were the parameter temperature, wavelength, voltage, current and intensity are adjustable. The system is created for high frequencies and can be used for every LED not only UV-LED.

References

- [1.] Föllinger, Otto; Dörrscheidt, Frank: *Regelungsethnik: Einführung in die Methoden und ihre Anwendung*. Heidelberg: Hüthig, 1994
- [2.] Patent US06964501: *Peltier-cooled led lighting assembly*. USA, 2002
- [3.] Patent WO2004/038290: *LED illuminated lamp with thermoelectric heat management*. Weltweit, 2004
- [4.] Patent EP00395259: *Temperature control system for solid state light source*. Europa, 1990
- [5.] Patent DE19756953: *Temperatursteuervorrichtung für eine optische Halbleitereinrichtung*. Deutschland, 1997
- [6.] Pauchard, Alexander: *Silicon Sensor Microsystem for Ultraviolet Detection*. Konstanz: Hartung-Gorre Verlag Konstanz, 2000
- [7.] Schubert, Fred: *Light-Emitting Diodes*. Cambridge: Cambridge University Press, 2003
- [8.] Linkenheld, Christian: *Basiswissen rund um die Fluoreszenz* (2002) [<http://www.mikroskopie.de/kurse/fluoreszenz/elektron.html>]
- [9.] Fütter, Richard; *Aufbau und Optimierung einer Versuchseinrichtung zur Blitzbeleuchtung im Bereich ultravioletter Strahlung*; TU Ilmenau, Ilmenau, 2010
- [10.] Osram-OS, *Datasheet BPW 34 B*, catalog.osram-os.com, 01.01.2011

Enhanced Method of the Quartz Resonator Self-Temperature-Sensing

^{1,2}V. Stofanik, ¹M. Minarik, ¹I. Balaz, ¹E. Cocherova, ²V. Bohac

¹ Dept. of Radio and Electronics, Faculty of Electrical Engineering and Information Technology, Slovak University of Technology, Bratislava, Slovak Republic.

² Institute of Physics, Slovak Academy of Sciences, Bratislava, Slovak Republic.
Email: vladimir.stofanik@savba.sk

Abstract. In this paper we introduce an extension of the self-temperature-sensing of stress compensated (SC) quartz resonator based on simultaneous excitation of two overtones (3rd and 5th overtone) - the slow thickness-shear modes (i.e. the c modes) in dual-mode crystal oscillator (DMXO). The extension is based on implementation of a self-identification of the differences between aging rates (long-term frequency instabilities) of the two mode's frequencies simultaneously excited in the quartz resonator. Processing of two excited c mode's frequencies enables to predict their shifts due to resonator's temperature variations in a wide range, where the characteristics of the c modes are free from significant anomalies.

Keywords: Dual-Mode Crystal Oscillator, SC-cut Resonator, Frequency Stability

1. Introduction

Conventional methods for sensing resonator's temperature in Temperature Compensated Crystal Oscillators (TCXO), for example, utilize a thermistor, placed in close proximity to the resonator. This method suffers from inaccuracies due to thermal lag stemming from differences in time constants and thermal gradients between the resonator and the thermistor, as well as thermistor aging. Simultaneous excitation of two modes of vibration in a piezoelectric resonator enables to realize the resonator self-temperature-sensing. The method eliminates temperature offset and lag effects, since no external temperature sensor is used. Possible applications of the self-temperature-sensing include: stabilization of the resonator's temperature with excellent accuracy; as well as precise compensation for frequency shifts due to the variations of the temperature in the resonator surrounding. Various applications related to the dual-mode excitation have been reviewed in [1], [2].

2. Enhanced SC-cut Self-Temperature-Sensing

We implemented an enhanced self-temperature-sensing of SC-cut quartz resonator with assistance of the DMXO and a field programmable gate array as it is illustrated in Fig. 1. The structure of particular crystal oscillators (XO) forming the DMXO we described in [3], [4], [5]. Digital circuitry, we have designed, consists of two frequency dividers, digital mixer and two binary counters, which periodically measure the time interval derived from the difference frequency f_d that is derived from the two excited c modes.

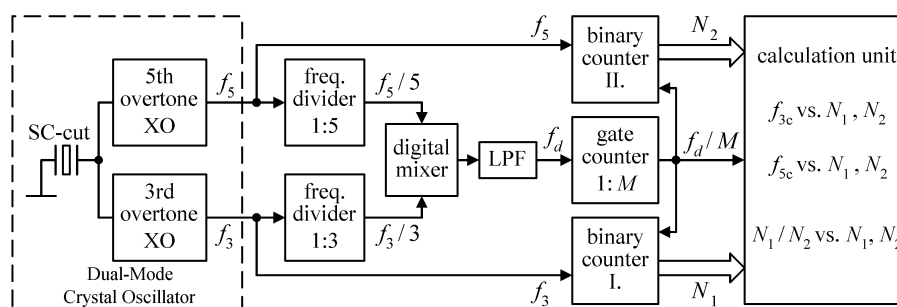


Fig. 1. Block diagram of the enhanced SC-cut resonator self-temperature-sensing implementation.

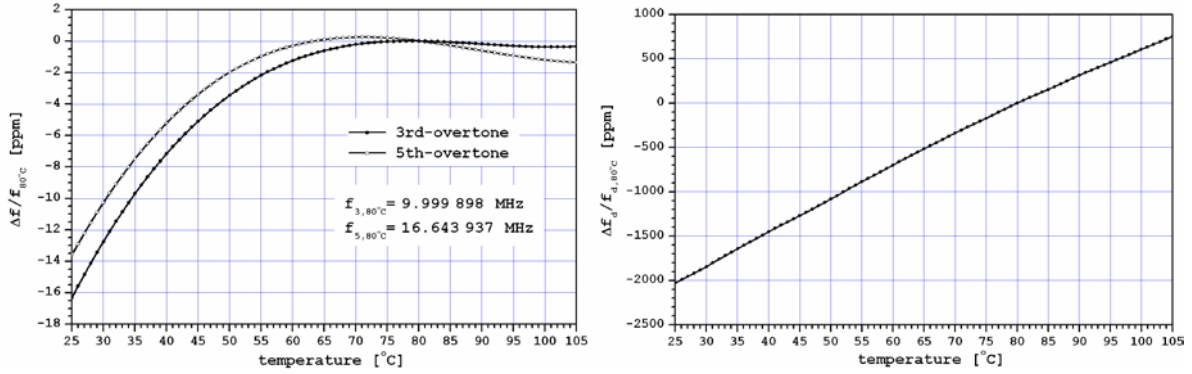


Fig. 2. Measured frequency vs. temperature dependencies of the two simultaneously excited modes in the SC resonator (left); the difference frequency vs. temperature (right).

The 5th overtone oscillator frequency divided by five is subtracted from the 3rd overtone oscillator frequency divided by three, with assistance of the digital mixer and low pass filter (LPF). The difference frequency at the LPF output can be expressed as follows:

$$f_d(\vartheta) = \frac{f_3(\vartheta)}{3} - \frac{f_5(\vartheta)}{5}, \quad (1)$$

where ϑ is the temperature of the SC-cut resonator. Figure 2 (left) shows the measured frequencies of the two simultaneously excited overtones in the SC-cut vs. temperature. Figure 2 (right) shows that the difference frequency f_d is almost linear function of temperature. The difference frequency f_d is close to 4.5 kHz and its relative value rising with temperature approximately by +38 ppm/ $^\circ\text{C}$. The gate counter (Fig. 1) produces approximately one-second time intervals (for $M=4460$), during which the binary counters accumulate clock pulses. Clock of the first binary counter is driven by the first excited c mode (the 3rd overtone frequency f_3), while the clock of the second binary counter is driven by the second excited c mode (the 5th overtone frequency f_5). At the end of each measuring cycle (time interval formed by the gate counter), the contents of both binary counters represent an actual temperature of the SC-cut resonator in the DMXO. After the clock pulses accumulation, the contents of the two binary counters can be expressed as follows:

$$N_1(\vartheta) = \text{int} \left(\frac{f_3(\vartheta)}{f_d(\vartheta)} \cdot M \right), \quad \text{where } M = 4460, \quad (2a)$$

$$N_2(\vartheta) = \text{int} \left(\frac{f_5(\vartheta)}{f_d(\vartheta)} \cdot M \right), \quad \text{where } M = 4460. \quad (2b)$$

Both the contents, $N_1(\vartheta)$ as well as $N_2(\vartheta)$, are again almost linear functions of temperature. The calculation unit (in Fig. 1) calculates actual frequencies of particular oscillators according to actual values of the independent variables $N_1(\vartheta)$, $N_2(\vartheta)$, with assistance of appropriate approximating polynomials, as follows:

$$f_{3c,1}(\vartheta) = \sum_{k=0}^9 a_k \cdot N^k, \quad \text{where } N = N_1(\vartheta) - N_{1,80^\circ\text{C}}, \quad (3a)$$

$$f_{3c,2}(\vartheta) = \sum_{k=0}^9 b_k \cdot N^k, \quad \text{where } N = N_2(\vartheta) - N_{2,80^\circ\text{C}}, \quad (3b)$$

$$f_{5c,1}(\vartheta) = \sum_{k=0}^9 c_k \cdot N^k, \quad \text{where } N = N_1(\vartheta) - N_{1,80^\circ\text{C}}, \quad (3c)$$

$$f_{5c,2}(\vartheta) = \sum_{k=0}^9 d_k \cdot N^k, \quad \text{where } N = N_2(\vartheta) - N_{2,80^\circ\text{C}}. \quad (3d)$$

The integers $N_{1,80^\circ\text{C}}$ and $N_{2,80^\circ\text{C}}$ in (3a) – (3d) represent the content of the two binary counters at selected temperature (e.g. at 80°C , which is approximately the lower turnover point temperature of the 3rd overtone) of the SC-cut. At first, the coefficients a_k , b_k , c_k and d_k in the polynomials (3a), (3b), (3c) and (3d), have to be determined according to collected data obtained from the calibration run. For each DMXO, the coefficients a_k , b_k , c_k and d_k have to be determined individually. During the calibration run, the temperature of DMXO, which is inserted into the temperature chamber, is set to the required value. When the temperature of DMXO is stabilized, the frequencies of the two modes are measured simultaneously, with assistance of precise counters. PC controls required temperature profiles in the chamber, controls the frequency measurements and collects all the measured data, as well.

Immediately after the DMXO calibration, the actual frequencies of the 3rd overtone XO calculated according to the polynomial (3a), as well as according to the polynomial (3b), have to be approximately the same; i.e. the differences between the two calculated values have to be within specified tolerance. However later, the two calculated values may start to differ due to different aging rates of resonant frequencies of particular modes, which are simultaneously excited in the SC-cut. If the two calculated values, according to the polynomial (3a) and according to the polynomial (3b), differ too much (i.e. the difference between the two calculated values is outside of the defined tolerance), then it indicates that probably the aging rates of particular modes differ too much also. In this case, the system with the DMXO has to be recalibrated. Similarly, in the case of the calculations of the actual frequencies of the 5th overtone XO, the calculated values according to the polynomial (3c), as well as according to the polynomial (3d), have to be approximately the same; i.e. the differences between the two calculated values have to be within specified tolerance. Moreover, the ratio between contents of the two binary counters $N_1(\vartheta)/N_2(\vartheta)$ indicates the ratio between the two excited c mode's frequencies $f_3(\vartheta)/f_3(\vartheta)$.

3. Results and Conclusions

Figures 3 and 4 illustrate that the frequency residuals approximately 0.1 ppm, including hysteresis, can be achieved in the temperature range between 25°C and 105°C . After performing initial calibration runs in the chamber, we can utilize the content of binary counters (N_1 , N_2) together with the ratio N_1 / N_2 for self-identification of the long-term frequency instabilities of the two c modes, which are simultaneously excited in the SC quartz resonator (Fig. 5), as well.

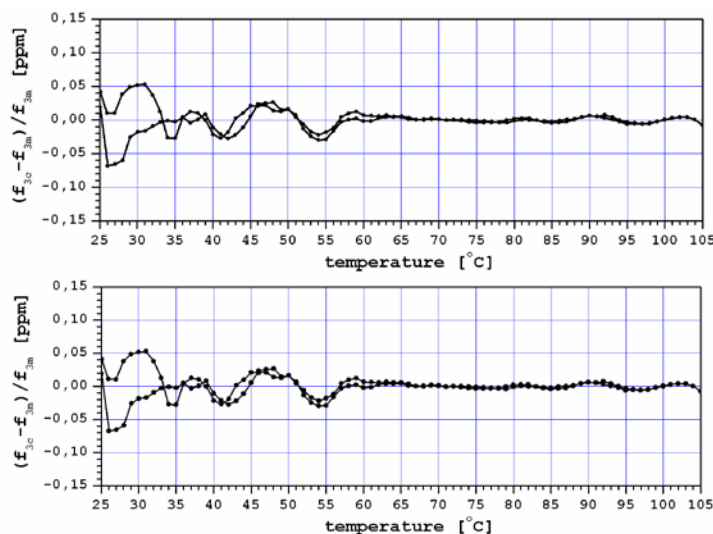


Fig. 3. Residuals vs. temperature in the case of 3rd overtone XO; data from calibration-run were fit to a single-segment 9th order polynomial (3a) – top, and polynomial (3b) – bottom.

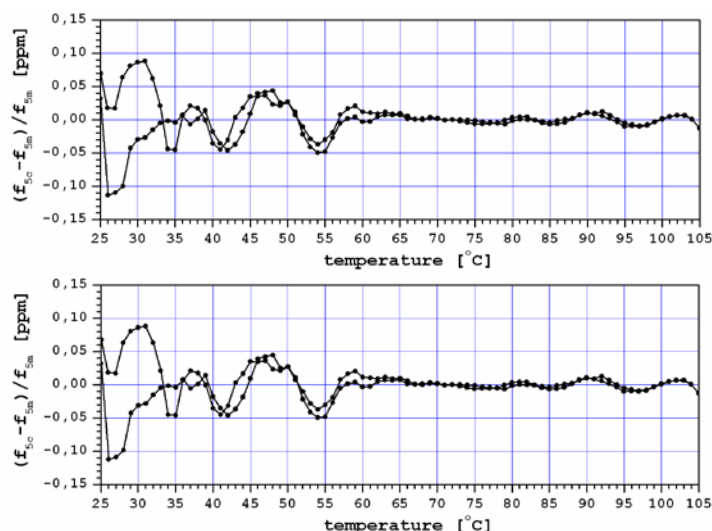


Fig. 4. Residuals vs. temperature in the case of 5th overtone XO; data from calibration-run were fit to a single-segment 9th order polynomial (3c) – top, and polynomial (3d) – bottom.

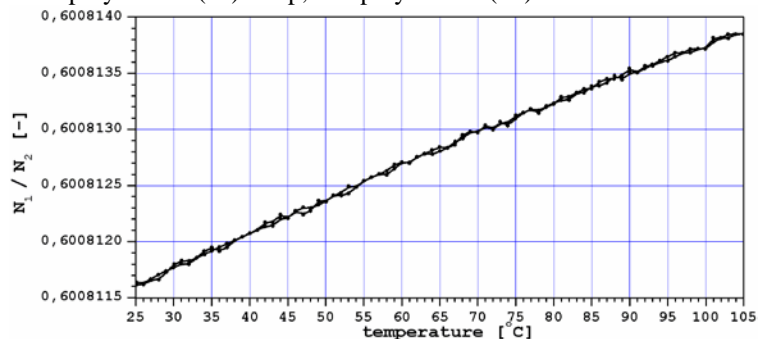


Fig. 5. Ratio of the numbers of clock pulses accumulated in the two binary counters N_1/N_2 vs. temperature of the SC-cut resonator; the clock pulses were accumulated during the time interval $4460/f_d$.

Acknowledgements

This work was supported by the Ministry of Education of Slovak Republic under the grants No. 1/0688/09 and No. 3/7411/09.

References

- [1] Vig JR. Dual-mode Oscillators for Clocks and Sensors. In proceedings of the 1999 IEEE Ultrasonics Symposium, 1999, 859-868.
- [2] Vig JR. Temperature-Insensitive Dual-Mode Resonant Sensors - A Review. *IEEE Sensors Journal*, 1 (1), 62-68, 2001.
- [3] Stofanik V, Balaz I, Minarik M. Dual-Mode Crystal Oscillator with Simultaneous Excitation of Two Overtones in a Stress Compensated Quartz Resonator. In proceedings of the joint 2007 European Frequency and Time Forum and the 2007 IEEE International Frequency Control Symposium, 2007, 227-229.
- [4] Stofanik V, Minarik M, Balaz I, Cocherova E. Investigation of Self-Temperature-Sensing of SC-Cut with Simultaneous Excitation of Two Higher Overtones in Dual-Mode Crystal Oscillator. In proceedings of the 2008 IEEE International Frequency Control Symposium, 2008, 170-173.
- [5] Stofanik V, Balaz I, Minarik M, Kozinka S. Multi-Mode Crystal Oscillator for Simultaneous Excitation of Three Thickness-Shear Modes in Stress Compensated Resonator. In proceedings of the Joint 2009 European Frequency and Time Forum and the 2009 IEEE International Frequency Control Symposium, 2009, pp 516-519.

Preparation and Characterization of $\text{Yb}_2\text{O}_3 - \text{Al}_2\text{O}_3$ Glass Microspheres with High Alumina Content

¹A. Prnová, ¹D. Galusek, ²M. Škrátek, ¹R. Karell, ¹R. Klement, ¹J. Kraxner

¹Vitrum Laugaricio – Joint Glass Center of the IIC SAS, TnU AD, FCHTP STU and Rona, a.s., Študenstská 2, SK-911 50 Trenčín, Slovak Republic

²Department of Magnetometry, Institute of Measurement Science, Slovak Academy of Sciences, Dúbravská cesta 9, 841 04 Bratislava, Slovak Republic

Email: prnova@tnuni.sk

Abstract. *In the paper we report on the preparation of ytterbia-alumina glass microspheres with high alumina content by flame synthesis. The microspheres with various alumina contents were prepared by using starting powders prepared by conventional mixing of aluminium oxide and ytterbium nitrates in appropriate proportions. The precursor powders were fed into methane-oxygen flame and after melting in the flame quenched by spraying with distilled water. The prepared microspheres were examined by optical microscopy, SEM, XRD, DTA and IR, in order to analyse the influence of experimental conditions and the way of preparation on homogeneity and the fraction of crystalline phases in prepared glasses, and to determine the temperature of maximum rate of crystallization of prepared systems. Mostly homogeneous glasses with low degree of crystallinity were prepared as microspheres in the pseudo-binary system $\text{Yb}_3\text{Al}_5\text{O}_{12}-\text{Al}_2\text{O}_3$. The presence of $\text{Yb}_3\text{Al}_5\text{O}_{12}$ (YbAG) crystalline phase together with two non-equilibrium orthorhombic and hexagonal YbAlO_3 (YbAP) phases was confirmed by XRD in prepared samples.*

1. Introduction

Modern solid state laser technology especially DPSSL (diode-pumping solid state laser) technology has become a very intense field of research in Physics. The replacement of flash-lamp pumping systems by direct laser-diode pumping systems requires development of new special and efficiency materials. Traditionally used host material – YAG ($\text{Y}_3\text{Al}_5\text{O}_{12}$ -yttrium aluminium garnet) is supplied by new materials such as YAP (YAlO_3 - yttrium-aluminium perovskite) and YAM (monoclinic yttrium-aluminate $\text{Y}_4\text{Al}_2\text{O}_9$), ytterbium-aluminium garnet (YbAG), and others, which have better thermal properties (for example low thermal conductivity ~ 0.13 W/mK)[1], high hardness and elastic modulus, greater chemical durability and very good non-hygroscopic properties. To produce high average power DPSSL, two rare-earth ions dominate: neodymium and ytterbium. At the beginning of the high-power laser development, the Nd-doped materials were preferred to the Yb-doped ones. It was mainly because of the four level nature of Nd ions and their many absorption lines, which are more convenient as far as flash lamp pumping is concerned. However, it seems obvious for more than one decade now, that Yb-doped materials are more suited for very efficient and very high-average-power diode-pumped lasers [2]. As it is clear from previous research [3, 4], Yb^{3+} ions with more simple energy level construction than Nd have some important advantages: low level of quantum defects (8.6%) between the pump and the laser photons, long storage lifetime of the upper laser level (1.3 ms) and no excited state absorption or up conversion loss. Due to the benefits of Yb^{3+} ions we expect better properties in doped single crystals and polycrystalline materials over other materials used for laser application, such as low thermal load, long upper state lifetime, large absorption width around the InGaAs laser emission range, relative large emission cross section, low thermal conductivity and strong

energy storing capacity [5 - 8]. However, these materials are commonly used in single crystal forms and their preparation is highly time, energy and financially consuming. Development of glass or polycrystalline transparent ceramic materials based on cubic oxides (YAG, YbAG) appears to be a highly economic solution, because fabrication of these materials is relatively easy and cheap. In recent years a number of works concerning preparation of very fine powders and their sintering was published [9]. These new materials are promising not only for laser applications but also as TBCs materials, or as oxidation and erosion resistant materials for design in military and commercial gas turbine engines or as optically active coating materials [5, 7, 10]. The aim of this work was preparation of fully amorphous or partially crystalline glass microspheres in systems $\text{Al}_2\text{O}_3\text{-Yb}_2\text{O}_3$ by flame synthesis and their characterisation.

Starting powders for flame synthesis were prepared by mixing of high purity Al_2O_3 with $\text{Yb}(\text{NO}_3)_3$ solution, which was prepared by dissolving Yb_2O_3 in HNO_3 . For flame synthesis methane-oxygen flame was used. All prepared binary, mostly glassy samples of various composition were examined by OM, XRD, SEM and DTA. The glass microspheres prepared in this way can be used as precursors for fabrication of transparent ceramic and glassceramic materials with good thermal, mechanical and optical properties.

2. Experimental

The compositions of the synthesized specimens (as weighed) are summarised in the Table 1. The samples A30Yb70M, A43Yb57M, A45Yb55M, A50Yb50M, and A54Yb46M were prepared using high-purity oxide powders (Yb_2O_3 - Treibacher Industrie AG, Austria, Al_2O_3 - Taimicron TM DAR, Krahn Chemie GmbH, Germany). The alumina powder was mixed with ytterbium oxide dissolved in nitric acid. The prepared mixture was homogenised by ball milling for 1 h. Then the ytterbium nitrate was converted to hydroxide by the addition of NH_4OH and the mixture was homogenized for another 1 h to complete the hydrolysis reaction. The precursor powders were finally dried, sieved, and pre-reacted for 4 h in order to increase the homogeneity of the mixture and form chemical bonds among individual components. The powders were fed into methane-oxygen flame. Molten particles were quenched by distilled water, separated, dried and calcined at 650°C in air for elimination of residua (e.g. soots from combustion process) from flame synthesis. Prepared microspheres were examined by optical microscopy (Nicon ECLIPSE ME 600) and SEM (Zeiss EVO 40HV at accelerating voltage 20kV). X-ray powder diffraction analysis (STOE Stadi-P, Germany, $\text{CuK}\alpha$ radiation, 2θ range $20\text{-}80^\circ$), IR spectroscopy (FTIR spectrometer Nicolet Magna 750, in the wavenumber range $400\text{-}4000\text{ cm}^{-1}$, standard KBr technique) and density measurement (by liquid pycnometry in hexamethyldisiloxane) were used for confirmation of amorphous or polycrystalline nature of prepared starting powders and glass microspheres. DTA measurements (DTA-TGA –simultaneous analyzer SDT 2960) were applied for determination of temperature of maximum rate of crystallization (T_x) of prepared samples.

3. Results and discussion

Composition and basic characteristics of prepared precursor powders and glass microspheres are summarized in Tab. 1. All prepared precursor powders were polycrystalline. The main phases identified in samples with higher alumina content (above 74.5 mol. %) were YbAG and $\alpha\text{-Al}_2\text{O}_3$. The X-ray diffraction data of the starting powders A30Yb70M, with lower alumina content (62.5 mol. %) showed the presence of YbAG together with traces of YbAlO_3 perovskite (YbAP). The $\alpha\text{-Al}_2\text{O}_3$ was not detected. The XRD patterns (Fig. 1) of glass microspheres were characteristic by high background, indicating highly amorphous nature of

prepared samples, but also contained separate diffraction peaks showing the traces of YbAG and YbAP crystalline phases. The presence of YbAP crystalline phase in the $\text{Al}_2\text{O}_3\text{-Yb}_2\text{O}_3$ binary system was unexpected: the stability of perovskite structure decreases with decreasing ionic radius. Moreover, increasing stability of monoclinic structure with decreasing ionic radius is assumed [12]. Also, the equilibrium binary phase diagrams $\text{Al}_2\text{O}_3\text{-Yb}_2\text{O}_3$ as published by various authors [11, 12, 13] recognize, apart from the YbAG crystalline phase, the existence of only one other thermodynamically stable binary compound, monoclinic ytterbium aluminate of the composition $2\text{Yb}_2\text{O}_3\cdot\text{Al}_2\text{O}_3$ (YbAM) in the temperature interval between 874 °C [12] and 1675 °C [11]. We therefore propose that the observed YbAP structures are non-equilibrium unstable phases associated with the transition of alumina and yttria to thermodynamically stable YbAM and YbAG phases. The traces of the YbAP phase in glass microspheres can be explained also by high temperature of methane-oxygen flame $\geq 2000^\circ\text{C}$, and high cooling rates applied during preparation of these systems. The prepared microspheres can be therefore considered as highly non-equilibrium system which, together with the presence of inhomogenities (Yb rich regions with the $\text{Y}_2\text{O}_3:\text{Al}_2\text{O}_3$ molar composition close to 1:1 similar to those observed during preparation of YAG)[14], give rise to formation of YbAlO_3 perovskite structures. The preliminary study of the structure of prepared glasses by IR spectroscopy (Fig. 2) revealed that the IR spectra of prepared glass microspheres contained two broad poorly resolved bands. The first band at $400\text{-}800\text{ cm}^{-1}$ corresponds to Al-O vibrations of tetrahedrally coordinated Al atoms in YbAG, the second one at $900\text{-}1100\text{ cm}^{-1}$, and observed also in the Yb_2O_3 spectra, could be attributed to Yb-O vibrations of octahedrally coordinated Yb atoms in the YbAG structure[5]. However, similar band with maximum at 1028 cm^{-1} was observed also in the spectra of yttrium aluminate glasses and could be attributed to change of coordination number of Al atoms from 4 to 6 in aluminate glasses[15].

Table 1. Prepared composition and their basic characteristic, p-c: partly crystalline, o-orthorhombic, h-hexagonal. The content of alumina is expressed both in weight and mole %. The content of Yb_2O_3 is the difference to 100 %.

sample	mol. % Al_2O_3	weight. % Al_2O_3	XRD	XRD quality		Tx [°C]
				powders	Microspheres	
A30Yb70	62.4	30	p-c	YbAG, YbAP h	YbAG, YbAPo	923.1
A43Yb57	74.5	43	p-c	YbAG, $\alpha\text{-Al}_2\text{O}_3$	YbAG, YbAPo, YbAPh	942.8
A45Yb55	75.9	45	p-c	YbAG, $\alpha\text{-Al}_2\text{O}_3$	YbAG	942.8
A50Yb50	79.4	50	p-c	$\alpha\text{-Al}_2\text{O}_3$, Yb_2O_3	YbAG, YbAPo	924.7 945.8
A54Yb46	81.9	54	p-c	YbAG, $\alpha\text{-Al}_2\text{O}_3$	YbAG	926 944

The morphology of prepared glass microspheres was examined by optical microscopy and SEM. Prepared particles were transparent (Fig. 3), fully remelted, with particle size $\leq 15\mu\text{m}$. However, detailed SEM examination (Fig. 4) revealed that some microspheres were fully or partially crystalline as can be seen from regular features and facets at the surface of microspheres with larger diameters ($\geq 10\mu\text{m}$). This feature is considered as undesirable, as the presence of crystallites might significantly influence the properties of prepared glasses, including the density, transparency, crystallization characteristic, or ability to densify by

viscous flow. The temperatures of maximum rate of crystallization T_X (Tab. 1) were determined by DTA.

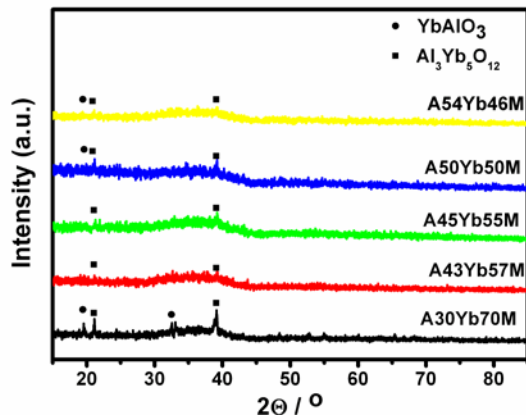


Fig. 1. XRD spectra of prepared glass microspheres

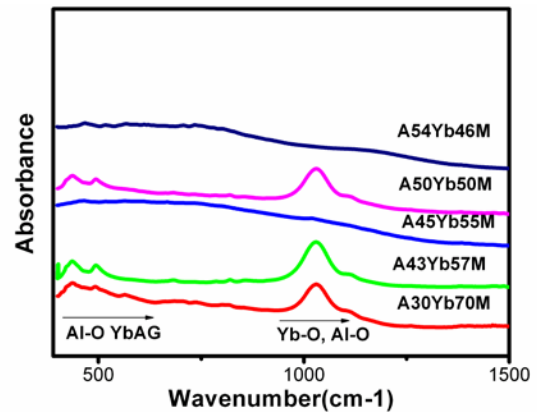


Fig. 2. IR spectra of prepared glass microspheres

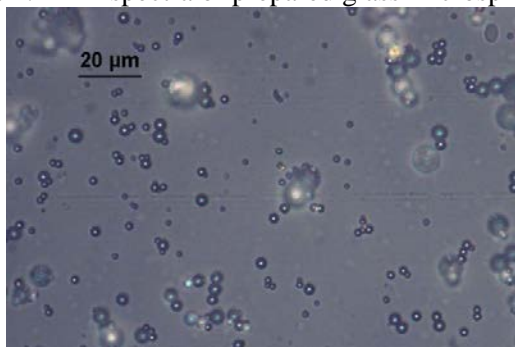


Fig. 3. Optical micrograph of the sample A50Yb50

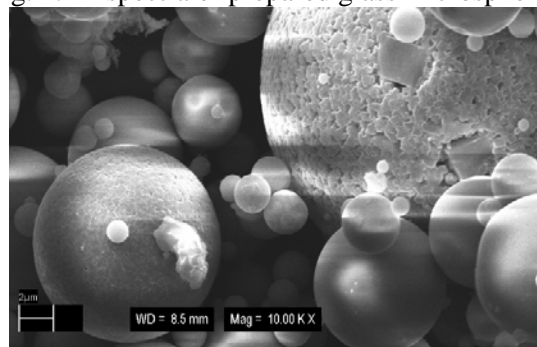


Fig. 4. SEM micrograph of the sample A50Yb50

While the compositions A30Yb70M, A43Yb57M and A45Yb55M showed only one crystallization peak on DTA records, the compositions with higher alumina content, such as A50Yb50M and A54Yb46M showed the presence of two closely spaced exothermic peaks. Based on the measured data or the information from the literature we could not find any plausible explanation for such behavior. Therefore, for detailed study of the structure and crystallization properties of these systems further examination of prepared microspheres by various methods, such as ^{27}Al MAS NMR, and high temperature XRD and DTA will be necessary. These will be further extended using fully amorphous glasses prepared by sol-gel methods, which contain no nuclei of the crystalline phases.

4. Conclusion

Glass microspheres in the system $\text{Al}_2\text{O}_3\text{-Yb}_2\text{O}_3$ with very low degree of crystallinity were prepared by flame synthesis. Examination of the microspheres revealed the presence of YbAG and traces of non-equilibrium phase YbAP. The IR spectra of studied systems contained only two broad unresolved bands between $400\text{-}800\text{ cm}^{-1}$ and $900\text{-}1100\text{ cm}^{-1}$. These were attributed to Al-O and Yb-O vibrations in the structure of YbAG, and to the change of Al coordination number in the structure of glass.

Acknowledgements

The financial support of this work by the grant VEGA 1/0603/09, and by the APVV grant LPP 0133-09 is gratefully acknowledged. This publication was created in the frame of the project "Centre of excellence for ceramics, glass, and silicate materials" ITMS code 262 20120056, based on the Operational Program Research and Development funded from

the ERDF. This publication is also the result of the project implementation „Centre of Excellence for Contaminants and Microorganisms in Food" supported by the Research & Development Operational Program funded by the ERDF.

References

- [1] Marchi J, Morais DS, Schneider J, Bressiani JC, Bressiani AHA, Characterization of rare earth aluminosilicate glasses, *Journal of Non-Crystalline Solids*, 351, 863-868, 2005.
- [2] Li J, Wang J, Tan H, Zhang H, Song F, Zhao S, Zhang J, Wang X, Growth and optical properties of Er, Yb:YAlO₃(BO₃)₄ crystal, *Materials Research Bulletin*, 39, 1329-1334, 2004.
- [3] Hou X, Zhou S, Jia T, Lin H, Teng H, Structural, thermal and mechanical properties of transparent Yb: (Y_{0.97} Zr_{0.03})₂O₃ ceramic, *Journal of European Ceramic Society*, Article in press, 2011.
- [4] Chénais S, Druon F, Forget S, Balembois F, Georges P, Review On thermal effects in solid-state lasers: The case of ytterbium-doped materials, *Progress in Quantum Electronics*, 30, 89-153, 2006.
- [5] Wang HM, Simmonds MC, Rodenburg JM, Manufacturing of YbAG coatings and crystallisation of the pure and LiO₂ doped Yb₂O₃-Al₂O₃ system by a modified sol-gel method, *Materials Chemistry and Physics*, 77, 802-807, 2002.
- [6] Xu X, Zhao Z, Xu J, Deng P, Distribution of ytterbium in Yb:YAG crystals and lattice parameters of the crystals, *Journal of Crystal Growth*, 255, 338-341, 2003.
- [7] Wu Y, Li J, Pan Y, Liu Q, Guo J, Synthesis of nano-sized Yb₃Al₅O₁₂ powders by the urea co-precipitation method, *Ceramics International*, 35, 25-27, 2009.
- [8] Fagundes-Peters D, Martynyuk N, Lunstedt K, Peters V, Petrmann K, Huber G, Basun S, Laguta V, Hofstaetter A, High quantum efficiency YbAG-crystals, *Journal of Luminiscence*, 125, 238-247, 2007.
- [9] Liu M, Wang S, Zhang J, An L, Chen L, Preparation and Upconversion Luminiscence of Y₃Al₅O₁₂:Yb³⁺, Er³⁺ Transparent Ceramics, *Journal of Rare Earths*, 24, 732-735, 2006.
- [10] Petermann K, Fagundes-Peters D, Johannsen J, Mond M, Peters V, Romero JJ, Kutovoi S, Speiser J, Giesen A, Highly Yb-doped oxides for thin-disc lasers, *Journal of Crystal Growth*, 275, 135-140, 2005.
- [11] Bondar A, Shirvinskaya AK, Popova VF, et al., "Thermal stability of orthoaluminates of yttrium-subgroup rare earths," *DAN SSSR*, 246, (5), 1132-1136, 1979.
- [12] Fabrichnaya O, Seifert HJ, Thermodynamic assessment of the ZrO₂-Yb₂O₃-Al₂O₃ system, *CALPHAD: Computer Coupling of Phase Diagrams and Thermochemistry*, 34, 206-214, 2010.
- [13] Lakiza SM, Red'ko VP, Lopato LM, Al₂O₃-ZrO₂-Yb₂O₃ phase diagram and phase equilibria in alloy solidification, *Powder Metallurgy and Metal Ceramics*, 4, 7-8, 2008.
- [14] Hay RS, Phase transformations and microstructure evolution in sol-gel derived yttrium-aluminum garnet films, *J.Mater Research*, 8, 578-604, 1993.
- [15] Wilding MC, McMillan PF, Navrotsky A, Thermodynamic and structural aspects of the polyamorphic transition in yttrium and other rare-earth aluminate liquids, *Physica A*, 314, 379 - 390, 2002.

The Measuring Workplace for Studying Basic Characteristic of Operational Amplifiers Distributing Through Internet

¹M. Godla, ²L. Michaeli, ³J. Šaliga, ⁴M. Sekerák

^{1,2,3}, Dept. of Electronics and Multimedia Communications, FEI TU of Košice ,
Slovakia,

Email: marek.godla@tuke.sk

Abstract. *This project was created for effective studying practical sections of object „Basics of electronics“ by a real remote control measuring workplace. The content of this measuring workplace are circuits of operational amplifiers and measure instruments. In circuits, it is possible to change a value of feedback resistors and setting parameters of measure instruments by PC. A virtual measuring workplace was created for comparison with this real workplace. The measuring workplace is distributed through the internet. The whole project is created in the development environment LABview with using the measuring card NI-DAQmx.*

Keywords: *Labview, Remote Control Measure Workplace, Operation Amplifier, Feedback Resistors, Remote Control Measure Instrument, NI-Daqmx.*

1. Introduction

Study of basic electronics without real measuring and exploring features of basic electronics components is not sufficient for students. A solution of this problem is real measuring in a laboratory. However this measure is problematic because of inadequate number of measuring instruments and fast destruction of measuring components. The destruction of electronics components is caused by often using.

A main task of this work is to design a measuring workplace, which can be controlled by a user via internet developed in the LabVIEW. LabVIEW development environment allows to remote access from any client with available web browser like Explore, Mozilla. In order to create laboratory stand as close as possible to the real situation stand alone instruments were used. Those instruments were controlled from the program using their interfaces. Moreover, the laboratory stand allows performing similar measurement off-line from the instruments. In order to increase the real feeling from the measuring stand a web camera was utilized displaying image from front panels of instruments.

2. Design and create measuring plant

Laboratory stand consist of four circuits for four laboratory exercises. Each measuring circuits is being controlled by a switching circuit which allow to change circuit component according command by a student from remote computer. The first two measuring circuits contain operational amplifiers connected as inverting and noninverting. Change of feedback elements caused different characteristic of amplifier. Resistors connected through the analog switching circuit show (fig. 1). Third measuring circuit represents integrator. Fourth circuit to be prepared for laboratory measurement was the rectifier with operational amplifier. The input signal from generator is being connected to all four circuits parallel.

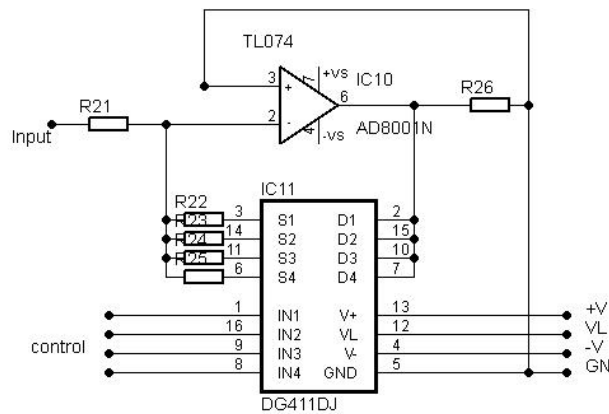


Fig. 1. Switching of feedback resistor on inverting circuits of operational amplifier

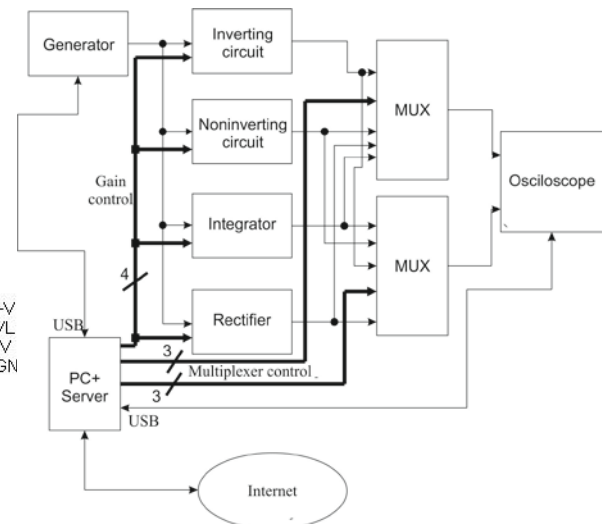


Fig. 2. Block scheme of laboratory stand

Each measuring node is connected to one of eight inputs at two analog multiplexers. Outputs from the multiplexers are connected to two inputs of oscilloscope. Selection of measured nodes by any multiplexer is performed independently by 3-bit addressing bus AB1 and AB2. The feedback resistors in both amplifiers and rectifier and feedback capacitors in the integrator are chosen simultaneously by control bus CB3 (fig.2). Multiplexers for control of the feedback resistors and selection of signals from measuring nodes are realized by integrated circuits DG 408, 409 and DG 412. The ON resistance DG 408, 409 is 100 Ω and DG 411 is 35 Ω . Multiplexers are controlled from measuring card NI-PCI 6251 with NI- SCC 68 is an I/O connector block. Schematic of whole plant is on figure 2.

3. Materials Supporting Students

Materials for preparation consist of necessary theoretical description of measurement stand, measurement tasks and project for simulation of the measured circuits.

User has on his disposal PSPICE simulation tool as a component of OrCAD program package. Simulation of the measured circuits allows students to compare simulation results with measured ones. Output plots acquired in the simulation environment for some values of component in the circuit are available for those who are not familiar with simulation software. Fig.3 shows output plot from the TRAN. analysis of operational amplifier as rectifier for 1 and 10 kHz input frequency.

4. Designing a web server for connection a workplace to the Internet

The web server is designed in the environment LabVIEW. The LabVIEW environment allows to generate the html web page from the panel diagram of the control program which is accessible from the client's computer. Program is running on server which is able to control laboratory stand, instruments and transfer image from the web camera. User from the clients computer can control program using Explorer or Mozilla. These web browsers have to allow pop-up application.

The link of this web page is set on the official web pages of the laboratory Department of electronics and multimedial communication.

5. Control program for control measuring Instruments

Control program allows changing basic setting-up of generator AGILENT 33220A and oscilloscope RIGOL DS1052E. Generator AGILENT 33220A represents arbitrary signal generator of frequency range 0-20 MHz. Oscilloscope RIGOL DS1052E is two channel digital oscilloscope with max 1GSa/s.

Multiplexing circuits for connection of selected measuring points into two inputs of oscilloscope were controlled from the digital outputs of the NI-DAQ board NI6251 by National Instruments. For any multiplexer three digital outputs were utilized. Other four digital outputs were used for control of combination feedback resistors simultaneously in all four circuits. Four digital inputs allow to set-up one of 4 resulting values of feedback resistor in each circuit.

Both instruments were controlled via USB link and using VISA standard.

Control program of oscilloscope allows controlling basic settings: time base, voltage range, triggering level, V and H position, DC or AC coupling of channels, AUTO button and RUN/STOP button.

Moreover program allows acquiring following parameters of the measured signals:

- measured signals from two input channels
- transferring values from oscilloscope determining parameters of measuring waves (amplitude, period, minimal voltage, maximal voltage, frequency)

Control program of generator allows controlling basic settings like signal form, signal amplitude, phase, offset, frequency and output polarity

Panels which control generator, oscilloscope and measuring nodes are on fig.4

6. Control program for web camera

This program allows users real watching of measure workplace. For better utilization of performing PC is show only consecutive pictures witch are refresh every 500ms. These pictures give user complete idea about measuring plant and instruments. Picture taken from the laboratory stand allow to get feeling of work in the real laboratory. Moreover user can check whether control commands are being received by measuring instruments (fig.5).

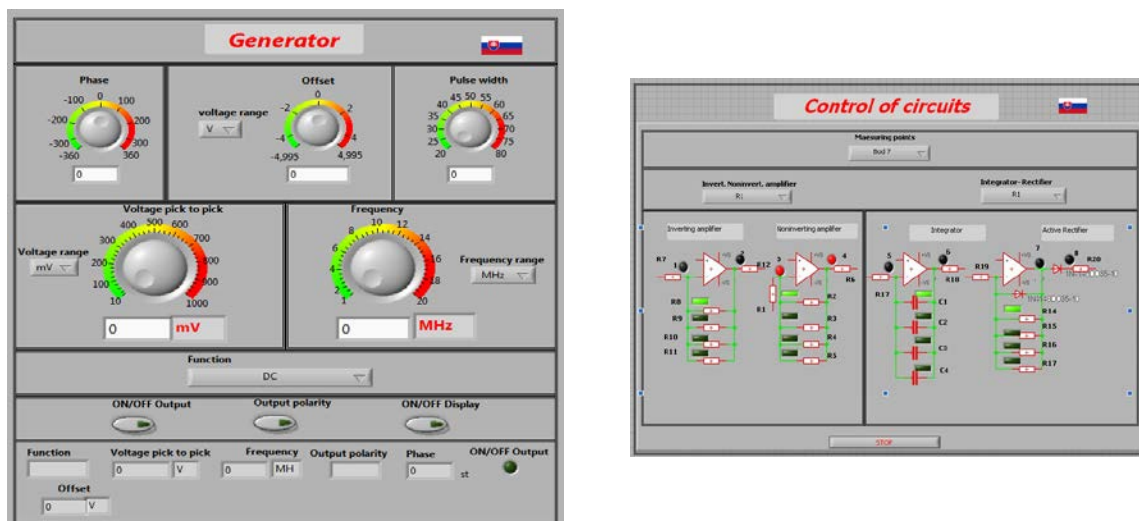


Fig. 3. Panels controlling generator, oscilloscope and measuring nodes.

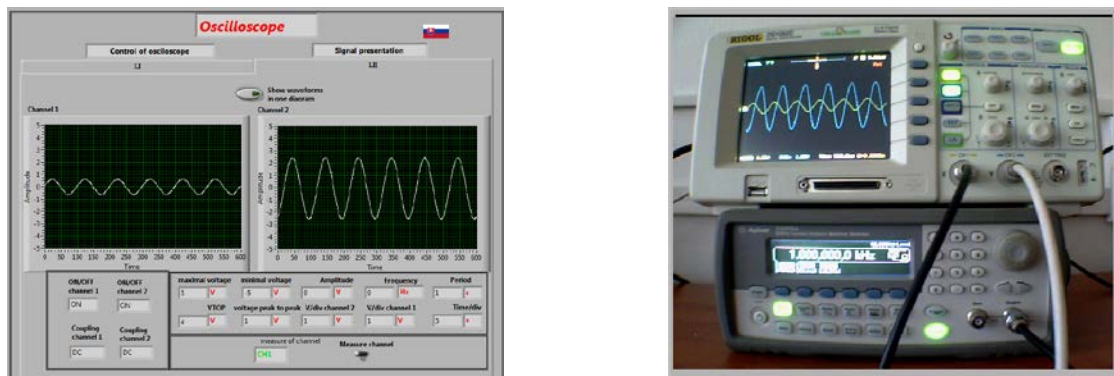


Fig. 4. Image from the laboratory stand acquired by a web camera

Conclusion

Presented laboratory stand controlled remotely through Internet serves students of Faculty of Electrotechnic and Informatics for distant laboratory exercises in the course of “Basic electronics”. Described stand is one of four stands which are in the trial phase. Three laboratory stands are controlled with DAQ board only. Described one has to increase feeling of work in the real laboratory. Results from questionnaire inquire among students showed that both methods how to control laboratory stands are for users similar. In the future all laboratory stands will be controlled by DAQ boards only. It allows to release instruments utilized here for laboratory stands devoted for laboratory exercises performed personally.

Acknowledgment

The work is a part of project supported by the Educational Grant Agency of Slovak republic (No. 3/7115/09)

This work was supported by Agency of the Ministry of Education of the Slovak Republic for the Structural Funds of the EU under the project Centre of Information and Communication Technologies for Knowledge Systems (project number: 26220120020).

References

- [1] www.ni.com
- [2] RIGOL, ”Programming guide DG 1022 Function/Arbitrary Waveform Generator, RIGOL Technologies Inc., August 2009
- [3] RIGOL ,”Programming guide DS1000, DS1000CA Series Digital Oscilloscope, Publication number: PGA02100-1210, RIGOL Technologies Inc, June 2008
- [4] USER GUIDE SCC- 68 ,”I/O Connector Block with 4 SCC Signal Conditioning Slots for DAQ Devices, National Instrumnets Corporation, 2006
- [5] Data Sheet, “DG408, DG409”, File Number 3283.5, Intersil Corporation, June 1999
- [6] Data Sheet, “TL074, TL074A – TL074B”, STMicroelectronics Group of Companies, December 1998
- [7] Godla,M.: “Diploma Work”, Technical University in Košice, Faculty of Electrical Engineering and Informatics, Slovak Republic, 2010
- [8] Grimaldi,D.: Workload measurement method into a Distributed Measurement Laboratory, In: Measurement. - ISSN 0263-2241. - Vol. 39, no. 7 (2006), p. 655-663.

Frequency Synthesizer Based on Flying Adder Architecture and Phase Locked Loop

M. Stork

Department of Applied Electronics and Telecommunications,
University of West Bohemia, Plzen, CZ
Email: stork@kae.zcu.cz

Abstract. Frequency synthesis is one of the most important and most actively researched subjects in the field of VLSI mixed-signal circuit design. Among the existing techniques in this area, phase locked loop fractional architecture is a widely used one for generating frequencies which are not integer multiple of the input reference frequency. Flying-Adder architecture is an emerging technique which is based on a new concept time-average-frequency, to generate frequencies. This paper presents fractional frequency synthesizer architecture based on concept flying-adder and phase locked loop principle. The simulation results concerning this system are presented.

Keywords: Direct Digital Synthesis, Flying Adder, Frequency Synthesis, Phase Locked Loop

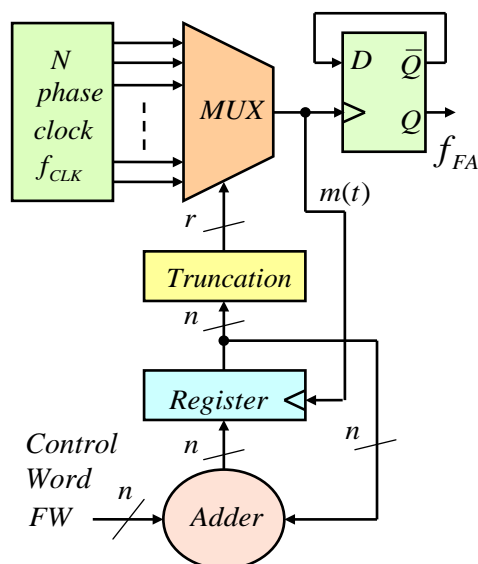


Fig. 1. The block diagram of fractional flying adder (FFA) frequency synthesizer consist of: N -phase clock generator (frequency f_{CLK}), multiplexer MUX, D-flip-flop, digital adder with control frequency word FW , register and truncation which convert n -bit word to r -bit word. Output frequency of FFA is f_{FA} .

1. Introduction

Along the history of frequency synthesis development, Phase-Lock Loop (PLL) based synthesis method is the mostly used approach. Within this approach, there are several milestone techniques: Integer- N architecture, Fractional- N architecture and Sigma-Delta Fractional- N architecture. Integer- N PLL is commonly used in the cases where frequency requirement is straightforward. Fractional- N PLL is a technique which can generate output frequencies that are fractional multiples of the input reference frequency. This is important step forward from the Integer- N PLL. However, this advancement is accompanied with a serious drawback. It degrades the spectrum purity of the output frequency. To overcome this problem, Sigma-Delta Fractional PLL was developed. The Flying-Adder architecture is an emerging technique in the field of frequency synthesis. The proof of concept was constituted

in 2000. It was built on the foundation of a new concept: Time-Average-Frequency. The theoretical foundation was established in 2008 [1, 2]. The more in-depth study is delivered in [3, 4]. The most distinguished features of this technique are its instantaneous response speed and the capability of generating arbitrary frequency. In this paper, the architecture of fractional flying adder (FFA) is used with conjunction of PLL. Compared to the pure structure FFA frequency synthesizer, the proposed approach can achieve the same frequency resolution with reduced fractional spurs.

2. Frequency Synthesizer Based on Flying Adder Principle

The FFA [3, 4], which is also referred to as direct digital period synthesizer or digital-to-frequency converter (DFC), is an independent frequency synthesis. The FFA shares some functionality with circuits that involve phase-switching prescalers and digital phase accumulators. The block diagram of basic FFA is shown in Fig. 1. The system is driven by the $N = 2^m$ clock phases with frequency f_{CLK} , one of which is selected by the N -to-1 multiplexer (MUX). The rising edges of MUX 's output (signal $m(t)$) is a trigger for the n -bit register changing its value from

$$x_{k+1} = (x_k + FW) \bmod 2^n \quad (1)$$

where FW is the n -bit long frequency control word and k is integer variable which presents counts of the rising edges of signal $m(t)$. The register value x_k , is then truncated by taking the first r , most significant bits to y_k according (2).

$$y_k = \frac{x_k}{2^{n-m}} \quad (2)$$

The y_k controls the MUX and therefore chooses the input phase that passes through the MUX . The signals $m(t)$ which is a sequence of pulses, or spikes is fed to the D-Flip-Flop which acts as a frequency divider by-2 providing the output signal f_{FA} .

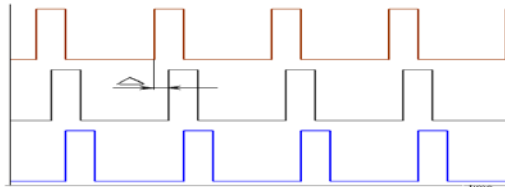


Fig. 2. Example of multiphase generator (8 phase generator, but only 3 phases are displayed) with phase difference Δ among the multiple outputs.

FFA employs a multiphase generator to generate multiple clock signals evenly distributed in a full clock cycle. These same-frequency-but-different-phases clock signals are used to synthesize desired frequency. The synthesized signal is directly related to the phase difference “ Δ ” among the multiple outputs from the generator (Fig. 2). The frequency control word FW sets the number of Δ before the synthesized clock toggles. The frequency of the f_{FA} is given by the following expression [1]:

$$f_{FA} = \frac{1}{FW \cdot \Delta} = \frac{1}{FW \frac{1}{f_{CLK} \cdot N}} = f_{CLK} \frac{N}{FW} \quad (3)$$

where N is the number of VCO stages. It is important to note that value x_k , eq. (1) in *Register* is limited to $2^n - 1$ (function $\bmod 2^n$) and therefore y_k , eq. (2) is also limited. Unlike the conventional PLL, the FFA consists of digital circuitry such as multiplexers, adders, and flip-flops, thereby resulting in fast switching time and wide tuning range. Specifically, an FFA architecture with an N -stage VCO has a frequency range of $0.5 \cdot f_{CLK}$ to $0.5 \cdot N \cdot f_{CLK}$ [5]. Due

to its wide tuning range and instant response time, the FFA frequency synthesizer is highly suitable for many System-on-Chip applications. The frequency control word could be an integer or a fractional number when high frequency resolution is desired. When FW is an integer, the FFA synthesizer can be viewed as a phase divider which can achieve finer resolution than frequency divider does. When FW is a fractional word, the FFA modulates the output frequency to achieve higher resolution. The frequency modulation results in spurious spikes in the frequency spectrum. Although dithering methods can be used to eliminate or effectively reduce the spurs, this approach comes at the cost of increased overall noise.

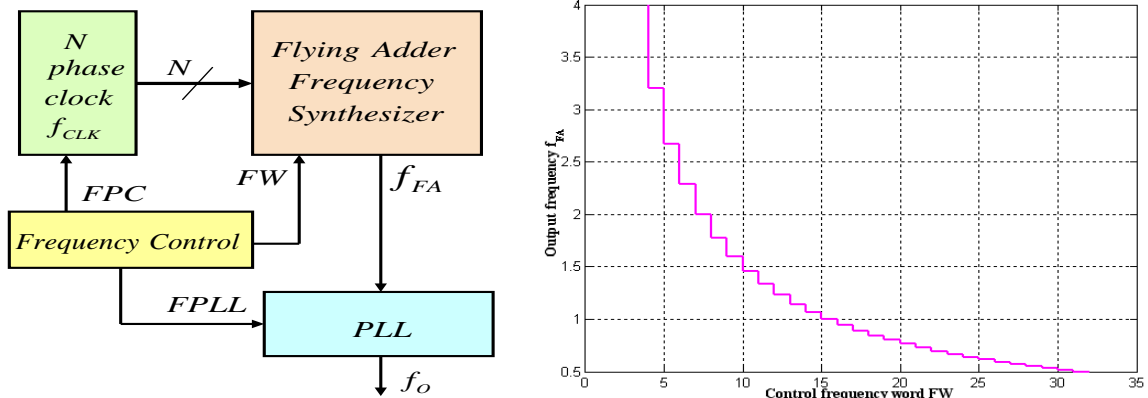


Fig. 3 and 4. The block diagram of fractional frequency synthesizer which consists of FFA and PLL (left) and output frequency of FFA, as function of control frequency word $FW <4; 31>$, for $n=5$ (right).

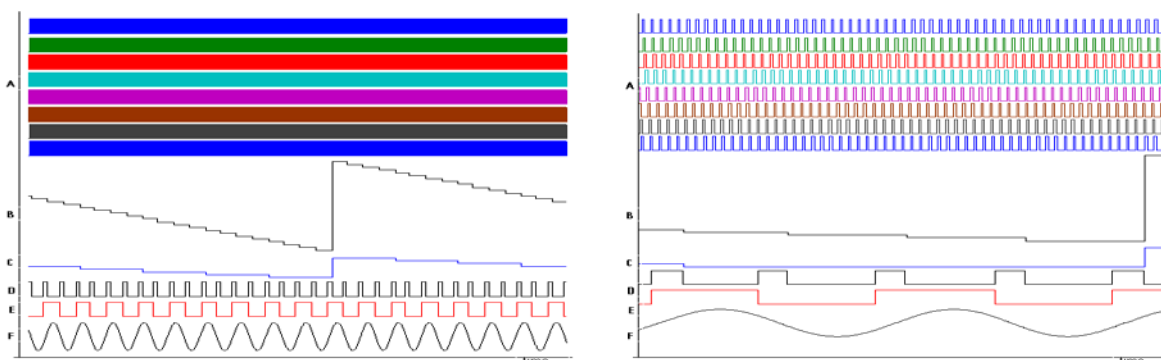


Fig. 5 and 6. The time diagram of signals in synthesizer for $n=5$, $r=3$, $N=8$ and control frequency word $FW=31$. A – 8th phase clock f_{CLK} , B – Register value (x_k) , C – Truncation value (y_k) , D – MUX output $m(t)$, E – D Flip-Flop output f_{FA} , F – PLL output f_o (left), (zoom of Fig. 5) (right).

3. Frequency Synthesizer Based on Flying Adders and PLL

The FFA synthesizer has a wide tuning range and a quick response time but has frequency spurs in the output spectrum when working in the fractional mode to achieve higher resolution. On the other hand, PLL technique can help reduce the spurs but fractional-N PLL architecture is complicated. This work introduces a frequency synthesizer architecture that incorporates the advantages of the FFA and conventional PLL architectures but avoid the drawbacks of each. The block diagram of synthesizer is shown in Fig. 3. This system contains also frequency control block which is used for coarse frequency setting in *N*-phase clock (signal FPC) and also in PLL (signal $FPLL$) and fine frequency setting (signal FW) connected to FFA. For coarse frequency setting the different principles can be used (depends on the types of system, e.g. oscillator switching etc.) and aren't described in this paper. The simulation results for 8 phase clock ($N=8$), 8 input MUX (3 bit address, $r=3$), 5 bit register ($n=5$) and conventional PLL with charge pump phase detector and voltage controlled oscillator with sinus signal output are presented. The output frequency of FFA, as function of

control frequency word FW (for $n=5$, $r=3$) is shown in Fig. 4. The FW step is 1, size of $\langle 4; 31 \rangle$. For better frequency resolution is possible to extend register, (increase of n), which means extend floating part of the number. The FFA architecture can generate any frequency, providing that there are sufficient fraction bits in the accumulator-register. On the other hand, the pulses on FFA output aren't equally distributed. The time diagram of signals in synthesizer are shown in Fig. 5 and zoom of this figure is shown in Fig. 6. The example of frequency spectrum of FFA without PLL is shown in Fig. 7. The comparison of previous results to proposed synthesizer (with PLL) is shown in Fig. 8. The spurious spikes of FFA are filtered by PLL low-pass filter.

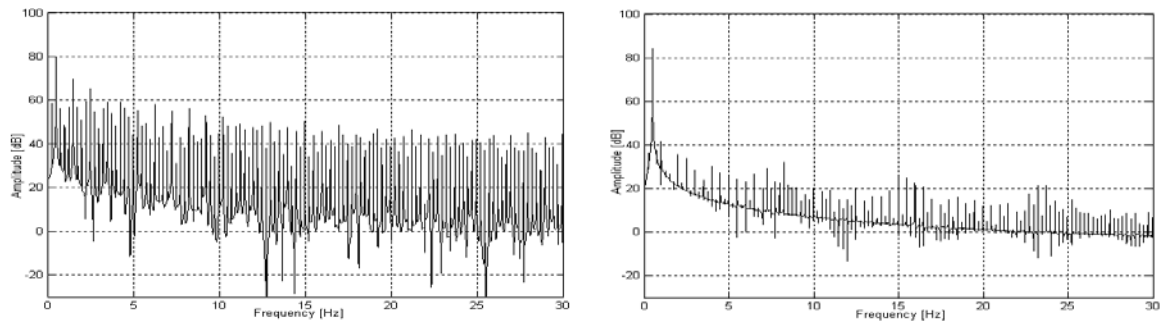


Fig. 7 and 8. The frequency spectrum of flying adder output f_{FA} , without PLL (left) and frequency spectrum of synthesizer output f_O with PLL (right)..

4. Conclusions

In this paper, a simple frequency synthesizer with reduced fractional spurs has been presented and simulated. The proposed approach uses Flying-Adder technique in cooperation with Phase Locked Loop. The tradeoff of this approach is that Flying-Adder loses its "instant response" advantage, because in a Phase Locked Loop low-pass filter is included.

Acknowledgements

Milan Stork's participation in preparing this paper has been supported by: Department of Applied Electronic and Telecommunication, University of West Bohemia, Plzen, CZ

References

- [1] XIU, L. The Concept of Time-Average-Frequency and Mathematical Analysis of Flying-Adder Frequency Synthesis Architecture. *IEEE Circuit And System Magazine*, 2008, Sept., 3rd quarter, pp.27-51.
- [2] XIU, L. A Flying-Adder PLL Technique Enabling Novel Approaches for Video/Graphic Applications. *IEEE Trans. on Consumer Electronic.*, 2008, vol. 54, pp.591-599.
- [3] SOTIRADIS, P. Theory of Flying-Adder Frequency Synthesizers, Part I: Modeling, Signals' Periods and Output Average frequency, *IEEE Transactions on Circuits and Systems—I*, 2010, vol. 57, no. 8, pp. 1935-1948.
- [4] SOTIRADIS, P. Theory of Flying-Adder Frequency Synthesizers, Part II: Time and Frequency Domain Properties of the Output Signal. *IEEE Transactions on Circuits and Systems—I*, 2010, vol. 57, no. 8, pp. 1949-1963.
- [5] Xiu, L., Zhihong, Y. A New Frequency Synthesis Method Based on Flying-Adder Architecture. *IEEE Trans. Circuits Syst. II, Analog Digit. Signal Processing*, 2003, vol. 50, no. 3, pp. 130-134.

Measurement in Biomedicine

An FPGA System for QRS Complex Detection Based on Integer Wavelet Transform

¹R. Stojanovic, ¹M. Mirkovic and ²D. Karadaglic

¹University of Montenegro, Podgorica, Montenegro

²University of Manchester, Manchester, United Kingdom

Email: stox@ac.me

***Abstract.** This paper presents the QRS complex detection design suitable for implementation in Field Programmable Gate Array (FPGA). It employs the simplest version of Integer Wavelet Transform for signal decomposition and techniques of zero crossing and double thresholding for extraction of R peaks which makes it suitable for application in real-time and cost effective personal healthcare assistance devices. Beside theoretical elaborations, the system architecture, simulation diagrams and working performances are presented.*

Keywords: QRS detection, FPGA, Wavelet Transform,

1. Introduction

The QRS complex is the most important segment in electrocardiogram (ECG) signal and its shape, time of occurrence and frequency gives us valuable information about heart condition. Many methods were tried on QRS complex detection, and an extensive review of the approaches proposed in the last decade can be found in [1].

The results of these studies have demonstrated that the Wavelet Transform (WT) in its discrete form - DWT (Discrete Wavelet Transform) - is the most promising method to extract characteristic points from the ECG signal. However, the most of the published algorithms are heavily processor demanding, therefore do not allow the real-time operation on personal computers.

In recent years, significant research, academic and industrial attention has been given to Telemedicine and Wearable Health Care (WHC) systems based on autonomous ultra-low-power devices capable performing real-time sampling, signal processing and wireless transfer. Such systems typically use general purpose microprocessors/microcontrollers and programmable devices.

The design of modern WHC systems therefore necessarily includes the aspects of effective algorithms, parallel processing and hardware architectures. FPGAs are kind of configurable digital circuits which can meet mentioned requirements. They mainly consist of reconfigurable logic, I/O and interconnections blocks and differ from microcontrollers and DSP processors which are Von Neumann machines. In addition to the parallelism, other advantages include: low price, flexibility of design, testing and rapid prototyping as well as ability to be transformed to Application Specific Integrated Circuits (ASICs). Also, the FPGA design can work with much higher throughput.

There are a few papers about implementing QRS detection in FPGA. Ref. [2] implements Pan-Tompkins algorithm, while Ref. [3] uses the wavelets. Both employ sophisticated filtering and other DSP blocks as well as state-machine blocks, resulting in complex design and huge occupation of silicon resources.

This paper proposes a cost and performance effective design methodology which integrates the positive characteristics of Wavelets, FPGAs and Integer Arithmetic for the purpose of QRS detection.

2. The design architecture

System Architecture

The proposed system, Fig. 1, consists of three blocks: Wavelet decomposition, Zero crossing and Double thresholding and Decision making.



Fig. 1. Architecture of proposed ECG QRS detection system

Wavelet decomposition

Unlike the Fourier transform, the DWT is suitable for application to non-stationary signals with transitory phenomena, whose frequency response varies in time, like an ECG. Mallat proposed the decomposition scheme, Fig. 2(a), which recursively employs downsampling, highpass (H) and lowpass (L) filters [4]. For each decomposition level, the H and L filters produce the details CD_i and approximations CA_i respectively. In order to detect the R peaks, the signal under test $x(t)$ is decomposed up to a desired level, 2^1 (CD_1), 2^2 (CD_2), 2^3 (CD_3), 2^4 (CD_4), 2^5 (CD_5), depending upon dominant frequency components in the signal, Fig. 2(b). Then specific details Di ($i=1, 2 \dots 5$) of the signal are selected and observed.

The detection of the QRS complex is based on modulus maxima of the specific details. This is because modulus maxima and zero crossings of the WT correspond to the sharp edges in the signal. The QRS complex produces two modulus maxima with opposite signs, with a zero crossing (ZC) between them (Fig. 2(b), CD_4). There are many approaches how to choose the most appropriate level for zero crossing detection. Some of them are based on the levels of signal energy through the scales.

The coefficients for the corresponding lowpass $h(n)$ and highpass $l(n)$ filters vary from the simplest, Haar's, over Doubisch's up to Quadratic Spline, having different vector lengths and, usually, floating point interpretation. For cost effective hardware implementation the key issue is to design as simple as possible L-H cell, maintaining all the positive characteristics of wavelets in spatial and frequency domains and satisfying the reconstruction conditions. One of the possible solutions, described in this paper, is to use one of simplest wavelet, such as Haar's, and to optimize it further for the implementation in FPGA hardware.

In our approach, the original filter coefficients are simplified in terms of integer arithmetic. The original Haar's coefficients $Lo=[1/\sqrt{2}, 1/\sqrt{2}]$, $Ho=[1/\sqrt{2}, 1/\sqrt{2}]$ are replaced with $L=[1/2, 1/2]$, $H=[1, -1]$, allowing the CA_j to be calculated by an adder and shifter $CA_j=(x_{2i}+x_{2i+1})\gg 1$ and the $CD_j=x_{2i}-x_{2i+1}$ by subtractor. The corresponding architecture of L-H Haar cell optimised in integer arithmetic is given in Fig. 3(a). The signal $clk_out=clk/2$ is used for downsampling and storing coefficients in output registers. The decomposition scheme is reduced to the pipelined structure of L-H cells, Fig. 3(b).

Zero crossing and double thresholding

In order to detect zero crossing for chosen coefficients CD_i , we need firstly to recognize the modulus maxima pair, Fig 4(a). Instead of using a classical way based on the local max or min, we prefer double thresholding technique. Negative and positive peaks are found by thresholding signal $x(t)$ by negative and positive thresholds $TR1$ and $TR2$, producing the digital signals $CRiTR1$ and $CRiTR2$, with zero crossing ZCi between. The $TR1$ and $TR2$ are chosen in a range $\max(x(t))/3 < \text{abs}(TR1)$, $TR2 < \max(x(t))/2$, while the ZCi is found by scanning the samples such that $x(n-1) < 0$ and $x(n) > 0$. The times t_1 , t_2 and t_0 correspond to the falling and rising edges of $CRiTR1$, $CRiTR2$ and ZCi 's trigger respectively.

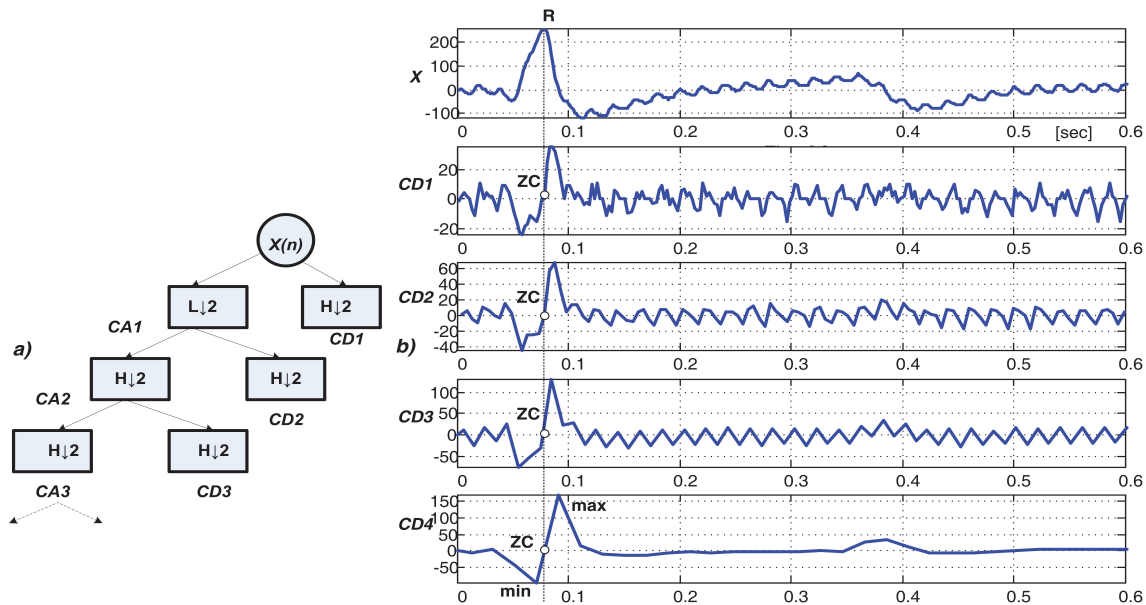


Fig. 2. a) Filter bank implementations of DWT; b) R peak detection using wavelet coefficients

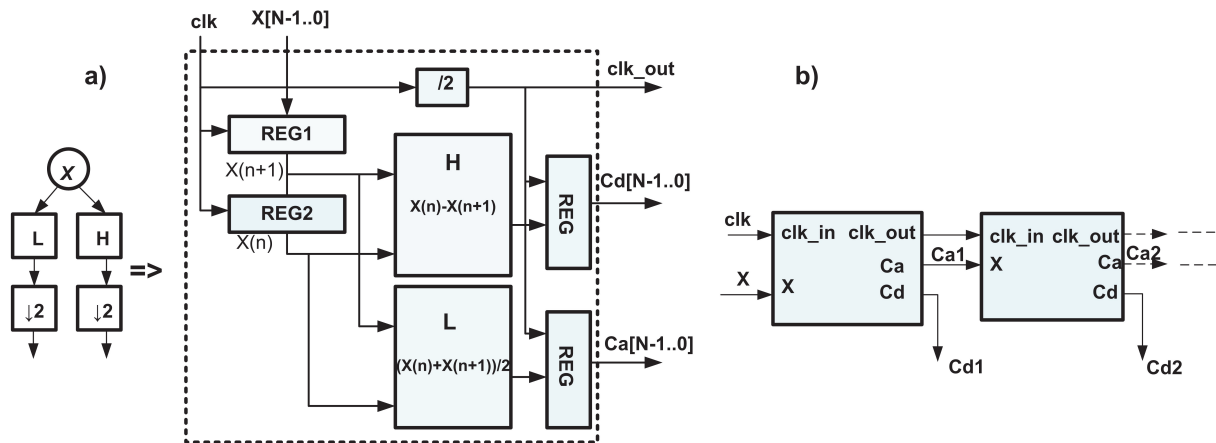


Fig. 3. a) Architecture of proposed L-H cell; b) Decomposition by pipelined structure of L-H cells

Decision making

Block for decision making receive the signals $CRiTR1$, $CRiTR2$ and ZCi for each decomposition level together with times $t1(i)$, $to(i)$ and $t2(i)$. The R peak can be recognised if for each or several decomposition levels valid $t1(i) < to < t2(i)$ and $\Delta T_{\min} < \Delta t(i) = t2(i) - t1(i) < \Delta T_{\max}$, where the ΔT depends on the inclination of the QRS complex and varies from $10\text{ms} < \Delta T < 50\text{ms}$ according to the ventricular activation time.

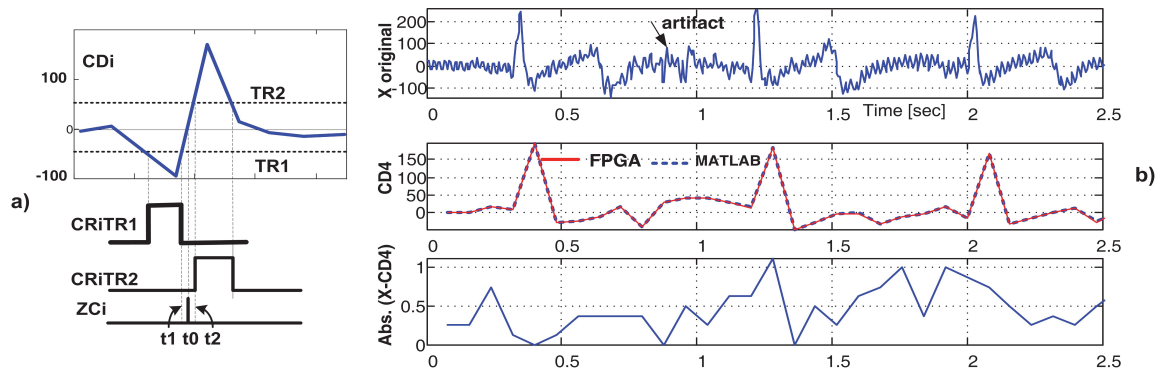


Fig. 4. a) Zero crossing and thresholding; b) FPGA-MATLAB comparison for proposed L-H decomposition

3. Results

The target FPGA chip for implementation of the proposed QRS detection system was Altera Cyclone EP1C12Q240. The data representation is with 9-bit signed integer. The performances of the system are tested in Quartus 9.1 development environment. The FPGA calculated CDi coefficients are compared with their MATLAB equivalents, Fig. 4(b). As shown, the absolute error is less than 1 count at 4th coefficient. The resource consumption and maximum frequency of the whole system are listed in Table 1. After compilation and simulation the chip is configured. The signal $x(n)$ presented the digital equivalents of MIT/BIH Arrhythmia database ECG and is fed to the input of system by serial port. There were totally 105,200 heart beats within $x(t)$ tested. The averaged accuracy is more than 95%.

Table 1. Performances of the system

Parameter	Value
Occupation of silicon resources (LCs) for system	410 (out of 5980)
Operating frequency for system	200MHz
Averaged accuracy of QRS detection	95.23%

4. Conclusion

The paper presents a real-time FPGA-based QRS detection design suitable for autonomous embedded systems. It uses the simplest Integer Wavelet Transform for signal decomposition and techniques of zero crossing and double thresholding for extraction of R peaks.

References

- [1] Kohler B. U, Hennig C and Orglmeister R. The principles of software QRS detection. *IEEE Eng. Med. Biol. Mag.*, 21: 42-57, 2002.
- [2] Pavlatos C, Dimopoulos A, Manis G and Papakonstantinou G. Hardware implementation of Pan & Tompkins QRS detection algorithm. In proceedings of the EMBE'05, IFMBE, 2005.
- [3] Chio I I, Mang I V and Peng U M. ECG QRS Complex Detection with Programmable Hardware. In Proceedings of the 30th Annual International IEEE EMBS Conference, 2008, 2920- 2923.
- [4] Mallat S. G. A theory for multiresolution signal decomposition: the wavelet representation. *IEEE Trans. Pattern Analysis and Machine Intelligence*, 11 (7), 674-693, 1989.

Cardiac Output Estimation Based on Oxygen Consumption during Exercise Test on Bicycle Ergometer

¹M. Stork, ²J. Novak, ²V. Zeman

¹ Department of Applied Electronics and Telecommunications,
University of West Bohemia, Plzen, CZ

² Institute of Sports Medicine, Medical Faculty, Charles University in Prague, CZ
Email: stork@kae.zcu.cz

Abstract. *Cardiac output (CO) is a cardinal parameter of cardiovascular state, and a fundamental determinant of global oxygen delivery. Historically, routine clinical measurement of CO has been limited to critically-ill patients, often with invasive indicator dilution methods such as thermodilution. A variety of cardiac output estimators have been developed over the past hundred years. The estimator evaluated in this paper is based on oxygen uptake measured during exercise test to estimate cardiac output and use heart rate (HR) to obtain also stroke volume (SV). Most important is that estimation is noninvasive and can be used during the exercises test. The results for well – trained, medium trained and untrained persons are also shown.*

Keywords: Cardiac output, stroke volume, heart rate, spiroergometric exercise test

1. Introduction

Cardiac output is a measure of the amount of blood pumped by either ventricle. In steady state, the outputs of both ventricles are the same. In a healthy adult male, *CO* is approximately 5 L/min. *CO* can vary, however, according to the body's physiological needs; for example, a well-trained athlete, while exercising, can increase *CO* to up to 30 L/min to increase the rate of transport of oxygen, nutrients, and wastes [1]. Abnormally low levels of *CO* can also be an indication of pathology. Each time the left ventricle contract, a volume of blood is ejected into the aorta. This *SV*, multiplied by the number of beats per minute (*HR*), equals the *CO*:

$$CO = SV*HR \quad [\text{ml/min, ml/min/beat, beats/min}] \quad (1)$$

CO indicates how well the heart is performing this function. *CO* is regulated principally by the demand for oxygen by the cells of the body. If the cells are working hard, with a high metabolic oxygen demand then the *CO* is raised to increase the supply of oxygen to the cells, while at rest when the cellular demand is low, the *CO* return to baseline. *CO* is regulated not only by the heart as it pumps, but also by the function of the vessels of the body as they actively relax and contract thereby increasing and decreasing the resistance to flow. When *CO* increases in a healthy but untrained individual, most of the increase can be attributed to an increase in *HR*. Increased sympathetic nervous system activity, and decreased parasympathetic nervous system activity can also increase *CO*. *HR* can vary by a factor of approximately 3, between 60 and 180 beats/ minute, while *SV* can vary between 70 and 120 ml, a ratio factor of only 1.7 ml. The ability to accurately measure *CO* is important in clinical medicine as it provides for improved diagnosis of abnormalities, and can be used to guide appropriate management. *CO* measurement, if it were accurate and non-invasive, would be adopted as part of every clinical examination from general observations to the intensive care ward, and would be as common as simple blood pressure measurements are now. Such practice, if it were adopted, may revolutionize the treatment of many cardiovascular diseases including hypertension and heart failure. This is the reason why *CO* measurement is now an important research and clinical focus in cardiovascular medicine [2].

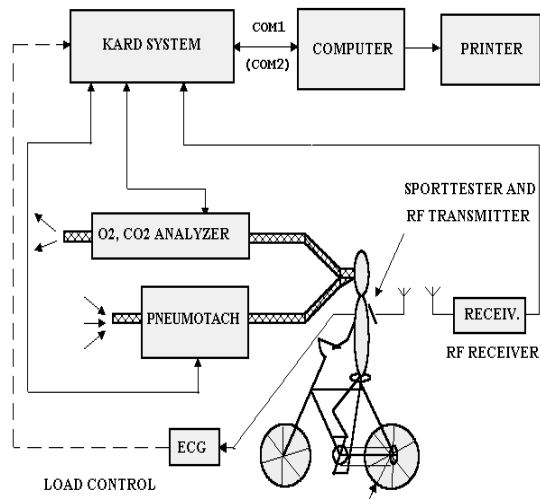


Fig. 1. Block diagram of measuring system for non-invasive CO estimation. The bicycle or treadmill ergometer can be used.

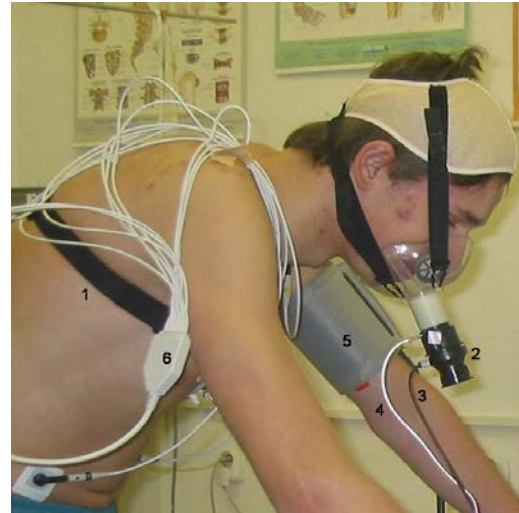


Fig. 2. The physiological parameter measurement: 1- HR belt (Sporttester), 2-turbine for ventilation measuring, 3-cable for ventilation pulses, 4-tube for exhausted gas samples, 5-cuff for blood pressure measuring, 6-cable for ECG electrodes.

The Fick method derives CO through calculating oxygen consumed over a given period of time by measuring oxygen consumption per minute with a spirometer, oxygen concentration of venous blood from the pulmonary artery, and oxygen concentration of arterial blood from a peripheral artery. Sometimes CO is expressed as a cardiac index (Ci), which is the CO divided by the estimated body surface area (BSA) in square meters.

$$BSA = (height * weight/3600)^{0.5} \quad [m^2, cm, kg] \quad (2)$$

The Ci is given by (5).

$$Ci = CO / BSA \quad [l/min/m^2, l/min, m^2] \quad (3)$$

Calculating the Ci normalizes CO to individuals of different size. A normal range for Ci is 2.6 to 4.2 $l/min/m^2$. While considered to be the most accurate method for CO measurement, Fick method is invasive. In this paper, CO was estimated noninvasively from oxygen uptake during exercise on cycle or treadmill ergometer.

2. Methods

Because both HR and VO_2 can be easily measured during standard incremental cardio-pulmonary exercise testing [1], both CO and SV could be accurately quantified if the simultaneous arteriovenous O_2 content difference ($C_A - C_V$) could be estimated [3, 4]. For noninvasive CO estimation, exercise tests were performed on an ergometer (or treadmill) controlled by computer. Subjects were familiarized with the apparatus and performed a continuous incremental symptom-limited maximal test for determination of VO_{2max} and lactic acidosis threshold (LAT). The block diagram of measuring system is shown in Fig. 1. The electrical signals from sensors were connected to microcontroller systems. The samples of expired gas samples were connected to gas analyzer (O_2 and CO_2 analyzer). All measured signals were processed in personal computer. Example of measuring (on bicycle regometer) is shown on Fig. 2. From the measured values workload [W] for cycle ergometer or [km/h] for treadmill, HR [beats/min] and VO_2 [l/min] the CO was estimated [3, 4]. Also SV and Ci were computed. The CO was calculated according formula (4):

$$CO = \frac{100 * VO_2}{5.721 + 0.1047 \frac{100 * VO_2}{VO_{2MAX}}} \quad [l/min] \quad (4)$$

Table 1. Spiroergometric values of 6 subjects. Sub=Subject, M-male, F-female, He=Height [cm], We=Weight [kg], $VO_{2m}=VO_{2max}$ [l], $VO_{2mk}=VO_{2max}/kg$ [ml/min/kg]

Sub	Age	He	We	VO_{2m}	VO_{2mk}
M1	28	177	70.3	6.75	81
M2	49	170	66.7	4.2	63
M3	65	166.5	65.2	3.15	39.7
F1	31	168.5	63.2	4.33	68.5
F2	11	156.5	42.8	1.6	37.5
F3	40	165.5	72	2.69	37.4

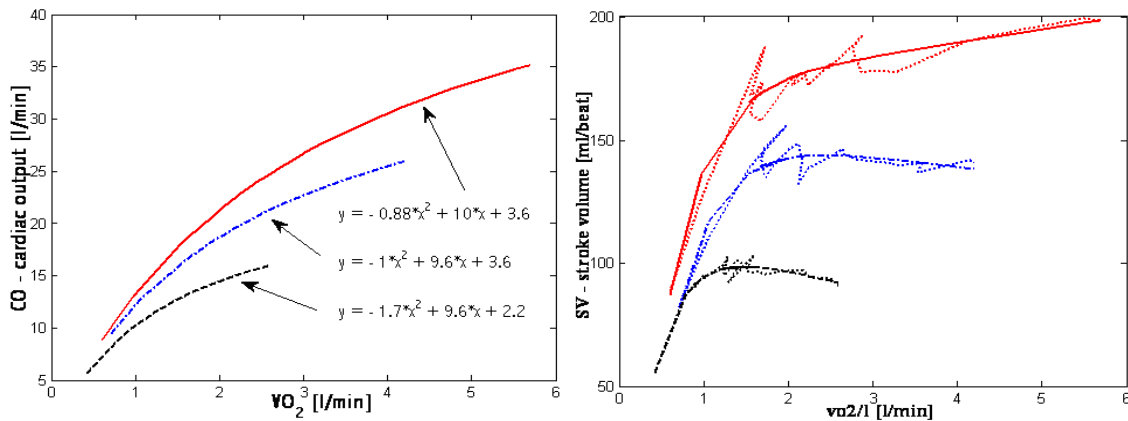


Fig. 3. CO in relation to VO_2 during stress-test M1-red, M2-blue (dash-dot), M3-black (dash), (left). SV in relation to VO_2 during the stress-test M1-red, M2-blue (dash-dot), M3-black (dash), (right).

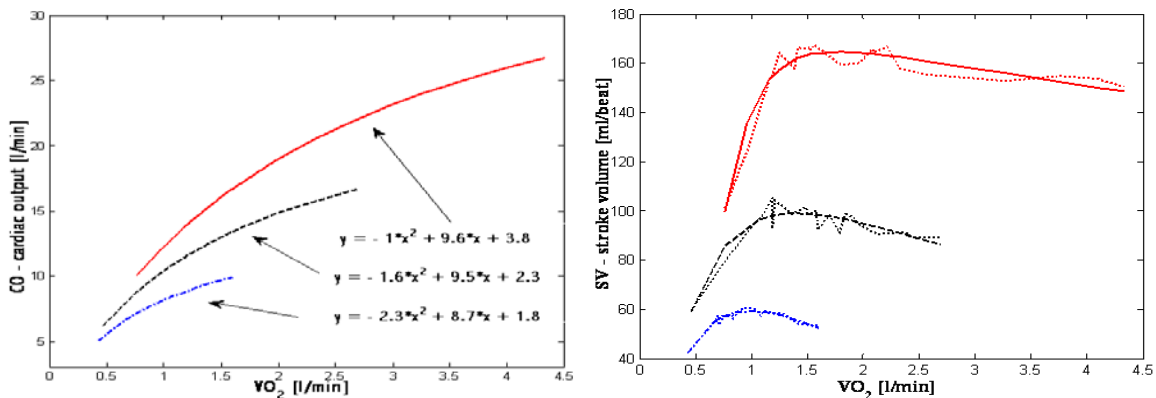


Fig. 4. CO in relation to VO_2 during stress-test F1-red, F2-blue (dash-dot), F3-black (dash), (left). SV in relation to VO_2 during the stress-test F1-red, F2-blue (dash-dot), F3-black (dash), (right).

3. Results

Six subjects (3 men and 3 women) of our data-base with very different athletic background were used to demonstrate the dynamics of CO and SV during standard spiroergometric test (Table 1). M1 – top-class cross-country skier, M2 – leisure „hobby” athlete, M3 – pre-surgery patient, F1 – top-class triathlete, F2 – young swimmer, F3 – leisure „hobby” athlete. The test used 3 three-minute sub-maximal warming-up workloads followed by step-wise increased

workload up to the exhaustion. Results (CO and SV in relation to VO_2 [l/min]) are presented in Fig. 3 for men and in Fig. 4 for women. Higher cardiac output as a function of higher stroke volume plays important role in increased transporting capacity of blood for oxygen and enables well trained subject to achieve significantly higher physical performance.

4. Discussion

A totally noninvasive determination of CO and SV during exercise would be very useful in healthy subjects as well as in patients with various degrees of cardiac insufficiency. This can provide a simple and low-cost assessment of cardiac function in response to exercise. Although it is generally assumed that CO increases linearly with VO_2 , the pattern of variation in VO_2 and CO as maximal O_2 consumption is approached has not been extensively investigated and may vary among individuals. According to Frank-Starling mechanism the amount of blood that the heart pumps works up to a limit of 3 times the normal cardiac output. When the peripheral tissues demand excessive amounts of blood flow, the nervous signals increase cardiac output [2, 3, 4]. Our examples document that the time course of these changes is very similar in the subjects of very different cardio-respiratory fitness level. However, these findings still need to be proved in the groups of subjects of different lifestyle, different athletic background, men and women, and even patients. Our pilot study indicates that top level endurance athletes can reach outstanding values of CO and SV at about 40 l/min and 200 ml/beat respectively. Hence, this method seems to offer another useful data to evaluate cardio-respiratory capacity and adaptation to physical activity and/or inactivity.

5. Conclusions

A variety of cardiac output estimators have been developed over the past hundred years. Stringer et. al. [3] proved that the data of oxygen uptake during exercise can be used to estimate noninvasively cardiac output. They used Fick's principle for CO estimation during exercise, and these results correlated with direct VO_2 measurements. Using their results we calculated CO in our subjects [4]. Estimation is noninvasive and can be used during the stress test.

Acknowledgements

Milan Stork's participation in preparing this paper has been supported by: Department of Applied Electronic and Telecommunication, University of West Bohemia, Plzen, CZ

References

- [1] Guyton A.C. and Hall J.E.: *Textbook of Medical Physiology*. Saunders and Company, 11th edition, 2005.
- [2] James X. Sun, MEng; Andrew T. Reisner, MD; Mohammed Saeed, MD, PhD; Thomas Heldt, PhD; Roger G. Mark, MD, PhD: The cardiac output from blood pressure algorithms trial, *Critical Care Medicine*, Vol. 37, No. 1, pp. 72-80, 2009.
- [3] Stringer W.W., Hansen J.E. and Wasserman K.: Cardiac output estimated noninvasively from oxygen uptake during exercise. *J. Appl. Physiol.* 82(3): 908–912, 1997
- [4] Beck K.C., Randolph L.N., Bailey K.R, Wood C.M, Snyder E.M. and Johnson B.D.: Relationship between cardiac output and oxygen consumption during upright cycle exercise in healthy humans. *J Appl Physiol* 101: 1474–1480, 2006.

Body Surface Potential Mapping Data Conversion Method

G. Tuboly

Department of Electrical Engineering and Information Systems, Faculty of
Information Technology, University of Pannonia, Veszprém, Hungary,
Email: tuboly.gergely@virt.uni-pannon.hu

***Abstract.** In body surface potential mapping, data conversion can be required whenever merging data sets taken by slightly different data acquisition systems. In this case, we face with a kind of conversion problem. This paper describes a method for solving the problem according to the least-square principle, so the datasets of physically different body surface potential mapping systems become compatible, thus their records can be handled the same way.*

Keywords: ECG, Body surface potential mapping systems, different electrode distribution, Data conversion

1. Introduction

High spatial and temporal resolution body surface potential mapping play an important role in sudden cardiac death risk assessment. These elaboration of decision rules require a high number of validated measurements. To achieve the statistically significant number of records, pooling of data bases recorded in different groups is a realistic approach. However, if the electrode layouts are not strictly identical in the cooperating groups, a measurement data conversion is needed for making the two systems compatible. In the following section, a method will be described for solving this problem with the help of our example, done at the Department of Electrical Engineering and Information Systems, University of Pannonia.

2. Subject and Methods

In the framework of our scientific cooperation with the Polish research group led by Professor Roman Maniewski we had to make compatible the records taken in Hungary and Poland. Since the Polish research group uses a slightly different lead arrangement, we had to elaborate the conversion method.

The two lead arrangements

The lead arrangements of our and the Polish body surface potential acquisition system is shown in Fig. 1 and Fig. 2.

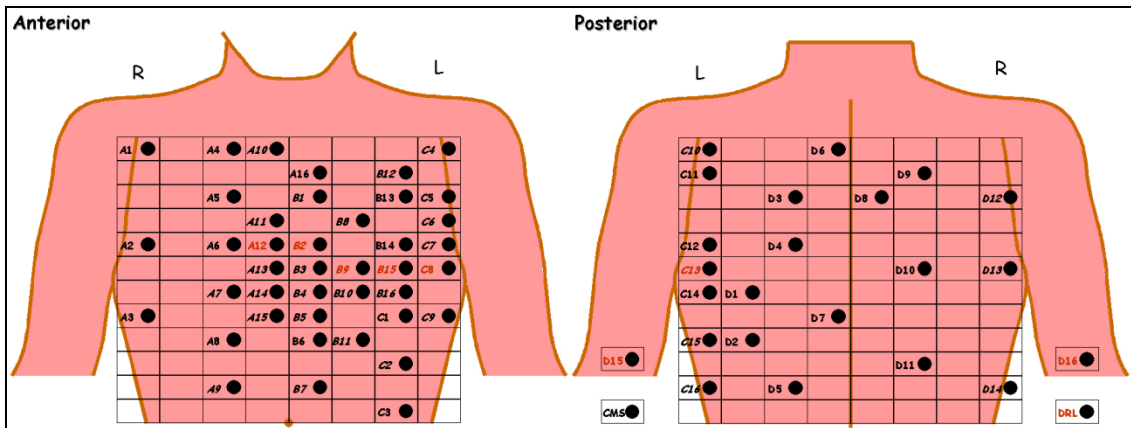


Fig. 1. Electrode positions of our Biosemi Mark-8 body surface potential mapper. Electrodes A1-D14 are on the torso, D15 is on the left arm and D16 is on the right arm. The leads are unipolar (reference is the WCT) [1].

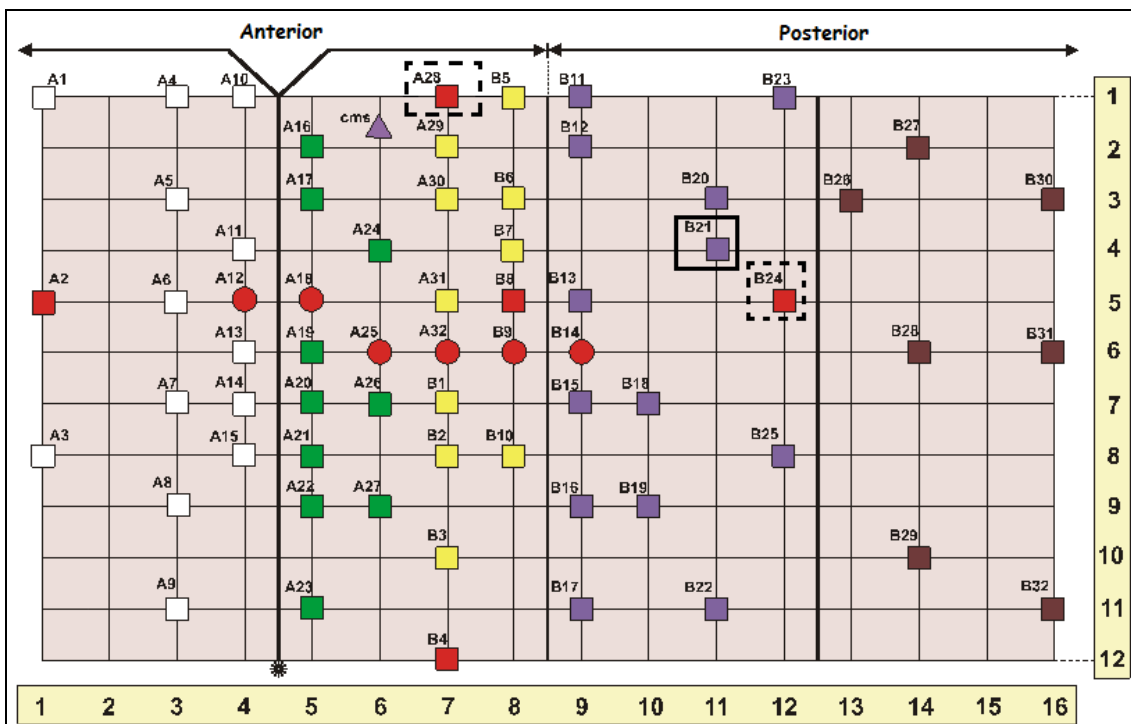


Fig. 2. Electrode positions of the Polish body surface potential mapper and the difference between the electrode locations of the two systems. Dashed frames mark the two leads missing from our system and solid frame signs the channel which is one unit higher than the corresponding D4 channel in our system. The other 61 leads are in the same positions regarding the two systems [2].

Principle of the method

There is a method based on least squares for estimating unknown lead data from known ones. The method was published by Robert L. Lux, et al. [3]. Its principle is as follows:

$$\phi_{est} = T \cdot \phi_m \tag{1}$$

where

φ_{est} : $k \times n$ matrix of estimated leads
 φ_m : $m \times n$ matrix of measured leads
 T : $k \times m$ estimating matrix
 k : number of estimated leads
 m : number of measured leads
 n : number of sampling points

To determine T we need a covariance matrix K , regarding all channels (both measured and estimated). T is defined as follows:

$$T = K'_{est} \cdot K_m^{-1} \quad (2)$$

where

K_{est} : $m \times k$ segment of K regarding estimated leads
 K_m : $m \times m$ segment of K regarding measured leads

We searched for a method for estimating our D4 lead from the 61 common leads (see Fig. 2), so we would be able to get the same 62 leads from the Polish records that we have. The steps of finding this method can be seen below in detail.

Determinating K

The more measurements we use, the more accurate our estimate will be, so we concatenated 52 records of our measurements considering leads A1-D14. This way we got a 62×10982400 matrix. Then we interpolated this data to 192 lead, so the matrix became 192×10982400 . After that we calculated the covariance matrix K (192×192):

$$K = \begin{bmatrix} \begin{bmatrix} k_{1,1} & k_{1,2} & \cdots & k_{1,62} \\ k_{2,1} & k_{2,2} & \cdots & k_{2,62} \\ \vdots & \vdots & \ddots & \vdots \\ k_{62,1} & k_{62,2} & \cdots & k_{62,62} \end{bmatrix} & \begin{bmatrix} k_{1,63} & k_{1,64} & \cdots & k_{1,192} \\ k_{2,63} & k_{2,64} & \cdots & k_{2,192} \\ \vdots & \vdots & \ddots & \vdots \\ k_{62,63} & k_{62,64} & \cdots & k_{62,192} \end{bmatrix} \\ \begin{bmatrix} k_{63,1} & k_{63,2} & \cdots & k_{63,62} \\ k_{64,1} & k_{64,2} & \cdots & k_{64,62} \\ \vdots & \vdots & \ddots & \vdots \\ k_{192,1} & k_{192,2} & \cdots & k_{192,62} \end{bmatrix} & \begin{bmatrix} k_{63,63} & k_{63,64} & \cdots & k_{63,192} \\ k_{64,63} & k_{64,64} & \cdots & k_{64,192} \\ \vdots & \vdots & \ddots & \vdots \\ k_{192,63} & k_{192,64} & \cdots & k_{192,192} \end{bmatrix} \end{bmatrix} = \begin{bmatrix} K_{11} & K_{12} \\ K_{21} & K_{22} \end{bmatrix} \quad (3)$$

The data is sorted like leads 1-62 are the leads before interpolation and leads 63-192 are the additional ones. Considering Fig. 1 it means, that lead 1 is A1, lead 2 is A2, ... and lead 62 is D14. And for the additional ones: lead 63 is the empty cell just below A1, lead 64 is two cells below A1, ... and finally lead 192 is just below D14.

Note that interpolation was unnecessary for this progress (only K_{11} will be used below), but we did it for further applicability.

Determinating K_m and K_{est}

K_m is quadratic and it represents the measured data, so we have to choose it so that it shall contain the covariances of the leads that will be measured (known) in the future. In this case

the measured leads will be the 61 common leads, thus K_m will be 61×61 . Considering Fig. 2 and Eq. 3 it can be seen that the matrix we are looking for is almost the same as K_{II} (62×62). The only difference is, that K_{II} contains the data of D4 too. It poses a problem, because that is the lead we would like to estimate. Since the covariances of D4 are in the 52th row and column, we can simply remove them, and the result will be K_m .

As written above, K_{est} is an $m \times k$ matrix containing the covariances regarding estimated leads, where m is the number of measured leads and k is the number of estimated leads. Because we would like to estimate one lead, K_{est} will be 61×1 . Due to the estimated lead will be D4, we can simply determine this matrix at the previously written K_m calculation: we have to remove the 52nd row from K_{II} first, then save the 52nd column as K_{est} , and remove the 52nd column from K_{II} after that.

Finally, substituting K_{est} and K_m to Eq. 2, T can be calculated.

3. Results

The covariance matrix was calculated from 52 measurements which means a relatively high population, therefore the estimation with the T matrix is accurate enough. Namely, the correlation between the estimated and measured data is 0.98.

4. Discussion

Whenever conversion has to be made between our and another "foreign" body surface potential mapping systems, a T matrix should be calculated as described above. During the calculation of the matrix, the "measured" data should represent the common channels of the two systems, while the "estimated" data mean the ones that exist in our system, but do not exist in the Polish one. The ones that appear only in the Polish system, can be simply neglected. After determination, the same T matrix can be used for any measurement of that particular device.

Acknowledgements

TÁMOP-4.2.2-08/1/2008-0018 – Livable environment and healthier people – Bioinnovation and Green Technology research at the University of Pannonia. The project is being co-financed by the European Social Fund with the support of the European Union.

References

- [1] http://www.biosemi.com/mark8_full_specs.htm (2010. április 11.) *Mark 8 specifications*
- [2] Fereniec M, Kacprzak M, Maniewski R, Zbiec A, Ircha D. The 64 channel system for high resolution ECG mapping. Institute of Biocybernetics and Biomedical Engineering PAS ul. Trojdena 4, 02-109 Warsaw. 2001.
- [3] Lux RL, Smith CR, Wyatt RF, Abildskov JA. Limited lead selection for estimation of body surface potential maps in electrocardiography. *IEEE Trans Biomed Eng.* 1978 May 25(3):270-6.

Assessment of Heart Position in a Torso Model Using an Inverse Solution

¹J. Švehlíková, ¹J. Lenková, ²A. Drkošová, ¹M. Foltin, ¹M. Tyšler

¹Institute of Measurement Science, SAS, Bratislava, Slovakia

²Faculty of Electrical Engineering., University of Zilina, Zilina, Slovakia

Email: umersveh@savba.sk

Abstract. Knowledge of actual heart position is important for finding results in inverse problem of electrocardiography. Magnetic resonance images of real subjects revealed large variability of the heart position in relation to ecg lead V2 usually placed in the 4th intercostal space and considered as the anatomical reference. The use of standard torso model in which the location of modeled heart is constant thus cannot reflect its actual position sufficiently. The method for finding the approximate position of heart in a standard torso model corresponding to the actual heart position in an observed subject is presented.

Position of single dipole obtained by an inverse solution from body surface potential measurements was used to locate the initial site of ventricular depolarization and suggested as representative position of the left ventricular septum. This approach was studied in 25 subjects with well documented geometry and measured ecg potentials in 62 leads. For each subject the heart in standard torso model was moved to a new position corresponding to the inversely estimated initial site of ventricular depolarization.

The individually estimated heart position in the standard torso model better corresponded to the real torso geometry configuration than that derived from the anatomical leads placement.

Keywords: standard torso model, inverse solution, integral maps, position of heart

1. Introduction

It is generally known that for correct solution of the inverse problem in electrocardiology the knowledge of individual realistic torso model is needed [1]. The best way to obtain such individual geometrical data is the use of CT or magnetic resonance imaging (MRI) technique. At present, however, this technique is still expensive and not always available in common cardiological practice. Recently we suggested to use the inverse solution for identification of one or two small ischemic lesions and tested the method on simulated data computed in a standard torso model [2]. However, the study on a set of 25 well documented geometrical data from normal subjects [3] revealed the great variability of heart position relative to the anatomically placed leads positions, mainly in vertical direction, that could strongly influence the inverse solution if only the standard torso model is used. In this work we suggest a method for individual approximation of real position of the heart from the electrocardiographic (ecg) data of the observed subject.

2. Subject and Methods

Data from 25 healthy subjects (15 men and 10 women) published in [1], [3] were used to study the possibility to assess individual position of their hearts. The geometry of each of them was obtained by MRI and then described by triangulated surfaces consisted of the model of torso, lungs, ventricular myocardium and the volume of ventricular cavities. The ecg data measured in 62 leads of the Amsterdam lead system were recorded for each subject. Positions of leads were documented along with the geometrical data. The precordial lead V2 was carefully placed with respect to the fourth intercostal space.

For each subject 62 raw signals recorded for 10 s with sampling rate of 1000 Hz were processed. The Lynn's low-pass filter with 50 Hz stop-band was applied in signal processing [4]. Then the signal was time averaged to create one representative time course of the heart cycle in each lead. Finally, the baseline of averaged signals was corrected by setting the mean potential of the PQ interval to zero. The QRS onset was defined manually from rms signal computed from all measured leads.

Five integral maps (IMs) for various time intervals up to 20 ms from the QRS onset were computed. Assuming that the knowledge of the heart position is not known, the position of the initial depolarization of ventricles was computed from IMs using the inverse solution to one dipole in homogeneous torso model. Location of a dipole that best represented the input IM was searched among positions of cubic 3 mm grid in the torso model and was considered as the estimated septum position.

First the similarity between the inverse solutions in individual models and the standard torso model was tested. For each measured subject the inverse solution was computed in its individual torso model obtained from MRI and also in the standard torso model. Then the vertical distance between the lead V2 and the inversely obtained dipole location was evaluated in each model.

After observing the results for the localization of initial ventricular depolarization in individual models and the corresponding individual position of the heart in each torso model, position of the individual reference point iRP was assigned in each individual heart to represent the position of the heart in torso as well as the site of the initial ventricular depolarization. Correspondingly, standard reference point sRP was assigned in the heart in the standard torso model. Then the heart in the standard torso model was moved to a new individual position such that the sRP corresponded to the inversely estimated location of the initial activation of ventricles computed in the standard model from individual ecg measurement. The improvement of the standard model configuration was evaluated.

3. Results

Because the variability of the heart position in relation to the lead system is studied in this work the base point representing the position of leads is considered the ecg lead V2 placed in the 4th intercostal space. Fig.1 demonstrates the vertical variability of the distance between the reference point in the heart in real chest models and the vertical position of lead V2. If the standard torso model for each subject is used this vertical distance is assumed to be constant.

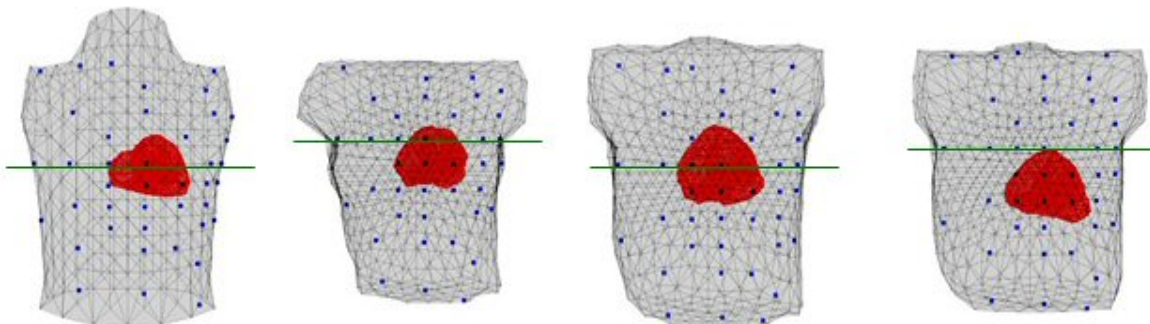


Fig. 1. The standard torso model (left) and examples of 3 real chest models. Dots indicate the leads placement, vertical position of lead V2 is marked by a horizontal line.

In each object the inversely estimated position of the initial ventricular activation was computed as the geometrical center of locations obtained from all 5 integral maps. In most

cases these locations were almost in the same place and were located in the volume of the left ventricle near septum. The mean standard deviation of the 5 results from their geometrical center for all observed subjects was 0.3 cm.

The inverse solution was computed from IMs of each subject in the individual torso as well as in the standard torso model. The vertical distance between the inversely estimated position of initial activation and the corresponding lead V2 in each model and each subject (denoted PP) is depicted in Fig. 2.

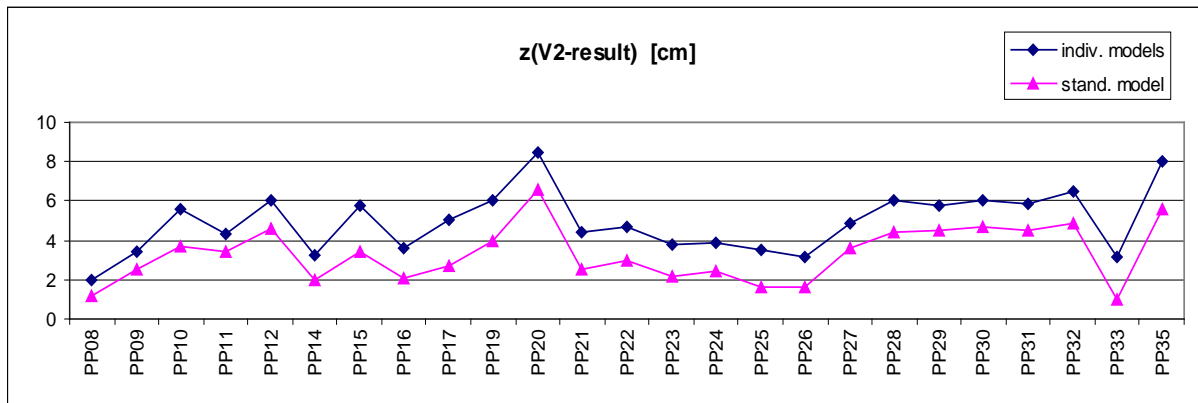


Fig. 2. The vertical distance between the inversely estimated position characterizing the initial ventricular activation and the position of the corresponding lead V2 computed for each measured subject in individual and standard torso model.

In agreement with the obtained localization of the initial ventricular activation in individual models, position of the individual reference point iRP in each heart model was defined in the left ventricular septum. The reference point sRP in the heart of the standard torso model was defined similarly.

For each individual subject the heart position in the standard torso model was adjusted by a vertical shift of the sRP to the inversely estimated vertical position of the initial site of ventricular of activation. The vertical distance between the reference point in the heart model and lead V2 in the original individual torso models, in adapted standard torso models and in the standard torso model is shown in Fig. 3. Most of the adapted standard torso models corresponded better to the original individual chests than the standard torso model.

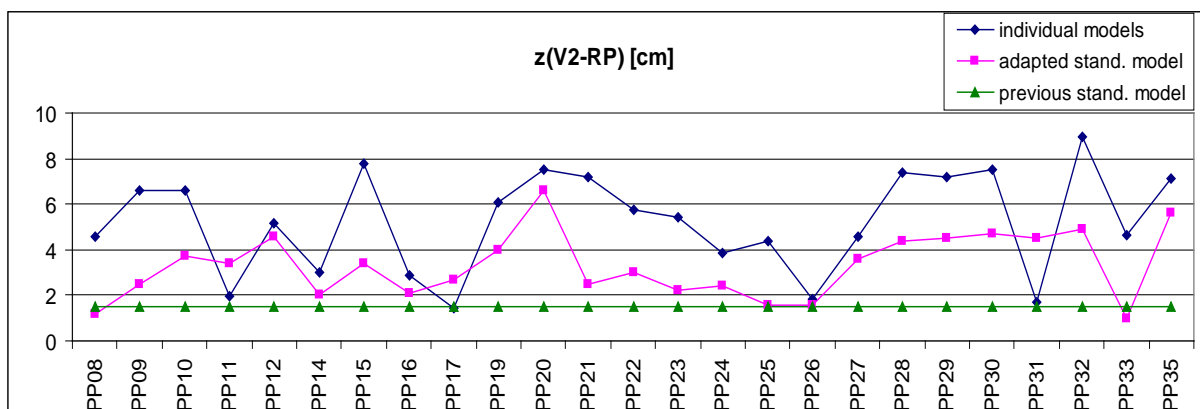


Fig. 3. The vertical distance between the reference point in the heart and the lead V2 in three types of models.

The mean difference between the vertical distance V2 to RP in individual torso models and in the standard torso model was 3.73 cm (std 2.2 cm); the mean difference between vertical distance of V2 to RP in individual torso models and in the adapted standard torso model decreased to 1.93 cm (std 1.9 cm).

4. Discussion

Although the suggested method improved the vertical position of the heart in the standard torso model, the mean error of almost 2 cm still remains remarkable. Two reasons for this large error could be considered. The first one is the inequality of outer geometry of the individual models and the standard one. In Fig.2 a systematic error is apparent between the results obtained in individual and standard torso model. The role of adaptation of the standard torso dimensions to the individual subject together with the placement of electrodes on the torso model should be evaluated.

The second reason for relatively large error in the present study could be the differences in electrophysiological properties of the volume torso conductor as well as the individual variability of the normal sequence of excitation of the ventricles. In spite of the fact that in individual models the geometry was known very precisely the position of the inversely located dipoles varied within the left ventricular septum in quite wide range. The reference point situated in the left ventricular septum was only approximate definition of the initial site of activation. For 25 subjects studied in this work the mean distance between the reference point and the inversely estimated initial site of activation was 2.17 cm (std 0.9 cm), the vertical distance only 0.5 cm but with std 1.7 cm.

5. Conclusions

From the results it can be stated that it is possible to adjust the vertical heart position in a standard torso model using information from measured ecg signals. Besides the adaptation of torso geometry to dimensions of an individual subject and proper placement of leads, the suggested method considerably improves the individual torso model configuration without using demanding CT or MRI techniques.

Acknowledgements

The authors would like to thank to prof. A.van Oosterom and R.Hoekema for providing the data from 25 subjects. The work was supported by research grant No. 2/0210/10 from the Vega Grant Agency in Slovakia.

References

- [1] Hoekema R, Uijen G, van Erning L, van Oosterom A. Interindividual variability of multilead electrocardiographic recordings. *Journal of Electrocardiology*, 32 (2): 137-148, 1999.
- [2] Tyšler M et al. Noninvasive Assessment of Local Myocardium Repolarization Changes using High Resolution Surface ECG Mapping. *Physiological Research*, 56 (Suppl. 1), 2007.
- [3] van Oosterom A, Hoekema R, Uijen G. Geometrical Factors Affecting the Interindividual Variability of the ECG and the VCG. *Journal of Electrocardiology*, 33 (Suppl):219-227, 2000.
- [4] Rozman J a kol. Elektronické přístroje v lékařství. Academia, Praha, 2006.

Computer Atlas of the Dipole Electrocardiotopography

¹E.A.I. Aidu, ¹V.G. Trunov, ¹L.I. Titomir,
²T.A. Sakhnova, ²E.V. Blinova

¹Institute for Information Transmission Problems, Russian Academy of Sciences,
Moscow, Russia,

²A.L. Myasnikov Research Institute of Clinical Cardiology, Russian Cardiology
Research-and- Production Complex, Ministry of Health and Social Development,
Moscow, Russia
Email: aidu@iitp.ru

Abstract. *Computer Atlas of the dipole electrocardiotopography (DECARTO-Atlas) contains decartograms, vectorcardiograms, and clinical data for more than 80 different pathological states of the heart. DECARTO-Atlas is equipped with interactive tools for navigating through the database of precedents. The decartograms of major pathological categories have representative, physiologically meaningful, and easy to remember patterns. This greatly simplifies the process of making informed and reasonable diagnostic decisions, especially when analyzing complicated combined pathology.*

Keywords: *Electrocardiotopography, Vectorcardiography, Cardioelectric Potential Visualization, Diagnostic Methods*

1. Introduction

Generally accepted standard electrocardiography does not always provide necessary reliability and diagnostic accuracy, especially at early stages of cardiovascular diseases. A more exact description of the electrophysiological state of the heart can be obtained through efficient mathematical processing and analysis of electrocardiographic data.

The DECARTO method proposed in [1] can significantly increase the diagnostic efficiency of electrocardiology. Theoretical background and the results of clinical and statistical studies of this method are described in a series of articles and monographs [2, 3]. New methods and criteria have been developed for the diagnosis of pathological states of the heart. The use of new decartography criteria has been shown to increase the diagnostic efficacy of the DECARTO in the clinical studies (e.g. [4, 5]). Compilation of the DECARTO-Atlas is a necessary step for summarizing the data previously obtained and further development and practical application of the method.

2. Subject and Methods

The Dipole ElectroCardioTopoGraphy (DECARTO) is mapping of electrophysiological processes and characteristics of the heart with reference to anatomical landmarks based on simple models containing background information obtained from three components of the heart vector (measured directly by the vectorcardiographic leads or synthesized from the 12 standard leads). Components of the heart vector are transformed into decartograms, i.e., maps of main states and electrophysiological characteristics of the myocardium projected onto a sphere tightly surrounding the heart. The main types of decartograms are listed below.

Instantaneous maps of depolarization – the distribution of the three major states of the myocardium: rest, activation (depolarization wave front spread), and total depolarization. Animation of these states allows visualization of spatial-temporal distribution of excitation.

Instantaneous maps of repolarization – the distribution of the myocardium polarization level at the consecutive time points of the repolarization process. These maps allow identification of vulnerability to arrhythmias.

Isochronous maps of depolarization – the distribution of time of arrival and departure of myocardial activation; these maps reflect the movement of the wave front of depolarization in the tangential direction to the wall of the heart; provide recognition of ventricular blockades, syndrome of pre-excitation of ventricles, and areas of postinfarction necrosis.

Activation duration maps – the distribution of the activation state duration, reflect the movement of the wave front of depolarization in the radial direction to the wall of the heart. These maps provide recognition of ventricular hypertrophy and blockades.

Atrial decartograms – show the distribution of isochrones of depolarization and size of the atrial wall; they are useful in recognizing the atrial enlargement.

3. Results

Reliably verified pathological cases were selected and included into the computer dipole electrocardiotopography DECARTO-atlas. The atlas presents decartograms, vectorcardiograms, and clinical data for various pathological states of the heart, such as left ventricular hypertrophy, right ventricular hypertrophy, left atrial enlargement, right atrial enlargement, biatrial enlargement, myocardial infarctions of different locations, conduction disturbances, etc.; normal cases are also presented. A short list of categories of pathological heart states contained in the atlas is shown in Fig. 1.

- Norm
 - Horizontal heart position
 - Vertical heart position
- Chamber hypertrophy and enlargement
 - Left ventricular hypertrophy
 - Right ventricular hypertrophy
 - Biventricular hypertrophy
 - Left atrial enlargement
 - Right atrial enlargement
 - Biatial enlargement
- Myocardial infarction
 - Anterolateral
 - Inferolateral
 - Lateral
 - Inferior
 - Posteroinferior
 - Inferoposterior
- Intraventricular block
 - Right bundle branch block
 - Left bundle branch block
 - Left anterior fascicular block
 - Left posterior fascicular block
 - Bifascicular block
- Wolf-Parkinson-White preexcitation
- Cardiomyopathy
 - Hypertrophic
- Combined pathology
 - Block & Infarction
 - Block & Hypertrophy
 - Block & Hypertrophy&Infarction
 - ...

Fig. 1. DECARTO-atlas. List of the main categories of pathological heart states.

4. Discussion

The decartograms of major pathological categories have representative, physiologically meaningful, and easy to remember patterns. This greatly simplifies the process of making

informed and reasonable diagnostic decisions, especially when analyzing complicated combined pathology.

Figure 2 shows decartograms for various complicated combined pathological states. Decartograms of the two consecutive ECGs with a considerable time interval between records are presented above; normal decartograms are given for comparison. Below the decartograms typical for individual components of the combined pathology are presented. The typical patterns are clearly seen on the first record: the right bundle branch block (a considerable delay of the activation arrival in the area marked with circle); the left anterior fascicular block (the activation moves right-up, as marked by the arrow). The second record reveals new pathological changes: left ventricular hypertrophy (increased activation duration in the left ventricle, seen as light grey area surrounded by dark grey on the activation duration decartogram); extensive myocardial injury scar of posterior location spreading to the lower left ventricular wall (the activation area is significantly decreased, as if there is a barrier to the spread of excitation appears; it is marked by the double black line).

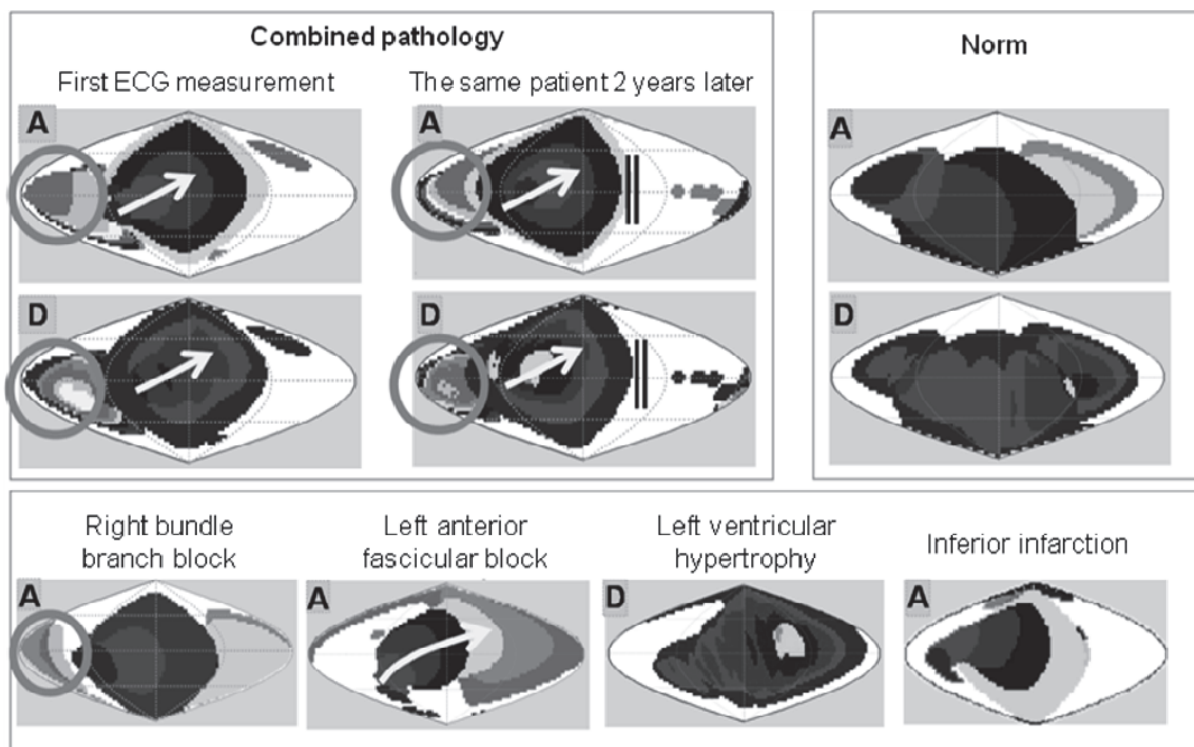


Fig. 2. Decartograms in complex combined pathology. A, activation arrival; D, activation duration.

5. Conclusions

The computer DECARTO-Atlas is a useful tool for making diagnostic conclusions. It will contribute to further accumulation of clinical experience and electrocardiographic statistical research. DECARTO-Atlas is designed for professionals and students, and for those interested in further improvement and development of the dipole electrocardiography.

Acknowledgements

This work was supported by the Basic Sciences for Medicine Program of the Presidium of the Russian Academy of Sciences.

References

- [1] Titomir LI, Ruttkay-Nedecký I. Chronotopography: A new method for presentation of orthogonal electrocardiograms and vectorcardiograms. *International Journal of Bio-Medical Computing*; 20(4): 275-182, 1987.
- [2] Titomir LI, Ruttkay-Nedecký I, Bakharova L. Comprehensive Electrocardiogram Analysis with Orthogonal Leads [in Russian]. Nauka, Moscow, 2001.
- [3] Titomir LI, Trunov VG, Aidu EAI, Kneppo P. Biophysical Basis of Electrocardiotopography Methods. Fizmatlit, Moscow, 2009.
- [4] Titomir LI, Trunov VG, Aidu EAI, Sakhnova TA, Blinova EV, Kneppo P. New approaches to the diagnosis of left and right ventricular hypertrophy by means of dipolar electrocardiotopography. *The Anatolian Journal of Cardiology*, 7(S1): 29-31, 2007.
- [5] Titomir LI, Trunov VG, Aidu EAI, Sakhnova TA, Blinova EV, Kneppo P. Electrocardiographic diagnosis of left ventricular hypertrophy on the basis of dipole electrocardiotopography method. *Journal of Electrocardiology*, 41(6): 697.e1-697.e6, 2008.

Individual vs. Adjusted Standard Torso Model in the Solution of the Inverse Problem in Electrocardiology

J. Lenkova, J. Svehlikova, M. Tysler

Institute of Measurement Sciences, Slovak Academy of Sciences, Bratislava, Slovakia

Email: jana.macugova@savba.sk

***Abstract.** To find a solution of the inverse problem of electrocardiography as precisely as possible, individual geometry of a patient's torso is required. The most precise method to obtain both the surface geometry and the position and shape of inner organs is an imaging method such as CT or magnetic resonance. In our work we tried to find a suitable surrogate torso model enabling to avoid the use of demanding imaging techniques and offering accurate enough results. We suggested doing that by adapting both the torso dimensions and positions of electrodes on an already existing parametrized standard torso model.*

Keywords: Individual Geometry, Standard Torso Model, Inverse Solution

1. Introduction

The topic of model geometry in the inverse problem of electrocardiography has been discussed for a long time. One of the overall accepted observations from numerous studies is that it is necessary to include inhomogeneities to the torso model – at least those most prominent, such as lungs and ventricular cavities, and that it is not possible to acquire an acceptably accurate result without individual geometry of a patient's body and the position of inner organs [1][2]. Other important observation is that the position of electrodes is to be adjusted to the heart position rather than to the reference point of the fourth intercostal space [3][4].

As opposed to imaging methods that have been used so far to acquire an individual human torso model (MRI, CT) and that require to construct a new torso model for each patient, different approach is employed in this study: a parametrized generic torso model that can be adjusted to fit the patient's individual torso shape. To do so, we pursued some procedures for torso- and electrodes position- adaptation. Our aim was to verify if a torso obtained by an imaging technique can be replaced with sufficient accuracy by a torso constructed in a much simpler way – using an adjusted standard realistically shaped torso model.

2. Subject and Methods

Simulation of body surface potentials

To simulate body surface ecg potential maps, we modeled 12 small ischemic lesions shaped as spherical caps, placed in the left ventricular myocardium, close to the positions of 3 main coronary arteries: Cx (circumflex artery), RCA (Right coronary artery) and LAD (left anterior descending artery). In each of these three positions, two subendocardial and two subepicardial lesions were modeled.

The model we used to simulate activation of ventricular myocardium used simplified analytical geometry of ventricles. The myocardium volume was divided into 1x1x1 mm cubic elements; each of them was assigned a realistically shaped action potential (AP) characteristic. In the elements within the ischemic lesion the AP was shortened to mimic the presence of ischemia. Activation sequence during ventricular depolarization and

depolarization was simulated in normal ventricles as well as in ventricles with ischemic lesions. Boundary element method was used to sum the electrical activity of the elementary sources and to compute the cardiac electric field in the torso volume conductor.

From simulated torso surface potentials QRST integral maps were constructed. Then, for every lesion a difference QRST integral map (DIM) was computed, by subtracting a map computed for normal activation from the map computed in case of particular ischemic lesion incorporated in the ventricular model. This DIM characterizes topographical changes in surface cardiac electrical field due to the ischemia.

Three torso models were used in the forward computations. The torso shape models were obtained using MRI scanning from 3 patients, 1 woman and 2 men, while they had electrodes put on [2]. Realistically shaped lungs and analytical model of ventricular myocardium with cavities were inserted into the torso. The set of inhomogeneities (lungs and ventricles) was the same for all the torso models; the electrical conductivity assigned to the inhomogeneities was 0.25 and 3 times the mean electrical conductivity of the torso, respectively. The original positions of electrodes, as scanned by MRI, were used in the forward computations as well. The lead system used was the modified Amsterdam 62 system used in Warsaw [5].

Solution of the inverse problem

For the inverse computations, 4 torso models (see Fig 1.) were used for each of the patients: a) torso 1 – the original torso model with electrodes as scanned using MRI, b) torso 2 – a standard torso model (STM), actually a modified Dalhousie torso [6] with inhomogeneities and regularly placed electrodes, c) torso 3 – an adjusted STM "stretched" to fit the shape of the original torso model as good as possible, with regularly placed electrodes, d) torso 4 – an adjusted STM, similar to torso 3 but with electrodes positions adjusted according to the original torso by horizontally shifting the electrodes of the original torso set-up so they would lie on the surface of the adapted torso model.

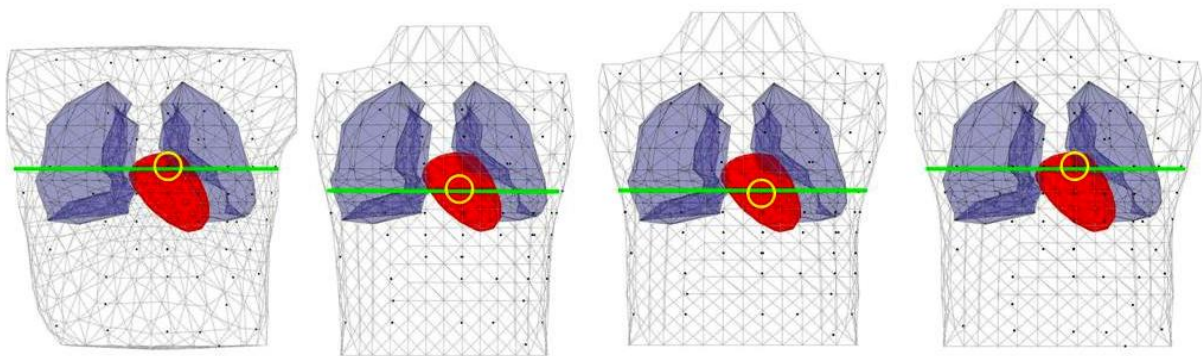


Fig 1. Four torso models created for patient 3 and used in the inverse solution. Left to right: torso 1, torso 2, torso 3 and torso 4 (described in text). The analytical model of ventricular cavities is surrounded by the epicardium, forming thus the ventricular myocardium model with lungs model on both sides. The square marks depict the electrodes of the used lead system, the line marks the level of the V2 lead (circled).

The model of ventricular myocardium consisting of 168 evenly laid segments as well as the models of lungs and ventricular cavities was the same for all torso models (torso 1 to 4) used in the inverse computations. In our inverse computations, difference integral maps were used as input data. Therefore, we searched the equivalent electrical source in form of an equivalent integral dipole (EID) that represented the difference over the whole QRST period between ischemic and normal activation. The position of EID was restricted to the centres of defined segments of ventricular model. The dipole moment of EID was computed for each of 168 possible positions using the equation

$$d_i = T_i^+ p \quad (1)$$

where d_i is the dipole moment of the EID placed in the i -th heart segment ($i=1,2,\dots,168$), T_i^+ is the pseudoinverse of the transfer matrix T_i describing how the EID positioned in the i -th segment and integral body surface potentials in measured points are related, p is the vector of integral potentials in measured points (corresponding DIM). To compute the equation (1), singular value decomposition was applied on the transfer matrix.

To assess the precision of the results for all 4 torso models used in the inverse computations for each of the patients, we evaluated a localization error parameter defined as the distance between the inversely localized EID and the gravity center of the simulated lesion that was looked for. The average localization error for all 12 lesions was then evaluated [5].

3. Results

As seen in Table 1, the best result for each patient was obtained when the torso 1 model was used in the inverse computation. In all three patients, the second best result was for torso 4, in case of patient 3, the result for torso 4 and torso 1 were the same. For patient 1, the third best result was achieved using torso 3, with the worst result being for the torso 2. In patients 2 and 3, the order of the torso models with two worst results was changed – the results for torso 2 were better than for torso 3.

Table 1. The results of the inverse computations. For each patient, four torso models were used in the inverse solution. For every torso set-up 12 DIMs (one for each lesion) were used as the input and the resulting localization error was averaged.

Mean localization error [cm]	Torso 1	Torso 2	Torso 3	Torso 4
Patient 1	0.59	2.88	2.62	0.97
Patient 2	0.49	1.04	1.31	0.76
Patient 3	0.49	1,70	1.80	0.49

4. Discussion and Conclusion

In this work we tried to suggest a surrogate torso model that could be used in the inverse solution with one dipole instead of a torso obtained from an imaging technique with sufficiently accurate results. We investigated the situation in 3 MR – scanned torso surface models with electrodes placed on them. For each original torso we suggested 3 types of simplified torso models to compare the accuracy of lesion location.

Our hypothesis was that the results of the inverse solution would show the least localization error parameter using the original torso+electrode set-up. From the other three torso models, the best results were expected for the torso with adapted electrode positions (torso 4). This proved to be true in all the three patients. The mean localization error was only 1.53 and 1.65 times higher for patient 1 and 2, respectively, and the same for patient 3, when compared to the mean localization error obtained by using the original torso model. The mean localization error values using the original torso model were not zero due to other factors such as the error coming from rough segmentation of the heart.

We supposed, that the third best results will be achieved using the torso model with adapted dimensions and with regularly distributed electrodes (torso 3) and that the worst results will come with using the STM with regular electrodes placement (torso 2). This, however, was

only true in patient 1 (a woman) while the other two men patients showed the localization results in reversed order. Determining the reason for this behaviour requires further observations.

It is worth noticing that the span between the value of the mean localization error for the adjusted torso with adjusted electrode positions and the value for the third best result (whichever torso model produced it) was rather large. Apparently, adjusting only the outer torso shape does not influence the results of the inverse solution as much as adjusting both, the torso shape and the electrode positions. However, it is not possible to omit the procedure of adjusting the torso model shape, since the standard torso model may not be large enough for the range of electrodes of the original lead system positioning to be kept.

Based on the obtained results we can conclude that using some standard torso model instead of realistic patient geometry obtained by imaging techniques can give sufficiently accurate inverse solution only if the dimensions of the standard torso are properly adjusted in accordance with patient torso dimensions and electrodes are positioned according to their original placement on the patient's body as well. It can be expected that the results could be even better if more precise position and orientation of the heart is available. That will be the subject of our future study.

Acknowledgements

The work has been supported by research grant No. 2/0210/10 of the Vega Grant Agency in Slovakia. We also thank to prof. van Oosterom and R. Hoekema for providing the data of three torso models obtained from MRI and used in the forward computations of surface potentials.

References

- [1] Huiskamp GJM, van Oosterom A: Tailored vs. realistic geometry in the inverse problem of electrocardiography. *IEEE Transaction on BME* 36 (8): 827-835, 1989.
- [2] Hoekema R, Uijen GJH, van Oosterom A. Geometrical aspects of the interindividual variability of multilead ECG recordings. *IEEE, Transactions on BME*, 48 (5): 551-559, 2001.
- [3] Hoekema R. Interindividual variability of multilead electrocardiographic recordings: Influence of heart position. *Journal of Electrocardiology*, 32 (2): 137-148, 1999.
- [4] Hyttinen J, Puurtinen HG et al. On the effects of model errors on forward and inverse ECG problems. *International Journal of Bioelectromagnetism*, 2 (2), 2000.
- [5] Tyšler, M., Kneppo, P., Turzová, M., Švehlíková, J., Karas, S., Hebláková, E., Hána, K., Filipová, S. (2007). Noninvasive assessment of local myocardium repolarization changes using high resolution surface ECG mapping. *Physiological Research* 56, Suppl. 1.
- [6] Horáček BM: Numerical model of an inhomogeneous human torso. *Advances in Cardiology*, 10: 51-57, 1974.

Infrared Thermography as a Screening Method for Carpal Tunnel Syndrome Diagnosis

¹M. Tkáčová, ²R. Hudák, ²J. Živčák, ³J. Švehlík

¹CEIT-KE, Košice, Slovakia,

²Technical University of Košice, Košice, Slovakia,

³Louis Pasteur University Hospital, Košice, Slovakia

Email: maja.tkacova@gmail.com

Abstract. *The presented study deals with thermographic (IRT) diagnosing of the Carpal Tunnel Syndrome (CTS). It is considered to be an approach to screening thermal manifestations of the difference between the physiological temperature distribution in the skin of dorsal hands and pathophysiological temperature distribution in hands affected by CTS. We created a database of 356 thermal images of dorsal and palmar side of 162 healthy ($n_{RS}=162$) and 16 pathological hands ($n_{CTS}=16$) with clinically diagnosed CTS of 9 patients. Pre-surgical thermograms of the hands with CTS of each subject were taken and stored using IRT (Thermocamera Fluke Ti55/20). We observed the temperature distribution in the entire hand and partial temperatures of the center point of carpals (D1/P1) as well as the area of distal phalanges on middle fingers (D5/P5). The Index of Median Nerve ($_{D}MI=(T_{D1}-T_{D5})$; $_{P}MI=(T_{P1}-T_{P5})$) was determined based on resulting data. Test results obtained from measurements of the two points on the dorsal side of hands showed that the temperature of CTS hands is typically higher in the phalanges as opposed to the wrist ($_{D}MI<0$, 62.5%), while the temperature is the lowest in distal phalanges (D5) of healthy hands ($_{D}MI\geq 0$, 81.5%). The sensitivity of IRT diagnostic test in our diagnostic process of CTS was calculated to be 0,625.*

Keywords: Thermography, Carpal Tunnel Syndrome, Index of Median Nerve

1. Introduction

The goal of the presented paper is to discuss the role of medical thermography in the diagnostics of neuro-vascular diseases of the human body such as the Carpal Tunnel Syndrome (CTS). Main issues include limits to investigating the median nerve area, diagnostic importance of measurements, etc.

Carpal Tunnel Syndrome

Carpal tunnel syndrome (CTS), or median neuropathy in the wrist, is a medical condition in which the median nerve is compressed at the wrist, which leads to paresthesia, numbness and muscle weakness in the hand. As a result of these predisposing factors, the finger flexor tendons cause friction as they move over one another and the generated heat causes local inflammation. This inflammation irritates the nerve and the resulting pain is what patients experience when they have CTS. The reason there is so much pain associated with CTS is because there is a lot of pressure on the Median Nerve.

CTS can be diagnosed with special tests and EMG, which is the only imaging diagnostic method. This method is based on myodynamia, but results from EMG are not always clear. In addition, EMG uses electrodes either in contact with the body or invasive electrodes. Modern medicine seeks to be contactless and noninvasive, which also makes thermography a suitable diagnostic method. A nerve conduction study, inflammation and temperature distribution may be of benefit to clarifying the diagnosis and this is the goal of this study. [1], [2], [3], [4], [10]

2. Subject and Methods

Contactless, noninvasive and painless infrared thermography (IRT) was used during these examinations. Skin temperature of the dorsal and palmar side of hands from our database ($n=356$) was measured with an infrared camera (ThermaCam Fluke Ti55/20, Fluke, USA). This thermographic camera generates a matrix (representing image points) of temperature values. They feature 320×240 (76 800 pixels) detectors with industry leading thermal sensitivity (≤ 0.05 °C; 50 mK NETD) for high resolution. The camera works in the spectral range from 8 to 14 μm (human body infrared radiation is the highest in the spectral range around 9.66 μm) and the calibrated temperature range from -20 to 100 °C. Data were obtained through high-speed (60Hz) analysis.

Emissivity of the skin was set up 0.98 in the camera, the ambient temperature was measured with an infrared (laser) thermometer (Pyrometer Testo 810) and a contact multimeter (Almemo Multimeter 2690, Ahlborn, Germany) was used for verification. The camera was calibrated using the system's internal calibration process before each recording. All thermograms ($n=356$) were processed using special software (SmartView 2.1, FLUKE, USA).

The database consists of reference thermograms (RT ; $n_{RT}=324$) and pathological (CTS) thermograms (CTS ; $n_{CTS}=32$). They are divided into dorsal (D_{RT} , $Dn_{RT}=162$; D_{CTS} , $Dn_{CTS}=16$) and palmar (P_{RT} ; P_{CTS}) thermograms. Current (thermographic) research focuses on the dorsal side of hands (D_{RT} , $Dn_{RT}=162$; D_{CTS} , $Dn_{CTS}=16$).

Conditions of Measurement

Measurements were carried out under the same conditions, always in the same room with the ambient temperature at 20 °C (± 2 °C). The blinds in the room were drawn in order to eliminate the impact of solar radiation and the room was air-conditioned to keep the same temperature during each measurement. [5], [6]

The Index of Median Nerve

We identified five points in the lines of the median nerve (on dorsal and palmar side of hand), on which we measured the temperature. For the dorsal side of hands, there are the center point of carpals (D_1), the center point of metacarpals (D_2) and the fingertips of the middle finger from proximal phalanges (D_3), the intermediate phalanges (D_4) to the distal phalanges (D_5). (see Fig.1)

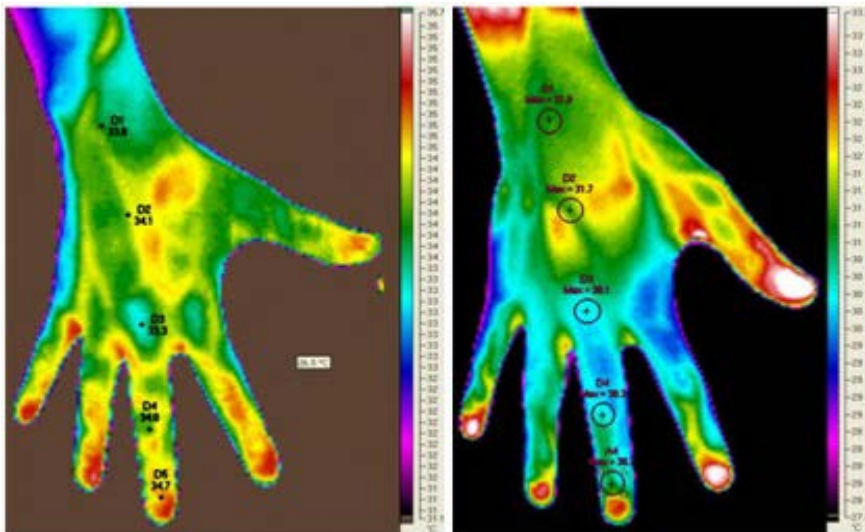


Fig. 1. Location of points D_i , the left thermogram shows a hand with CTS (D_{CTS}), the right one shows a hand from reference thermograms (D_{RT})

3. Results

The data showed that the skin temperatures of median nerve distribution area on dorsal hands varied significantly between CTS and the control group. Results will be confirmed by further terminal screening of a statistically significant group of patients.

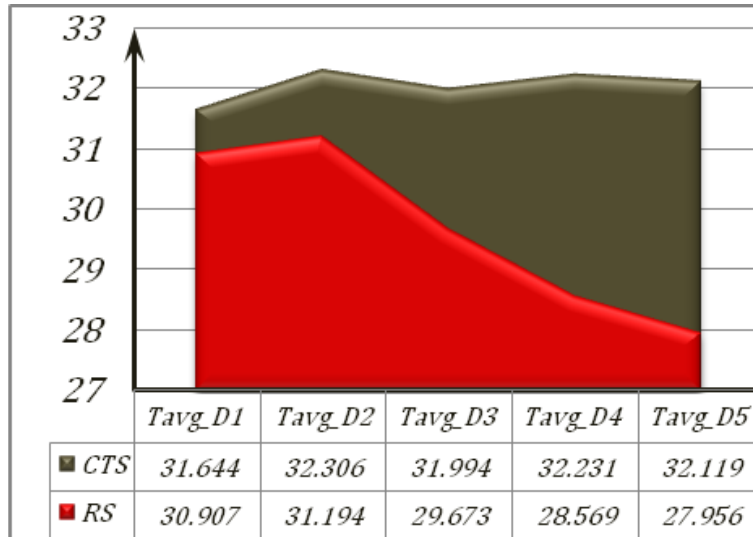


Fig. 2. Arithmetic average of the temperature of hands on the dorsal side of hand (line of median nerve)

Graph (Fig. 2) illustrates the relationship between points of line of the median nerve from D_{RT} ($D_{N_{RT}}=162$) and D_{CTS} ($D_{N_{CTS}}=16$).

The cumulative averages of temperature distribution, which were taken from reference and pathological thermograms on the dorsal side of the line of the median nerve, show a big difference between healthy and CTS hands. To be precise, there were 4°C between average temperatures which were taken from $_{CTS}D_5$ and $_{RT}D_5$. This difference was the main reason to establish the Index of Median Nerve. The following equation is used to calculate the Index of Median Nerve on the dorsal side of hands (MI; Graph 2, 3, 4):

$${}_D MI = T_{D_1} - T_{D_5} \tag{1}$$

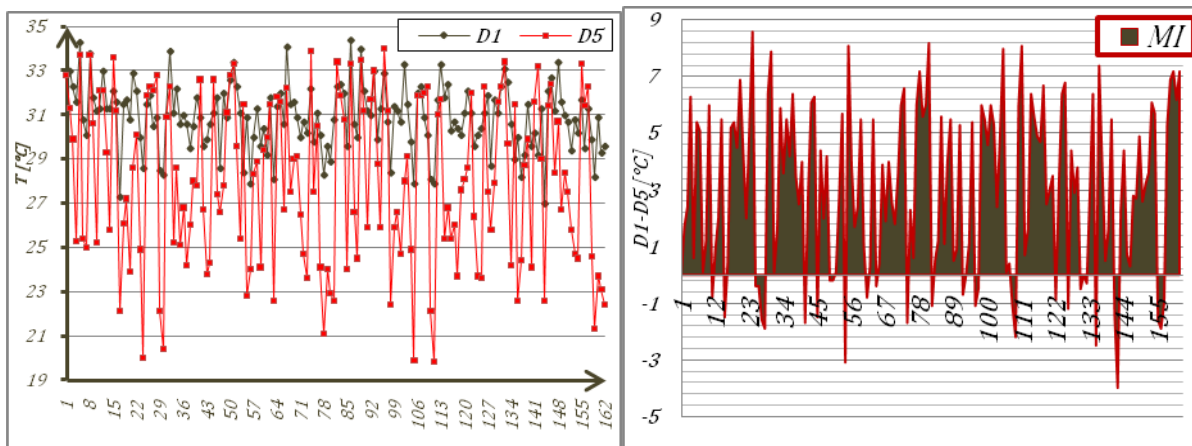


Fig. 3. Index of the Median Nerve (${}_D MI_{RT}$) from D_{RT} ($D_{N_{RT}}=162$)

A negative difference D_1-D_5 ($D_{MI}<0$) from D_{RT} ($D_{n_{RT}}=162$) was detected in 30 healthy hands which account for 18.5% of total normal thermograms from the dorsal side of D_{RT} , see Fig. 3.

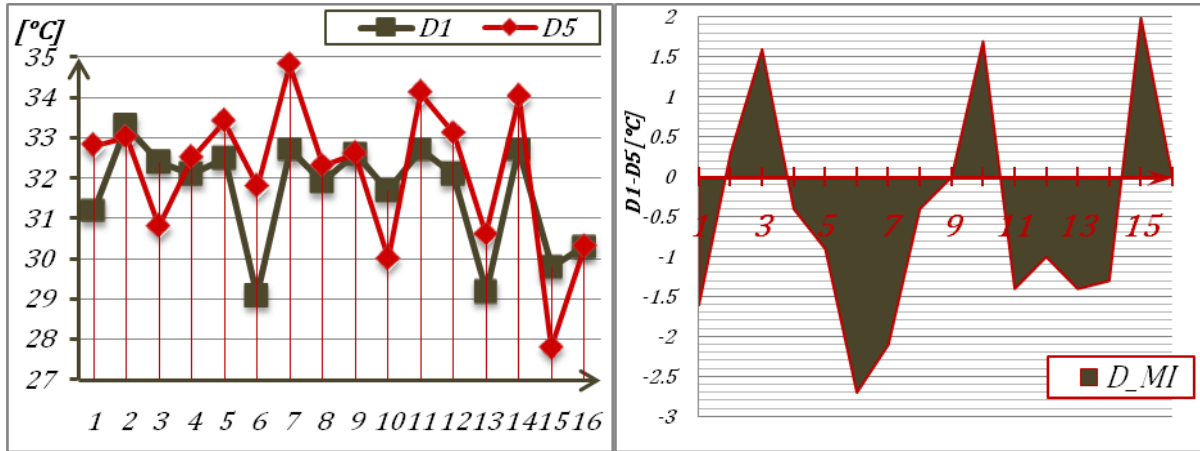


Fig. 4. Index of the Median Nerve ($D_{MI_{CTS}}$) from D_{CTS} ($D_{n_{CTS}}=16$)

A negative difference $D_{MI_{CTS}}$ ($D_{MI}<0$) from D_{CTS} ($D_{n_{CTS}}=16$, dorsal side of hands from CTS patients) was detected in 10 cases (that is 62.5% from D_{CTS}), see Fig. 4, Fig. 5.

Table 1. The Index of Median Nerve (D_{MI}).

The Index of Median Nerve (MI)		
$D_{MI} = T_{D_1} - T_{D_5}$	[°C] \pm SD	$D_{MI}<0$ [%]
D_{CTS}	- 1,165 \pm 2,944	62,5%
D_{RT}	2,937 \pm 2,936	18,5%

Estimation of index test results

The diagnostic test performance includes consideration of validity and reliability of the test (infrared thermography). (See table 2).

Table 2. Assessment of validity of a diagnostic test

		Reference test [EMG]	
		Positive	Negative
Diagnostic test [Thermography]	Positive	a = 10	b = 30
	Negative	c = 6	d = 132
Total sample size		$n_1 = 16$	$n_2 = 162$

Based on Tab.3 above, measures of validity and 95% confidence intervals were calculated: confidence interval for sensitivity: $0.625_{\pm 0.237}$ and confidence interval for specificity: $0.815_{\pm 0.060}$.

4. Discussion

Calculated sensitivity (0.625) and specificity (0.815) of diagnostic test showed that thermography could be the promising method in diagnostic process of CTS, but we need more

pathological thermograms for study for evidence. From our results thermogram of dorsal side of the hand has more significant importance for diagnostic process than the palmar side of hand what correlates with other studies in the world. [1], [2], [3], [4], [8]

5. Conclusions

Sensitivity and specificity of thermographic diagnostic tests were realized on 162 healthy hands ($D_{nRT}=162$) whose dorsal side was scanned (D_{RT}) and 16 pathological hands ($D_{nCTS}=16$) whose dorsal side was also scanned (D_{CTS}). An EMG diagnostic method was applied as a referential test. Sensitivity and specificity were calculated using standart formulas and argument $D_{MI} = (T_{D1}-T_{D5})$ from the database of dorsal scans. The calculated sensitivity of diagnostic test (0.625) with the confidence interval $0.625_{\pm 0.237}$ and specificity of diagnostic test (0.815) with the confidence interval $0.815_{\pm 0.060}$ showed that thermography could be a promising method in the diagnostic process of CTS, its advantages being its non-invasiveness and contactlessness. More statistically significant measurements are required to confirm obtained results.

Acknowledgements

This contribution is the result of the project implementation: Center for research of control of technical, environmental and human risks for permanent development of production and products in mechanical engineering (ITMS:26220 120060) supported by the Research & Development Operational Programme fund ed by the ERDF.

References

- [1] Jesensek Papez B, Palfy M, Mertik M, Turk Z., Infrared thermography based on artificial intelligence as a screening method for carpal tunnel syndrome diagnosis; J Int Med Res. 2009 May-Jun;37(3):779-90; PMID: 19589261.
- [2] Niehof, S. P. at al., Thermography imaging during static and controlled thermoregulation in complex regional pain syndrome type 1: diagnostic value and involvement of the central sympathetic system; BioMedical Engineering OnLine 2006, 5:30 doi:10.1186/1475-925X-5-30; Published: 12 May 2006.
- [3] Jesensek Papez B, Palfy M, Turk Z., Infrared thermography based on artificial intelligence for carpal tunnel syndrome diagnosis, J Int Med Res. 2008 Nov-Dec;36(6):1363-70
- [4] Ming Z, Siivola J, Pietikainen S, Närhi M, Hänninen O., Postoperative relieve of abnormal vasoregulation in carpal tunnel syndrome., Clin Neurol Neurosurg. 2007 Jun;109(5):413-7. Epub 2007 Apr 2., PMID: 17400369.
- [5] Ring E, Ammer K. The technique of infrared imaging in medicine. Thermology International 2000;10:7-14.
- [6] Jones C, Ring E, Plassmann P, Ammer K, Wiecek B. Standardisation of infrared imaging: a reference atlas for clinical thermography—initial results. Thermology International 2005; 15:157-8.
- [7] Wang H, Wade D, Kam J. IR imaging of blood circulation of patients with vascular disease. Proceedings of Thermosense XXVI; 2004 Apr 13-15; Bellingham, WA.
- [8] http://arthritis.about.com/od/carpal/ss/carpaltunnelqa_6.htm
- [9] Dziuban, E., Human body temperature measurement- class program, Joint IMEKO TC-1 & XXXIV MKM Conference 2002, Wroclaw, 2002, 35-959.

Industrial Computed Tomography in Biomedical Engineering

P. Kat'uch, R. Hudák, J. Živčák

Department of Biomedical Engineering, Automation and Measurement
Faculty of Mechanical Engineering, Technical University of Kosice, Kosice, Slovakia
Email: peter.katuch@tuke.sk

Abstract. *Computed tomography scanners (or CT scanners) are very popular medical equipments for tens of years. Its invention initiated a revolution in diagnostic technology by allowing us to look inside a person and obtain a very clear anatomical image without violating the outer surface of his body, in other words, non-invasively [10]. Just few years ago this technology found way to the area of industrial applications. Presented paper describes metrological possibilities of industrial tomography in the area of biomedical engineering in order to hardware limitations and software functions.*

Keywords: industrial computed tomography, biomedical engineering, measurement

1. Introduction

More than one hundred years ago X-ray technology started its triumphal procession when Wilhelm Conrad Roentgen discovered a new kind of radiation in his laboratory in Wuerzburg, Germany in the year 1895. Up to this moment most of the developments on X-ray technologies and computer tomography have been focused on special medical applications. Another twenty years later computer tomography (CT) has become a powerful, well accepted tool in industrial applications as well. Today industrial CT is on its way to become a major tool of industrial quality control in high-tech branches, not only for material testing but for geometry analysis as well. Industrial CT uses a series of 2-dimensional (2 D) images taken at specific intervals around the entire sample. Basically any type of industrial CT system uses three principal components: an X-ray tube, an X-ray detector, and a rotational stage. Everything is enclosed within a radiation shielding steel/lead/steel cabinet. Micro computed tomography (micro-CT) is primarily the same as standard CT except it uses a micro focus tube instead of a traditional tube. A micro-CT scan yields resolutions in microns because the focal spot of a micro focus tube is only a few micrometers in size. For comparison, micro-CT resolution is about 100 times better than the best CT scan in the medical field.

2. Possibilities of industrial tomography

Metrotomography presented by Metrotom device uses X-ray technology based on a simple principle: an x-ray source illuminates an object with an electro-magnetic beam – the x-ray beams. The beams meet on a detector surface and are recorded in varying degrees of intensity depending on the thickness of the material and its absorption characteristics. The result is a two-dimensional gray-scale image. However, this image is only meaningful for visual inspection when shown as a cross section. Metrotom rotates the component 360° around its own axis, thus producing a 3D image of the interior of the part.

Nowadays, the industrial tomographs are designed to scan with the high precision. Thanks to this, their use will be extended from the diagnosis area to the metrology area. In the metrology, they will improve the control of the shapely-complicated parts that could not have been measured until now. The main industrial tomography areas of the use are:

- testing: - quality of the connections in assemblies

- analysis of the porosity
- analysis of the defects
- inspection of the material
- measuring the dimensions of the inner and outer elements
- reverse engineering (obtaining the CAD model from the real part)
- comparing the nominal with actual geometry

3. Application in biomedicine

Technology center of computed tomography at Technical university of Kosice serves as support for many kind of researches. Biomedical research or research in prosthetics and orthotics are important supported areas. Tomography can be used for various evaluations. One of the most used is digitalization of very complicated shaped objects. In biomedical engineering there are many objects with so complex surfaces, that they are not measurable by any other methods of digitalization. Touching probes, lasers or optic scanners can not reach areas which are mostly hidden or unobtainable. With CT scanners we obtain 100% information about object shape. Because of that for example animal skull (fig. 1) can be digitized. VGStudio Max is software which allow extract STL model from surface points. STL is universal triangular model which can be imported to almost every CAD/CAE/FEM/RP software for further processing.

With CAD software it is possible to do parameterization or design a supplement for scanned object. In FEM (Finite element method) software the stress/strain analysis can be performed. STL model is ideal type of model for Rapid Prototyping. With 3D printer the plastic or metal copy of real object can be done. On the pictures bellow (fig. 1) can be seen original and printed copy of monkey skull. More about express creation of complex shaped object copy can be found in authors other publications [10].

X-ray is kind of radiation which can penetrate through objects. Because of that we have information not only about surface of object, but also about inner volume. After reconstruction of point cloud we can look inside the object by using virtual cross-sections without destroying of real object or separate materials with different density.



Fig. 1. STL model of monkey skull generated from point cloud (left) and copy of skull made with rapid prototyping technology compared to real skull (right)

In the figure 2 the separation of different plastics, composite materials and wood is shown. Prosthesis contains components which are not visible. On reconstructed point cloud we can set transparency for polyurethane and inner components appear in 3D rendered visualization.

Another research supported by CT technology at our laboratory was porosity analysis at two samples of human bones. The research was focused to compare amount of solid phase of two

human demineralised bone matrices, where one of them was cultivated with mesenchymal stem cells (MSC) for two weeks.

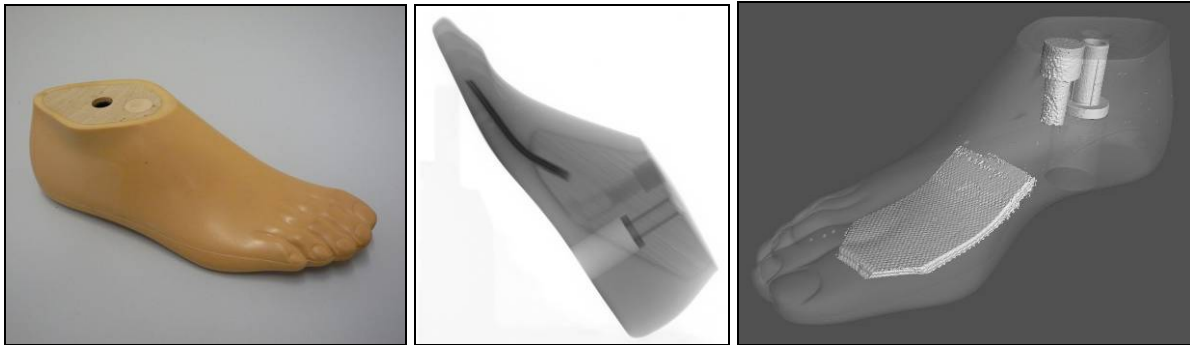


Fig. 2. Prosthesis (left), its x-ray image in selected position (middle) and rendered point cloud with predetermined transparency of PUR material (right)

After cultivation the amount of solid phase increased rapidly and the results can be seen also on figure 3. Porosity of selected regions of interests have been calculated and compared. Results of research can be found in authors' publication [5].

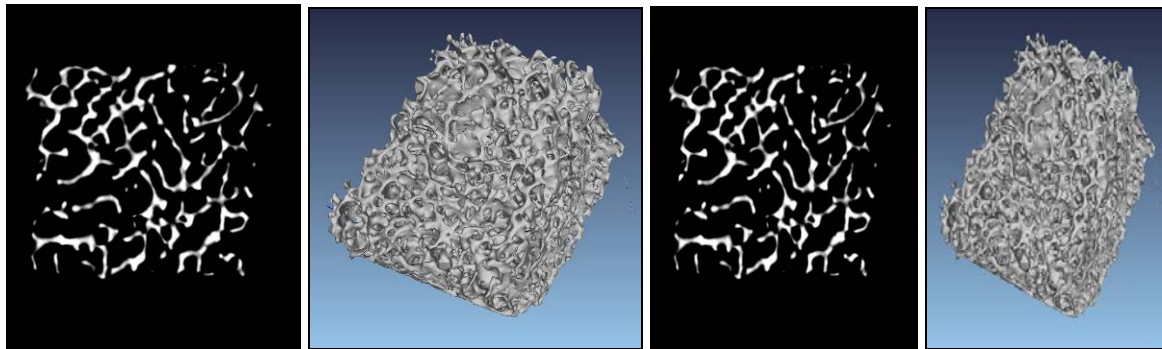


Fig. 3. Demineralised human bone matrix without hMSCs (left) and demineralised human bone matrix with hMSCs after two weeks of cultivation (right) in cross-section views and 3d rendered views

Industrial tomography is a branch of technology which gives not only advantages of nondestructive testing and viewing of inner structure, but the reconstructed data are so accurate, that this technology can be used for very precise geometrical measurements. Also in biomedical applications it is necessary to measure characteristics, which are difficultly measurable by any other technology without destruction. Spherical form of used acetabular component was measured with Calypso software. This metrological software is used for almost all coordinate measuring machines from Carl Zeiss. With Calypso we can evaluate characteristics of objects and make a protocols or graphical presentations of results. Graphical interpretation of form deviations at acetabular component in magnification are presented on figure 4. Deviations have been filtered to eliminate scratches on the spherical surface.

Quality of reconstructed point cloud and accuracy of measured data markedly depends on density and cumulative wall thickness of scanned object. Because of that material with lower density are more suitable for scanning than denser materials. Titanium, in comparison with other metals (steel, copper, etc.), is a metal with relatively low density and because of that small components made from titanium are measurable without restrictions.

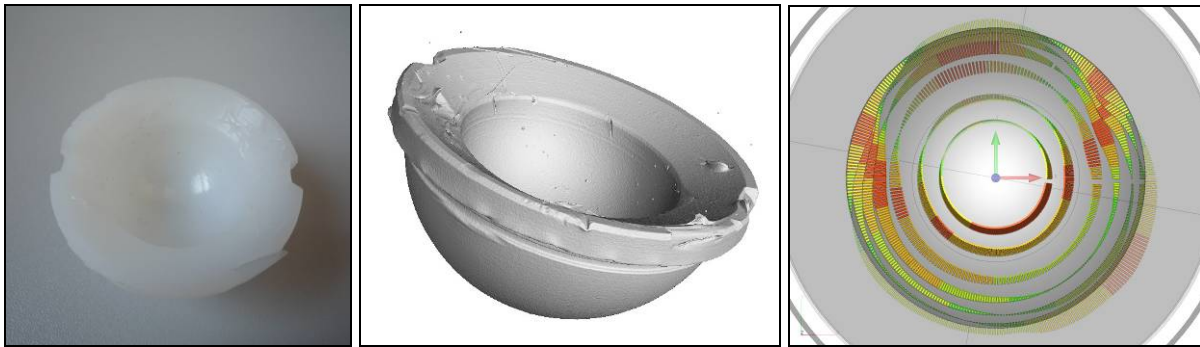


Fig. 4. Used acetabular component (left), rendered point cloud (middle) and form deviations on spherical surface (right)

One of the latest researches supported by our laboratory is digitalization of titanium dental implants. Analyses of material homogeneity, porosity, assembly quality and geometry have been performed on four different implants (fig. 5).

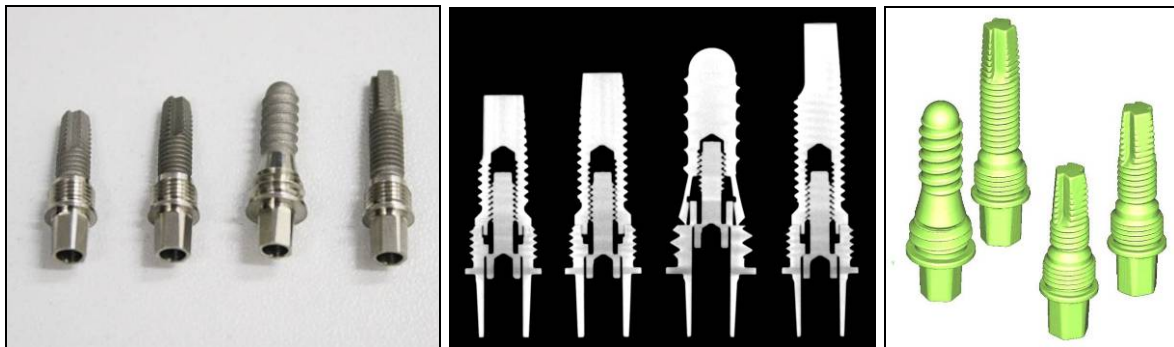


Fig. 5. Four dental implants (left), cross-section of point-cloud (middle) and STL files imported to metrology software Calypso prepared for measurement

4. Conclusions

The paper deals with relatively new technology - industrial tomography - and application oriented to biomedical engineering. This technology with its advantages can increase quality of biomedical products. A possibility of analysis of osteosynthetic junctions, analysis of total replacements in order to endoprosthesis release and analysis of biomechanical properties of materials (monitoring of cavities, composites research, etc.), analysis of junction in medical devices, 3D modeling by reverse engineering and following rapid manufacturing are just few of applications.

Acknowledgements

This contribution is the result of the project implementation: Creation and promotion of technologies in diagnostics of components and junctions with computed tomography (ITMS:26220 220038) supported by the Research & Development Operational Programme funded by the ERDF.

References

- [1] Ritman EL. Micro-Computed Tomography - Current Status And Developments. *Annual Review of Biomedical Engineering*, Vol. 6: 185-208, 2004.

- [2] Lettenbauer H, Georgi B, Weiß D. Means to Verify the Accuracy of CT Systems for Metrology Applications (In the Absence of Established International Standards), DIR 2007 - *International Symposium on Digital industrial Radiology and Computed Tomography*. Lyon, 2007.
- [3] Noel J. Advantages of CT in 3D Scanning of Industrial Parts. *3D Scanning Technologies Magazine*. 2008.
- [4] Andreu, J. P. and Rinnhofer, A.: Modeling Knot Geometry in Norway Spruce from Industrial CT Images, Springer-Verlag Berlin Heidelberg, SCIA 2003, LNCS 2749, 2003. 786–791.
- [5] Gromošová S, Rosocha J, Živčák J, Hudák R, Kneppo P. New modular semiautomatic system for preparation of the demineralized bone matrix for clinical transplantation. *World Congress on Medical Physics and Biomedical Engineering - WC 2006: Imaging the future medicine: August 27 - September 1, 2006 COEX Seoul, Korea*. Heidelberg: SpringerLink, 2006.
- [6] Toporcer T, Grendel T, Vidinský B, Gál P, Sabo J, Hudák R. Mechanical properties of skin wounds after atropa belladonna application in rats. *Journal of Metals, Materials and Minerals*. vol. 16, no. 1 2006, 25-29.
- [7] Sidun J, Dabrowski J, R. Investigation of Osseointegration of Porous Materials for Orthopedic Implants, *Acta Mechanica Slovaca*, Volume 14, No.2/2010
- [8] Brajliah T, Valentan B, Balic J, Drstvensek I. Speed and accuracy evaluation of additive manufacturing machines. *Rapid Prototyping Journal*, Volume 17, Number 1, 2011, 64-75.
- [9] Cierniak R. X-Ray Computed Tomography in Biomedical Engineering. Springer London, 2011.
- [10] Gajdos I, Katuch P. Complex approach to the reverse engineering techniques. *Scientific Papers of University of Rzeszow : Zeszyty Naukowe Politechniki Rzeszowskiej: Mechanika* z. 80. No. 273, 2010, 81-86.

Magnetic Resonance Imaging Methods Used for Weak Magnetic Materials Detection

I. Frollo, P. Andris, J. Přibíl, L. Vojtíšek, T. Dermek, L. Valkovič,
D. Gogola, O. Štrbák

Institute of Measurement Science, SAS, Bratislava, Slovakia,
frollo@savba.sk

Abstract. *Imaging based on nuclear magnetic resonance (MRI) for mapping and imaging of the weak magnetic field materials placed into the homogenous magnetic field of an NMR imager, is proposed. A sample made of a weak magnetic material was constructed, theoretical computation and testing on an MRI 0.178 T Esaote Opera imager were accomplished. In our experiments a homogeneous phantom (reference medium) - a container filled with doped water - was used. The resultant image represents the magnetic field distribution in the homogeneous phantom. For detection a carefully tailored gradient-echo (GRE) imaging method, susceptible to magnetic field homogeneities, was used. The first results showed the feasibility of the method and some of the possibilities offered in this field of material research.*

Keywords: magnetic resonance imaging, weak magnetic material, gradient echo

1. Introduction

Imaging of proton density based on Nuclear Magnetic Resonance (NMR) methods used for biological and physical structures is a routine investigating procedure. Special case is observed when an object that consists of a weak magnetic material is inserted into a stationary homogeneous magnetic field. This results in a deformation of the basic stationary magnetic field. Using a special homogeneous phantom, filled with a water containing substance, near the sample, it is possible to image the contours of this sample. The acquired image represents a modulation of the basic magnetic field of the imager detectable by gradient echo imaging sequence.

First attempt of a direct measurement of the magnetic field created in living and physical tissue by a simple wire fed by a current was reported in [1]. A method utilizing the divergence in gradient strength that occurs in the vicinity of a thin current-carrying copper wire was introduced in [2]. A simple experiment with thin, pulsed electrical current-carrying wire and imaging of a magnetic field using a plastic sphere filled with agarose gel as phantom, was published in [3]. First attempt of the indirect susceptibility mapping of thin-layer samples using phantoms were described in [4].

In this paper we propose a magnetic resonance imaging method used for weak magnetic materials detection, computation of the magnetic field distribution based on double-layer magnetic theory and a comparison of theoretical results with experimental images.

2. Subject and Methods

We suppose that the magnetic double layer is positioned in the x-y plane of the rectangular coordinate system ($\mathbf{i}_x, \mathbf{j}_y, \mathbf{k}_z$) and the thickness of the layer is neglected.

According to Fig. 1, we suppose the layer is limited by lengths of $2a$ and b , with the left - right symmetry. The layer is moved in +y direction by distance of g . The basic magnetic

field B_0 of the NMR imager is parallel with the z-axis. The task is to calculate the $B_z(x,y,z)$ component of the magnetic field in the point $A[x_0, y_0, z_0]$.

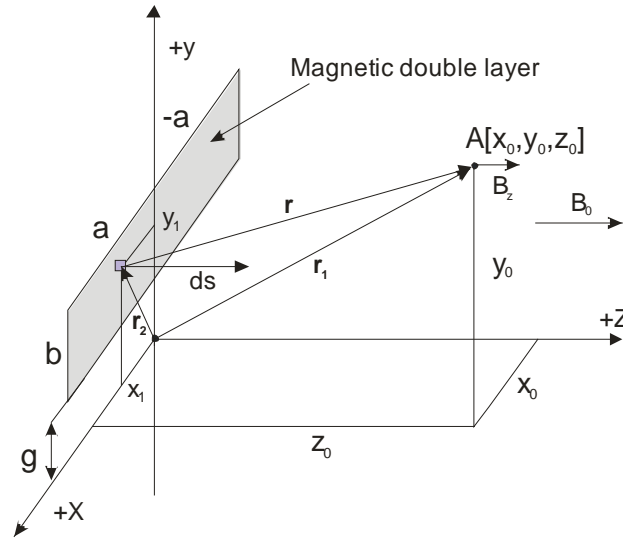


Fig. 1. Basic configuration of the magnetic double layer sample positioned in x-y plane of the rectangular coordinate system. The thickness of the layer is neglected.

In a general definition the magnetic double layer can be considered to have magnetic dipoles continuously distributed on a surface $S(a,b)$. Such a planar magnetic dipoles distribution is called magnetic double layer that is characterised by a surface density of a magnetic dipole moment \mathbf{M} :

$$\mathbf{m}_s = \int_S \mathbf{M}_s(\mathbf{r}) dS \quad \text{and} \quad \mathbf{M}_s = I \mathbf{n} \quad (1)$$

where \mathbf{r} - is a position vector, I - is a current equivalent to planar density of dipole moment of the magnetic double layer and \mathbf{n} - is a unite normal vector of a surface S in a particular point. The formula for magnetic field in the point $A[x_0, y_0, z_0]$ is supposing to use the Biot-Savart law in vector form assuming the equivalency of a current loop and a magnetic double layer (the curve integral is replaced by a surface integral):

$$\mathbf{B} = -\frac{\mu_0 I}{4\pi} \oint \frac{\mathbf{r} \times d\mathbf{s}}{r^3} = \frac{\mu_0 I}{4\pi} \int_S \left(\frac{3\mathbf{r} \cdot \mathbf{r}}{r^5} - \frac{\mathbf{I}}{r^3} \right) \cdot d\mathbf{S} \quad (2)$$

From the physical interpretation the calculated magnetic field assuming:

$$\mathbf{r} \cdot \mathbf{r} = r^2 = (x_0 - x)^2 + (y_0 - y)^2 + (z_0 - z)^2$$

we can write the final formula in a double integral form as follows:

$$B_z(x, y, z) = \frac{\mu_0 I}{4\pi} \int_{-a}^a \left[\int_d^h \frac{3 - I}{r^3} dy \right] dx, \quad (3)$$

where limits for integration are: $[-a, a]$ and $[d = g, h = g+b]$, see Fig.1.

After integration of a indefinite double integral (3) we get the final formula for practical calculation as follows:

$$B_z(x, y, z) = \frac{1}{z_0} \text{ArcTan} \frac{(x - x_0)(b + g - y_0)}{z_0 \sqrt{b^2 + 2bg + g^2 + (x - x_0)^2 - 2by_0 - 2gy_0 + y_0^2 + z_0^2}} + \frac{1}{z_0} \text{ArcTan} \frac{(x - x_0)(b - g - y_0)}{z_0 \sqrt{b^2 - 2bg + g^2 + (x - x_0)^2 + 2by_0 - 2gy_0 + y_0^2 + z_0^2}}$$

Assuming the following relative values: $\mu_0 I / 4\pi = 1$, $z_0 = 0.5$, $a = 7$, $b = 1$, $g = 5$, the resultant 3D and 2D -plots of magnetic field of relative values for $\{x_0, -10, 10\}$, $\{y_0, 0, 10\}$ are depicted in Fig. 2.

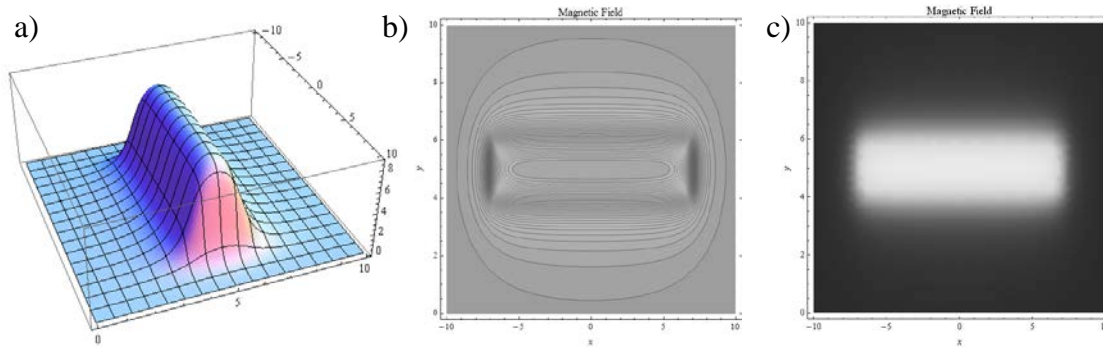


Fig. 2. Calculated magnetic field $B_z(x,y,z)$ of the magnetic double layer sample positioned in x-y plane of the rectangular coordinate system. a) 3D-plot, b) contour plot, c) density plot.

3. Experimental Results

As a physical model, a sample made of 4 low magnetic tapes was used. The sample was placed at the centre of a plastic holder – homogeneous phantom filled with 0,1 wt% solution of CuSO_4 in distilled water, see Fig.3.



Fig. 3. Horizontal field RF coil, active measuring volume (homogeneous phantom), dimensions 90 x 90 mm.

An NMR imager (ESAOTE Opera), permanent magnet 0,178 T with vertical orientation of the basic magnetic field B_0 was used. The gradient-echo NMR sequence was selected for the measurement. A special feature of this sequence is its sensitivity to basic magnetic field inhomogeneities. The original sample, calculated 3D image of the magnetic field distribution and an NMR image of the double cross sample are seen in Fig.4. and Fig.5.

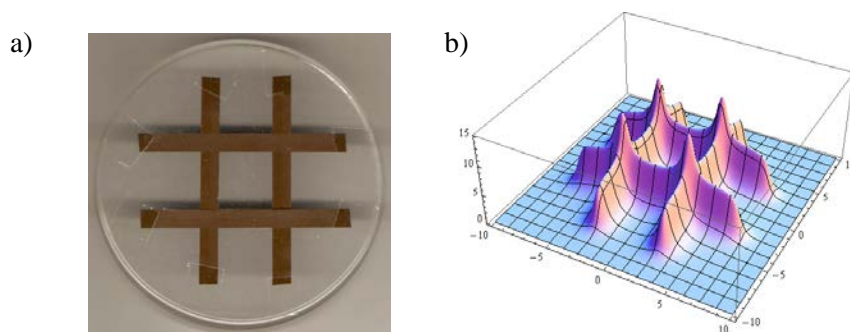


Fig. 4. a) Original sample made of 4 low magnetic tapes, double cross, 6 x 70 mm, distance between tapes 25 mm, audio cassette tape, thickness 11 μm , densely packed pure grained ferric particles. b) Calculated 3D image of the magnetic field distribution.

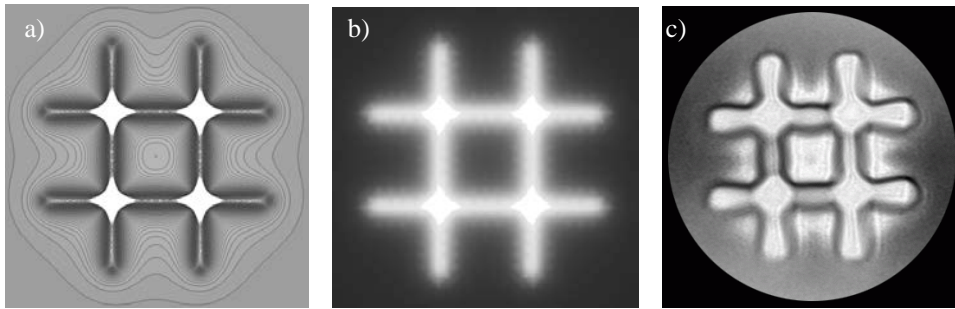


Fig. 5. a) Calculated image of the magnetic field, contour plot, b) density plot, c) NMR image of the double cross sample using GRE imaging sequence.

4. Discussion

A sample made of 4 low magnetic tapes for verification of this methodology was used. Careful adjustment of the GRE imaging sequence parameters to detect weak magnetic materials was necessary. It is evident that imaging of the magnetic field of the weak magnetic samples can be performed by GRE method based on a exteriorization of magnetic field of the sample into a homogeneous planar phantom. Furthermore this magnetic field may cause artefacts if weak magnetic samples are present in the MRI. This effect is strongest if the vector of the static magnetic field $B_0 = B_z$ is perpendicular to the phantom plain. Our experimental results are in good correlation with the simulations. This validates the suitability of the proposed method for detecting weak magnetic materials by MRI.

5. Conclusions

A new method for mapping and imaging of the planar weak magnetic samples placed into the homogenous magnetic field of an NMR imager is proposed. First results showed the feasibility of the method and the importance of detecting the field changes caused by weak magnetic materials, that may cause image artefacts even in the low-field MRI.

Acknowledgements

The financial supports by the Grant Agency of the SAS, project no. VEGA 2/0090/11, The State program ŠPVV no. 2003SP200280203 and project “Creation of the Centre of Excellence for the Research and Development of Construction Composite Materials for Mechanical and Building Engineering and Medical Applications” based on the support of Operational Program Research and Development financially supported by European Regional Development Fund, CEKOMAT, ITMS No. 26240120006 are gratefully acknowledged.

References

- [1] Joy M., Scott G., Henkelman M. In vivo imaging of applied electric currents by magnetic resonance imaging, *Magnetic Resonance Imaging*, Vol.7, 1989, 89-94.
- [2] P. T. Callaghan and J. Stepisnik, “Spatially-distributed pulsed gradient spin echo NMR using single-wire proximity,” *Phys. Rev. Lett.*, vol. 75, no. 24, pp. 4532–4535, 1995.
- [3] Sekino M., Matsumoto T., Yamaguchi K., Iriguchi N., and Ueno S. A method for NMR imaging of a magnetic field generated by electric current, *IEEE Trans. on Magnetics*, Vol. 40, 2004, 2188-2190.
- [4] Frollo I., - Andris P., - Pribil J., - Juráš V. Indirect Susceptibility Mapping of Thin-Layer Samples Using Nuclear Magnetic Resonance Imaging, *IEEE Trans. on Magnetics*, Vol. 43, no. 8, (2007), 3363-3367.

Development of Dedicated dGEMRIC Protocol for Biochemical Imaging of the Temporomandibular Joint Disc at 3 Tesla: A Feasibility Study

^{1,3} P. Szomolányi, ^{1,2} E. Pittschieler, ^{1,3} V. Juráš, ³ I. Frollo, ¹ S. Trattinig

¹MR Centre – High Field MR, Medical University of Vienna, Vienna, Austria

²Bernhard Gottlieb University Clinic of Dentistry, Vienna, Austria

³Institute of Measurement Science, Slovak Academy of Sciences, Bratislava, Slovakia

Email: pavol.szomolanyi@meduniwien.ac.at, pavol.szomolanyi@savba.sk

Abstract. *The temporomandibular joint (TMJ) is one of the most complex joints in the human body. TMJ degenerative changes are studied by means of MRI morphological techniques. So far, to our best knowledge, there was no attempt to show the biochemical ultrastructure of cartilage in the TMJ in humans in-vivo. Our feasibility study show that the tracer accumulation occurs within 30 minutes and an inversion recovery technique in combination with application of delayed-Gadolinium Enhanced Magnetic Resonance Imaging of Cartilage can reveal biochemical composition of TMJ in terms of GAG content.*

Keywords: MRI, Temporomandibular joint, MRI biochemistry, MR contrast agents

1. Introduction

Temporomandibular joint and muscle disorders refer to a complex set of conditions that can cause pain in the area of the jaw joint and associated muscles and/or problems using the jaw. Both or just one of the TMJ may be affected. This can affect a person's ability to speak, eat, chew, swallow, make facial expressions, breathe, cause head and neck pain, a jaw that is locked or difficulty to open, and popping/clicking noises. The TMJ is a hinge and gliding joint that is the most often used joint in the body. TMJ and muscle disorder has been reported of occurring in 5% to 44% of persons examined in epidemiologic and clinical studies [1-3].

MR diagnostic techniques extensively tested, optimized and clinically applied for articular cartilage of the human body are now further optimized for TMJ. MR protocols has to be adapted due to a complicated anatomy and small size. Higher nominal in-plane resolution and thin slice are required in order to prevent partial-volume effects during subsequent image evaluation. Promising methodology for TMJ enhancement in MR imaging is application of gadolinium based contrast agents and its dynamics during uptake and washout period. The aim of the present feasibility-study is to develop delayed Gadolinium enhanced MR imaging techniques for the cartilage tissues in the TMJ. Furthermore, certain pathologies (internal derangements, osteoarthritis) of the TMJ or reactions of the soft tissues after splint use or with functional orthodontic appliances could be assessed.

2. Subject and Methods

The TMJ is one of the most complex joints in humans. It is a synovial articulation between the processus condylaris of the mandibular condyle and the fossa articularis of the temporal bone. The TMJ is classified as a ginglymoarthrodial (hinge-gliding) joint. The upper joint space is separated from the lower joint space by an ovoid mixed-fibrous and fibrocartilagenous disc or meniscus [4]. Figure 1 shows detail of the TMJ anatomy [1]. The disc is thin in the center (1mm) and thick peripherally (2,8mm posteriorly and 2mm anteriorly), thus being “erythrocyte-shaped”. The disc is attached to the circumference of the

joint by a tough, fibrous joint capsule. Posterior to the joint, there is the bilaminar zone, formed superiorly by the elastic ligamentous insertion of the disc into the tympanic bone and inferiorly by the fibrous ligamentous insertion into the subcondylar region [5]. TMJ disorders are very common. Approximately 70% of the general population exhibit signs of TMJ disorder, but only about 5% seek medical or dental treatment [6].

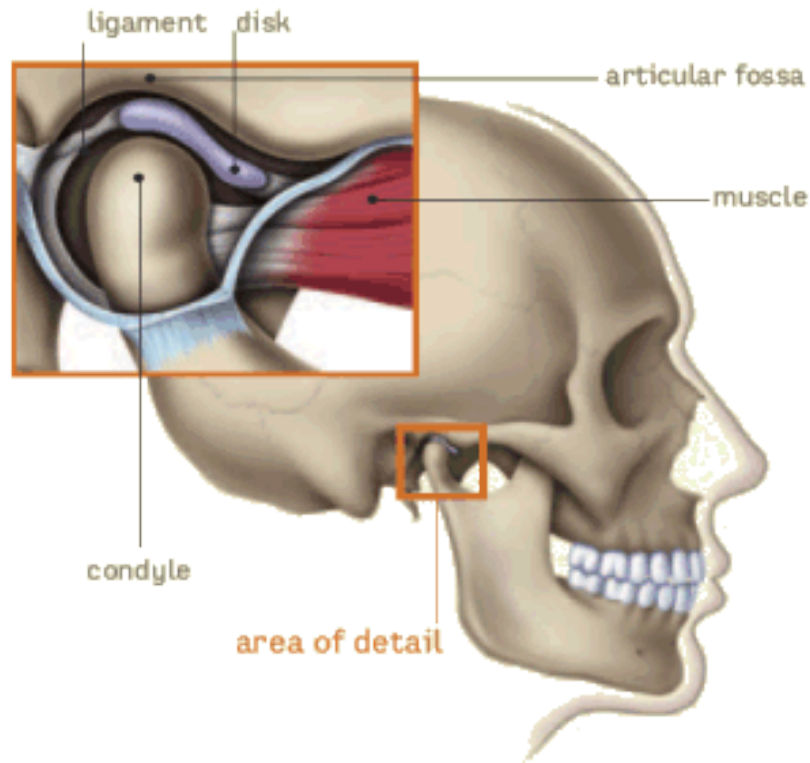


Fig. 1. TMJ anatomy

MRI technique has proven its ability to follow differences in T_1 relaxation time constant before and after CA administration in case of articular cartilage. T_1 relaxation time constant dropped down after CA administration followed by the intense exercise to approximately 50% of native T_1 values in case of articular cartilage. This technique of contrast agent application known as a delayed-Gadolinium Enhanced Magnetic Resonance Imaging of Cartilage (dGEMRIC) has proven good correlation with glycosaminoglycan (GAG) amount, which is one of the principal components of the articular cartilage in human body. Main objective of presented feasibility study is therefore to optimize MR protocols in combination with dGEMRIC for the TMJ in-vivo study.

Figure 2 shows example MR image of the TMJ. Measurements were performed using Inversion Recovery (IR) technique. This technique is known for robustness and insensitivity to the B_1 RF field inhomogeneity. Disadvantage of the inversion recovery technique is long measurement time and consequently low time resolution. Furthermore, the probability of the movement artifacts is high if measurement takes long time. The total measurement time limited to 30 minutes allowed to perform 9 inversion time measurements. Subsequently ROIs were evaluated on 9 images by an experienced dentist (E.P.) and mean values and standard deviations were recorded. Measurements were performed on the 3T Siemens Trio (Siemens Medical, Erlangen, Germany) MR system using flexible eight-channel coil, consisting of two separate components with 4 channels on each side (Noras MRI products, H"ochberg, Germany).



Fig. 2. MRI of the volunteer: left TMJ with ROI drawn. T_1 mean value and standard deviation (SD) are displayed above ROI. Sequence parameters are depicted on the Figure as well.

3. Results

Figure 3 shows the T_1 relaxation time behavior of the TMJ cartilage. Contrast agent uptake was quick and caused significant drop of T_1 from the starting value of 678ms before contrast agent administration to the 332ms 30 minutes after contrast agent administration, 325ms 60 minutes after CA, 367ms 120 minutes after CA and 358ms 180 minutes after CA.

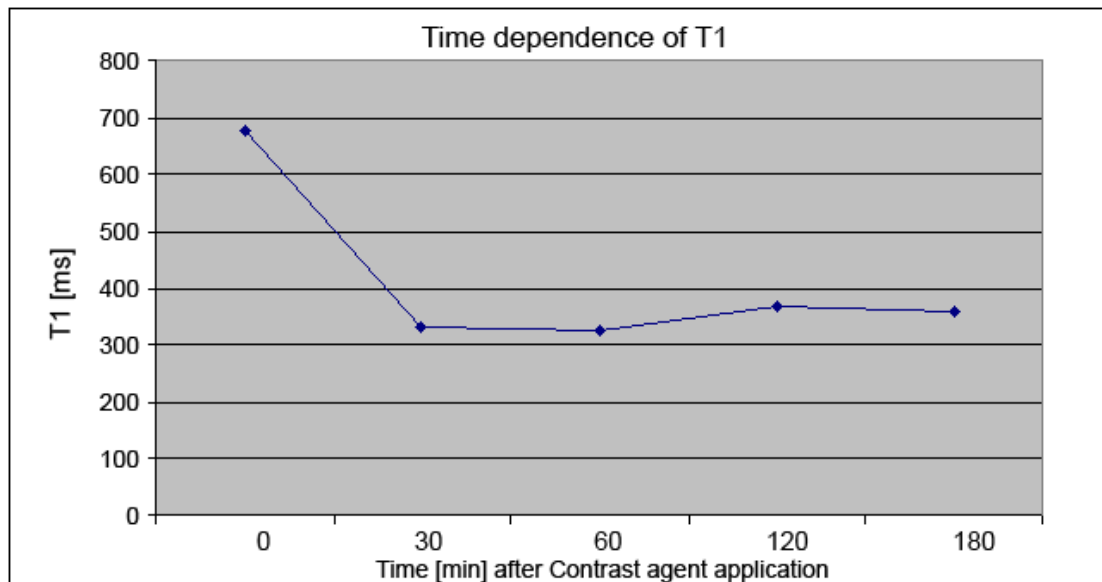


Fig. 3. Native T_1 relaxation time constant (time 0) and T_1 values in different post-contrast times.

Levenberg-Marquardt least-squares fit was performed using IDL (RSI, Builder, Colorado) routine. Asterisk on a figure 4 represent measured values. Line represents fitting curve. R^2 equal to 0.970713 represents quality of fit.

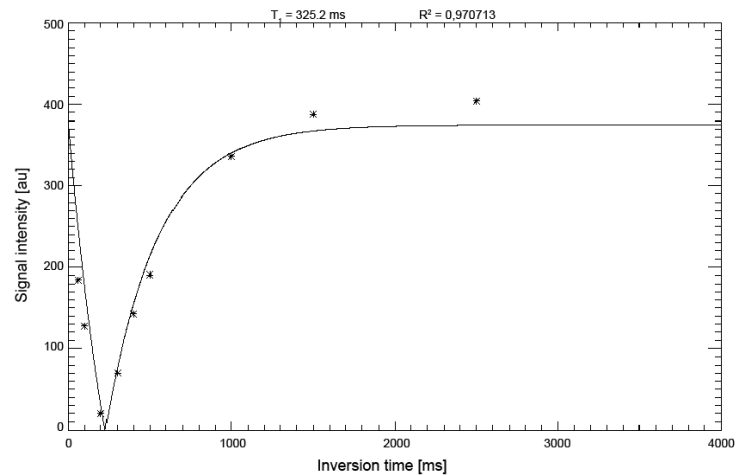


Fig.4. An example of curve fitting using non-linear least squared method

4. Discussion

As apparent from the figure 3, dramatic drop of the T_1 relaxation time constant after a contrast agent administration can be resolved only in steps of 30 minutes, due to slow Inversion Recovery measurement. Alternative to this technique could be dual-flip angle 3D-spoiled GRE technique (VIBE), which is much faster but at the same time also less precise, due to its high sensitivity to the B_1 imperfections.

5. Conclusions

Presented study show that biochemical properties of the TMJ can be evaluated by the dGEMRIC MR techniques. It is known that amount of gadolinium based contrast agent is inversely proportional to the GAG content. By measuring T_1 relaxation time constant of the TMJ we found that after 30 minutes contrast agent penetration has reached stable level. The first successful volunteer experiments encourage us to further optimize biochemical sequences for the TMJ of healthy volunteers.

References

- [1] National Institute of Dental and Craniofacial Research. National Institutes of Health. Prevalence of TMJD and Its Signs and Symptoms. <http://www.nidcr.nih.gov/DataStatistics/FindDataByTopic/FacialPain/PrevalenceTMJD.htm>, February 11, 2011.
- [2] Hansson T, Nilner M, *A study of the occurrence of symptoms of diseases of the temporomandibular joint, masticatory musculature, and related structures*. J Oral Rehabil, **2**: p. 313 – 324, 1975.
- [3] Heloe B, Heloe L A, *Frequency and distribution of myofascial pain-dysfunction syndrome in a population of 25-year-olds*. Community Dent Oral Epidemiol, **7**: p. 357 – 360, 1979
- [4] L, Hylander W, ed. *Functional anatomy of the TMJ*. 3rd ed. The temporomandibular joint: a biological basis for clinical practice, ed. L.D.M. Sarnat B G. Charles C Thomas: Springfield. 85-113, 1979,
- [5] A, Bell K, ed. *Computed Tomography of the Temporomandibular Joint*. Magnetic Resonance of the Temporomandibular Joint, ed. V.G.E. Palacios E, Shannon M, Reed C F., Georg Thieme Verlag: Stuttgart - New York. 28 – 38, 1990
- [6] G, Dimitroulis, *Temporomandibular disorders: a clinical update*. B M J. **317**: p. 190 – 194, 1998

Radiofrequency Coil Array Design and Optimisation for Magnetic Resonance Low Field Imaging

¹L. Vojtíšek, ¹I.Frollo, ¹L. Valkovič, ¹D. Gogola, ¹T. Dermek, ^{1,2} V. Juráš,
^{1,2} P. Szomolányi

¹ Institute of Measurement Science, Department of Imaging Methods, Slovak Academy of Sciences, Dubravská cesta 9, 841 04, Bratislava, Slovakia

² Medical University of Vienna, Department of Radiology, Vienna General Hospital, Waeringer Guertel 18-20, A-1090, Vienna, Austria

Email: lubomir.vojtisek@savba.sk

Abstract. Radiofrequency (RF) coil phased arrays are getting more and more important for accelerating the imaging speed and for gaining better signal to noise ratio (SNR) in magnetic resonance imaging (MRI). The approach is conceptually similar to phased array used in radar techniques hence it is used to be called MRI phased array coils. To get maximum benefits from this technique, coil and preamp decoupling and coil geometry optimization are necessary to ensure independence of the individual coil channels. Qualitative design and a method for optimization of geometric properties of the coil elements in phased arrays, with aim to increase SNR, G-factor and to limit noise correlation, are proposed in this paper. Simulating by the finite element method (FEM) using Comsol Multiphysics we obtained the sensitivity maps of coils. The introduced Matlab program is primarily calculating the G-factor along with other parameters that can be calculated from sensitivity maps. By an optimization algorithm the program is setting the parameters of the coil and afterwards is driving the FEM simulations.

Keywords: MRI, coil array optimization, phased array

1. Introduction

Parallel Imaging

Usually, the data are acquired sequentially using different magnetic field gradients. Parallel imaging technique in MRI uses spatial information about the origin of detected MR signal from sensitivity maps of particular RF receivers of the array. This information may be used for the image generation. As coil sensitivity map does not depend on the examined object it can be obtained prior the measurement and just once for each coil. Thus, it can significantly shorten the time of image acquisition, e.g. by using less phase encoding steps (without losing the image quality), or increase the image quality in the normal acquisition time. Careful design of suitable phased coil array is essential for optimal parallel imaging [1], [2].

Receivers in array are connected to the independent preamplifier, amplifier and separately digitalized. Data from each channel are later combined in optimal way with focus on the origin of the signal by Sensitivity Encoding (SENSE) reconstruction algorithm or Generalized Auto-calibrating Partially Parallel Acquisitions (GRAPPA) [3], [4], etc.. Using these methods, it is possible to acquire SNR of local coil with a field-of-view (FOV) typical to a volume receiver [5].

Noise in Parallel Imaging - Geometry Factor

Serious limitation of all techniques in MR is level of noise or SNR. Phased array techniques and parallel imaging is not an exception. As was already mentioned, in arrays is higher number of individual coils used instead of one global. Because one part of noise is generated

by the sample which is hard to eliminate, it is possible to increase the SNR by using the array coils. Applicability of array for parallel imaging might be represented by the so called geometry factor (G-factor), that is most depended on geometry of the coil and can be defined by the formulas of Pruessmann [2]:

$$g = \frac{SNR^{full}}{SNR^{red} \sqrt{R}} \quad , \quad (1)$$

where g is a geometry factor and it is always equal or higher than one, SNR^{full} is SNR in full encoding acquisition, SNR^{red} denotes SNR in sample-reduced acquisition and R is a factor by which the number of samples is reduced in comparison to full acquisition. For SENSE reconstruction was derived a formula:

$$g_{\rho} = \sqrt{\frac{\left[(S^H \Psi^{-1} S)^{-1} \right]_{\rho, \rho}}{(S^H \Psi^{-1} S)_{\rho, \rho}}} \quad (2)$$

where g_{ρ} is a local geometry factor, ρ denote the index of the voxel, S^H transposed sensitivity matrix, Ψ receiver noise matrix. For the GRAPPA reconstructions a different formula for quantitative G-factor must be used [4].

Decoupling

Mutual inductances and parasitic capacitances may cause coupling - an undesired transfer of signal and also of the noise between the coils. This causes loosing of the spatial information and also decreases the SNR. So, the reduction of this unwanted interactions between coils with overlapping FOVs is critical in phased array techniques. This might be performed in several ways (or their combination): By the mutual position of the coils in array (the overlap of the neighboring coils or as in our case a gap - distance between the coils); By "preamplifier decoupling" using either high impedance or low impedance input preamplifier; By coil decoupling by lumped elements mutual capacitors or inductances; By coil shielding (passive or active), etc. More information can be found in [6], [1].

2. Subject and Methods

Analytical precalculations

For the study of the butterfly coil behavior have been used an analytical calculations in Wolfram Mathematica derived from Biot-Savart law:

$$H(r) = \frac{I}{4\pi} \int \frac{dl \times r}{|r|^2} \quad (3)$$

Vector of magnetic field $H(r)$ is calculated in simplified model as four infinite strip conductors fed by current I . Thickness of the strips is here neglected. For one strip were derived formulas (4) and (5). The x-component of magnetic field H_x can be written as follows:

$$H_x = \frac{15}{2\pi} \left[\tan^{-1} \left(\frac{-a-x+f}{y+b} \right) - \tan^{-1} \left(\frac{a-x+f}{y+b} \right) \right] \quad (4)$$

For the y-component of the magnetic field H_y was written the following expression [7]:

$$H_x = \frac{15}{4\pi} \left[\text{Log} \left\{ (-a-x+f)^2 + (y+b)^2 \right\} - \text{Log} \left\{ (a-x+f)^2 + (y+b)^2 \right\} \right] \quad (5)$$

where a is the width of the strip, x and y are coordinates in two dimensional Cartesian coordinate system, f is a shift of the strip on x axis, b is a shift of the strip on y axis.

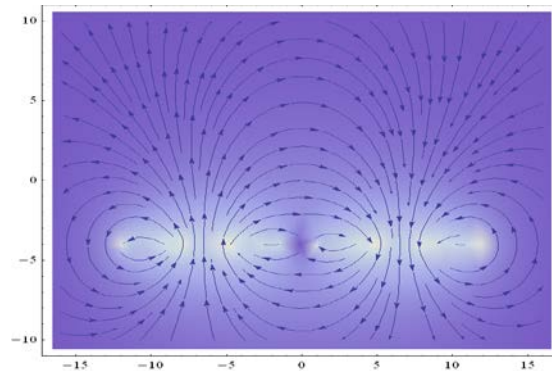


Fig. 1. Magnetic field $H_{x,y}(x,y)$ of the one butterfly coil from Fig.2, calculated from equations (4), (5).

Design of coils

Small cavity of the G-Scan together with B_0 direction perpendicular to scanner cavity, does not allow usage of typical design of phased array coil. Hence a design combined from two square loops and two so called butterfly coils was selected. The advantage of butterfly coil is a significant sensitivity to the longitudinal magnetic field components (this means field perpendicular to the face of the coil).

FEM Analyses – Comsol multiphysics

For FEM analyses Comsol Multiphysics package with an interface to Matlab was used. This allows preparing of all models by a code written in Matlab and also running all Comsol simulations from Matlab. Data extracted from the simulations are processed and parameters like G-factor might be calculated. According to the calculated parameter new dimensions of the coil are proposed and calculated by Comsol Kernel. Due to the long duration (minutes) of each simulation and many parameters of the coil that are adjusted, a short optimization algorithm should be used. As the coil parameters can slightly change with the loading, the model will always slightly differ. So, the optimization convergence limit can be set on quite high level. Finally the optimal setting of the array in seven steps of the optimization algorithm was reached.

3. Results

A method for optimization of phased array receivers uses simulations of electromagnetic fields by finite element methods available in Comsol Multiphysics. Optimization routine was written in Matlab. Description of the coil array and setting of the parameters of the Comsol simulation was based on common interface of the Matlab and Comsol. An optimal array setting for SENSE G-factor was reached by adjusting of the seven dimensional parameters, in seven steps of the optimization algorithm.

Table 1. Results of the optimization steps of the 4-channel phased array for ^3He lung imaging in ESAOTE G-Scan. Optimized on G-factor calculated by (2) with $R=4$

Step	0	1th	2nd	3rd	4th	5th	6th	7th
Width of square loop	19	24	24	24	24	24	24	24
Length of Square loop	24	20	26	20	20	20	23	26,5
Width of copper strip sq. Loop	1,5	1	0,5	0,5	0,5	0,5	0,5	0,5
Width of butterfly coil	8	5,5	5,5	6,5	5,5	5,5	5,5	5,5
Length of butterfly	30	25,5	33	38	32,5	40	40	40
Width of butterfly coil strip	1,5	1	1,5	1	1	0,5	0,5	0,5
Gap on butterfly	5	4,5	3	4	3	4	3	3
G-Factor	3,02	2,19	2,04	1,96	1,84	1,73	1,67	1,67

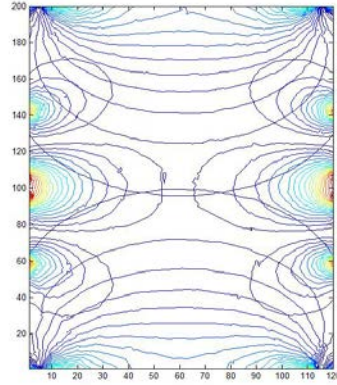
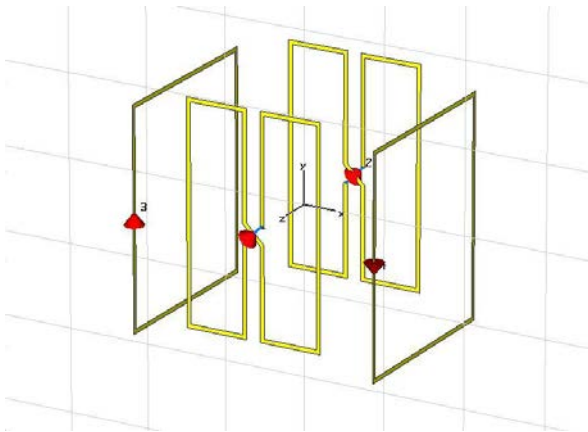


Fig. 2. Model of the 4 channel phased array coil system designed for ESAOTE G-Scan tomograph Fig. 3. Coil sensitivity maps of the array from Fig.2 calculated in Comsol Multiphysics

4. Discussion and Conclusion

The paper is proposing a method for optimization of phased array resonators by using simulations of electromagnetic fields by finite element methods in Comsol Multiphysics and optimization routine written in Matlab. Description of the coil array and setting of the parameters of the simulation is based on common interface of the Matlab and Comsol. By using of this method the four channel coil array for ESAOTE G-scan for thorax imaging was designed and optimized for SENSE G-factor. Currently the coil was manufactured and currently is under testing. Advantage of the proposed method is in versatility of the usage, in effective and fast calculation and in relative simplicity.

Acknowledgements

The work was supported by the European Commission through its Marie Curie Actions (MRTN-CT2006-036002) and by Slovak Scientific Grant Agency VEGA 2/0090/11.

References

- [1] Ohliger, M.A. and D.K. Sodickson, An introduction to coil array design for parallel MRI. *Nmr in Biomedicine*, 19(3): p. 300-315, 2006.
- [2] Pruessmann, K.P., M. Weiger, M.B. Scheidegger, et al., SENSE: Sensitivity encoding for fast MRI. *Magnetic Resonance in Medicine*, 42(5): p. 952-962, 1999.
- [3] Griswold, M.A., P.M. Jakob, R.M. Heidemann, et al., Generalized Autocalibrating Partially Parallel Acquisitions (GRAPPA). *Magnetic Resonance in Medicine*, 47(6): p. 1202-1210, 2002.
- [4] Breuer, F.A., S.A.R. Kannengiesser, M. Blaimer, et al., General Formulation for Quantitative G-factor Calculation in GRAPPA Reconstructions. *Magnetic Resonance in Medicine*, 62(3): p. 739-746, 2009.
- [5] Roemer, P.B., W.A. Edelstein, C.E. Hayes, et al., The Nmr Phased-Array. *Magnetic Resonance in Medicine*, 16(2): p. 192-225, 1990.
- [6] Lee, R.F., R.O. Giaquinto, and C.J. Hardy, Coupling and decoupling theory and its application to the MRI phased array. *Magnetic Resonance in Medicine*, 48(1): p. 203-213, 2002.
- [7] Frolo, I., P. Andris, J. Přibil, et al., Magnetic Field Measurement of a Planar Coil Using Magnetic Resonance Imaging Method. *Measurement Science Review*, 10(3): p. 97-101 2009.

Dynamic Measurement of Body Inclination in Walking by Body Area Network Sensing System

S. Takayama, Y. Matsuda, N. Takahashi, T. Tanaka, K. Kariya

Dept.E.E.Engng. Fac.Sci.&Engng. Ritsumeikan Univ.BKC, Shiga, JAPAN

Email: s-tkym@se.ritsumei.ac.jp

***Abstract.** This paper shows the dynamic measurement system and result of body inclination in walking by monitoring acceleration at waist. To monitor the acceleration in walking, the sensing system had been constructed as a wearable and small scale wireless network system (body area network sensing system [BANSS]) put on body. BANSS is constructed with a host system and plural sensing nodes. Sensing node has sensors, microprocessor and near field communication device (NFC). In this study, the sensing node measures the acceleration at waist of user in walking, and sends them to the host system regularly. By analysing the acceleration data at host system, the situation of body inclination in walking was estimated dynamically. It has been confirmed that the body inclination generates for everybody regardless their consciousness.*

Keywords: sensing system, body inclination, dynamic measurement

1. Introduction

In daily life, quality of life (QOL) is the highest concern for all of people. They hope to keep it well and enhance it. Parameters of QOL are many kinds and different to each person. The parameters are concerning to the situations of living, health, family, friends, job, money, meal, hobby, social activity and so on. Especially, physical condition like health is the most basic and indispensable parameter. The physical condition depends on physical activity in daily life and changes dynamically. Then, to know the state of physical condition in detail, it is necessary to measure that continuously in daily life. Wearable and wireless body area network sensing system (BANSS) is the most suitable system to measure the dynamical physical condition continuously. Concerning the measurement system of body motion in walking, there are several kinds[1-5]. In this study, to detect body inclination in walking, BANSS collects the acceleration at waist dynamically, analyses the data and sends the information to host system. The body inclination in motion becomes the cause of heavy load and strong pain at a hip joint and a knee. Most of people do not feel their body inclination in daily life. The detection of body inclination in walking is to discover the sign of them.

2. Body Area Network Sensing System (BANSS)

To measure physical conditions in motion like walking, running and various kinds of physical activities in daily life, there are several parameters which are heart rate(HR), SPO2(Oxygen density in blood), body temperature, skin temperature, accelerations at many points of body (shoulders, waist, knees and feet [ankles]), impact transmitting in bones and so on. The measuring points of these parameters are distributed on body area. And users should be not limited their behaviours in motion by devices and wires of the monitoring system. Then, the formation of sensing system should be light and easy to use, wearable and near field wireless network to communicate measuring data and commands on and around body area. In this paper, that system is called as the wearable and wireless Body Area Network Sensing System (BANSS). Fig.1 shows the conceptual construction of the wearable and wireless BANSS.

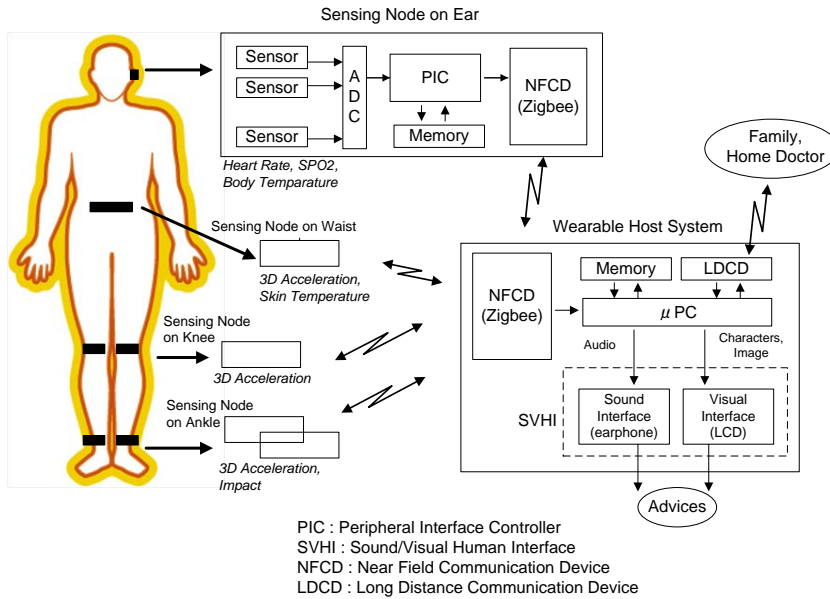


Fig.3. Concept of body area network sensing system (BANSS)

3. Measurement of body inclination in walking

Using a function of BANSS, body inclination in walking has been measured dynamically. Fig.2 shows the concept of the detection of body inclination by acceleration sensor. User puts 3D acceleration sensor on waists. The data of X axis of the sensor output expresses the movement of up-down direction of user. The data of Z axis expresses the movement of front-back direction. And the output signal of Y axis of the sensor expresses the movement of right-left direction. Fig.3 shows the detection of body inclination by analysing the signal of Y axis of acceleration sensor. Fig.3(a) shows the output signal of Y axis of 3D acceleration sensor. It is seen that the signal is fluctuating around zero. The movement of right-left direction in walking is not so high speed. Blue line in Fig.3(b) shows the signal filtered by LPF (less than 0.1 Hz). The filtered signal has the bias changing slowly. To detect the bias locally, the average of the filtered signal in a constant time interval is calculated. The series of green squares in Fig.3(b) shows the fluctuation of local average each 30 sec..

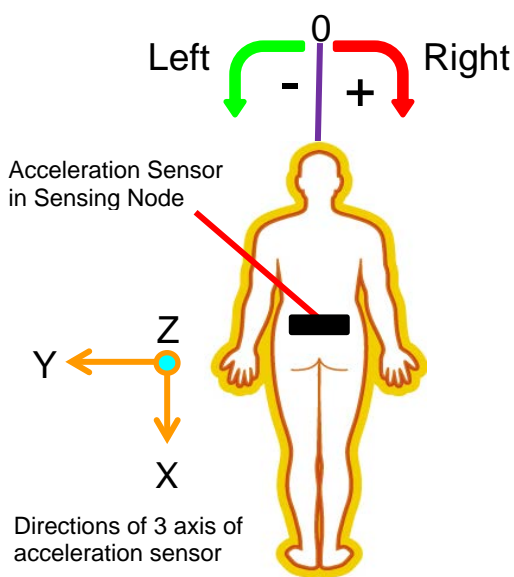


Fig.2. Concept of the detection of body inclination by acceleration sensor.

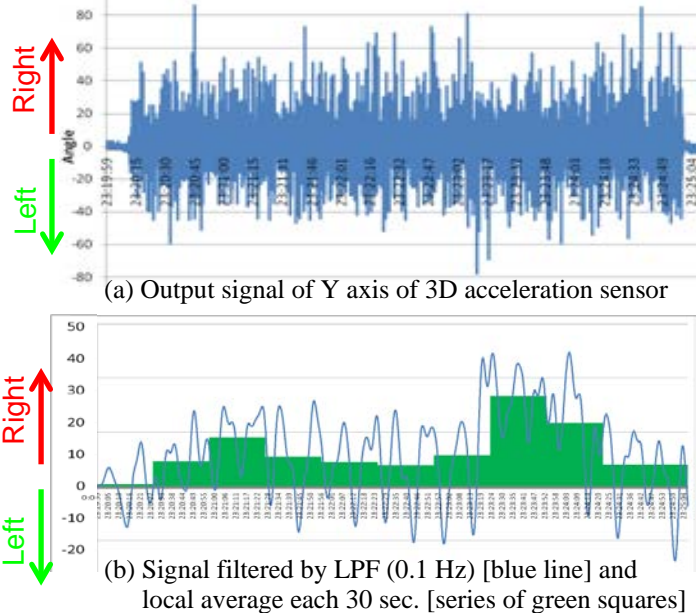


Fig.3. Detection of body inclination by analysing the signal of Y axis of acceleration sensor.

In Fig.3(b), it is confirmed that the series of local average each 30 sec. has shifted to right side. By this observation, it has been estimated that the body inclination of user is right in walking.

To confirm the system operation obviously, the body inclination by unbalance sandals was estimated. Fig.4 shows unbalance sandals. Fig.5 shows walking path, the distance of which is 82m/round. Subject walked two times around the square path. He used with balance sandals in the 1st walking, with unbalance sandals in the 2nd walking. Fig.6 shows the estimated results. Using balance sandals, body inclination was zero mostly. On the other hand, using unbalance sandals, body inclination became right side. As the right heel is lower than left heel, the acceleration to right side became strong in walking.



Fig.4. Different heights of heels.

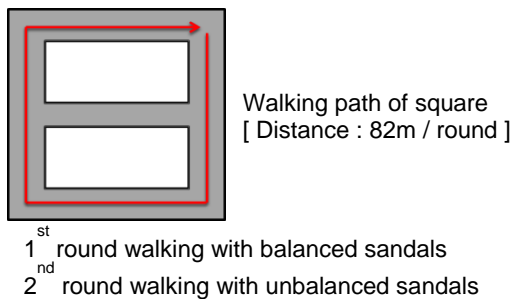


Fig.5. Walking path

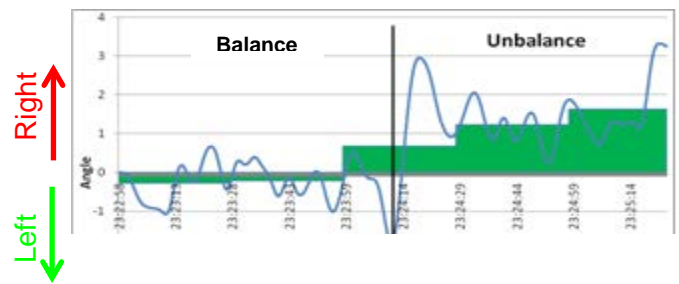
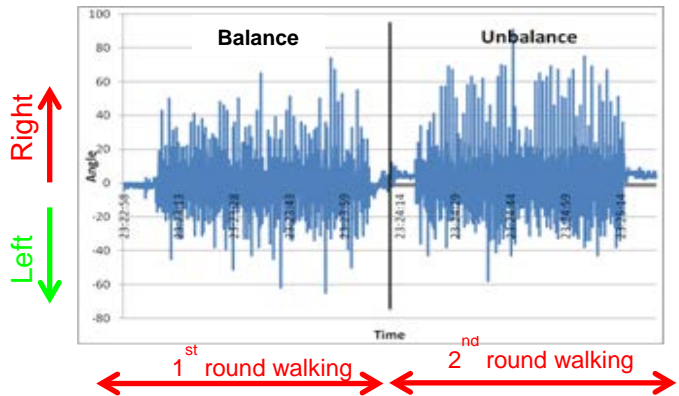
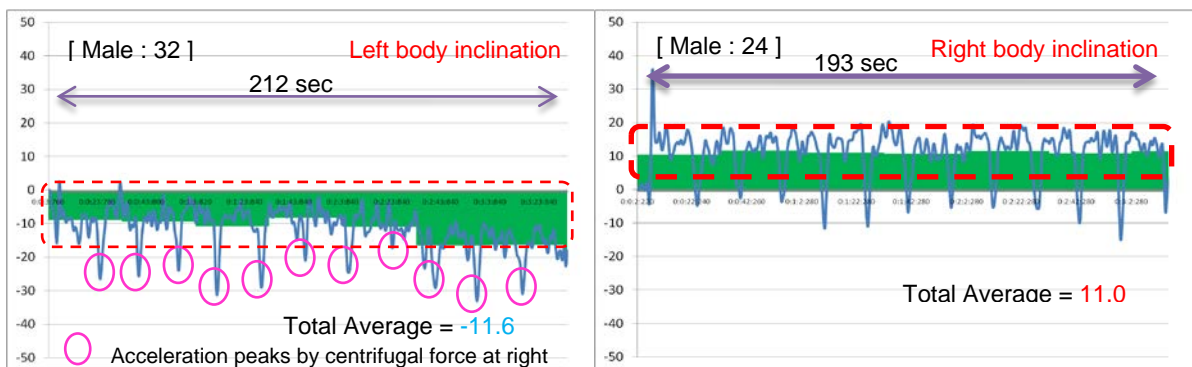


Fig.6 Different body inclinations by balance and unbalance heels.

By using this system, the body inclinations in walking of 5 Laboratory staffs were measured. They walked on same path 3 times continuously with their own shoes. As a remark, they have no consciousness concerning to body inclination at standing and in any motions in daily life. Fig. 7 shows the measurement results. In Fig. 7a, acceleration signal has 11 peaks to left side. These are caused by centrifugal force at right turns.



(a) in case of Male 32 years old

(b) in case of Male 24 years old

Fig.7 a, b. Estimation of body inclination in walking.

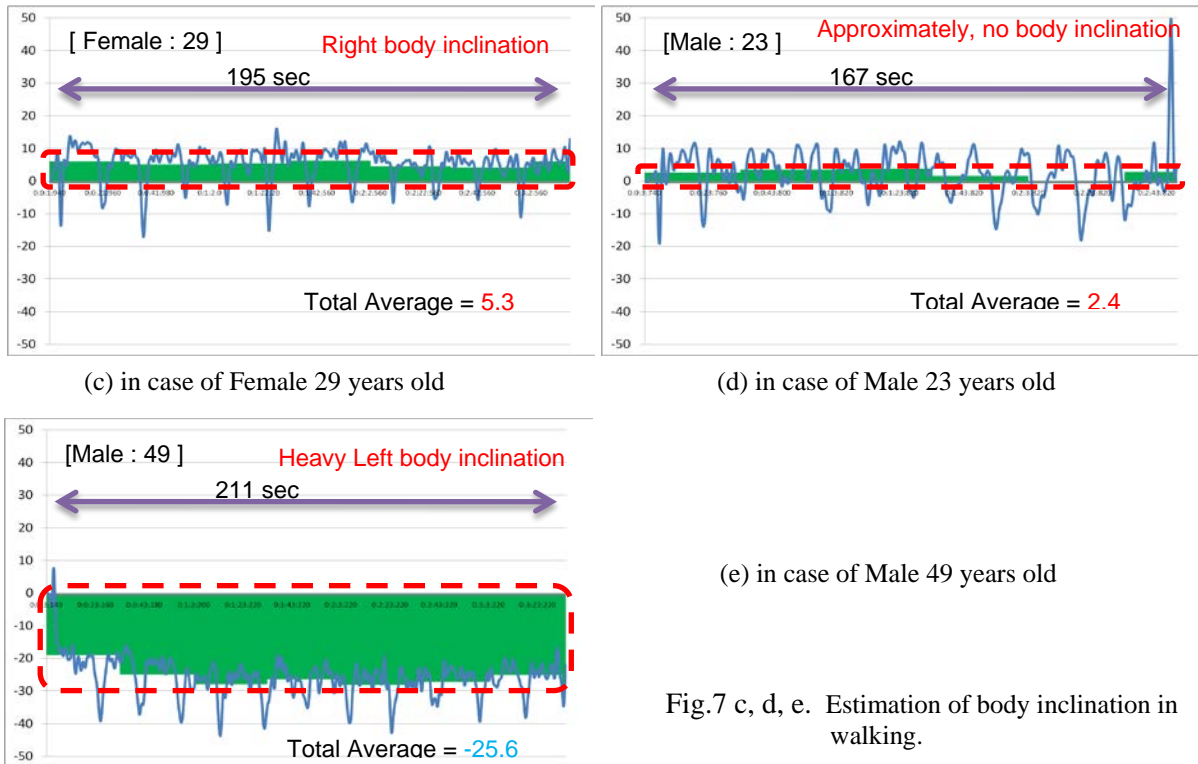


Fig.7 c, d, e. Estimation of body inclination in walking.

In Fig. 7d, the series of local average are around zero. Then, the body inclination was not observed approximately. In Fig. 7e, the body inclination is heavy to left side. It seems that his waist (hip joints) and left knee have got strong load in walking.

4. Conclusions

Body inclination in motion causes unbalance of physical activity and gives heavy load to waist (hip joints) and knees. Mostly, the body inclination occurs without consciousness at the beginning. By using wearable and wireless BANSS, it was confirmed that the body inclination in walking was estimated dynamically. As future works, the body inclination in running and walking for long time will be measured. BANSS is useful tool to measure the physical parameters at various parts on body and estimate physical condition dynamically in motion. That does not become obstacle to various motions. By reconstructing BANSS as small and robust system, the application fields will spread more and more.

References

- [1] Hisao Oka and Tomonori Inoue, Monitoring of physical Activity by Accelerometer, *Technical Report of IEICE MBE98-50*, 1998.
- [2] Kiyoshi Teramoto and Nagao Usui, Effect of Pelvis Adjusting Method on Leg Length Inequality and Centre of Gravity of Patients with Hip Joint Disorder, *Rigakuryoho Kagaku* 11(4): 201-206, 1996.
- [3] Naofumi Tanaka, Shigeru Sonoda, Yoshihiro Muraoka, Yutaka Tomita, Naoichi Chino, Reproducibility and Validity of Gait Analysis Using Portable Accelerometer, *Jpn J Rehabil Med* 33: 549 – 553, 1996.
- [4] Yosinori Nishijima, Tatuo Kato, Takahide Baba, Masatada, Yoshizawa, Effect of Stride Frequency on EMG during Level Walking and Stair Ascending, *Walking Research*, No.7, 2003.
- [5] Masuo Hanawaka, Masaharu Sawamura, Naoyuki Fujimoto, Akira Satoh, Gait Measurement System and its Applications, *YOKOGAWA TECHNICAL Report* Vol.51, No.3, 2007.

Assessment of Human Balance during Stance using Accelerometer Sensors

F. Hlavačka, D. Bzdúšková, Z. Halická, J. Lobotková, V. Szathmáry

Institute of Normal and Pathological Physiology, Slovak Academy of Sciences,
Bratislava, Slovakia,
Email: frantisek.hlavacka@savba.sk

Abstract. *The paper describes a system for assessment of postural activity during stance with data acquired from two biaxial accelerometer sensors and from a force platform. We examined balance in healthy subjects during the quiet stance under the static conditions: at stance on a firm surface or on a foam surface with eyes either open or closed. Body sway was evaluated from the centre of pressure (CoP) positions and outputs of 2D accelerometers attached to the backside of lower and upper trunk during a 50 sec interval. The parameters from CoP and from accelerometers were evaluated to assess quiet stance in two age groups: juniors and seniors. For better presentation, power spectral densities of CoP displacements and outputs of both accelerometer sensors in forward-backward direction were compared. We found that most of CoP parameters were significantly different when comparing juniors and seniors. The useful insight into the balance control during quiet stance was provided also by the rate of change of acceleration (jerk) at lower and upper trunk levels in forward-backward direction. Our results showed that data acquired from accelerometers placed at trunk during quiet stance may indicate small balance impairment due to age.*

Keywords: human balance, accelerometer sensor, age-related posture control.

Introduction

Stabilometry based on recording of the magnitude and direction of the resultant ground reaction force (CoP) by the force platform during stance is an objective method often used for assessment of the human balance in experimental and clinical studies [1]. In recent years the interest in using accelerometer-based systems for measurement of body segment tilts has increased [2]. They range from simple monitoring of daily activities to integrating miniature sensors to enhance the function of devices to perform motor tasks [3]. Because of small dimensions and light weights, these accelerometer sensors can be easily attached to the upper body segments. Its output signals provide useful insight in balance control and gait in healthy subjects [4] and also in patients with balance disorders [5].

Subject and Methods

Fifteen young subjects within the range of 22-29 years (6 men and 9 women, mean age 25.4 years, mean height 172 cm) and sixteen elderly within the range of 64-85 years (7 men and 9 women, mean age 72.1 years, mean height 166 cm) participated in the study. None of the subjects reported previous or present disease or injuries associated with gait and/or balance impairments. All subjects gave written informed consent prior to participation and the local Science Ethical Committee approved the experimental protocol.

The balance control of juniors and seniors was measured during the quiet stance in four conditions: stance on a firm surface with eyes open (EO); stance on a firm surface with eyes closed (EC); stance on a foam surface (thickness 10 cm) with eyes open (FEO) and stance on a foam surface with eyes closed (FEC). The participants were informed to stand upright and relaxed on the force platform barefoot with heels together and feet displayed at angle of about 30°. Before the onset of measuring in each condition, the subjects stood in the same central position of the feet related to the force platform. In conditions with eyes open, the subjects

were instructed to keep eyes open fixing to a black point with a diameter 2 cm placed on a white scene in front of them at a distance of 2 m. Each trial lasted 50 s and 1-3 min rest period was allowed between trials.

The body sway was quantified by displacements of the center of pressure (CoP) in the forward-backward (FB) and left-right (LR) direction. We used custom-made force platform with automatic subject's weight normalization.

Trunk tilts in FB and LR directions were measured by two ADXL203 dual-axis accelerometers with signal conditioned voltage outputs. Sensors measure both dynamic and static acceleration with a full-scale range of ± 1.7 g. The acceleration output was low-pass filtered with cut-off frequency of 5 Hz and the output (trunk inclination) was calibrated in stationary conditions for a ± 10 degrees range of body tilt. The accelerometers were positioned (see Fig.1) at the spinal column of the upper trunk at the level of the fourth thoracic vertebra (Th4) and the lower trunk at the level of the fifth lumbar vertebra (L5).

The CoP displacements and the angle of trunk tilts were sampled at 100 Hz and recorded on MacPC. Obtained data were evaluated and analyzed with MATLAB program. For each subject, the CoP displacements and the trunk tilt angles were averaged for each experimental condition. Group averages were calculated from the individual subjects' averages.

The differences between juniors and seniors in the parameter the rate of change of acceleration (Jfb) were statistically analyzed using t-test and p values < 0.05 were considered significant.

Results

The results showed that data from accelerometer sensors placed at trunk levels during quiet stance indicated small balance differences between young and elderly subjects. We found that time courses of CoP displacement were quite similar to trunk tilts characterized by outputs of accelerometer sensors at L5 and Th4 levels. The data indicated that body during quiet stance is often swaying as inverted pendulum around ankle (ankle strategy). This is noticeable on fig. 1 in time interval from 15 to 20 s where both trunk segments moved in the same direction as CoP displacement.

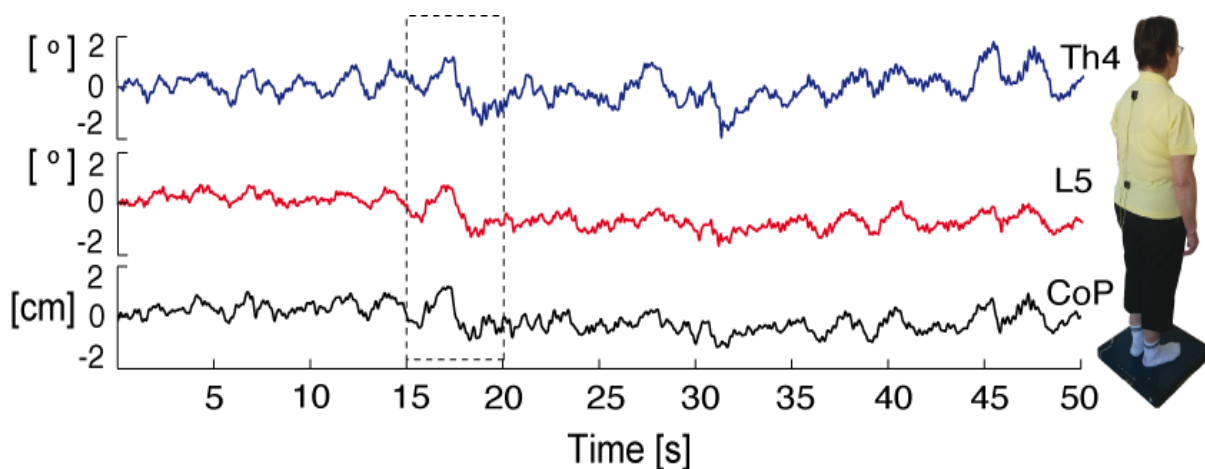


Fig. 1. Time courses of body sway in forward-backward direction recorded by the force platform (CoP) and by accelerometer sensors at lower trunk (L5) and upper trunk (Th4). The outputs of accelerometers were calibrated in degrees – body segment tilt toward vertical line.

The frequency spectrum of CoP displacements and trunk tilts showed very similar curves, which were not so much influenced by age. These frequency profiles indicated that the tilting of trunk during quiet stance oscillated with low frequency (lower than 1 Hz). Results from fig. 2 supported our idea that the calibration of output of accelerometer sensors in degree related to vertical line is acceptable for measurement of the trunk tilts during quiet stance.

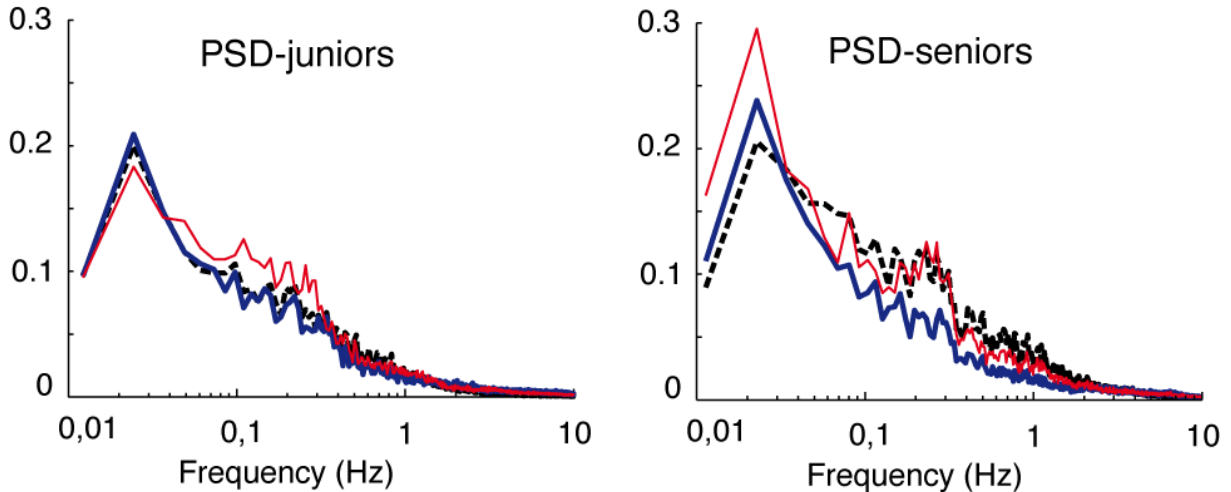


Fig.2. PSD – power spectral density of CoP displacements (dashed line) and accelerometer outputs at lower trunk (thick line) and upper trunk (thin line) in forward-backward direction.

Data analysis of outputs from accelerometer sensors at trunk levels during quiet stance showed the small imbalance in elderly subjects. A first derivation of acceleration - the rate of change of acceleration (jerk-Jfb) at lower trunk in forward-backward direction was considered as a sensitive parameter. The value created by the mean of jerk at lower trunk was the most sensitive to age-related changes in balance of the quiet stance.

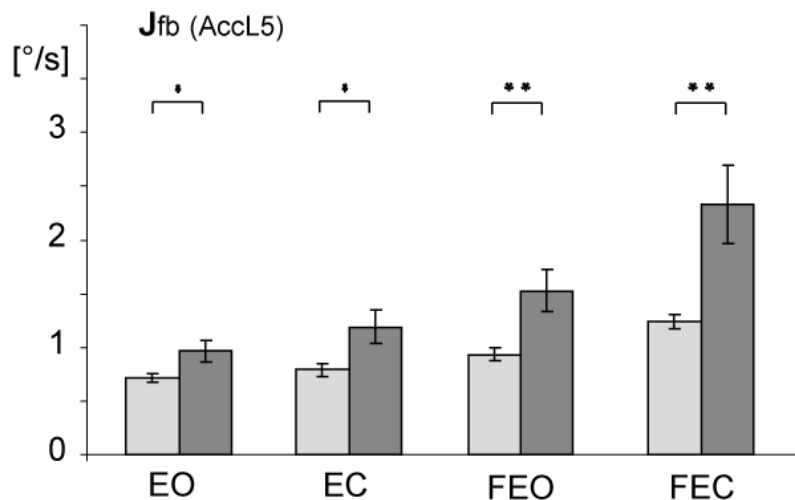


Fig. 3. Comparison of jerk (derivation of acceleration) at lower trunk in forward-backward direction between juniors (white) and seniors (black) in all experimental conditions. The asterisks denote significant differences * P<0.05; ** P<0.01 between the young and elderly subjects. The values of jerk are expressed as group averages \pm standard error of mean.

Discussion

Our results showed that data acquired from accelerometer sensors at trunk levels during quiet stance provided useful information about balance control. The jerk parameter created as the first derivation of acceleration was also appropriate for assessment of differences in balance between juniors and seniors. Similar conclusion about age-related changes in CoP parameters was found in all static conditions [1]. It was reported that the most sensitive view on postural steadiness during quiet stance was provided by CoP amplitude and velocity in FB direction.

If we assume that the acceleration at the level of L5 has a similar time course as the CoP displacement in the same direction, then it is obvious that the rate of change of acceleration in time should be sensitive indication of age-related changes in balance control. This conclusion is supported by the findings of authors [1] concerning about the velocity of CoP as a good indicator of postural changes due to age.

Our data confirmed also the inverted pendulum prediction that forward-backward and left-right accelerations of the trunk were related to the subsequent CoP displacements. These findings are in agreement with those of Zijlstra and Hof [4]. Furthermore, the accelerations show a more complex pattern than is expected based upon an inverted pendulum movement alone. Accelerometers afford opportunity to differ between ankle and hip strategy.

Both stabilometry and accelerometers provide valid information about postural control, but different information about postural strategies. The body-mounted sensors are accurate, inexpensive and portable and allow long-term recordings in clinical, sport and ergonomics settings. The body-mounted sensors do not hinder natural movement [2], because they can be unobtrusively attached to the body or can be part of clothing items [3]. Stabilometry is less sensitive in differing between ankle and hip strategy and also in assessing slight changes in postural control. For these reasons we advise using accelerometers as supplement or alternation of stabilometry in postural control research.

Acknowledgements

This work was supported by grant 2/0186/10 from Slovak grant agency VEGA.

References

- [1] Abrahamová D, Hlavačka F. Age-Related Changes of Human Balance during Quiet Stance. *Physiological Research*, 57: 957-964, 2008
- [2] Mayagoitia RE, Nene AV, Veltink PH. Accelerometer and rate gyroscope measurement of kinematics: an inexpensive alternative to optical motion analysis systems. *Journal of Biomechanics*, 35(4):537-42, 2002
- [3] Bonato P. Advances in wearable technology and applications in physical medicine and rehabilitation. *Journal of NeuroEngineering and Rehabilitation*, 25;2(1):2, 2005
- [4] Zijlstra W, Hof AL. Assessment of spatio-temporal gait parameters from trunk accelerations during human walking. *Gait & Posture*.18(2):1-10, 2003
- [5] Janssen M, Stokroos R, Aarts J, van Lummel R, Kingma H. Salient and placebo vibrotactile feedback are equally effective in reducing sway in bilateral vestibular loss patients. *Gait & Posture*, 31(2):213-7, 2010

Iron Oxides Particles in Globus Pallidus of Human Brain

¹M. Kopáni, ²M. Melník, ³M. Čaplovičová, ⁴J. Ivan, ⁵J. Maňka, ¹J. Jakubovský

¹Institute of Pathology, Faculty of Medicine, Comenius University, Bratislava, Slovakia,

²St. Elizabeth University, College of Health, Bratislava, Slovakia

³Department of Geology of Mineral Deposits, Faculty of Natural Sciences Comenius University, Bratislava, Slovakia,

⁴Institute of Materials and Machine Mechanics, ⁵Institute of Measurement Science Slovak Academy of Sciences, Bratislava, Slovakia

Email: martin.kopani@fmed.uniba.sk

Abstract. Iron is essential element used for fundamental cell functions, catalyst for chemical reaction. We used scanning and transmission electron microscopy, energy-dispersive microanalysis, electron diffraction, UV and EPR measurements for investigation of iron particles in globus pallidus of human brain. Scanning electron microscopy revealed iron rich complexes with Na, Si, P, S, Cl, Ca and Cu. Transmission electron microscopy revealed bumpy, solid particles of platy and sometimes rounded shape with the size around 3 μm. These ones were identified as hematite. Spectral measurements showed the presence of Fe(III), Cu(II) and some amount of Fe(II). We consider low-temperature process of hematite formation in human globus pallidus by aggregation-dehydration-rearrangement in aqueous environment through ferrihydrite influenced by organic and inorganic factors.

Keywords: iron, copper, brain, hematite

1. Introduction

Bio-mineralization process in organism is results of the interaction between metabolic processes products and the surrounding environment. Iron can be found in human body mainly in the form of ferritin. The size of ferritin core is 8 nm and has polyphasic structure consisting of ferrihydrite, hematite and magnetite. Pathological bio-mineralization may happen under some circumstances. The result of this process depends on many other factors such as chemical elements, temperature/pH and time. Iron induces reactive oxygen species (ROS), which react with iron resulting in iron oxides, hydroxides and oxide hydroxides.

2. Subject and Methods

Samples

Postmortem tissues were taken from globus pallidus externa of nine human brains without any clinico-pathological findings on a disease of central nervous system.

Scanning electron microscopy (SEM) and energy-dispersive X-ray analysis (EDX)

We used 3% fixation solution of glutar(di)aldehyde buffered by phosphate for scanning electron microscopy. Samples at autopsy were dehydrated in graded acetone, subjected to critical point drying of CO₂ (CPD 030, BAL-TEC, BG PRŮFZERT). Specimens were mounted on carbon stubs and coated with layer of carbon in ion sputtering apparatus (SCD 050, BALZERS, Lichtenstein). They were examined JXA 840 A (JEOL, Japan) with the accelerating voltage of 15 kV. Simultaneous EDX analysis was performed with the aid of

KEVEX 3205-1200 (Kevex, Valencia, Ca). The time period of spectrum collection was 200 s with the energy range 0.160 to 9 keV.

Transmission electron microscopy (TEM) and electron diffraction

The samples at autopsy for transmission electron microscopy investigation were fixed in glutar(di)aldehyde solution (SERVA, Heidelberg, Germany) for two hours. After dehydration the tissue by alcohol, samples were embedded into Durcupan ACM (Fluka AG, Busch, Switzerland) and cut by ultramicrotome with thickness 200 nm (C. Reichert, Wien, Austria). Noncontrasted ultrathin sections were investigated by selective electron diffraction in transmission electron microscope CM 100 (Philips, Eindhoven, Netherlands) with acceleration voltage of 80 kV.

Spectral measurements

Electronic spectra of the powdered samples in nujol mulls were recorded at room temperature on Specord 200. EPR spectra were measured using either a Bruker ER 200E SRC with an internal marker for determining the frequency on a Bruker EMX series with an ER 035 NMR gaussmeter and System Donner EMX frequency counter. The EPR spectra were measured in polycrystalline form at room temperature.

3. Results

SEM examination of globus pallidus samples shows iron-oxygen rich particles (see Fig. 1). The size of them with organic envelope was in the range of 0.5 – 3 μm . The shape of the complex is irregular. The chemical composition of iron rich complex is Na, P, S, Cl, and Ca. Some complexes contain also various amount of Cu (Cu K α 8,04 keV).

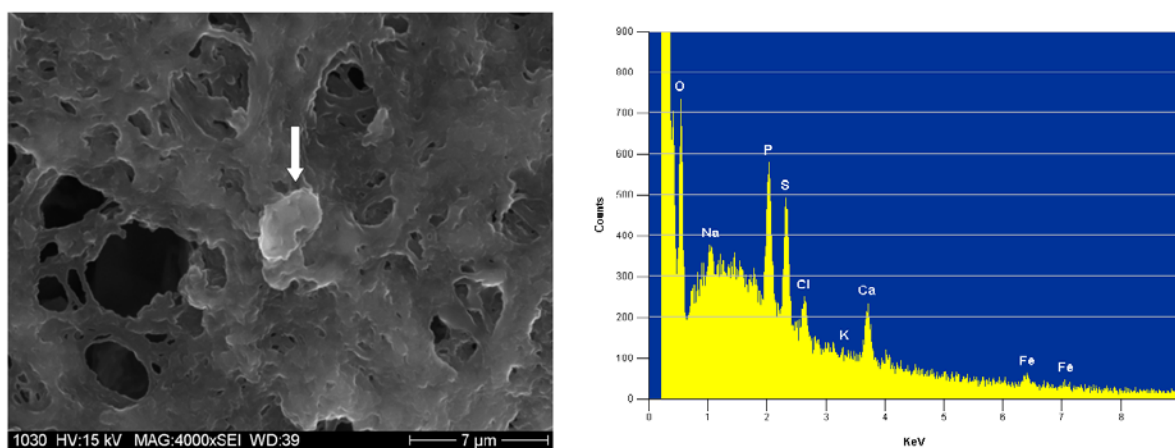


Fig. 1. Iron-oxide rich complex in globus pallidus of human brain (arrow) in SEM. EDX spectrum reveals the presence of Na, P, S, Cl, Ca and Fe. Range 0.160 to 9 keV, spectrum time collection was 200 s.

TEM investigation reveals bumpy, solid particles of irregular shape (see Fig. 2). Their size is 1-4 μm .

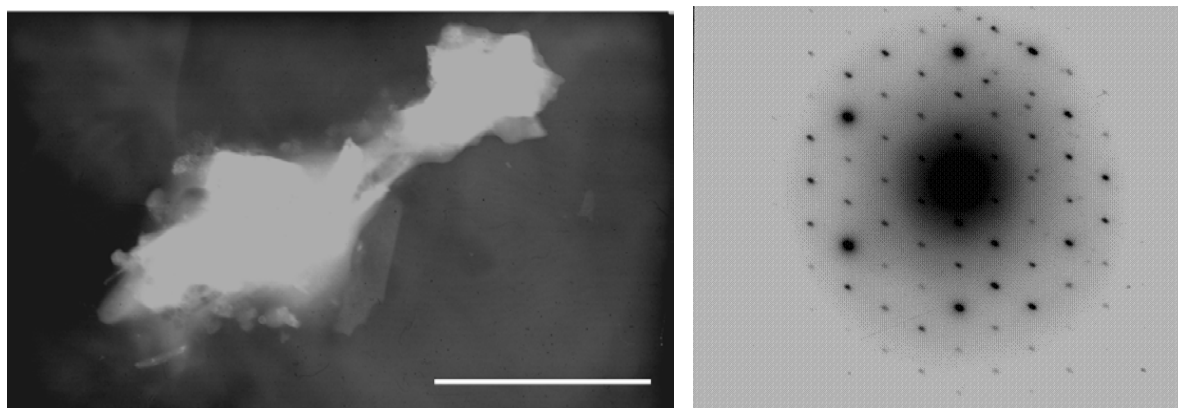


Fig. 2. Iron-oxide rich particle in TEM from globus pallidus of human brain (left) and its diffraction pattern corresponding to α -Fe₂O₃ (hematite). Scale bar = 3 μ m.

Selective electron diffraction in TEM shows well crystalline α -Fe₂O₃ with hexagonal structure with lattice parameters $a = 0.503$ nm, $c = 1.375$ nm corresponding to hematite (see Fig. 2).

The absorption features in the spectra are primarily charge transfer in origin with various weak features in are assigned as d-d transitions. Because of the oxidizing power of Fe(III), ligand to metal charge transfer bands often observe the very low intensity d-d absorption. However, it can be present some amount of Fe(II) as well. The solid state electronic spectra of the samples are almost identical with the band approximately at 398(\pm 2), 278(\pm 2), 230(\pm 2) and 214(\pm 2) nm. The EPR spectra of the samples are similar and complex. The pseudo rhombic spectra indicate the presence of Fe(III). The spectra show the additional bands at about 300(4) and 230(5) mT, which indicate the presence of Cu(II).

4. Discussion

Hematite is the end product of phase transformation of various iron oxides. The water/OH is fundamental for non-thermal conversion of ferrihydrite to hematite (α -Fe₂O₃). The most important chemical elements influencing iron oxides formation are phosphorus and sulphur. The higher concentration of phosphate is associated with non-crystallinity of iron biominerals. The iron overload leads to ROS induction and subsequently to the regulation of antioxidant defenses involving thiol (-SH) metabolism. Cysteine, amino acid with -SH group, effect ferrihydrite transformation into hematite, goethite and lepidocrocite at pH 6 – 8 [1]. It was observed spontaneous ferrihydrite transformation to well crystalline hematite with little goethite at room temperature for 20,4 years in closed vessels in aqueous system [2]. In globus pallidus of human brain there are conditions that favor hematite formation [3]. EPR spectra of the samples indicate the presence of Fe(III) iron, what is in good agreement with electron diffraction measurements. But the presence of Fe(II) can not be ruled out. Copper like iron has crucial role as redox active metal in biological reactions. But its elevated level is involved in the pathogenesis of many neurological diseases. ROS are scavenged by antioxidant enzymes Cu-Zn superoxide dismutase (Cu-Zn-SOD). Copper-iron interactions in the body have significant physiological and pathological relevance [4].

5. Conclusions

Iron is essential element used for fundamental cell functions, catalyst for chemical reaction in the brain. Its bio-mineralization process in the brain is the interaction between metabolic processes products, surrounding environment, chemical elements and compounds. Hematite is stable phase and is the end product of transformation of other iron oxides. In globus pallidus of human brain there are conditions that favor hematite formation. From this point of view copper-iron interaction may play significant role.

Acknowledgements

This work was supported by Agency of the Ministry of Education of the Slovak Republic for the Structural Funds of the EU, Operational Programme Research and Development (OPVaV-2008/4.1/01-SORO), Project Code 262 401 200 11 and by VEGA grant 2/0160/10.

References

- [1] Cornell RM, Schneider W, Giovanoli R. Phase-transformations in The ferrihydrite-cysteine system. *Polyhedron*, 8 (23): 2829-2836, 1989.
- [2] Schwertmann U, Friedl J, Stanjek H. From Fe(III) ions to ferrihydrite and then to hematite. *Journal of Colloid Interfaces Science*, 209: 215-223, 1999.
- [3] Schwertmann U, Murad E. Effect of pH on the formation of goethite and hematite from ferrihydrite. *Clays and Clay Minerals*, 31: 277-284, 1983
- [4] Collins JF, Prohaska JR, Knutson MD. Metabolic crossroads of iron and copper. *Nutrition Review*, 68:133-147, 2010

Spectral Analysis of Cardiovascular Parameters of Rats Under Irregular Light-Dark Regime

¹M. Teplan, ²L. Molčan, ²M. Zeman

¹Institute of Measurement Science, Slovak Academy of Sciences,
Bratislava, Slovak republic,

²Department of Animal Physiology and Ethology, Faculty of Natural Sciences,
Comenius University Bratislava, Slovak republic
Email: michal.teplan@savba.sk

Abstract.

Our study is related to shift work that possibly brings negative consequences on public health. Adaptation of cardiovascular parameters in rats to rotating phase delay shift in light regime was addressed. Prolongation of circadian rhythms was observed for blood pressures, heart rate and locomotive activity. Relative amount of circadian in comparison to ultradian rhythms was strongly activated by shifted regime in its first weeks, while being the lowest during persistent light conditions. Results contribute to understanding of physiological changes that accompany shift work.

Keywords: spectral analysis, Lomb-Scargle periodogram, unevenly sampled data

1. Introduction

Work connected with shifted day regime is a common feature of modern society. However, it can alter biological rhythms in humans. Chronic disturbances of biological clocks results in the suppression of circadian rhythms with possible negative consequences on the cardiovascular, neuroendocrine and gastrointestinal system. Such regime can contribute to the development of many neurological, cardiovascular [1] and cancer diseases [2].

In epidemiologic studies many factors are usually simultaneously involved, thus they can hardly elucidate all negative effects of shift work on physiologic parameters or reveal hidden causal interrelationships. Moreover, results of epidemiological studies linking shift work and various health risk factors often claim opposite effects. Therefore it is the advantage of animal model with treatment under controlled conditions, which can analyze different factors separately. Experimental studies using animal models are needed for better understanding of biological mechanisms of endogenous biological clocks and the way how they control variety of body functions.

Biological clocks control physiological and behavioural processes in all organisms, including humans. Regular synchronization is a necessary prerequisite for their normal function. Light is the most significant stimulus for resetting biological clocks in higher vertebrates [3]. The light signal is transferred from the retina to the central oscillator via the retinohypothalamic tract. In the central oscillator a rhythmic, circadian, transcription of clock genes occurs and the signal is transferred by output pathways into all organs of the body. In this work we assessed effects of light regime as the main factor, which can affect the central oscillator, on the control of cardiovascular system of rats.

The aim of this study was to analyze the effect of irregular light-dark regime on endogenous circadian and ultradian rhythms of selected physiological parameters in rats. In this part of the work cardiovascular parameters and locomotive activity are addressed. In particular, we

investigated how rotating phase delay shifts impact rhythmic changes of systolic and diastolic blood pressure (SP and DP), hearth rate (HR) and locomotive activity (LA) of rats.

2. Subject and Methods

Cardiovascular and locomotive variables were measured telemetrically using the telemetric sensor TA 11 PA-C40 (DSI St. Paul, Minnesota, USA). Monitoring begun two weeks after the surgical implantation of sensors into the abdominal aorta of 4 female normotensive rat (*Rattus norvegicus*, 12 month old of the beginning of the experiment). During a time span of 18 weeks the rats were exposed to the following set of conditions: control 12:12 light/dark (LD) for a period of one week; phase delay shifts of light-dark regime by eight hours every second day (Shift) for a period of 12 weeks; again LD 12:12 regime for one week; and finally continuous light (LL) for the last 4 weeks. The particular Shift conditions aimed to simulate light/dark conditions of shift work on fast rotation program. As the dark phase was prolonged by 8 h every second day, it is the most common shift work. Further details on experimental design, technical and animal treatment can be found in [4].

Measured variables were recorded every 10 s, stored in PC by program A.R.T Gold 4.1 (DSI, St. Paul, Minnesota, USA). Permanent and wireless data acquisition enabled on-line monitoring of recording variables in order to control overall functioning of the recording system and animal conditions. For further data control and preprocessing manipulation Microsoft Excel and MatLab programs were used.

For spectral analysis modified Lomb-Scargle periodogram (LSP) [5] was adapted in MatLab environment (MatLab 2008b, MathWorks, Inc. USA). LSP approach is identical with estimation of harmonic content of a data set at a given frequency by linear least-squares fitting to the model. This method has several advantages in comparison with traditional fitting techniques. The basic characteristic of our large data sets was the absence of regular sampling in recorded signal. Several reasons contributed to these irregularities: Manual weighting of the experimental animals, when wireless communication of the sensor with receiving plate was interrupted for a few minutes. Also occasional shorter malfunction of the recording system were involved. Still, our task was not to discard the data recorded for a number of days but rather to apply methods of analysis that are capable to deal with unevenly sampled data. Traditional spectral estimators need to modify irregularly sampled series by interpolation and even re-sampling. Unlike conventional Fourier analysis, LSP approach is capable to overcome dropout of smaller data fractions in time series. Another advantage of LSP approach is a possible choice of arbitrarily fine frequency step and examination of frequencies higher than the mean Nyquist frequency. Moreover, weighting of single power points occurs rather on a 'per point' basis instead of on a 'per frequency interval' basis. This means that the height of the peak is stable unlike in the case of Fourier types of analysis where height of a peak is confined with frequency step. As all other methods in the search for periodic signals, the LSP requires the assumption of independent Gaussian noise on the error term. Under this assumption one can estimate level of significance of resulting peaks. Peaks probability distribution is evaluated according to observance of certain amount of independent peaks. Basically, the LS algorithm is quite time demanding, however several less time consuming modifications with sufficiently exact approximation were developed, working at the level of $N \cdot \log N$ computational time demand (N is a number of frequency components to be estimated).

3. Results and discussion

Spectra obtained by LSP approach reveal animal reactions to different regime conditions. In our analysis we focus on circadian (20-30 h) and ultradian (2-6) rhythms. Strength and period localization of power peaks in these ranges was changing (Fig.1) according to the conditions. While during LL conditions circadian contribution is highly suppressed, during Shift conditions 24 h peak is elongated to longer periods.

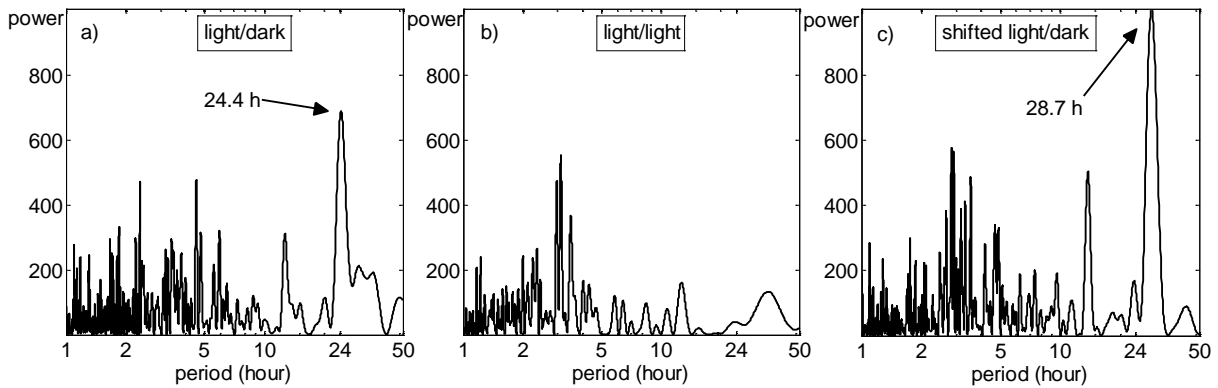


Fig. 1: Periodogram calculated by LSP approach for diastolic pressure of rat #1 for 3 different conditions: a) 12:12 light/dark revealing circadian peak near 24 h, b) persisting light conditions with emphasized activity of ultradian rhythms, and c) delayed shift in light/dark conditions with prolongation of circadian rhythm.

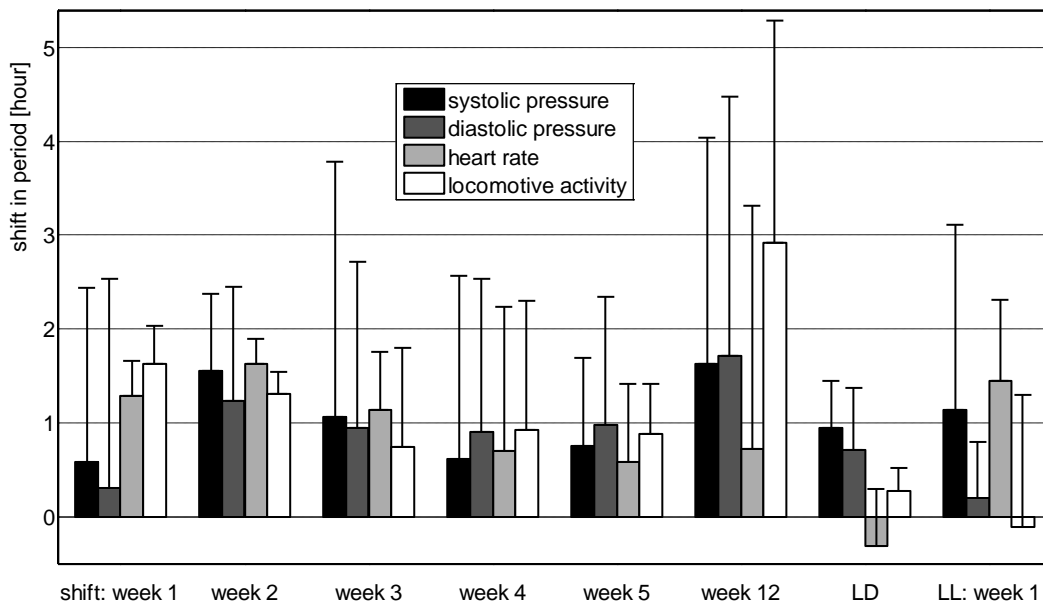


Fig. 2. Drift of main circadian periods from 24 h period represented by zero value on Y-axis. X-items represent week intervals under shift, light/dark and light/light regime. Mean data from all rats with standard deviations in a form of error bars are presented.

In Fig.2 the shift of circadian peak of 24 h is evaluated. The strongest drift occurred during the second and 12th week of the Shift conditions, suggesting more complex adaptation mechanisms of inner clocks. Initial wave of adaptation was weakened during the next weeks. Unfortunately, during week 6-11 no telemetry measurements were performed. Increased shift of SP and DP during LD conditions could be affected by tightly preceding of Shift conditions, while HR and LA seemed to be more flexible according to their reaction in this particular time point of the experiment. Whereas from the point of view of Fig.2 there were two

vertexes in deviation of 24 h peak – in Shift week no. 2 and 12, in Fig.3 there is substantial difference between these 2 weeks. Relative amount of LSP power from circadian range in comparison to the amount of power in ultradian range was more strongly activated only in the first and second week of Shift regime. During the last two weeks of persistent light conditions circadian rhythms were relatively eliminated in the highest extend.

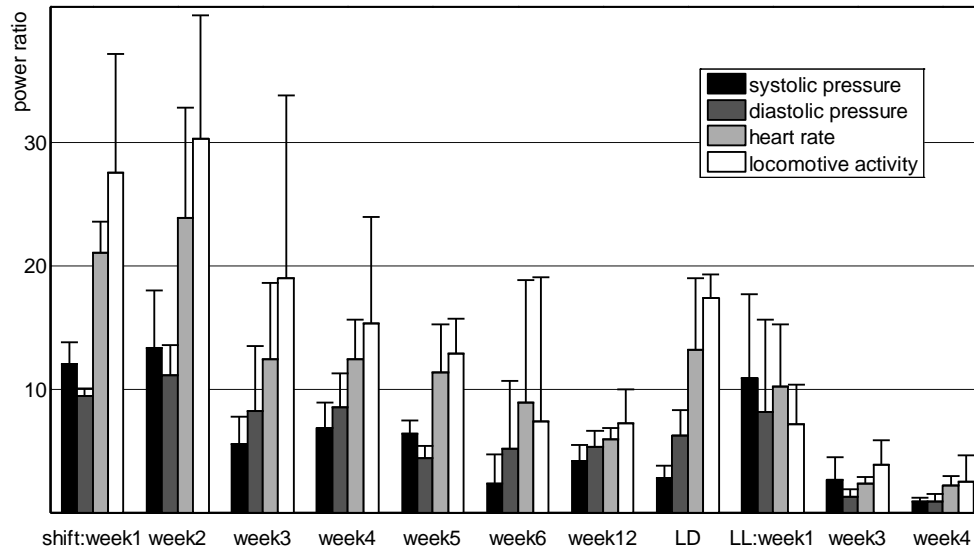


Fig. 3: Ratio of the power between circadian band (20-30 h) and ultradian band (2-6 h) during different regime conditions. X-items represent week intervals under shift, light/dark and light/light regime. Mean data from all rats with standard deviations in a form of error bars are presented.

We showed that the cardiovascular system of rats (blood pressure, heart rate) is able to adapt to delay shifts in light regime by lengthening of endogenous period of cardiovascular parameters. Moreover, ratio of circadian and ultradian cycles is changing. Results contribute to understanding of physiological changes that accompany shift work. In further work shifted regime in opposite – advanced direction will be spectrally analyzed.

Acknowledgements

This work was supported by Slovak Grant Agency for Science (grant VEGA No 2/0019/10 and APVV-0214-07).

References

- [1] Knutsson A. Health disorders of shift workers, *Occup Med (Lond)*, 53:103-108, 2003.
- [2] Davis S., Mirick D.K. Circadian disruption, shift work and the risk of cancer, *Cancer Causes Control*, 17:539-545, 2006.
- [3] Boivin, D.B., James, F.O. Light treatment and circadian adaptation to shift work, *Ind. Health*, 43:34-48, 2005.
- [4] Molčan, L. Effect of lightning regimen simulating shift work on rhythmic changes in the cardiovascular system and its regulation, Master thesis, Comenius University in Bratislava, Faculty of Natural Sciences, Dep. of Animal Physiology and Ethology, 2010.
- [5] Press, W.H., Teukolsky, S. Numerical recipes in C: The art of scientific computing. Cambridge University Press, 1992, 575-583.

3D Ultrasound Transmission Tomography Using Synthetic Aperture Focusing and Regularized Algebraic Reconstruction

¹R. Jiřík, ¹I. Peterlík, ¹J. Jan, ¹J. Fousek, ²M. Zapf, ²N. Ruiter

¹ Dept. of Biomedical Engineering, Brno University of Technology, Czech Republic,

² Karlsruhe Institute of Technology, Germany

Email: jirik@feec.vutbr.cz

Abstract. *Ultrasound transmission tomography is presented as an imaging modality for breast cancer diagnosis. A 3D reconstruction technique is proposed for estimation of sound-speed images for the Karlsruhe 3D ultrasound transmission tomograph. The problems of sparse spatial distribution of ultrasound transducers and of low signal-to-noise ratio are approached using synthetic aperture focusing. The image reconstruction is done based on regularized algebraic reconstruction. The proposed method is tested on simulated data as well as on measured phantom data.*

Keywords: ultrasound transmission tomography, sound speed, synthetic-aperture focusing, regularization

1. Introduction

Ultrasound computed tomography (USCT) is an imaging modality intended as an alternative to X-ray and conventional ultrasound imaging for breast cancer diagnostics. The acquisition setup is similar to X-ray computed tomography (CT) [1]. The imaged object is immersed in a water tank, surrounded by ultrasound transducers, where one transducer emits ultrasound wave while other transducers receive the transmitted and reflected/scattered signals. Images of several diagnostically important parameters can be reconstructed from the received signals: reflectivity, sound-speed and attenuation. This contribution focuses on sound-speed image reconstruction.

The USCT systems are still in the stage of research, mainly due to the complexity caused by phenomena inherent to ultrasound signal propagation, such as diffraction and refraction. Most published USCT devices are constructed as 2D systems (e.g. [2]), with a ring of fairly large transducers. Our approach is based on the Karlsruhe 3D USCT system, described in [3], where transducers are positioned on the surface of a cylindrical tank. Such transducer distribution enables fast acquisition of spatial 3D data and potentially a better spatial resolution of reflectivity images. However, it brings also several challenges, mainly sparse transducer distribution and low signal-to-noise ratio (SNR) due to small transducer size.

An approach to overcome the sparse transducer distribution and low SNR by means of synthetic-aperture focusing is presented. Example results reconstructed from synthetic data and data measured on a breast phantom are shown.

2. Subject and Methods

The problem of 3D sound-speed image reconstruction can be formulated as reconstruction from projections. Here, the projections are formed by time-of-flight (TOF) values, i.e. the ultrasound propagation times measured for each emitter-receiver combination. The sound-speed image reconstruction is solved as a 3D regularized algebraic reconstruction [4]. In contrast to the widely used filtered backprojection method, the algebraic reconstruction enables regularization of the reconstruction. Here, the regularization imposes piecewise

smoothness of the resulting sound-speed map, while preserving edges (details can be found in [4]). In addition, the algebraic reconstruction approach enables incorporation of non-straight propagation paths, e.g. due to refraction (not implemented here).

The data acquisition is done in 6 steps. After each step the whole USCT system is rotated, in order to increase the number of effective transducer positions [3]. Hence, the system has 6 times more “virtual transducer positions” than the physical number of transducers. The received radiofrequency transmission signals are measured and stored for all emitter-receiver combinations within each rotation position. This allows us to use a synthetic aperture formed of nearby virtual transducer positions by appropriately delaying and summing their radiofrequency signals. The aperture size is given by the number of neighbouring transducers used for focusing.

The focusing procedure is done in two steps: first, focusing on the receiver side (delay and sum of the radiofrequency signals) is done with the focal point positioned to each emitter of the emitter aperture. Then, the resulting focused signals are focused (i.e. accordingly delayed) so that the emitter aperture is focused to the center of the receiver aperture.

As it is practically impossible to run the above described processing on a standard PC computer (a dataset consists of about 3.5 million radiofrequency signals, which needs approximately 20 GB of storage capacity), the algorithm was parallelized and implemented using Matlab® Parallel Computing Toolbox™ and Matlab® Distributed Computing Server™ in a heterogeneous computing cluster environment.

3. Results

Simulated data

The sound-speed reconstruction was first tested on synthetic data. The simulation software was implemented to mimic the Karlsruhe 3D USCT system in the geometry and the data acquisition scheme. The radiofrequency signals were generated assuming propagation of spherical waves, with the centre frequency of 3 MHz and a bandwidth of 1.2 MHz. Frequency-independent attenuation along the propagation path was implemented. The propagation path between each emitter and receiver was assumed straight, i.e. no refraction was simulated. The resulting synthetic radiofrequency signals were distorted by additive Gaussian white noise. The signal-to-noise was set to 11 dB, which corresponds to the ratio estimated from the data measured using the Karlsruhe 3D USCT system. The simulated object was a simple model of breast immersed in water. It consisted of several homogeneous regions with different ultrasound speed values. The hemisphere simulating a breast shape included three spherical objects simulating various lesions. The simulated sound-speed values corresponded to the expected values for breast tissues [5] (1493 m/s for normal breast tissue, 1550 m/s for breast cancer lesion, 1568 m/s for cyst and 1584 m/s for fibroadenoma). The attenuation coefficient for the breast tissues was 0.7 dB/cm/MHz and for water regions it was set to 0 dB/cm/MHz.

The accuracy of the estimated sound-speed maps for various focusing apertures was evaluated in terms of the mean squared difference between the estimated map and the reference sound-speed map used for synthetic-data generation. The error values for some synthetic apertures are shown in Table 1 (note that the spacing between emitter and receiver elements are different). They show that too small and too large aperture size deteriorate the image quality. An optimal size of the emitting and receiving apertures has to be selected as a compromise between a too small aperture (influence on noise) and a too large aperture (geometry distortion due to loss of spatial information).

Table 1. Mean square errors of sound-speed maps for simulated USCT data, various combinations of the synthetic aperture sizes.

Emitting and receiving apertures [no. of virtual transducer positions]	Emitting and receiving apertures [mm x mm]	Mean square error [(m/s) ²]
1 x 1, 1 x 1	1 x 1, 1 x 1	72
3 x 3, 7 x 7	12 x 12, 18 x 18	54
7 x 7, 13 x 13	24 x 24, 36 x 36	79

Measured phantom data

The sound-speed reconstruction with synthetic-aperture focusing described above was tested on data recorded with the Karlsruhe 3D USCT system on a breast phantom with embedded cyst-mimicking lesions (CIRS triple modality breast phantom). To evaluate visually the sound-speed maps based on known outlines of structures in the selected slice, a reflectivity image was reconstructed using an algorithm described in [3] (Fig. 1 a, b). The breast-phantom outlines are denoted by dotted lines. Sound-speed maps in the selected slices are shown for the optimal aperture sizes in Fig. 1 c, d. Examples of images obtained for no focusing and too large synthetic apertures are shown in Fig. 2. The images show that optimal focusing substantially improves the spatial consistence over no focusing (which lacks spatial consistence) and over too large aperture used for focusing (which leads to blurred images). The sound-speed of the main-body material was in accordance with the phantom specifications (approximately 1450 m/s).

The reconstructed 3D images showed clear outlines of the breast phantom. However the phantom geometry was slightly deformed. The breast object appeared smaller than in the reflectivity images. The lesions from the reflectivity images were visible also in the sound-speed image (consistently in neighboring layers) but in shifted positions. This can be explained by beam refraction. Due to the cone-like shape of the breast phantom, for some emitter-receiver combinations the ultrasound beam path is close to a tangent to the breast surface. The refraction effect is not taken into account by the presented image reconstruction because it assumes straight beams.

4. Discussion and Conclusions

The presented synthetic-aperture focusing improves the reconstruction of sound-speed images in case of sparse distribution of small transducers in USCT. The synthetic aperture size has to be chosen as a compromise. Larger aperture leads on one hand to better suppression of diffraction and higher SNR, while, on the other hand, decreasing the spatial resolution of the reconstructed images.

To account for beam refraction, this effect will be included in the algebraic reconstruction algorithm by assuming non-straight beam-propagation path. The evaluation will be extended by construction and imaging of a sound-speed phantom with completely known reference sound-speed values for all used materials.

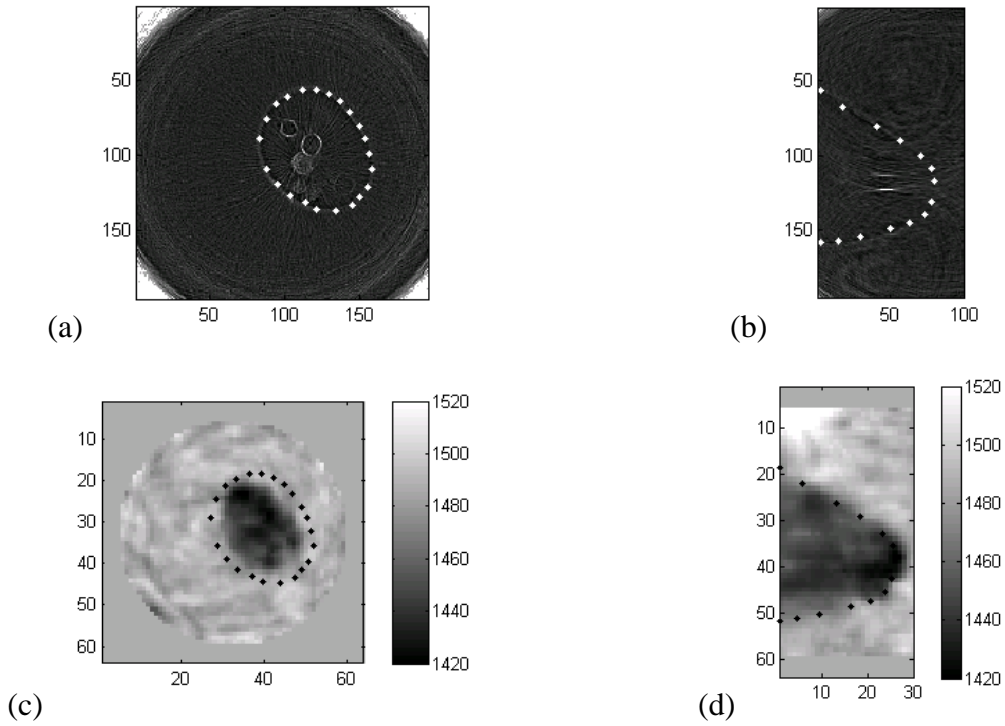


Fig. 1. (a), (b) Reflectivity images, coronal and sagittal slices, respectively. (c), (d) Sound-speed images, coronal and sagittal slices, respectively, optimal synthetic aperture size (12x12, 18x18 mm for emitter and receiver apertures).

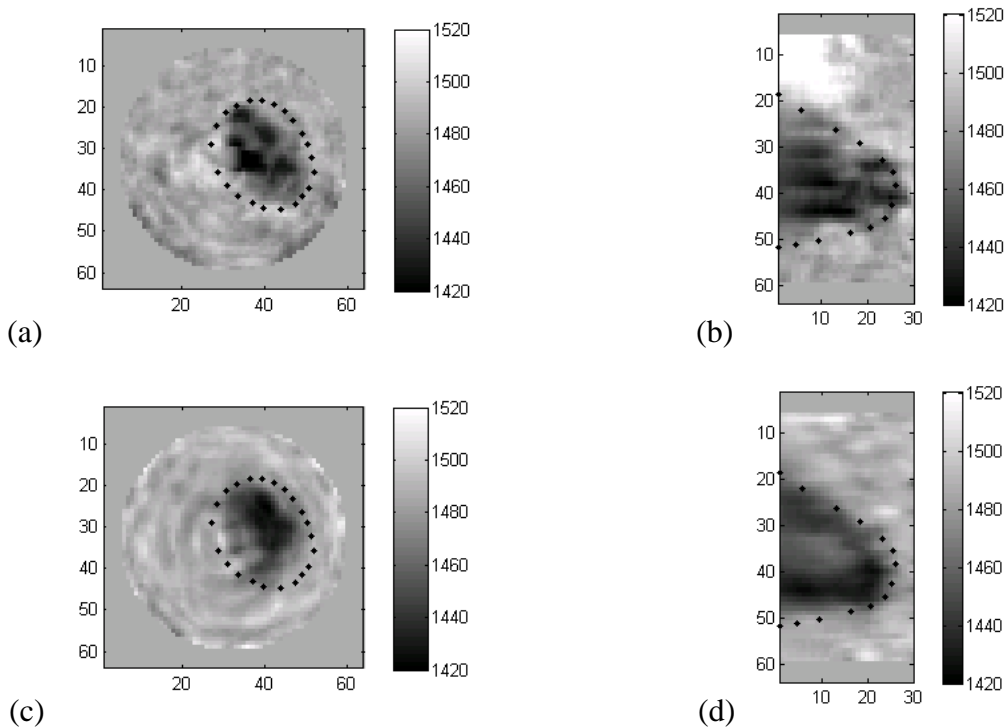


Fig. 2. (a), (b) Sound-speed images, coronal and sagittal slices, respectively, no focusing. (c), (d) Sound-speed images, coronal and sagittal slices, respectively, too large synthetic aperture size (24x24, 36x36 mm for emitter and receiver apertures).

Acknowledgements

The project has been supported by the Czech Ministry of Education, Youth and Sports (Research Center DAR, proj. no. 1M6798555601) and the joint program of the German Academic Exchange Service and the Czech Academy of Science, partly also by the research frame of the Czech Ministry of Education, Youth and Sports (grant no. CEZ MS 0021630513). We are also grateful to MetaCentrum, an activity of the CESNET association, for offering the distributed-computing resources.

References

- [1] Kak AC, Slaney M. Principles of Computerized Tomographic Imaging. Society of Industrial and Applied Mathematics; 2001.
- [2] Duric N, Littrup P, Poulou L, Babkin A, Pevzner R, Holsapple E, Rama O, Glide C. Detection of breast cancer with ultrasound tomography: First results with the Computed Ultrasound Risk Evaluation (CURE) prototype. *Med Phys* 2007;34:773–785.
- [3] Gemmeke H, Ruiter NV. 3D Ultrasound Computer Tomography for Medical Imaging. *Nuclear Instruments and Methods in Physics Research*. 2007; 550:1057–1065.
- [4] Jiřík R, Peterlík I, Jan J, Ruiter NV, Zapf M. 3D Regularized Speed-Map Reconstruction in Ultrasound Transmission Tomography. 2009 IEEE International Ultrasonics Symposium, Roma, Sept. 2009. 2272–2275.
- [5] Glover GH, Sharp JC. Reconstruction of ultrasound propagation speed distribution in soft tissue: Time-of-flight tomography. *IEEE Trans. Sonic and Ultrasonics* 1977; 24:229–234.

In Vivo Measurement of Fast Transversal Relaxation Times of Achilles Tendon Using Ultra-High Field MRI

^{1,2} V. Juras, ²S. Zbyn, ²Ch. Pressl, ^{1,2}P. Szomolanyi, ¹I. Frollo, ²S. Trattnig

¹Institute of Measurement Science, Slovak Academy of Sciences, Bratislava, Slovakia

² Medical University of Vienna, Dept. of Radiology, Vienna General Hospital, Austria
Email: Vladimir.Juras@savba.sk

Abstract. *The aim of the study was to investigate proton transverse relaxation times combined with local magnetic field non-uniformities (T_2^*) of human Achilles tendon in vivo as a prospective marker for diagnosis of early pathological changes. Achilles tendon consists mainly of highly oriented collagen fibres resulting in lower water mobility, and therefore fast relaxation processes of protons. Mapping of ultra-short T_2^* using conventional MR techniques is considered challenging using conventional sequences. Ten volunteers and two patients with chronic tendonitis were included in the study. 3D ultra-short time echo (TE) sequence with radial sampling was used. From the images acquired at different TEs (0.07, 0.20, 0.30, 0.46, 0.59, 0.74, 1.00, 1.50 ms), T_2^* map was constructed by pixel-by-pixel fitting of signal intensities to mono-exponential function. Resulting maps were evaluated in various anatomical regions (tendon-muscle junction, medial part and insertion). Mean bulk T_2^* in volunteers was 0.56 ± 0.18 ms. In patients with chronic Achillotendonitis, T_2^* values were higher in comparison to healthy volunteers. Advanced quantitative imaging of human Achilles tendon has a potential to benefit from early diagnosis of degenerative processes and so prevent the development of serious tendon damage, such as partial tear or rupture.*

Keywords: MRI, Achilles tendon, T_2^* , ultra-short

1. Introduction

The conventional clinical MRI sequences are predominately used for visualizing the tissues with relatively long transversal T_2 relaxation times. In the human body, however, there are some tissues characterized by a very short T_2 . These highly oriented tissues, such as tendons ($T_2 \sim 1.5$ ms), menisci ($T_2 \sim 5$ ms), ligaments ($T_2 \sim 5-10$ ms) or cortical bone ($T_2 \sim 0.5$ ms), give little to no signal using conventional sequences so they appear black on standard MR images [1].

Considering the relaxation times in Achilles tendon (AT) to be in order of 1 ms, a very short echo time (TE) must be used to acquire signal directly from the tendon. Recent developments of UTE made this sequence to be clinically applicable in a whole variety of cases. UTE pulse sequences have TEs (in sense of ultra-short imaging, TE is often referred to as 'time of encoding') about 10 to 20 times shorter than the shortest generally available on modern clinical systems. Signal is produced by half-radiofrequency excitation with radial sampling from the centre of the k-space. Using UTE imaging, it is possible to come to a detectability of tissues with T_2 relaxation times of 0.1 to 0.01 ms [2].

The aim of this study was to investigate ^1H transverse relaxation times combined with local magnetic field non-uniformities (T_2^*) of Achilles tendon in vivo in healthy volunteers with 3D-UTE sequence. T_2^* may prospectively serve as a marker for diagnosis of early pathological changes in Achilles tendon.

2. Subject and Methods

Ten volunteers (5 males, 5 females, mean age of 25 +/- 3 years, free of any pain and any abnormality in the Achilles tendon in the past) and 3 patients (1 male, 2 females, mean age of 28 +/- 4 years) with chronic Achillotendinitis were included in the study. The ankle of each subject was placed within the coil in the way that the foot platform and the axis of tibia created 110° angle and the Achilles tendon was parallel to the static magnetic field B₀ as much as possible (taking into account a natural curvature of the tendon). Volunteers underwent MRI examination at 7T, (Siemens Healthcare, Erlangen Germany). The investigational 7T MR system is equipped with the same gradient strength. Twenty-eight channels transmit/receive knee coil (QED, Quality Electrodynamics, Mayfield Village, OH, USA) with diameter of 18 cm was used. To acquire a signal from Achilles tendon, half-pulse 3D-UTE sequence with radial k-space sampling was used. The data were sampled on the projection originating from the center of the k-space and the ending points of all projections covered a spiral on a sphere. The reconstruction was performed using regridding algorithm and 3D-iFFT to produce resulting images [3].

Eight different TEs were used [0.07, 0.20, 0.30, 0.46, 0.59, 0.74, 1.00, 1.50] ms. The rest of the sequence parameters was the same in each scanning: TR, 400ms; averages, 2; bandwidth, 560 Hz/px; matrix, 256 x 256 x 256 (isotropic); flip-angle, 12°, FOV, 300mm, number of projections 12.000. Standard shimming method implemented on both scanners by manufacturers was used. Total scanning time was 12 min (8 x 1:30 min) at 7T.

T_2^* maps were generating by mono-exponential three parameter fitting on pixel-by-pixel basis in custom-built IDL (Interactive Data Language, RSI, Boulder, CO) script using mpcurvefit routine (Craig B. Markwardt, NASA/GSFC Code 662, Greenbelt, MD20770) for each slice. Coefficient of determination (R^2) was stored for later T_2^* correction [4].

3. Results

Mean bulk T_2^* was 0.56 ± 0.18 ms; Example T_2^* map and corresponding fitting curve are depicted on Fig. 1 and Fig. 2, respectively. The individual T_2^* values for all subareas are summarized in the Table 3. When looking at the anterior-posterior differences of Achilles tendon in the sense of T_2^* , statistically significant differences were observed for bulk values and so for individual subareas. Regarding the precision of T_2^* calculation, R^2 was 0.90 ± 0.03 in average.

Table 1. The summary of T_2^* measured in healthy Achilles tendon

	T_2^* [ms]	stdev	area [mm ²]	SNR
UA	0.495	0.153	93.73	137.17
UP	0.551	0.170	90.57	54.82
MA	0.452	0.180	35.20	131.65
MP	0.574	0.177	61.39	95.82
LA	0.448	0.184	27.10	118.14
LP	0.812	0.352	25.25	109.60
BULK	0.555	0.181	333.25	107.87

In patients with tendinitis (Fig. 3), significant increase of T_2^* values was found in lower part of Achilles tendon (0.66 ± 0.09 ms in anterior region and 0.65 ± 0.15 ms in posterior region). In average, T_2^* in patients was 0.80 ± 0.13 in anterior region and 0.73 ± 0.12 in posterior region. An example of MR examination of patient with Haglund's disease accompanied with Achillotendonitis and corresponding T_2^* map are depicted on Fig. 3. Compared to healthy

volunteers, the T_2^* were higher in patients of +42% (anterior), +11% (posterior) and +27% (bulk).

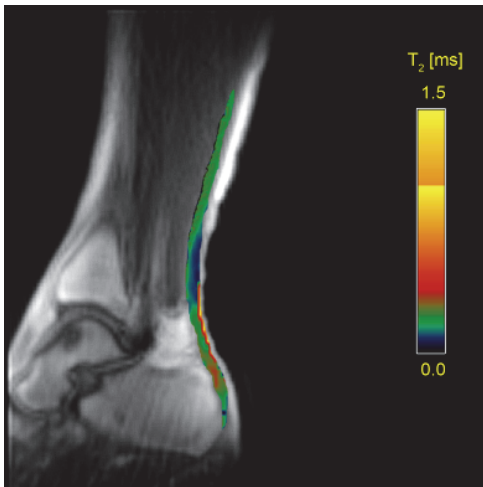


Fig. 1. Pseudo-color coded T_2^* map of healthy 25 years old volunteer acquired by 3D-UTE at 7T (overlaid on image acquired at the minimum TE 0.07 ms).

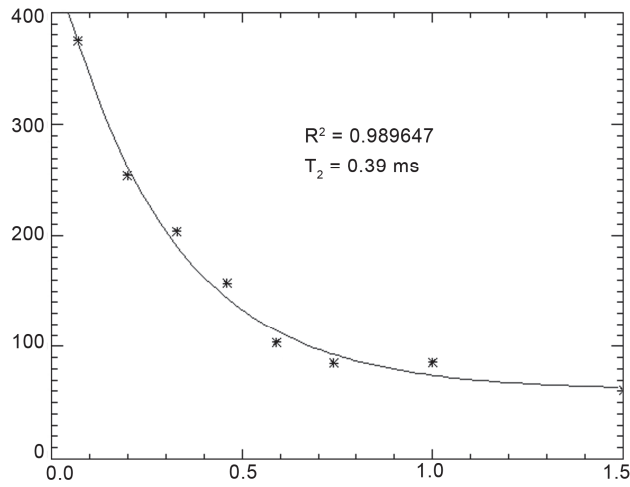


Fig. 2. Exponential decay from representative pixel selected in Achilles tendon of healthy volunteer. On both images, stars represent the measured intensity values, while the solid line is the mono-exponential fitting curve. Offset of the curve is caused by the hardware noise.

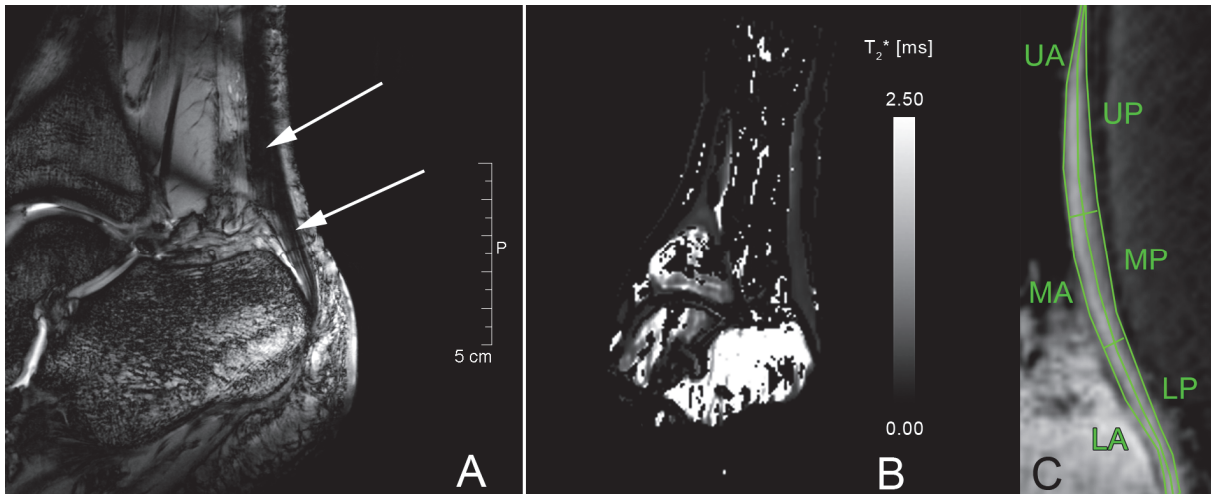


Fig. 3. A) 3D TRUFI T_2 -weighted morphological image of 26 years old patient with Haglund's disease and tendonitis measured at 7T. The thickening of the Achilles tendon is obvious (upper arrow) and hyper-intense signal in the lower region signalizes the inflammation process. B) T_2^* values in Achilles tendon in patients were considerably increased in comparison to healthy volunteers. The definitions of ROI segmentation are sketched on the C) with this meaning of labels: UA: upper anterior, UP: upper posterior, MA: medial anterior, MP:medial posterior, LA: low anterior, LP: low posterior.

4. Discussion and Conclusion

In this study, the first results of the quantitative assessment of Achilles tendon at ultra-high field MR are presented. 3D-UTE sequence used at ultra high-field provided a remarkable contrast of Achilles tendon by acquiring the signal directly from tissue.

To compare our results with already published studies at different field strength, Du et al. observed T_2^* of 0.78 ± 0.07 ms at 3T using 2D-UTE sequence [5]. Robson et al. demonstrated region-dependent T_2^* values in Achilles tendon - in anterior region 88% of

short component ($T_2^* \sim 0.53$ ms) and 12% of long component ($T_2^* \sim 4.80$ ms), and in posterior region 70% of short component ($T_2^* \sim 0.60$ ms) and 30% of long component ($T_2^* \sim 4.20$ ms) [6]. Filho et al. reported the T_2^* values in lateral, central, medial and bulk region of 2.10 ± 0.43 , 2.23 ± 0.31 , 1.89 ± 0.34 and 2.18 ± 0.30 , respectively [7]. These values are different from those measured in our study which may be caused by tissue changes in cadaver samples and non-physiological tense. Henkelman et al. used CPMG sequence for T_2 mapping; they measured relatively high values - 7.2 ± 0.6 ms at 0° (angle between tendon and static magnetic field) and 23 ± 2 ms at 55° . T_2 and T_2^* effects cannot be distinguished using the UTE sequence [8]. One of the limitations of the study is the in-plane resolution of images. The used matrix was 256×256 and FOV 300×300 mm which leads to resolution of 1.17 mm per pixel. This limits the examination of some clinically interesting areas, such as tendon insertion. Theoretically, it would be possible to increase the resolution, but this would cause even stronger k-space undersampling and therefore stronger artefacts and in addition the total acquisition time would dramatically increase. For the investigation of the Achilles tendon at higher resolution, the 2D-UTE sequence is more suitable.

In conclusion, advanced qualitative and quantitative imaging of human Achilles tendon using 3D-UTE sequence may provide additional information to standard clinical imaging in reasonable scan times. It has the potential to provide early diagnosis of degenerative processes and so prevent the development of serious tendon damage, such as partial tear or rupture.

Acknowledgements

Funding for this study was provided by the Vienna Spots of Excellence des Wiener Wissenschafts- und Technologie-Fonds (WWTF) -Vienna Advanced Imaging Center - VIACLIC and the Slovak Scientific Grant Agency VEGA 2/0090/11.

References

- [1] Wang, J.H., Mechanobiology of tendon. *J Biomech*, 2006. 39(9): p. 1563-82.
- [2] Gatehouse, P.D. and G.M. Bydder, Magnetic resonance imaging of short T2 components in tissue. *Clin Radiol*, 2003. 58(1): p. 1-19.
- [3] Nielles-Vallespin, S., et al., 3D radial projection technique with ultrashort echo times for sodium MRI: clinical applications in human brain and skeletal muscle. *Magn Reson Med*, 2007. 57(1): p. 74-81.
- [4] Juras, V., et al., Regression error estimation significantly improves the region-of-interest statistics of noisy MR images. *Med Phys*, 2010. 37(6): p. 2813-21.
- [5] Du, J., et al., Orientational analysis of the Achilles tendon and enthesis using an ultrashort echo time spectroscopic imaging sequence. *Magn Reson Imaging*, 2009. 28(2): p. 178-84.
- [6] Robson, M.D., et al., Magnetic resonance: an introduction to ultrashort TE (UTE) imaging. *J Comput Assist Tomogr*, 2003. 27(6): p. 825-46.
- [7] Filho, G.H., et al., Quantitative characterization of the Achilles tendon in cadaveric specimens: T1 and T2* measurements using ultrashort-TE MRI at 3 T. *AJR Am J Roentgenol*, 2009. 192(3): p. W117-24.
- [8] Henkelman, R.M., et al., Anisotropy of NMR properties of tissues. *Magn Reson Med*, 1994. 32(5): p. 592-601.

Low-Field BOLD Effect Induced by Alcohol and Caffeine Measured in the Upper Limb: A Feasibility Study

¹L. Valkovic, ^{1,2}V. Juras, ¹D.Gogola, ¹L.Vojtisek, ¹I. Frollo

¹Institute of Measurement Science, Department of Imaging Methods, Slovak Academy of Sciences, Bratislava, Slovakia

²Medical University of Vienna, Department of Radiology, Vienna General Hospital, Vienna, Austria

Email: ladval@chello.sk

Abstract. *Low-field magnetic resonance imaging (MRI) is even in the time of high-field strength scanners still widely used in many applications. Unfortunately, low-field MRI has many physical and technical limitations and therefore is not being used for special MR methods like functional MRI (fMRI), diffusion tensor imaging (DTI) or MR spectroscopy. In this paper, we focused on testing a feasibility of a modern low-field system for a blood-oxygen level dependent (BOLD) imaging. For this purpose, a study based on alcohol and caffeine consumption was performed, since these substances capability of influencing the blood flow. Low-field system is shown to be a feasible system to image the BOLD effect and therefore has potential for future fMRI examinations.*

Keywords: BOLD, alcohol, caffeine, low field, fMRI

Introduction

Even though MR hardware developers concentrate mainly on constructing high-field strength scanners with strong gradient systems, not every application profits from these technological advantages. Interventional and intra-operative MRI as well as orthopaedic MRI under load call for space and accessibility, which is usually, provided by low- to ultra-low field MR scanners with open bore or sandwich-design, [1, 2]. While advanced MRI methods such as functional MRI, diffusion weighted MRI or magnetic resonance spectroscopy would be advantageous in this context, technical (e.g. gradient design) as well as physical (e.g. susceptibility effects, SNR) limitations largely prevent their application especially in ultra-low field intra-operative MRI. Especially functional MRI is considered to be a high-field strength phenomenon and is not used in MR scanners below 1 T. Functional MRI combines at once the high spatial resolution anatomic imaging capabilities of conventional MRI with hemodynamic specificity of nuclear tracer techniques (positron emission tomography). This allows spatially accurate mapping of human brain function to underlying anatomy and tomographically image the second-by-second time course of the hemodynamic and metabolic responses to neuronal activation, [3]. Hence, the focus of this study is feasibility testing of low-field blood-oxygen level dependent (BOLD) MRI at commercial 0.18 T scanner with regard to its potential for future intra-operative applications.

In general, the BOLD effect is influenced by blood flow, blood volume and oxygen consumption, but not all of these aspects need to be influenced to measure the changes in signal intensity. Therefore substances capable of changing the blood flow, like alcohol and caffeine [4, 5] are used for the purposes of this study. Caffeine's primary biological effect is the competitive antagonism of adenosine receptor, [6]. And as such it has vasoconstriction effect, thus decreasing the blood flow and blood volume and therefore has negative effect on the BOLD signal. On the other hand, alcohol in low concentrations has vasodilatation effect, thus increasing the blood flow and blood volume. Therefore after alcohol consumption positive BOLD effect can be measured.

The changes in the signal intensity due to blood volume and blood flow changes in the hand are in this study referred to as induced "BOLD" effect. It is shown that negative and positive BOLD responses can be detected in the hand, using low-field MR system, after intake of caffeine and alcohol respectively.

Materials and Methods

The MR images before and after alcohol/caffeine consumption from 5 volunteers (1 female, 4 male; mean age 29 +/- 2.5; range 25-31 years; all fair alcohol and no caffeine users) were used. For alcohol experiments an average amount of 50 ml of 40 % pale alcohol was used with consideration of body weight. For caffeine experiments was used a standard 330 ml energy drink containing 105.6 mg of caffeine. MR examinations were performed on a 0.18 T MR scanner (E-scan Opera, Esaote Genoa, Italy) and MR signal was acquired using a wrist coil equipped with motion diminishing system and reference phantom for intensity normalization, described in [7]. The GRE sequence parameters were set as follows: TE of 22 ms, TR of 700 ms, FA of 40°, FOV of 150×150 mm², 256×256 pixels matrix, slice thickness of 4 mm and number of slices 12. The total protocol time for one substance was 30 minutes, consisting of a baseline-reference measurement followed by oral substance consumption (in-situ) and following-measurements in time intervals 5 and 15min after the consumption. The pre-processing consisted of image realignment, intensity normalization and spatial smoothing. Afterwards the difference between pre and post images was calculated and thresholded for information extraction. Mean values of selected ROIs (skin of a hand dorsum containing three of the superficial veins as depicted on Fig. 1) of pre and post alcohol/caffeine consumption images were compared by a T-test (P-values <0.05 were considered statistically significant).

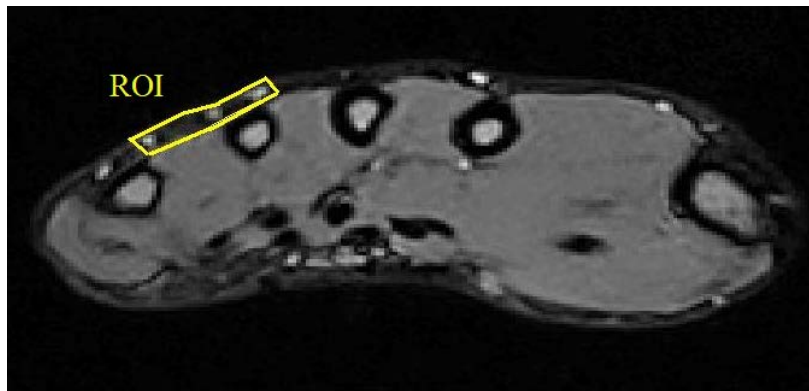


Fig. 1. T₂* baseline image showing ROI selection on the dorsal skin area

Results

The mean signal intensity value of a selected ROI of a baseline image was for the alcohol measurement across the volunteers 815.84 with the mean SNR of 40.3. After 15 min after alcohol consumption the mean signal intensity value was 932.698 with the mean SNR value of 46.38. The average increase of signal intensity for this measurement was 116.86. The relationship between the signal intensity in the selected ROI and the alcohol consumption was substantial ($p < 0.01$). For the caffeine experiment the mean signal intensity value of the ROI of a baseline image was 984.54 with the mean SNR of 58.04. In the measurement after 15 minutes after the caffeine consumption decreased the mean signal intensity value of the ROI to 781.53 with the mean SNR level of 60.37. The average decrease of signal intensity for the caffeine measurement was 203.01. T-test for comparison of signal intensity means after caffeine consumption reached significant level ($p < 0.005$).

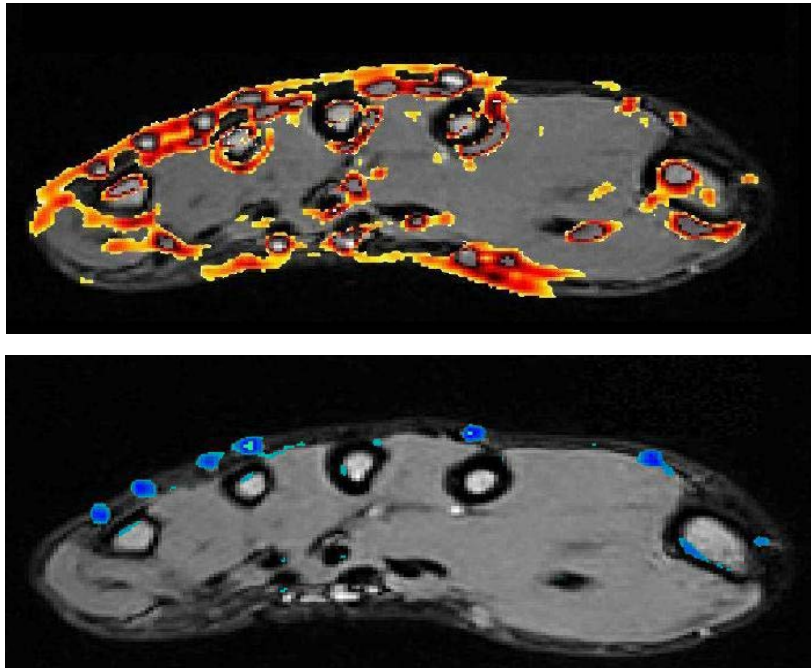


Fig. 2. Thresholded difference images overlaid over the corresponding after consumption images. The alcohol influence is depicted in the image on the top and the caffeine influence in the image on the bottom. The change in the signal intensity in the venal areas is clearly visible. The small artefacts visible inside the hand are caused by the hand fixation and movement of the inner tissue.

Discussion

Our results showed that it is possible to observe the signal intensity change near the veins after consumption of either alcohol or caffeine using very low-field MRI. It was possible to measure positive BOLD response in case of alcohol and negative BOLD response in case of caffeine (Fig. 2). The signal intensity change in the selected ROI was determined to be statistically significant in both cases. The reason for the signal intensity increase in the case of alcohol could be the decrease of deoxygenated haemoglobin concentration caused by blood flow and blood volume increase. The signal intensity decrease in case of caffeine is very likely caused by an opposite effect.

The effect has a very fast onset and increases over time. This was observed by the difference in the two time moments when the measurement was performed. After 5 minutes was the effect in the case of alcohol non-significant and in the case of caffeine just above the significance level. But in 15 minutes after the substance consumption the signal intensity change reached significant level in both cases. The earlier significance level of signal intensity change after caffeine consumption can be explained by longer drinking time.

As alcohol and caffeine have long-term effects there was no need of fast imaging methods like EPI and the sensitivity of a low field MR scanner is sufficient to measure the induced BOLD response as our results clearly showed.

In the next step, in order to use conventional low-field system without any modification to the hardware as was done in the only intra-operative fMRI feasibility study so far [8], a functional brain paradigm with long blocks of activation and baseline will be designed to provide enough time to acquire gradient echo images. These experiments are the base for potential developments and implementation of an EPI capable gradient system for clinical low-field MRI.

Conclusions

Low-field BOLD imaging is a very important step towards interventional and intra-operative fMRI measurements. This study has shown that modern commercial low-field systems are sensitive enough without any additional hardware and therefore feasible to provide fMRI measurement, but need a long term paradigms or a fast gradient systems capable of EPI sequences.

Acknowledgements

This work was supported by Grant Agency of the Slovak Academy of Sciences, VEGA 2/0090/11 and by State program ŠPVV no. 2003SP200280203.

References

- [1] Blanco, R.T., et al. Interventional and intraoperative MRI at low field scanner--a review. *Eur J Radiol.* 56(2): 130-42, 2005.
- [2] Yoshioka, H., et al. Low-field compact magnetic resonance imaging system for the hand and wrist in rheumatoid arthritis. *Journal of Magnetic Resonance Imaging.* 23(3): 370-6, 2006.
- [3] Rosen, B.R., R.L. Buckner, and A.M. Dale. Event-related functional MRI: Past, present, and future. *Proceedings of the National Academy of Sciences of the United States of America.* 95(3): 773-780, 1998.
- [4] Esposito, F., et al. Alcohol increases spontaneous BOLD signal fluctuations in the visual network. *Neuroimage.* 53(2): 534-43, 2010.
- [5] Chen, Y. and T.B. Parrish. Caffeine dose effect on activation-induced BOLD and CBF responses. *Neuroimage.* 46(3): 577-83, 2009.
- [6] Chou, T.M. and N.L. Benowitz. Caffeine and Coffee - Effects on Health and Cardiovascular-Disease. *Comparative Biochemistry and Physiology C-Pharmacology Toxicology & Endocrinology.* 109(2): 173-189, 1994.
- [7] Valkovic, L., et al. The effect of stress on MR image contrast in the human hand at low field NMR. In proceedings of the ELITECH'10. Slovakia. 2010.
- [8] Gering, D.T. and D.M. Weber. Intraoperative, real-time, functional MRI. *Jmri-Journal of Magnetic Resonance Imaging.* 8(1): 254-257, 1998.

Design and Construction of a Head Probe Coil for Vocal Tract Imaging

D. Gogola, L. Valkovič, J. Příbil, T. Dermek, L. Vojtíšek, I. Frollo
Institute of Measurement Science of the Slovak Academy of Sciences,
Dubravská cesta 9, Bratislava, Slovakia

Abstract. *Magnetic resonance imaging (MRI) is nowadays a most widely use in medicine for diagnostic imaging and in research studies. At the present time many research studies follow with problematic about human vocal tract modeling. This paper is devoted to the design and optimization of head probe coil for vocal tract imaging. For the reason of requirement voice recording during measurement, this head probe coil was made and tuned for MR tomograph with field strength 0.178 T. This produces less noise like MR tomograph with stronger magnetic field.*

Keywords: probe coil, MR tomography, voice tract imaging

1. Introduction

The human vocal tract imaging is necessary for the three-dimensional modeling of human vocal tract. The three-dimensional (3D) modeling of human vocal tract is necessary for understanding the basic physical principles for the creation of human speech and voice as close to reality as possible. Such models are helpful for modeling the real clinical situation, such as influence of various inborn defects in human supraglottal spaces on speech and voice or simulations of various post surgical states in patients [1].

The human voice is made up of oscillation of vocal cords due to airflow from the lungs. Resonant frequency of the vocal cords is basic frequency of voice. While most of the acoustic energy of the human voice and speech is contained in the frequency range between 70 Hz to 5 kHz high-fidelity simulation of human voice and speech aims at producing sounds within the whole audible frequency range, i.e. 20 Hz - 20 kHz. Consequently, it is important to develop models that are able to simulate the acoustic properties of the vocal tract with a high accuracy. These models should allow simulating pathological changes or voice quality variations due to slight geometry modifications of the human supraglottal acoustic space. [2]. In previous studies it has been shown that even small changes in vocal tract geometry significantly affect the frequency above 4 kHz [1].

3D models of human glottal acoustic space during the formation vowels are acquired on the basis of magnetic resonance images.

Head probe coils are commonly produced for MR tomographs with strong magnetic field, but these systems produce a lot of unwanted acoustic noise. Because of the need of simultaneous voice recording for the vocal tract MRI, the MR tomographs with strong magnetic field cannot be used. The solutions to the acoustic noise problems are low field MR scanners, but these are not usually provided with the head/neck coils.

Therefore, in this study the focus is to develop MR receiving head coil, for a tomograph with low magnetic field, for imaging of human vocal tract.

2. Subject and Methods

For the best signal to noise ratio, receiving coil should be exactly matched to the preamplifier and tuned to the main working frequency of MR tomograph. For this reason, variable

capacitors must be used [3]. Because these capacitors are part of the resonance circuit, they should be situated near the receiving coil as close as possible. This resonance circuit is placed into the main magnetic field of the MR scanner; therefore variable capacitors with ultra-low magnetic susceptibility must be used. Next requirements for capacitor for MR probes include high quality Q, high voltage, ultra-low piezoelectric effects, and high temperature stability [4]. During sample excitation by the RF pulse, the coil can induce a high voltage. For this reason, the detuning circuit was used, as a part of the resonance circuit of coil, like a protection of preamplifier, before this high voltage. For a good homogeneity in the center of the coil, as shown in Fig. 1, our probe coil was made as elliptical solenoid.

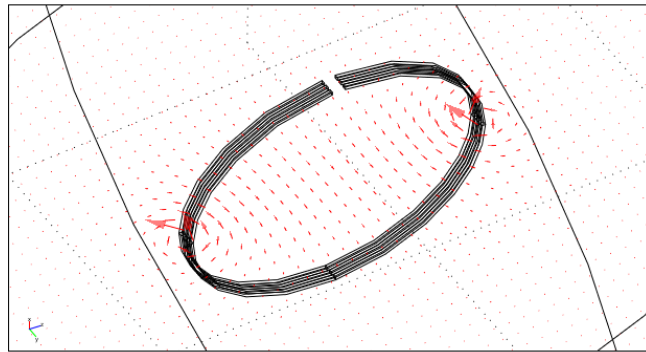


Fig.1. Magnetic flux density of a probe coil

The coil was designed and simulated in Comsol Multiphysics program (Comsol AB, Los Angeles, USA). Homogeneity of the magnetic field of coil was calculated from the simulation in the program Comsol Multiphysics. Theoretic calculation of magnetic induction, as shown in Fig.2, was made in Mathematica program.

Signal to noise ratio (SNR) and contrast to noise ratio (CNR) were calculated from the image which was produced with our coil.

The magnetic field B_z of a simple circular coil can be calculated using equation (1), [5] :

$$B_z = \frac{EllipticK[k] + \frac{EllipticE[k](R_1^2 - r^2 - (z - z_1)^2)}{(R_1 - r)^2 + (z - z_1)^2}}{\sqrt{(z - z_1)^2 + (R_1 + r)^2}}, \quad \text{where } k = \frac{4R_1r}{(R_1 + r)^2 + (z - z_1)^2}. \quad (1)$$

Where $R_1 = 0.09$ [m] is a radius of coil, r denotes a variable in radius direction, z is variable in z direction, $z_1 = 0.007$ [m] is distance of each wire loop.

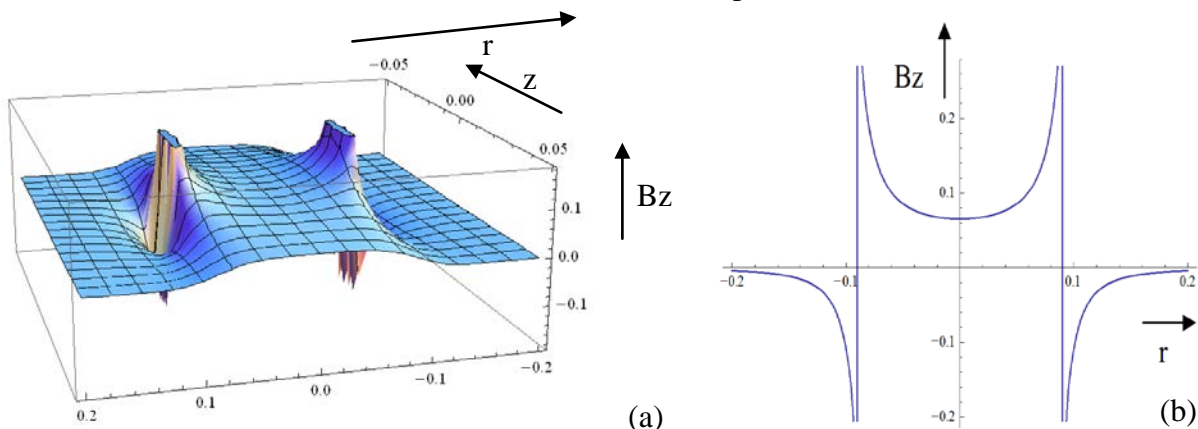


Fig.2. Image of magnetic field induction, in 3D (a) and in

plane $z = 0$ (b)

The induction of magnetic field B_1 in center of solenoid coil is described by the equation (2), [4]:

$$B_1 = \frac{\mu_0 n I}{2h \sqrt{1 + 4 \left(\frac{r}{h}\right)^2}} \quad (2)$$

where

μ_0 - permeability of free space, n - number of turns, I - electric current, h - high of coil and r - radius of coil.

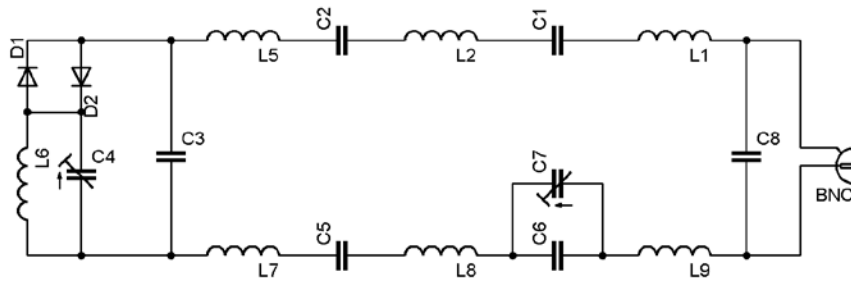


Fig.3. Equivalent circuit of head probe coil, with detuning (protection) circuit on the left side.

This coil is created by the three turns of wire with diameter 2.5mm. Loop diameter is 22cm. Each thread is divided into two parts, which are connected by the capacitors, as shown in equivalent circuit of Fig. 3.

All experiments were done on the 0.178 T MR scanner Opera [6].

3. Results

The magnetic field homogeneity calculated from the simulated field was ± 4.2 ppm.

The constructed head probe coil was tuned and tested in low-field MR scanner. The measured image of volunteer is depicted in Fig.4. The SNR of the tissues surrounding the vocal tract in the measured image, as seen in Fig.5, were as follows: soft palate 26.84, tongue 22.36 and epithelium 15.36. The CNR of the tissues against the cavities was as follows: soft palate 26.45, tongue 14.96 and epithelium 21.96.



Fig.4. MR image of vocal tract with following para-

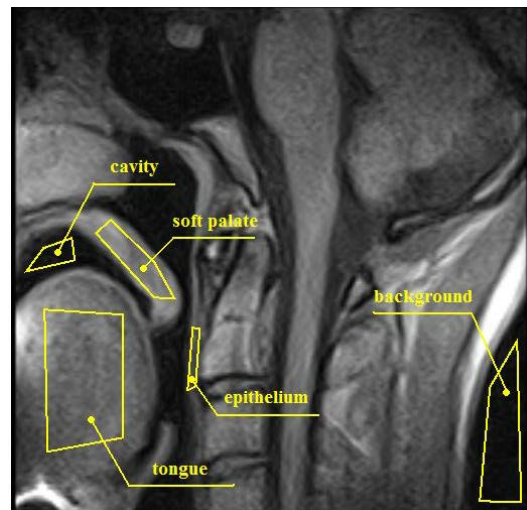


Fig.5. Image of vocal tract with described regions

meters TR: 900, TE: 26, slice thickness: 5mm

of interest

4. Discussion and conclusions

The prototype of receiver coil design with partitioning of turns seems to be feasible for obtaining reasonable signal to noise ratio. The calculated contrast to noise ratio of the tissues surrounding the vocal tract against the cavities was acceptable, and thus the vocal tract is in the image easily recognized.

According to design a head probe coil was made and afterwards tested in Opera ESAOTE tomograph. An image with relative high SNR (see Fig.3) can be measured with only two averages, thus in reasonably short acquisition time.

From our results it is clear that our head coil developed for low-field MR scanners is suitable for vocal tract MRI, as seen in Fig. 3. Imaging of the throat and mouth cavity in short time along with voice recording is therefore possible without enormous acoustic noise. In our case, the mouth cavity is not fully visible due to the imaging sequence restrictions (Field of View - FOV). The increase of FOV is the focus of our future developments.

This prototype of a low-field MR probe head coil has fair properties, but not yet optimal. In further research we will primarily focus on the selection of more suitable materials for the construction of the coil to increase the coil quality and thus improve the signal to noise ratio. For the same purpose will also the development of high impedance differential amplifier be part of further research.

For automatic fine-tuning and better compatibility with Opera ESAOTE system will be air variable tuning capacitor replaced by the varicap.

Acknowledgements

This work was supported by Grant Agency of the Slovak Academy of Sciences, VEGA 2/0090/11 and by State program ŠPVV no. 2003SP200280203.

References

- [1] Vampola T, Horáček J, Švec G.J. FE Modeling of Human Vocal Tract Acoustics. *Acta Acustica united with Acustica*: 94, 433-447, 2008.
- [2] Vampola, T., Horáček, J., Vokřál, J., and Černý, L. FE modeling of human vocal tract acoustics: Part II – Influence of velopharyngeal insufficiency on phonation of vowels”, *Acta Acustica United with Acustica*, 94, 448-460, 2008.
- [3] Andris P, Frollo I. Varicaps for NMR receiving coil matching and sensitivity changes. *Journal of ELECTRICAL ENGINEERING*: vol. 58, no.5, 291-293, 2007.
- [4] Doty F.D. Solid State NMR Probe Design. *Encyclopedia of Magnetic Resonance*, 2007.
- [5] Frollo, I.: Generation and application of gradient magnetic fields in NMR measurement and imaging. *Scientific Instrumentation*, 4, 1989, 2, 41-51.
- [6] E-scan Opera. Image Quality and Sequences manual. 830023522 Rev. A, Esaote S.p.A., Genoa, April 2008.

Noise Reduction of Recorded Speech in an NMR Imager during Phonation for 3D Vocal Tract Modeling

¹J. Přibil, ²J. Horáček, ³P. Horák, ¹I. Frollo

¹Institute of Measurement Science, SAS, Dúbravská cesta 9, Bratislava, Slovakia

²Institute of Thermomechanics, AS CR, v.v.i., Dolejškova 5, Prague, Czech Republic

³Institute of Photonics and Electronics, AS CR, v.v.i., Prague, Czech Republic

Email: Jiri.Pribil@savba.sk

***Abstract.** The paper presents two methods of noise reduction of recorded speech signal during phonation for the human vocal tract modeling in an NMR imager. The noise is mainly produced by gradient coils, have a mechanical character, and can be processed in spectral domain. Our first noise reduction method use real cepstrum limitation and clipping the “peaks” corresponding to the harmonic frequencies of mechanical noise. The second method is coming out from substitution of the short-time spectra of two signals recorded withal: the first includes speech and noise, and the second is consisted of the noise only.*

Keywords: Speech processing, Noise reduction, NMR imaging

1. Introduction

Better knowledge of the inner structures of human body is enabled by using CT or NMR investigations. The noninvasive magnetic resonance scanning of vocal tract spaces of subjects for speech configuration or in phonation position of their resonant cavities for each vowel enables to develop the three-dimensional (3D) computer models of the vocal tract. The primary volume models of the human acoustic supraglottal spaces created from the NMR images can then be transformed into the 3D finite element (FE) models [1]. The FE models open new possibilities in simulating and understanding production of human voice and speech. The FE models of the human vocal tract enable to perform numerical simulations of voice production. These models should allow simulating pathological changes or voice quality variations due to slight geometry modifications of the human supraglottal acoustic space.

The purpose of future studies is to develop computational models of human vocal tract that allow more accurate representation of the 3D wave propagation, and especially real-time numerical simulations of phonation useful in modeling real clinical situations. The FE modelling enables also to simulate the influence of the acoustic impedance changes of the vocal tract by phonating into glass tubes or straws used in voice training and therapy in clinical practice [2]. The quality of the developed FE models has to be checked by a sufficiently accurate numerical simulation of the subject phonation during the NMR scanning and therefore the simultaneous acoustic recording of subject voice during the scan procedure is very important.

There exist several approaches to reduce the noise in speech. One group of these speech enhancement methods is based on the spectral subtraction of the estimated background noise [3]. The noise estimation techniques, usually coming out on statistical approaches [4], were not able to track the real variations in the noise thereby resulting in an artificial residual fluctuating noise and distorted speech. Other noise estimation techniques performed relatively better for stationary and slowly varying noise but showed degradations when the noise was non-stationary. For that reason we use another approach, based on cepstral speech modeling.

2. Reduction of NMR coil noise in speech signal using the cepstral model

In contradiction to other speech description principles (LPC etc.), the cepstral speech analysis is performed in the frequency domain. The cepstral speech synthesis (reconstruction of speech signal) is realized by a digital filter implementing approximate inverse cepstral transformation. For voiced speech the filter is excited by a combination of an impulse train and high-pass filtered random noise, for unvoiced speech the excitation is formed by a random noise generator. The transfer function of the vocal tract model is approximated by Padé approximation of the continued fraction expansion of the exponential function. The error of this inverse cepstral approximation depends on the number and the values of applied cepstral coefficients and the used approximation structure [5].

The fundamental frequency (F0) of voiced speech is represented by a typical peak in the real cepstrum, as well as the mechanical frequencies of gradient coils producing the noise into NMR imager. Our first noise reduction method is based on the limitation of the real cepstrum and clipping the “wrong peaks” corresponding to the harmonic frequencies of the mechanical noise. The second approach is based on the substitution of the short-time spectra from two parallel processed signals: from the first microphone including the speech and noise, and from second microphone consisting only of the noise.

Single channel noise reduction by cepstrum clipping

Cepstral analysis of speech and noise signal is performed in the following way: from the input samples (after segmentation and weighting by a Hamming window) the complex spectrum by the FFT algorithm is calculated. In the next step the powered spectrum is computed and the natural logarithm is applied – see the block diagram in Fig. 1. Application of inverse FFT algorithm gives the symmetric real cepstrum. By limitation to the first $N_0 + 1$ coefficients, the Z-transform of the real cepstrum can be obtained. The truncated cepstrum represents an approximation of a log spectrum envelope

$$E(f) = c_0 + 2 \sum_{n=1}^{N_0} c_n \cos(n \cdot 2\pi f) \quad (1)$$

where the first cepstral coefficient c_0 corresponds to the signal energy.

The whole algorithm works in four steps:

- 1) Calculation of real cepstrum, pitch-period detection, F0 calculation.
- 2) Determination position of peaks in cepstrum corresponding to the frequencies of mechanical noise, and minimum number N_0 of cepstral coefficients (for sufficient log spectrum approximation [5]).
- 3) Limitation of real cepstrum and clipping peaks.
- 4) Reconstruction of input signal by the pitch-synchronous cepstral speech synthesizer.

Two channel noise reduction by spectral subtraction

Generally is the noisy speech signal $x(k)$ interpreted as addition of a clean speech signal $s(k)$ and a additive noise $n(k)$. The noisy signal is segmented and windowed to obtain a short

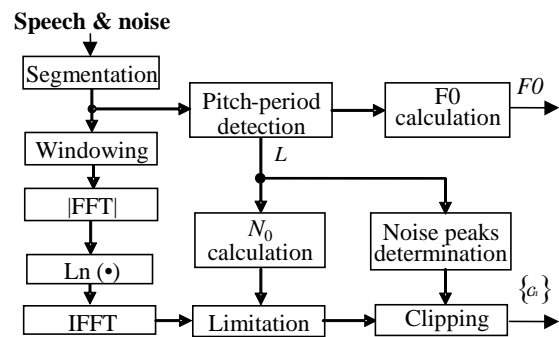


Fig. 1. Block diagram of cepstral analysis of the speech and noise signal.

time-frame of noisy speech. By transformation to the frequency domain using the FFT, we get the short-time spectrum $X(f, n)$. The enhanced speech spectrum can be obtained by subtracting a noise magnitude spectrum loaded by the microphone Mic. 2 from the noisy speech magnitude spectrum (of signal loaded by the first microphone Mic. 1):

$$S(f, n) = \left(|X(f, n)| - |N(f, n)| \right) \cdot e^{\varphi_n(f, n)}, \quad (2)$$

where $e^{\varphi_n(f, n)}$ represents the phase of noisy speech spectrum, and n is index of processed frame. On the resulting spectrum is applied natural logarithm and IFFT, whereby the limited real cepstrum is next obtained – see the block diagram in Fig. 2. The final clean signal is reconstructed also by cepstral speech synthesizer.

3. Experiments and Results

Our experiments were performed in the open-air 0.178T imager Esaote OPERA [6]. An arrangement of speech and noise recording measurement was following: the bed with testing person was set to 60 deg position (originated from the left corner – maximum rotation angle is 180 deg) – see Fig. 3. For the speech and RF coils noise signal recording, the front microphone (Mic. 1) was located on the 150 deg position; for recording the noise signal only, the back microphone (Mic. 2) was placed on the 30 deg position. Both microphones were located in the 10 cm above the bed (in the middle between both coils), and in the 60 cm radius of the central point of scanning area (RF coil). The measurement was realized with running scanning sequence: gradient echo, T1, coronal (TE = 18 ms), the background noise intensity (generated mainly by a temperature stabilizer) was $I_0 = 55$ dB (measured by DT-8820 device).

Speech as well as noise was recorded with the help of the M-Audio FireWire 1814 equipment connected to a personal computer through high-performance, high-resolution multi-channel interface of the IEEE 1394 (FireWire) bus. As the Mic. 1, the professional 1" Behringer dual diaphragm condenser microphone B-2 PRO (cardioids, omnidirectional or figure eight pickup pattern) was used. For Mic. 2 the RØDE NTK 1" condenser microphone with cardioid directional pattern was chosen. Signals from both microphones originally were recorded at 32 kHz, and resampled to 16 kHz. Collected database of speech and noise signals consists of 90 records of five separate phonated long vowels "a:", "e:", "i:", "o:", and "u:" from three male and three female non-professional speakers with mean time duration about 8 sec. The frame length depends on the mean pitch period L_0 of the processed signal. In our experiment, we use 24-ms frames for male voice, and 20-ms frames for female voice. The parameter for limitation of real cepstrum (chosen in correspondence on the period of noise part of signal

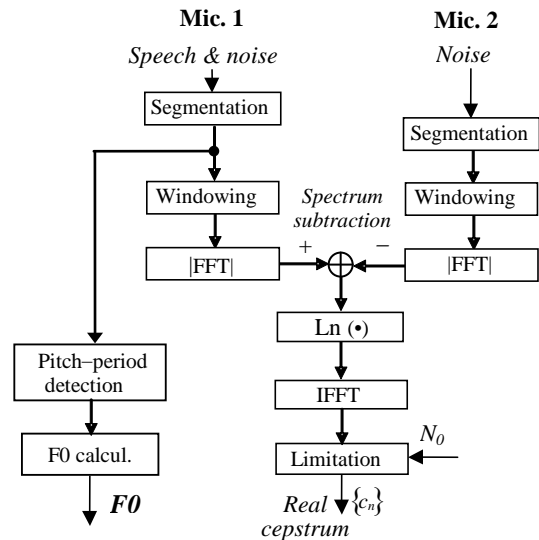


Fig. 2. Block diagram of two channel spectral subtraction method and cepstral analysis.



Fig. 3. An experiment arrangement: bed with testing person (1), front read microphone 1 (2), patient's head into RF coil (3), back read microphone 2 (4).

L_n), was set as $N_0 = 256$ (when $N_{FFT} = 1024$) for both voices; the minimum-phase cepstral coefficients $\{\hat{s}_n\}$ [5] were subsequently used for signal reconstruction.

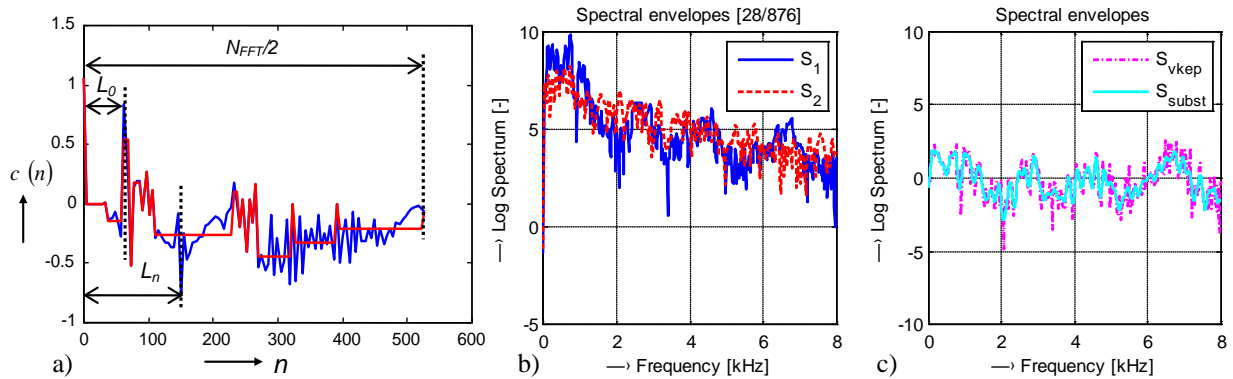


Fig. 4. Graphic examples of applied noise reduction method: real cepstrum clipping and limitation (a), two log spectral envelopes (b), resulting envelope after subtraction and cepstral reconstruction (c); processed speech and noise signal of vowel “a”, female voice ($F_0 \approx 220$ Hz, processed 28th frame of total 876).

4. Conclusions

Performed experiment confirms usability of both applied noise reduction methods based on the cepstral speech model. The significant audible differences between the noisy and cleaned speech signal were observed for all of processed samples. Used professional condenser microphones have no effect on the homogeneity of low-magnetic field B_0 of the NMR imager, needed for obtaining the sufficient image quality. When the cardioid directional pattern is set for both microphones, the background noise can be ignored. From obtained results follows, that sufficient noise suppression can be reached by using of simple one microphone method (the two microphone approach is generally complicated for realization, and not bring any significant effect).

In the near future, we will use the listening tests for detail audio comparison of final speech signal cleared by these two methods. As an objective comparison criterion, the recognition score parameter of an Automatic Speech Recognition (ASR) system can be also applied too.

Acknowledgements

The work has been supported by the Grant Agency of the Slovak Academy of Sciences, project VEGA no. 2/0090/11, and by the Grant Agency of the Czech Republic (GA102/09/0989).

References

- [1] Vampola, T., Horáček, J., and Švec, J.G., FE modeling of human vocal tract acoustic. Part I: Production of Czech vowels. *Acta Acustica United Acustica*, 94, 2008, 433-447.
- [2] Laukkanen, A.M., Titze, I.R., Hoffman, H., and Finnegan, E.M., Effects of a semi-occluded vocal tract on laryngeal muscle activity and glottal adduction in a single female subject. *Folia Phoniatrica et Logopaedica*, 60, 2008, 298-311.
- [3] Boll, S.F., Suppression of Acoustic Noise in Speech using Spectral Subtraction. *IEEE Trans. On ASSP*, Vol. 27, No. 2, 1979, 113-120.
- [4] Martin, R., Spectral Subtraction Based on Minimum Statistics. *Proc. of EUSIPCO 1994*, 1182-1185.
- [5] Vích, R., Cepstral Speech Model, Padé Approximation, Excitation, and Gain Matching in Cepstral Speech Synthesis. *Proc. of EURASIP Conference Biosignal 2000*, 77-82.
- [6] E-scan Opera. Image Quality and Sequences manual. 830023522 Rev. A, Esaote S.p.A., Genoa, April 2008.

The Measurement System for Experimental Investigation of Middle Ear Mechanics

¹M. Kwacz, ²M. Mrowka, ²J. Wysocki

¹Institute of Micromechanics and Photonics WUT, Warsaw, Poland,

²Institute of Physiology and Pathology of Hearing, Warsaw/Kajetany, Poland

Email: m.kwacz@mchtr.pw.edu.pl

Abstract. *This paper presents a measurement system for non-contact measurements of vibration parameters of the structural elements of the organ of hearing. It proposes an original methodology of in-vitro measurements of the human ear, round window membrane motions. It was found that the Scanning Laser Doppler Vibrometry (LDV) technique is a useful research tool in micro- and nanometer scales, not only for technical, but also for biological objects.*

Keywords: laser Doppler vibrometry, middle ear mechanics, round window membrane

1. Introduction

The human middle ear is a complex mechanical system, which transmits sound from the external ear canal to the inner ear structures. The ossicular chain is the most important part of that system. The physiological range of the middle ear structural elements displacement amplitudes in the process of sound conduction does not exceed 100 nm. Both, diagnosis of the hearing organ in its physiological condition, and the hearing organ after ossicular chain reconstruction, require measuring equipment which enables non-contact measurements of vibration parameters in very low amplitudes and in a wide range of acoustic frequencies. Laser Doppler Vibrometry (LDV), especially scanning one, is a modern measurement method which meets such requirements.

The objective of this study is experimental verification of the applicability of the LDV method in non-contact, human ear, round window (RW) membrane vibration measurements, in specimens in their physiological condition, pathological condition and post-implantation of various kinds of ossicular chain prosthesis. The measurement results can be used to model the process of sound transmission [1], to test middle ear prostheses [2,3], to diagnose of pathologies [4,5] and for intraoperative control of otosurgery effectiveness [6]. Despite significant advances in this field, the relation between the sound transmission process and the structure of hearing organ remains under-researched. Therefore, it is purposeful to expand on this topic in research works of both, an experimental, as well as theoretical and model nature. Developing LDV-based diagnostic equipment and introducing it into otorhinolaryngological practice is of great necessity.

2. Subject and Methods

Our research was conducted in-vitro with the use of appropriately prepared fresh human temporal bone specimens obtained postmortem. The experiments consisted of measuring the amplitude and phase of RW membrane motions depending on the sound frequency (400 Hz – 10 kHz) with the sound pressure entering the external auditory canal at 90 dB. The amplitude and phase functions of velocity transmission were defined according to the experimental results, depending on the ossicular chain state. The course of the designated functions can differentiate middle ear pathologies and can be used to optimize the construction of auditory prostheses.

Preparing the specimen

Literature sources [7,8] show, that the functioning of middle ear structures in fresh cadaver temporal bones is the same as their functioning in physiological condition. Our procedure of preparing the physiological specimen required the following steps to be taken: (1) harvesting a segment of the temporal bone within 48 hours after death, (2) microscopic inspection of the specimen, (3) reaming until the tympanic membrane was fully exposed (the bony rim around the tympanic annulus was left intact), (4) conducting a wide posterior tympanotomy (sometimes sacrificing part of the facial nerve canal with the facial nerve) and making the round window and stapes visible, (5) gluing a foam earmold onto the remaining bony rim, (6) placing the microphone tube (approx. 2 mm away from the tympanic membrane) and a ER3-04 loudspeaker adapter (approx. 4-5 mm away) in the earmold, (7) periodically dipping the specimen in a saline solution to maintain the proper hydration of the structure.

Acoustic system

The acoustic signal introduced into the substitute external auditory canal of the temporal bone specimen induces the tympanic membrane vibrations, and causes vibration of the ossicular chain. A sound is produced by a probe loudspeaker connected to an adapter placed into the external auditory canal. In our study an input sound signal generated by a computer system (VIBSOFT, Polytec PI) and amplified by an acoustic amplifier (Revox A78) was supplied to the earmold placed into the specimen. The procedure of acoustic stimulation involves: (1) calibrating the VIBSOFT system, the loudspeaker and probe microphone, (2) selecting and setting the sound level intensity of the stimulating signal (90dB SPL), (3) selecting and setting the frequency of the input signal (sounds with a center frequency of successive one-third octave bands were transmitted into the external auditory canal), (4) transmitting sounds into the external auditory canal with the aid of a loudspeaker (ER-2, Etymotic Research) attached to an adapter (ER3-04, Etymotic Research) placed into the earmold, (5) controlling the sound intensity level of the stimulating sound with a probe microphone (ER-7C, Etymotic Research) placed in the microphone tube approx. 2 mm away from the tympanic membrane (TM).

Optical system

The optical measurement system was created from a commercially available SLDV PSV 400 scanning laser Doppler vibrometer produced by Polytec GmbH, Waldbronn, Germany. The vibrometer in use is characterized by the following parameters: scanning surface of 512 by 512 measuring points, scanning laser head equipped with a type He-Ne 633 nm laser of < 1 mW power, vibrometer sensor (OFV-505), scanning unit (OFV 040) featuring a +/- 20° scanning range and < 0,002° resolution, and a VTC 24 video camera featuring Auto Focus and a 72x zoom, vibrometer controller (OFV-5000) equipped with a RS-232 port, which enables measuring velocity in the 0,01 $\mu\text{m/s}$ – 10 m/s range for frequencies in the 0 MHz – 1 MHz range, a PSV E 400 interface for connecting the measuring head and vibrometer controller with the measurement data compiling system, measurement data compiling system, comprised of a PC computer with software and a generator of low-intensity signals.

Figure 1 shows the scheme of the experiments (measurements of the parameters of the round window membrane motions in a physiological specimen in the frequency function) and a partial view of the measurement system.

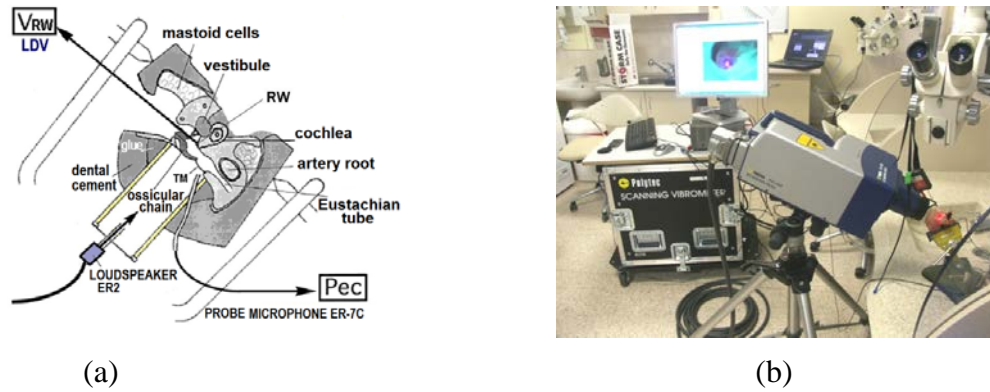


Fig. 1. (a) Scheme of the experimental measurements (Stage 1), (b) View of the measurement system.

3. Results

The original research comprised of measuring parameters of the human ear round window membrane vibrations. The scanning LDV method was used to measure the following vibration parameters of 34 targets on the round window membrane in frequency function of the acoustic input signal: (1) displacement amplitude, (2) velocity amplitude and (3) phase displacement, where the determined characteristic parameter was the sound pressure level of the input signal of 90 dB SPL. The amplitude-frequency characteristics for targets located on the surface of the RW membrane are shown in Figure 2. The characteristics of the RW membrane vibrations were determined based on measurements of displacement in the grid nodes when the sound pressure is 90 dB SPL and frequencies ranging from 400 Hz up to 10 kHz in the external auditory canal.

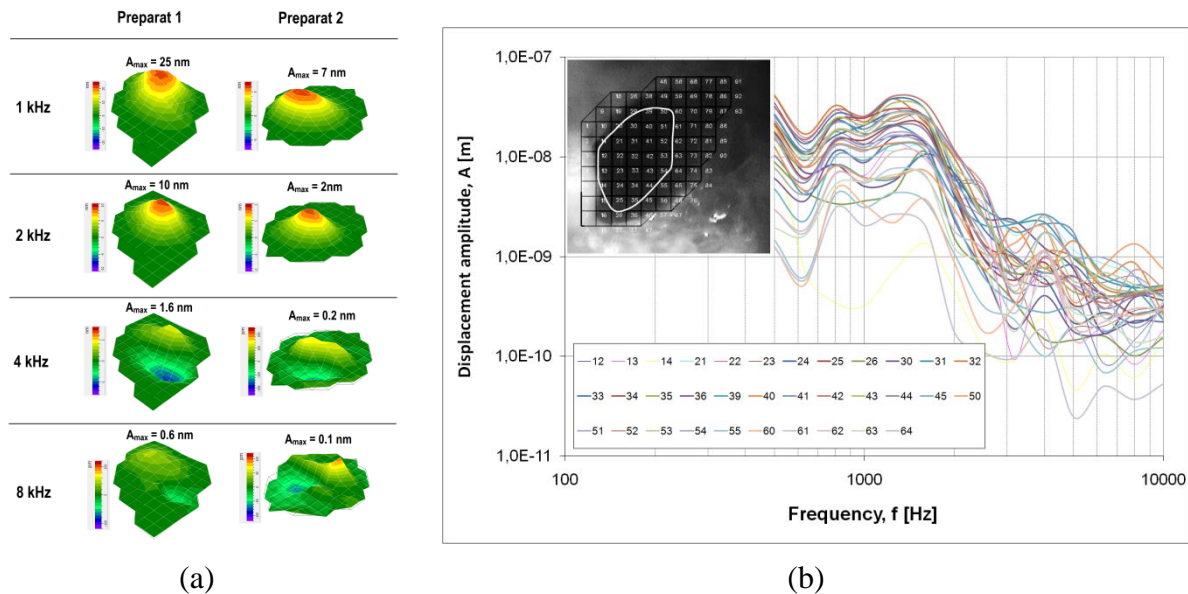


Fig. 2. (a) The vibration pattern of the RW membrane at 1, 2, 4 and 8 kHz, (b) Magnitude of the displacement amplitude of 34 measurement targets on the RW membrane. The result is from specimens in physiological state stimulated with an AC when the sound pressure level is 90 dB SPL in the external auditory canal.

In both physiological specimens, the Preparat 1 and Preparat 2 at 1 and 2 kHz vibration frequencies all measurement targets oscillate in the same phase, yet a difference in the location of points characterized by the greatest displacement amplitude values located on the RW membrane is noticeable (Fig.2a). The displacement amplitude for all measurement points

in the low-frequency range (0.5–2 kHz) is 10-15 times greater than in the high frequency range (2–10 kHz). Characteristic resonant frequencies of the middle ear are noticeable.

4. Discussion

The measurement results for the human ear RW membrane vibrations in two fresh cadaver temporal bone specimens for air conduction at 90 dB SPL in the external auditory canal showed that the maximum displacement amplitude in the central area of the RW membrane is different in both specimens. This difference of the maximum vibration amplitude was related to different shapes and sizes of the RW membrane in each specimen, which is a characteristic trait of biological objects demonstrating individual variability. The decrease in the displacement amplitude of vibrations for frequencies above 2 kHz is related to different vibration phases in each measurement point on the RW membrane. The circumferential ring pattern of displacement maxima in Fig.2 is consistent with the presence of standing waves on the RW surface at frequencies below 2kHz. Based on a detailed iso-amplitude chart analysis it was found that the vibrations of measurement points spread across the entire surface of the RW membrane for all examined specimens in low-frequency ranges were single-phase vibrations. Above 1250 Hz – 2000 Hz frequencies, the phase of vibration for points placed in various parts of the RW membrane was different. When examining the iso-phase contours, indications of both modal and traveling waves can be seen. 3D visualization shows that modal vibration was dominating at the low frequencies and traveling wave motion at the high frequencies.

The motion of the RW membrane can be used to measure the cochlear stimulation for the evaluation of middle ear ossicle reconstruction. Therefore one can assume that as a result of conducting a standard implanting procedure, a significant change in biomechanical parameters of the middle ear conductive apparatus takes place, which causes a significant change in the input impedance of the cochlea and a significant decrease in perilymph stimulation levels. The result of a decrease in stimulation of the perilymph in the post-implantation condition, in comparison with its physiological condition, in case of otologic surgery conducted in-vivo, could be the incomplete closure of the air-bone gap resulting in hearing outcomes showing signs of conductive hearing loss.

5. Conclusions

The LDV method is a useful research tool in micro- and nanometer scales. The latest scanning systems enable taking measurements of vibrations in the picometer amplitude range and can be used not only to examine technical but also biological objects. The presented experimental method of measuring vibration parameters of structural elements of the middle ear can be applied to: (1) research aiming to explore the phenomenon of conducting sound through physiological, pathological and reconstructed structures of the middle ear, (2) verifying computer- modeling and simulating procedures of sound conduction by the structures of the middle ear and examining the influence of various parameters on the effectiveness of stimulation of the perilymph in the cochlea of the inner ear, (3) aiding the process of constructing various kinds of middle ear prosthetics (including optimizing the build and methods of implantation) by experimental research on prototypes of such prostheses, (4) in-vivo diagnostics whose purpose is to differentiate pathological conditions (tympanosclerosis, otosclerosis, ossicular chain disruption, diagnosing the inner ear by measurement of acoustic otoemissions) and predicting results of hearing improvements achieved after otological procedures, (5) supporting the process of surgery (intraoperative diagnostics).

Acknowledgements

The authors would like to thank the IPPH Director, Professor Henryk Skarzynski for granting permission to use facilities at the ICHS Head and Neck Clinical Anatomy Laboratory in Kajetany in order to conduct the research.

Research was funded by the Research Project Nr N N518 377637.

References

- [1] Gan R, Reeves B, Wang X. Modeling of Sound Transmission from Ear Canal to Cochlea. *Annals of Biomedical Engineering*, 35 (12): 2180-2195, 2007.
- [2] Chien W, Rosowski R, Merchant S. Investigation of the Mechanics of Type III Stapes Columella Tympanoplasty Using Laser-Doppler Vibrometry. *Otol Neurotol*, 28 (6): 782-787, 2007.
- [3] Puria S, Kunda L, Roberson J Jr, Perkins R. Malleus-to-footplate ossicular reconstruction prosthesis positioning: cochleovestibular pressure optimization. *Otol Neurotol*, 26 (3): 368-379, 2005.
- [4] Huber A, Schwab C, Linder T, Stoeckli S, Ferrazzini M, Dillier N, Fisch U. Evaluation of Eardrum Laser Doppler Interferometry as a Diagnostic Tool. *The Laryngoscope*, 111: 501-507, 2001.
- [5] Nakajima H, Ravicz M, Rosowski J, Peake W, Merchant S. Experimental and clinical studies of malleus fixation. *The Laryngoscope*, 115 (1): 147-154, 2005.
- [6] Huber A, Linder T, Ferrazzini M, Schmid S, Dillier N, Stoeckli S, Fisch U. Intraoperative assessment of stapes movement. *Ann Otol Rhinol Laryngol*, 110 (1): 31-35, 2001.
- [7] Rosowski J, Davis P, Merchant S, Donahue K, Coltrera M. Cadaver Middle Ears as Models for Living Ears: Comparison of Middle Ear Input Immitance. *Ann Otol Rhinol Laryngol*, 99: 403-412, 1990.
- [8] Goode R, Ball G, Nishihara S. Measurement of umbo vibration in human subjects - method and possible clinical applications. *Am J Otol*, 14: 247-251, 1993.

Application of the Wavelet Based Denoising Methods for T-Wave Alternans Analysis in High Resolution ECG Maps

¹D. Janusek, ¹M. Kania, ²R. Zaczek, ¹H. Zavala-Fernandez,
¹A. Zbieć, ²G. Opolski, ¹R. Maniewski

¹ Nalecz Institute of Biocybernetic and Biomedical Engineering, Warsaw, Poland

² First Department of Cardiology, Medical University of Warsaw, Warsaw, Poland

Email: djanusek@ibib.waw.pl

Abstract. *T-wave alternans (TWA) allows for identification of patients at an increased risk for ventricular arrhythmia. Stress test, which increase heart rate, is used for TWA measurement. The TWA analysis is often disturbed by muscular interference. The evaluation of wavelet based denoising methods was performed to find optimal algorithm for TWA analysis.*

Keywords: *T-wave alternans, wavelet denoising, stress test, arrhythmia, sudden cardiac death*

1. Introduction

Sudden cardiac death (SCD) is the leading cause of cardiovascular mortality in developed countries [1]. The efforts of many medical scientists and physicians are concentrated on the prediction and the prevention of SCD by different diagnostic tools and therapies. At present, there is no generally accepted non-invasive risk index of SCD. T-wave Alternans (TWA) is a very promising marker of the vulnerability to ventricular arrhythmia [2]. It is defined as a beat-to-beat change in the T-wave amplitude that repeats every other heart beat and indicates the spatial heterogeneity of the ventricular repolarization. Both temporal and spatial distribution of the electrical potentials generated by heart on the surface of the body could be investigated by high resolution Body Surface Potential Mapping (BSPM) [3]. In the presented study the results of the TWA assessment by using FFT-based method are shown [4]. Patients were examined with use of electrocardiographic stress test.

The aim of the study was to evaluate T-wave alternans amplitude in the BSPM signals denoised with use of different wavelet functions [5].

2. Subject and Methods

The study group consisted of 12 patients with myocardial ischemia (7 with detected TWA). Two minute ECG maps (67 channels) were recorded during stress test performed on supine ergometer (heart rate 100 bpm \pm 5). The Fast Wavelet Transform [6] was applied and soft thresholding procedure was used [7]. For the final analysis 3 wavelets functions were chosen: Daubechies 1 level 6, Symlet 3 levels 4 and 5 and Symlet 8 levels 4 and 5.

3. Results

Wavelet function Daubechies 1 level 6 (db1lev6) was found to be the best for denoising ECG signals for TWA analysis. The average value of TWA magnitude calculated in denoised signals was 25% greater than in raw data with detectable TWA. The difference between TWA magnitude calculated in signals denoised with use of the db1lev6 method and another methods was 2% (SD = 3) which is not significant. The main advantage of using db1lev6 method is that the number of leads, where diagnostic significant value of TWA was found, was 30% greater than in raw data. In signals where another denoising methods were used the

increase was 10% (SD=35). There are no significant difference between TWA magnitude calculated in signals without detectable TWA before and after denoising (0.3%, SD = 0.04).

4. Conclusion

The wavelet denoising with application of Daubechies function increases probability of TWA detection. It is directly connected with the higher TWA magnitude as well as with greater number of ECG leads where the TWA shows significant diagnostic value.

Acknowledgements

This work was supported by Polish Ministry of Science and Higher Education project number NN 518 504 339.

References

- [1] Bayes A., Guindo J.: Sudden Cardiac Death. MCR, Spain, 1989.
- [2] Buxton AE. Risk stratification for sudden death in patients with coronary artery disease. *Heart Rhythm*. 2009 Jun;6(6):836-47
- [3] Fereniec M, Stix G, Kania M, Mroczka T, Janusek D, R. M. Risk assessment of ventricular arrhythmia using new parameters based on high resolution body surface potential mapping. *Med Sci Monit*. 2011;17(2).
- [4] Rosenbaum D., Jackson L., Smith J., Garan H., Ruskin J., Cohen R.: Electrical alternans and vulnerability to ventricular arrhythmias, *N. Engl. J. Med.*, 1994, 330, 235-241.
- [5] Kania M, Fereniec M, Maniewski R. Wavelet denoising for multi-lead high resolution ECG signals. *Measurement Science Review*. 2007;7 (Section 2, No. 3):30-3
- [6] Mallat S.: A theory for multiresolution signal decomposition: the wavelet representation. *IEEE Pattern Anal. and Machine Intel.*, 1989, vol. 11, no. 7, pp. 674-693
- [7] Donoho D. L.: De-Noising by soft-thresholding. *IEEE Trans. on Inf. Theory*, 1995, vol. 41, 3, pp. 613-627

Evaluation of Heart Rate Variability Using Recurrence Analysis

¹J. Schlenker, ¹T. Funda, ²T. Nedělka

¹Czech Technical University, Faculty of Biomedical Engineering, Prague, Czech republic,

²Department of Neurology 2nd Medical School Charles University, Prague, Czech republic

Email: jakub.schlenker@fbmi.cvut.cz

Abstract. *This paper presents a new method of evaluating heart rate variability based on nonlinear analysis. We can describe selected processes generated in living organism much more effectively using specific methods of nonlinear analysis. The main tool of recurrence analysis is represented by recurrence plots which visualise the recurrence behaviour of the phase space trajectory of dynamical systems.*

Keywords: recurrence analysis, recurrence plot, nonlinear analysis, heart rate variability,

Introduction

Heart rate variability shows heart's ability to adapt to changing circumstances. The clinical significance of HRV has been known for many years. HRV is, for example, a strong and independent instrument for the prediction of mortality from acute myocardial infarction in cardiology [1]. HRV provides information on the activities of the autonomic nervous system in neurology.

Evaluation of HRV is currently based on time domain or frequency analysis. To obtain complex information about HRV it is necessary to know the results of both these methods. There is an increasing importance of nonlinear analysis of biological data in the last few years. Recurrence analysis - the subject of this study - is one of these techniques. In biomedicine, recurrence analysis was initially used in special cases. However, recent studies [2, 3, 4, 5] suggest possibilities of wider application of recurrent analysis of biological data.

Recurrence plots (RP) - the basic instrument of recurrence analysis allow visualization of phase space trajectories using two-dimensional graph. RPs allow analysis of multidimensional systems. RP can be used to detect transitions between different states or to find interrelations between several systems [6, 7].

The structures created in RP represent the basis for so-called recurrence quantification analysis (RQA). It is a set of parameters introduced by Zbilut and Webber [7] for the possibility of quantitative evaluations of RP. The parameters are based on diagonal lines of the structures of RP [6, 7]. Compared to other traditional methods of nonlinear analysis, a great advantage of RQA is its ability to capture the chaotic properties without a need of a long data series and the fact that it is relatively immune to noise and nonstationarity. RQA is a sensitive tool for detecting any dynamic changes, but it can be easily affected by settings. One of the critical parameters of RQA is the threshold distance ε_i . Even a small change of ε_i can dramatically affect the results of RQA [3, 4]. Currently, we meet with various studies and articles dealing with the choice of threshold distance ε_i [4, 5, 8].

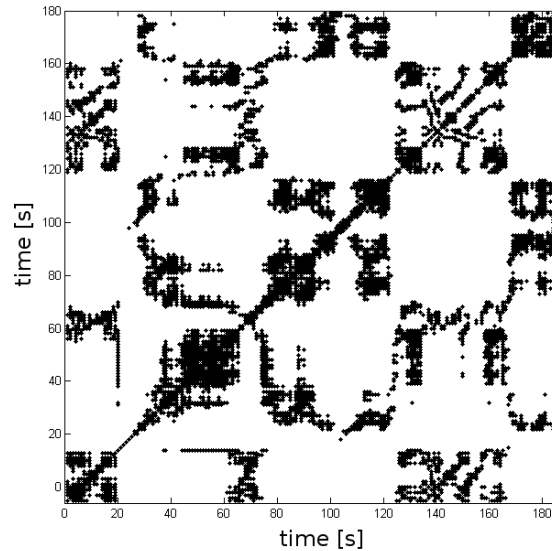


Fig. 1. A representative example of the recurrence plot.

Subject and Methods

In cooperation with the Neurological Clinic of the Motol hospital, we used recurrence analysis for the evaluation of heart rate variability in both patients and healthy subjects. The length of RR intervals measured during the orthostatic test was used as input signal. The main data set for the analysis was patients' data from the clinic. The most commonly represented diseases were neuropathy (CMT), complex regional pain syndrome (CRPS), phobic postural vertigo (FPV) and the conditions of collapse (PRE-COLL). Pre-collapse state is intolerance while standing, without finished collapsing with impaired consciousness, usually in patients with vagotonus standing. The control group consisted of healthy subjects who underwent a clinical orthostatic test. Orthostatic load is carried by the adjustment of the human body from a lying to standing. The load causes stagnation of blood in legs, thus reducing venous return and cardiac stroke volume. In response, heart rate increases, peripheral vasoconstriction occurs and cardiac blood volume and blood pressure equalize in healthy humans.

For the analysis we used a script created in MATLAB. The input parameters are the time delay τ , the dimension m and threshold p . The threshold distance is determined by the percentage of each record so that

$$\epsilon = \frac{S_{max} - S_{min}}{100} \cdot p \quad (1)$$

where

- ϵ the threshold value,
- S_{max} the maximum in the matrix,
- S_{min} the minimum in the matrix,
- p an input parameter threshold.

The calculated parameters of RQA were processed in a form of boxplot graphs. Two-sided t-tests were then calculated for selected graphs.

Results

We found significantly higher percentage of recurrent points from RQA measurement in patient with CMT and FPV compared with control group. RQA measurement based on diagonal lines showed significantly higher percentage of points forming diagonal lines (the

value of DET parameter - determinism), in group with CRPS and PRE-COLL compared on the control group.

RQA measurement based on vertical lines showed significant difference in longest vertical line MAXV between PRE-COLL and control group. The last parameter which showed significant difference was entropy ENTR. The values of ENTR were significantly higher in CMT and PRE-COLL groups compared to the control group. Unfortunately, there was no significant difference among individual groups with diseases. In other words, the only differences we found were just between the groups with diseases and the control group.

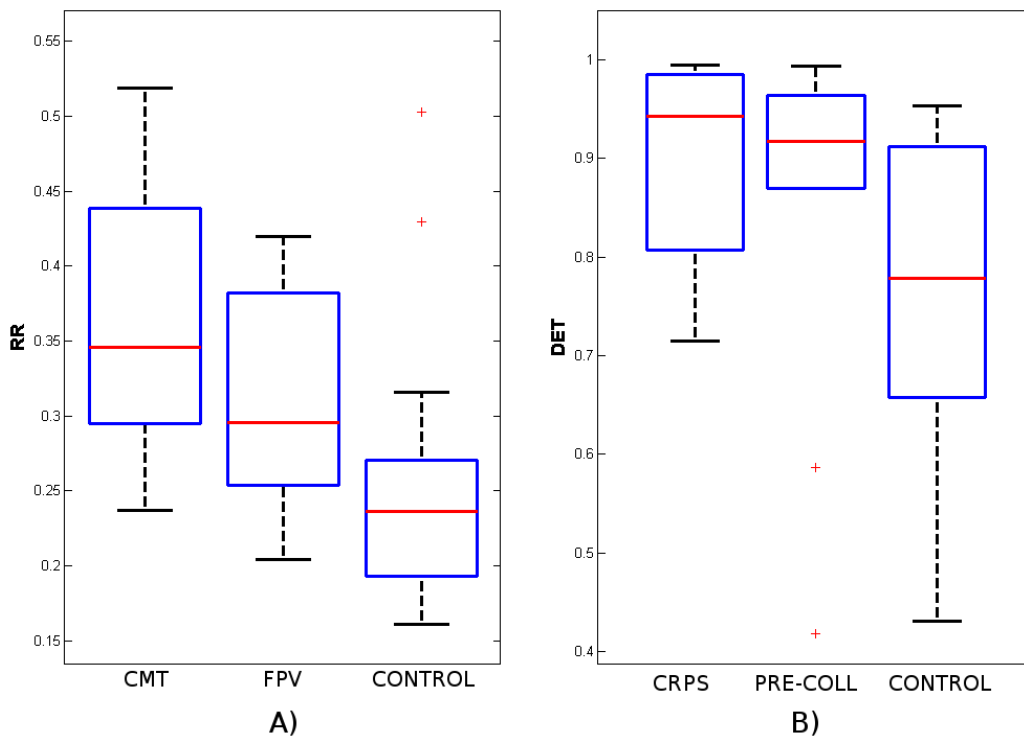


Fig. 2. A) Box plot illustrating the comparison of percentage of recurrence points (RR) between control group and FPV ($P=0.025$) and between control group and CMT ($P=0.005$). B) Box plot illustrating the comparison of percentage of determinism (DET) between control group and PRE-COLL ($P=0.005$) and between control group and CRPS ($P=0.1$). Box plot shows interquartile range of values with central line indicates median.

Discussion

The main goal of our study was to verify the possibilities of recurrence analysis in neuroscience. We demonstrated significant differences in the values of RQA parameters for healthy and ill subjects. Higher percentage of recurrence points and higher values of DET, ENTR or MAXV show the changes in HRV, that may indicate pathological conditions.

The main advantage of RPs in comparison to other traditional methods of non-linear analysis is that they can be applied to rather short and even nonstationary time series. RQA is a sensitive tool for detecting any dynamic changes, but can be easily affected by parameter settings. As we mentioned before, one of the critical parameters for the RQA is the threshold distance ε_i . We determine the threshold distance as a percentage. New experiments, however suggest greater accuracy when using the standard deviation method [10] describe above. The next limitation of our pilot study is a small number of patients in the groups. At this time, we are working on new studies, that eliminate these shortcomings and are specifically focused.

Conclusions

We have verified the possibility of using recurrence analysis for the evaluation of heart rate variability. The RQA parameters can be used together with commonly used parameters of HRV to evaluate the heart rate variability in neuroscience. The main RQA parameters suitable for the evaluation of HRV are recurrence rate (RR), determinism (DET), entropy (ENTR) and longest vertical line (MAXV).

Acknowledgements

This study was supported by Research Project MSM6840770012 Transdisciplinary Research in the Field of Biomedical Engineering II.

References

- [1] Malik M. Heart rate variability – Standards of measurement, physiological interpretation, and clinical use. Task Force of The European Society of Cardiology and The North American Society of Pacing and Electrophysiology (Membership of the Task Force listed in the Appendix). *European Heart Journal*, Vol. 17, March 1996, pp. 354- 381
- [2] Ding H., Crozier S., Wilson S. A new heart rate variability analysis method by means of quantifying the variation of nonlinear dynamic patterns. *IEEE transactions on bio-medical engineering*. 2007, 54 (9), s. 1590-1597.
- [3] García G.M.A., Fernández Ch.M., Ramos C.J. Errors in the estimation of approximate entropy and other recurrence-plot-derived indices due to the finite resolution of RR time series. *IEEE transactions on bio-medical engineering*. 2009, 56 (2), s. 345-351.
- [4] Ding H., Crozier S., Wilson S. Optimization of Euclidean distance threshold in the application of recurrence quantification analysis to heart rate variability studies. *Elsevier*. 2008, 38, s. 1457-1467.
- [5] Javorka M. et al. Recurrences in heart rate dynamics are changed in patients with diabetes mellitus. *Clinical Physiology and Functional Imaging*. 2008, 28, s. 326-331.
- [6] Traut M. MATLAB® Recipes for Earth Sciences. Potsdam: Springer, 2007. 288s. ISBN 978-3-540-72748-4.
- [7] Marwan N. Encounters with neighbours: current developments of concepts based on recurrence plots and their applications. Potsdam, 2003. 331 s. Dizertační práce. University of Potsdam. Dostupné z WWW: < <http://www.recurrence-plot.tk/furtherreading.php> >. ISBN 3000123474, 9783000123474.
- [8] Schinkel, Stefan; Dimigen, Olaf; Marwan, Norbert. Selection of recurrence threshold for signal detection. *European Physical Journal: Special Topics*. 2008, 164, s. 45-53.

Measuring System with Compound Software Architecture for Measurement and Evaluation of Biosignals from Isolated Animal Hearts

P. Kaľavský, V. Rosík, S. Karas, M. Tyšler

Department of Biomeasurements, Institute of Measurement Sciences, SAS
Dúbravská cesta 9, 841 04 Bratislava, Slovakia
Email: umerkala@savba.sk

Abstract. *Biomedical measuring system for acquisition, processing and evaluation of ECG signal, blood and perfusion pressure and drug dosage is introduced. Mentioned signals are obtained during experiments on small animal hearts making use of a Langendorff setup. The USB powered system is conceived as a virtual instrument with an external measuring unit controlled by a microprocessor and connected to a host computer with running application software. The novelty of the approach presented is purposeful compound architecture of the application software. For real-time data acquisition graphical programming language LabVIEW was used, due to the offered possibility of easier parallelization of processes. For off-line biophysical parameter analysis MATLAB, one of the most widely used signal processing tool, was applied.*

Keywords: *USB-based device, Langendorff setup, compound LabVIEW and MATLAB software architecture, biosignal processing, parallelism*

1. Introduction

Software development is a time consuming process, especially in so sensitive field as medical sciences [1]. In order to dynamically respond to continual technological progress and to solve technical computing problems within few weeks or months, small scientific teams prefer LabVIEW or MATLAB instead of traditional programming languages like C, C++ or Java.

Measuring part of our application software is developed in graphical programming environment LabVIEW that has been widely adopted as the standard for data acquisition and instrument control [2]. Dataflow code developed with LabVIEW allows for automatic parallelization. Parallelism is important in advanced computer programs because it can unlock performance gains in comparison to purely sequential programs due to recent changes in computer processor designs [3]. Analytical part of our application software is developed in high-level technical computing language MATLAB and makes use of its signal processing toolboxes. Proposed software concept controls a communication between the measuring unit and the host computer, processes data stream during an acquisition, formats, visualizes and records measured signals and consequently realizes off-line processing and analysis of the measured signals.

2. Methods and results

Measuring system BioLab-P

Based on previous experience with BioLab series measuring systems [4], the USB powered measuring system BioLab-P was developed. The system consist of selected biosignals sensors, a signal conditioning module and a data acquisition module (Fig. 1a) that are placed in the measuring unit (Fig. 1b) and the host computer with a compound application software.

The BioLab-P measuring system allows to monitor and record one of two possible triples of biosignals. Either the electrocardiogram (ECG), left ventricular pressure (PS1) and drug

dosage (DD) or ECG, PS1 and perfusion pressure (PS2) can be measured. The external sensors for sensing these four types of signals are part of the Langendorff experimental setup and their outputs are attached to corresponding connectors on the front panel of the measuring unit (Fig. 1). The Langendorff measuring system is suitable for „in-vitro“ investigation of isolated heart of small animals, such as rat, hamster or guinea-pig. It is used for evaluation of potential response of myocardial cells evoked by pharmacological stimulation. ECG signal is sensed by 2 specially designed monopolar Ag-AgCl electrodes. Peak-to-peak ECG signal amplitude is about 100 mV. Pressure signals (PS1 and PS2) are sensed by high sensitive pressure sensors PX181B-006G5V (Omega Engineering, Inc) that allow registration of pressure variances from 0 to 6 psi (0 – 40 kPa). Drug dosage signal (DD) represents an output TTL signal of a drop-type flowmeter. Each 5 ms wide TTL impulse corresponds to a drops volume of about 50 μ l.

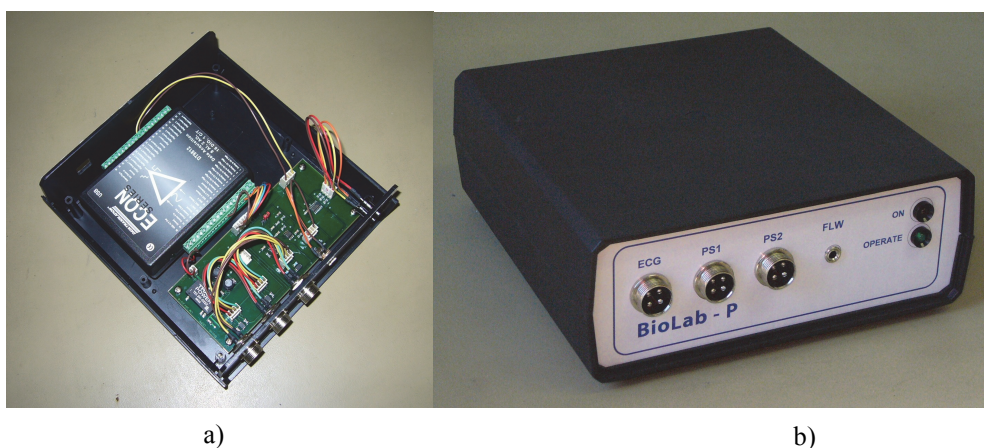


Fig. 1. a) The signal conditioning module and the data acquisition module inside the measuring unit BioLab-P; b) The measuring unit BioLab-P

The signal conditioning module and the acquisition module are placed in a patient terminal box of small geometric dimensions (190x200x70 mm). The signal conditioning module adjusts electrical signals from the external voltage, pressure and flow sensors. Its outputs are through individual cables connected to the screw terminal of the Data Translation DT9812-10V acquisition module. The data acquisition module is an economy, multifunction mini-instrument that provides one USB connector, one 12 bit A/D converter with 8 channel multiplexer, input signal range of ± 10 V and programmable gains of 1, 2, 4 a 8 allowing more effective input ranges. The per-channel sampling rate is set to 1000 Hz in the application software. The data acquisition module is through a plug-in connector connected to an USB 2.0 port of the host computer. All electric circuits of the measuring unit are powered from the USB, what eliminates the need for an external power supply. Utilization of the USB interface facilitates bidirectional data transfer between the measuring unit and the host computer. Their mutual communication is managed by the application software.

Application software

BioLab-P application software consists of a measuring part and an analytical part developed in different programming languages regarding their suitability.

The measuring software is intended for real-time acquisition. It must process large amount of data within a few milliseconds. Our measuring program developed in LabVIEW (version 8.6) and destined for multicore computing systems can significantly reduce the execution time. Fig. 2 depicts the proposed modular multiple-loop application framework. The key features of

this framework are four parallel loops running simultaneously and independently of one another. Messaging between these loops is accomplished using Queue constructs (Queue is the most commonly used messaging construct. It is an ordered set of elements [2] and in our application it serves as a FIFO buffer). Such parallel processing algorithm helps to divide processor usage among multiple cores [5]. In Fig. 2, the Data Acquisition Loop continuously acquires data even if there is a delay in any other loop. The extra samples are simply stored in the FIFO in the meantime.

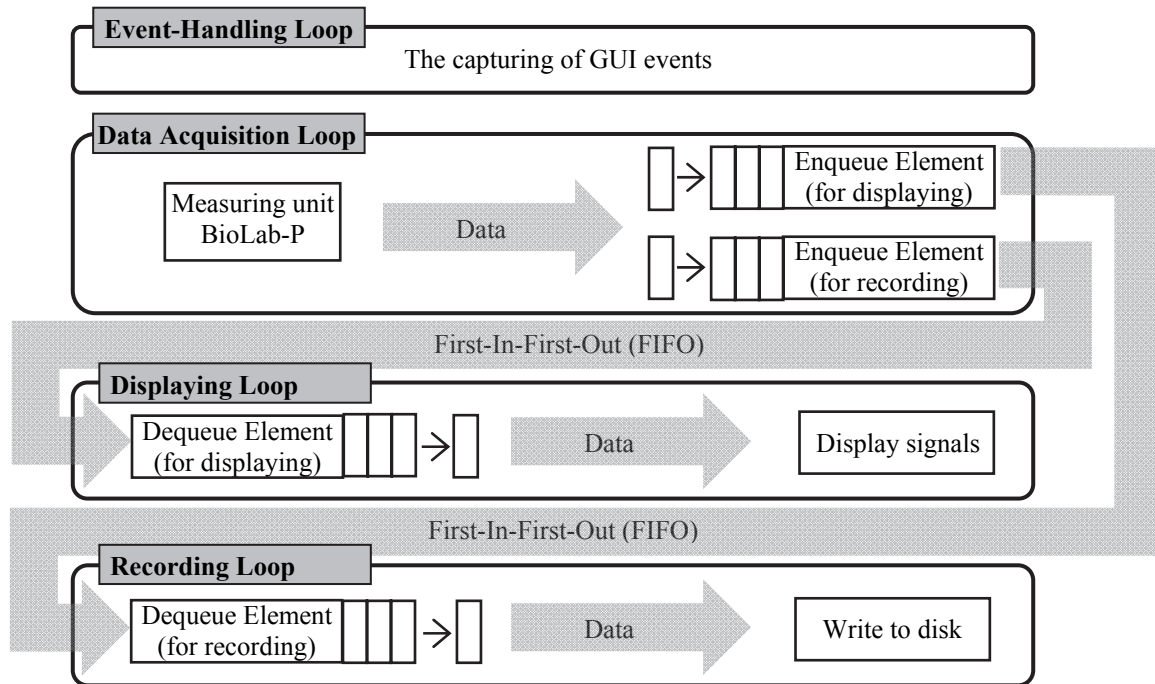


Fig. 2. A block diagram of modular multiple-loop application framework of the proposed measuring application. The diagram consists of the Event-Handling Loop for processing GUI activity, the Data Acquisition Loop for acquisition of sampled data from the acquisition unit, the Displaying Loop for visualization of measured biosignals, the Recording Loop for saving raw data to disk and the queue-based messaging scheme that accomplishes synchronization and transmission of data between the loops.

Communication over the USB port is based on a DLL that supports Data Translation's DT9812-10V acquisition module. DLL functions are fully compatible with DT-Open Layers™, a set of standards for developing integrated modular application programs under Windows [6].

Using the GUI of the measuring software, the user can set e.g. the triple of measured signals, a time base rate, an update mode, or can modify the gain of amplifiers for optimal signal resolution and appropriate visualization on the computer screen. There is also a possibility to save all signals and eventually also their descriptive stamps on a hard disk.

The real-time data acquisition is followed by the off-line data processing and evaluation. Relevant application software is developed in MATLAB (version 7) and includes simultaneous tracing of selected signals, zooming, filtration by finite impulse response type filters, searching for defined type of events in the time domain, automatic computation of 28 parameters for each signal (e. g. number of drops, number of QRS complexes, heart frequency, number of extrasystoles, time derivation of signals), transferring of requested group of parameters to an Excel sheet, spectral analysis of the signals (e. g. computation of PSD, CSA, spectrogram), etc.

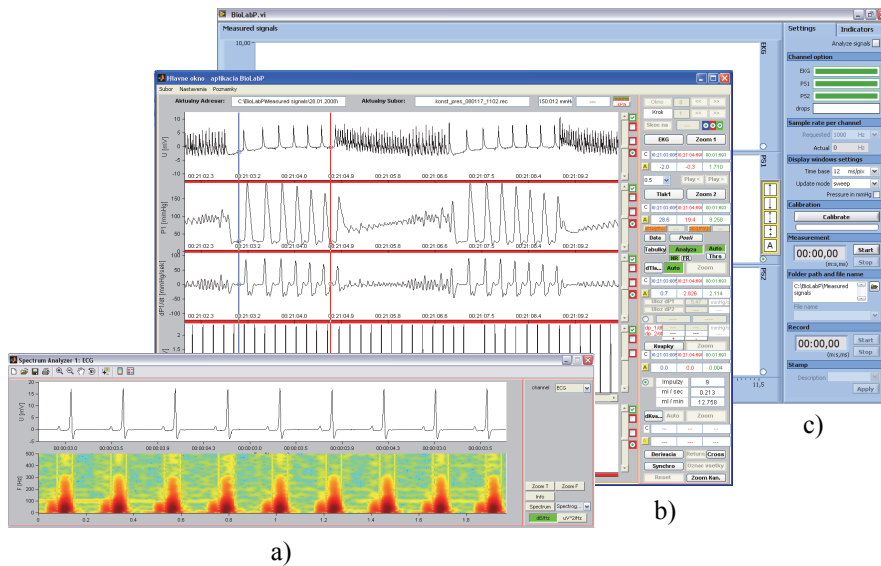


Fig. 3. The screen shots of the BioLab-P user interfaces. a) The spectral analysis window with time-frequency analysis of an ECG signal; b) The main window of the analytical application with data loaded from experiments; c) The part of the main window of the measuring application.

3. Discussion and conclusion

The measuring system BioLab-P in conjunction with existing experimental setup represents a low cost, versatile solution for pharmacological researchers investigating animal hearts following drug challenges. Modularity of the whole BioLab-P system enables to change partial hardware and software modules if more advanced tools will be available. After compilation, the BioLab-P application software can be deployed as a stand-alone application on any computer with Windows XP and later OS.

As CPU manufacturers have moved to new chip architectures with multiple processor cores on a single chip, parallel programming is rapidly becoming a necessity in order to make the most of the newest multicore processors. Advanced applications has to be optimized for these multicore processors, otherwise the expected increased performance will not be reached [7]. This is also the reason why the parallel application framework for the real-time processing was introduced.

Acknowledgements

This work has been supported by research grant No. 2/0210/10 of the Vega Grant Agency.

References

- [1] Bronzino D. J. Biomedical Engineering Handbook. CRC Press, 1995.
- [2] Travis J, Kring J. LabVIEW for Everone: Graphical Programming Made Easy and Fun. Prentice Hall, 2006.
- [3] <http://www.ni.com/labview/whatis/graphical-programming/>
- [4] Karas S., Švehlíková J., Tyšler M. Measurement and evaluation of biosignals from isolated hearts of small animals. In proceedings of the ESF project conference with international participation MEDITECH, 2008, 131 – 136.
- [5] Blume P. A. The LabVIEW Style Book. Prentice Hall, 2007.
- [6] DataAcq SDK User's Manual. Data Translation, 2010.
- [7] <http://www.ni.com/labview/whatis/multicore/>

Information Function of the Heart. A Measurement Model

V. Uspenskiy

The 2-nd Central Military Clinical Hospital named after P.V.Mandryka,
Moscow, Russia

Email: medddik@yandex.ru

***Abstract.** The paper deals with a measurement model of various diseases the semantics of which is embedded in electrocardiosignals. The development of the model described included: measuring the basic parameters of the electrocardiosignals, creating an alphabet of the symbols corresponding to available versions for the dynamics of measurement parameters of each subsequent cycle with respect to a previous one, encoding no less than 600 recorded signals in their serial stream, selecting combinations of symbols of the 100% occurrence which can be met in the patterns of healthy people and patients with different diseases, getting on these basis of these symbols code images (below called "patterns") of the norm and particular diseases. The experience gained in applying the patterns of the norm and diseases as diagnostic standards, has shown their high efficiency in the diagnostics of diseases.*

***Keywords:** Information Function of the Heart, Electrocardiosignals, Measurement Model, Semantics of Diseases*

1. Introduction

The reliable diagnostics of diseases, particularly at early stages, is one of the most important tasks of the contemporary medicine. In the scientific literature there are some publications the authors of which describe their experience in diagnosing diseases on the basis of an analysis of the pulse [1]-[3]. However, these works are supported with some other measurement models the diagnostic capabilities of which are constricted by limits of the functional diagnostics.

In [4], [5] published in 2008, a biophysical reasoning of the information function of the heart is given, and a measurement model containing patterns of the norm and diseases, used as the basis of the computer diagnostic system providing an information analysis of electrocardiosignals, is suggested.

The medical testing of the computer diagnostic system for analyzing information the electrocardiosignals contain has shown its high efficiency in diagnosing the norm and diseases most widely spread, as well as the possibility to apply this system both in biology and medicine for analyzing the semantics of signals of any biophysical nature.

2. The object and methods

To perform investigations a special electrocardiography complex, "KAD-3", was developed and produced in Russia according to technical requirements [5]. This device differs from regular cardiographs in its broader frequency band of input signals (from 0.5 to 500 Hz) and higher accuracy. Electrocardiographs with such parameters are not produced in the world.

Therapeutic investigations of the QRS-ventricular complexes, which demonstrate the electrical activity of the heart, are applied in everyday medical practice. Usually, time intervals T_n between the QRS-ventricular complexes are measured, and the configuration of signals is visually estimated. The accuracy of such measurements is not sufficient for solving the problem. According to conventional procedures (with the exception of ECG-monitoring),

5 - 15 cardiocycles are recorded, which does not enable obtaining information for diagnostics of the whole body diseases.

In the process of investigations, there was established a set of the electrocardiosignal parameters, which, at the minimum, were required for performing measurements. For each patient, 2 parameters are measured in addition to T_n (Table 1):

- amplitude or swing of the QRS-ventricular complexes taking into account their configuration;
- value of tga , where α is the conventional angle between a “zero” line of the QRS-complexes and the straight line drawn from the beginning of the interval T_n to the point corresponding to the maximum value of the signal that completes the interval.

The uncertainty of amplitude or swing measurements is no more than 5 mkV, while the uncertainty of T_n measurements is no more than 0.01 ms. To obtain reliable information, the electrocardiosignals are registered in a number of 600 (in a continuous mode). The readout of electrocardiosignals is performed within the time interval from 5 to 12 min depending on the pulse frequency of persons to be examined.

Comparison of the given set of three parameters (amplitude or swing, T_n , and tga) of each subsequent signal with respect to corresponding parameters of the previous signal allows the electrocardiosignals variation in time to be characterized. From all versions of changes experienced by the relationship of the cardiosignal parameters, six versions of them were selected as the main ones. Such signals were coded by symbols from which an alphabet was formed: A, B, C, D, E, F. Each symbol of the alphabet shows one of possible versions of the parameter dynamics for two adjacent QRS-complexes. Processing of the signals is performed with the help of special software.

The data base of the study included the electrocardiosignals obtained from both 198 healthy persons and 2760 patients with various internal diseases of a noninfectious nature. An overall diagnostics of patients under observation was simultaneously done using clinical and laboratory-instrumentation methods.

3. Results

The positive sequential coding of the parameter dynamics in a massive of 600 electrocardiocomplexes allows a pattern to be obtained. Some sets of combinations, which contained no less than three symbols with the 100 % occurrence in the corresponding groups of patients being observed, were revealed with the help of the comparative analysis of patterns belonging to the groups of observed healthy persons and patients with internal diseases. The sets of such combinations taken as patterns, i.e., specific standards of the norm and 23 widespread internal diseases, constituted a data base of diagnostic standards for the computer diagnostic system of the first generation. These diseases include, for example, diabetes, cholelithiasis, essential hypertension and ulcer, and many others.

As an example some patterns of the cholelithiasis (FAA, FFA, FCA, AAF, ADF, AFF, AEF, DFA, FBA, AAD, DFC, CAD, ACF, EFF) and those of the diabetes (AFC, CAF, AFA, FAE, AFB, BAF, BAD, EFC, EFA, CFC) are given.

In the process of testing the diagnostic system, it was found that in no less than 90 % of cases, the patterns of the norm and diseases allowed the diseases of patients recognized as ill people on the basis of traditional observation results to be identified. At the same time, in 98 % of cases the corresponding diagnoses coincided. The reproducibility of the diagnostics results was 80 – 100 %.

Table 1. The basic types of the QRS ventricular complex and versions of measurements of their main parameters.

No	QRS complex	Measurements
1		Amplitude R_n Time interval $T_n = t_{R_n} - t_{R_{n+1}}$
2		Swing QR_n Time interval $T_n = t_{R_n} - t_{R_{n+1}}$
3		Swing RS_n Time interval $T_n = t_{R_n} - t_{R_{n+1}}$
4		Swing RS_n Time interval $T_n = t_{R_n} - t_{R_{n+1}}$
5		Swing R^1S_n Time interval $T_n = t_{R^1_n} - t_{R^1_{n+1}}$
6		Amplitude QS_n Time interval $T_n = t_{QS_n} - t_{QS_{n+1}}$
7		Swing R^2S_n Time interval $T_n = t_{R^2_n} - t_{R^2_{n+1}}$

4. Discussion

The biophysical specific features of electrocardiosignals registered within an input signal frequency band from 0,5 to 500 Hz, are characterized by a probabilistic variability of the signal amplitude and frequency. This corresponds to a random transient (stochastic) process of modulation of these parameters in accordance with information about the health state [5]. The same properties are intrinsic to the pulses of a magnetic and hydrodynamic nature, which are generated by the heart. The experience gained in using the patterns as the specific diagnostic standards of the norm and diseases, obtained with the help of the proposed measurement model of processing the electrocardiosignals, completely agrees with a centuries-old experience of the China pulse diagnostics [1]. The hydrodynamic pulses (pulse waves) generated by the heart are subjected to modulation simultaneously with electrical and magnetic pulses. All this is an evidence of the uniformity of mechanisms participating in generating information that is introduced into the pulses. The specific pulse wave patterns used in the pulse diagnostics, perform the function similar to that they fulfill in the technology of the information analysis of electrocardiosignals.

The theory of information function of the heart the author suggests completely agrees with the main principles of the modern information theory as well as the theory of signals and their propagation. However, the transformation (modulation) of cardiopulses into signals of the magnetic and hydrodynamic nature, channels of signal propagation in an organism and mechanisms of perceiving information (semantics of the norm and diseases) introduced into cardiosignals by organs, have specific features peculiar to the biological system alone and, particularly, to the organism of man [5]. They are the objects for further investigations.

5. Conclusion

The measurement model suggested by the author provides a basis for information analysis of electrocardiosignals with the purpose to diagnose the norm and internal diseases. It takes into account the biological features of the information function of the heart and can be used in biology and medicine in analyzing pulse signals of any biophysical nature.

References

- [1] Nguen Van Ngi. Traditional Chinese medicine. Pathogenesis of Diseases. Diagnostics. Therapeutics. Tekhart-plaz, Moscow, 2000.
- [2] Prokop D., Cysewska-Sobusiak A., and Hulewicz A.. Application of a multi-sensor set for comparative evaluation of the photoplethysmographic waveforms. In proceedings of the 1st International Conference on Sensor Device Technologies and Applications, Venice , Italy, 18-25 July 2010, 242 - 245.
- [3] Desova A.A., Gukchuk V.V., Dorofeyuk A.A., Anokhin A.M. Investigation of regularities of the rate structure of quasi-periodical biosignals by the example of a pulse signal of the radial artery. In thye proceedings of the conference “Instruments and software of systems for control, verification and measurement (UKI-10)”, Moscow, Russia, Institute of Control Sciences, 18 -20 October, 2010. 7 p.
- [4] Uspenskiy V.M. Information Function of the Heart. *Clinical Medicine*, 5 (86): 4 – 13, 2008.
- [5] Uspenskiy V.M. The Heart Informational Function. Theory and Practice of Diagnosing the Internal Diseases on the Basis of an Information Analysis of Electrocardiosignals. Economics and Information, Moscow, 2008.

Dielectric Characterization of Limited Volume of Human Blood by Open-Ended Coaxial Measurement Probe

¹A. Takeda, ²K. Takata, ³J. Wang, ³O. Fujiwara

¹Chubu Daigaku Techno-Medical College, Nagoya, Japan,

²Toyota National College of Technology, Toyota, Japan

³Nagoya Institute of Technology, Nagoya, Japan

Email: takeda@chubu-jr.ac.jp

Abstract. To evaluate the quality of hemodialysis from the limited volume of human blood using a commercially available open-ended coaxial probe, we used pure water in lieu of blood to measure the complex relative permittivity in the frequency range from 200 MHz to 6 GHz with respect to its measured liquid volume. We then obtained the measurement errors relative to the calculated values from an empirical formula Udo developed for water permittivity. As a result, we found that 0.9 ml water in a beaker with a diameter of 24 mm and a depth of 2 mm gives a variation within $\pm 0.5\%$ for the real part and $\pm 7\%$ for the imaginary part. Taking into account the finding for water, we measured for normal healthy subjects the dielectric properties of 2.5 ml whole blood with a temperature of 25 °C in a syringe with a diameter of 20 mm and a depth of 8 mm. There was an agreement between the measurement and the data Gabriel reported for human blood with a temperature of 37 °C.

Keywords: Open-Ended Coaxial Probe, Pure Water, Human Blood, Limited Liquid Volume, Complex Relative Permittivity

1. Introduction

An open-ended coaxial probe has often been used to measure dielectric properties in combination with a network-analyzer [1], though it can be applied to semi-infinite homogeneous materials. For thickness and size of materials to be measured, on the other hand, the probe response on measurement accuracy has not been well examined [2]. With such an open-ended coaxial probe, we seek to determine the dielectric characterization of dialysis fluid in order to show the possibility for evaluating the quality of hemodialysis. Due to the limited volume of human blood, therefore, it is essential to learn how small an amount of blood may provide measurement data with acceptable accuracy. In this study, using a commercially available open-ended coaxial probe, we first measured the complex relative permittivity of pure water in lieu of blood in the frequency range from 200 MHz to 6 GHz with respect to the measured water volume, and investigated relative measurement errors in relation to the calculated values from an empirical formula [3] Udo developed for water permittivity to find out the minimum volume of water providing acceptable measurement accuracy. In view of the finding obtained for water, the complex relative permittivity of a limited amount of whole blood for healthy subjects was measured to compare with the data Gabriel [4][5] reported for human blood.

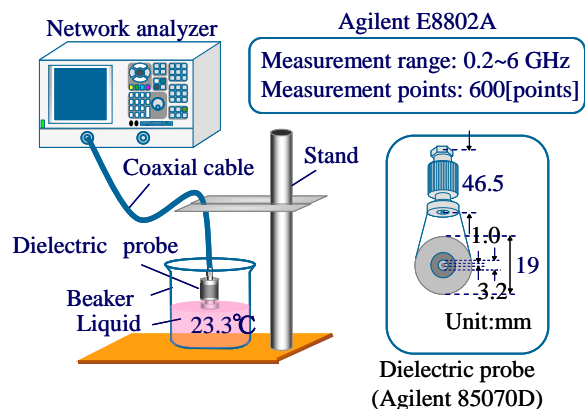


Fig. 1. Measurement setup and open-ended coaxial probe.

2. Method

Figure 1 shows a setup for measuring complex permittivity with a network analyzer (Agilent E8802A) and an open-ended coaxial probe called dielectric probe (Agilent 85070D). Also shown in the same figure are the appearance and dimensions of the probe. Due to the limited availability of human blood, we alternatively used pure water with a temperature of 23.3 °C in a beaker with a diameter of 62 mm. Measurement was conducted in the following way. With the dielectric probe connected to a network analyzer as shown in Figure 1, we measured complex relative permittivity of pure water in the beaker with respect to the water volume in the frequency range from 200 MHz to 6 GHz, when changing the distance from the probe face to the beaker bottom. In order to validate the measured results, we compared them with those calculated from an empirical formula Udo proposed for complex relative permittivity ϵ_r of pure water with temperature of T [°C], which can be expressed as in [3]:

$$\left. \begin{aligned} \epsilon_r(j\omega) &= \epsilon_r' - j\epsilon_r'' = \epsilon_r(\infty) + \frac{\epsilon_r(0) - \epsilon_r(\infty)}{1 + j\omega\tau} \\ \epsilon_r(0) &= 10^{1.94404 - 1.991 \times 10^{-3} \times T} \\ \epsilon_r(\infty) &= 5.77 - 0.0274 \times T \\ \tau [\text{ps}] &= 3.745 \times 10^{-3} \times \left\{ 1 + 0.7 \times \left[\frac{T - 27.5}{100} \right]^2 \right\} \times e^{\frac{2.2957 \times 10^3}{T + 273.15}} \end{aligned} \right\} \quad (1)$$

where $\epsilon_r(0)$ is the DC relative permittivity, $\epsilon_r(\infty)$ is the relative permittivity at infinite frequency, and τ is the relaxation time constant. In this study, considering the calculated results from (1) as the true values of complex relative permittivity for pure water, we evaluated relative measurement errors with respect to the water volume.

For validation of the complex relative permittivity of human blood, our measured results, which will be described in the next chapter, were compared with those calculated from the multiple Cole-Cole dispersion formula Gabriel developed for human biological tissues [4]:

$$\epsilon_r(j\omega) = \epsilon_r(\infty) + \sum_{k=1}^4 \frac{\Delta\epsilon_k}{1 + (j\omega\tau_k)^{1-\alpha_k}} + \frac{\sigma}{j\omega\epsilon_0} \quad (2)$$

where α_k is the distribution index or a measure of the broadening of dispersion, σ is the conductivity and $\Delta\epsilon_k = \epsilon_{rk}(0) - \epsilon_{rk}(\infty)$. Gabriel also derived these parameters for human blood [4] based on experimental data, which were used for calculation.

3. Results and Discussion

Figures 2(a) and 2(b) show the measured frequency characteristics of complex relative permittivity for pure water and

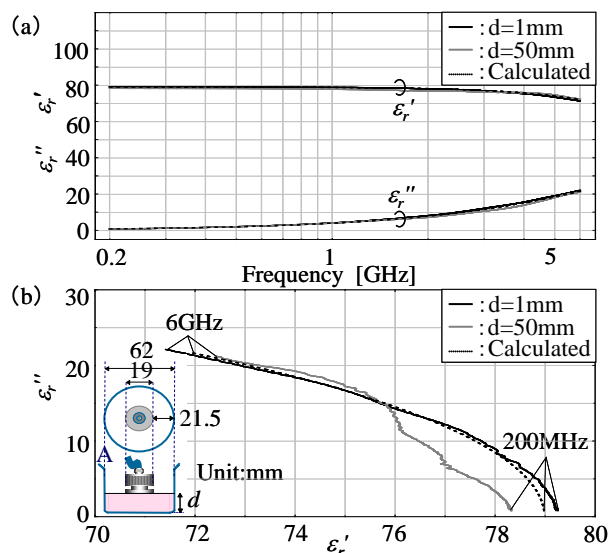


Fig. 2. Measured results of complex relative permittivity when changing distance d from probe face to bottom of beaker: (a) frequency characteristics and (b) Cole-Cole plots.

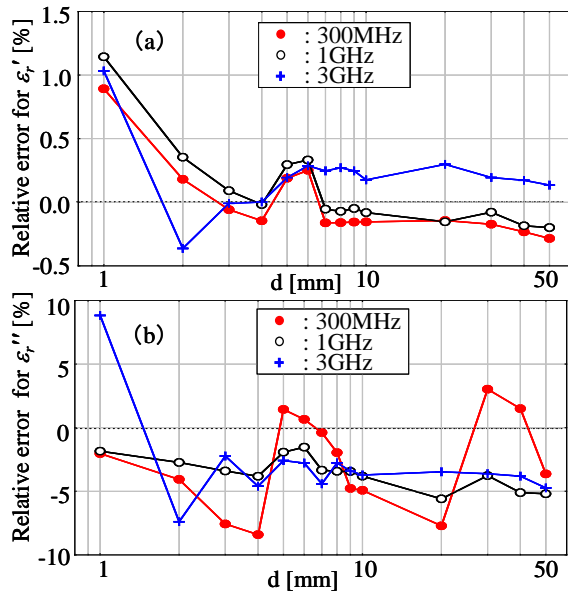


Fig. 3. Relative errors to calculated values of complex relative permittivity when changing distance d from probe face to bottom of beaker.

their Cole-Cole plots, respectively, when changing distance d from the probe face to the bottom of the beaker. Thick and thin solid lines indicate the measured results for $d = 1$ mm and $d = 50$ mm, respectively. Dotted lines indicate the calculated results from (1). Figure 2(a) shows good agreement between the measured and calculated results regardless of the distance d , while Figure 2(b) shows some discrepancies between the measured results particularly for $d = 1$ mm and the calculated result. Figures 3(a) and 3(b) show measurement errors relative to the calculated values of real and imaginary parts, respectively, for complex relative permittivity measured at frequencies of 300 MHz, 1 GHz and 3 GHz, which reveal that the water volume in a beaker with a depth of over $d = 2$ mm gives the variations within $\pm 0.5\%$ for a real part and $\pm 7\%$ for an imaginary part. Furthermore, we measured the complex relative permittivity when changing the distance between the sides of the probe and the beaker, which showed that the side distance has almost no effect on the measured results, and gives the variations within $\pm 0.3\%$ for the real part and -5.5% for the imaginary parts.

Again, according to Gabriel [4], on the other hand, the dielectric properties of human blood show that in comparison with those of water the permittivity is smaller, while the conductivity is larger. This suggests that the same amount of blood as water should provide measurement data with more acceptable accuracy due to the larger loss angle or dissipation factor. In view of the finding obtained for water, therefore, to measure the complex relative permittivity of human blood, we used 2.5 ml of whole blood in a syringe with a diameter of 20 mm and a depth of 8 mm for four healthy subjects, which are summarized along with their sex, age and blood temperature (25.1°C) in Table 1. For all blood samples used, ethylenediaminetetraacetic acid was added for anti-coagulant, which hardly affects the dielectric properties [6].

Figures 4(a) and 4(b) show the measured frequency characteristics of complex relative permittivity of whole blood for four subjects and their Cole-Cole plots, respectively. Also shown in the figure is a setup for measurement. It should be noted that different blood

Table 1. Subjects and their sex, age and blood temperature.

Subject	Sex	Age [year]	Blood temperature [$^\circ\text{C}$]
A	Male	52	25.1
B	Male	53	25.1
C	Female	23	25.1
D	Female	37	25.1

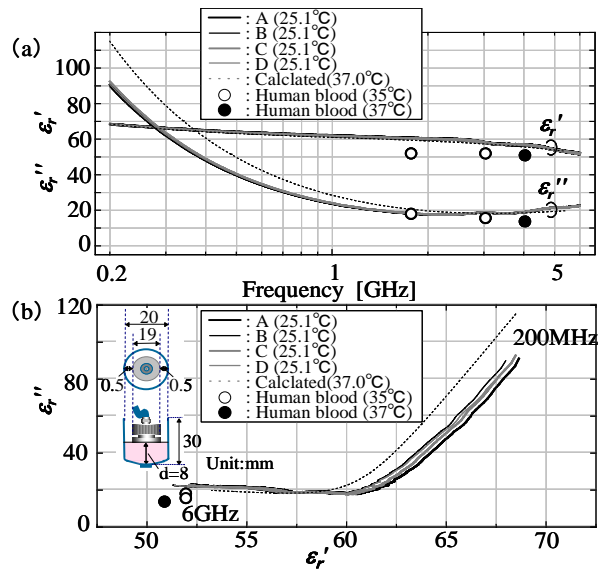


Fig. 4. Measured results of complex relative permittivity of blood for four healthy subjects. (a) frequency characteristics and (b) Cole-Cole plots.

samples give almost the same results. Dashed lines in these figures indicate the calculated results from (2) for whole blood with a temperature of 37°C. Open and closed circles are the data cited in [5] for human blood with 35°C and 37°C, respectively. Figure 4 shows that the measured real parts agree well with the calculated results and cited data despite different blood temperatures, while the imaginary measured parts are 20% smaller at most than the calculated ones at frequencies less than 1 GHz despite good agreement between them at over 1 GHz.

4. Conclusions

Using an open-ended coaxial probe in combination with a network-analyzer, we seek to measure the dielectric properties of dialysis fluid in order to evaluate the conditions and quality of hemodialysis. Due to the limited availability of human blood, however, it is essential to grasp how small an amount of blood may provide measurement data with acceptable accuracy. In this study, with a commercially available open-ended coaxial probe, in lieu of blood, we measured the complex relative permittivity of pure water in the frequency range from 200 MHz to 6 GHz with respect to its measured volume to obtain the measured errors relative to the calculated values from an empirical formula Udo proposed for water permittivity. Results showed that 0.9 ml water in a beaker with a diameter of 24 mm and a depth of 2 mm gives the variation within $\pm 0.5\%$ for the real part and $\pm 7\%$ for the imaginary part. Taking into account the finding, we measured the dielectric properties of 2.5 ml blood with a temperature of 25 °C in normal healthy subjects in a syringe with a diameter of 20 mm and a depth of 8 mm to reveal agreement between the measurement and the data Gabriel reported for human blood with a temperature of 37°C.

In a future study, we will measure the dielectric properties of blood and plasma for subjects with kidney disease before/after dialyses.

References

- [1] Delanghe P., Martens L. and Zutter D. De: Design rules for an experimental setup using an open-ended coaxial probe based on theoretical modeling. *IEEE Transactions on Instrumentation and Measurement*, 43: 810-817, 1994.
- [2] Hagl D. M., Popovic D., Hagness S. C., Booske J. H., and Okoniewski M.: Sensing volume of open-ended coaxial probes for dielectric characterization of breast tissue at microwave frequencies., *IEEE Transactions on Microwave Theory & Techniques*, 51(4): 1194-1206, 2003.
- [3] Kaatze U.: Complex permittivity of water as a function of frequency and temperature. *Journal of Chemical and Engineering Data*: 34: 371-374, 1989.
- [4] Gabriel C.: The dielectric properties of biological tissues: III. Parametric models for the dielectric spectrum of tissues. *Physics in Medicine and Biology*, 41: 2271–2293, 1996.
- [5] Gabriel C.: The dielectric properties of biological tissues: II. Measurements in the frequency range 10 Hz to 20. *Physics in Medicine and Biology*, 41: 2251–2269, 1996.
- [6] Wakatsuchi H., Hanazawa M, Watanabe S., Nishikata A., Kouzai M., Kojima M., Yamashiro Y., Sasaki K. and Hashimoto O.: The measurements of the complex permittivities of blood samples in quasi-millimeter and millimeter wave bands, *IECE Transactions on Communications*, E90-B(6): 1357-1359, 2007.

Dynamic Measurement to Keep Suitable Physical Strength in Exercise by Body Area Network Sensing System

S. Takayama, T. Tanaka, N. Takahashi, Y. Matsuda, K. Kariya

Dept.E.E.Engng. Fac.Sci.&Engng. Ritsumeikan Univ.BKC, Shiga, JAPAN

Email: s-tkym@se.ritsumei.ac.jp

***Abstract.** This paper shows the dynamic measurement system to keep a constant physical strength by monitoring a heart rate in exercise. To monitor the heart rate, the measurement system had been constructed as a wearable and small scale wireless network system put on body. That was named Body area network sensing system(BANSS). BANSS is constructed with a host system and plural sensing nodes. Sensing node has sensors, microprocessor and near field communication device(NFCD). The sensing node is the subsystem which measures the physical parameters of user in exercise, and sends them to the host system regularly. BANSS is not only the system to measure physical parameters. By analysis of them, BANSS estimates present physical condition and generate a suitable advice to keep constant physical strength and informs it to the subject in exercise. In actual exercise by using BANSS, it is confirmed that constant physical strength is kept. This means that the interaction between user and BANSS has functioned successively.*

Keywords: sensing system, physical strength, dynamic measurement

1. Introduction

In daily life, quality of life (QOL) is the highest concern for all of people. They hope to keep it well and enhance it. Parameters of QOL are many kinds and different to each person. The parameters are concerning to the situations of living, health, family, friends, job, money, meal, hobby, social activity and so on. Especially, physical condition like health is the most basic and indispensable parameter. The physical condition depends on physical activity in daily life and changes dynamically. Then, to know the state of physical condition in detail, it is necessary to measure it continuously in daily life. Wearable and wireless body area network sensing system(BANSS) is the most suitable system to measure the dynamical physical condition continuously. Concerning to the measurement system like BANSS, there are several kinds of system [1-5]. In general, BANSS collects physical parameters on several measuring points on body, and send the data and information to host system. BANSS does not only measure physical parameters but also informs the state of physical conditions and give advices to control physical strength adequately to user. Additionally, BANSS will send the measurement data and the objective information of physical condition of user to family or home doctor.

2. Body Area Network Sensing System (BANSS)

To measure physical conditions in motion like walking, running and various kinds of physical activities in daily life, there are several parameters which are heart rate(HR), SPO2(Oxygen density in blood), body temperature, skin temperature, accelerations at measuring points of body (waist and foots [ankles]), impact transmitting in bones and so on. As measuring points of these parameters are distributed on body area, the sensing system forms near field wireless network to communicate measuring data and commands. Fig.1 shows a conceptual system construction.

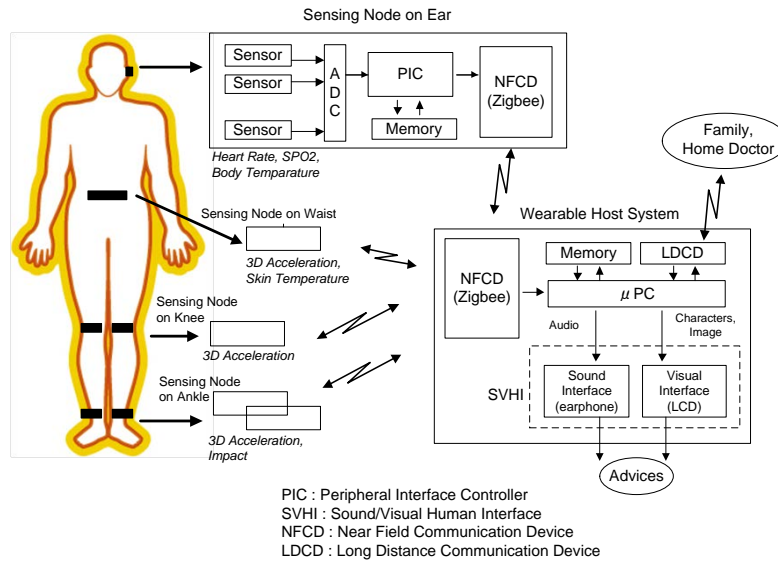


Fig.1. Concept of body area network sensing system (BANSS)

Sensing node is mainly constructed with some sensors, Analog-Digital Converter (8 channels, 10bits resolution, 0 - 3.3V input), Peripheral Interface Controller (PIC)(30MHz, 256kB memory, 32ch Digital I/O), some kinds of memory (total 1MB) and near field communication device (NFC ; Zigbee) (communication distance 80cm, 8 channels). The kinds of sensors are different each sensing node like heart rate, SPO2 and body temperature sensor on ear, acceleration and skin temperature sensors on waist, acceleration sensor on knees and acceleration and impact sensor on ankles. The main role of sensing node is the detection, analysis and transmission of physical condition parameters of user in exercise.

Host system is constructed with micro processor(SH3DSP), some kinds of memory, near field communication device (NFC ; Zigbee), long distance communication device (LDCD) and sound/visual human interface (SVHI ; earphone, small size display[LCD]). The main role of host system is the objective estimation of physical conditions, the presentation of some advices to adjust physical conditions and the report of to family and home doctor. SVHI is the system for user to present current physical condition and advices for health condition. LDCD is the device to report the information of physical conditions of user to family and home doctor. The most suitable LDCD is handy phone using commercial telephone network.

3. Management of Suitable physical strength in Exercise by BANSS

Fig.2 shows the time transition of heart rate (blue line) in a motion sequence of quiet, walking, quiet, running and quiet(Lab. student ; male, age:23) which is measured by BANSS.

It has been confirmed that the heart rate responses according to human motions. In walking, the heart rate increased gradually. In the second quiet, the heart rate decreased gradually. In running, his heart rate increased quickly. He felt so tired at finish to run. This means that his physical condition became hard. In the third quiet, the heart rate decreased quickly.

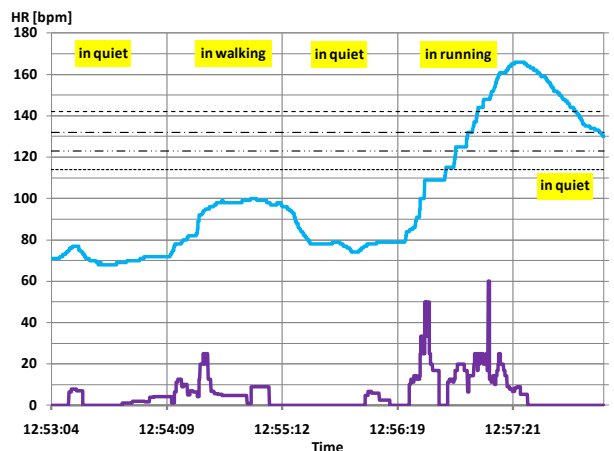


Fig.2. Time transition of heart rate in a motion sequence (blue line)

MET (Metabolic Equivalent) is well known as a unit to express strength of physical exercise. By using the heart rate, MET is calculated as follows,

$$MET = (HR - HR_{min}) / (HR_{max} - HR_{min}) \quad [\text{Karvonen Formula}] \quad (1).$$

HR_{min} : heart rate in quiet,
 HR_{max} : heart rate in the most heavy exercise

The MET is defined according with the strength of physical exercise roughly.(Table 1)

Table 1. Relation of MET and strength of physical exercise

40-50	light exercise (walking)
50-60	medium exercise (slow running)
60-85	stressed exercise
85-100	heavy exercise (professional level)

By selection of MET, suitable heart rate (HR) is calculated as follows:

$$HR = (HR_{max} - HR_{min}) \times MET + HR_{min} \quad (2).$$

To keep a constant strength of physical exercise, BANSS supplies several advices to current exercise under conditions that are value and trend of HR. Table 2 and Table 3 show the selection of advices by these conditions.

Table 2. Selection of advices to keep a constant strength of physical exercise Table 3 List of six advices

Trend of HR \ Value of HR	Even or slow down	Rising up gradually	Rising up	Advices
HR < HR _{by_min MET}	Advice_1		Advice_3	Advice_1 Pace up gradually
HR _{by_min.MET} < HR < HR _{Thr1}	Advice_1	Advice_2		Advice_2 Keep pace
HR _{Thr1} < HR < HR _{Thr2}	Advice_2			Advice_3 Pace down gradually
HR _{Thr2} < HR < HR _{by_max.MET}	Advice_2	Advice_4	Advice_5	Advice_4 Pace down
HR _{by_max.MET} < HR	Advice_6			Advice_5 Pace down quickly
				Advice_6 Stop exercise now, have short rest

where HR_{by_min MET} : Heart rate at minimum MET ,
 HR_{by_max.MET} : Heart rate at maximum MET ,
 HR_{Thr1} : 1/3 (HR_{by_max.MET} - HR_{by_min MET}) + HR_{by_min MET} ,
 HR_{Thr2} : 2/3 (HR_{by_max.MET} - HR_{by_min MET}) + HR_{by_min MET} .

Fig. 3 and Fig. 4 show the time transition (blue line) of heart rate kept medium exercise (MET: 40 - 60) controlled by advices of BANSS. In this experiment, each HRs are as follows:
 in Fig. 3, (Male;23) HR_{by_min MET} : 114, HR_{by_max.MET}: 142, HR_{Thr1}: 123, HR_{Thr2}: 132,
 in Fig. 4, (Male;32) HR_{by_min MET} : 111, HR_{by_max.MET}: 136, HR_{Thr1}: 119, HR_{Thr2}: 127.

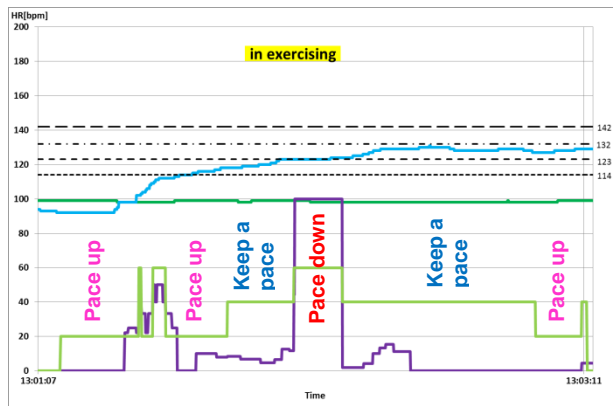


Fig.3. Heart rate(bule line) in medium exercise (MET : 40 - 60) controlled by advices of BANSS (male, age: 23)

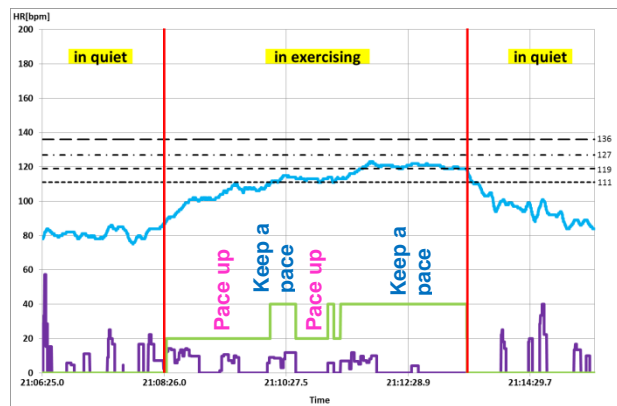


Fig.4. Heart rate(bule line) in medium exercise (MET: 40-60) controlled by advices of BANSS (male, age: 32)

Subject in Fig.3 is same in Fig.2. The heart rate (blue line) has increased gradually in the previous half. In the latter half, the heart rate has kept within 123 – 132 bpm. BANSS is advising to the subject continuously by monitoring and analysing the time transition of heart rate. Especially, BANSS is changing advices frequently. It has been confirmed that constant medium exercise (MET : 40 - 60) is realized well in the latter half.

In Fig.4 shows the result by other subject (male; 32) in motion sequence; quiet, exercise and quiet. The subject switched on BANSS just at start of exercise, and switched off just at end of that. In exercising, it is confirmed that BANSS controls heart rate into the range of HR_{Thr1} and HR_{Thr2} by several advices.

4. Conclusions

It was confirmed to keep suitable physical strength in exercise by the interaction between BANSS and user that was the monitoring dynamic physical parameters of user and the advising exercise level to user. BANSS is useful tool to measure the physical parameters at various parts on body and estimate physical condition dynamically in motion. That does not become obstacle to various motions. By reconstructing BANSS as small and robust system, the application fields will spread more and more.

References

- [1] Lee J. A., Cho S. H., Lee J. W., Lee K. H. and Yang H. K., Wearable Accelerometer System for Measuring the Temporal Parameters of Gait. *Proceedings of the 29th Annual International Conference of the IEEE EMBS. France.* 483 – 486, 2007.
- [2] Wertsch J. J., Webster J. G. and Tompkins W. J., A portable insole plantar pressure measurement system, *Journal of Rehabilitation Research and Development*, 29(1), 13-18, 1992.
- [3] Westerterp K. R., Physical activity assessment with accelerometers, *International Journal of Obesity*, 23, S45 – S49, 1999.
- [4] Rolian C., Lieberman D. E., Hamill J., Scott J. W. and Werbel W., Walking, running and the evolution of short toes in humans, *The Journal of Experimental Biology*, 212, 713 - 721, 2009.
- [5] Hyuma Makizako, Tutomu Abe, Shinichi Fujii, Kumiko Sumiya, Tatsuki Yoshimatsu, Rie Tokuhara, Shuji Kobayashi, Akira Kubo, Examination of Gait Measurement in Home-Based Rehabilitation – Gait Ability Evaluation Using a 1.5 Meters Walking Test -, *The Society of Physical Therapy Science*, 2005.

Telemonitoring of Blood Glucose and Energy Expenditure of Patients with Diabetes Mellitus to Support Optimization of Insulin Dosing

¹A. Wolf, ¹V. Caithaml, ¹L. Nestával

¹Czech Technical University in Prague, Faculty of Biomedical Engineering,
Joint Department of Biomedical Engineering CTU and Charles University in Prague,
Czech Republic,
Email: adam.wolf@fbmi.cvut.cz

***Abstract.** There are patients with diabetes mellitus who have to measure their blood glucose several times a day. The purpose of such measurements is to estimate optimal dose of insulin they should take. The amount of insulin needed depends on several aspects: previous insulin dose, amount of sugar in consumed food, previous physical activity of the patient – amount of metabolized energy and of course the measured blood glucose level. It is mostly the patient's responsibility to take into account those values. In case of inappropriate dosing the patient is exposed to a possible hyperglycemic or hypoglycemic shock. Our proposed telemonitoring system allows storing on-line data of patient's movement activity and without any additional patient's control also transmits all measured patient's blood glucose values. This can increase the patient's safety. The system could be useful especially for patients with reduced ability such as very old people.*

Keywords: telemedicine; diabetes mellitus, patient monitoring

Introduction

Diabetes is rapidly growing in prevalence worldwide. The number of people with diabetes was 171 million in 2000 and will grow to 366 million by 2030. One reason for this is a growing elderly population, but younger people are increasingly likely to develop diabetes due to an increase in mean weight and a decrease in exercise. The increasing resources needed to modify lifestyle and appropriately manage diabetes are a worldwide healthcare burden. Promising solutions arise among others from wireless technologies and mobile solutions [1].

Problems which can be solved by mobile solutions require regular monitoring of events and a fast, appropriate reaction to them. In diabetes, the stability of blood glucose level in normal life is an important objective. In addition, promotion of physical activity and exercise as well as dietary compliance may be supported by mobile solutions [1].

One of the most important values which have to be monitored by a patient with diabetes is the blood glucose level. Personal glucometers are often used for measuring. Most glucometers today use an electrochemical method. Test strips contain a capillary that sucks up a reproducible amount of blood. The glucose in the blood reacts with an enzyme electrode containing glucose oxidase. The enzyme is reoxidized with an excess of a mediator reagent. The mediator in turn is reoxidized by reaction at the electrode, which generates an electrical current. The total charge passing through the electrode is proportional to the amount of glucose in the blood that has reacted with the enzyme. For future applications non-invasive devices may enable continuous monitoring. Research is being done on non-invasive methods for measuring blood glucose, such as using infrared or near-infrared light, electric currents, and ultrasound. For now we must settle for a set of discrete measurements.

Telemonitoring system proposal

In our laboratory we have developed a home care mobile patient monitoring system [2]. Currently it is a running complex service including basic patient's mobile telemetric unit, secure centralised server solution, monitoring software and non-stop assistance service [3]. The mobile unit measures movements and location of the patient. The system also checks itself constantly by measuring several technical parameters. The patient can call for help by pressing the only one button it has. The personal inspect mobile unit is shown in Fig. 1 (left). Nowadays this basic standalone unit is used mostly by seniors living alone in their home environment. The service is going to be advantageously extended by further wireless medical peripherals for different sorts of patients.

Diabetics

For the diabetic extension of the system several glucometers have been tested. Finally we have chosen the FORA G31 Blood Glucose Monitoring system, shown in Fig. 1 (right). This glucometers have a possibility to store last thousand measured values in memory and are equipped with an integrated Bluetooth interface.



Fig. 1. Personal inspect mobile sensing unit (left) with wirelessly connected blood glucose meter (right).

Hardware of our 2nd generation mobile unit has been adjusted, another type of 3D accelerometer (ADXL327) has been used and the Bluetooth interface has been added into it. We have used Laird BTM411 modules for this. The firmware has been modified so the mobile unit is wirelessly paired with the glucometer. It detects when the glucometer turns on. After that it waits for receiving just measured value or it can receive other values stored in memory. Finally these values are sent to the server and there processed and stored. All this happens automatically without any additional patient's control. The unit also measures the patient's movement activity, processes signals from the accelerometer and sends them to the server. Trends can be observed from the client application (by the patient or his diabetological specialist). Alarm thresholds to avoid hyperglycemic state or hypoglycemic shock can be set.

Pilot measurements

The system is being tested in cooperation with The Research Center for Diabetes, Metabolism and Nutrition 3rd Medical Faculty, Charles University in Prague. First group of testing patients are pregnant diabetic women or women having gestational diabetes. The percentage of patients with diabetes mellitus consists of a population of about 1.5-2.0% of pregnant women. In case of gestational diabetes is the presence of about 3-4% of all pregnant women. Perinatal morbidity of children of mothers with diabetes mellitus is approximately 3 times higher than children of healthy mothers [4]. Measurement of blood sugar runs eight times a day, movement activity is monitored continuously 24 hours a day.

Results

An option how to monitor the patient's blood glucose level remotely in his home environment has been demonstrated. Working sample of such a system has been made and tested. The system is able to work without any additional patient's control. From the measured movement activity of the patient can be estimated his energy expenditure and the dose of insulin can be than optimized.

Discussion

There is work to be done around algorithms for accurate calculation of energy released during daily exercise. In case of well-located sensing unit measured data are sufficient for this and the calculation may be done by the server side. Algorithms for processing blood glucose trends may be also improved to be able to prevent some critical states. This is going to be discussed with diabetological specialists.

Acknowledgements

We would like to thank ForaCare Suisse AG Switzerland for providing us with their blood glucose meters including data communication protocols. We also thank MUDr. Kateřina Andělová from the Research Center for Diabetes, Metabolism and Nutrition 3rd Medical Faculty, Charles University in Prague and her patients for valuable testing of our system.

References

- [1] E. ALASAARELA, N. S. OLIVER.: Wireless Solutions for Managing Diabetes: A Review and Future Prospect, *Department of Electrical and Information Engineering, University of Oulu*, 2010, pp. 1-19.
- [2] K. HÁNA, P. SMRČKA, R. FIALA, J. MUŽÍK - ET.AL.: The system for monitoring of the human psychophysiological state, *Czech Office of Industrial Ownership*, 2009.
- [3] CleverTech [online], 2011, <<http://www.cleverttech.cz/>>.
- [4] K. ANDĚLOVÁ.: Diabetes mellitus in pregnancy, Recommended practices, *ČLS JEP*, 2001, pp. 1-5.

Some Aspects of Liver Iron Stores Measurement with the SQUID System

M. Škrátek, I. Šimáček, A. Dvurečenskij and J. Maňka

Institute of Measurement Science, Slovak Academy of Sciences

Bratislava, Slovakia

Email: martin.skratek@savba.sk

Abstract. Direct method of measurement liver iron stores using SQUID gradiometer system is presented. A method for correction of the results, which should be applied depending on the size, shape of the liver and its position against the sensor is given. The possibility of using this noninvasive method in clinical practice is presented.

Keywords: SQUID Gradiometer System, Liver Iron Quantification, Ferritin

1. Introduction

Iron occurs in the liver in the form of a protein called ferritin. For this reason the liver susceptibility χ differs from the surrounding diamagnetic tissue. In a healthy human body there can be up to 4 g of iron with 400 mg (on the average) of iron storage in the liver [1]. Liver χ varies according to the concentration of iron c_{Fe} ($\text{mg}_{\text{Fe}}/\text{g}_{\text{tissue}}$), and therefore in the magnetic field it results in corresponding change of the liver magnetization M_m . As the measured values of the M_m are very small it is reasonable to use the SQUID system. Our biomagnetic system consists of the RF SQUID, 2nd-order gradiometer, electronic modules, movable patient bed and the magnetization system with Helmholtz coils generating the uniform magnetic field in the direction of gradiometer axis. The magnetization system is driven by AC current [2, 3] with the frequency of 2.8 Hz. The gradiometer measures magnetic induction B_m above the abdomen and it is placed close to the surface near the liver [4].

2. Methods and results

To define the relation between the SQUID gradiometer output voltage U_{pp} and c_{Fe} , the reference phantom of the adult torso has been constructed, Fig 1. The phantom consisted of two acrylic containers filled with distilled water, which simulated a diamagnetic environment of the thorax and abdominal cavity with the volume of 0.023 m^3 and 0.02 m^3 , respectively. Inside these containers there were placed two air-filled polyethylene 0.001 m^3 models of lung lobes and cylindrical or ellipsoidal model of liver with volume of 0.001 m^3 filled with the specific aqueous solution of paramagnetic $\text{FeCl}_3 \cdot 6\text{H}_2\text{O}$, where c_{Fe} was ranging from 0.1 - 5 $\text{mg}_{\text{Fe}}/\text{g}_{\text{water}}$. Using this phantom, from four measurements of B_m , the dependence of average c_{Fe} on U_{pp} and the 95% confidence interval for this SQUID biomagnetic system has been determined, Fig. 2. Measurements proved the linear relationship $c_{\text{Fe}} = f(U_{\text{pp}})$, however, also a relatively large uncertainty in determining the values of low c_{Fe} , which practically makes impossible to distinguish the reduced value of c_{Fe} (iron deficiency) from normal levels (0.1-0.5 $\text{mg}_{\text{Fe}}/\text{g}_{\text{tissue}}$). On the contrary, pathologically high values of c_{Fe} , above 1.5 $\text{mg}_{\text{Fe}}/\text{g}_{\text{tissue}}$, will be determined more reliably. As the mass susceptibility of $\text{FeCl}_3 \cdot 6\text{H}_2\text{O}$ is approximately by one-half less than the mass susceptibility of ferritin $\sim 1.6 \times 10^{-6} \text{ m}^3 \text{ kg}^{-1}$ [5], the dependence of $c_{\text{Fe}} = f(U_{\text{pp}})$ derived from the model measurement has been recomputed to the ferritin value, see right axis in Fig. 2. Measurements of c_{Fe} are mainly influenced by i) the position of the gradiometer towards the liver and ii) the volume and the shape of the liver. To enable the



Fig. 1. Configuration of the phantom of thorax and abdomen consists of two containers filled with distilled water, models of lungs and liver. A part of the SQUID system is shown above.

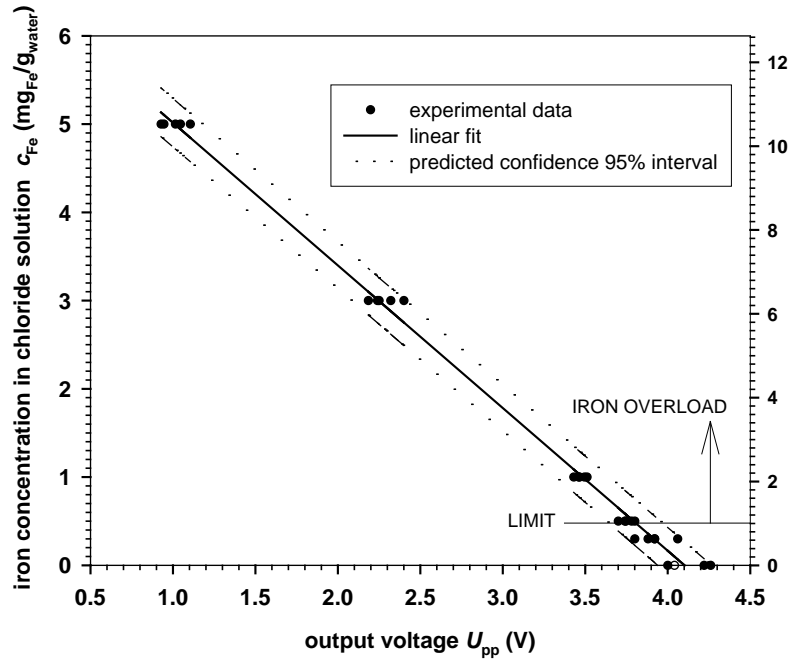


Fig. 2. Correlation between the iron concentration c_{Fe} and output voltage U_{pp} for determining the iron in chloride solution $FeCl_3 \cdot 6H_2O$ and ferritin.

comparing of various measured values of c_{Fe} , the theoretical calculations of B_m have been made: amorphous shape of the liver and middle part of the model were replaced by the defined spherical volumes V_N and using the MR images of the abdominal cavity, these spherical volumes were placed in the nearest position to the gradiometer axis, Fig.3. The measurements demonstrated, that the detection characteristics of the used 2nd order gradiometer is relatively narrow, therefore we estimated that lateral and distant parts of the liver will not significantly affect the overall measured value of B_m . The calculation of B_m also assumes that ferritin is in the liver dispersed homogenously, liver tissues and surrounding diamagnetic tissues have the same properties as water and B_m will be always measured at a distance of 0.01 m from the surface of the model, or the abdomen above the right greater part of the liver.

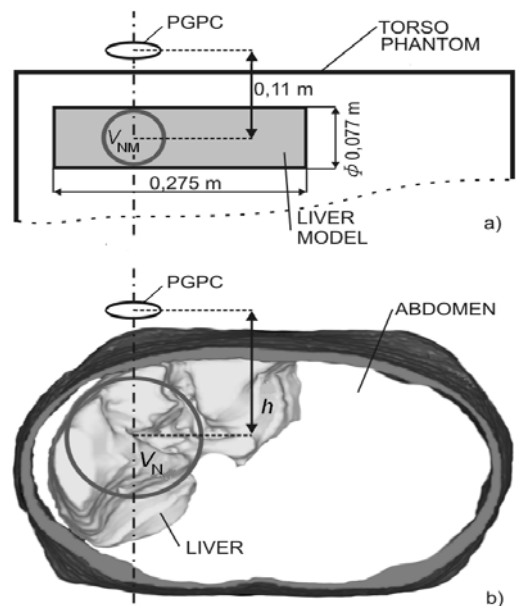


Fig. 3. Approximation of the model (a) and the liver shape (b) by spherical volumes V_{NM} and V_N using MR images of the transversal section of the abdomen, PGPC – proximal gradiometer pick-up coil.

Theoretical calculation B_m comprising the size, shape and position of the liver can be performed if V_N is divided into small elements (with the volume of 10^{-6} m^3) which are located on rings (of the width of 0.01 m) around the gradiometer axis. As all elements have the same magnetic moment \vec{m} oriented in the direction of the magnetic field, values B_m can be calculated consecutively for each of gradiometer coil due to relation [6]

$$\vec{B}_m(\vec{m}, \vec{r}) = \frac{\mu_0}{4\pi} \left[\frac{3(\vec{m} \cdot \vec{r})\vec{r}}{r^5} - \frac{\vec{m}}{r^3} \right] \quad (1)$$

where \vec{r} is the position vector of pertinent magnetic element towards the sensing coil. From the nature of relation (1) is clear, that for each of small magnetized element is sufficient to calculate only the variable component, so-called position parameter $A(x, h, ib)$ by formula

$$A(x, h, ib) = \frac{3(h + ib)^2}{\left[\sqrt{x^2 + (h + ib)^2} \right]^5} - \frac{1}{\left[\sqrt{x^2 + (h + ib)^2} \right]^3} \quad (2)$$

where x is the radius of the rings, h is the vertical distance between the center of V_N and the center of the proximal gradiometer pick-up coil (PGPC), b is the baselength and $i = 0, 1, 2$. By summation of all values $A(x, h, ib)$ related to a given V_N , applying to all gradiometer coils, the cumulative positional parameter $A_C(V_N, h)$ for h in the range from 0.08 to 0.22 m and V_N 0.00025 to 0.002 m^3 were obtained, Fig. 4. When the cylindrical model was replaced by the spherical model with $V_{NM} = 0.00024 \text{ m}^3$, which was located at the distance of $h_M = 0.11 \text{ m}$ from the PGPC, the cumulative positional parameter for the liver model $A_{CM}(V_{NM}, h_M) = 3.15 \times 10^{-7} \text{ m}^{-3}$ was calculated.

Then the correction factor k was defined as

$$k = A_C(V_N, h) / A_{CM}(V_{NM}, h_M) \quad (3)$$

where $A_C(V_N, h)$ is cumulative positional parameter for given h and V_N of the measured liver. Then the actual concentration of iron in the liver, which is corrected to the size, shape and position of the measured liver is $c_{Fe k} = k c_{Fe}$, where c_{Fe} is determined from the relationship $c_{Fe} = f(U_{pp})$, see Fig. 2, ferritin axis.

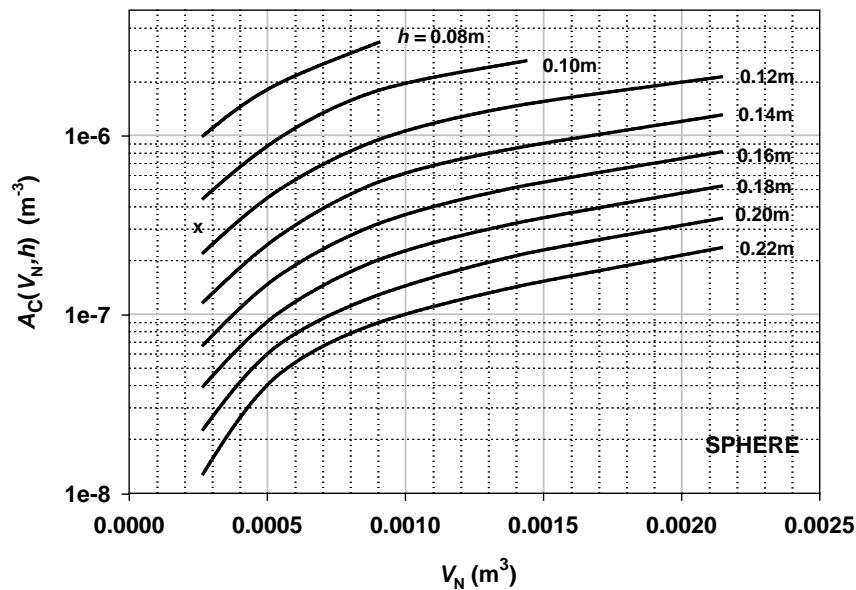


Fig. 4. The cumulative position parameter $A_C(V_N, h)$ depending on the spherical volume V_N and the distance h between PGPC and the center of the sphere. The dagger shows the value of the cumulative position parameter $A_{CM}(V_{NM}, h_M)$.

The exact location of the gradiometer above the liver plays an important role, especially regarding repeated measurements. On the liver model with the ellipsoidal shape, the influence of the gradiometer deflection (in two perpendicular directions) on U_{pp} has been studied. Even by change of gradiometer position ± 0.01 m from the center of the ellipsoid, the value of U_{pp} increased by about 13%, what could be eventually rated as a lower c_{Fe} in comparison to reality.

3. Discussion

It is clear that non-invasive magnetometric determination of iron content in the liver is associated with relatively large uncertainties. In order to obtain the relevant c_{Fe} in the liver it is necessary to correct the measured values depending on the position, shape and volume of the measured object. Model measurements showed that we could measure with the uncertainty under 10% only if c_{Fe} is higher than $4 \text{ mg}_{Fe}/\text{g}_{tissue}$. A particular improvement of the relative accuracy can be achieved by stabilization of the magnetizing field homogeneity which is affected by temperature changes in the coils of the Helmholtz system. In any case, the decisive influences on the accuracy of measurement liver iron stores are: to find the exact position of the liver to the sensor, and to define the liver volume and its shape.

Acknowledgements

This work was supported by Agency of the Ministry of Education of the Slovak Republic for the Structural Funds of the EU, Operational Programme Research and Development (OPVaV-2008/4.1/01-SORO), Project Code 262 401 200 11 and by VEGA grant 2/0160/10.

References

- [1] Bauman JH, Harris JV. Estimation of hepatic iron stores by in vivo measurement of magnetic susceptibility. *Jour. Lab. & Clin. Med.*, 70 (2): 246-257, 1967.
- [2] Carneiro AAO, Fernandes JP, Vilela GR, Baffa O, Angulo IL, Covas DT. Preliminary Liver Iron Evaluation Using an Superconducting Magnetic Susceptometer. In proceedings of 13th International Conference of Biomagnetism, BIOMAG 2002, 2002.
- [3] Penna SD, Gratta C, Luizio S, Pizzella V, Torquati K and Romani GL. The use of an inhomogeneous applied field improves the spatial sensitivity profile of an in vivo SQUID susceptometer. *Phys. Med Biol.*, 44 (3): N21-N29, 1999.
- [4] Boháková F, Šimáček I, Jurdák P. Basic quantification of magnetic particles in solid substance and human tissue by the SQUID gradiometer., *Sensors and Actuators A*, (129), 150-153, 2006.
- [5] Carneiro AAO, Fernandes JP, Angulo LL, Zago MA, Covas DT, and Baffa O. An alternating current superconductor susceptometric system to evaluate liver iron overload. *Review of Scientific Instruments*. 6 (74), 3098-3103, 2003.
- [6] Kötitz R, Matz H, Trahms I, Koch H, SQUID Based Remanence Measurements for Immunoassays, *IEEE Trans. On Applied Superconductivity*, 2 (7), 3678-3681, 1997.

Selected Methods for Automatical Classification of Psychophysiological States in Experimentally Controlled Psychological Load

R. Kliment, P. Smrčka, J. Jeřábek, M. Vítězník

Joint Department of Biomedical Engineering CTU and Charles University in Prague,
Prague, Czech Republic
Email: radim.kliment@gmail.com

***Abstract.** In this work we deal with acquiring and consecutive processing and last but not least with data analysis, acquired at the Charles University, Faculty of Science in real experiments. The data consists of psychological factors computed from psychological questionnaires helping to determinate level of dominance or submissiveness. The second part of data consists of electrophysiological parameters acquired in double tests, including stressful part and relaxation part. We discovered a correlation between psychological factors and few parameters of HRV analysis. The usage of psychological factors helps to better classify the stress part.*

Keywords: stress, HRV analysis, dominance, psycho-physiological correlates

1. Introduction

Detection of stress as one of important psychophysiological aspects could help in many areas of human activity, where a wrong decision can lead to very serious consequences, e.g. army or health care. By detection of stress we can improve the quality of life, because we know that long-term exposure to a stress has a destructive influence on cardiovascular system. These people exposed to long-term incidence of stress have higher probability of cardiovascular diseases [3][4]. The aim of this work is to prove correlation between psychological factors and parameters of HRV analysis. We want to add another piece to a mosaic of non-invasive measuring quantity of stress of organism and quantification of stress in real time.

The data are coming from experiments which were led by prof. Flégr at the Charles University. These real experiments are part of a research that monitors influence of parasite *Toxoplasma Gondii* on a human psychophysiology [2]. All probands in experiments are blood donors tested on *Toxoplasma Gondii* antigens. The experiments were composed from several parts. In the beginning probands had an interview with a psychologist. After that they filled out several psychological questionnaires which determined their submissiveness or dominance in different aspects of their lives. After the questionnaires were filled out probands were connected to a wireless non-invasive telemetric measuring system VLV2 by a person of opposite sex. In the first part of measurement they were given crayons with different colors. They were asked to put them together side by side according to the colours and according to their own colour preferences. In the second part, the stress part, the person of opposite sex opened a case with BDSM stuff and took out of this case a inform consent on which the proband had to tick BDSM techniques which they are willing to practice. After that the proband had to sign this document. Once they signed that form, the probands were told by the person of opposite sex that the experiment is over. This was followed by a short conversation about proband's feelings that he had during the experiment. The Charles University is preparing a new wider cycle of experiments. It is necessary to technically optimize measuring units for those new experiments.

2. Subject and Methods

Bio-telemetrical system VLV2

For measuring experiments was on joint department of Biomedical Engineering CTU in Prague, Albertov, developed a modular telemetric units that are able to noninvasively measure signals. Units are wireless, working with wifi technology. A system is able to measure and record data in real time from twelve units at once. This is a benefit, it saves time. And it can be used in new experiments, where prof. Flégr wants to measure an influence between probands . As at the Charles University were planned new massive experiments, we had to technically optimize the measuring units, so we put a crypt module into the units. This module was added because it was important to secure measured data, which are personal, non-public. This module was created within a student grant. To encrypt was used a library Crypto++ [5], which was ported to our used architecture of microprocessor [6]. This library contains crypt algorithms (Blowfish, AES) that can be used for crypt in a real time. The module is built into the system – as it is visible in Figure 1.

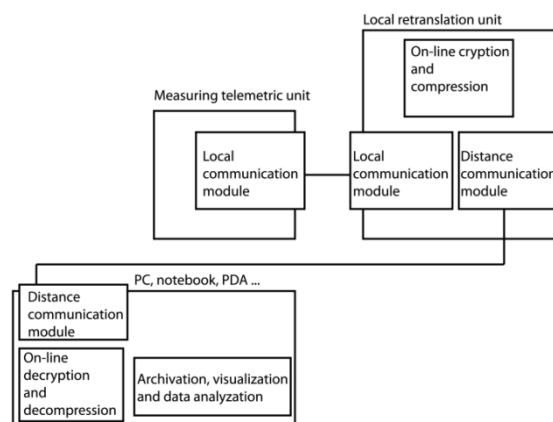


Fig. 1. Block diagram of crypt module

Measured data

The data were measured in real experiments at the Charles University. We measured 71 probands, 25 men, 46 women. The probands filled out few questionnaires, from these questionnaires the psychological factors were computed out of these questionnaires. We computed a cardiogram from ECG. Detection of QRS complex was performed by QRSDet plugin which is a part of VLV system [7]. In final analysis we worked with psychological factors and parameters from HRV analysis, computed from cardiogram in Kubios [1] software. Prof. Flégr computed psychological factors, which were based on psychological questionnaires. The questionnaires were intended to find affection to dominance or submissiveness in various aspects of human life. Table 1 shows these factors.

Table 1. Psychological factors

Factor	Nature	Range
Shawl	Proband likes tying?	-2,65 – 1,68
Democrat	Proband cling on equality?	-2,32 – 2,89
Non-dominance	Proband is non-dominant?	-2,4 – 1,95
Judith	Dominance on psychologist	-2,09 – 3,63
Film	Excitement from dominance in film?	-3,68 – 2,18
Cattell	Dominance by Cattell test	-2,73 – 1,98
Non-cooperation	willingness to cooperate	-2,44 – 2,36

Results

We studied an influence of these factors separation to a relax state and stress state with individual HRV parameters. Factors were used like filters. In Microsoft Excel was created a framework that allowed application of filters and creating of graphs in real time. With boxplot graphs (figure 2) we were looking for a parameters that separate both states (stress, relax).

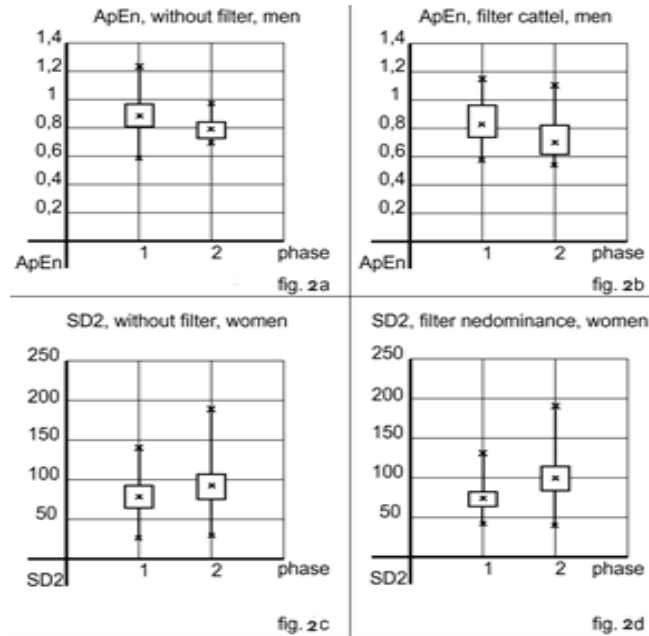


Fig. 2. Boxplot graphs HRV parameters with filters and without filters

The best HRV parameter for detection of stress for men was parameter ApEn (fig 2a) and SD2 (fig 2c) for women. These two parameters are able to separate both states. Better separation of relax and stress state can be achieved by using of psychological factors. The best ability of separation of states for women had “non-dominance” factor on HRV parameters HF/LF and SD2 (fig 2d). The best ability of separation for men had factor “Cattel” on ApEn parameter (fig 2b). Table 2 shows filters and HRV parameters, which have the best separation of states.

Table 2. Psychological filters

Filter	Adjustment	Sex	Parameter*	Classification Error
Non-dominance	(-10) – (-0,07)	Women	SD2	29,46%
Non-dominance	(-10) – (-0,07)	Women	LF/HF	30,88%
Non-dominance	(-10) – (-0,07)	Men	Shannon	21,64%
Non-cooperation	0,18 – 10	Women	SampEn	29,16%
Cattel	0,1 – 10	Man	ApEn	31,18%

* **SD2** – Non-linear Poincare plot parameter; **LF/HF** – Low frequencies / High frequencies; **Shannon** – Shannon entropy coefficient; **SampEn** – Sample Entropy is the negative natural logarithm of an estimate of the conditional probability that subseries (epochs) of length *m* that match pointwise within a tolerance *r* also match at the next point. [12]; **ApEn** – quantifies the unpredictability of fluctuations in a time series such as an instantaneous heart rate time series [12].

Discussion

The aim of this work was to acquire a process for classification of stress from cardiogram recording. We found markers in HRV analysis that demonstrably carry information about stress. These markers were found on women and men, too. For better

classification of stress can be used psychological factors, computed from psychological questionnaires. We designed and constructed new optimized versions of units for next experiments at the Charles University. Our next work is aimed to automate and improve the process of classification. We want to create accurate and fully automated system for detection stress state, which can be calibrated for particular cases, by psychological parameters.

Acknowledgements

Supported by projects No. FR—TI3/703 and FT-TA5/135 (Ministry of Industry and Trade of the Czech Republic) and project No. VG20102015002, Ministry of the Interior of the Czech Republic and CTU internal student grant No. OHK4-045/10.

References

- [1] Biosignal analysis and Medical imaging group „HRV analysis software“: <http://kubios.uku.fi/>.
- [2] FLEGR, J. Effects of Toxoplasma on human behaviour. *Schizophrenia Bulletin*, 2007: 33, 757-760.
- [3] Paul A. Landsbergis, Susan J. Schurman, Barbara A. Israel, Peter L. Schnall, Margit K. Hugentobler, Janet Cahill, and Dead Baker: Job stress and heart disease, Scientific Solutions, Summer 1993.
- [4] Schnall, P. L., Landsbergis, P. A. Baker, D. "Job Strain and Cardiovascular Disease," *Annual Review of Public Health*, 1994 (under review).
- [5] Wei Dai: Crypto++ ® Library 5.6.0 [online]. 2004 [cat. 2010-01-31] at. WWW: <<http://www.crzptopp.com>>.
- [6] Horňáková, A. : Encryption and compression in real-time biological data transfer. 2010
- [7] Pavel Smrčka, Jan Kašpar, Karel Hána, Jiří Brada, Jan Mužík: Multiparametrické mobilní zařízení pro snímání biologických signal, funkční vzor TZ-FVZ- 144233-VLVH2 1.0.
- [8] Bayevski et al.: HRV Analysis under the usage of different electrocardiography systems (Methodical recommendations), Committee of Clinic Diagnostic Apparatus and the Committee of New Medical Techniques of Ministry of Health of Russia - protocol №4 from the 11-th of April, 2002.
- [9] Smrčka, P. - Hána, K. - Kašpar, J. - Brada, J. - Fiala, R.: Multifractal Analysis of Heart Rate Variability in Sleep Deprivation and Alcohol Intoxication. In: The 3rd European Medical and Biological Engineering Conference — EMBEC'05 [CD-ROM]. Praha: Společnost biomedicínského inženýrství a lékařské informatiky ČLS JEP, 2005, vol. 11, s. 2583–2586. ISSN 1727–1983.
- [10] Roman Bittner, Pavel Smrčka, Miroslav Pavelka, Petr Vysoký, Lubomir Pousek: Fatigue Indicators of Drowsy Drivers Based on Analysis of Physiological Signals, in: Medical Data Analysis, Second International Symposium, ISMDA 2001, Madrid, Spain, October 8-9, 2001, Proceedings. Lecture Notes in Computer Science 2199 Springer 2001, ISBN 3-540-42734-1, pp. 62-68.
- [11] Nedělka - Smrčka - Jeřábek: ROLE ROVNOVÁŽNÉHO ÚSTROJÍ V REGULACI AUTONOMNÍCH FUNKCÍ, *Neurol. prax*, 2007; 6: 346 – 348.
- [12] Goldberger AL, Amaral LAN, Glass L, Hausdorff JM, Ivanov PCh, Mark RG, Mietus JE, Moody GB, Peng CK, Stanley HE. PhysioBank, PhysioToolkit, and PhysioNet: Components of a New Research Resource for Complex Physiologic Signals. *Circulation* 101(23): e215-e220 [Circulation Electronic Pages; <http://circ.ahajournals.org/cgi/content/full/101/23/e215>]; 2000 (June 13).

A Reference for Human Eye Surface Temperature Measurements in Diagnostic Process of Ophthalmologic Diseases

¹M. Tkáčová, ²J. Živčák, ²P. Foffová

¹CEIT-KE, Košice, Slovakia,

²Technical University of Košice, Faculty of Mechanical Engineering, Košice, Slovakia

Email: maja.tkacova@gmail.com

Abstract. *The study is focused on the area using infrared diagnostics for ophthalmic applications, with the aim to obtain the physiological surface temperatures database of healthy eyes. The contactless, noninvasive and painlessness infrared thermography (IRT) was used (Thermocamera Fluke Ti 55/20, Fluke, USA and the software SmartView 2.1, Fluke, USA) to create a database of 28 thermograms of healthy human eyes. As an identification markers - a circular polygon and three points T1, T2 and T3 on the linear horizontal axis of the eye were assessed. The results show that the overall average temperature of the cornea of the eye is $34,5 \pm 0,8$ °C.*

Keywords: Thermography, Ophthalmology, Temperature

1. Introduction

For many years temperature is the first measurement of a physical property for determination of diagnosis in the medicine. From electromagnetic theory it is a form of infrared energy being emitted from the first molecular surface of a body (skin). Infrared imaging is the detection and conversion of energy from a section of the infrared spectrum, into the visible spectrum. Surface energy levels are affected by the environment, operational conditions, heat transfer processes of a human body and the surface characteristics.

Thermography is a non-invasive, contactless temperature measurement technique used to produce a colored visualization of thermal energy emitted by the measured surface. Each pixel in the image depicts the radiance falling on the focal plane array/ microbolometer– type detector used in an IR camera.

Current applications infrared thermography in ophthalmology include:

- diagnosis of glaucoma, an eye disorder in which the optic nerve suffers damage, permanently impacting vision in the affected eye(s) and progressing to complete blindness if untreated. It is often, but not always, associated with increased pressure of the fluid in the eye;
- monitoring surface temperature of a healthy eye;
- thermographic monitoring of tear ocular film;
- thermography and comparison of normal, ischemic and hyperaemic eye;
- the impact of contact lenses for the eye surface temperature and other

Our study is based on monitoring the temperature of the healthy eye to get the reference database for diagnostic process support of ophthalmologic diseases.

2. Subject and Methods

Skin temperature on human eyes from our database (n= 28) were measured with an infrared camera (ThermaCam Fluke Ti55/20, Fluke, USA) with 10,5 mm lens (10,5 mm F/0,8; 8-14 μm). The thermal sensitivity of the camera is 0.05°C at 30°C of a blackbody. Camera works in the spectral range from 8 to 14 μm (human body infrared radiation is highest in the spectral

range around $9,66 \mu\text{m}$) and the calibrated temperature range from -20 to $100 \text{ }^\circ\text{C}$. Camera resolution is 320×240 pixels (total 76.800 pixels). Data were obtained through a high-speed (60Hz) analysis.

Emissivity of the skin was set in the camera software to 0,98, the ambient temperature was measured by handheld thermometer (Testo 810). Before each recording the camera was calibrated using the system's internal calibration process. All thermograms ($n=28$) were processed by SmartView 2.1 software.

Object of our measurements were volunteers, their average age was 24 years.

Methodology of Measurement

Our measurements were carried out under the same conditions, same room (air-conditioned) ambient temperature $20 \text{ }^\circ\text{C}$ ($\pm 1 \text{ }^\circ\text{C}$). Each eye was scanned separately. The 10.5 mm lens was used and constant distance between camera lens and the human eye was maintained ($d = 5 \text{ cm}$) as it is shown in Fig. 1.

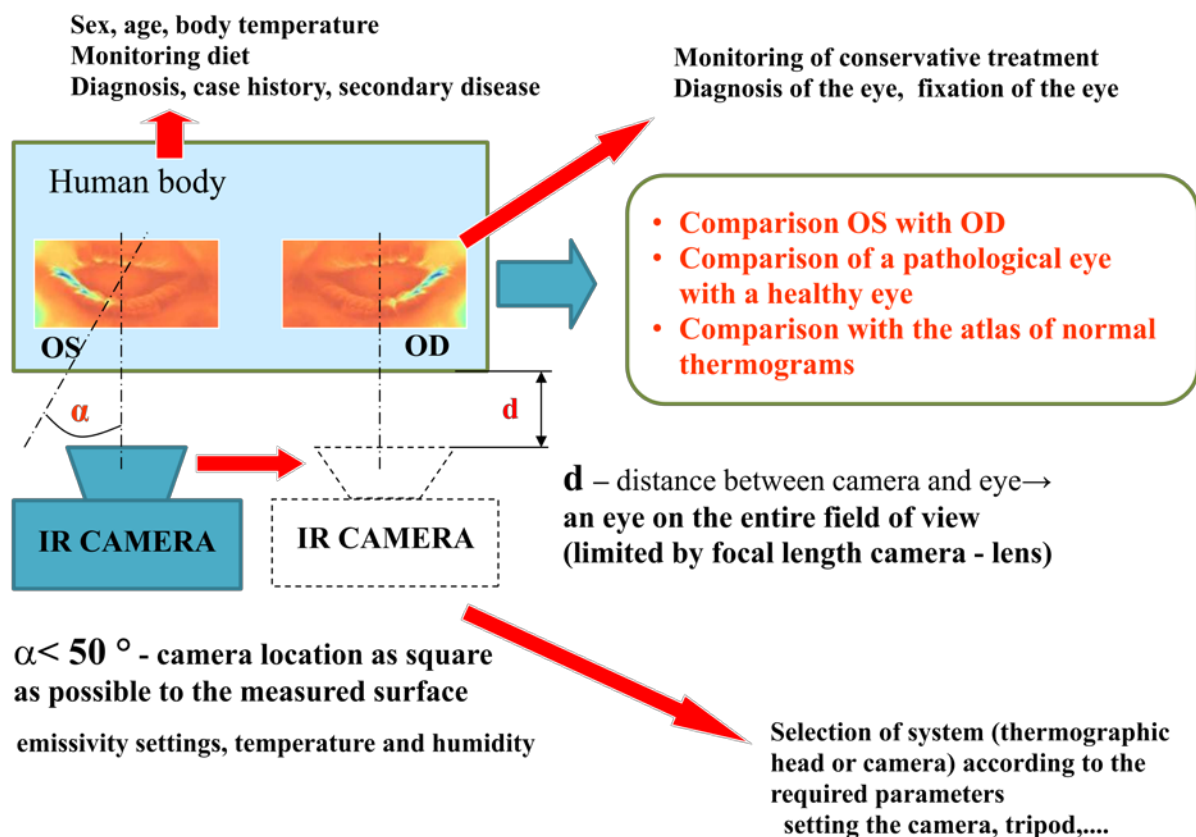


Fig. 1. Methodology of measurement

For identification of the area of interest, a circular polygon and three points T1, T2 and T3, which on linear horizontal axis on the eye were defined, see Fig. 2.

3. Results

The following average temperatures in T1, T2, T3 markers were obtained: $\bar{x}_{CT1} = 34,70 \text{ }^\circ\text{C}$, $\bar{x}_{CT2} = 34,17 \text{ }^\circ\text{C}$, $\bar{x}_{CT3} = 34,74 \text{ }^\circ\text{C}$, where \bar{x}_{CT1} is average temperatures in T1, \bar{x}_{CT2} is average temperatures in T2 and \bar{x}_{CT3} is average temperatures in T3. The total average temperature in all markers where calculated $\bar{x}_{CT1,T2,T3} = 34,54 \text{ }^\circ\text{C}$ with the standard deviation of $\pm 0,81 \text{ }^\circ\text{C}$.

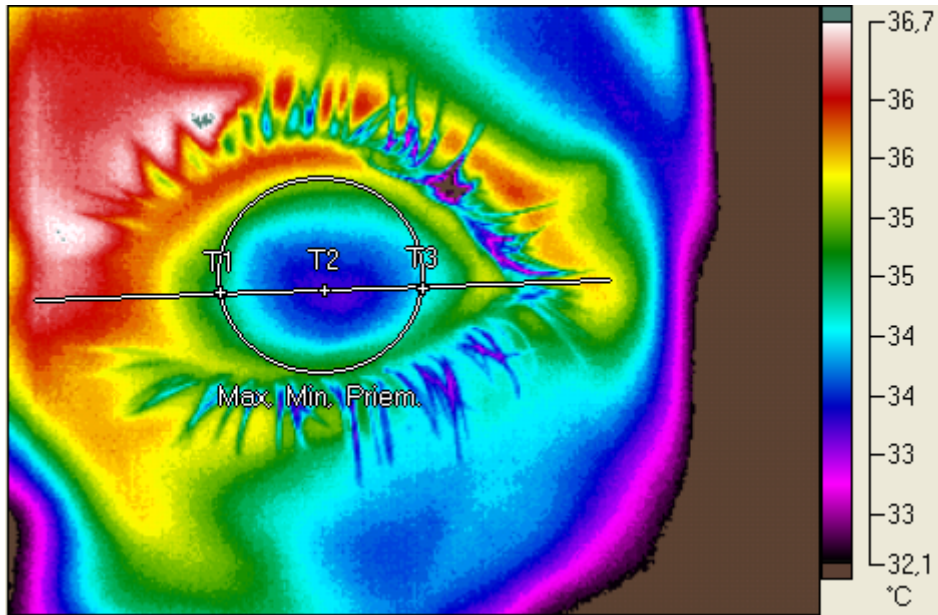


Fig. 2. Thermogram of the left eye with defined points of measurement.

Maximum, average and minimum temperature were obtained from defined points (T1, T2, T3), like in Fig. 3.

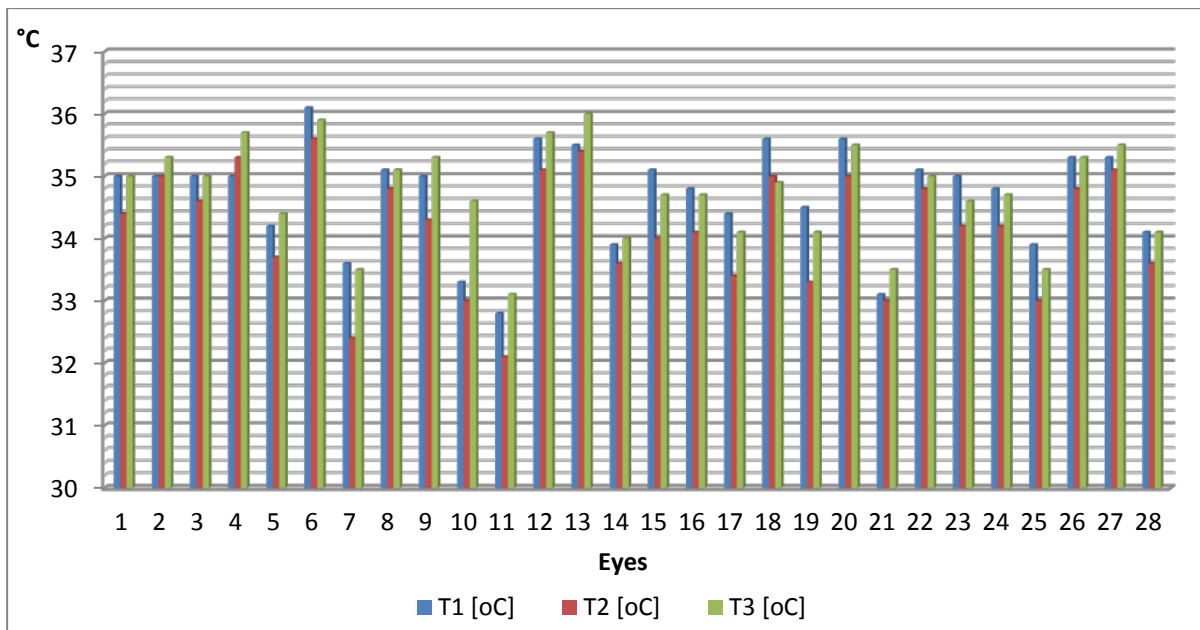


Fig. 3. Graph of temperature value from defined points of measurement

4. Discussion

Studies published worldwide indicate that thermography is a valuable diagnostic method in ophthalmology, in order to objective detection of some ophthalmologic diseases and conditions (monitoring of tear ocular film, ischemic and hyperaemic eye, diagnosis of glaucoma, etc.). The database of healthy eye surfaces temperature is important to differentiate the healthy eye and pathological condition of the eye in specific ophthalmologic diseases.

5. Conclusions

In the study a methodology of thermographic measurements was assessed. After the processing of the thermograms, the average temperatures of the cornea in all measured subjects were calculated. Results show, that a total average temperature in the cornea of the eye in markers T1, T2 a T3 is $34,51 \pm 0,82$ °C. The minimum temperature of the cornea eye was $33,82 \pm 1,10$ °C and maximum temperature $35,41 \pm 0,73$ °C. The results show that the overall average temperature of the eye surface is $34,51 \pm 0,82$ °C. The bigger statistically significant group is planned to get the significant reference values.

Acknowledgements

This contribution is the result of the project implementation: Center for research of control of technical, environmental and human risks for permanent development of production and products in mechanical engineering (ITMS:26220 120060) supported by the Research & Development Operational Programme funded by the ERDF.

References

- [1] Gordon, M; Thurdals, M: Repolarization Changes Displayed in Surface ECG Maps. A Simulation Study. *International Journal of Bioelectromagnetism*, 4 (5): 92-104, 2002.
- [2] Nowakowski, A.; Kaczmarek M., Ruminski J.; Hryciuk M.; Renkielska A.; Grudzinski J.; Siebert J.; Jagielak D.; Rogowski J.; Roszak K.; Stojek W.: Medical applications of model based dynamic thermography, Proc. SPIE, v. 4360, 2001, 492 – 503.
- [3] Murawski, P.; Jung A.; _uber J., Kalicki B., The project of an open and extendable database for thermal images archiving, IFMBE Proc. 2-nd European Medical and Biological Engineering Conf., Vienna, 2002, 1618 – 1619.
- [4] Jones, B.; Plassman, P.: Computational approaches to image processing for improved interpretation and analysis, IEEE Eng. in Medicine and Biology, v. 21, 6, 2002, 41 - 48.
- [5] Ring, E.; Ammer, K.: The technique of infrared imaging in medicine. *Thermology International* 2000;10:7-14.
- [6] Jones, C.; Ring, E.; Plassmann, P.; Ammer, K.; Wiecek, B.: Standardisation of infrared imaging: a reference atlas for clinical thermography—initial results. *Thermology International* 2005; 15:157-8.
- [7] Morgan, P.; Tullo, A.; Efron, N.: Infrared thermography of the tear film in dry eye. Manchester, 1995. s. 615-618.
- [8] Betney, S.; Morgan, P.; Doyle, S.; Efron, N.: Corneal temperature changes during photorefractive keratectomy. Philadelphia, 1997. s. 158-161.
- [9] Morgan, PB, Soh MP, Efron N, Tullos AB. Potential applications of ocular thermography. *Optom Vis Sci* 1993;70:568–76.
- [10] Tan, Jen-Hong; Ng, E.Y.K.; Rajendra Acharya, U.; Chee, C.: Study of normal ocular thermogram using textural parameters; *Infrared Physics & Technology*; Volume 53, Issue 2, March 2010, Pages 120-126.

AUTHORS INDEX

- Aidu E. A., 301
Anderson P. I., 107
Andreev N.K., 221
Andris P., 166, 319
Arendacká B., 69
Atuchin V.V., 257
Bačić I., 145
Bajla I., 59
Baksheeva Yu., 141
Balaz I., 265
Bartošová K., 76
Bartušek K., 131, 213, 217
Bas G., 12
Bazin V.S., 201
Bednarik M., 127
Beňačka Š., 119
Bittera M., 229
Blinova E. V., 301
Bodermann B., 95
Boháč V., 182, 265
Bosse H., 95
Brand U., 95
Buhr E., 95
Bütefisch S., 95
Bzdúšková D., 335
Caithaml V., 395
Čáp M., 213
Čaplovičová M., 339
Chmelíková M., 127
Chromik Š., 119
Chugui Yu.V., 197
Chukwuchekwa N., 107
Chvosteková M., 16
Cocherová E., 265
Dai G., 95
Danzebrink H.U., 95
Dermek T., 319, 327, 360
Dieška P., 182
Dittrich P.G., 209
Drexler P., 217
Drkošová A., 297
Dujavová A., 119
Düntsch E., 209
Durakbasa M.N., 12, 135
Ďuriš S., 24
Dvorák T., 123
Dvurečenskij A., 398
Ehret G., 95
Fiala P., 217
Florek R., 123
Flügge J., 95
Foffová P., 406
Foltín M., 297
Fotowicz P., 3
Fousek J., 347
Frollo I., 115, 166, 319, 323, 327, 352, 356, 360, 364
Fuchs P., 38
Fujiwara O., 178, 387
Funda T., 375
Fütterer R., 261
Galusek D., 269
Garbe H., 178
Gaži Š., 119
Godla M., 28, 274
Gogola D., 115, 319, 327, 360
Göpfert A., 205, 261
Grman J., 233
Güclü E., 12
Haessler-Grohne W., 95
Hain M., 123, 192
Halaj M., 88
Halická Z., 335
Hall J. P., 107
Hallon J., 229
Hanus R., 32
Hart'anský R., 225, 229, 241
Hernych M., 150
Hlavačka F., 335
Hofmann D., 209
Hokr M., 150
Holčík J., 46, 65
Holder S., 205
Holzer R., 127

- Horáček J., 364
Horák P., 364
Horníková A., 12, 135
Hornišová K., 73
Hribík J., 38
Hudák R., 309, 314
Hüser D., 95
Ivan J., 339
Jakubovský J., 339
Jan J., 347
Janusek D., 373
Jeřábek J., 402
Jiřík R., 347
Juráš V., 323, 327, 352, 356
Kaľavský P., 379
Kalichkin S.V., 201
Kalikin V.E., 201
Kamenský M., 42
Kania M., 373
Karadaglic D., 285
Karas S., 379
Karell R., 269
Kariya K., 331, 391
Karovič K., 80
Kaťuch P., 314
Kawate E., 192
Kemppinen J., 111
Khasanov T., 257
Kienast S., 205
Klement R., 269
Kliment R., 402
Kochubey V.A., 257
Kollár M., 84
Köning R., 80, 95
Kopáni M., 339
Kořínek R., 131
Košek M., 170, 245
Kováč K., 42, 84, 229
Kovářová K., 127
Kowalczyk A., 32
Krakovská A., 51, 55
Krammer A., 225
Kraxner J., 269
Kubičár Ľ., 182
Kureková E., 88
Kwacz M., 237, 368
Lackner F., 111
Laurinavičius L., 158
Lenková J., 297, 305
Linss G., 205, 253, 261
Lobotková J., 335
Loebl T., 88
Lojko B., 38
Mainaud Durand H., 111
Makarov S.N., 201
Malarić K., 145
Malatsion A.S., 221
Maniewski R., 373
Maňka J., 339, 398
Marcon P., 213
Marques N., 154
Maršalka L., 241
Matsuda Y., 331, 391
Melník M., 339
Mezeiová K., 51, 55
Michaeli L., 28, 274
Miglierini M., 188
Minárik M., 265
Mirkovic M., 285
Molčan L., 343
Mori I., 178
Moses A. J., 107
Mrowka M., 237, 368
Musil M., 131
Nedělka T., 375
Nespor D., 217
Nestával L., 397
Nesterov V., 95
Nosko M., 123
Novák J., 249, 289
Novák M., 245
Okrouhlý M., 249
Opolski G., 373
Osanna P. H., 135
Otomański P., 3
Pacheco C., 154

- Pacheco de Carvalho J., 154
 Palenčár P., 24, 28, 88
 Pavúk M., 188
 Peterlík I., 347
 Pittschieler E., 323
 Pokrovsky L.D., 257
 Pressl Ch., 352
 Přibil J., 319, 364
 Prnová A., 269
 Ravas R., 233
 Regtien P.P.L., 174
 Reis A., 154
 Richter A., 170
 Řimnáč M., 150
 Rosenberger M., 261
 Rosík V., 379
 Rublík F., 7
 Rückwardt M., 205, 261
 Ruiter N., 347
 Sagbas B., 135
 Sakhnova T. A., 301
 Šaliga J., 28, 274
 Sapozhnikova K., 141
 Savkov S.G., 201
 Schellhorn M., 205, 261
 Schlenker J., 375
 Sekerák M., 274
 Senchenko E.S., 197, 257
 Ševčík R., 127
 Šimáček I., 398
 Šimančík F., 123
 Škoviera R., 59
 Škrátek M., 269, 398
 Slavík L., 245
 Šmatko V., 119
 Smieško V., 229
 Smrčka P., 402
 Špánek R., 150
 Štofanič V., 265
 Stojanovic R., 285
 Štolc S., 59
 Štork M., 278, 289
 Štrbák O., 115, 319
 Štrbík V., 119
 Štuller J., 150
 Stupakov O., 162
 Švehlík J., 309
 Švehlíková J., 297, 305
 Švendová V., 65
 Svoboda P., 150
 Syrová L., 233
 Szathmáry V., 335
 Szlachta A., 32
 Szomolányi P., 323, 327, 352
 Takahashi N., 331, 391
 Takata K., 387
 Takayama S., 331, 391
 Takeda A., 387
 Tanaka T., 331, 391
 Taymanov R., 141
 Teplan M., 343
 Titomir L. I., 301
 Tkáčová M., 309, 406
 Trattinig S., 323, 352
 Truhlář M., 170, 245
 Trunov V. G., 301
 Tuboly G., 293
 Tyl P., 150
 Tyšler M., 297, 305, 379
 Uspenskiy V., 383
 Valentín K., 59
 Valkovič L., 319, 327, 356, 360
 Valky G., 42
 Van Wieringen I.M.P., 174
 Vávra I., 119
 Veiga H., 154
 Verkhogliad A.G., 201
 Vítězník M., 402
 Vogel M., 253
 Vojtíšek L., 319, 327, 360
 Vondrák J., 131
 Vrabček P., 119
 Vretenár V., 182
 Wang J., 387
 Weissensee K., 253
 Williams P. I., 107

Wimmer G., 80

Witkovský V., 80

Wolf A., 395

Wurm M., 95

Wysocki J., 237, 368

Xu X. T., 107

Zaczek R., 373

Zakrzewski J., 20

Zapf M., 347

Zavala-Fernandez H., 373

Zbieć A., 373

Zbyn S., 352

Zeman V., 289, 343 ,

Živčák J., 309, 314, 406